

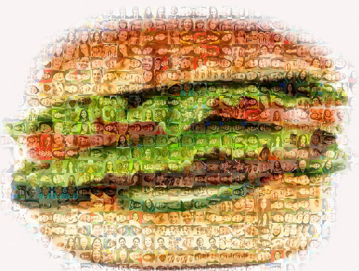


Volume 163
Number 5

November 19, 2015

cell





What to Eat? Check Your Microbiome!

ZEEVI ET AL., PAGE 1079

Personalized diets, based on the integration of people's different responses to meals and their microbiome, may successfully lower post-meal blood glucose and its consequences for metabolic diseases.

*H*specially Important Network for Dengue

TAGUWA ET AL., PAGE 1108

Chaperone network components are required at distinct steps of Dengue viral lifecycle, with compounds that allosterically modulate Hsp70 showing potent antiviral activity against Dengue and other flavivirus pathogens.

Antibodies from Privileged Exons

YEAP ET AL., PAGE 1124

An in vivo assay elucidating the role of DNA substrate sequences in AID-initiated antibody diversification finds that the variable (V)-region exon is specifically selected. Gut-associated B lymphocytes provide a reservoir of such variable exons that allow for highly diversified antibody repertoires.

Case Closed for V(D)J Recombination

WU ET AL., PAGE 1138

Cryo-EM structures of synaptic RAG complexes reveal a recombination signal sequence (RSS)-induced closed conformation that enables catalytic activation and explain the molecular basis for the 12/23 rule that conveys recombination fidelity, whereby RAG forms synaptic complexes only with 12- and 23-base-pairs-long RSS spacers.

Getting into the Habit

KIM ET AL., PAGE 1165

A population of dopamine neurons in the basal ganglia is involved in learning and in sustaining habitual behavior in monkeys, providing a possible neural framework for the dysfunction in performing daily routines in Parkinson's disease.

GPCR Odd Couple

KERN ET AL., PAGE 1176

GPCR heterodimerization between a dopamine receptor and a ghrelin receptor that is not associated with ghrelin initiates a non-canonical, cAMP-independent signaling pathway that regulates dopaminergic regulation of hippocampal memory.

An Excited "STOP" from the Brainstem

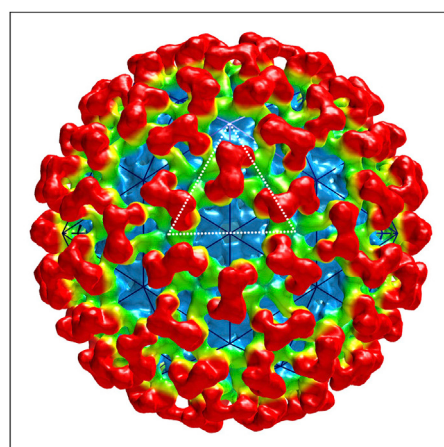
BOUVIER ET AL., PAGE 1191

The ability to stop locomotion is regulated by genetically and spatially segregated excitatory neurons in the brain stem that project to the spinal cord, where they depress locomotor rhythm generation.

Anti-Alpha Antibodies

FOX ET AL., PAGE 1095

A class of broadly neutralizing monoclonal antibodies protecting against multiple alphaviruses, including chikungunya, bind a discrete epitope on the alphavirus E2 glycoprotein, blocking viral entry and egress.





Innate Wins in Fear Contest

ISOSAKA ET AL., PAGE 1153

A population of serotonin receptor-expressing cells in the central amygdala integrates innate and learned behaviors and acts as a hierarchy generator to prioritize innate over learned fear.

Making Dystrophy All Bark and No Bite

VIEIRA ET AL., PAGE 1204

A genetic modifier of Duchene muscular dystrophy phenotype has been found in two exceptional dogs that display functional muscle and normal lifespan despite the complete absence of dystrophin.

Time and Temperature

TATAROGLU ET AL., PAGE 1214

Temperature shifts the phase of the *Drosophila* circadian clock through the regulated degradation of the pacemaker protein TIMELESS.

Wnt without Transcription

KOCH ET AL., PAGE 1225

While canonical Wnt signaling necessitates β -catenin-dependent transcription, a multifaceted set of Wnt functions in sperm development is implemented post-transcriptionally through mechanisms that may be relevant to other tissues as well.

Oncogenic Secrets of K-Ras

WANG ET AL., PAGE 1237

The interaction between K-Ras and calmodulin (CaM) modulates tumor formation through inhibition of CaM kinase activity and suppression of Wnt/Ca²⁺ signaling; disruption of this interaction by the natural product prostratin represses tumor growth.

Telomere's Meiotic Hat

SHIBUYA ET AL., PAGE 1252

During meiosis, telomeres experience a cap exchange process in which a protein complex localized at the inner nuclear membrane replaces the protective cap of chromosomes to ensure telomere tethering for correct chromosome recombination.

Ribosome Gymnastics with RNA and Peptide Spotters

CHEN ET AL., PAGE 1267

The ribosome can "hop" over a section of phage mRNA while in the midst of translating it, and single-molecule techniques indicate that these dynamics require interactions between the mRNA secondary structure, the nascent peptide, and the ribosome that advances in a non-canonical rotated state.

Matters of Size

Size does matter. At least that's what the tagline of the movie *Godzilla* claims (one of the many renditions of the franchise). A quick glance at the great beasts of our past—dinosaurs, marine animals, snakes, why even disturbingly massive dragonflies, scorpions and camels—would make it appear as if increased body size conferred some sort of advantage then. Yet biologists concur that overall, the body sizes of most species on Earth have been subjected to rather stringent limitations by factors such as land area, climate change, predation, and adaptability to changing environments (Roy, 2008; Smith et al., 2010).

Larger animals typically live longer than smaller ones. Elephants should and will almost always outlive mice. But when one looks closer within a species, a more complex picture emerges. In dogs, for example, smaller breeds such as chihuahuas outlive Great Danes and St. Bernards (Galis et al., 2007), with the sole determinant of size being a single gene—insulin-like growth factor-1 (IGF-1) (Sutter et al., 2007). In fact, there is much evidence to support the link between reduced body size and organismal longevity. A moderate reduction in cellular signaling pathways such as IGF-1, PI3K, or mTOR signaling results in enhanced resistance against various stresses and extrinsic insults and significantly increases lifespan across a number of species (Narasimhan et al., 2009). Whether this regulation exclusively occurs at the cellular level or whether there are cell non-autonomous mechanisms at play is not entirely clear. The link between cell size and organ size—and by extension organism size—is not necessarily linear. Studies in *C. elegans* and *Drosophila* provide evidence for both, the convergence and uncoupling of the pathways controlling cell size and cell proliferation that may then impact organ and/or organism size. While body size scaling and increases in cell size as well as number are important during development, organ and or-

ganism size are stably maintained through homeostatic regulatory pathways during adulthood (Lloyd, 2013).

Humans today come in all shapes and sizes but was there some sort of selection on our earliest ancestors? Biologists estimate that the divergence between apes and hominids occurred sometime between 8–20 million years ago. Alba and colleagues now propose that the grand ancestor of apes and humans, a newly identified species, was not in fact the size of a large great-ape as previously thought but rather small, akin to a gibbon (Alba et al., 2015). This ape, *Pliobates cataloniae*, weighed no more than 4–5 kg and bore anatomical features that were a mosaic of primitive and hominoid species, including forearm rotation abilities like ours. Their finding challenges previous reports suggesting that another large ape, *Proconsul*, was the ancestral species. The great human race, it turns out, may have ultimately arisen from something rather small.

Moving further over time, the evolution of hominids itself is a matter of active debate—two recent studies identified a new species in southern Africa, *Homo naledi*, that lived nearly 2 million years ago, a time that is thought to mark the very initiation of the *Homo* genus. Anatomical and morphological reconstruction studies suggest that size-wise *H. naledi* was somewhat of a hybrid between early hominids and Neanderthals as well as modern humans and is overall considered to be of moderate size (Berger et al., 2015 and Dirks et al., 2015). Other extinct species along the chart of human evolution have been marginally smaller or larger but among these none are as baffling as the 1-m-tall *Homo floresiensis*, the “hobbit”-like species of humans that existed just 13,000 years ago in a small island in the Indonesian archipelago (Stringer, 2014). Given this timeline, is it possible that there were then two species of “humans,” our ancestor *Homo erectus* and *H. floresiensis*, that co-existed the same point of time but the latter population was somehow selected against? Did *H. floresiensis* suffer from IGF-1 or growth hormone deficiency, microcephaly or some other form of dwarfism that may have contributed to their extinction? Modern day humans with deficiencies in IGF-1 and growth hormone suffer from dwarfism but demonstrate remarkable protection from cancer and diabetes, very much along the lines of what has been observed in model organisms bearing these genetic mutations (Guevara-Aguirre et al., 2011). While resistance to two debilitating diseases sounds like a useful fitness trait, mutations in these pathways are in fact rare and there is little evidence for their positive selection in humans or other organisms. For example, nematodes carrying the same mutations found in these humans are extremely long-lived and stress-resistant under laboratory conditions but die sooner than wild-type animals in natural soil (Van Voorhies et al., 2005).

Humans today are bigger, taller, and longer-lived than ever before but this is attributed largely to good nutrition and medical facilities rather than evolutionary pressures, especially since average modern human height did not really increase until the 19th century. Big or small, large or petite—in today's world, body size and body image are almost



The biology of size is complex, and it is unclear what evolutionary pressures drive selection in favor of either large or small animals.
Image from iStock/GlobalP.

interchangeably used. Evolutionary biology teaches us that there are advantages to both—bigger organisms emerge victorious in battles over food, dominance, or mating while smaller animals possibly are quicker, adapt faster, and may endure changes more easily. With no clear answers in favor of one over the other, the bottom line is that perhaps it is context that matters, not size.

REFERENCES

- Alba, D.M., Almécija, S., DeMiguel, D., Fortuny, J., Pérez de los Ríos, M., Pina, M., Robles, J.M., and Moyà-Solà, S. (2015). *Science* 350, aab2625.
- Berger, L.R., Hawks, J., de Ruiter, D.J., Churchill, S.E., Schmid, P., Delezene, L.K., Kivell, T.L., Garvin, H.M., Williams, S.A., DeSilva, J.M., et al. (2015). *eLife* 4. <http://dx.doi.org/10.7554/eLife.09560>.
- Dirks, P.H., Berger, L.R., Roberts, E.M., Kramers, J.D., Hawks, J., Randolph-Quinney, P.S., Elliott, M., Musiba, C.M., Churchill, S.E., de Ruiter, D.J., et al. (2015). *eLife* 4. <http://dx.doi.org/10.7554/eLife.09561>.
- Galis, F., van der Sluijs, I., van Dooren, T.J., Metz, J.A., and Nussbaumer, M. (2007). *J. Exp. Zoolog. B Mol. Dev. Evol.* 308, 119–126.
- Guevara-Aguirre, J., Balasubramanian, P., Guevara-Aguirre, M., Wei, M., Madia, F., Cheng, C.W., Hwang, D., Martin-Montalvo, A., Saavedra, J., Ingles, S., et al. (2011). *Sci. Transl. Med.* 3, 70ra13.
- Lloyd, A.C. (2013). *Cell* 154, 1194–1205.
- Narasimhan, S.D., Yen, K., and Tissenbaum, H.A. (2009). *Curr. Biol.* 19, R657–R666.
- Roy, K. (2008). *Science* 321, 1451–1452.
- Smith, F.A., Boyer, A.G., Brown, J.H., Costa, D.P., Dayan, T., Ernest, S.K., Evans, A.R., Fortelius, M., Gittleman, J.L., Hamilton, M.J., et al. (2010). *Science* 330, 1216–1219.
- Stringer, C. (2014). *Nature* 514, 427–429. <http://dx.doi.org/10.1038/514427a>.
- Sutter, N.B., Bustamante, C.D., Chase, K., Gray, M.M., Zhao, K., Zhu, L., Padukasahasram, B., Karlins, E., Davis, S., Jones, P.G., et al. (2007). *Science* 316, 112–115.
- Van Voorhies, W.A., Fuchs, J., and Thomas, S. (2005). *Biol. Lett.* 1, 247–249.

Sri Narasimhan

Illuminating the Genome's Dark Matter

The Deeper Genome: Why There Is More to the Human Genome Than Meets the Eye

Author: John Parrington

New York, NY, USA: Oxford University Press (2015).

272 pp. \$29.95

John Parrington's book *The Deeper Genome* provides us with a closer look at the enigma of junk DNA. Often referred to as the dark matter of the genome, junk DNA is an important but often overlooked part of the human genome. (Perhaps, in light of recent discoveries, this term might be somewhat problematic; however, it is the term that Parrington uses and we will follow that here.) The dark matter metaphor is particularly apt: akin to the great expanses of dark matter within our universe, junk DNA makes up the vast majority of the genome. And just like dark matter, whose properties can only be inferred from its effects on observable matter, much of our junk DNA can only currently be characterized by its regulatory effects on the smaller fraction of coding DNA. Further, just like dark matter is presumed to account for discrepancies in our understanding of the universe—between what's theoretically predicted versus actually observed—junk DNA is thought to account for the majority of associations with genetic diseases found by genome-wide association studies (GWAS). Insofar as this is the case, junk DNA is medically relevant and contains actionable information. Finally, just like dark matter contains historical evidence of events from the primordial universe, junk DNA, lacking the evolutionary pressures on protein-coding genes, contains vestigial information relating to the molecular history of our species.

The Deeper Genome is unique in that it provides an entertaining tale of personalities with lots of useful technical knowledge. We highly recommend the book as a supplement for classroom teaching as it covers fundamental concepts in an easily readable format.

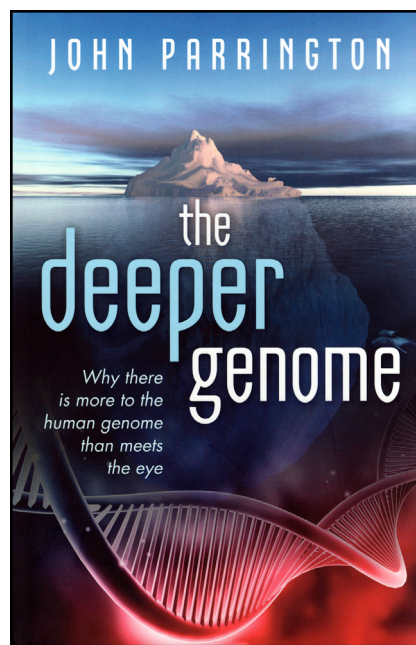
Students will likely find it even more interesting than many of the more standard textbooks. For example, the book

goes through the classic story of the double helix, starting all the way from Aristotle and eventually working its way through Darwin, Wallace, Mendel, and Morgan to more contemporary times, with Gilbert and Sanger. To wit, Parrington ably describes how early abstractions related to genetic inheritance were concretized over time and culminates in quite readable descriptions of current scientific research and experimentation. He provides lucid textual descriptions of the canonical theory of Darwinian evolution and its synthesis with the work of Mendel by Fisher and others. He even covers a somewhat forgotten alternative theory: the pre-Darwinian Lamarckian evolutionary theory and its recent resurgence—e.g., in Eugene Koonin's two-stroke process, with an initial Lamarckian epigenetics phase and a subsequent Darwinian selection phase. Finally, the

book contains a great description of the actual structure of DNA, excellently describing in prose the intricate 3D structure of the sugar-phosphate backbone. It also has a number of spare but incisive figures to illustrate key concepts, without detracting from the primarily textual description.

In one of its most interesting parts, the book expertly provides both the scientific and historical progression of how repressors were first abstractly described as fundamental principles of gene regulation by Nobel laureates Jacob and Monod through to the recent in-depth molecular understanding of these as transcription factors. Here, in elucidating aspects of scientific culture—like he does in a number of other places in the book—the author quotes James Watson in describing the relationship between Walter Gilbert and Mark Ptashne, who isolated and characterized the first transcription factors: “take young researchers, put them together in virtual seclusion, give them an unprecedented degree of freedom, and turn up the pressure by fostering competitiveness.” This is what makes this book particularly enjoyable—Parrington’s ample use of tangential anecdotes and sidebars relating to the very-human aspects of the scientific process.

The book also provides an extensive discussion on how genes are linked to disease, with a particular focus on classic examples such as Huntington’s, Phenylketonuria (PKU), and cystic fibrosis. Parrington helps the reader understand an important distinction in the nascent but quickly growing field of genetic testing: he provides clear examples that distinguish across the spectrum of informative to actionable genetic tests. For some diseases, such as Huntington’s, we can test for the statistical likelihood of developing the late-onset disease but otherwise cannot provide medical intervention to prevent its onset. For other diseases like cystic fibrosis, which has become part of the standard prenatal genetic testing panel, parents can be forewarned and incorporate genomic technologies to prevent having children with the disease. And for yet a third group, like PKU, genetic testing can lead to early medical intervention such as dietary modifications that will greatly alleviate the disease effects. In



combining his research training and journalistic credentials, Parrington seamlessly delves into original research papers in the scientific literature and also describes their interpretation in the popular press. In particular, he contrasts the excitement surrounding the initial sequencing of the human genome in 2000 with the current sobering reflection that the expected breakthroughs have yet to arrive. In light of Parrington's time as a journalist actually covering the ENCODE rollout, the book uses the post-2012 ENCODE debate to frame his analysis and theories for junk DNA. While this is an effective method of piquing interest in the subject matter, Parrington sometimes cherry picks quotes to exaggerate the storminess of the debate. Parrington, whose coverage in this area was focused on the British protagonists, sometimes also provided less information regarding the global perspective on the ENCODE effort.

The book concludes with a discussion of human origin and neurogenomics. There is a nice description of how RNA sequencing studies comparing human and chimp brains give some insight into the developmental time of synapse formation and what the comparisons with the Neanderthal genome actually mean.

Finally, the book tempts the reader to think about how the genome project relates to its progenies: efforts to catalog all proteins (the proteome), RNA molecules (the transcriptome), metabolites (the metabolome), interactions (the interactome), and the foreshadowed neuroscience project relating to the connectome.

As this book is nominally devoted to discussing the genome, it would have been informative to discuss some other prominent genomics projects in greater detail—particularly those relevant to constraint in non-coding regions, such as the HapMap, 1000 Genomes, and GTEx Projects. Parrington could have also included more about related innovations, such as next-generation DNA sequencing, that make many of these large projects possible. It would have also been helpful to have a more technical discussion related to selection—i.e., exactly what is the absence of constraint (i.e., the state of being “junk”) and how does one measure this with well-known statistics such as the enrichment of rare alleles and the ratio of synonymous to non-synonymous changes.

Additionally, given the book's focus on junk DNA, it seems strange that there isn't any mention of the most common

constituents of junk DNA: the LINE and Alu elements. Likewise, the discussion of pseudogenes could have delved further and included, for example, recent research that suggests that transcribed pseudogenes actually function as regulatory non-coding RNAs, rather than as translated proteins.

Finally, it would have been interesting for Parrington to have drawn out conclusions and actionable repercussions of interest to the lay reader. In particular, issues of privacy vis-a-vis the genome loom large for the public, yet they are given little attention in the book. For example, an issue of notable significance to the lay public has been the use of non-coding junk DNA sequences by the police and others in DNA fingerprinting. In light of ENCODE, the public's concerns have been compounded—that databases of heretofore identifying but not descriptive DNA may now be more descriptive than previously thought, raising, among other concerns, significant privacy issues. That said, *The Deeper Genome* is a great read that definitely imparts knowledge in an entertaining fashion and connects the almost 99 percent of the genome that is not protein coding to all sorts of interesting questions. We highly recommend it.

Dov Greenbaum^{1,2,*}
and Mark Gerstein^{2,*}

¹Interdisciplinary Center Herzliya, Herzliya, 4610101, Israel

²Yale University, New Haven, CT 06520, USA

*Correspondence: dov.greenbaum@yale.edu (D.G.), mark@gersteinlab.org (M.G.)
<http://dx.doi.org/10.1016/j.cell.2015.10.073>

When Science Is a Family Tradition

A Shared Passion for Neuroscience



Anne Churchland
Cold Spring Harbor Laboratory
Mark Churchland
Columbia University

Family efforts are commonplace in many professions. Dedication to suits united the Brooks Brothers, and enthusiasm for books brought Wiley & Sons together. In our family, it's a passion for understanding the brain. Our parents were drawn to the subject when they realized that their own field, philosophy of mind, was uninformed by developments in neuroscience. To discover what philosophy might gain from neuroscience, they trekked to labs at the University of Manitoba medical school, once even bringing back Tupperware-encased brains to dissect in our kitchen. The brain dissection fascinated us as kids, and even more critical was the accompanying conversation, conveying a conviction that understanding the brain was the great scientific challenge of our time.

This inspired us to choose neuroscience for our own careers. Though our professional interests have diverged somewhat, there remain many points of intersection. Our shared passion means that we have a common language for discussing subjects of mutual interest. This common language is the best part of having a sibling who is also a close colleague. We don't always agree. At family dinners, strong words are exchanged over topics both large—what will be the limits of the human brain in understanding itself—and small—what approach should be used to analyze neural variability. But a colleague who understands your ideas makes possible a dialogue that can help those ideas develop. Our discussions today don't usually center around the same topics as our parents' did, but our belief in the importance of neuroscience is the same, as we help each other contribute to that shared enterprise.

Scientific Imprinting



Robert B. Darnell
Rockefeller University & HHMI

My apprenticeship from my father (pictured above, center), James Darnell, happened at the dinner table. There I first learned the vocabulary of science. By the time I was 12, I was pretty convinced that "polyadenylation precedes splice site selection." Growing up with the second language of science facilitated the transition from fluency in terminology to fluency in scientific thought. There was no confusing transcription and translation in my family! Fast-forwarding, my father and I now think critically together about transcriptional dynamics and RNA regulation versus the bland information present in steady-state RNA analyses.

At our dinner table, once a month my mother—an intellectual, but not a scientist—would ask my father what was new in the lab. Her question and her interest itself I always found wonderful. Explanations using jargon underscored the difficulty of putting the complex into understandable words. The importance of simple communication is a lesson I carry with me to this day.

Our dinner table and house was also full of people I knew were scientists, but who I thought of first as people. Experiences like waking up in the morning and jumping on a sleeping Lennart Philipson, bringing out his warmth and mirth, allowed me to experience scientists' humanity first-hand. The privilege of seeing the warm people underneath towering scientific personas, whether it was Lennart, Harry Eagle, David Baltimore, Aaron Shatkin, Jim Watson, or Bob Roeder, even as I overheard the intensity of their science discussions, led me to see intellectual intensity as a natural part of life. I knew their shared secrets—humanity underlying shared scientific passion. And this has been the biggest privilege for me—aiming to emulate their idealism rather than aiming to become a persona.

Getting Signal out of Noise



Andre Nussenweig
National Cancer Institute, NIH

Even though I grew up in a family full of scientists, I can tell you that I didn't have a particular interest in being a scientist. Nothing against it, but dinner conversations about "complementary determining regions" (CD this and CD that) sounded pretty boring. Despite the background noise, one thing that came through loud and clear was the four P's: the *patience*, *passion*, and *persistence* to which my parents approached science, obviously leading to great *pleasure*—perhaps even to a fault. Every single day (including weekends), they would go to work. When they were on vacation at our country house, there were plenty of articles lying around from *Science* and *Nature*. Of course I flipped through them, but these were no *Time* magazines—a few pictures but with that same unintelligible fine print that my parents seemed so passionate about.

In addition to science journals, there were bookshelves and coffee tables full of photography, art, poetry, biographies, mysteries, and thrillers. This pre-selected library has always been an excellent source of fascinating reads on a range of topics. With all of these stimuli, it took me a long time to figure out what I wanted to do. I tried my best to avoid science with music, basketball, philosophy, psychology, computers, and art history. But I realized that only science seemed to satisfy my four P's. I first trained in physics (perhaps influenced by my uncle, who is a theoretical physicist) but eventually made a transition to biology. That's another story in itself, but I can tell you that CD this and CD that doesn't sound so bad anymore.

From physics to systems biology

Nikolaus Rajewsky
Max Delbrück Center, Berlin

No Other Choice

Bernardo L. Sabatini
Harvard/HHMI
David M. Sabatini
Whitehead Institute/MIT/HHMI

DNA Lit the Way

Alan Jian Zhu
Peking University

Discussions at our lunch table in Cologne were rarely about my dad Klaus's immunology and genetics work but much more frequently about society and politics because my mom was a political scientist. But as a young boy, I loved visiting my dad in his lab, and the humming of the big machines sounded like music. Music was and is very important to me. However, a summer vacation changed my life. When I was 15, Janos Hajdu, a family friend, taught me calculus, differential equations, and Newtonian mechanics during the vacation. I fell in love with math and physics and eventually finished a Ph.D. in theoretical physics in 1998. However, a workshop about biology excited me when I was a postdoc with Joel Lebowitz in Rutgers University. Biology offers the most exciting scientific questions amenable to me! So I started a second postdoc with Eric Siggia at Rockefeller University, working computationally on transcriptional regulation. Meanwhile, Klaus moved to Harvard Medical School. Great! It was easy to visit and to discuss our science. He became interested in my computational approaches and my work on miRNAs that I had started at my own lab at NYU in 2003. This led to highly enjoyable interdisciplinary collaborations between Klaus and myself.

I moved to Max Delbrück Center (MDC) in 2006 and in 2008 started building an Institute for Systems Biology, where we synergize computation and experiments. Klaus later left Boston and joined the MDC. I think it is a real joy and very precious for us to be able to have a family life that includes science and music, which is now perhaps tighter than that in the early days.

Each family has its peculiarities, and children usually assume that the oddities that surround them represent the norm. Thus, growing up in a microcosm of Argentinians transplanted to New York, populated exclusively by carnivorous physicians and scientists, never seemed odd to us. We must have appeared quite bizarre to the outsider, as we didn't understand American football but could explain protein trafficking through the Golgi apparatus.

Like many foreigners, our parents have classical educations that fostered, at gatherings of expats, heated conversations on arts, literature, history, politics, and, of course, science and medicine. With them, we travelled the world and had experiences—picking up hitchhiking armed soldiers in Israel, crossing Checkpoint Charlie into communist Berlin, and roaming the streets of Kyoto playing pachinko—that opened our young minds to the diversity of customs, beliefs, and tensions that fill the world. In each locale, with its own accents and foods, we encountered intellectuals and writers who were essentially family, both in their intense affection for our parents and in a shared pursuit of a stimulating life that was comfortable yet devoid of overt material pursuit. This childhood imbued in us a deep appreciation not directly for science but, rather, for the joy that arises from impactful pursuits driven by curiosity and free of intellectual constraints. It was the embrace of this lifestyle that inevitably led to us choose careers in science.

I grew up in an academic family in China in the 1980s. My father, Zuoyan Zhu, ran a laboratory in the Institute of Hydrobiology, studying fish biology. My decision to become a scientist came very naturally after gradual exposure to the research environment in my father's laboratory.

When I was a kid, I often went to my father's office to do homework after school. Homework was easy for me, and I got bored very quickly. To escape the boredom, I sometimes sneaked into the laboratory adjacent to his office. That was the beginning of my exposure to a research environment from a tender age. I remember vividly my first experiment: helping a graduate student load a DNA molecular weight marker onto an agarose gel. I was taught at school that DNA carries biological information but is too tiny to be seen with naked eye. So I was amazed to find out that I could actually see, behind a facial mask, the glowing red DNA ladder migrating through the gel before my eyes. I was immediately hooked. It was in that very room where I learned how to perform molecular cloning to put together different DNA pieces and later observed the hatch of a fish embryo injected with the transgene I helped construct. It was after that exciting period when I decided to follow my father's path to become a scientist.

The Center for Life Sciences at the Peking University, where I have my own laboratory, runs a program inviting local high school students into research laboratories. From my own experience, I believe this initiative will help kids become interested in science and, hopefully, will lead to future careers in science.

Siri, What Should I Eat?

Reiner Jumpertz von Schwartzenberg^{1,2} and Peter J. Turnbaugh^{1,*}

¹University of California, San Francisco, Department of Microbiology and Immunology, G.W. Hooper Research Foundation, 513 Parnassus Avenue, HSE 1001F, San Francisco, CA 94143-0552, USA

²Charité Universitätsmedizin Berlin, Department of Endocrinology and Metabolic Diseases, Charitéplatz 1, 10117 Berlin, Germany

*Correspondence: peter.turnbaugh@ucsf.edu

<http://dx.doi.org/10.1016/j.cell.2015.11.012>

Zeevi et al. report that extensive monitoring of a human cohort for variations in dietary intake, life-style, host phenotype, and the gut microbiome has enabled the development of a machine-learning algorithm that accurately predicts the individual glycemic response to meals, providing an important first step toward personalized nutrition.

Nearly 1 in 10 adult Americans now suffers from type 2 diabetes (T2D), placing it among the top ten leading causes of death (National Diabetes Statistics Report, 2014). Insulin resistance and impaired insulin secretion characterize T2D, ultimately leading to persistent dysregulation of plasma glucose. Besides fasting glucose levels, post-meal glucose levels are increasingly recognized as important risk factors for the development of cardiovascular disease and mortality (Cavalot et al., 2011), and the introduction of continuous glucose monitoring has improved glycemic control; for example in type 1 diabetics (Juvenile Diabetes Research Foundation Continuous Glucose Monitoring Study Group et al., 2008).

The post-meal rise in plasma glucose levels after ingestion of carbohydrates is reflected by a food's glycemic index (incremental area under the curve of plasma glucose levels relative to a pure glucose load); however, the combination with other macronutrients in a meal adds substantial variation. For example, meals with high fat content may impair glycemic response by delayed gastric emptying. Numerous additional factors, such as anthropometrics, meal times, sleep-wake cycle, physical activity, intestinal disorders, insulin sensitivity/resistance, lifestyle, and the trillions of microbes residing in the gastrointestinal tract (the gut microbiome), among other variables, may all contribute to the high degree of inter-individual variation of glycemic response to a given food (Dodd et al., 2011). In fact, one person may exhibit an exaggerated glucose response to a meal that results in a flat

or even negative glucose curve in others. Thus, prediction of individual glucose responses is fraught with issues, and given the substantial health burden of glycemic disorders and associated secondary diseases, improved predictions represent a grand challenge for modern medicine.

In this issue of *Cell*, Zeevi et al. (2015) provide a framework to systematically address this challenge. The authors collected extensive phenotypic data from 800 individuals, which were then used to train a machine-learning algorithm that could accurately predict glycemic response to various meals. Their remote data collection is enabled by a smartphone "app," providing a glimpse into a brave new world wherein our mobile devices, trained with extensive host and microbiome data, provide real-time advice on our dietary consumption and other lifestyle choices (Figure 1).

The resulting algorithm integrates many variables, including well-established contributors to glycemic response, such as carbohydrate intake or anthropometrics, but also various other traits like sleep-wake cycle, physical activity, age, HbA1c, calories, time of meal ingestion, and preceding measurements of glycemic response via continuous glucose monitors. The authors also include data on the gut microbiome, based on prior human studies showing that caloric intake and macro-nutrient composition can rapidly alter gut microbial community structure (e.g., David et al., 2014; Jumpertz et al., 2011) and that the gut microbiome is correlated with glucose regulation (Qin et al.,

2012). The algorithm accurately predicts glycemic response in a separate validation cohort and in a follow-up dietary intervention study. Notably, it also yields similar, if not markedly more accurate, predictions of glycemic response compared with an expert nutritionist.

This study provides a generalizable framework for the unbiased development of algorithms that predict other clinically relevant phenotypes. However, in part due to the complexity of the model, many critical questions remain to be addressed. What are the major data-points responsible for the accurate prediction of glycemic response? Could similarly accurate predictions be accomplished by a more limited set of already established determinants of glucose response, such as body composition, caloric and macronutrient content of meals, and age? The authors show that their model out-performs carbohydrate and caloric intake, but how does a model based on a more comprehensive analysis of dietary intake (e.g., including micronutrients) perform? Could this be improved by including information on each carbohydrate's glycemic index and/or susceptibility to host versus microbial digestion? Finally, what contribution did the gut microbiome make to these predictions and to what degree does this represent a causal versus casual link to glucose regulation? The answers to these questions are not just scientifically intriguing but will also be critical to translate these findings into a cost effective strategy for predicting glucose levels in patients.

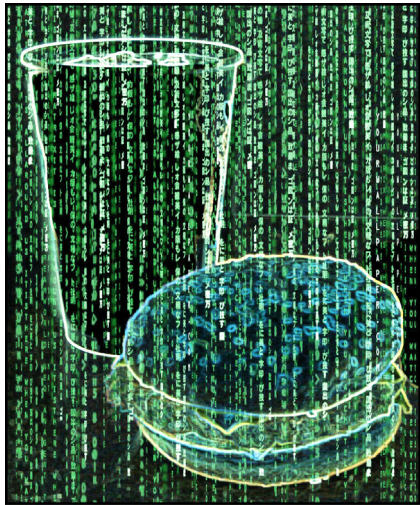


Figure 1. Computational Models Are Opening the Way toward a More Quantitative and Personalized Approach to Nutrition

Vast datasets on diet, lifestyle, host, and the microbiome can be used to predict the glycemic response to a given food.

Nonetheless, the current study is an important proof-of-principle for the utility of tailoring nutritional and/or pharmaceutical interventions to each individual. Precise predictions of glycemic response could represent a powerful tool to optimize dosing of insulin (or dietary interventions) in type 1 or even type 2 diabetics to avoid hypoglycemic episodes and more

efficiently control HbA1c levels. Follow-up studies will be essential to determine whether or not such personalized approaches reduce the risk of secondary disease and death. It will also be important to refine and validate app-based methods to monitor dietary intake and other relevant lifestyle traits in large cohorts. Machine-learning algorithms could be more broadly applicable to pharmacology and toxicology, especially for drugs with a narrow therapeutic window, such as those used for heart failure (Haisser et al., 2013) or cancer (Wallace et al., 2010). Currently, drug dosage can be adjusted based on body surface area and kidney/liver function; however, the more comprehensive approach introduced here could lead to more accurate strategies to improve response rates and reduce the side effects of such therapeutics. Interpreting these models will require inter-disciplinary efforts to establish causal relationships and identify the host and microbial genetic variants that are most relevant and those that can be safely ignored. Finally, it is important to remember that even with a perfect diagnostic tool we would still all be subject to the age-old struggle to maintain this now more personalized “healthy” diet, necessitating a concerted revolution in agriculture, food distribution, and food preparation.

REFERENCES

- Cavalot, F., Pagliarino, A., Valle, M., Di Martino, L., Bonomo, K., Massucco, P., Anfossi, G., and Trovati, M. (2011). *Diabetes Care* 34, 2237–2243.
- David, L.A., Maurice, C.F., Carmody, R.N., Gootenberg, D.B., Button, J.E., Wolfe, B.E., Ling, A.V., Devlin, A.S., Varma, Y., Fischbach, M.A., et al. (2014). *Nature* 505, 559–563.
- Dodd, H., Williams, S., Brown, R., and Venn, B. (2011). *Am. J. Clin. Nutr.* 94, 992–996.
- Haiser, H.J., Gootenberg, D.B., Chatman, K., Sarsani, G., Balskus, E.P., and Turnbaugh, P.J. (2013). *Science* 341, 295–298.
- Jumpertz, R., Le, D.S., Turnbaugh, P.J., Trinidad, C., Bogardus, C., Gordon, J.I., and Krakoff, J. (2011). *Am. J. Clin. Nutr.* 94, 58–65.
- Juvenile Diabetes Research Foundation Continuous Glucose Monitoring Study Group, Tamborlane, W.V., Beck, R.W., Bode, B.W., Buckingham, B., Chase, H.P., Clemons, R., Fiallo-Scharer, R., Fox, L.A., Gilliam, L.K., et al. (2008). *N. Engl. J. Med.* 359, 1464–1476.
- National Diabetes Statistics Report (2014). <http://www.cdc.gov/diabetes/pubs/statsreport14/national-diabetes-report-web.pdf>.
- Qin, J., Li, Y., Cai, Z., Li, S., Zhu, J., Zhang, F., Liang, S., Zhang, W., Guan, Y., Shen, D., et al. (2012). *Nature* 490, 55–60.
- Wallace, B.D., Wang, H., Lane, K.T., Scott, J.E., Orans, J., Koo, J.S., Venkatesh, M., Jobin, C., Yeh, L.-A., Mani, S., and Redinbo, M.R. (2010). *Science* 330, 831–835.
- Zeevi, D., Korem, T., Zmora, N., Israeli, D., Rothchild, D., Weinberger, A., Ben-Yacov, O., Lador, D., Avnit-Sagi, T., Lotan-Pompan, M., et al. (2015). *Cell* 163, this issue, 1079–1094.

Potent Antibody Protection against an Emerging Alphavirus Threat

Margaret Kielian^{1,*} and Erica Ollmann Saphire^{2,3,*}

¹Department of Cell Biology, Albert Einstein College of Medicine, Bronx, NY 10461, USA

²Department of Immunology and Microbial Science

³The Skaggs Institute for Chemical Biology

The Scripps Research Institute, La Jolla, CA 92037, USA

*Correspondence: margaret.kielian@einstein.yu.edu (M.K.), erica@scripps.edu (E.O.S.)

<http://dx.doi.org/10.1016/j.cell.2015.11.006>

Chikungunya virus recently caused large outbreaks world-wide. In this issue of *Cell*, Fox et al. describe several potently neutralizing antibodies against multiple alphaviruses. The structure of the virus in complex with one of the antibodies reveals the antibody-induced rearrangement and crosslinking of the viral surface proteins that result in neutralization.

The alphavirus Chikungunya virus (CHIKV) was originally isolated in Africa. Although it caused sporadic large outbreaks in Africa, it largely flew under the scientific radar. CHIKV is transmitted by mosquito vectors, and the emergence of this pathogen has been fueled by its adaptation to new mosquito species and by the spread of these vectors into new areas. In 2004, CHIKV emerged as a global pathogen when it generated a much larger pandemic of millions of cases and a number of deaths in countries around the Indian Ocean (Schwartz and Albert, 2010). CHIKV was first reported in the Americas in 2013 and since then has spread rapidly in the New World, with more than a million cases in at least 43 countries, including the United States (Johansson, 2015). CHIKV is transmitted by mosquito vectors, and the emergence of this pathogen has been fueled by its adaptation to new mosquito species and by the spread of these vectors into new areas. CHIKV causes fever and arthritis, with resultant joint problems that can linger for years. There are currently no licensed vaccines or antiviral therapies for CHIKV or for other alphavirus pathogens, including Eastern and Western equine encephalitis viruses. Those two viruses are endemic in the United States, where they cause low numbers of cases but have high fatality rates. A better understanding of the immune response against the array of alphavirus pathogens would promote the development of necessary vaccines and immunotherapeutics. Given the high mutation rate of

RNA viruses, broadly reactive antibody strategies may be of particular importance.

In this issue of *Cell*, a multidisciplinary team of investigators led by Michael Diamond screened a panel of mouse and human monoclonal antibodies raised against CHIKV and found that, of the 60 that neutralized CHIKV, 19 also bound to other alphaviruses such as the African O'nyong'nyong virus (86% identical to CHIKV) and South American Mayaro virus (60% identical to CHIKV), with differing abilities to neutralize these disparate viruses (Fox et al., 2015). The most potent of these broadly reactive mAbs, termed CHK-265, also protected mice from CHIKV, O'nyong'nyong, and Mayaro virus challenge.

Alphaviruses are small enveloped viruses with highly organized structures and infect host cells by receptor-mediated endocytosis and low-pH-triggered membrane fusion (Kuhn, 2013). On the surface are two transmembrane glycoproteins, the class II fusion protein E1 and the receptor-binding protein E2. These proteins are arrayed symmetrically on the viral surface to form 80 spikes, each a trimer of E2-E1 heterodimers. E2 has three domains with immunoglobulin-like folds: a central domain A, a distal domain B, and a membrane-proximal domain C. E2 covers much of the E1 protein on the viral surface and clamps the fusion loop at the membrane-distal tip of E1 between its domains A and B. E2 regulates E1's fusion activity, and a key step in fusion is the low-pH-triggered dissociation/rearrangement of the E2-E1 dimer, thus allowing E1 to insert into the endosome membrane and refold to the hairpin conformation that drives fusion (Gibbons et al., 2004). A first step in this process is the "uncapping" of the E1 fusion loop by the movement of the E2 B domain (Li et al., 2010; Voss et al., 2010). E2 is the principal target of neutralizing antibodies, which have been mapped to locations across its outer surface, while the E2 A and B domains are implicated in receptor interaction (reviewed in Voss et al., 2010).

Here, Fox et al., perform cryoelectron microscopy on CHK-265 Fabs in complex with virus particles. The resulting structures illustrate that binding of this potent neutralizing antibody occurs with a concomitant structural rearrangement of the envelope proteins.

CHK-265 is primarily directed toward domain B of the E2 protein, and binding of the antibody induces a slight rotation of domain B from its unbound position. Unexpectedly, binding of CHK-265 also causes a concomitant large repositioning of domain A up and out of each envelope trimer, involving a ~20 Å translation and 70° rotation about E1 (Figure 1). Ultimately, each copy of CHK-265 bridges domain B of one spike to domain A of a neighboring trimer on the viral surface, with each Fab binding 19 residues of domain B and 4 residues of the neighboring trimer's domain A. The effect of CHK-265 binding is a cross-linking network across the virus surface. Fab fragments of CHK-265 were less potent than IgG, suggesting that the IgG could induce additional cross-linking and

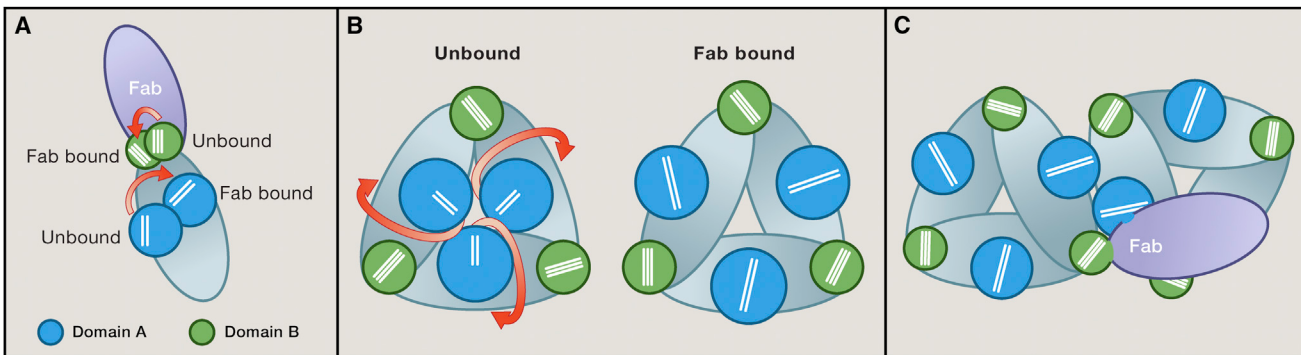


Figure 1. Antibody-Induced Rearrangements of Chikungunya Virus Envelope Proteins

(A) Binding of Fab CHK-265 induces a rearrangement of domains A and B of envelope protein E2. The rest of E2 and the E1 protein are both colored as a single gray oval for simplicity. Illustrated is one monomer. White lines represent the axes of major β strands in the domain structure.
 (B) Domain rotation illustrated for an envelope trimer, before and after binding of Fab CHK-265.
 (C) Fab CHK-265 bridges domain A of one copy of E2 to domain B of a different copy of E2 belonging to a neighboring trimer. Figure: Christina Corbaci, TSRI.

perhaps a steric blockage of viral entry as well.

Although the orientation of domain A is changed radically, E2's receptor-binding activity is unchanged. Notably, CHIKV still attaches to cells in the presence of CHK-265, so the block achieved by this antibody is not at receptor engagement but, rather, at events downstream. CHK-265 partially inhibits virus fusion and partially inhibits egress: its total dampening of infectivity may result from a sum of separate functions at separate steps. Based on the structure, CHK-265 could function by inhibiting the uncapping step by domain B or by "clamping" the E2-E1 dimer to impede its dissociation. Alternatively, antibody-mediated crosslinking of adjacent spikes could inhibit more global rearrangements of the virus particle surface that occur during fusion, as has been previously observed for West Nile virus (Kaufmann et al., 2010).

Unlike viruses with structurally related fusion proteins, such as Dengue virus,

there is to date no compelling evidence that antibodies to the alphavirus envelope proteins cause antibody-dependent enhancement of infection. Vaccine candidates, including those based on virus-like particles, measles virus chimeras, or attenuated CHIKV, are under development (reviewed in Cassone, 2015; Weaver et al., 2012). The correlations shown in this paper between broadly neutralizing CHIKV antibodies and the structure of the epitopes on the viral particle may prove important to developing and evaluating these vaccines. While the CHIKV antibodies discussed here did not cross-neutralize the single encephalitic alphaviruses tested, development of a potent neutralizing antibody could be an important strategy against these viruses as well.

REFERENCES

- Cassone, A. (2015). *Pathog. Glob. Health* **109**, 43.
- Fox, J.M., Long, F., Edeling, M.A., Lin, H., van Duijlen-Richter, M.K.S., Fong, R.H., Kahle, K.M., Smit, J.M., Jin, J., Simmons, G., et al. (2015). *Cell* **163**, this issue, 1095–1107.
- Gibbons, D.L., Vaney, M.-C., Roussel, A., Vigouroux, A., Reilly, B., Lepault, J., Kielian, M., and Rey, F.A. (2004). *Nature* **427**, 320–325.
- Johansson, M.A. (2015). *Trends Parasitol.* **31**, 43–45.
- Kaufmann, B., Vogt, M.R., Goudsmit, J., Holdaway, H.A., Aksyuk, A.A., Chipman, P.R., Kuhn, R.J., Diamond, M.S., and Rossman, M.G. (2010). *Proc. Natl. Acad. Sci. USA* **107**, 18950–18955.
- Kuhn, R.J. (2013). Togaviridae. In *Fields Virology*, D.M. Knipe and P.M. Howley, eds. (Lippincott, Williams and Wilkins), pp. 629–650.
- Li, L., Jose, J., Xiang, Y., Kuhn, R.J., and Rossman, M.G. (2010). *Nature* **468**, 705–708.
- Schwartz, O., and Albert, M.L. (2010). *Nat. Rev. Microbiol.* **8**, 491–500.
- Voss, J.E., Vaney, M.C., Duquerroy, S., Vonrhein, C., Girard-Blanc, C., Crublet, E., Thompson, A., Bricogne, G., and Rey, F.A. (2010). *Nature* **468**, 709–712.
- Weaver, S.C., Osorio, J.E., Livengood, J.A., Chen, R., and Stinchcomb, D.T. (2012). *Expert Rev. Vaccines* **11**, 1087–1101.

A Common Mechanism that Underpins Antibody Diversification

Cornelis Murre^{1,*}¹Department of Molecular Biology, Division of Biological Sciences, University of California, San Diego, La Jolla, CA 92093, USA

*Correspondence: cmurre@ucsd.edu

<http://dx.doi.org/10.1016/j.cell.2015.10.075>

Targeting of AID to antibody variable (V) regions results in somatic hypermutation, whereas its recruitment to switch (S) regions leads to class-switch recombination. Yeap et al. find that the mechanism by which variable and switch regions recruit AID essentially is the same but that the two regions differ in the density of double-stranded DNA breaks that are generated. These lead to either point mutations in V exons in somatic hypermutation or deletion of intervening DNA sequences during class switch recombination.

During the developmental progression of B-lineage cells, antibody genes are being assembled by unique combinations of gene segments encoding for variable (V), diversity (D), and joining (J) elements, a process frequently referred to as V(D)J recombination. In the primary lymphoid organs such as the fetal liver and the bone marrow, VDJ recombination ultimately leads to a diverse antibody repertoire expressed on the cell surface of the antigen-inexperienced mature B cell population. Upon expression of an innocuous B cell receptor (BCR), naive B cells exit the primary lymphoid organs and migrate to the spleen and lymph nodes. Once exposed to invading pathogens, B cells move to specialized micro-anatomical structures, named germinal centers. Here, B cells are subject to two distinct sets of genomic modifications: class switch recombination (CSR) and/or somatic hypermutation (SHM) (Chandra et al., 2015). Somatic point mutations in germinal center B cells that lead to increased affinity of the antigen receptor are selected for further maturation, while mutations that lead to a decline in antigen receptor affinity are being depleted within the population. Frequently, but not exclusively, CSR is also initiated in the germinal centers and can be induced *in vitro* by culturing naive B cells in the presence of the appropriate stimuli. During CSR, dsDNA breaks are generated at highly repetitive sequences, named S regions, that are located adjacent to exons encoding for the ensemble of antibody isotypes. DNA breaks generated during CSR find

each other through thermal motion, leading to the joining of two S regions that replace the IgM constant region with that of other isotypes, including IgG, IgE, or IgA. Ultimately, this highly orchestrated series of genomic changes generates a population of effector B cells with distinct functions that express a diverse and high-affinity antibody repertoire.

The process of SHM and CSR requires activation-induced cytidine deaminase (AID). AID converts cytosine (C) into uracil (U), leading to DNA lesions (Muramatsu et al., 2007; Di Noia and Neuberger, 2007). Such DNA lesions generate double-stranded DNA breaks across switch regions or point mutations that are associated with exons encoding for V regions (Nussenzweig and Nussenzweig, 2010; Alt et al., 2013). Distinct DNA repair modules are used to repair and modify the DNA lesions, including mismatch DNA repair, base excision repair, and error-prone DNA polymerases.

AID predominantly, but not exclusively, targets RGYW consensus sequences (R relates to purine, Y to pyrimidine, W to A or T) (Hackney et al., 2009). The RGYW motif is enriched, albeit modestly, across the majority of the V region repertoire. The RGYW sequence is found in S regions more densely than within V exons. The high density of the RGYW consensus sequences at S regions and its palindromic nature permit the targeting of AID to both the sense and anti-sense DNA strands across the S regions (Zarrin et al., 2004). This then leads to double-stranded breaks and deletion of the intervening genomic sequences.

The RGYW motif (Figure 1) is not restricted to V exons. Rather it is present at other locations in the genome that are not subjected to AID targeting. If it is not specific to V exons and S regions, then what is the role of the RGYW motif in AID targeting? Furthermore, is the role of the RGYW motif equivalent to promote class switch recombination and somatic hypermutation? In this issue of *Cell*, Yeap et al. (2015) have designed an elegant experimental approach to address this question. Briefly, a strategy was developed to measure AID activity on a spectrum of test sequences, named passenger alleles. This assay permits the testing of a passenger against a V exon expressing a productive in-frame antibody allele in the same normal V-region genomic location and with the same transcriptional machinery (known to target AID). The mutations associated with passenger alleles were then compared to the sequences of a productive V region known to interact with a specific antigen, termed 4-hydroxy-3-nitropheylactyl (NP). This approach was combined with throughput DNA sequencing that permitted “surrogate kinetic” analyses of somatic mutations in both productive and passenger alleles. Furthermore, in the approach developed by Yeap et al. (2015), selection for NP does not occur within the time-frame that spans the short-term immunization protocols and that the passenger allele is not translated, and consequently, there is no bias by selection for antigen or against mutations that inactive the antibody. Interestingly, the authors found that AID

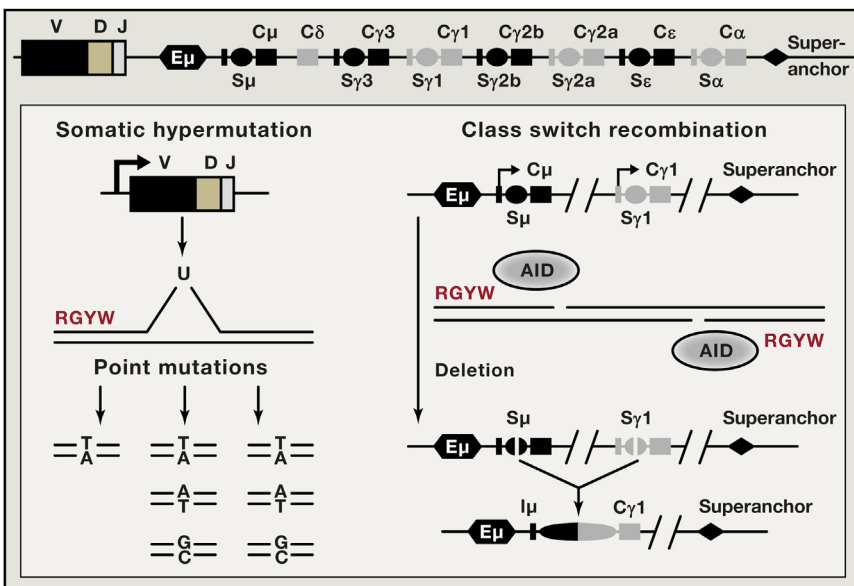


Figure 1. Schematic Diagram Depicting the Role of the RGYW Motif in Class-Switch Recombination and Somatic Hypermutation

Adapted and modified from Chandra et al. (2015).

acted on the most dominant RGYW targets in V exons and S regions, pointing to a conserved mechanism by which AID activates class switch recombination or somatic hypermutation. Given this striking similarity, the authors next addressed why targeting to V exons would yield point mutations rather than genomic deletions observed during class switch recombination. Using their reporter system, Yeap et al. (2015) observed that, surprisingly, somatic hypermutation did in fact lead to double-stranded breaks and genomic deletions in V exons, similar to class switch recombination process. Thus, no specialized mechanism is required for generating

deletions that have been observed in subsets of antibodies, including those in neutralizing antibodies isolated from patients infected with HIV. These findings are intriguing, suggesting that the ability of S regions to be subjected to double-stranded breaks with limited AID exposure may have evolved to permit efficient class switch recombination, avoiding mutations associated with V regions that, in principle, could affect antibody affinity and/or specificity.

These data also provide insight into the special nature of V exons compared to other regions in the genome as it relates to being targeted by AID (Odegard and

Schatz, 2006). The authors found that non-Ig DNA sequences, including bacterial DNA, that were inserted as passengers V-region location accumulated point mutations at RGYW sequences at levels similar to V exons. Thus, it is the genomic location, exons encoding for V regions, that matter for AID targeting. A wide spectrum of possible mechanisms has been proposed, including AID recruitment motifs distinct from that of the RGYW motif, enhancer activity, and ongoing ncRNA transcription. Now that Yeap et al. (2015) have resolved the role of RGYW motifs in AID targeting, the search begins to understand why and how the AID targeting machinery senses genomic location.

REFERENCES

- Alt, F.W., Zhang, Y., Meng, F.L., Guo, C., and Schwer, B. (2013). *Cell* 152, 417–429.
- Chandra, V., Bortnick, A., and Murre, C. (2015). *Trends Immunol.* 36, 527–535.
- Di Noia, J.M., and Neuberger, M.S. (2007). *Annu. Rev. Biochem.* 76, 1–22.
- Hackney, J.A., Misaghi, S., Senger, K., Garris, C., Sun, Y., Lorenzo, M.N., and Zarrin, A.A. (2009). *Adv. Immunol.* 101, 163–189.
- Muramatsu, M., Nagaoka, H., Shinkura, R., Begum, N.A., and Honjo, T. (2007). *Adv. Immunol.* 94, 1–36.
- Nussenzweig, A., and Nussenzweig, M.C. (2010). *Cell* 141, 27–38.
- Odegard, V.H., and Schatz, D.G. (2006). *Nat. Rev. Immunol.* 6, 573–583.
- Yeap, L.-S., Hwang, J.K., Du, Z., Meyers, R.M., Meng, F.-L., Jakubauskaitė, A., Liu, M., Mani, V., Neuberg, D., Kepler, T.B., et al. (2015). *Cell* 163, this issue, 1124–1137.
- Zarrin, A.A., Alt, F.W., Chaudhuri, J., Stokes, N., Kaushal, D., Du Pasquier, L., and Tian, M. (2004). *Nat. Immunol.* 5, 1275–1281.

Microbiota's No Wasting Policy

Miguel P. Soares^{1,*}¹Instituto Gulbenkian de Ciéncia, Rua da Quinta Grande 6, 2780-156 Oeiras, Portugal

*Correspondence: mpsoares@igc.gulbenkian.pt

<http://dx.doi.org/10.1016/j.cell.2015.10.077>

Schieber et al. demonstrate that a specific gut microbiota bacterial strain induces a host-mediated protection mechanism against inflammation-driven wasting syndrome. This salutary effect confers a net survival advantage against bacterial infection, without interfering with the host's pathogen load, revealing that host-microbiota interactions regulate disease tolerance to infection.

Immune-driven resistance mechanisms are usually perceived as the central defense strategy preventing the pathological outcome of infections. We now realize, however, that additional defense strategies are required to achieve this goal (Medzhitov et al., 2012). These include an evolutionary conserved defense strategy known as disease tolerance, which preserves host homeostasis during infection without interfering with the host's pathogen load (Medzhitov et al., 2012). The study by Schieber et al. (2015) published in *Science* highlights how host/microbiota interactions manipulate this defense strategy to confer host protection against bacterial infections and ultimately preserve homeostasis.

There is now a growing body of experimental evidence to suggest that tissue damage control mechanisms (Soares et al., 2014) play a central role in sustaining disease tolerance to viral (Rodrigue-Gervais et al., 2014), bacterial (Larsen et al., 2010), or protozoan (Ferreira et al., 2011; Råberg et al., 2007) infections. While host microbiota/interactions are known to regulate immune-driven resistance mechanisms against viral (Ichinohe et al., 2011), bacterial (Cash et al., 2006), or protozoan infections (Yilmaz et al., 2014), whether this was also the case for tissue damage control mechanisms regulating disease tolerance to these infections remained unknown.

Schieber et al. (2015) demonstrate that a specific bacterial member of the gut microbiota, namely *Escherichia coli* (*E. coli*) O21:H⁺, confers a strong survival advantage against enteric and lung bacterial infections in mice. This occurs without interfering with pathogen growth (i.e., host pathogen load), revealing that

E. coli O21:H⁺ confers disease tolerance to bacterial infections.

The mechanism via which the protective effect of *E. coli* O21:H⁺ is exerted involves sensing of this microbiota component by a host inflammasome signaling platform containing the NOD-like receptor (NLR) family CARD domain-containing protein 4 (NLrc4) (Figure 1). While engagement of the NLrc4 inflammasome was well known to trigger the cleavage and secretion of interleukin (IL)-18 and IL-1 β , the authors now show that IL-18 and, to a lesser extent, IL-1 β are critical to maintain systemic levels of insulin-like growth factor-1 (IGF-1) during bacterial infections. This

is required to activate a downstream signal transduction pathway in muscle cells, involving the Phosphoinositide 3-kinase (PI3K)/Akt and antagonizing muscle wasting via a process that represses the expression of the E3 ubiquitin ligases Atrogin-1 and Murf1 (Figure 1). This tissue damage control mechanism prevents the development of wasting syndrome and accounts for the survival advantage conferred by *E. coli* O21:H⁺ against bacterial infections (Figure 1).

Surprisingly, the protective effect exerted by *E. coli* O21:H⁺ requires its active translocation from the gut into white adipose tissue. The mechanism via which

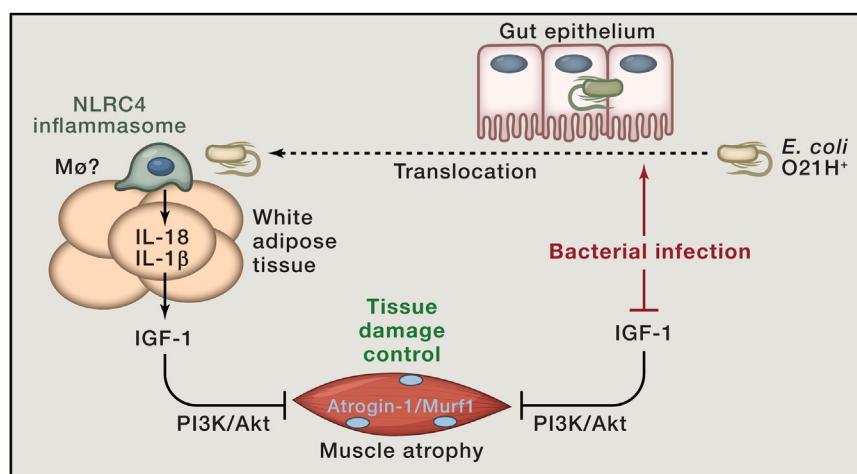


Figure 1. Protective Effect of *E. coli* O21:H⁺ against Bacterial-Infection-Driven Muscle Atrophy

At steady state, *E. coli* O21:H⁺ remains in the gut lumen. However, upon bacterial infections, *E. coli* O21:H⁺ translocates across the gut epithelial barrier and accumulates specifically in white adipose tissue. This occurs via an unknown mechanism that does not require disruption of the intestinal barrier. Once in white adipose tissue, *E. coli* O21:H⁺ is sensed by the NLrc4 inflammasome (presumably expressed in resident macrophages; Mø?). This triggers the production of IL-1 β and IL-18, possibly acting synergistically to induce IGF-1 production in white adipose tissue and sustain systemic levels of IGF-1 during bacterial infections. IGF-1 signaling via PI3K/Akt activation in muscle cells prevents the upregulation of atrophy associated programs involving the muscle-specific E3 ubiquitin ligases Murf1 and Atrogin1 and leading to muscle wasting. This tissue damage control mechanism confers disease tolerance to bacterial infections.

this occurs is not yet established but is shown to act independently of the host Nlrc4 inflammasome. As a final note, the study by Schieber et al. (2015) suggests that manipulation of the IGF-1/PI3K/Akt/Atrogin-1;Murf1 signaling transduction pathway may be a valuable therapeutic approach to induce tissue damage control and to confer disease tolerance to bacterial infections. This should be particularly relevant to the treatment of severe sepsis, given the relative contribution of muscle wasting to the overall morbidity and mortality of this infectious disease.

ACKNOWLEDGMENTS

M.P.S. is supported by Fundação Calouste Gulbenkian and by grants from the Fundação para a

Ciência e Tecnologia (PTDC/SAU TOX/116627/2010, HMSCP-ICT/0022/2010) and by the European Community 7th Framework Grant ERC-2011-AdG. 294709-DAMAGECONTROL.

REFERENCES

- Cash, H.L., Whitham, C.V., Behrendt, C.L., and Hooper, L.V. (2006). *Science* 313, 1126–1130.
- Ferreira, A., Margutti, I., Bechmann, I., Jeney, V., Chora, A., Palha, N.R., Rebelo, S., Henri, A., Beuzard, Y., and Soares, M.P. (2011). *Cell* 145, 398–409.
- Ichinohe, T., Pang, I.K., Kumamoto, Y., Peaper, D.R., Ho, J.H., Murray, T.S., and Iwasaki, A. (2011). *Proc. Natl. Acad. Sci. USA* 108, 5354–5359.
- Larsen, R., Gozzelino, R., Jeney, V., Tokaji, L., Bozza, F.A., Japiassú, A.M., Bonaparte, D., Cavalcante, M.M., Chora, A., Ferreira, A., et al. (2010). *Sci. Transl. Med.* 2, 51ra71.
- Medzhitov, R., Schneider, D.S., and Soares, M.P. (2012). *Science* 335, 936–941.
- Råberg, L., Sim, D., and Read, A.F. (2007). *Science* 318, 812–814.
- Rodrigue-Gervais, I.G., Labbé, K., Dagenais, M., Dupaul-Chicoine, J., Champagne, C., Morizot, A., Skeldon, A., Brincks, E.L., Vidal, S.M., Griffith, T.S., and Saleh, M. (2014). *Cell Host Microbe* 15, 23–35.
- Schieber, A.M.P., Lee, Y.M., Chang, M.W., Leblanc, M., Collins, B., Downes, M., Evans, R.M., and Ayres, J.S. (2015). *Science*. Published online October 30, 2015. <http://dx.doi.org/10.1126/science.aac6468>.
- Soares, M.P., Gozzelino, R., and Weis, S. (2014). *Trends Immunol.* 35, 483–494.
- Yilmaz, B., Portugal, S., Tran, T.M., Gozzelino, R., Ramos, S., Gomes, J., Regalado, A., Cowan, P.J., d'Apice, A.J., Chong, A.S., et al. (2014). *Cell* 159, 1277–1289.

Improving Cancer Treatment via Mathematical Modeling: Surmounting the Challenges Is Worth the Effort

Franziska Michor^{1,2,*} and Kathryn Beal^{3,*}

¹Department of Biostatistics and Computational Biology, Dana-Farber Cancer Institute, Boston, MA 02215, USA

²Department of Biostatistics, Harvard T.H. Chan School of Public Health, Boston, MA 02115, USA

³Department of Radiation Oncology, Memorial Sloan-Kettering Cancer Center, New York, NY 10065, USA

*Correspondence: michor@jimmy.harvard.edu (F.M.), bealk@mskcc.org (K.B.)

<http://dx.doi.org/10.1016/j.cell.2015.11.002>

Drug delivery schedules are key factors in the efficacy of cancer therapies, and mathematical modeling of population dynamics and treatment responses can be applied to identify better drug administration regimes as well as provide mechanistic insights. To capitalize on the promise of this approach, the cancer field must meet the challenges of moving this type of work into clinics.

Cancer research and oncology has entered a new era of targeted therapy (Sawyers, 2004) and patient-tailored therapeutic intervention (Shrager and Tenenbaum, 2014), but resistance (Gottesman et al., 2002; Holohan et al., 2013) and tumor heterogeneity (Anderson et al., 2011; Burrell et al., 2013; Ding et al., 2012; Gerlinger et al., 2012; Landau et al., 2013) have been a barrier for realizing the clinical impact of these discoveries. This barrier is, in essence, a quantitative population genetics problem—the need to quantitatively describe heterogeneous tumor cell populations and their dynamics over time and during treatment. Using such mathematical descriptions, it is then possible to evaluate which drugs, combinations, and schedules are best for a given patient. For instance, if drugs are administered at sufficiently low doses, no drug holidays are necessary to limit the side effects and reduce patient toxicity; however, if drugs are administered at more concentrated doses, which may lead to higher cell kill, then rest periods are needed to limit side effects. Such drug holidays can lead to an exponential rebound of the tumor cell population and hence pose a significant risk for the emergence of resistance. It is unclear, *a priori*, which of these two example strategies are going to be more effective in reducing tumor burden and preventing the emergence or outgrowth of a resistant tumor subclone. In order to answer this question, several clinical studies have been performed to identify optimum dosing frequencies (Hryniuk, 2001; Lake and Hudis, 2004). However, it is both unethical and too time consuming to test all possible dosing schedules in pre-clinical or clinical studies, and therefore only limited clinical experimentation can be performed.

Mathematical modeling of the treatment response of heterogeneous cell populations represents an attractive avenue toward narrowing the set of possibilities that should be tested in pre-clinical models and in the clinical setting (Figure 1). Mathematical modeling can, in principle, be used to systematically search through the millions of possible dose administration strategies (each determined by a unique dose-time profile) and combination schedules (each determined by a combination of different drugs administered at different dose-time profiles) to identify the schedules that maximally extend patient survival. Indeed, a

significant amount of research effort has been devoted to developing mathematical models that identify the most effective chemotherapeutic administration regimens using optimization and control techniques (Coldman and Murray, 2000; Costa et al., 1992, 1995; Katouli and Komarova, 2011; Kimmel and Swierniak, 2006; Ledzewicz and Schattler, 2009; Martin et al., 1992; Martin and Teo, 1993; Murray and Coldman, 2003). These models are in general aimed at rapidly minimizing the total tumor burden. However, long-term patient survival depends not only on quickly decimating the total number of tumor cells, but also on controlling drug-resistant subpopulations within the tumor. The simultaneous achievement of these two goals is complicated by the fact that they are often accomplished by exerting opposing evolutionary selection pressures. Furthermore, both long-term toxicity and dose-limiting side effects must be avoided.

Below, we will highlight several examples of promising, modeling-based findings, some of which represent the few that have been or will soon be tested clinically. We will then discuss the challenges that the field must meet to enable more extensive clinical testing of mathematically discovered treatment modalities. In a landmark study, Norton and Simon (Norton and Simon, 1977) observed that clinical experience was at odds with a fundamental concept that had been instrumental in designing dose schedules for the treatment of human cancer: that small tumors were more sensitive to cytotoxic therapy than larger tumors of the same histology. The underlying assumption was that smaller tumors have a large fraction of actively dividing cells. However, Norton and Simon observed that, in many cases, the low-dose low-concentration schedules used for smaller tumors were inferior to more high-concentration, dose-dense protocols that were a relatively novel approach at that time. To understand this observation, they probed the relationship between tumor size and sensitivity to therapy by inspecting growth curves of tumors exposed to anti-cancer agents. They found that most untreated malignancies can be described using a Gompertzian growth law, which predicts an S-shaped growth curve. According to this law, the growth rate

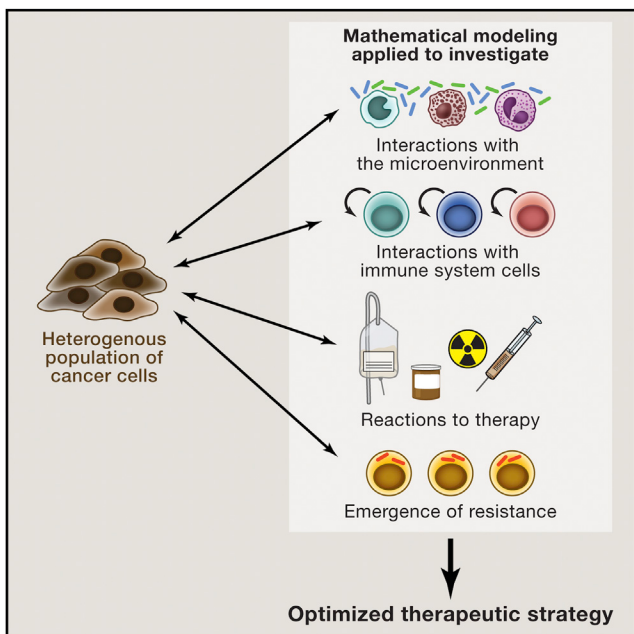


Figure 1. Exploring Complex Dependencies in Cancer Biology with Mathematical Modeling

The complexity of cancer includes not only the heterogeneous cell population of a tumor, but also its interaction with the microenvironment and immune system and responses to different kinds of treatments. Mathematical modeling of the impact of these factors on tumor cell population dynamics facilitates the generation testable hypotheses regarding the evolution of resistance and identifying prospectively optimum treatment strategies designed to maximize the chance of a cure.

of tumor cells is smallest for both very small and very large tumors but is maximum at the inflection point. Their resulting mathematical model led to the conclusion that a dose schedule capable of dramatically depleting a tumor of intermediate size may not be sufficient to cure a small tumor. They thus suggested more intense schedules, higher doses, and prolonged therapy. The authors later set out to validate their predictions in a large randomized clinical trial (Citron et al., 2003) of axillary node-positive breast cancer. They found, as predicted, that dose-dense schedules significantly increased disease-free survival and overall survival. Their approach thus became the first mathematical model providing clinically validated predictions.

The model by Norton and Simon was based on the observation that treatment efficacy can drop if insufficient drug is administered at a time when the tumor is kinetically less sensitive to treatment. This "kinetic resistance" is unlike acquired resistance due to genetic and/or epigenetic events that prevent the drug from entering the cell, binding to its target, or other mechanisms. This "biochemical" type of resistance was first mathematically addressed by Goldie and Colman, who developed a mathematical model relating the probability of drug sensitivity of a tumor to the rate at which cells accumulate changes that enable them to become resistant to therapy (Goldie and Colman, 1979). The model assumed that there is a certain probability per cancer cell division that a resistance-causing (epi)genetic change arises. By calculating the probability of resistance and the

expected number of resistant cells, the authors found not only that an increase in the mutation rate increases the probability of a resistant phenotype emerging, but also that the probability of there being at least one resistant cell will increase dramatically during a very short interval in the biological history of the tumor. The clinical recommendation based on these results was that therapy be initiated as quickly as possible to maximize the probability of a cure. This approach was later also predicted to maximize patient survival due to the emergence of more lethal cancer states such as metastases (Haeno et al., 2012).

A subsequent extension of this mathematical model considered two types of resistant cells, each insensitive to a different chemotherapeutic agent (Goldie et al., 1982). The goal of the model was to take both types of resistance into account and identify treatment schedules that would maximize the chance of a cure by preventing the emergence of doubly resistant cells. Using a computer program to simulate the development of such doubly resistant cells, the authors predicted that alternating the treatment regimen of the two drugs at every cycle would be the most effective strategy to prevent resistance. This prediction became known as the Goldie-Coldman hypothesis. A clinical trial in Italy tested this hypothesis in women with resectable mammary carcinoma and more than three positive axillary lymph nodes (Bonadonna et al., 1995). The patients were randomized into two treatment arms, either receiving treatments sequentially or in an alternating fashion. The primary endpoints were relapse free, and overall survival and the median duration of follow-up was 9 years. The trial results demonstrated significantly longer survival, both progression free and overall, for patients who received the sequential regimen as compared to the alternating regimen. A subsequent phase II study also evaluated the efficacy of alternating and sequential regimens of docetaxel and doxorubicin as first-line chemotherapy for metastatic breast cancer (Paridaens et al., 2003). The alternating and sequential groups achieved similar objective tumor response rates and median duration of response, but medial survival times were significantly shorter in the alternating than the sequential group. Furthermore, patients receiving sequential therapy were more likely to complete the planned eight chemotherapy cycles and had a lower incidence of side effects.

These trial results suggest that, at least in those clinical settings, the Goldie-Coldman hypothesis did not hold. However, the possibility remains that the hypothesis might lead to better survival times in other cancer types and/or treatment approaches (such as chemotherapy and radiation therapy). Indeed, several studies have investigated the outcome of radiation therapy followed by chemotherapy versus chemotherapy concomitant with radiation therapy. For example, in non-metastatic breast cancer, both radiation and chemotherapy are often used as adjuvant treatment following surgery. A randomized study performed in the 1990s comparing the sequencing options (of radiation versus chemotherapy first) showed a reduction in the rate of distant metastases in the group that received chemotherapy first (Recht et al., 1996). However, those results were later updated (Bellon et al., 2005) and shown to be non-significant and were then disputed in a meta-analysis of three well-documented randomized trials designed to study this question (Hickey et al., 2013). Thus, the findings regarding implementations of the

Goldman-Coldie hypothesis in the clinic remain mixed, and no clear validation of the hypothesis has been obtained so far. In fact, other recent approaches have suggested that it would be beneficial to administer combination treatment upfront to prevent the outgrowth of resistance (Bhang et al., 2015; Bozic et al., 2013; Glickman and Sawyers, 2012).

To determine whether modeling approaches could be applied to specific resistance mechanisms to individual drugs, we developed a mathematical model of non-small cell lung cancer cell response to treatment with the epidermal growth factor receptor (EGFR) inhibitor erlotinib (Chmielecki et al., 2011) in which resistance was considered to arise predominantly due to a second-site EGFR mutation (Pao et al., 2005), T790M, which emerges with a low probability during each sensitive cell division. The model, similar to the approach by Goldie and Coldman, was based on a stochastic branching process in which erlotinib-sensitive cells proliferate and die according to rates determined in a patient-derived cell line. Resistant cells then also proliferate and die according to rates determined in cells isogenic to the sensitive line apart from the T790M mutation. These in vitro cell culture experiments demonstrated that resistant cells had a fitness lower than sensitive cells in the absence of treatment, a finding explaining the low frequencies of pre-existing T790M-positive clones in patients (Chmielecki et al., 2011). The mathematical model was then used to search through the space of all clinically tolerated erlotinib schedules to identify the one that would significantly delay the emergence of T970M-driven resistance. Unlike the FDA-approved schedule of 150 mg per day, the optimum consisted of administering a low dose of 50 mg per day together with twice weekly high-dose pulses at the clinically determined maximally tolerated dose; the clinical study testing this hypothesis was initiated at Memorial Sloan-Kettering in 2013 (<http://clinicaltrials.gov/show/NCT01967095>). Preliminary results show that this schedule is well tolerated and might reduce the rate of progression in patients with brain metastases (H.A. Yu et al., 2015, ASCO, poster).

Although only these three population-based modeling approaches have so far led to clinical implementation, several other frameworks have been developed that might soon be tested in the clinic. These include a mathematical model suggesting the use of an adaptive therapeutic approach that changes in response to the variability in both space and time of the tumor microenvironment, cell phenotype, and response to treatment (Gatenby et al., 2009) and a model investigating alternative radiation schedules in primary glioblastoma (Leder et al., 2014). Another recent approach incorporates genetic heterogeneity in the context of selecting optimum combination strategies (Zhao et al., 2014). Other groups have used evolutionary game theory to investigate optimal combination therapies (Basanta et al., 2012) or have used patient-derived data on tumor stem cell turnover to identify prognostic factors (Stiehl et al., 2015).

These studies serve as examples of quantitative descriptions of heterogeneous cell populations responding to treatment. The potential of this approach is obvious—it enables us to systematically investigate hypotheses and test alternative options for treatment. While mathematical models and pre-clinical studies of optimized treatment schedules are encouraging, limitations of the approach are also plentiful, as illustrated by the

lack of resolution regarding the efficacy of alternating versus sequential treatments discussed above. The predictive utility of a model parameterized using a particular pre-clinical model depends on the accuracy not only of the mathematical model, but also the in vitro or in vivo model vis a vis the human cancer that it models, as well as the biological assumptions and quality of the data. The ability of the modeling predictions to be verified or falsified—not just in a model system, but eventually in a clinical study—is the essential test. In addition, knowledge is evolving: more complex aspects of tumor biology are emerging and need to be incorporated into quantitative modeling approaches. These include single-cell genetic and epigenetic heterogeneity (Van Loo and Voet, 2014) and interactions between cancer cells and the immune system (Sharma et al., 2011) as well as the microenvironment. The analysis of datasets that comprehensively and quantitatively capture such features may require novel mathematical approaches and simulation tools that, for instance, can take advantage of today's most powerful supercomputers.

Importantly, translation of these concepts and ideal models into a clinical setting presents both logistical and patient-specific challenges related to the tumor micro-environment. It is always difficult to translate a result from a cell line or animal model into a human clinical study; while there are logistical concerns related to administering any type of cancer-related treatment, we will discuss the complexities of treating brain tumor patients with radiation as a specific example. The first challenge regarding scheduling altered or “optimized” scheduled radiation, for instance, as proposed in Leder et al. (2014), reflects the process of treating patients at a specific time each day. There are staffing concerns with respect to hours of operation and coordination of scheduling multiple patients throughout the day on each linear accelerator. There is also the potential of treatment- or tumor-related toxicity that may fluctuate daily and may affect whether or not patients can tolerate treatment at very specific time(s) each day. Most patients are also fatigued and may have neurologic symptoms related to their brain tumors or treatment, which makes it difficult to adhere to a complicated or specific timing schedule. With careful patient selection and consideration of scheduling constraints, though, these challenges may be overcome. The observation of variable tumor volume among patients reflects the fact that there is great variability among patients with the extent of their brain tumor resection related to the location of their tumors in different regions of the brain and the original extent of the tumor. A patient who has a gross total resection with only microscopic residual disease may have a very different response to an altered or optimized treatment schedule than a patient who has a large, relatively intact tumor. The potential variability of tumor volume between brain tumor patients is much greater than in the breast cancer studies referred to above. This variability could certainly affect the outcome of an optimized radiation schedule clinical trial.

Other challenges are related to variability in the tumor micro-environment that may be the result of molecular differences among patients' tumors or even more simply the wide range of medications, or chemotherapy, that brain tumor patients often require as part of the management of their brain tumors. These medications may alter the cancer cells' sensitivity to radiation

or may change the vascular environment and thus indirectly affect sensitivity to radiation. Even if a study were designed that controlled for the use of common medications for brain tumor patients, such as corticosteroids, antiepileptics, or temozolamide, the requirements of some medications are likely to change during the course of radiation, or patients may discontinue some medications in the midst of their course of radiation due to toxicity. There are innumerable possibilities of drug combinations during radiation therapy for brain tumors that could both positively and negatively impact the effect of radiation. The exact schedule of those standard adjuvant chemotherapies, or perhaps investigational immunotherapies, may also alter the radiosensitivity, or clonal expansion, possibilities at any given moment. A fully optimized model would need to incorporate those possible influences as well.

Despite these challenges in designing and effectively executing a clinical trial to test treatment regimes derived from mathematical modeling and preclinical data, the endeavor should be pursued. The results with the current standard treatment are suboptimal, with a median survival of only 15 months for patients with primary glioblastoma, the most common type of malignant brain tumor. However, following surgery, radiation remains the most effective therapy for glioblastoma, and thus optimizing the effect of radiation remains an attractive option. Historically there have been many studies of various schedules of radiation for glioblastomas, including dose escalation, but the results from all are disappointing to date (Brada et al., 1999; Horiot et al., 1988; W.J. Curran et al., 1996, Proc. Am. Soc. Clin. Oncology, abstract). Notably, none of these studies have been based upon a mathematically optimized schedule. A hypothesis worth testing is that a clinical trial of a mathematically optimized radiation schedule could yield an improved result and could identify altered radiation scheduling as an opportunity for improved outcomes in other types of brain tumors or other cancer types.

Despite the logistical, tumor-, and patient-specific challenges listed above, a trial of an optimized radiation schedule is an achievable goal with careful patient selection, patient management, and support from all of the stakeholders, including clinicians, scientists, and the patients and their families. The glioblastoma mouse model study comparing a standard schedule to an optimized schedule (Leder et al., 2014) proves the concept that an altered radiation schedule can affect survival. This theory must be tested in humans with glioblastoma, as these patients need every opportunity possible to improve their outcome.

Despite the operational, biological, and mathematical obstacles that need to be overcome for successful implementation of a mathematically predicted treatment strategy in the clinic, we strongly believe that surmounting these challenges is worth the effort. The Norton-Simon hypothesis was the first demonstration that a mathematically derived schedule might be clinically superior, but many recent and forthcoming approaches hold great promise, and we have high expectations that rational quantitative investigations might contribute to new hope for cancer patients.

REFERENCES

- Anderson, K., Lutz, C., van Delft, F.W., Bateman, C.M., Guo, Y., Colman, S.M., Kempski, H., Moorman, A.V., Titley, I., Swansbury, J., et al. (2011). Genetic variegation of clonal architecture and propagating cells in leukaemia. *Nature* 469, 356–361.
- Basanta, D., Gatenby, R.A., and Anderson, A.R. (2012). Exploiting evolution to treat drug resistance: combination therapy and the double bind. *Mol. Pharm.* 9, 914–921.
- Bellon, J.R., Come, S.E., Gelman, R.S., Henderson, I.C., Shulman, L.N., Silver, B.J., Harris, J.R., and Recht, A. (2005). Sequencing of chemotherapy and radiation therapy in early-stage breast cancer: updated results of a prospective randomized trial. *J. Clin. Oncol.* 23, 1934–1940.
- Bhang, H.E., Ruddy, D.A., Krishnamurthy Radhakrishna, V., Caushi, J.X., Zhao, R., Hims, M.M., Singh, A.P., Kao, I., Rakiec, D., Shaw, P., et al. (2015). Studying clonal dynamics in response to cancer therapy using high-complexity barcoding. *Nat. Med.* 21, 440–448.
- Bonadonna, G., Zambetti, M., and Valagussa, P. (1995). Sequential or alternating doxorubicin and CMF regimens in breast cancer with more than three positive nodes. Ten-year results. *JAMA* 273, 542–547.
- Bozic, I., Reiter, J.G., Allen, B., Antal, T., Chatterjee, K., Shah, P., Moon, Y.S., Yaqubie, A., Kelly, N., Le, D.T., et al. (2013). Evolutionary dynamics of cancer in response to targeted combination therapy. *eLife* 2, e00747.
- Brada, M., Sharpe, G., Rajan, B., Britton, J., Wilkins, P.R., Guerrero, D., Hines, F., Traish, D., and Ashley, S. (1999). Modifying radical radiotherapy in high grade gliomas: shortening the treatment time through acceleration. *Int. J. Radiat. Oncol. Biol. Phys.* 43, 287–292.
- Burrell, R.A., McGranahan, N., Bartek, J., and Swanton, C. (2013). The causes and consequences of genetic heterogeneity in cancer evolution. *Nature* 501, 338–345.
- Chmielecki, J., Foo, J., Oxnard, G.R., Hutchinson, K., Ohashi, K., Somwar, R., Wang, L., Amato, K.R., Arcila, M., Sos, M.L., et al. (2011). Optimization of dosing for EGFR-mutant non-small cell lung cancer with evolutionary cancer modeling. *Sci. Transl. Med.* 3, 90ra59.
- Citron, M.L., Berry, D.A., Cirrincione, C., Hudis, C., Winer, E.P., Gradowitz, W.J., Davidson, N.E., Martino, S., Livingston, R., Ingle, J.N., et al. (2003). Randomized trial of dose-dense versus conventionally scheduled and sequential versus concurrent combination chemotherapy as postoperative adjuvant treatment of node-positive primary breast cancer: first report of Intergroup Trial C9741/Cancer and Leukemia Group B Trial 9741. *J. Clin. Oncol.* 21, 1431–1439.
- Coldman, A.J., and Murray, J.M. (2000). Optimal control for a stochastic model of cancer chemotherapy. *Math. Biosci.* 168, 187–200.
- Costa, M.I., Boldrini, J.L., and Bassanezi, R.C. (1992). Optimal chemical control of populations developing drug resistance. *IMA J. Math. Appl. Med. Biol.* 9, 215–226.
- Costa, M.I., Boldrini, J.L., and Bassanezi, R.C. (1995). Drug kinetics and drug resistance in optimal chemotherapy. *Math. Biosci.* 125, 191–209.
- Ding, L., Ley, T.J., Larson, D.E., Miller, C.A., Koboldt, D.C., Welch, J.S., Ritchey, J.K., Young, M.A., Lamprecht, T., McLellan, M.D., et al. (2012). Clonal evolution in relapsed acute myeloid leukaemia revealed by whole-genome sequencing. *Nature* 481, 506–510.
- Gatenby, R.A., Silva, A.S., Gillies, R.J., and Frieden, B.R. (2009). Adaptive therapy. *Cancer Res.* 69, 4894–4903.
- Gerlinger, M., Rowan, A.J., Horswell, S., Larkin, J., Endesfelder, D., Gronroos, E., Martinez, P., Matthews, N., Stewart, A., Tarpey, P., et al. (2012). Intratumor heterogeneity and branched evolution revealed by multiregion sequencing. *N. Engl. J. Med.* 366, 883–892.
- Glickman, M.S., and Sawyers, C.L. (2012). Converting cancer therapies into cures: lessons from infectious diseases. *Cell* 148, 1089–1098.
- Goldie, J.H., and Coldman, A.J. (1979). A mathematic model for relating the drug sensitivity of tumors to their spontaneous mutation rate. *Cancer Treat. Rep.* 63, 1727–1733.
- Goldie, J.H., Coldman, A.J., and Gudauskas, G.A. (1982). Rationale for the use of altering non-cross-resistant chemotherapy. *Cancer Treat. Rep.* 66, 439–449.

- Gottesman, M.M., Fojo, T., and Bates, S.E. (2002). Multidrug resistance in cancer: role of ATP-dependent transporters. *Nat. Rev. Cancer* 2, 48–58.
- Haeno, H., Gonen, M., Davis, M.B., Herman, J.M., Iacobuzio-Donahue, C.A., and Michor, F. (2012). Computational modeling of pancreatic cancer reveals kinetics of metastasis suggesting optimum treatment strategies. *Cell* 148, 362–375.
- Hickey, B.E., Francis, D.P., and Lehman, M. (2013). Sequencing of chemotherapy and radiotherapy for early breast cancer. *Cochrane Database Syst. Rev.* 4, CD005212.
- Holohan, C., Van Schaeybroeck, S., Longley, D.B., and Johnston, P.G. (2013). Cancer drug resistance: an evolving paradigm. *Nat. Rev. Cancer* 13, 714–726.
- Horiot, J.C., van den Bogaert, W., Ang, K.K., Van der Schueren, E., Bartelink, H., Gonzalez, D., de Pauw, M., and van Glabbeke, M. (1988). European Organization for Research on Treatment of Cancer trials using radiotherapy with multiple fractions per day. A 1978–1987 survey. *Front. Radiat. Ther. Oncol.* 22, 149–161.
- Hryniuk, W. (2001). Dosage parameters in chemotherapy of breast cancer. *Breast Dis.* 14, 21–30.
- Katouli, A.A., and Komarova, N.L. (2011). The worst drug rule revisited: mathematical modeling of cyclic cancer treatments. *Bull. Math. Biol.* 73, 549–584.
- Kimmel, M., and Swierniak, A. (2006). Control theory approach to cancer chemotherapy: Benefiting from phase dependence and overcoming drug resistance. In *Tutorials in Mathematical Biosciences III*, A. Friedman, ed. (Springer), pp. 185–221.
- Lake, D.E., and Hudis, C.A. (2004). High-dose chemotherapy in breast cancer. *Drugs* 64, 1851–1860.
- Landau, D.A., Carter, S.L., Stojanov, P., McKenna, A., Stevenson, K., Lawrence, M.S., Sougnez, C., Stewart, C., Sivachenko, A., Wang, L., et al. (2013). Evolution and impact of subclonal mutations in chronic lymphocytic leukemia. *Cell* 152, 714–726.
- Leder, K., Pitter, K., Laplant, Q., Hambarzumyan, D., Ross, B.D., Chan, T.A., Holland, E.C., and Michor, F. (2014). Mathematical modeling of PDGF-driven glioblastoma reveals optimized radiation dosing schedules. *Cell* 156, 603–616.
- Ledzewicz, U., and Schattler, H. (2009). On the optimality of singular controls for a class of mathematical models for tumor anti-angiogenesis. *Discrete Continuous Dyn. Syst. Ser. B* 11, 691–715.
- Martin, R.B., and Teo, K.L. (1993). Optimal Control of Drug Administration in Cancer Chemotherapy (World Scientific Pub Co Inc).
- Martin, R.B., Fisher, M.E., Minchin, R.F., and Teo, K.L. (1992). Optimal control of tumor size used to maximize survival time when cells are resistant to chemotherapy. *Math. Biosci.* 110, 201–219.
- Murray, J.M., and Coldman, A.J. (2003). The effect of heterogeneity on optimal regimens in cancer chemotherapy. *Math. Biosci.* 185, 73–87.
- Norton, L., and Simon, R. (1977). Tumor size, sensitivity to therapy, and design of treatment schedules. *Cancer Treat. Rep.* 61, 1307–1317.
- Pao, W., Miller, V.A., Politi, K.A., Riely, G.J., Somwar, R., Zakowski, M.F., Kris, M.G., and Varmus, H. (2005). Acquired resistance of lung adenocarcinomas to gefitinib or erlotinib is associated with a second mutation in the EGFR kinase domain. *PLoS Med.* 2, e73.
- Paridaens, R., Van Aelst, F., Georgoulia, V., Samonigg, H., Cocquyt, V., Zielinski, C., Hausmaninger, H., Willemse, P., Boudraa, Y., Wildiers, J., et al. (2003). A randomized phase II study of alternating and sequential regimens of docetaxel and doxorubicin as first-line chemotherapy for metastatic breast cancer. *Ann. Oncol.* 14, 433–440.
- Recht, A., Come, S.E., Henderson, I.C., Gelman, R.S., Silver, B., Hayes, D.F., Shulman, L.N., and Harris, J.R. (1996). The sequencing of chemotherapy and radiation therapy after conservative surgery for early-stage breast cancer. *N. Engl. J. Med.* 334, 1356–1361.
- Sawyers, C. (2004). Targeted cancer therapy. *Nature* 432, 294–297.
- Sharma, P., Wagner, K., Wolchok, J.D., and Allison, J.P. (2011). Novel cancer immunotherapy agents with survival benefit: recent successes and next steps. *Nat. Rev. Cancer* 11, 805–812.
- Shrager, J., and Tenerbaum, J.M. (2014). Rapid learning for precision oncology. *Nat. Rev. Clin. Oncol.* 11, 109–118.
- Stiehl, T., Baran, N., Ho, A.D., and Marciniak-Czochra, A. (2015). Cell division patterns in acute myeloid leukemia stem-like cells determine clinical course: a model to predict patient survival. *Cancer Res.* 75, 940–949.
- Van Loo, P., and Voet, T. (2014). Single cell analysis of cancer genomes. *Curr. Opin. Genet. Dev.* 24, 82–91.
- Zhao, B., Hemann, M.T., and Lauffenburger, D.A. (2014). Intratumor heterogeneity alters most effective drugs in designed combinations. *Proc. Natl. Acad. Sci. USA* 111, 10773–10778.

Establishment and Dysfunction of the Blood-Brain Barrier

Zhen Zhao,¹ Amy R. Nelson,¹ Christer Betsholtz,² and Berislav V. Zlokovic^{1,*}

¹Department of Physiology and Biophysics and the Zilkha Neurogenetic Institute, Keck School of Medicine of the University of Southern California, Los Angeles, CA 90089, USA

²Department of Immunology, Genetics, and Pathology, Rudbeck Laboratory, 75185 Uppsala, Sweden

*Correspondence: zlokovic@usc.edu

<http://dx.doi.org/10.1016/j.cell.2015.10.067>

Structural and functional brain connectivity, synaptic activity, and information processing require highly coordinated signal transduction between different cell types within the neurovascular unit and intact blood-brain barrier (BBB) functions. Here, we examine the mechanisms regulating the formation and maintenance of the BBB and functions of BBB-associated cell types. Furthermore, we discuss the growing evidence associating BBB breakdown with the pathogenesis of inherited monogenic neurological disorders and complex multifactorial diseases, including Alzheimer's disease.

Introduction

Blood vessels in the brain are organized with surprising precision, supporting the major brain circuits tasked with sensation, memory, and motion (Andreone et al., 2015; Blinder et al., 2013; Zlokovic, 2011). Proper structural and functional brain connectivity, synaptic activity, and information processing all require precise regulation of cerebral blood flow (CBF), oxygen delivery, and energy metabolite supply (Attwell et al., 2010; Iadecola, 2013). These key central nervous system (CNS) functions are maintained by the highly coordinated activity of multiple cell types within the neurovascular unit (NVU), including vascular cells (endothelial cells, pericytes, smooth muscle cells), glia (astrocytes, oligodendroglia, microglia), and neurons (Figure 1) (Zlokovic, 2011).

Within the NVU, the endothelial cells form the blood-brain barrier (BBB) that limits entry of potentially neurotoxic plasma components, blood cells, and pathogens into the brain (Winkler et al., 2011). Importantly, these endothelial cells express multiple substrate-specific transport systems that control transport of nutrients, energy metabolites, and other essential molecules from blood into the brain and the transport of metabolic waste products from the brain's interstitial fluid (ISF) into the blood. The meningeal lymphatic vessels contain cerebrospinal fluid (CSF) and immune cells and drain into the deep cervical lymph nodes (Aspelund et al., 2015; Louveau et al., 2015). Thus, the BBB serves as a key homeostatic site of the nervous system, connecting CNS, systemic circulation, and major systems in the body such as respiratory, renal, hepatic, and immune systems.

In this Perspective, first we examine the cellular and molecular mechanisms regulating the formation and maintenance of the BBB. We then look into how major NVU cell types contribute to BBB functions and how molecular alterations and aberrant signal transduction within the NVU leads to BBB breakdown that is associated with secondary neuronal injury and neurodegeneration. In particular, we discuss the role of NVU and BBB breakdown in the etiology and pathogenesis of inherited mono-

genic neurological disorders and complex neurodegenerative disorders such as Alzheimer's disease (AD). Finally, we discuss key questions in the field for future investigation.

BBB Development

Different stages of BBB formation are illustrated in Figure 2A. The neural microenvironment provides initial cues for CNS angiogenesis and induction of the BBB properties (Obermeier et al., 2013). At embryonic day E10 in mice, the angioblasts of the perineurial vascular plexus penetrate the neuroectoderm guided by neuro-ectoderm-secreted vascular endothelial growth factor (VEGF), which results in formation of the nascent "leaky" blood vessels (Potente et al., 2011). Wnt ligands secreted by neural cells elicit canonical Wnt signaling in the endothelium by binding to the Frizzled receptors (Wang et al., 2012b) and the co-receptors low-density lipoprotein receptor-related protein (LRP) 5 and 6, which in turn activates β -catenin-dependent pathways (Daneman et al., 2009; Liebner et al., 2008; Zhou et al., 2014) (Figure 2B). Activation of Wnt/ β -catenin signaling leads to induction of genes critical for the BBB formation, such as glucose transporter Glut1 (Stenman et al., 2008) and death receptors DR6 and TROY (Tam et al., 2012). In addition, an orphan G-protein-coupled receptor, Gpr124, acts as a specific co-activator of Wnt/ β -catenin signaling at the BBB (Kuhnert et al., 2010; Zhou and Nathans, 2014).

The primitive BBB is formed at embryonic day E15 in mice (Ben-Zvi et al., 2014; Daneman et al., 2010), but the exact timing is species dependent and varies regionally. It is debatable, whether humans and/or other mammals are born with a fully functional BBB (Saunders et al., 2013). Recruitment of pericytes to the developing endothelial capillary wall is critical for the formation and maintenance of the BBB (Armulik et al., 2010; Bell et al., 2010; Daneman et al., 2010). While some pathways have been implicated, it remains unclear exactly which signals are involved in the pericyte-mediated induction and regulation of the BBB (Figure 2B). Astrocytes recruited at a later stage further

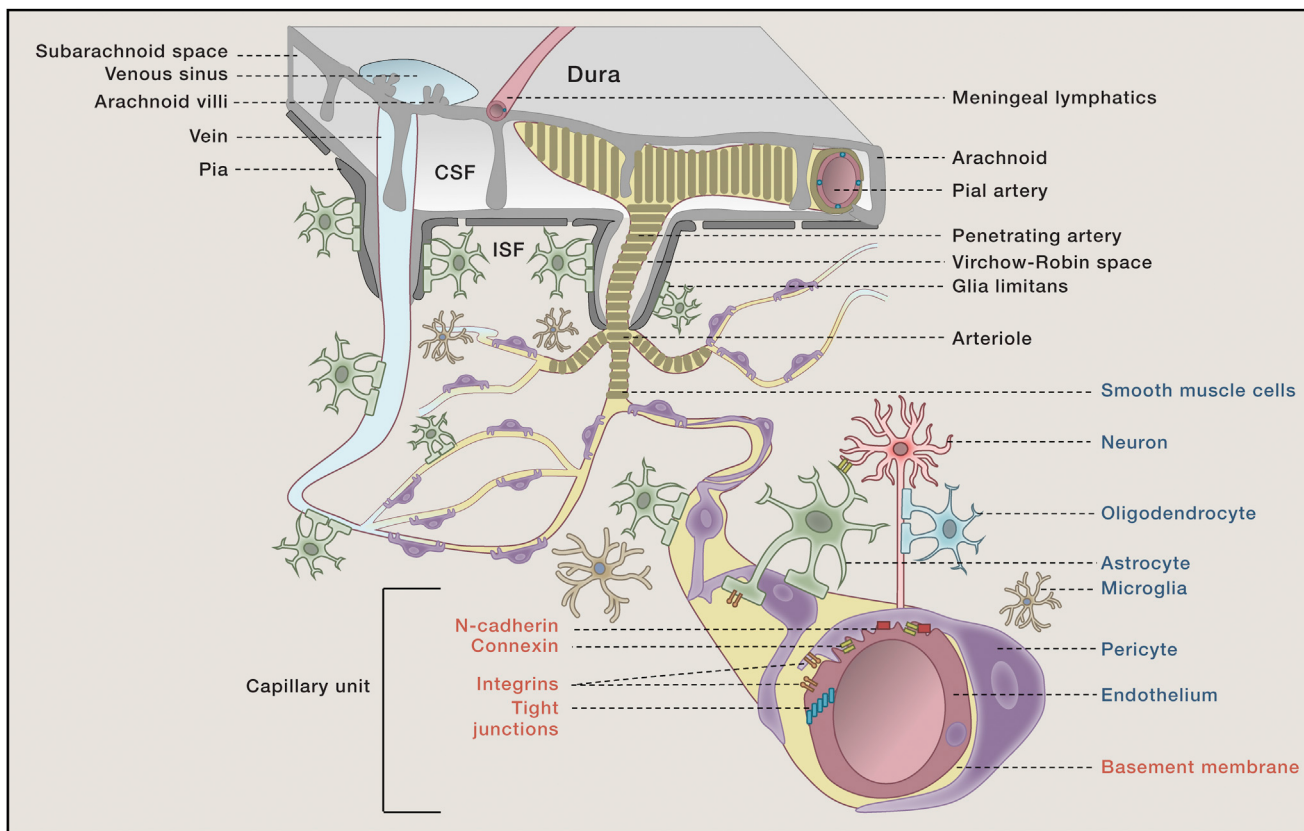


Figure 1. Neurovascular Unit

Vessels in the subarachnoid space. The subarachnoid space contains cerebrospinal fluid (CSF) that drains via arachnoid villi into the venous sinuses. Cerebral arteries branch into smaller pial arteries. Cerebral veins empty into dural venous sinuses. Meningeal lymphatic vessels carry CSF and immune cells to deep cervical lymph nodes. *Intracerebral vessels*. Pial arteries give rise to the penetrating arteries that branch into arterioles all covered by vascular smooth muscle cells (blue). The penetrating arteries are separated from brain parenchyma by the glia limitans, an astrocytic endfeet layer that forms the outer wall of the Virchow-Robin spaces containing brain interstitial fluid (ISF). Arterioles branch off into capillaries, and the vessels enlarge as they become venules and veins. *Brain capillary unit*. Endothelial cells (red) connected by tight junctions form the blood-brain barrier. Pericytes (purple) and endothelium share a common basement membrane (yellow) and connect with each other with several transmembrane junctional proteins, including N-cadherin and connexins. Astrocytes (green) connect with pericytes, endothelial cells, and neurons (peach). Microglia (brown) regulate immune responses. Oligodendrocytes (aqua) support neurons with axonal myelin sheath. Integrins make connections between cellular and matrix components.

assist endothelium in acquiring BBB characteristics, barrier properties, and CNS immune quiescence (Alvarez et al., 2011) (Figure 2B).

The BBB functions continue to mature after birth, but the exact time window remains elusive and is likely species dependent (Hagan and Ben-Zvi, 2015; Saunders et al., 2013). At a mature stage, the mammalian BBB is stabilized by highly specialized perivascular structures (Figure 2C).

Cellular Components of the BBB

Endothelial Cells and Cellular Junctions

A number of factors contribute to the physical barrier of BBB, including endothelial tight junction (TJ) and adherens junction (AJ) proteins, inhibition of non-selective fenestrae, pinocytosis, and bulk-flow transcytosis, as well as suppression of leukocyte adhesion molecules (Obermeier et al., 2013). Endothelium allows rapid free diffusion of oxygen from blood to brain and carbon dioxide from brain to blood, which is essential for normal brain metabolism and regulation of pH in the brain ISF, neurons, and

other NVU cells. Small lipophilic molecules and drugs, with a molecular weight of <400 Da and form of <8 hydrogen bonds, can cross the BBB (Pardridge, 2015).

The major endothelial transport systems and cellular junction molecules are briefly discussed below and are described in detail elsewhere (Daneman and Prat, 2015; Hagan and Ben-Zvi, 2015; Tietz and Engelhardt, 2015; Zlokovic, 2008, 2011). A preliminary molecular atlas of the BBB based on manual collection of available data on protein and RNA expression, as well as physiological measurements from different published investigations, is provided in Table 1. It is noteworthy that some of the listed components are not confirmed in recent RNA-seq data (see, e.g., http://web.stanford.edu/group/barres_lab/brain_rnaseq.html). Since expression may be species, strain, disease, or context dependent, we provide Table 1 as an all-inclusive data source and encourage the readers to explore and critically examine the specifics in existing literature.

Active Efflux. Multiple ATP-binding cassette (ABC) proteins are expressed on the luminal, blood-facing endothelial plasma

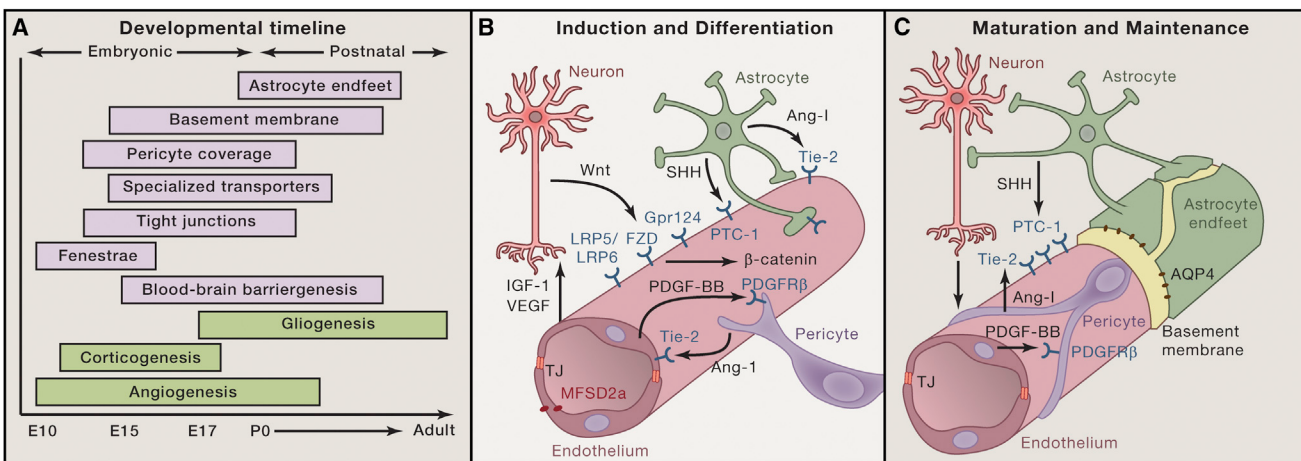


Figure 2. Blood-Brain Barrier Development in the Murine Central Nervous System

(A) Developmental timeline. Restriction of paracellular and transcellular transport of solutes is accomplished by elimination of endothelial fenestrae and pinocytosis, formation of a continuous endothelial monolayer connected with the tight junctions, creation of highly selective endothelial transport systems, and establishment of specialized perivascular structures, including the basement membrane and the coverage of the endothelial capillary wall by pericytes and astrocytic endfeet. E, embryonic days; P, postnatal days.

(B) Induction and differentiation. Wnt ligands (*Wnt7a/7b*) secreted by neural cells bind to endothelial Frizzled receptors (FZD) and the co-receptors low-density lipoprotein receptor-related protein (LRP) 5 and 6, which activate β-catenin signaling, leading to the induction of BBB specific genes. G protein coupled receptor 124 (Gpr124) co-activates Wnt/β-catenin signaling. Endothelial cells secrete platelet-derived growth factor BB (PDGF-BB), which interacts with platelet derived growth factor receptor-β (PDGFR-β) in pericytes, inducing pericyte recruitment. Pericytes and astrocytes secrete angiopoietin-1 (Ang-1) that acts on endothelial Tie-2 receptor leading to microvascular maturation and highly stable and impermeable BBB. Pericytes are required for the expression of endothelial major facilitator superfamily domain-containing protein 2a (MFSD2a) that is critical for the BBB formation and maintenance. Astrocytes secrete sonic hedgehog (SHH) that acts on endothelial patched homolog 1 (PTC-1) receptor eliciting signaling which contributes to the BBB formation. Endothelial cells secrete vascular growth factor (VEGF) and insulin growth factor (IGF-1) contributing to proper neurovascular patterning. Additional signal transduction pathways may also participate in BBB formation. TJ, tight junction.

(C) Maturation and maintenance. Postnatally, brain capillaries are covered by mature pericytes sharing the basement membrane with endothelium. Astrocytic endfeet form the outer layer of the mature capillaries. Pericytes and astrocytes continue secreting matrix proteins (yellow) of the basement membrane. Signaling pathways mediating BBB induction and differentiation likely continue to play a role in BBB maturation and maintenance and their dysregulation may lead to BBB breakdown causing different central nervous system pathologies. AQP4, aquaporin-4 water channel.

membrane of the BBB, which restricts the permeability of a large number of toxins, including therapeutic agents (Miller, 2015). ABC transporters are ATP-driven efflux pumps for xenobiotics and endogenous metabolites. Their high expression at the BBB contributes to CNS pharmacoresistance (Table 1). Decreased expression and/or functional activity of ABC BBB transporters were reported in patients with Alzheimer's disease (AD) and Parkinson's disease (PD) (Zlokovic, 2011) and were shown to lead to accumulation of amyloid β-peptide (Aβ) in the brain in an animal model of AD (Cirrito et al., 2005). The clinical potential of targeting ABC transporters for disease management and drug delivery improvement, however, remains elusive.

Carrier-Mediated Transport (CMT). CMT systems are expressed by genes within the solute carrier (SLC) transporter gene family, including >300 transporter genes encoding membrane-bound proteins that facilitate the transport of a wide array of substrates across biological membranes (Lin et al., 2015). At the BBB, the SLC proteins facilitate the trans-cellular transport of a variety of molecules, including carbohydrates, amino acids, monocarboxylic acids, hormones, fatty acids, nucleotides, organic anions, amines, choline, and vitamins (Table 1) (Daneman and Prat, 2015; Pardridge, 2015; Zlokovic, 2008). Human genetic studies have provided important insight into the roles of the more recently characterized SLC transporters in both rare and common diseases. As discussed below, genetic

alterations in brain endothelial SLC2A1 (Glut1) that transports glucose into the brain and maintains the BBB integrity (Winkler et al., 2015) and in SLC16A2 that transports T3 thyroid hormone into the brain have been implicated in the development of neurological disorders (Benarroch, 2014; Kersseboom et al., 2013). Screening for BBB-penetrating small molecules that can use the existing CMT systems at the BBB as surrogate ligands have been recently proposed as a new model for CNS discovery programs (Pardridge, 2015).

Receptor-Mediated Transport (RMT). Peptide bonds prevent larger peptides and proteins from using the amino acid CMT systems to cross the BBB (Zlokovic et al., 1985). However, certain neuroactive peptides (Zlokovic, 1995), regulatory proteins, hormones, and growth factors can use RMT systems to slowly cross the BBB (Pardridge, 2015; Zlokovic, 2008) (Table 1). For example, Aβ can cross the BBB to enter the circulation through LRP1 (Deane et al., 2004) or the other way around via the receptor for advanced glycation end products (RAGE) on RAGE-expressing endothelium, particularly under pathological conditions (Deane et al., 2003, 2012). Moreover, RMT systems—for example, the transferrin receptor (TfR)—have been utilized for the CNS drug delivery (Bray, 2015).

Major Facilitator Superfamily. Docosahexaenoic acid (DHA), an essential omega-3 fatty acid, is transported into the brain by the endothelial major facilitator superfamily domain-containing

Table 1. Molecular Atlas of the Blood-Brain Barrier: Transport Systems and Cellular Junctions

Transport Systems	Transporters	Abbreviation	Gene Name	Substrates	Direction of Transport
Active efflux	ABC transporters	MDR1/P-gp	<i>ABCB1</i>	Drugs, xenobiotics	Endothelium to blood
		ABCA2	<i>ABCA2</i>	—	
		BCRP	<i>ABCG2</i>	Drugs, xenobiotics	
		MRP1	<i>ABCC1</i>	Drugs, drug conjugates	
		MRP2	<i>ABCC2</i>		
		MRP3	<i>ABCC3</i>		
		MRP4	<i>ABCC4</i>	Nucleosides	Bidirectional
		MRP5	<i>ABCC5</i>		Endothelium to blood
Solute carrier-mediated transport	Carbohydrate transporters	GLUT1	<i>SLC2A1</i>	Glucose	Bidirectional
		SGLT1	<i>SLC5A1</i>		Blood to brain
		HMIT	<i>SLC2A13</i>	Myoinositol	Blood to brain
		SMIT	<i>SLC5A3</i>		
	Amino acid transporters	CAT1	<i>SLC7A1</i>	Cationic L-amino acids (y+) (e.g., lysine, arginine)	Bidirectional
		CAT3	<i>SLC7A3</i>		
		LAT1	<i>SLC7A5</i>	Large neutral amino acids (L) (e.g., tryptophan, tyrosine)	Bidirectional
		LAT2	<i>SLC7A6</i>		
		SNAT1	<i>SLC38A1</i>	Glutamine and small neutral amino acids (A)	Brain to blood
		SNAT2	<i>SLC38A2</i>		
		SNAT 3	<i>SLC38A3</i>	Glutamine (N)	
		SNAT 5	<i>SLC38A5</i>		Bidirectional
		ASCT1	<i>SLC1A4</i>	Neutral amino acids (ASC)	Brain to blood
		ASCT2	<i>SLC1A5</i>		
Monocarboxylic acid transporter	EAAT1	EAAT1	<i>SLC1A3</i>	Excitatory amino acids (EAAT) (e.g., glutamate, aspartate)	
		EAAT2	<i>SLC1A2</i>		
	EAAT3	EAAT3	<i>SLC1A1</i>		
		GLYT1	<i>SLC6A9</i>	Glycine	
	Hormone transporter	TAUT	<i>SLC6A6</i>	Taurine, GABA	
		MCT1	<i>SLC16A1</i>	Lactate, ketone bodies	Bidirectional
	Fatty acids	MCT2	<i>SLC16A7</i>	Lactate (proton exchanger)	Brain to blood
		MCT8	<i>SLC16A2</i>	T3 thyroid hormone	Blood to brain
Nucleotide transporters	FATP-1	FATP-1	<i>SLC27A1</i>	Fatty acids	Blood to brain
		FATP-4	<i>SLC27A4</i>		
	Organic anion and cation transporters	CNT2	<i>SLC28A2</i>	Nucleotides, nucleobases	Brain to blood
		ENT1	<i>SLC29A1</i>		Bidirectional
		ENT2	<i>SLC29A2</i>		
	Amine transporter	OAT3	<i>SLC22A8</i>	Organic anions (e.g., indoxyl sulfate, benzylpenicillin aminohippuric acid)	Brain to blood
		OATP1A4	<i>SLCO1A4</i>		Bidirectional
		OATP2B1	<i>SLCO2B1</i>		
		OATP1C1	<i>SLCO1C1</i>	Thyroxine	
		OCT1	<i>SLC22A1</i>	Organic cations (e.g., morphine, MPTP, creatinine)	Blood to brain
		OCT2	<i>SLC22A2</i>		
		OCT3	<i>SLC22A3</i>		
Choline transporter	Vitamin transporters	OCTN2	<i>SLC22A5</i>	Organic cations, carnitine	Bidirectional
		PMAT	<i>SLC29A4</i>	Organic cations, MPP+	Brain to blood
		CTL1	<i>SLC44A1</i>	Choline	Bidirectional
	SMVT	<i>SLC5A6</i>	Multivitamins	Blood to brain	

(Continued on next page)

Table 1. Continued

Transport Systems	Transporters	Abbreviation	Gene Name	Substrates	Direction of Transport
Receptor-mediated transport	Protein ligands	V1	<i>AVPR1A</i>	Arginine-vasopressin	Bidirectional
		TfR	<i>TFRC, TFR2</i>	Transferrin	Blood to brain
		LEP-R	<i>LEPR</i>	Leptin	
		IR	<i>INSR</i>	Insulin	
		LRP1	<i>LRP1</i>	Apolipoproteins, amyloid- β , etc.	Brain to blood
		LRP2	<i>LRP2</i>		
		RAGE	<i>AGER</i>	Glycosylated proteins, A β , S-100, etc.	Blood to brain
Major facilitators	Fatty acids	MFSD2a	<i>MFSD2a</i>	Docosahexaenoic acid	Blood to brain
Cellular Junctions	Components	Abbreviation	Genes	Functions	
Tight junctions	Occludin	Occludin	<i>OCLN</i>	Not required for TJ formation	
	Claudins	Claudin-1	<i>CLDN1</i>	Sealing BBB	
		Claudin-3	<i>CLDN3</i>	Unknown	
		Claudin-5	<i>CLDN5</i>	Size-selective barrier to small molecules (< 800 D)	
		Claudin-12	<i>CLDN12</i>	Unknown	
	Membrane-associated guanylate kinases	ZO-1	<i>TJP1</i>	Multi-domain scaffolding proteins, cytoskeleton anchorage for TJ proteins	
		ZO-2	<i>TJP2</i>		
		ZO-3	<i>TJP3</i>		
Adherens junctions	Adherens junctions	Cadherins	<i>CDH5</i>	Cytoskeleton link, modulating receptor signaling, regulating trans-endothelial migration of lymphocytes	
Other junctional molecules	JAMs	PECAM-1	<i>PECAM1</i>		
		JAM-A	<i>F11R</i>	Modulating junctional tightness, regulating trans-endothelial migration of lymphocytes	
		JAM-B	<i>JAM2</i>		
	JAM-C	<i>JAM3</i>			
	ESAM	ESAM	<i>ESAM</i>		
Gap junctions	Connexin hemichannels	CX30	<i>GJB6</i>	Cell-cell communication, required for BBB	
		CX43	<i>GJA1</i>		
Cytoskeleton	Dystrophin	Dystrophin	<i>DMD</i>	Organization of actin cytoskeleton	

protein 2a (MFSD2a) (Nguyen et al., 2014). Mice lacking *Mfsd2a* show brain DHA deficits and develop BBB breakdown (Ben-Zvi et al., 2014), suggesting that MFSD2a has the dual function of transporting fatty acids into the brain and maintaining BBB integrity (Betsholtz, 2014; Zhao and Zlokovic, 2014).

TJ proteins seal brain endothelia, contributing to the anatomical barrier (Table 1). Mutations in and loss of some TJ proteins lead to BBB breakdown and are associated with neurological disorders, as discussed below (Tietz and Engelhardt, 2015; Zlokovic, 2008). TJ proteins are connected to cortical actin cytoskeleton via multi-domain scaffolding proteins of the peripheral membrane-associated guanylate kinase (MAGUK) family, i.e., ZO-1, ZO-2, and ZO-3 (Tietz and Engelhardt, 2015). ZO-1 deficiency disrupts TJs, and reduced ZO-1 levels are associated with BBB breakdown in many neurological disorders (Zlokovic, 2011) (Figure 3). AJ proteins such as cadherins and platelet endothelial cell adhesion molecule-1 also contribute to barrier properties, and the space between these proteins is ~20 nm, which is wider compared to that between TJs (Tietz and Engelhardt, 2015) (Table 1; Figure 3). Brain endothelial cells are anchored to the basement membrane through integrins, which interact with extracellular matrix (ECM) proteins, such as laminin, collagen, and perlecan, and mediate signaling by activating ECM

ligands, growth factors, and growth factor receptors (Baeten and Akassoglou, 2011). Mice lacking β 1-integrins in endothelial cells develop aberrant cadherin signaling, loss of junctional claudin-5, and immature BBB (Yamamoto et al., 2015). Similarly, mice lacking astrocyte-secreted laminin exhibit BBB breakdown (Yao et al., 2014).

Pericytes

Pericytes share a basement membrane with endothelial cells and form direct synaptic-like peg-socket focal contacts with endothelium through N-cadherin and connexins, allowing exchanges of ions, metabolites, second messengers, and ribonucleic acids between the two cell types (Armulik et al., 2011). Pericytes play important roles in maintaining BBB integrity, aiding in angiogenesis and microvascular stability (Armulik et al., 2011; Winkler et al., 2011), regulating capillary diameter and CBF (Hall et al., 2014; Peppiatt et al., 2006), and phagocytosing toxic metabolites (Sagare et al., 2013). They have also been reported to have multipotent stem cell capabilities (Nakagomi et al., 2015). Pericyte degeneration and injury occur in many neurological diseases, including AD (Baloyannis and Baloyannis, 2012; Farkas and Luiten, 2001; Halliday et al., 2015; Sengillo et al., 2013), mild dementia (Montagne et al., 2015), amyotrophic lateral sclerosis (ALS) (Winkler et al., 2013), and stroke (Hall et al., 2014).

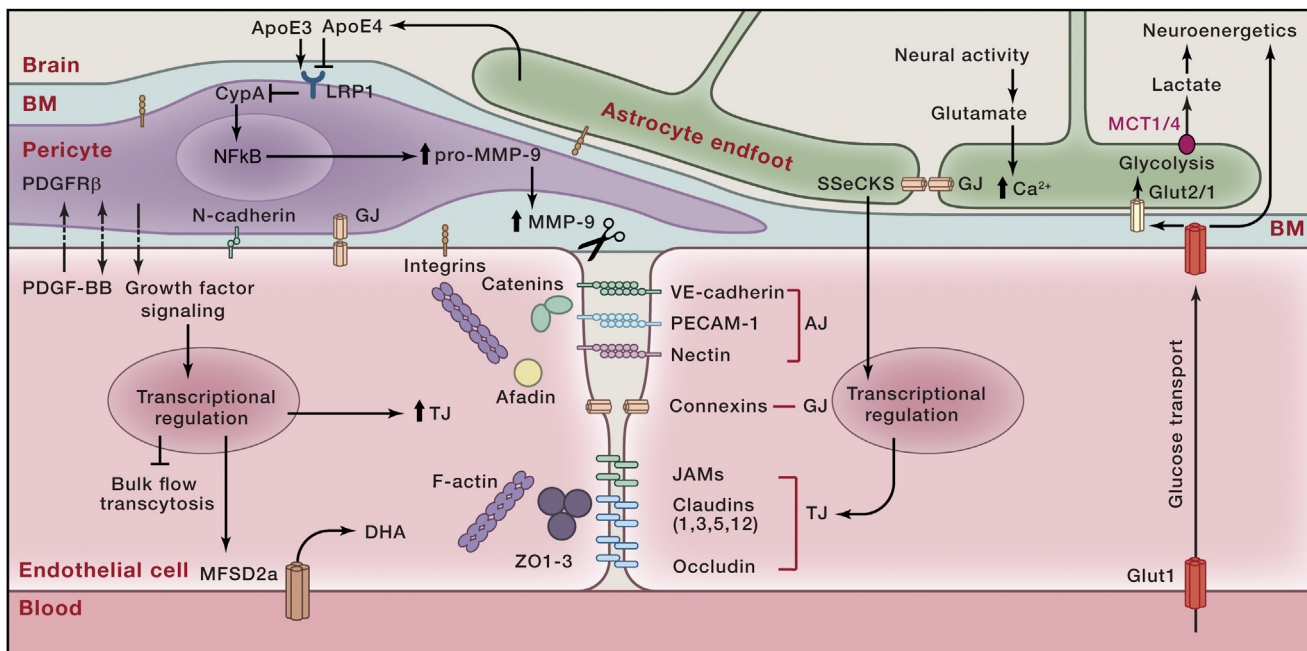


Figure 3. The Vascular Triad of the Blood-Brain Barrier

Endothelial cells are connected with each other through the tight junction (TJ), adherens junction (AJ) and gap junction (GJ) proteins. In the TJs, occludin, claudins and junctional adhesion molecules (JAMs) form an impermeable barrier to fluids and are connected to F-actin filaments by the zonula occludens ZO-1, ZO-2 and ZO-3 multi-domain scaffolding proteins of the membrane-associated guanylate kinase family. GJs formed by connexin hemichannels are specialized for direct intercellular communications. AJs are formed by homotypic binding of VE-cadherin, platelet endothelial cell adhesion molecule-1 (PECAM-1) and Nectin. Catenins link VE-cadherin to F-actin, while nectin is secured to F-actin by afadin.

Pericytes communicate with the endothelial cells via growth factor-mediated signaling (unidirectional or bidirectional), adhesion via N-cadherin homotypic binding and GJs. Pericyte can modulate BBB permeability by regulating gene expression in the endothelial cells resulting in upregulation of TJ proteins, inhibition of bulk flow transcytosis and upregulation of brain endothelial specific docosahexaenoic acid (DHA) transporter, a major facilitator domain-containing protein 2A (MFSD2a). Both endothelial cells and pericytes are embedded in the basement membrane (BM) and anchored to BM via integrins. PDGF-BB, platelet-derived growth factor BB; PDGFR β , platelet-derived growth factor receptor- β .

Astrocytes regulate expression of matrix metallo-proteinase-9 (MMP-9) in pericytes by secreting apolipoprotein E (ApoE). ApoE3, but not ApoE4, binds to the low density lipoprotein receptor-related protein 1 (LRP1) in pericytes, which suppresses the proinflammatory cyclophilin A (CypA) nuclear factor κ B (NFkB) MMP-9 pathway and degradation of TJ and BM proteins causing BBB breakdown. Astrocytes signal endothelial cells by Src-suppressed C-kinase substrate (SSeCKS) to increase TJ protein expression. Neural activity-dependent glutamate release increases $[Ca^{2+}]$ in the astrocytic endfeet, which regulates vascular tone. The GJs connect the adjacent astrocytic endfeet. Glucose gets into the brain via the endothelial Glut1 transporter and is taken up by neurons via Glut3. Glucose is taken up by astrocytes mainly by Glut2 and is metabolized to lactate, which is exported to neurons by the monocarboxylic MCT1 and MCT4 transporters.

Much of the insight into pericyte biology stems from the analysis of pericyte-deficient mice with disrupted platelet-derived growth factor BB (PDGF-BB)/platelet-derived growth factor receptor β (PDGFR β) signaling (Armulik et al., 2011). PDGF-BB secreted by endothelial cells binds to heparan sulfate proteoglycans in the basement membrane, and its concentration gradient regulates pericyte proliferation, migration, and recruitment to the vessel wall through PDGFR β receptor in pericytes. PDGF-B or PDGFR β null mice have a complete loss of pericytes, resulting in rupture of CNS microvessels, microaneurysms, and embryonic lethality (Lindahl et al., 1997; Tallquist et al., 2003). Pericytes are essential for maintaining BBB integrity in the adult and aging CNS (Armulik et al., 2010; Bell et al., 2010; Daneman et al., 2010) (Figure 3). Implications of disrupted PDGF-B/PDGFR β signaling for human neurological disorders are discussed below. Multiple signaling pathways in pericytes contribute to CNS vascular stability, as examined in detail elsewhere (Armulik et al., 2011; Winkler et al., 2011). Moreover, signaling between astrocytes and pericytes exerts significant impact on BBB integrity. On one hand, studies in

transgenic apolipoprotein E (APOE) mice have shown that APOE4, a major genetic risk factor for AD (Zlokovic, 2013), leads to disruption of BBB integrity by activating the proinflammatory cyclophilin-A (CypA) nuclear factor κ B matrix metalloproteinase 9 (MMP-9) pathway in pericytes, which in turn leads to degradation of the basement membrane and TJ proteins, causing chronic BBB breakdown followed by neuronal dysfunction and secondary neurodegenerative changes (Bell et al., 2012). In contrast, apoE3 and apoE2, which confer a lower risk for AD, suppress the CypA-MMP-9 pathway through LRP1 on pericytes, supporting the maintenance of BBB functions (Figure 3). On the other hand, pericyte loss leads to the loss of astrocyte-derived components from the endfeet (Armulik et al., 2010), but the pericyte-derived signal(s) in this case are unknown.

Astrocytes

Astrocytes contribute to a variety of dynamic regulations in the neural system and play a vital role in CNS inflammation in neurodegenerative diseases (Clarke and Barres, 2013; Sofroniew, 2015). However, it remains unclear whether astrocytes

are essential for BBB maintenance. The glial limitans ensheathing the penetrating arterial blood vessels and the outer layer of mature capillaries are formed by astrocytic endfeet (*Figure 3*). Yet, genetic lineage tracing and ablation studies showed that regional ablation had no effect on BBB permeability (*Tsai et al.*, 2012). In contrast, others have shown that Src-suppressed C-kinase substrate (SSeCKS) in astrocyte progenitors regulates angiogenesis and formation of TJs at the BBB by modulating VEGF and Ang-1 expression (*Lee et al.*, 2003). Future studies should provide more definitive answers as to whether astrocytes play a role in BBB maintenance in the adult and aging brain.

BBB and Monogenic Neurological Disorders

Several genetic diseases appear to originate in individual cell types of the NVU and link to specific roles in BBB development, function, and regulation. Such diseases, while rare, offer insights into causal pathogenic links and chains of events. Below, we briefly discuss some of these diseases, the relevant cell types (*Table 2*), and the potential pathogenic role of BBB dysfunction.

Endothelial Cells

Several inherited CNS diseases are caused by mutations in genes that play pivotal roles in endothelial cells or in the endothelium-derived ECM. These genes encode proteins that are either structural components or regulators of the endothelial cell-cell junctions, the vascular basement membrane, or transporters critically involved in BBB maintenance. For instance, mutations in the genes encoding the TJ proteins occludin (*O'Driscoll et al.*, 2010) and junctional adhesion molecule C (JAM-C) (*Woodfin et al.*, 2011) lead to severe problems in brain growth, hemorrhage, and calcification (*Table 2*). These pathologies may result from uncontrolled leakage of solutes and plasma proteins across the endothelial junctions and/or neuroinflammatory changes due to increased trans-endothelial migration of leukocytes, a process inhibited by JAM-C. Another example is familial cerebral cavernous malformations (CCM), occurring in hereditary or sporadic forms and together affecting ~0.5% of the population. CCM is caused by mutations in three genes, *CCM1–3*, leading to similar thin-walled, leaky vascular lesions of venous origin (*Fischer et al.*, 2013). The CCM proteins likely act together in a complex that maintains endothelial junctional organization and polarization and inhibits endothelial-to-mesenchymal transition (*Maddaluno et al.*, 2013). Collagen *COL4A1* and *COL4A2* are abundant in all basement membranes and are expressed by many cell types, including vascular endothelial cells. Mutations in these genes are associated with a diverse range of problems in several organs, including the brain, where they are associated with cerebral hemorrhage and small vessel disease (*Gould et al.*, 2006). Work in animal models with *Col4a1* deficiency suggests that increased vessel fragility could make the animal susceptible to hemorrhage either upon mild trauma or due to the anatomy of the vessel that is particularly sensitive to increased hemodynamic stress (*Kuo et al.*, 2012).

Among transporters mutated in brain disorders, two striking examples of BBB endothelial proteins are GLUT1 and MFSD2a. GLUT1, the major glucose transporter at the BBB, is mutated and functionally inactivated in human GLUT1 defi-

ciency syndrome, a disease associated with early-onset seizures and microcephaly (*Wang et al.*, 2000). This is consistent with the importance of sufficient GLUT1 levels and glucose transport across the BBB for brain function and its role in maintaining the BBB integrity (*Winkler et al.*, 2015). Similar to GLUT1, MFSD2a is highly expressed on brain endothelial cells. It transports lipids in the form of lysophosphatidylcholine coupled to certain long fatty acyl chains and is critical for the maintenance of the BBB integrity (*Ben-Zvi et al.*, 2014; *Nguyen et al.*, 2014). Microcephaly syndrome was recently shown to be caused by inactivating mutations in *MFSD2A*, the severity of the syndrome correlating with the degree of functional inactivation of the MFSD2A protein (*Alakbarzade et al.*, 2015; *Gomez-Gamboa et al.*, 2015). These studies provide insight into the cause of a rare disease but, perhaps more importantly, are an illustration to how basic physiological knowledge may come from human and mouse genetics and offer a fundamental insight into the mechanisms by which brain transports lipids across the BBB (*Betsholtz*, 2015) and maintains BBB integrity (*Betsholtz*, 2014; *Zhao and Zlokovic*, 2014). A third example of a brain disease associated with a BBB transporter is Allan-Herndon-Dudley syndrome, a psychomotor retardation syndrome caused by inactivating mutations in the triiodothyronine (T3) transporter SLC16A2 (MCT8) (*Dumitrescu et al.*, 2004; *Friesema et al.*, 2004). It is thought that the severe intellectual disability and movement problems observed in these patients are due to deficient transport of T3 from the blood to the brain, resulting in impairment of neuronal development and function. Indeed, different degrees of SLC16A2 inactivation correlate with the phenotypic consequences in patients (*Capri et al.*, 2013).

Vascular Mural Cells

CADASIL (cerebral autosomal dominant arteriopathy with subcortical infarcts and leukoencephalopathy) is a relatively common (2–4/100,000 individuals) autosomal-dominant stroke syndrome caused by mutations in NOTCH3, a gene known to be specifically expressed in vascular mural cells (*Chabriat et al.*, 2009). Although, the precise pathogenic mechanisms of CADASIL remain unresolved, recent studies of Notch 3 null mice demonstrated focal disruption of the BBB with tracer leakage and perivascular fibrin deposits in the CNS (*Henshall et al.*, 2015). Primary familial brain calcification (PFBC, a.k.a., idiopathic basal ganglia calcification [IBGC] or Fahr's disease) is characterized by early-onset microvascular calcification occurring in certain deep brain regions, most notably the basal ganglia. Disease symptoms include motoric and cognitive problems suggestive of significant neuronal dysfunction. The recent description of loss-of-function mutations in *PDGFB* and *PDGFRB* genes in PFBC (*Keller et al.*, 2013; *Nicolas et al.*, 2013) suggests a role for pericytes in this disease. In different mouse models based on mutations in *Pdgfb* that led to variable levels of defect in PDGF-B/PDGFR β signaling, a correlation was noted among the extent of pericyte loss, BBB deficiency, and brain calcification (*Keller et al.*, 2013). This is suggestive of a role for BBB dysfunction in PFBC, possibly involving changes in phosphate transport, since mutations in the phosphate transporters SLC20A2 and XPR1 also cause PFBC (*Legati et al.*, 2015; *Wang et al.*, 2012a).

Table 2. Human Monogenic Inherited Diseases with Blood-Brain Barrier Dysfunction

Disease	Symptoms	Cell Types	Subcellular Components	Proteins	Genes
Band-like calcification with simplified gyration and polymicrogyria (BLC-PMG)	Early-onset seizures, severe microcephaly, developmental delay with bilateral polymicrogyria, and a band of gray matter calcification on brain imaging.	Endothelial cells	Tight junctions	Occludin	<i>OCLN</i>
Hemorrhagic destruction of the brain, subependymal calcification, and congenital cataracts	Brain hemorrhage, subependymal calcification, congenital cataracts, spasticity, exaggerated deep-tendon reflexes, and seizures			JAM-C	<i>JAM3</i>
Familial cerebral cavernous malformations (CCM)	Seizures, headaches, intracerebral hemorrhages, focal neurological deficits, and gait ataxia		Cytoplasm and nucleus	CCM1 CCM2 CCM3	<i>KRIT1</i> <i>CCM2</i> <i>PDCD10</i>
Cerebral small vessel disease	Lacunar ischemic strokes, deep intracerebral hemorrhages, white matter hyperintensities		Basement membrane	COL4A1 COL4A2	<i>COL4A1</i> <i>COL4A2</i>
GLUT1 deficiency syndrome (De Vivo syndrome)	Early-onset seizures, microcephaly, mild movement disorder, and developmental delay		Transporters	GLUT1	<i>SLC2A1</i>
Microcephaly	Lethal or non-lethal microcephaly, intellectual disability, spasticity, and absent speech			MFSD2a	<i>MFSD2a</i>
Allan-Herndon-Dudley syndrome (AHDS)	Severe psychomotor retardation and altered serum thyroid parameters			MCT8	<i>SLC16A2</i>
Cerebral autosomal-dominant arteriopathy with subcortical infarcts and leukoencephalopathy (CADASIL)	Migraines, progressive dementia, mood disorders, and minor strokes	Vascular smooth muscle cells	Receptor	CADASIL	<i>NOTCH3</i>
Primary familial brain calcification (Idiopathic basal ganglia calcification, Fahr's disease)	Calcifications in the basal ganglia, cerebellum, thalamus, and brainstem lead to motor, cognitive, and psychiatric symptoms	Pericytes	Growth factor Receptor Transporter Receptor	PDGF-BB PDGFR β PIT2 SYG1	<i>PDGFB</i> <i>PDGFRB</i> <i>SLC20A2</i> <i>XPR1</i>
Alexander disease	Infantile form: megalencephaly, seizures, and impaired physical and mental development, early death; later-onset: bulbar signs, including difficulties with coordination, speech, and swallowing	Astrocytes	Cytoskeleton	GFAP	<i>GFAP</i>
Megalencephalic leukoencephalopathy with subcortical cysts (MLC)	Macrocephaly and cerebral white matter swelling and subcortical cysts, increased water content in the brain, and myelin and astrocyte vacuolation		Membrane protein	MLC1 GLIALCAM	<i>MLC1</i> <i>HEPACAM</i>
Congenital muscular dystrophy 1A (MDC1A)	Muscular weakness, raised creatine phosphokinase, cerebral white matter abnormalities, respiratory insufficiency, early death		Basement membrane	LAMM	<i>LAMA2</i>
Nasu-Hakola disease (NHD)	Progressive senile dementia characterized by extensive demyelination, accumulation of axonal spheroids, and multifocal bone cysts	Microglia	Membrane protein	DAP12 TREM2	<i>TYROBP</i> <i>TREM2</i>

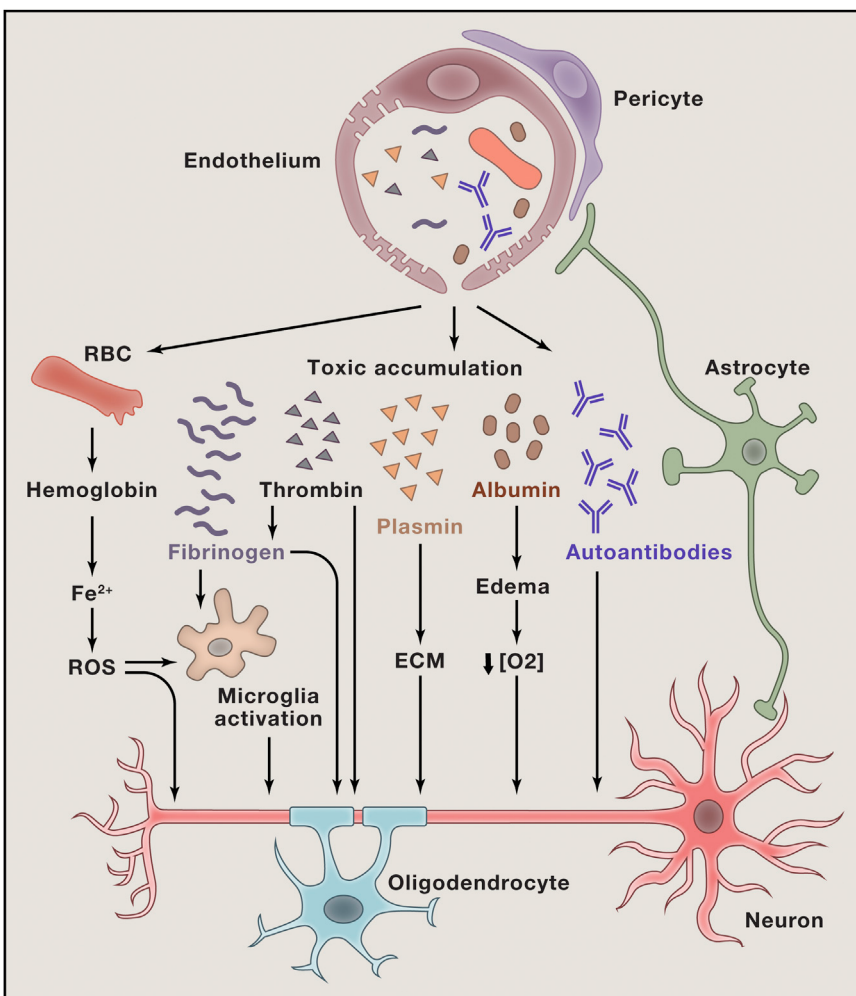


Figure 4. Vascular-Mediated Neurodegeneration

Aberrant pericyte-endothelial or astrocyte-pericyte signal transduction leads to BBB breakdown, resulting in brain accumulation of: (1) red blood cell (RBC)-derived neurotoxic hemoglobin and iron (Fe^{2+}), causing production of reactive oxygen species (ROS) and oxidant stress to neurons; (2) neuronal toxic blood-derived proteins such as fibrinogen, thrombin, and plasminogen, which could be converted into plasmin that, in turn, degrades neuronal extracellular matrix (ECM) and leads to detachment of neurons and cell death; (3) fibrinogen that activates microglia, promotes neuroinflammation and demyelination, and prevents myelination by oligodendrocyte progenitor cells; (4) albumin that contributes to the development of vasogenic edema, capillary hyperperfusion, and hypoxia. BBB breakdown can also lead to the loss of immune privilege, resulting in development of anti-brain antibodies against different axonal and membrane components of neurons.

2015; Sweeney et al., 2015) and other neurodegenerative disorders, such as ALS (Winkler et al., 2013), PD (Korcyn, 2015), and Huntington disease (HD) (Drouin-Ouellet et al., 2015), are increasingly recognized. A number of vascular dysfunctions are frequently associated with neurodegeneration, including hypertension, cerebrovascular disorder, BBB breakdown, etc. (Iadecola, 2013; Montagne et al., 2015; Snyder et al., 2015). Experimental studies in murine transgenic models with a chronic BBB breakdown due to aberrant endothelial-pericyte and/or astrocyte-pericyte signaling

Astrocytes and Microglia

Mutations in astrocyte-specific genes are associated with various neurological disorders, such as glial fibrillary acidic protein (GFAP) in Alexander disease and MLC1 and HEPACAM in megalecephalic leukoencephalopathy with subcortical cysts. These mutations may affect BBB integrity. However, the involvement of brain vascular dysfunction in these diseases remains to be established. Laminin $\alpha 2$ chains (LAMA2), an astrocyte gene encoding the basement membrane protein LAMA2, is mutated in congenital muscular dystrophy, a disease that affects the brain in some patients in ways that are suggestive of a defective BBB (e.g., brain edema) (Alkan et al., 2007). Reactive microglia are commonly found in association with leaky brain vessels. Mutations in the microglia-specific genes DAP12 and TREM2 cause Nasu-Hakkola disease (Sasaki et al., 2015), a neurodegenerative disorder with unclear pathogenesis. It remains to be determined whether Nasu-Hakkola disease is associated with a dysfunctional BBB.

BBB and Multifactorial Neurodegenerative Diseases

Vascular contributions to dementia and AD (Iadecola, 2013; Montagne et al., 2015; Montine et al., 2014; Snyder et al.,

have shown that accumulation in the CNS, particularly in neurons, of blood-derived neurotoxic proteins, including fibrinogen, thrombin, red-blood-cell-derived hemoglobin, iron-containing hemosiderin, free iron, and/or plasmin, can initiate and/or contribute to neurodegeneration (Armulik et al., 2010; Bell et al., 2010, 2012; Daneman et al., 2010; Davalos et al., 2012). ApoE knockout mice with dysfunctional BBB, but not wild-type mice with normal BBB, develop psychotic behavioral impairment when injected with N-methyl-D-aspartate receptor antibody-positive serum, suggesting that seroprevalence in neuropsychiatric diseases could be related to an insult to BBB integrity (Hammer et al., 2014). The model that we propose in Figure 4 may apply to various types of vascular-mediated neurodegeneration.

Accumulations of blood-derived proteins in the hippocampus and cortex (e.g., immunoglobulins, albumin, fibrinogen, and thrombin) were observed in post-mortem human studies, indicating BBB damage in AD (Halliday et al., 2015; Hultman et al., 2013; Sweeney et al., 2015; Zipser et al., 2007) and ALS (Winkler et al., 2013), both associated with degeneration of pericytes (Baloyannis and Baloyannis, 2012; Farkas and Luiten, 2001; Halliday et al., 2015; Sengillo et al., 2013; Winkler et al.,

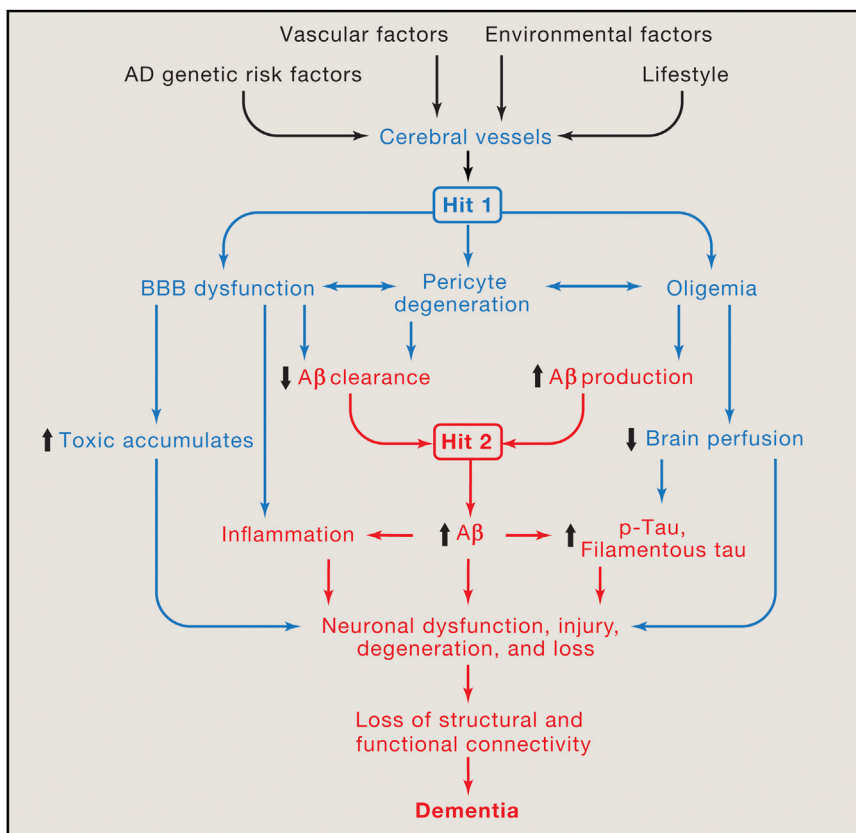


Figure 5. The Neurovascular Hypothesis for Alzheimer's Disease

AD genetics, vascular factors, environment, and lifestyle can independently and/or synergistically lead to cerebrovascular injuries, including BBB dysfunction, pericyte degeneration, and cerebral blood flow reductions (oligemia), initiating a cascade of events that can either: (1) directly cause neuronal injury and damage independently of A β (hit 1, blue) and/or (2) accelerate the A β -dependent neurodegeneration (hit 2, red). In the A β -dependent pathway, BBB dysfunction leads to faulty clearance of A β from brain, whereas reduced brain perfusion increases A β production, both causing A β accumulation in the brain. Reduced brain perfusion (hit 1) and elevated levels of A β (Hit 2) can independently and/or synergistically lead to Tau hyperphosphorylation (p-Tau) and formation of filamentous Tau pathology. Additionally, the two hits can exacerbate neuroinflammation.

2013). BBB impairments were also found in other neurological disorders, including multiple sclerosis, PD, and HD (Drouin-Ouellet et al., 2015; Korczyn, 2015; Zlokovic, 2011). Moreover, microbleeds and accumulation of iron were observed in the brains of patients with preclinical and clinical AD symptoms (Yates et al., 2014; Zonneveld et al., 2014), particularly in the hippocampus (Raven et al., 2013). It has also been shown that age-dependent early BBB breakdown is accelerated in individuals with mild dementia (Montagne et al., 2015). Some studies using the CSF-to-plasma ratio of blood-derived albumin also reported BBB damage in AD particularly associated with vascular risk factors or in individuals at a genetic risk for AD (Sweeney et al., 2015). Thus, findings in complex human brain diseases support, at least in part, the proposed model of vascular-mediated neurodegeneration (Figure 4). Below, we discuss AD in greater detail.

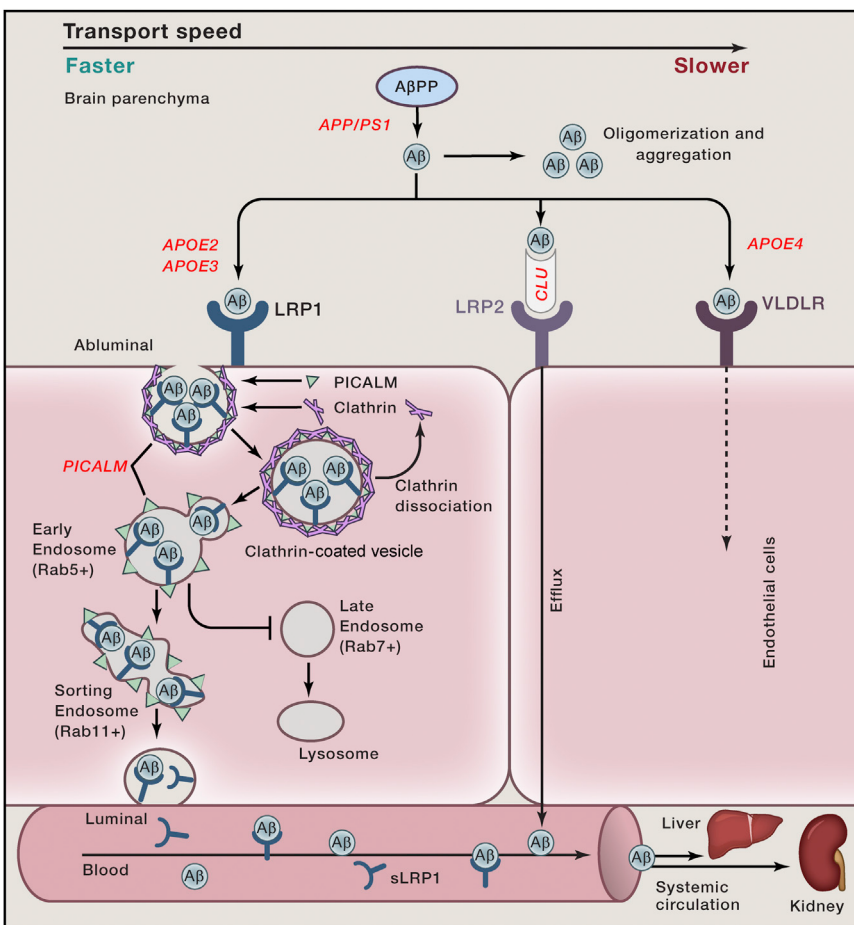
AD patients develop an early neurovascular dysfunction, progressive neurodegeneration, selective loss of neurons, and accumulation in the brain of A β pathology and neurofibrillary tangles composed of aggregated hyperphosphorylated Tau (Querfurth and LaFerla, 2010; Zlokovic, 2011). Strikingly, AD affects all cell types of the NVU depending on the disease stage, including endothelial and mural cells, glia, and neurons (Sweeney et al., 2015). The neurovascular hypothesis of AD proposes that cerebrovascular dysfunction and disruption in the neurovascular integrity contribute to the onset and progression of cognitive decline and that cerebral blood vessels are the converging point

of pathogenic events leading to dementia (Zlokovic, 2011). Vascular damage can be triggered by genetics, vascular risk factors, environmental factors, and lifestyle (Sagare et al., 2013; Sweeney et al., 2015; Zlokovic, 2011). Primary damage of the cerebrovasculature leads to brain accumulation of blood-derived neurotoxins, and the decrease in brain perfusion can cause neuronal injury. Vascular damage also influences neurodegeneration pathway mediated by A β .

In combination, vascular damage and elevated A β have a striking synergistic effect on neuronal Tau phosphorylation and pathology, leading to accelerated loss of neurons (Sagare et al., 2013) (Figure 5).

Faulty A β clearance from the brain leads to elevated A β in patients with sporadic AD (Mawuenyega et al., 2010). Experimental studies have shown that, in various animal models, A β is cleared from the brain primarily by trans-vascular clearance across the BBB (70%–85%), whereas a minor portion is removed by the ISF flow (Bading et al., 2002; Deane et al., 2004; Tarasoff-Conway et al., 2015). The molecular mechanism for A β clearance across the BBB has been recently elucidated in greater detail (Figure 6). In brief, A β produced in the brain binds to LRP1 at the abluminal side of the BBB, causing its rapid internalization into endothelial cells and clearance through the blood. Phosphatidylinositol-binding clathrin assembly protein (PICALM) is critical for clathrin/PICALM-mediated internalization of LRP1-A β complexes by the endothelium and guides intracellular trafficking of A β -containing endocytic vesicles across endothelium by sequential fusion with Rab5-positive early endosomes and Rab11-positive sorting endosomes for exocytosis at the luminal side of the BBB, which completes A β transcytosis cycle across the BBB (Zhao et al., 2015).

In plasma, the soluble form of LRP1 (sLRP1) generated by the proteolytic cleavage of LRP1 by β -secretase binds and sequesters free A β 40 and A β 42 (Sagare et al., 2007), mediating A β



transport via blood to the excretory organs (Zlokovic et al., 2010) (Figure 6). A β 42 can bind to Clusterin (CLU or apoJ) in the brain ISF, and apoJ-A β complexes are transported across the BBB into circulation by LRP2 (Bell et al., 2007). Enzymatic degradation of A β by neprilysin, insulin-degrading enzyme, matrix metalloproteinases, plasmin, and tissue plasminogen activator contributes to its clearance from brain (Querfurth and LaFerla, 2010).

Several frequently studied genes, of which the mutations are associated with high risk for sporadic and familial AD, play a role in the cerebrovascular system. For instance, APOE4 is the strongest genetic risk factor for late-onset AD that exerts direct toxic cerebrovascular effects (Zlokovic, 2013). Compared to the other two APOE isoforms, i.e., APOE3 or APOE2, APOE4 increases BBB damage, cerebral amyloid angiopathy, and fibrinogen and iron deposition in the brain of AD patients (Halliday et al., 2013, 2015; Hultman et al., 2013; Sweeney et al., 2015; Zipser et al., 2007; Zonneveld et al., 2014). Consistently, findings in APOE4 transgenic mice suggest that vascular changes may precede neuronal changes and behavioral deficits (Bell et al., 2012). ApoE can bind to A β . While ApoE2-A β and ApoE3-A β complexes are rapidly cleared across the BBB via LRP1, the removal rate of ApoE4-A β complexes is lower, mediated by slow internalization and transcytosis via very low-density lipo-

Figure 6. Alzheimer's Amyloid β -Peptide Clearance across the Blood-Brain Barrier

Transvascular A β clearance. LRP1 binds A β at the abluminal side of endothelium, which recruits PICALM, resulting in PICALM/clathrin-dependent endocytosis of LRP1-A β complexes. Next, PICALM guides the trafficking of A β -LRP1 endocytic vesicles to Rab5 $^+$ early endosomes and then to Rab11 $^+$ sorting endosomes for exocytosis at the luminal side of the BBB, resulting in A β transcytosis. PICALM guides A β away from Rab7 $^+$ late endosomes and lysosomes. Apolipoprotein J (apoJ; CLU) facilitates A β 42 clearance across the BBB via LRP2. **Systemic A β clearance.** A β binds to soluble LRP1 (sLRP1) in plasma. Circulating sLRP1-A β complexes are transported to liver and kidney for elimination from the body. **Genetic risk factors.** APOE2 and APOE3 carry lower risk for AD compared to APOE4. CLU variants influence risk for sporadic AD, but their effects on A β clearance are presently unknown. Some protective PICALM variants lead to increased PICALM expression and enhanced A β clearance across the BBB. PSEN1 mutations causing early autosomal-dominant AD lead to increased production of A β —particularly A β 42, which increases A β load for clearance across the BBB.

protein receptor (VLDLR) (Bell et al., 2007; Deane et al., 2008) (Figure 6).

Another example is PICALM, a validated genetic risk factor for AD (Harold et al., 2009; Lambert et al., 2009). PICALM mediates endocytosis and internalization of cell receptors and intracellular trafficking of endocytic proteins (Treusch et al., 2011; Zhao et al., 2015). It is highly expressed in brain endothelium of the

BBB (Parikh et al., 2014; Zhao et al., 2015) and plays a central role in A β clearance across the BBB (Figure 6). A recent study suggested that, compared to the protective allele, the non-protective allele of the rs3851179 PICALM variant leads to decreased PICALM expression in endothelial cells and substantially lower A β clearance in an *in vitro* model of the BBB (Zhao et al., 2015), suggesting that PICALM variants may affect AD pathogenesis, potentially through a vascular mechanism.

Similarly, mutations in Clusterin (CLU, apoJ) are associated with sporadic AD (Harold et al., 2009; Lambert et al., 2009). CLU binds to several different proteins, including A β , and has been shown to prevent aggregation and promote clearance of A β peptides across the BBB (Bell et al., 2007) (Figure 6). Presenilin (PSEN) mutations cause autosomal-dominant AD and increase A β production in the brain (Querfurth and LaFerla, 2010). PSEN1 mutations also lead to major cerebrovascular pathology in humans, including degeneration of pericytes and mural cells, BBB breakdown, and A β deposits in small cerebral vessels (Sweeney et al., 2015). Similar cerebrovascular pathology was found in transgenic PSEN1 mice (Gama Sosa et al., 2010), although it is worth noting that how vascular pathology relates to the increased A β production during disease progression remains elusive.

Conclusions and Future Directions

Recent advances in human genetics and the corresponding transgenic models indicate that almost every non-neuronal cell type of the NVU could be affected by some monogenic inherited disorders. This association can provide insights into the potential pathogenic links among BBB dysfunction, neuronal injury, neurodegeneration, and neurological disorders caused by NVU disruption and BBB breakdown. On the other hand, the relationship among neurovascular integrity, brain structural and functional connectivity, cognitive function, and neurological symptomatology in complex disorders such as AD still awaits to be directly explored in the most relevant *in vivo* context, which has only recently became possible with the development of novel state-of-the-art neuroimaging and molecular biomarker approaches. Experimental studies combining genetic, environmental, and lifestyle factors hold promise to further advance our knowledge of multifactorial CNS disorders and to establish the concept that the loss of healthy cerebral blood vessels and BBB integrity influences the course and clinical phenotype of neurological disorders in a region-specific manner.

Some important questions remain to be addressed. First, it is still unclear whether in the living human brain, cerebrovascular changes and BBB breakdown can drive the initial pathogenic events that lead to neuronal injury, disrupted structural and functional brain connectivity, and early neurological symptoms, such as cognitive decline in AD and motor changes in ALS, PD, or HD. Second, further studies are warranted to test whether the underlying molecular mechanisms of NVU disruption and BBB breakdown might point to new targets for therapeutic development to prevent and/or treat neurodegenerative disorders. Third, technological advance is required to determine whether neurovascular dysfunction and BBB breakdown are detectable in the living human brain prior to the development of the full spectrum of neurological symptoms. Last but not least, future investigations need to address whether molecular and imaging biomarkers of neurovascular dysfunction can serve as reliable prognostic and/or diagnostic tools to predict the development of neurodegenerative disorders.

From the basic science side, pushing the envelope further to generate a comprehensive proteomics and RNA-seq molecular atlas of the BBB in animals and humans would provide a valuable resource for discovering and studying new targets and signaling pathways mediating the crosstalk among different cell types within the NVU. This may lead to the development of new transgenic animal models—pluripotent stem cell models of the BBB, NVU, and different neurological disorders—serving as valuable platforms for drug discovery and for testing novel drug delivery approaches.

AUTHOR CONTRIBUTIONS

Z.Z. and A.R.N. contributed equally in preparing some sections of this Perspective.

ACKNOWLEDGMENTS

The work of B.V.Z. is supported by the National Institutes of Health grants R01AG023084, R01NS090904, R01NS034467, and R01AG039452 and the

Cure Alzheimer's Fund. The work of C.B. is supported by the European Research Council (ERC advanced grant number 294556 BBBARRIER), the Knut and Alice Wallenberg Foundation, Leducq Foundation (Sphingonet), Swedish Cancer Foundation, the Swedish Science Council, and Uppsala University. We apologize to authors whose work we could not cite because of the limit on the number of references; in some instances, we mostly cited the overview articles.

REFERENCES

- Alakbarzade, V., Hameed, A., Quek, D.Q.Y., Chioza, B.A., Baple, E.L., Cazenave-Gassiot, A., Nguyen, L.N., Wenk, M.R., Ahmad, A.Q., Sreekantan-Nair, A., et al. (2015). A partially inactivating mutation in the sodium-dependent lysophosphatidylcholine transporter MFSD2A causes a non-lethal microcephaly syndrome. *Nat. Genet.* 47, 814–817.
- Alkan, A., Sigirci, A., Kutlu, R., Aslan, M., Doganay, S., and Yakinci, C. (2007). Merosin-negative congenital muscular dystrophy: diffusion-weighted imaging findings of brain. *J. Child Neurol.* 22, 655–659.
- Alvarez, J.I., Dodelet-Devillers, A., Kebr, H., Ifergan, I., Fabre, P.J., Terouz, S., Sabbagh, M., Wosik, K., Bourbonnière, L., Bernard, M., et al. (2011). The Hedgehog pathway promotes blood-brain barrier integrity and CNS immune quiescence. *Science* 334, 1727–1731.
- Andreone, B.J., Lacoste, B., and Gu, C. (2015). Neuronal and vascular interactions. *Annu. Rev. Neurosci.* 38, 25–46.
- Armulik, A., Genové, G., Mäe, M., Nisancioglu, M.H., Wallgard, E., Niaudet, C., He, L., Norlin, J., Lindblom, P., Strittmatter, K., et al. (2010). Pericytes regulate the blood-brain barrier. *Nature* 468, 557–561.
- Armulik, A., Genové, G., and Betsholtz, C. (2011). Pericytes: developmental, physiological, and pathological perspectives, problems, and promises. *Dev. Cell* 21, 193–215.
- Aspelund, A., Antila, S., Proulx, S.T., Karlsen, T.V., Karaman, S., Detmar, M., Wiig, H., and Alitalo, K. (2015). A dural lymphatic vascular system that drains brain interstitial fluid and macromolecules. *J. Exp. Med.* 212, 991–999.
- Attwell, D., Buchan, A.M., Charpak, S., Lauritzen, M., Macvicar, B.A., and Newman, E.A. (2010). Glial and neuronal control of brain blood flow. *Nature* 468, 232–243.
- Bading, J.R., Yamada, S., Mackie, J.B., Kirkman, L., Miller, C., Calero, M., Ghiso, J., Frangione, B., and Zlokovic, B.V. (2002). Brain clearance of Alzheimer's amyloid-beta40 in the squirrel monkey: a SPECT study in a primate model of cerebral amyloid angiopathy. *J. Drug Target.* 10, 359–368.
- Baeten, K.M., and Akassoglou, K. (2011). Extracellular matrix and matrix receptors in blood-brain barrier formation and stroke. *Dev. Neurobiol.* 71, 1018–1039.
- Baloyannis, S.J., and Baloyannis, I.S. (2012). The vascular factor in Alzheimer's disease: a study in Golgi technique and electron microscopy. *J. Neurol. Sci.* 322, 117–121.
- Bell, R.D., Sagare, A.P., Friedman, A.E., Bedi, G.S., Holtzman, D.M., Deane, R., and Zlokovic, B.V. (2007). Transport pathways for clearance of human Alzheimer's amyloid beta-peptide and apolipoproteins E and J in the mouse central nervous system. *J. Cereb. Blood Flow Metab.* 27, 909–918.
- Bell, R.D., Winkler, E.A., Sagare, A.P., Singh, I., LaRue, B., Deane, R., and Zlokovic, B.V. (2010). Pericytes control key neurovascular functions and neuronal phenotype in the adult brain and during brain aging. *Neuron* 68, 409–427.
- Bell, R.D., Winkler, E.A., Singh, I., Sagare, A.P., Deane, R., Wu, Z., Holtzman, D.M., Betsholtz, C., Armulik, A., Sallstrom, J., et al. (2012). Apolipoprotein E controls cerebrovascular integrity via cyclophilin A. *Nature* 485, 512–516.
- Ben-Zvi, A., Lacoste, B., Kur, E., Andreone, B.J., Mayshar, Y., Yan, H., and Gu, C. (2014). Mfsd2a is critical for the formation and function of the blood-brain barrier. *Nature* 509, 507–511.
- Benarroch, E.E. (2014). Brain glucose transporters: implications for neurologic disease. *Neurology* 82, 1374–1379.

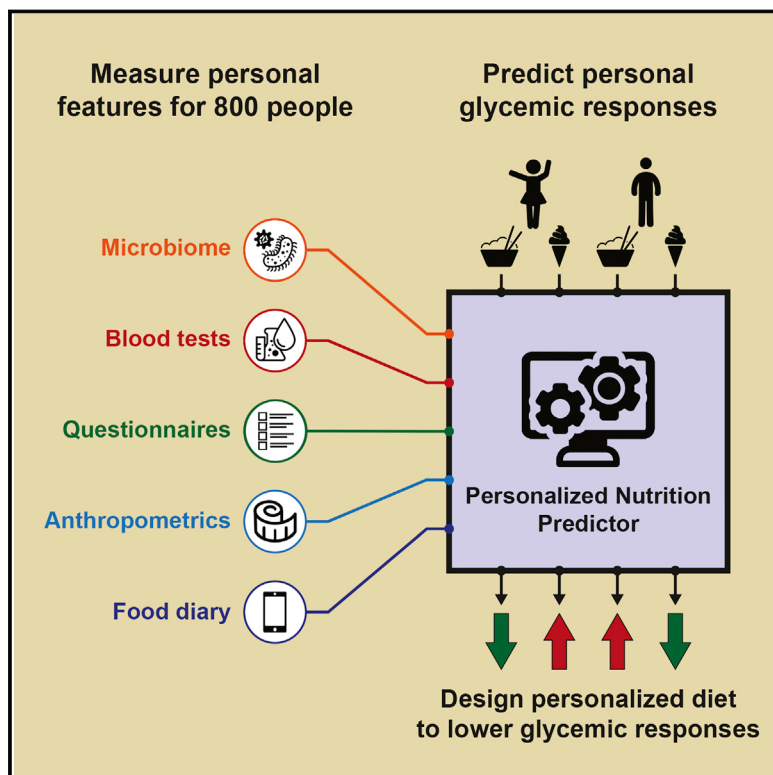
- Betsholtz, C. (2014). Physiology: Double function at the blood-brain barrier. *Nature* 509, 432–433.
- Betsholtz, C. (2015). Lipid transport and human brain development. *Nat. Genet.* 47, 699–701.
- Blinder, P., Tsai, P.S., Kaufhold, J.P., Knutson, P.M., Suhl, H., and Kleinfeld, D. (2013). The cortical angiome: an interconnected vascular network with noncolumnar patterns of blood flow. *Nat. Neurosci.* 16, 889–897.
- Bray, N. (2015). Biologics: Transferrin' bispecific antibodies across the blood-brain barrier. *Nat. Rev. Drug Discov.* 14, 14–15.
- Capri, Y., Friesema, E.C.H., Kersseboom, S., Touraine, R., Monnier, A., Eyraud-Pierre, E., Des Portes, V., De Michele, G., Brady, A.F., Boespflug-Tanguy, O., et al. (2013). Relevance of different cellular models in determining the effects of mutations on SLC16A2/MCT8 thyroid hormone transporter function and genotype-phenotype correlation. *Hum. Mutat.* 34, 1018–1025.
- Chabriat, H., Joutel, A., Dichgans, M., Tournier-Lasserre, E., and Bousser, M.-G. (2009). Cadasil. *Lancet Neurol.* 8, 643–653.
- Cirrito, J.R., Deane, R., Fagan, A.M., Spinner, M.L., Parsadanian, M., Finn, M.B., Jiang, H., Prior, J.L., Sagare, A., Bales, K.R., et al. (2005). P-glycoprotein deficiency at the blood-brain barrier increases amyloid-beta deposition in an Alzheimer disease mouse model. *J. Clin. Invest.* 115, 3285–3290.
- Clarke, L.E., and Barres, B.A. (2013). Emerging roles of astrocytes in neural circuit development. *Nat. Rev. Neurosci.* 14, 311–321.
- Daneman, R., and Prat, A. (2015). The blood-brain barrier. *Cold Spring Harb. Perspect. Biol.* 7, a020412.
- Daneman, R., Agalliu, D., Zhou, L., Kuhnert, F., Kuo, C.J., and Barres, B.A. (2009). Wnt/beta-catenin signaling is required for CNS, but not non-CNS, angiogenesis. *Proc. Natl. Acad. Sci. USA* 106, 641–646.
- Daneman, R., Zhou, L., Kebede, A.A., and Barres, B.A. (2010). Pericytes are required for blood-brain barrier integrity during embryogenesis. *Nature* 468, 562–566.
- Davalos, D., Ryu, J.K., Merlini, M., Baeten, K.M., Le Moan, N., Petersen, M.A., Deerinck, T.J., Smirnoff, D.S., Bedard, C., Hakozaiki, H., et al. (2012). Fibrinogen-induced perivascular microglial clustering is required for the development of axonal damage in neuroinflammation. *Nat. Commun.* 3, 1227.
- Deane, R., Du Yan, S., Subramanyan, R.K., LaRue, B., Jovanovic, S., Hogg, E., Welch, D., Manness, L., Lin, C., Yu, J., et al. (2003). RAGE mediates amyloid-beta peptide transport across the blood-brain barrier and accumulation in brain. *Nat. Med.* 9, 907–913.
- Deane, R., Wu, Z., Sagare, A., Davis, J., Du Yan, S., Hamm, K., Xu, F., Parisi, M., LaRue, B., Hu, H.W., et al. (2004). LRP/amyloid beta-peptide interaction mediates differential brain efflux of Abeta isoforms. *Neuron* 43, 333–344.
- Deane, R., Sagare, A., Hamm, K., Parisi, M., Lane, S., Finn, M.B., Holtzman, D.M., and Zlokovic, B.V. (2008). apoE isoform-specific disruption of amyloid-beta peptide clearance from mouse brain. *J. Clin. Invest.* 118, 4002–4013.
- Deane, R., Singh, I., Sagare, A.P., Bell, R.D., Ross, N.T., LaRue, B., Love, R., Perry, S., Paquette, N., Deane, R.J., et al. (2012). A multimodal RAGE-specific inhibitor reduces amyloid β-mediated brain disorder in a mouse model of Alzheimer disease. *J. Clin. Invest.* 122, 1377–1392.
- Drouin-Ouellet, J., Sawiak, S.J., Cisbani, G., Lagacé, M., Kuan, W.-L., Saint-Pierre, M., Dury, R.J., Alata, W., St-Amour, I., Mason, S.L., et al. (2015). Cerebrovascular and blood-brain barrier impairments in Huntington's disease: Potential implications for its pathophysiology. *Ann. Neurol.* 78, 160–177.
- Dumitrescu, A.M., Liao, X.-H., Best, T.B., Brockmann, K., and Refetoff, S. (2004). A novel syndrome combining thyroid and neurological abnormalities is associated with mutations in a monocarboxylate transporter gene. *Am. J. Hum. Genet.* 74, 168–175.
- Farkas, E., and Luiten, P.G. (2001). Cerebral microvascular pathology in aging and Alzheimer's disease. *Prog. Neurobiol.* 64, 575–611.
- Fischer, A., Zalvide, J., Faurobert, E., Albiges-Rizo, C., and Tournier-Lasserre, E. (2013). Cerebral cavernous malformations: from CCM genes to endothelial cell homeostasis. *Trends Mol. Med.* 19, 302–308.
- Friesema, E.C.H., Grueters, A., Biebermann, H., Krude, H., von Moers, A., Reeser, M., Barrett, T.G., Mancilla, E.E., Svensson, J., Kester, M.H.A., et al. (2004). Association between mutations in a thyroid hormone transporter and severe X-linked psychomotor retardation. *Lancet* 364, 1435–1437.
- Gama Sosa, M.A., Gasperi, R.D., Rocher, A.B., Wang, A.C.-J., Janssen, W.G.M., Flores, T., Perez, G.M., Schmeidler, J., Dickstein, D.L., Hof, P.R., and Elder, G.A. (2010). Age-related vascular pathology in transgenic mice expressing presenilin 1-associated familial Alzheimer's disease mutations. *Am. J. Pathol.* 176, 353–368.
- Gould, D.B., Phalan, F.C., van Mil, S.E., Sundberg, J.P., Vahedi, K., Massin, P., Bousser, M.G., Heutink, P., Miner, J.H., Tournier-Lasserre, E., and John, S.W. (2006). Role of COL4A1 in small-vessel disease and hemorrhagic stroke. *N. Engl. J. Med.* 354, 1489–1496.
- Guemez-Gamboa, A., Nguyen, L.N., Yang, H., Zaki, M.S., Kara, M., Ben-Orran, T., Akizu, N., Rosti, R.O., Rosti, B., Scott, E., et al. (2015). Inactivating mutations in MFSD2A, required for omega-3 fatty acid transport in brain, cause a lethal microcephaly syndrome. *Nat. Genet.* 47, 809–813.
- Hagan, N., and Ben-Zvi, A. (2015). The molecular, cellular, and morphological components of blood-brain barrier development during embryogenesis. *Semin. Cell Dev. Biol.* 38, 7–15.
- Hall, C.N., Reynell, C., Gesslein, B., Hamilton, N.B., Mishra, A., Sutherland, B.A., O'Farrell, F.M., Buchan, A.M., Lauritzen, M., and Attwell, D. (2014). Capillary pericytes regulate cerebral blood flow in health and disease. *Nature* 508, 55–60.
- Halliday, M.R., Pomara, N., Sagare, A.P., Mack, W.J., Frangione, B., and Zlokovic, B.V. (2013). Relationship between cyclophilin A levels and matrix metalloproteinase 9 activity in cerebrospinal fluid of cognitively normal apolipoprotein e4 carriers and blood-brain barrier breakdown. *JAMA Neurol.* 70, 1198–1200.
- Halliday, M.R., Rege, S.V., Ma, Q., Zhao, Z., Miller, C.A., Winkler, E.A., and Zlokovic, B.V. (2015). Accelerated pericyte degeneration and blood-brain barrier breakdown in apolipoprotein E4 carriers with Alzheimer's disease. *J. Cereb. Blood Flow Metab. Off. J. Int. Soc. Cereb. Blood Flow Metab.* <http://dx.doi.org/10.1038/jcbfm.2015.44>.
- Hammer, C., Stepienik, B., Schneider, A., Papiol, S., Tantra, M., Begemann, M., Sirén, A.-L., Pardo, L.A., Sperling, S., Mohd Jofry, S., et al. (2014). Neuropsychiatric disease relevance of circulating anti-NMDA receptor autoantibodies depends on blood-brain barrier integrity. *Mol. Psychiatry* 19, 1143–1149.
- Harold, D., Abraham, R., Hollingworth, P., Sims, R., Gerrish, A., Hamshere, M.L., Pahwa, J.S., Moskina, V., Dowzell, K., Williams, A., et al. (2009). Genome-wide association study identifies variants at CLU and PICALM associated with Alzheimer's disease. *Nat. Genet.* 41, 1088–1093.
- Henshall, T.L., Keller, A., He, L., Johansson, B.R., Wallgard, E., Raschperger, E., Mäe, M.A., Jin, S., Betsholtz, C., and Lendahl, U. (2015). Notch3 is necessary for blood vessel integrity in the central nervous system. *Arterioscler. Thromb. Vasc. Biol.* 35, 409–420.
- Hultman, K., Strickland, S., and Norris, E.H. (2013). The APOE ε4/ε4 genotype potentiates vascular fibrin(ogen) deposition in amyloid-laden vessels in the brains of Alzheimer's disease patients. *J. Cereb. Blood Flow Metab.* 33, 1251–1258.
- Iadecola, C. (2013). The pathobiology of vascular dementia. *Neuron* 80, 844–866.
- Keller, A., Westenberger, A., Sobrido, M.J., García-Murias, M., Domingo, A., Sears, R.L., Lemos, R.R., Ordoñez-Ugalde, A., Nicolas, G., da Cunha, J.E.G., et al. (2013). Mutations in the gene encoding PDGF-B cause brain calcifications in humans and mice. *Nat. Genet.* 45, 1077–1082.
- Kersseboom, S., Kremers, G.-J., Friesema, E.C.H., Visser, W.E., Klootwijk, W., Peeters, R.P., and Visser, T.J. (2013). Mutations in MCT8 in patients with Allan-Herndon-Dudley-syndrome affecting its cellular distribution. *Mol. Endocrinol.* 27, 801–813.
- Korcyn, A.D. (2015). Vascular parkinsonism—characteristics, pathogenesis and treatment. *Nat. Rev. Neurol.* 11, 319–326.

- Kuhnert, F., Mancuso, M.R., Shamloo, A., Wang, H.-T., Choksi, V., Florek, M., Su, H., Fruttiger, M., Young, W.L., Heilshorn, S.C., and Kuo, C.J. (2010). Essential regulation of CNS angiogenesis by the orphan G protein-coupled receptor GPR124. *Science* 330, 985–989.
- Kuo, D.S., Labelle-Dumais, C., and Gould, D.B. (2012). COL4A1 and COL4A2 mutations and disease: insights into pathogenic mechanisms and potential therapeutic targets. *Hum. Mol. Genet.* 21 (R1), R97–R110.
- Lambert, J.-C., Heath, S., Even, G., Campion, D., Sleegers, K., Hiltunen, M., Combarros, O., Zelenika, D., Bullido, M.J., Tavernier, B., et al.; European Alzheimer's Disease Initiative Investigators (2009). Genome-wide association study identifies variants at CLU and CR1 associated with Alzheimer's disease. *Nat. Genet.* 41, 1094–1099.
- Lee, S.-W., Kim, W.J., Choi, Y.K., Song, H.S., Son, M.J., Gelman, I.H., Kim, Y.-J., and Kim, K.-W. (2003). SSeCKS regulates angiogenesis and tight junction formation in blood-brain barrier. *Nat. Med.* 9, 900–906.
- Legati, A., Giovannini, D., Nicolas, G., López-Sánchez, U., Quintáns, B., Oliveira, J.R.M., Sears, R.L., Ramos, E.M., Spiteri, E., Sobrido, M.-J., et al. (2015). Mutations in XPR1 cause primary familial brain calcification associated with altered phosphate export. *Nat. Genet.* 47, 579–581.
- Liebner, S., Corada, M., Bangsow, T., Babbage, J., Taddei, A., Czupalla, C.J., Reis, M., Felici, A., Wolburg, H., Fruttiger, M., et al. (2008). Wnt/beta-catenin signaling controls development of the blood-brain barrier. *J. Cell Biol.* 183, 409–417.
- Lin, L., Yee, S.W., Kim, R.B., and Giacomini, K.M. (2015). SLC transporters as therapeutic targets: emerging opportunities. *Nat. Rev. Drug Discov.* 14, 543–560.
- Lindahl, P., Johansson, B.R., Levéen, P., and Betsholtz, C. (1997). Pericyte loss and microaneurysm formation in PDGF-B-deficient mice. *Science* 277, 242–245.
- Louveau, A., Smirnov, I., Keyes, T.J., Eccles, J.D., Rouhani, S.J., Peske, J.D., Derecki, N.C., Castle, D., Mandell, J.W., Lee, K.S., et al. (2015). Structural and functional features of central nervous system lymphatic vessels. *Nature* 523, 337–341.
- Maddaluno, L., Rudini, N., Cuttano, R., Bravi, L., Giampietro, C., Corada, M., Ferrarini, L., Orsenigo, F., Papa, E., Boulday, G., et al. (2013). EndMT contributes to the onset and progression of cerebral cavernous malformations. *Nature* 498, 492–496.
- Mawuenyega, K.G., Sigurdson, W., Ovod, V., Munsell, L., Kasten, T., Morris, J.C., Yarasheski, K.E., and Bateman, R.J. (2010). Decreased clearance of CNS beta-amyloid in Alzheimer's disease. *Science* 330, 1774.
- Miller, D.S. (2015). Regulation of ABC transporters blood-brain barrier: the good, the bad, and the ugly. *Adv. Cancer Res.* 125, 43–70.
- Montagne, A., Barnes, S.R., Sweeney, M.D., Halliday, M.R., Sagare, A.P., Zhao, Z., Toga, A.W., Jacobs, R.E., Liu, C.Y., Amezcuia, L., et al. (2015). Blood-brain barrier breakdown in the aging human hippocampus. *Neuron* 85, 296–302.
- Montine, T.J., Koroshetz, W.J., Babcock, D., Dickson, D.W., Galpern, W.R., Glymour, M.M., Greenberg, S.M., Hutton, M.L., Knopman, D.S., Kuzmichev, A.N., et al.; ADRD 2013 Conference Organizing Committee (2014). Recommendations of the Alzheimer's disease-related dementias conference. *Neurology* 83, 851–860.
- Nakagomi, T., Kubo, S., Nakano-Doi, A., Sakuma, R., Lu, S., Narita, A., Kawahara, M., Taguchi, A., and Matsuyama, T. (2015). Brain vascular pericytes following ischemia have multipotential stem cell activity to differentiate into neural and vascular lineage cells. *Stem Cells* 33, 1962–1974.
- Nguyen, L.N., Ma, D., Shui, G., Wong, P., Cazenave-Gassiot, A., Zhang, X., Wenk, M.R., Goh, E.L.K., and Silver, D.L. (2014). Mfsd2a is a transporter for the essential omega-3 fatty acid docosahexaenoic acid. *Nature* 509, 503–506.
- Nicolas, G., Pottier, C., Maltête, D., Coutant, S., Rovelet-Lecrux, A., Legallic, S., Rousseau, S., Vaschalde, Y., Guyant-Marechal, L., Augustin, J., et al. (2013). Mutation of the PDGFRB gene as a cause of idiopathic basal ganglia calcification. *Neurology* 80, 181–187.
- O'Driscoll, M.C., Daly, S.B., Urquhart, J.E., Black, G.C.M., Pilz, D.T., Brockmann, K., McEntagart, M., Abdel-Salam, G., Zaki, M., Wolf, N.I., et al. (2010). Recessive mutations in the gene encoding the tight junction protein occludin cause band-like calcification with simplified gyration and polymicrogyria. *Am. J. Hum. Genet.* 87, 354–364.
- Obermeier, B., Daneman, R., and Ransohoff, R.M. (2013). Development, maintenance and disruption of the blood-brain barrier. *Nat. Med.* 19, 1584–1596.
- Pardridge, W.M. (2015). Blood-brain barrier endogenous transporters as therapeutic targets: a new model for small molecule CNS drug discovery. *Expert Opin. Ther. Targets* 19, 1059–1072.
- Parikh, I., Fardo, D.W., and Estus, S. (2014). Genetics of PICALM expression and Alzheimer's disease. *PLoS ONE* 9, e91242.
- Peppiatt, C.M., Howarth, C., Mobbs, P., and Attwell, D. (2006). Bidirectional control of CNS capillary diameter by pericytes. *Nature* 443, 700–704.
- Potente, M., Gerhardt, H., and Carmeliet, P. (2011). Basic and therapeutic aspects of angiogenesis. *Cell* 146, 873–887.
- Querfurth, H.W., and LaFerla, F.M. (2010). Alzheimer's disease. *N. Engl. J. Med.* 362, 329–344.
- Raven, E.P., Lu, P.H., Tishler, T.A., Heydari, P., and Bartzokis, G. (2013). Increased iron levels and decreased tissue integrity in hippocampus of Alzheimer's disease detected *in vivo* with magnetic resonance imaging. *J. Alzheimers Dis.* 37, 127–136.
- Sagare, A., Deane, R., Bell, R.D., Johnson, B., Hamm, K., Pendu, R., Marky, A., Lenting, P.J., Wu, Z., Zarcone, T., et al. (2007). Clearance of amyloid-beta by circulating lipoprotein receptors. *Nat. Med.* 13, 1029–1031.
- Sagare, A.P., Bell, R.D., Zhao, Z., Ma, Q., Winkler, E.A., Ramanathan, A., and Zlokovic, B.V. (2013). Pericyte loss influences Alzheimer-like neurodegeneration in mice. *Nat. Commun.* 4, 2932.
- Sasaki, A., Kakita, A., Yoshida, K., Konno, T., Ikeuchi, T., Hayashi, S., Matsuo, H., and Shiota, K. (2015). Variable expression of microglial DAP12 and TREM2 genes in Nasu-Hakola disease. *Neurogenetics* 16, 265–276.
- Saunders, N.R., Daneman, R., Dziegielewska, K.M., and Liddelow, S.A. (2013). Transporters of the blood-brain and blood-CSF interfaces in development and in the adult. *Mol. Aspects Med.* 34, 742–752.
- Sengillo, J.D., Winkler, E.A., Walker, C.T., Sullivan, J.S., Johnson, M., and Zlokovic, B.V. (2013). Deficiency in mural vascular cells coincides with blood-brain barrier disruption in Alzheimer's disease. *Brain Pathol.* 23, 303–310.
- Snyder, H.M., Corriveau, R.A., Craft, S., Faber, J.E., Greenberg, S.M., Knopman, D., Lamb, B.T., Montine, T.J., Nedergaard, M., Schaffer, C.B., et al. (2015). Vascular contributions to cognitive impairment and dementia including Alzheimer's disease. *Alzheimers Dement.* 11, 710–717.
- Sofroniew, M.V. (2015). Astrocyte barriers to neurotoxic inflammation. *Nat. Rev. Neurosci.* 16, 249–263.
- Stenman, J.M., Rajagopal, J., Carroll, T.J., Ishibashi, M., McMahon, J., and McMahon, A.P. (2008). Canonical Wnt signaling regulates organ-specific assembly and differentiation of CNS vasculature. *Science* 322, 1247–1250.
- Sweeney, M.D., Sagare, A.P., and Zlokovic, B.V. (2015). Cerebrospinal fluid biomarkers of neurovascular dysfunction in mild dementia and Alzheimer's disease. *J. Cereb. Blood Flow Metab.* 35, 1055–1068.
- Tallquist, M.D., French, W.J., and Soriano, P. (2003). Additive effects of PDGF receptor beta signaling pathways in vascular smooth muscle cell development. *PLoS Biol.* 1, E52.
- Tam, S.J., Richmond, D.L., Kaminker, J.S., Modrusan, Z., Martin-McNulty, B., Cao, T.C., Weimer, R.M., Carano, R.A.D., van Bruggen, N., and Watts, R.J. (2012). Death receptors DR6 and TROY regulate brain vascular development. *Dev. Cell* 22, 403–417.
- Tarasoff-Conway, J.M., Carare, R.O., Osorio, R.S., Glodzik, L., Butler, T., Fieremans, E., Axel, L., Rusinek, H., Nicholson, C., Zlokovic, B.V., et al. (2015). Clearance systems in the brain-implications for Alzheimer disease. *Nat. Rev. Neurol.* 11, 457–470.
- Tietz, S., and Engelhardt, B. (2015). Brain barriers: Crosstalk between complex tight junctions and adherens junctions. *J. Cell Biol.* 209, 493–506.

- Treusch, S., Hamamichi, S., Goodman, J.L., Matlack, K.E.S., Chung, C.Y., Baru, V., Shulman, J.M., Parrado, A., Bevis, B.J., Valastyan, J.S., et al. (2011). Functional links between A β toxicity, endocytic trafficking, and Alzheimer's disease risk factors in yeast. *Science* 334, 1241–1245.
- Tsai, H.-H., Li, H., Fuentealba, L.C., Molofsky, A.V., Taveira-Marques, R., Zhuang, H., Tenney, A., Murnen, A.T., Fancy, S.P.J., Merkle, F., et al. (2012). Regional astrocyte allocation regulates CNS synaptogenesis and repair. *Science* 337, 358–362.
- Wang, D., Kranz-Eble, P., and De Vivo, D.C. (2000). Mutational analysis of GLUT1 (SLC2A1) in Glut-1 deficiency syndrome. *Hum. Mutat.* 16, 224–231.
- Wang, C., Li, Y., Shi, L., Ren, J., Patti, M., Wang, T., de Oliveira, J.R.M., Sobrido, M.-J., Quintáns, B., Baquero, M., et al. (2012a). Mutations in SLC20A2 link familial idiopathic basal ganglia calcification with phosphate homeostasis. *Nat. Genet.* 44, 254–256.
- Wang, Y., Ratner, A., Zhou, Y., Williams, J., Smallwood, P.M., and Nathans, J. (2012b). Norrin/Frizzled4 signaling in retinal vascular development and blood brain barrier plasticity. *Cell* 151, 1332–1344.
- Winkler, E.A., Bell, R.D., and Zlokovic, B.V. (2011). Central nervous system pericytes in health and disease. *Nat. Neurosci.* 14, 1398–1405.
- Winkler, E.A., Sengillo, J.D., Sullivan, J.S., Henkel, J.S., Appel, S.H., and Zlokovic, B.V. (2013). Blood-spinal cord barrier breakdown and pericyte reductions in amyotrophic lateral sclerosis. *Acta Neuropathol.* 125, 111–120.
- Winkler, E.A., Nishida, Y., Sagare, A.P., Rege, S.V., Bell, R.D., Perlmuter, D., Sengillo, J.D., Hillman, S., Kong, P., Nelson, A.R., et al. (2015). GLUT1 reductions exacerbate Alzheimer's disease vasculo-neuronal dysfunction and degeneration. *Nat. Neurosci.* 18, 521–530.
- Woodfin, A., Voisin, M.-B., Beyrau, M., Colom, B., Caille, D., Diapouli, F.-M., Nash, G.B., Chavakis, T., Albelda, S.M., Rainger, G.E., et al. (2011). The junctional adhesion molecule JAM-C regulates polarized transendothelial migration of neutrophils in vivo. *Nat. Immunol.* 12, 761–769.
- Yamamoto, H., Ehling, M., Kato, K., Kanai, K., van Lessen, M., Frye, M., Zeuschner, D., Nakayama, M., Vestweber, D., and Adams, R.H. (2015). Integrin β 1 controls VE-cadherin localization and blood vessel stability. *Nat. Commun.* 6, 6429.
- Yao, Y., Chen, Z.-L., Norris, E.H., and Strickland, S. (2014). Astrocytic laminin regulates pericyte differentiation and maintains blood brain barrier integrity. *Nat. Commun.* 5, 3413.
- Yates, P.A., Desmond, P.M., Phal, P.M., Steward, C., Szoek, C., Salvado, O., Ellis, K.A., Martins, R.N., Masters, C.L., Ames, D., et al.; AIBL Research Group (2014). Incidence of cerebral microbleeds in preclinical Alzheimer disease. *Neurology* 82, 1266–1273.
- Zhao, Z., and Zlokovic, B.V. (2014). Blood-brain barrier: a dual life of MFSD2A? *Neuron* 82, 728–730.
- Zhao, Z., Sagare, A.P., Ma, Q., Halliday, M.R., Kong, P., Kisler, K., Winkler, E.A., Ramanathan, A., Kanekiyo, T., Bu, G., et al. (2015). Central role for PICALM in amyloid- β blood-brain barrier transcytosis and clearance. *Nat. Neurosci.* 18, 978–987.
- Zhou, Y., and Nathans, J. (2014). Gpr124 controls CNS angiogenesis and blood-brain barrier integrity by promoting ligand-specific canonical wnt signaling. *Dev. Cell* 31, 248–256.
- Zhou, Y., Wang, Y., Tischfield, M., Williams, J., Smallwood, P.M., Ratner, A., Taketo, M.M., and Nathans, J. (2014). Canonical WNT signaling components in vascular development and barrier formation. *J. Clin. Invest.* 124, 3825–3846.
- Zipser, B.D., Johanson, C.E., Gonzalez, L., Berzin, T.M., Tavares, R., Hulette, C.M., Vitek, M.P., Hovanessian, V., and Stopa, E.G. (2007). Microvascular injury and blood-brain barrier leakage in Alzheimer's disease. *Neurobiol. Aging* 28, 977–986.
- Zlokovic, B.V. (1995). Cerebrovascular permeability to peptides: manipulations of transport systems at the blood-brain barrier. *Pharm. Res.* 12, 1395–1406.
- Zlokovic, B.V. (2008). The blood-brain barrier in health and chronic neurodegenerative disorders. *Neuron* 57, 178–201.
- Zlokovic, B.V. (2011). Neurovascular pathways to neurodegeneration in Alzheimer's disease and other disorders. *Nat. Rev. Neurosci.* 12, 723–738.
- Zlokovic, B.V. (2013). Cerebrovascular effects of apolipoprotein E: implications for Alzheimer disease. *JAMA Neurol.* 70, 440–444.
- Zlokovic, B.V., Begley, D.J., and Chain-Eliash, D.G. (1985). Blood-brain barrier permeability to leucine-enkephalin, D-alanine2-D-leucine5-enkephalin and their N-terminal amino acid (tyrosine). *Brain Res.* 336, 125–132.
- Zlokovic, B.V., Deane, R., Sagare, A.P., Bell, R.D., and Winkler, E.A. (2010). Low-density lipoprotein receptor-related protein-1: a serial clearance homeostatic mechanism controlling Alzheimer's amyloid β -peptide elimination from the brain. *J. Neurochem.* 115, 1077–1089.
- Zonneveld, H.I., Goos, J.D.C., Wattjes, M.P., Prins, N.D., Scheltens, P., van der Flier, W.M., Kuijer, J.P.A., Muller, M., and Barkhof, F. (2014). Prevalence of cortical superficial siderosis in a memory clinic population. *Neurology* 82, 698–704.

Personalized Nutrition by Prediction of Glycemic Responses

Graphical Abstract



Authors

David Zeevi, Tal Korem, Niv Zmora, ..., Zamir Halpern, Eran Elinav, Eran Segal

Correspondence

eran.elinav@weizmann.ac.il (E.E.), eran.segal@weizmann.ac.il (E.S.)

In Brief

People eating identical meals present high variability in post-meal blood glucose response. Personalized diets created with the help of an accurate predictor of blood glucose response that integrates parameters such as dietary habits, physical activity, and gut microbiota may successfully lower post-meal blood glucose and its long-term metabolic consequences.

Highlights

- High interpersonal variability in post-meal glucose observed in an 800-person cohort
- Using personal and microbiome features enables accurate glucose response prediction
- Prediction is accurate and superior to common practice in an independent cohort
- Short-term personalized dietary interventions successfully lower post-meal glucose



Personalized Nutrition by Prediction of Glycemic Responses

David Zeevi,^{1,2,8} Tal Korem,^{1,2,8} Niv Zmora,^{3,4,5,8} David Israeli,^{6,8} Daphna Rothschild,^{1,2} Adina Weinberger,^{1,2} Orly Ben-Yacov,^{1,2} Dar Lador,^{1,2} Tali Avnit-Sagi,^{1,2} Maya Lotan-Pompan,^{1,2} Jotham Suez,³ Jemal Ali Mahdi,³ Elad Matot,^{1,2} Gal Malka,^{1,2} Noa Kosower,^{1,2} Michal Rein,^{1,2} Gili Zilberman-Schapira,³ Lenka Dohnalová,³ Meirav Pevsner-Fischer,³ Rony Bikovsky,^{1,2} Zamir Halpern,^{5,7} Eran Elinav,^{3,9,*} and Eran Segal^{1,2,9,*}

¹Department of Computer Science and Applied Mathematics, Weizmann Institute of Science, Rehovot 7610001, Israel

²Department of Molecular Cell Biology, Weizmann Institute of Science, Rehovot 7610001, Israel

³Immunology Department, Weizmann Institute of Science, Rehovot 7610001, Israel

⁴Internal Medicine Department, Tel Aviv Sourasky Medical Center, Tel Aviv 6423906, Israel

⁵Research Center for Digestive Tract and Liver Diseases, Tel Aviv Sourasky Medical Center, Sackler Faculty of Medicine, Tel Aviv University, Tel Aviv 6423906, Israel

⁶Day Care Unit and the Laboratory of Imaging and Brain Stimulation, Kfar Shaul Hospital, Jerusalem Center for Mental Health, Jerusalem 9106000, Israel

⁷Digestive Center, Tel Aviv Sourasky Medical Center, Tel Aviv 6423906, Israel

⁸Co-first author

⁹Co-senior author

*Correspondence: eran.elinav@weizmann.ac.il (E.E.), eran.segal@weizmann.ac.il (E.S.)

<http://dx.doi.org/10.1016/j.cell.2015.11.001>

SUMMARY

Elevated postprandial blood glucose levels constitute a global epidemic and a major risk factor for prediabetes and type II diabetes, but existing dietary methods for controlling them have limited efficacy. Here, we continuously monitored week-long glucose levels in an 800-person cohort, measured responses to 46,898 meals, and found high variability in the response to identical meals, suggesting that universal dietary recommendations may have limited utility. We devised a machine-learning algorithm that integrates blood parameters, dietary habits, anthropometrics, physical activity, and gut microbiota measured in this cohort and showed that it accurately predicts personalized postprandial glycemic response to real-life meals. We validated these predictions in an independent 100-person cohort. Finally, a blinded randomized controlled dietary intervention based on this algorithm resulted in significantly lower postprandial responses and consistent alterations to gut microbiota configuration. Together, our results suggest that personalized diets may successfully modify elevated postprandial blood glucose and its metabolic consequences.

INTRODUCTION

Blood glucose levels are rapidly increasing in the population, as evident by the sharp incline in the prevalence of prediabetes and impaired glucose tolerance estimated to affect, in the U.S. alone, 37% of the adult population (Bansal, 2015). Prediabetes, charac-

terized by chronically impaired blood glucose responses, is a significant risk factor for type II diabetes mellitus (T2DM), with up to 70% of prediabetics eventually developing the disease (Nathan et al., 2007). It is also linked to other manifestations, collectively termed the metabolic syndrome, including obesity, hypertension, non-alcoholic fatty liver disease, hypertriglyceridemia, and cardiovascular disease (Grundy, 2012). Thus, maintaining normal blood glucose levels is considered critical for preventing and controlling the metabolic syndrome (Riccardi and Rivelles, 2000).

Dietary intake is a central determinant of blood glucose levels, and thus, in order to achieve normal glucose levels it is imperative to make food choices that induce normal postprandial (post-meal) glycemic responses (PPGR; Gallwitz, 2009). Postprandial hyperglycemia is an independent risk factor for the development of T2DM (American Diabetes Association., 2015a), cardiovascular disease (Gallwitz, 2009), and liver cirrhosis (Nishida et al., 2006) and is associated with obesity (Blaak et al., 2012), and enhanced all-cause mortality in both T2DM (Cavalot et al., 2011) and cancer (Lamkin et al., 2009).

Despite their importance, no method exists for predicting PPGRs to food. The current practice is to use the meal carbohydrate content (American Diabetes Association., 2015b; Bao et al., 2011), even though it is a poor predictor of the PPGR (Conn and Newburgh, 1936). Other methods aimed at estimating PPGRs are the glycemic index, which quantifies PPGR to consumption of a single tested food type, and the derived glycemic load (Jenkins et al., 1981). It thus has limited applicability in assessing the PPGR to real-life meals consisting of arbitrary food combinations and varying quantities (Dodd et al., 2011), consumed at different times of the day and at different proximity to physical activity and other meals. Indeed, studies examining the effect of diets with a low glycemic index on T2DM risk, weight loss, and cardiovascular risk factors yielded mixed results (Greenwood et al., 2013; Kristo et al., 2013; Schwingshackl and Hoffmann, 2013).

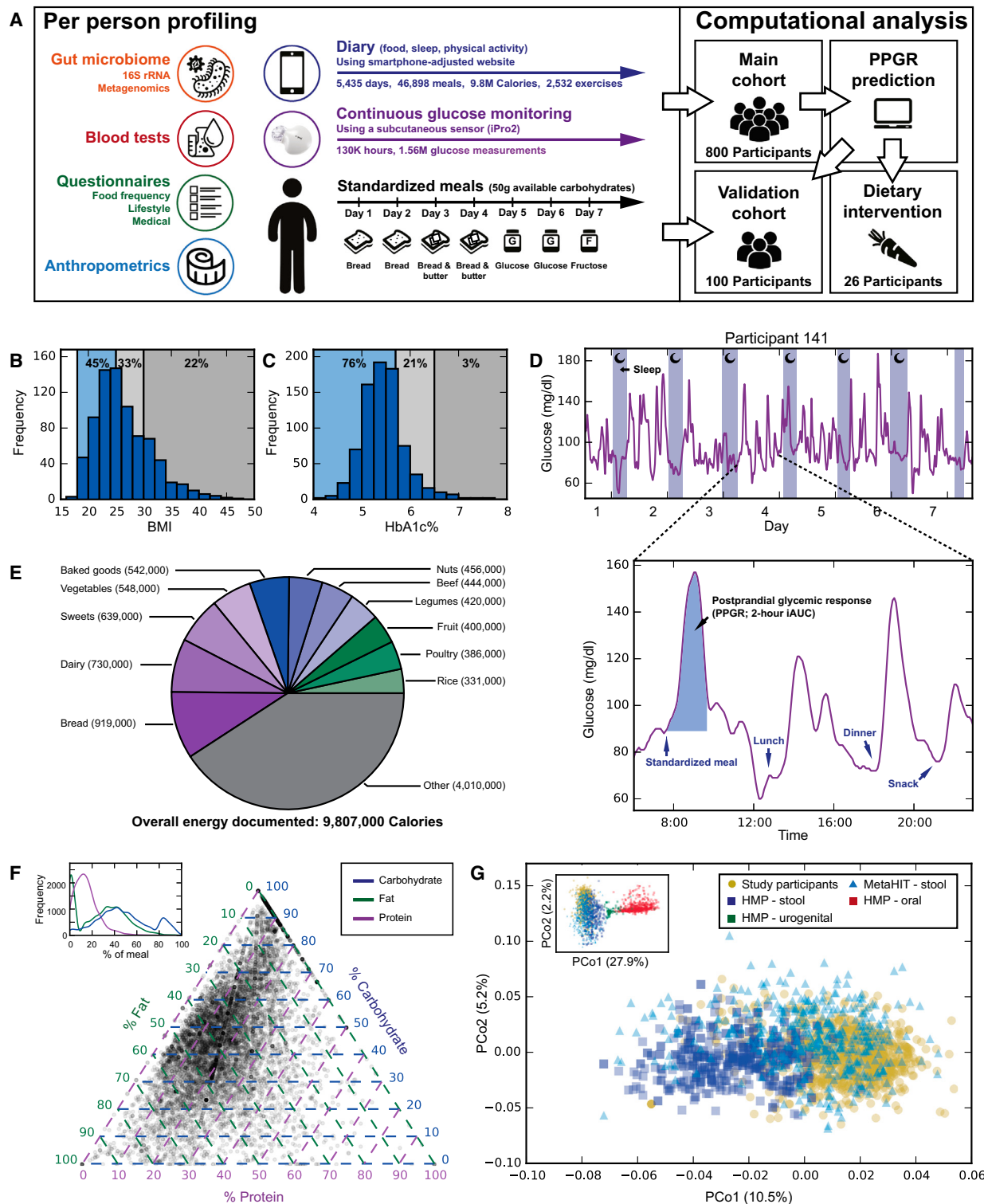


Figure 1. Profiling of Postprandial Glycemic Responses, Clinical Data, and Gut Microbiome

(A) Illustration of our experimental design.

(B and C) Distribution of BMI and glycated hemoglobin (HbA1c%) in our cohort. Thresholds for overweight ($\text{BMI} \geq 25 \text{ kg/m}^2$), obese ($\text{BMI} \geq 30 \text{ kg/m}^2$), prediabetes ($\text{HbA1c\%} \geq 5.7\%$) and T2DM ($\geq 6.5\%$) are shown.

(legend continued on next page)

Table 1. Cohorts Description

	Main Cohort	Validation Cohort	KS p Value
Number of participants (n)	800	100	
Sex (% female)	60%	60%	1
Age (y) Mean ± SD	43.3 ± 13.1	42.4 ± 12.6	0.972
BMI (kg/m ²) Mean ± SD	26.4 ± 5.1	26.5 ± 4.8	0.867
BMI ≥ 25	428 (54%)	50 (50%)	
BMI ≥ 30	173 (22%)	18 (18%)	
HbA1c% Mean ± SD	5.43 ± 0.45	5.50 ± 0.55	0.492
HbA1c% ≥ 5.7	189 (24%)	31 (31%)	
HbA1c% ≥ 6.5	23 (3%)	3 (3%)	
Total cholesterol (non-fasting, mg/dl) Mean ± SD	186.8 ± 37.5	182.7 ± 35.7	0.231
HDL cholesterol (non-fasting, mg/dl) Mean ± SD	59.0 ± 17.8	55.0 ± 16.1	0.371
Waist-to-hip circumference ratio Mean ± SD	0.83 ± 0.12	0.84 ± 0.07	0.818

KS - Kolmogorov-Smirnov test. See also [Figure S1](#).

More broadly, ascribing a single PPGR to each food assumes that the response is solely an intrinsic property of the consumed food. However, the few small-scale ($n = 23\text{--}40$) studies that examined interpersonal differences in PPGRs found high variability in the response of different people to the same food (Vega-López et al., 2007; Vrolix and Mensink, 2010), but the factors underlying this variability have not been systematically studied.

Factors that may affect interpersonal differences in PPGRs include genetics (Carpenter et al., 2015), lifestyle (Dunstan et al., 2012), insulin sensitivity (Himsworth, 1934), and exocrine pancreatic and glucose transporters activity levels (Gibbs et al., 1995). Another factor that may be involved is the gut microbiota. Pioneering work by Jeffrey Gordon and colleagues previously showed that it associates with the propensity for obesity and its complications, and later works also demonstrated associations with glucose intolerance, T1DM, hyperlipidemia, and insulin resistance (Le Chatelier et al., 2013; Karlsson et al., 2013; Qin et al., 2012; Suez et al., 2014; Turnbaugh et al., 2006; Zhang et al., 2013). However, little is known about the association of gut microbiota with PPGRs.

Here, we set out to quantitatively measure individualized PPGRs, characterize their variability across people, and identify factors associated with this variability. To this end, we continuously monitored glucose levels during an entire week in a cohort of 800 healthy and prediabetic individuals and also measured

blood parameters, anthropometrics, physical activity, and self-reported lifestyle behaviors, as well as gut microbiota composition and function. Our results demonstrate high interpersonal variability in PPGRs to the same food. We devised a machine learning algorithm that integrates these multi-dimensional data and accurately predicts personalized PPGRs, which we further validated in an independently collected 100-person cohort. Moreover, we show that personally tailored dietary interventions based on these predictions result in significantly improved PPGRs accompanied by consistent alterations to the gut microbiota.

RESULTS

Measurements of Postprandial Responses, Clinical Data, and Gut Microbiome

To comprehensively characterize PPGRs, we recruited 800 individuals aged 18–70 not previously diagnosed with T1DM ([Figure 1A](#), [Table 1](#)). The cohort is representative of the adult non-diabetic Israeli population (Israeli Center for Disease Control, 2014), with 54% overweight ($\text{BMI} \geq 25 \text{ kg/m}^2$) and 22% obese ($\text{BMI} \geq 30 \text{ kg/m}^2$, [Figures 1B](#), [1C](#), and [S1](#)). These properties are also characteristic of the Western adult non-diabetic population (World Health Organization, 2008).

Each participant was connected to a continuous glucose monitor (CGM), which measures interstitial fluid glucose every 5 min for 7 full days (the “connection week”), using subcutaneous sensors ([Figure 1D](#)). CGMs estimate blood glucose levels with high accuracy (Bailey et al., 2014) and previous studies found no significant differences between PPGRs extracted from CGMs and those obtained from either venous or capillary blood (Vrolix and Mensink, 2010). We used blinded CGMs and thus participants were unaware of their CGM levels during the connection week. Together, we recorded over 1.5 million glucose measurements from 5,435 days.

While connected to the CGM, participants were instructed to log their activities in real-time, including food intake, exercise and sleep, using a smartphone-adjusted website (www.personalnutrition.org) that we developed ([Figure S2A](#)). Each food item within every meal was logged along with its weight by selecting it from a database of 6,401 foods with full nutritional values based on the Israeli Ministry of Health database that we further improved and expanded with additional items from certified sources. To increase compliance, participants were informed that accurate logging is crucial for them to receive an accurate analysis of their PPGRs to food (ultimately provided to each of them). During the connection week, participants were asked to follow their normal daily routine and dietary habits, except for the first meal of every day, which we provided as one of four different types of standardized meals, each consisting of 50 g of available carbohydrates. This resulted in a total of 46,898 real-life meals with close-to or full nutritional values (median of 54

(D) Example of continuous glucose monitoring (CGM) for one participant during an entire week. Colored area within zoom-in shows the incremental area under the glucose curve (iAUC) which we use to quantify the meal's PPGR.

(E) Major food components consumed by energy intake.

(F) Distribution of meals (dots) by macronutrient content. Inset shows histogram of meals per macronutrient.

(G) Bray-Curtis based PCoA of metagenome-based bacterial abundances of stool samples in our cohort and in the U.S. HMP and European MetaHIT cohorts. Inset shows PCoA when samples from other HMP body sites are added. See also [Figure S2](#).

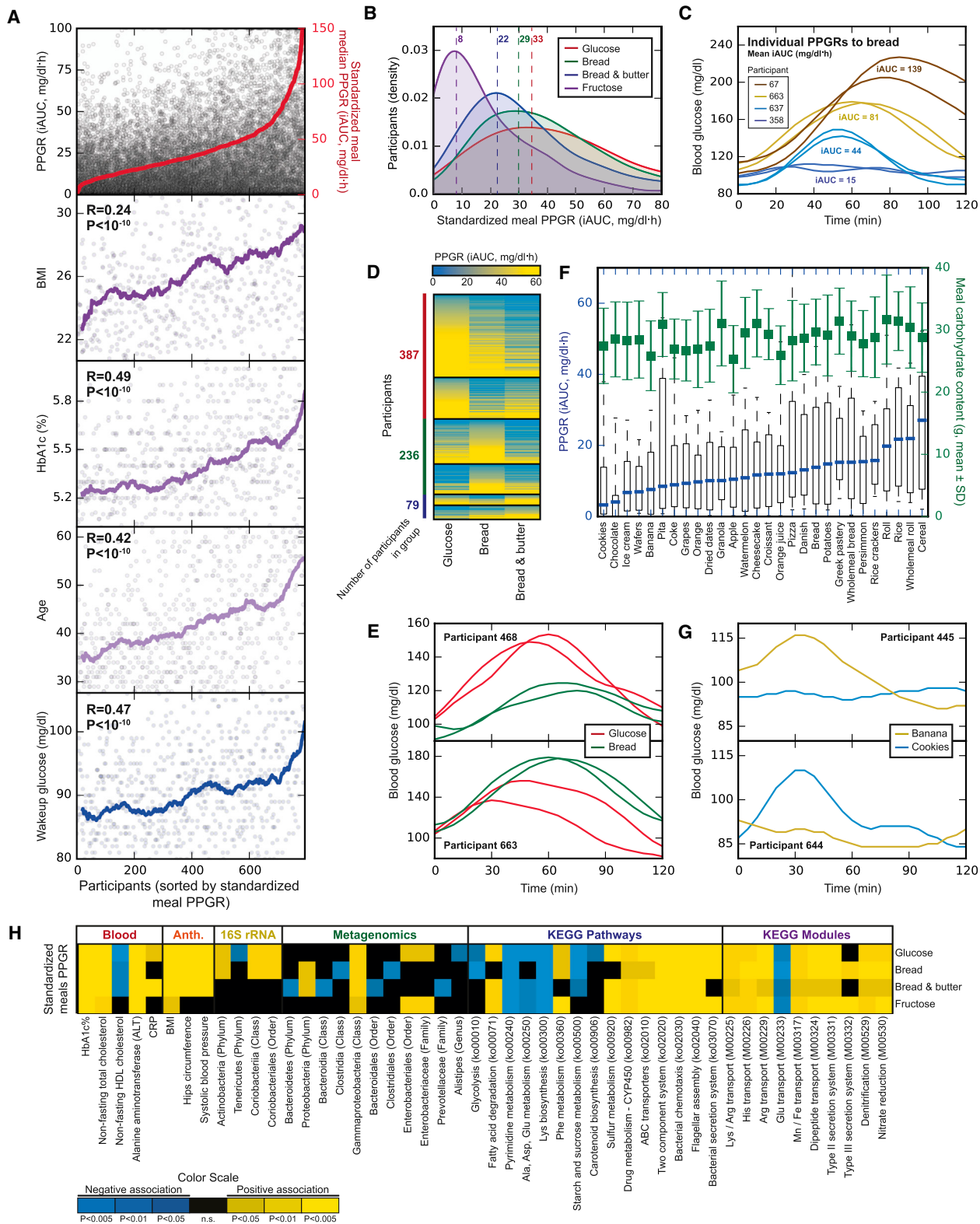


Figure 2. High Interpersonal Variability in the Postprandial Glycemic Response to the Same Meal

(A) PPGRs associate with risk factors. Shown are PPGRs, BMI, HbA1c%, age, and wakeup glucose of all participants, sorted by median standardized meal PPGRs (top, red dots). Correlation of factors with the median PPGRs to standardized meals is shown along with a moving average line.

(legend continued on next page)

meals per participant) and 5,107 standardized meals. The PPGR of each meal was calculated by combining reported meal time with CGM data and computing the incremental area under the glucose curve in the 2 hr after the meal (iAUC; [Wolever and Jenkins, 1986](#); [Figure 1D](#)).

Prior to CGM connection, a comprehensive profile was collected from each participant, including: food frequency, lifestyle, and medical background questionnaires; anthropometric measures (e.g., height, hip circumference); a panel of blood tests; and a single stool sample, used for microbiota profiling by both 16S rRNA and metagenomic sequencing.

With a total of ~10,000,000 Calories logged, our data provide a global view into the cohort's dietary habits, showing the fraction that each food source contributes to the cohort's overall energy intake (e.g., dairy, 7%; sweets, 6%; [Figure 1E](#)), and macronutrient intake ([Figures S2B–S2D](#)). Analysis of the caloric breakdown of every meal by macronutrients revealed that protein intake varies relatively little across meals (80% of meals have 5%–35% protein), while fat and carbohydrates have a wide and bimodal distribution, where one of the modes corresponds to fat-free meals and constitutes 18% of all meals ([Figure 1F](#)).

Principal coordinates analysis (PCoA) on the Bray-Curtis dissimilarity between metagenome-based relative abundances (RA) revealed a similar degree of variability in the microbiomes of our cohort and stool samples of the US HMP ([Human Microbiome Project Consortium, 2012](#)) and European MetaHIT ([Nielsen et al., 2014](#)) cohorts ([Figure 1G](#)). The first two principal coordinates show some distinction between our cohort and the other cohorts, but when HMP samples from other body sites are added to the PCoA, stool samples from all three cohorts cluster together and separate from the rest, indicative of overall similarity in the gut microbiota composition of individuals from these three distinct geographical regions ([Figure 1G](#)).

Postprandial Glycemic Responses Associate with Multiple Risk Factors

Our data replicate known associations of PPGRs with risk factors, as the median standardized meal PPGR was significantly correlated with several known risk factors including BMI ($R = 0.24$, $p < 10^{-10}$), glycated hemoglobin (HbA1c%, $R = 0.49$, $p < 10^{-10}$), wakeup glucose ($R = 0.47$, $p < 10^{-10}$), and age ($R = 0.42$, $p < 10^{-10}$, [Figure 2A](#)). These associations are not confined to extreme values but persist along the entire range of PPGR values, suggesting that the reduction in levels of risk factors is continuous across all postprandial values, with lower values associated with lower levels of risk factors even within the normal value ranges ([Figure 2A](#)).

Utilizing the continuous nature of the CGMs, we also examined the association between risk factors and the glucose level of each participant at different percentiles (0–100) with respect to all glucose measurements from the connection week. These levels are affected by the PPGRs while also reflecting the general glycemic control state of the participant. All percentiles significantly associated with risk factors (wakeup glucose, BMI, HbA1c%, and age; [Figures S3A–S3D](#)). The percentile at which the glucose level correlation was highest varied across risk factors. For example, BMI had the highest correlation with the 40th glucose value percentile, whereas for HbA1c% percentile 95 had the highest correlation ([Figures S3A](#) and [S3C](#)). These results suggest that the entire range of glucose levels of an individual may have clinical relevance, with different percentiles being more relevant for particular risk factors.

High Interpersonal Variability in the Postprandial Response to Identical Meals

Next, we examined intra- and interpersonal variability in the PPGR to the same food. First, we assessed the extent to which PPGRs to three types of standardized meals that were given twice to every participant ([Figure 1A](#)), are reproducible within the same person. Indeed, the two replicates showed high agreement ($R = 0.77$ for glucose, $R = 0.77$ for bread with butter, $R = 0.71$ for bread, $p < 10^{-10}$ in all cases), demonstrating that the PPGR to identical meals is reproducible within the same person and that our experimental system reliably measures this reproducibility. However, when comparing the PPGRs of different people to the same meal, we found high interpersonal variability, with the PPGRs of every meal type (except fructose) spanning the entire range of PPGRs measured in our cohort ([Figures 2B](#), [2C](#), and [S3E–S3H](#)). For example, the average PPGR to bread across 795 people was $44 \pm 31 \text{ mg/dl}^{\cdot}\text{h}$ (mean \pm SD), with the bottom 10% of participants exhibiting an average PPGR below 15 mg/dl $^{\cdot}$ h and the top 10% of participants exhibiting an average PPGR above 79 mg/dl $^{\cdot}$ h. The large interpersonal differences in PPGRs are also evident in that the type of meal that induced the highest PPGR differs across participants and that different participants might have opposite PPGRs to pairs of different standardized meals ([Figures 2D](#) and [2E](#)).

Interpersonal variability was not merely a result of participants having high PPGRs to all meals, since high variability was also observed when the PPGR of each participant was normalized to his/her own PPGR to glucose ([Figures S3I–S3K](#)). For white bread and fructose, for which such normalized PPGRs were previously measured, the mode of the PPGR distribution in our cohort had excellent agreement with published values ([Foster-Powell et al.,](#)

(B) Kernel density estimation (KDE) smoothed histogram of the PPGR to four types of standardized meals provided to participants (each with 50 g of available carbohydrates). Dashed lines represent histogram modes (See also [Figure S3](#)).

(C) Example of high interpersonal variability and low intra-personal variability in the PPGR to bread across four participants (two replicates per participant consumed on two different mornings).

(D) Heatmap of PPGR (average of two replicates) of participants (rows) to three types of standardized meals (columns) consumed in replicates. Clustering is by each participant's relative rankings of the three meal types.

(E) Example of two replicates of the PPGR to two standardized meals for two participants exhibiting reproducible yet opposite PPGRs.

(F) Box plot (box, IQR; whiskers, 10–90 percentiles) of the PPGR to different real-life meals along with amount of carbohydrates consumed (green; mean \pm std).

(G) Same as (E), for a pair of real-life meals, each containing 20 g of carbohydrates.

(H) Heatmap (subset) of statistically significant associations ($p < 0.05$, FDR corrected) between participants' standardized meals PPGRs and participants' clinical and microbiome data (See also [Figure S4](#) for the full heatmap).

2002), further validating the accuracy of our data (bread: 65 versus 71; fructose: 15 versus 19, [Figures S3I](#) and [S3K](#)).

Next, we examined variability in the PPGRs to the multiple real-life meals reported by our participants. Since real-life meals vary in amounts and may each contain several different food components, we only examined meals that contained 20–40 g of carbohydrates and had a single dominant food component whose carbohydrate content exceeded 50% of the meal's carbohydrate content. We then ranked the resulting dominant foods that had at least 20 meal instances by their population-average PPGR ([Figure 2F](#)). For foods with a published glycemic index, our population-average PPGRs agreed with published values ($R = 0.69$, $p < 0.0005$), further supporting our data ([Table S1](#)). For example, the average PPGR to rice and potatoes was relatively high, whereas that for ice cream, beer, and dark chocolate was relatively low, in agreement with published data ([Atkinson et al., 2008](#); [Foster-Powell et al., 2002](#)). Similar to standardized meals, PPGRs to self-reported meals highly varied across individuals, with both low and high responders noted for each type of meal ([Figures 2F](#) and [2G](#)).

Postprandial Variability Is Associated with Clinical and Microbiome Profiles

We found multiple significant associations between the standardized meal PPGRs of participants and both their clinical and gut microbiome data ([Figures 2H](#) and [S4](#)). Notably, the TIIDM and metabolic syndrome risk factors HbA1c%, BMI, systolic blood pressure, and alanine aminotransferase (ALT) activity are all positively associated with PPGRs to all types of standardized meals, reinforcing the medical relevance of PPGRs. In most standardized meals, PPGRs also exhibit a positive correlation with CRP, whose levels rise in response to inflammation ([Figure 2H](#)).

With respect to microbiome features, the phylogenetically related Proteobacteria and Enterobacteriaceae both exhibit positive associations with a few of the standardized meals PPGR ([Figure 2H](#)). These taxa have reported associations with poor glycemic control, and with components of the metabolic syndrome including obesity, insulin resistance, and impaired lipid profile ([Xiao et al., 2014](#)). RAs of Actinobacteria are positively associated with the PPGR to both glucose and bread, which is intriguing since high levels of this phylum were reported to associate with a high-fat, low-fiber diet ([Wu et al., 2011](#)).

At the functional level, the KEGG pathways of bacterial chemotaxis and of flagellar assembly, reported to increase in mice fed high-fat diets and decrease upon prebiotics administration ([Everard et al., 2014](#)), exhibit positive associations with several standardized meal PPGRs ([Figure 2H](#)). The KEGG pathway of ABC transporters, reported to be positively associated with TIIDM ([Karlsson et al., 2013](#)) and with a Western high-fat/high-sugar diet ([Turnbaugh et al., 2009](#)), also exhibits positive association with several standardized meal PPGRs ([Figure 2H](#)). Several bacterial secretion systems, including both type II and type III secretion systems that are instrumental in bacterial infection and quorum sensing ([Sandkvist, 2001](#)) are positively associated with most standardized meal PPGRs ([Figure 2H](#)). Finally, KEGG modules for transport of the positively charged amino acids lysine and arginine are associated with high PPGR to standardized foods, while transport of the negatively charged

amino acid glutamate is associated with low PPGRs to these foods.

Taken together, these results show that PPGRs vary greatly across different people and associate with multiple person-specific clinical and microbiome factors.

Prediction of Personalized Postprandial Glycemic Responses

We next asked whether clinical and microbiome factors could be integrated into an algorithm that predicts individualized PPGRs. To this end, we employed a two-phase approach. In the first, discovery phase, the algorithm was developed on the main cohort of 800 participants, and performance was evaluated using a standard leave-one-out cross validation scheme, whereby PPGRs of each participant were predicted using a model trained on the data of all other participants. In the second, validation phase, an independent cohort of 100 participants was recruited and profiled, and their PPGRs were predicted using the model trained only on the main cohort ([Figure 3A](#)).

Given non-linear relationships between PPGRs and the different factors, we devised a model based on gradient boosting regression ([Friedman, 2001](#)). This model predicts PPGRs using the sum of thousands of different decision trees. Trees are inferred sequentially, with each tree trained on the residual of all previous trees and making a small contribution to the overall prediction ([Figure 3A](#)). The features within each tree are selected by an inference procedure from a pool of 137 features representing meal content (e.g., energy, macronutrients, micronutrients); daily activity (e.g., meals, exercises, sleep times); blood parameters (e.g., HbA1c%, HDL cholesterol); CGM-derived features; questionnaires; and microbiome features (16S rRNA and metagenomic RAs, KEGG pathway and module RAs and bacterial growth dynamics - PTRs; [Korem et al., 2015](#)).

As a baseline reference, we used the “carbohydrate counting” model, as it is the current gold standard for predicting PPGRs ([American Diabetes Association., 2015b](#); [Bao et al., 2011](#)). On our data, this model that consists of a single explanatory variable representing the meal's carbohydrate amount achieves a modest yet statistically significant correlation with PPGRs ($R = 0.38$, $p < 10^{-10}$, [Figure 3B](#)). A model using only meal Caloric content performs worse ($R = 0.33$, $p < 10^{-10}$, [Figure 3C](#)). Our predictor that integrates the above person-specific factors predicts the held-out PPGRs of individuals with a significantly higher correlation ($R = 0.68$, $p < 10^{-10}$, [Figure 3D](#)). This correlation approaches the presumed upper bound limit set by the 0.71–0.77 correlation that we observed between the PPGR of the same person to two replicates of the same standardized meal.

Validation of Personalized Postprandial Glycemic Response Predictions on an Independent Cohort

We further validated our model on an independent cohort of 100 individuals that we recruited separately. Data from this additional cohort were not available to us while developing the algorithm. Participants in this cohort underwent the same profiling as in the main 800-person cohort. No significant differences were found between the main and validation cohorts in key parameters, including age, BMI, non-fasting total and HDL cholesterol, and HbA1c% ([Table 1](#), [Figure S1](#)).

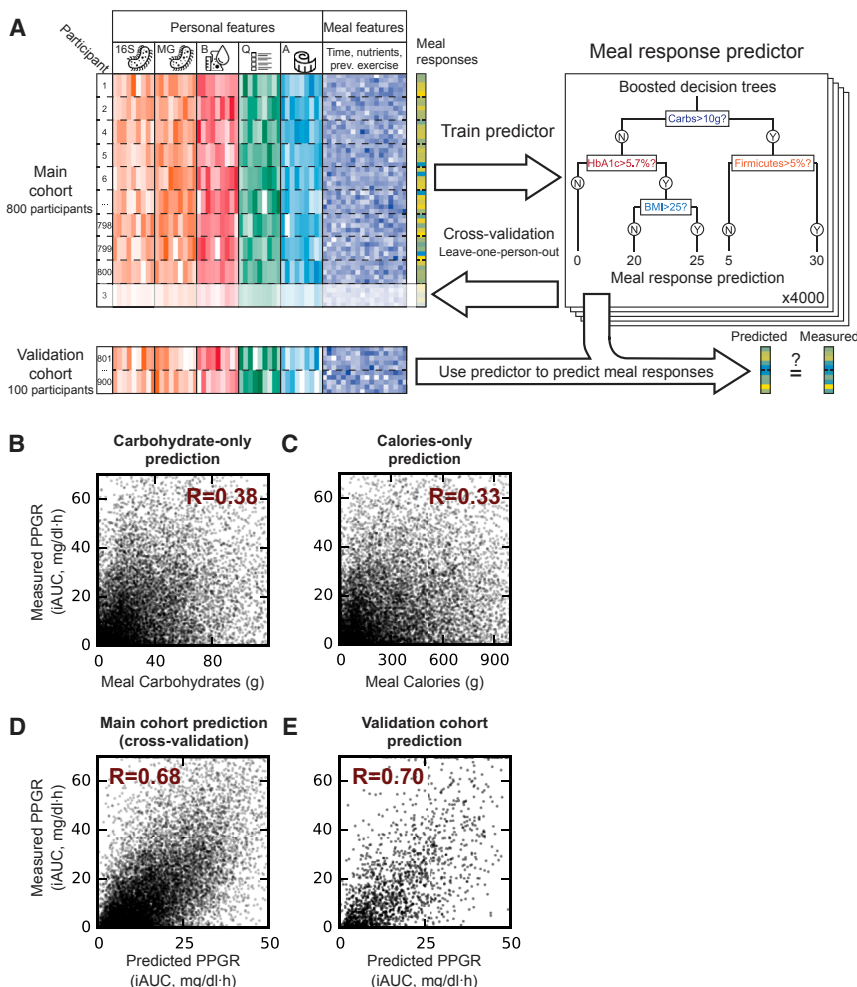


Figure 3. Accurate Predictions of Personalized Postprandial Glycemic Responses

(A) Illustration of our machine-learning scheme for predicting PPGRs. (B–E) PPGR predictions. Dots represent predicted (x axis) and CGM-measured PPGR (y axis) for meals, for a model based: only on the meal's carbohydrate content (B); only on the meal's Caloric content (C); our predictor evaluated in leave-one-person-out cross validation on the main 800-person cohort (D); and our predictor evaluated on the independent 100-person validation cohort (E). Pearson correlation of predicted and measured PPGRs is indicated.

Notably, our algorithm, derived solely using the main 800 participants cohort, achieved similar performance on the 100 participants of the validation cohort ($R = 0.68$ and $R = 0.70$ on the main and validation cohorts, respectively, **Figures 3D** and **3E**). The reference carbohydrate counting model achieved the same performance as in the main cohort ($R = 0.38$). This result further supports the ability of our algorithm to provide personalized PPGR predictions.

Factors Underlying Personalized Predictions

To gain insight into the contribution of the different features in the algorithm's predictions, we examined partial dependence plots (PDP), commonly used to study functional relations between features used in predictors such as our gradient boosting regressor and an outcome (PPGRs in our case; [Hastie et al., 2008](#)). PDPs graphically visualize the marginal effect of a given feature on prediction outcome after accounting for the average effect of all other features. While this effect may be indicative of feature importance, it may also be misleading due to higher-order interactions ([Hastie et al., 2008](#)). Nonetheless, PDPs are commonly used for knowledge discovery in large datasets such as ours.

As expected, the PDP of carbohydrates (**Figure 4A**) shows that as the meal carbohydrate content increases, our algorithm predicts, on average, a higher PPGR. We term this relation, of higher predicted PPGR with increasing feature value, as non-beneficial (with respect to prediction), and the opposite relation, of lower predicted PPGR with increasing feature value, as beneficial (also with respect to prediction; see PDP legend in **Figure 4**). However, since PDPs display the overall contribution of each feature across the entire cohort, we asked whether the relationship between carbohydrate amount and PPGRs varies across people. To this end, for each participant we computed the slope of the linear regression between the PPGR and carbohydrate amount of all his/her meals. As expected, this slope was positive for nearly all (95.1%) participants, reflective of higher PPGRs in meals richer in carbohydrates. However, the magnitude of this slope varies greatly across the cohort, with the PPGR of some people correlating well with the carbohydrate content (i.e., carbohydrates “sensitive”) and that of others exhibiting equally high PPGRs but little relationship to the amount of carbohydrates (carbohydrates “insensitive”; **Figure 4B**). This result suggests that carbohydrate sensitivity is also person specific.

The PDP of fat exhibits a beneficial effect for fat since our algorithm predicts, on average, lower PPGR as the meal's ratio of fat to carbohydrates (**Figure 4C**) or total fat content (**Figure S5A**) increases, consistent with studies showing that adding fat to meals may reduce the PPGR ([Cunningham and Read, 1989](#)). However, here too, we found that the effect of fat varies across people. We compared the explanatory power of a linear regression between each participant's PPGR and meal carbohydrates, with that of regression using both fat and carbohydrates. We then used the difference in Pearson R between the two models as a quantitative measure of the added contribution of fat (**Figure 4D**). For some participants we observed a reduction in PPGR with the addition of fat, while for others meal fat content

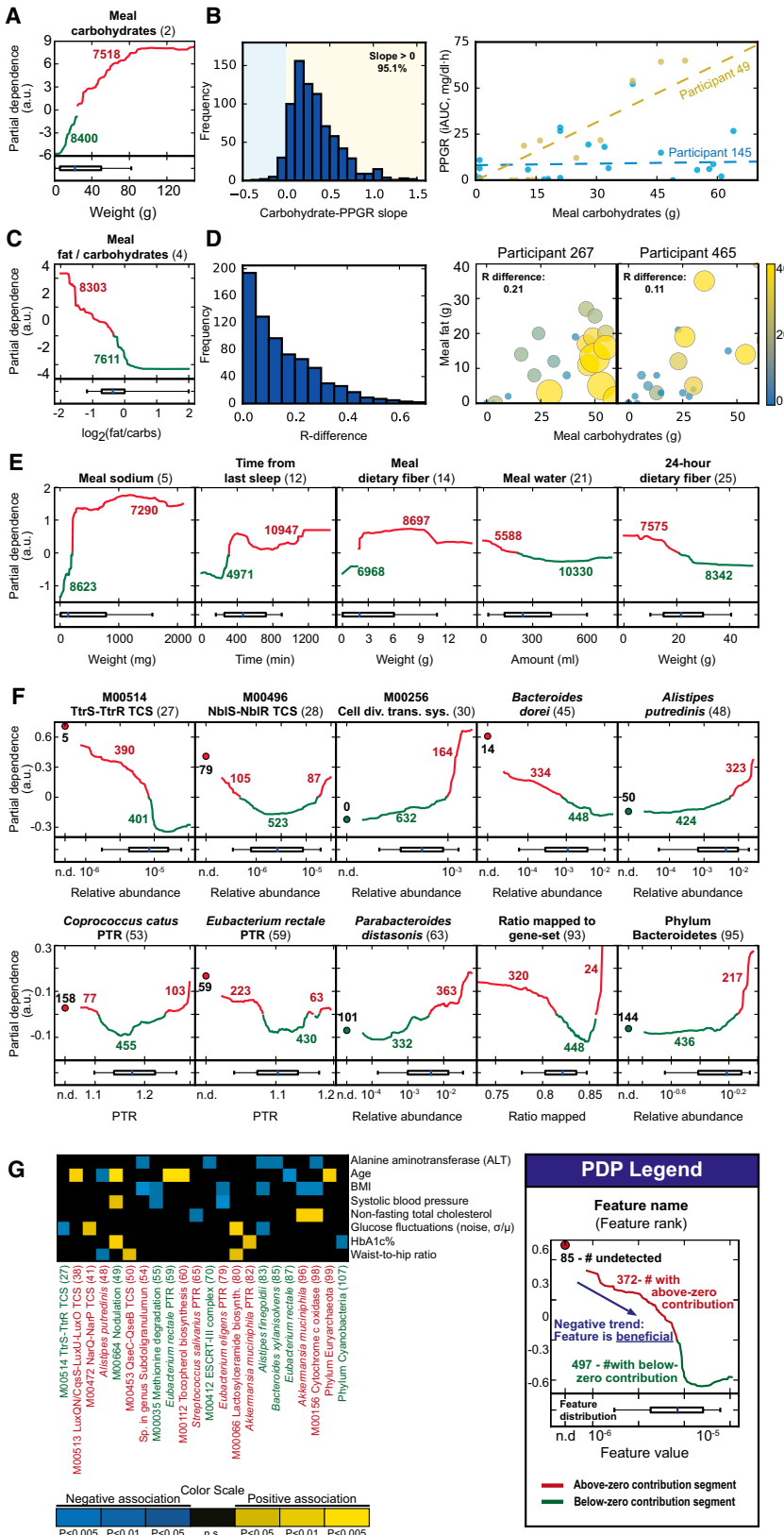


Figure 4. Factors Underlying the Prediction of Postprandial Glycemic Responses

(A) Partial dependence plot (PDP) showing the marginal contribution of the meal's carbohydrate content to the predicted PPGR (y axis, arbitrary units) at each amount of meal carbohydrates (x axis). Red and green indicate above and below zero contributions, respectively (number indicate meals). Boxplots (bottom) indicate the carbohydrates content at which different percentiles (10, 25, 50, 75, and 90) of the distribution of all meals across the cohort are located. See PDP legend.

(B) Histogram of the slope (computed per participant) of a linear regression between the carbohydrate content and the PPGR of all meals. Also shown is an example of one participant with a low slope and another with a high slope.

(C) Meal fat/carbohydrate ratio PDP.

(D) Histogram of the difference (computed per participant) between the Pearson R correlation of two linear regression models, one between the PPGR and the meal carbohydrate content and another when adding fat and carbohydrate*fat content. Also shown is an example of the carbohydrate and fat content of all meals of one participant with a relatively low R difference (carb alone correlates well with PPGR) and another with a relatively high difference (meals with high fat content have lower PPGRs). Dot color and size correspond to the meal's PPGR.

(E) Additional PDPs.

(F) Microbiome PDPs. The number of participants in which the microbiome feature was not detected is indicated (left, n.d.). Boxplots (box, IQR; whiskers 10–90 percentiles) based only on detected values. (G) Heatmap of statistically significant correlations (Pearson) between microbiome features termed

beneficial (green)

did not add much to the explanatory power of the regressor based only on the meal's carbohydrates content (Figure 4D).

Interestingly, while dietary fibers in the meal increase the predicted PPGR, their long-term effect is beneficial as higher amount of fibers consumed in the 24 hr prior to the meal reduces the predicted PPGR (Figure 4E). The meal's sodium content, the time that passed since last sleeping, and a person's cholesterol levels or age all exhibit non-beneficial PDPs, while the PDPs of the meal's alcohol and water content display beneficial effects (Figures 4E and S5A). As expected, the PDP of HbA1c% shows a non-beneficial effect with increased PPGR at higher HbA1c% values; intriguingly, higher PPGRs are predicted, on average, for individuals with HbA1c% above ~5.5%, which is very close to the prediabetes threshold of 5.7% (Figure S5A).

The 72 PDPs of the microbiome-based features used in our predictor were either beneficial (21 factors), non-beneficial (28), or non-decisive (23) in that they mostly decreased, increased, or neither, as a function of the microbiome feature. The resulting PDPs had several intriguing trends. For example, growth of *Eu bacterium rectale* was mostly beneficial, as in 430 participants with high inferred growth for *E. rectale* it associates with a lower PPGR (Figure 4F). Notably, *E. rectale* can ferment dietary carbohydrates and fibers to produce metabolites useful to the host (Duncan et al., 2007), and was associated with improved post-prandial glycemic and insulinemic responses (Martínez et al., 2013), as well as negatively associated with T1DM (Qin et al., 2012). RAs of *Parabacteroides distasonis* were found non-beneficial by our predictor (Figure 4F) and this species was also suggested to have a positive association with obesity (Ridaura et al., 2013). As another example, the KEGG module of cell-division transport system (M00256) was non-beneficial, and in the 164 participants with the highest levels for it, it associates with a higher PPGR (Figure 4F). *Bacteroides thetaiotaomicron* was non-beneficial (Figure S5B), and it was associated with obesity and was suggested to have increased capacity for energy harvest (Turnbaugh et al., 2006). In the case of *Alistipes putredinis* and the Bacteroidetes phylum, the non-beneficial classification that our predictor assigns to both of them is inconsistent with previous studies that found them to be negatively associated with obesity (Ridaura et al., 2013; Turnbaugh et al., 2006). This may reflect limitations of the PDP analysis or result from a more complex relationship between these features, obesity, and PPGRs.

To assess the clinical relevance of the microbiome-based PDPs, we computed the correlation between several risk factors and overall glucose parameters, and the factors with beneficial and non-beneficial PDPs across the entire 800-person cohort. We found 20 statistically significant correlations ($p < 0.05$, FDR corrected) where microbiome factors termed non-beneficial correlated with risk factors, and those termed beneficial exhibited an anti-correlation (Figure 4G). For example, higher levels of the beneficial methionine degradation KEGG module (M00035) resulted in lower PPGRs in our algorithm, and across the cohort, this module anti-correlates with systolic blood pressure and with BMI (Figure 4G). Similarly, fluctuations in glucose levels across the connection week correlates with nitrate respiration two-component regulatory system (M00472) and with lactosylceramide biosynthesis (M00066), which were both termed

non-beneficial. Glucose fluctuations also anti-correlate with levels of the tetrathionate respiration two-component regulatory system (M00514) and with RAs of *Alistipes finegoldii*, both termed beneficial (Figure 4G). In 14 other cases, factors with beneficial or non-beneficial PDPs were correlated and anti-correlated with risk factors, respectively.

These results suggest that PPGRs are associated with multiple and diverse factors, including factors unrelated to meal content.

Personally Tailored Dietary Interventions Improve Postprandial Responses

Next, we asked whether personally tailored dietary interventions based on our algorithm could improve PPGRs. We designed a two-arm blinded randomized controlled trial and recruited 26 new participants. A clinical dietitian met each participant and compiled 4–6 distinct isocaloric options for each type of meal (breakfast, lunch, dinner, and up to two intermediate meals), accommodating the participant's regular diet, eating preferences, and dietary constraints. Participants then underwent the same 1-week profiling of our main 800-person cohort (except that they consumed the meals compiled by the dietitian), thus providing the inputs (microbiome, blood parameters, CGM, etc.) that our algorithm needs for predicting their PPGRs.

Participants were then blindly assigned to one of two arms (Figure 5A). In the first, "prediction arm," we applied our algorithm in a leave-one-out scheme to rank every meal of each participant in the profiling week (i.e., the PPGR to each predicted meal was hidden from the predictor). We then used these rankings to design two 1-week diets: (1) a diet composed of the meals predicted by the algorithm to have low PPGRs (the "good" diet); and (2) a diet composed of the meals with high predicted PPGRs (the "bad" diet). Every participant then followed each of the two diets for a full week, during which they were connected to a CGM and a daily stool sample was collected (if available). The order of the 2 diet weeks was randomized for each participant and the identity of the intervention weeks (i.e., whether they are "good" or "bad") was kept blinded from CRAs, dietitians and participants.

The second, "expert arm," was used as a gold standard for comparison. Participants in this arm underwent the same process as the prediction arm except that instead of using our predictor for selecting their "good" and "bad" diets a clinical dietitian and a researcher experienced in analyzing CGM data (collectively termed "expert") selected them based on their measured PPGRs to all meals during the profiling week. Specifically, meals that according to the expert's analysis of their CGM had low and high PPGRs in the profiling week were selected for the "good" and "bad" diets, respectively. Thus, to the extent that PPGRs are reproducible within the same person, this expert-based arm should result in the largest differences between the "good" and "bad" diets because the selection of meals in the intervention weeks is based on their CGM data.

Notably, for 10 of the 12 participants of the predictor-based arm, PPGRs in the "bad" diet were significantly higher than in the "good" diet ($p < 0.05$, Figure 5C). Differences between the two diets are also evident in fewer glucose spikes and fewer fluctuations in the raw week-long CGM data (Figure 5B). The

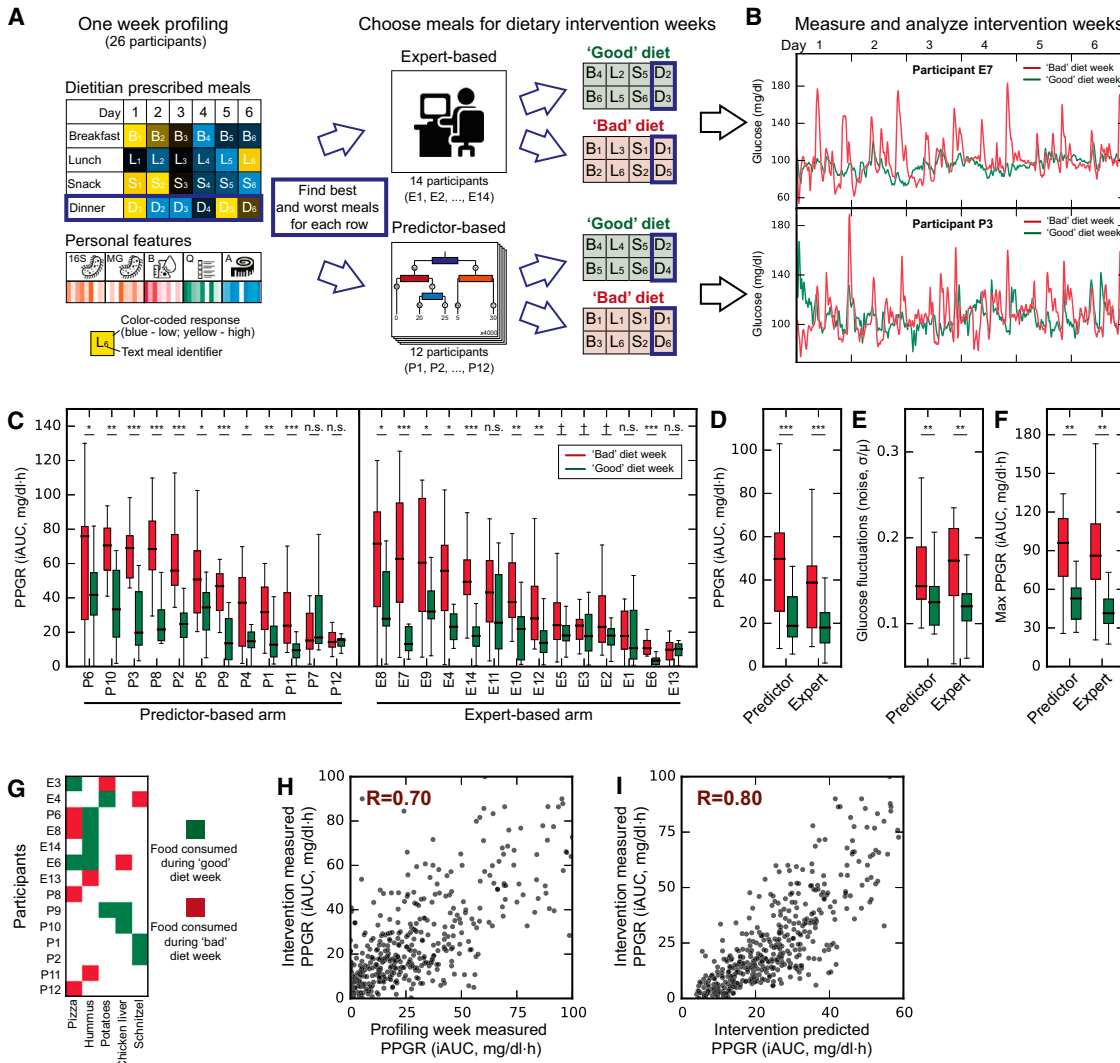


Figure 5. Personally Tailored Dietary Interventions Improve Postprandial Glycemic Responses

- (A) Illustration of the experimental design of our two-arm blinded randomized controlled trial.
- (B) Continuous glucose measurements of one participant from the expert arm (top) and another from the predictor arm (bottom) across their "good" (green) and "bad" (red) diet weeks.
- (C) Boxplot of meal PPGRs during the "bad" (red) and "good" (green) diet weeks for participants in both the predictor (left) and expert (right) arms. Statistical significance is marked (Mann-Whitney U-test, ***p < 0.001, **p < 0.01, *p < 0.05, †p < 0.1, n.s. not significant).
- (D) As in (C), but for a grouping of all meals of all participants in each study arm (p, Wilcoxon signed-rank test).
- (E) Boxplot of the blood glucose fluctuations (noise) of participants in both the "bad" (red) and "good" (green) diet weeks for both study arms. Blood glucose fluctuations per participant are defined as the ratio between the standard deviation and mean of his/her weeklong blood glucose levels (p, Wilcoxon signed-rank test).
- (F) As in (E), but for the maximum PPGR of each participant.
- (G) Subset of dominant food components prescribed in the "good" (green) diet of some participants and in the "bad" (red) diet of other participants. See also Figure S6 for the full matrix.
- (H) Dot plot between the CGM-measured PPGR of meals during the profiling week (x axis) and the average CGM-measured PPGR of the same meals during the dietary intervention weeks (y axis). Meals of all participants in both study arms are shown.
- (I) As in (H), but when PPGRs in the dietary intervention weeks are predicted by our predictor using only the first profiling week data of each participant. Boxplots - box, IQR; whiskers 1.5*IQR.

success of the predictor was comparable to that of the expert-based arm, in which significantly lower PPGRs in the "good" versus the "bad" diet were observed for 8 of its 14 participants ($p < 0.05$, 11 of 14 participants with $p < 0.1$, Figure 5C).

When combining the data across all participants, the "good" diet exhibited significantly lower PPGRs than the "bad" diet ($p < 0.05$, Figure 5D) as well as improvement in other measures of blood glucose metabolism in both study arms, specifically,

lower fluctuations in glucose levels across the CGM connection week ($p < 0.05$, Figure 5E), and a lower maximal PPGR ($p < 0.05$, Figure 5F) in the “good” diet.

Both study arms constitute personalized nutritional interventions and thus demonstrate the efficacy of this approach in lowering PPGRs. However, the predictor-based approach has broader applicability since it can predict PPGRs to arbitrary unseen meals, whereas the “expert”-based approach will always require CGM measurements of the meals it prescribes.

Post hoc examination of the prescribed diets revealed the personalized aspect of the diets in both arms in that multiple dominant food components (as in Figure 2F) prescribed in the “good” diet of some participants were prescribed in the “bad” diet of others (Figures 5G and S6). This occurs when components induced opposite CGM-measured PPGRs across participants (expert arm) or were predicted to have opposite PPGRs (predictor arm).

The correlation between the measured PPGR of meals during the profiling week and the average CGM-measured PPGR of the same meals during the dietary intervention was 0.70 (Figure 5H), which is similar to the reproducibility observed for standardized meals ($R = 0.71\text{--}0.77$). Thus, as in the case of standardized meals, a meal’s PPGR during the profiling week was not identical to its PPGR in the dietary intervention week. Notably, using only the first profiling week data of each participant, our algorithm predicted the average PPGRs of meals in the dietary intervention weeks with an even higher correlation ($R = 0.80$, Figure 5I). Since our predictor also incorporates context-specific factors (e.g., previous meal content, time since sleep), this result also suggests that such factors may be important determinants of PPGRs.

Taken together, these results show the utility of personally tailored dietary interventions for improving PPGRs in a short-term intervention period, and the ability of our algorithm to devise such interventions.

Alterations in Gut Microbiota Following Personally Tailored Dietary Interventions

Finally, we used the daily microbiome samples collected during the intervention weeks to ask whether the interventions induced significant changes in the gut microbiota. Previous studies showed that even short-term dietary interventions of several days may significantly alter the gut microbiota (David et al., 2014; Korem et al., 2015).

We detected changes following the dietary interventions that were significant relative to a null hypothesis of no change derived from the first week, in which there was no intervention, across all participants (Figures 6A and 6B). While many of these significant changes were person-specific, several taxa changed consistently in most participants ($p < 0.05$, FDR corrected, Figure 6C and S7). Moreover, in most cases in which the consistently changing taxa had reported associations in the literature, the direction of change in RA following the “good” diet was in agreement with reported beneficial associations. For example, *Bifidobacterium adolescentis*, for which low levels were reported to be associated with greater weight loss (Santacruz et al., 2009), generally decrease in RA following the “good” diet and increase following the “bad” diet (Figure 6C,D). Similarly, TIIIM has been associated with low levels of *Roseburia inulinivorans* (Qin et al.,

2012; Figure 6E), *Eubacterium eligens* (Karlsson et al., 2013), and *Bacteroides vulgatus* (Ridaura et al., 2013), and all these bacteria increase following the “good” diet and decrease following the “bad” diet (Figure 6C). The Bacteroidetes phylum, for which low levels associate with obesity and high fasting glucose (Turnbaugh et al., 2009), increases following the “good” diet and decreases following the “bad” diet (Figure 6C). Low levels of Anaerostipes associate with improved glucose tolerance and reduced plasma triglyceride levels in mice (Everard et al., 2011) and indeed these bacteria decrease following the “good” diet and increase following the “bad” diet (Figure 6C). Finally, low levels of *Alistipes putredinis* associate with obesity (Ridaura et al., 2013) and this bacteria increased following the “good” diet (Figure 6C).

These findings demonstrate that while both baseline microbiota composition and personalized dietary intervention vary between individuals, several consistent microbial changes may be induced by dietary intervention with a consistent effect on PPGR.

DISCUSSION

In this work we measured 46,898 PPGRs to meals in a population-based cohort of 800 participants. We demonstrate that PPGRs are highly variable across individuals even when they consume the same standardized meals. We further show that an algorithm that integrates clinical and microbiome features can accurately predict personalized PPGRs to complex, real-life meals even in a second independently collected validation cohort of 100 participants. Finally, personalized dietary interventions based on this algorithm induced lower PPGRs and were accompanied by consistent gut microbiota alterations.

Our study focused on PPGRs, as they were shown to be important in achieving proper glycemic control, and when disturbed are considered an independent disease risk factor (American Diabetes Association., 2015a; Gallwitz, 2009). PPGRs in our study also associated with several risk factors, including BMI, HbA1c%, and wakeup glucose. In addition to its centrality in glucose homeostasis, PPGRs serves as a convenient and accurate endpoint, enabling continuous “point-of-care” collection of dozens of quantitative measurements per person during a relatively short follow up period. Such continuous assessment of PPGRs is complementary to other equally important clinical parameters such as BMI and HbA1c%, for which changes typically occur over longer timescales and are thus difficult to correlate to nutritional responses in real time.

In line with few small-scale studies that previously examined individual PPGRs (Vega-López et al., 2007; Vrolix and Mensink, 2010), we demonstrate on 800 individuals that the PPGR of different people to the same food can greatly vary. The most compelling evidence for this observation is the controlled setting of standardized meals, provided to all participants in replicates. This high interpersonal variability suggests that at least with regard to PPGRs, approaches that grade dietary ingredients as universally “good” or “bad” based on their average PPGR in the population may have limited utility for an individual.

We report several associations between microbiome features and variability in PPGRs across people. In some cases, such as for Actinobacteria, Proteobacteria, and Enterobacteriaceae, the

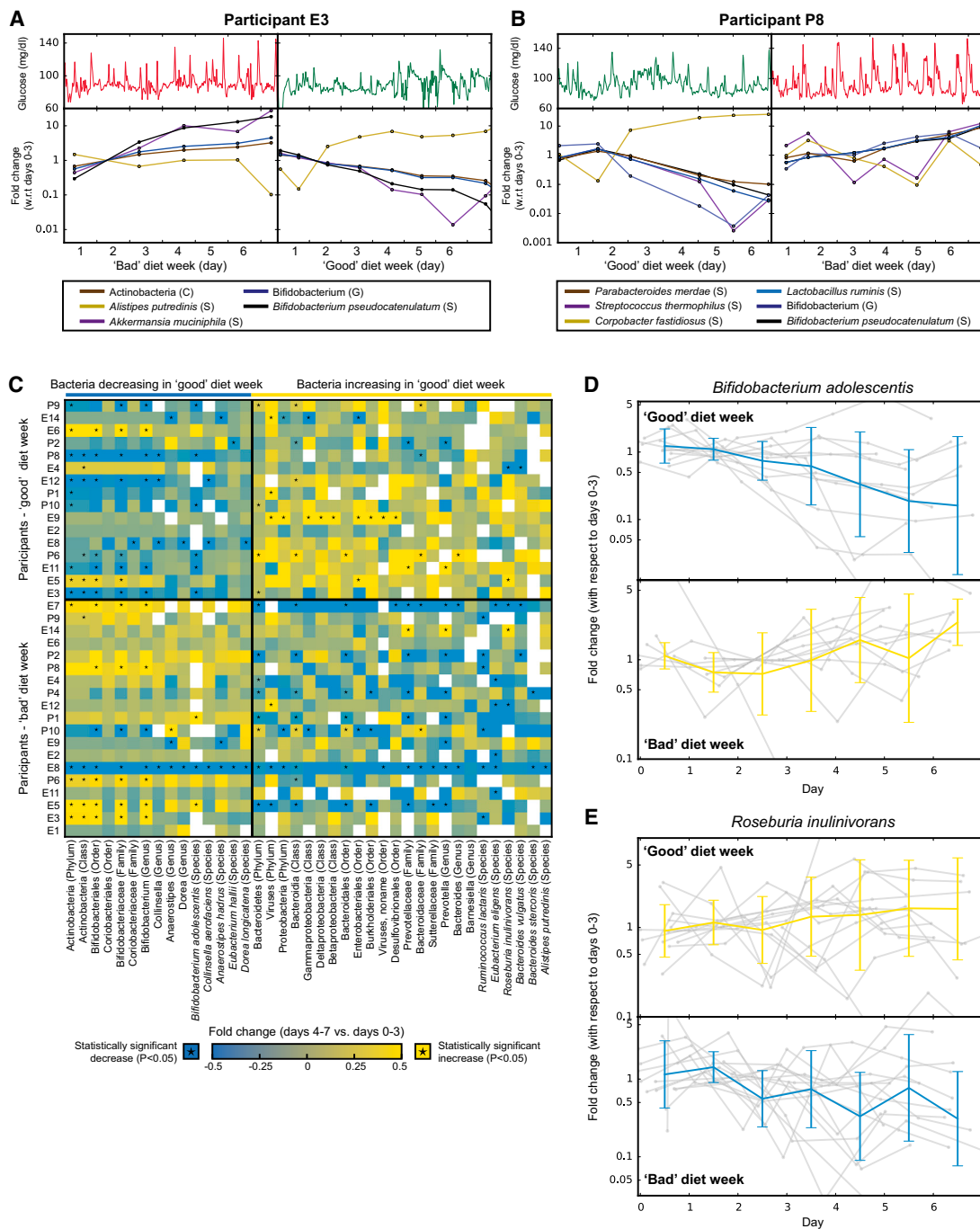


Figure 6. Dietary Interventions Induce Consistent Alterations to the Gut Microbiota Composition

(A) Top: Continuous glucose measurements of a participant from the expert arm for both the “bad” diet (left) and “good” diet (right) week. Bottom: Fold change between the relative abundance (RA) of taxa in each day of the “bad” (left) or “good” (right) weeks and days 0–3 of the same week. Shown are only taxa that exhibit statistically significant changes with respect to a null hypothesis of no change derived from changes in the first profiling week (no intervention) of all participants.

(B) As in (A) for a participant from the predictor arm. See also Figure S7 for changes in all participants.

(C) Heatmap of taxa with opposite trends of change in RA between “good” and “bad” intervention weeks that was consistent across participant and statistically significant (Mann-Whitney U -test between changes in the “good” and “bad” weeks, $p < 0.05$, FDR corrected). Left and right column blocks shows bacteria increasing and decreasing in their RA following the “good” diet, respectively, and conversely for the “bad” diet. Colored entries represent the (log) fold change between the RA of a taxon (x axis) between days 4–7 and 0–3 within each participant (y axis). Asterisks indicate a statistically significant fold change. See also Figure S7 for all changes.

(legend continued on next page)

direction of our associations are consistent with previous associations reported between these taxa and higher-level phenotypes such as dietary habits, obesity and overall glycemic control (Wu et al., 2011; Xiao et al., 2014), raising testable hypotheses about how these taxa may mediate these host metabolic effects. However, in most other cases we identify yet unknown associations with particular biosynthesis pathways or transport and secretion systems, which may be contributed by different taxa in different individuals. These correlations thus provide concrete new pointers for further mechanistic research, aimed at establishing causal roles for these bacterial taxa and functional pathways in determining PPGRs.

Our study further attempts to analyze real-life meals that are consumed in complex food combinations, at different times of the day, and in varying proximity to previous meals, physical activity, and sleep. While clearly of higher translational relevance, the use of "real-life" nutritional input also introduces noise into the meal composition data. Despite that, our results show that predictions for such meals can be made informative by integrating data from a large cohort into a carefully structured predictor. Even better predictions can likely be achieved with further research.

Our algorithm takes as input a comprehensive clinical and microbiome profile and employs a data-driven unbiased approach to infer the major factors that are predictive of PPGRs. Introspecting the resulting algorithm shows that its predictions integrate multiple diverse features that are unrelated to the content of the meal itself. These include contents of previous meals, time since sleep, proximity to exercise, and several microbiome-based factors. With respect to microbiome factors, our algorithm identifies multiple functional pathways and bacterial taxa as either beneficial or non-beneficial, such that in participants with increasing levels for these factors the algorithm predicts a lower or higher PPGR, respectively. In many such cases, microbiome factors found to be beneficial with respect to PPGRs are also negatively associated with risk factors such as HbA1c% and cholesterol levels.

Dietary interventions based on our predictor showed significant improvements in multiple aspects of glucose metabolism, including lower PPGRs and lower fluctuations in blood glucose levels within a short 1-week intervention period. It will be interesting to evaluate the utility of such personalized intervention over prolonged periods of several months and even years. If successful, prolonged individualized dietary control of the PPGR may be useful in controlling, ameliorating, or preventing a set of disorders associated with chronically impaired glucose control, including obesity, prediabetes, T1DM, and non-alcoholic fatty liver disease (Grundy, 2012). These intriguing possibilities, and the microbiome changes that accompany them, merit further studies. Of equal interest and importance, our individualized nutritional study protocols may be applicable to address other clinically relevant issues involving nutritional modifications,

such as T1DM and T1DM patient-specific determination of medication (e.g., insulin and oral hypoglycemics) dosing and timing.

Employing similar individualized prediction of nutritional effects on disease development and progression may also be valuable in rationally designing nutritional interventions in a variety of inflammatory, metabolic, and neoplastic multi-factorial disorders. More broadly, accurate personalized predictions of nutritional effects in these scenarios may be of great practical value, as they will integrate nutritional modifications more extensively into the clinical decision-making scheme.

EXPERIMENTAL PROCEDURES

Human Cohorts

Approved by Tel Aviv Sourasky Medical Center Institutional Review Board (IRB), approval numbers TLV-0658-12, TLV-0050-13 and TLV-0522-10; Kfar Shaul Hospital IRB, approval number 0-73; and Weizmann Institute of Science Bioethics and Embryonic Stem Cell Research oversight committee. Reported to <http://clinicaltrials.gov/>, NCT: NCT01892956.

Study Design

Study participants were healthy individuals aged 18–70 able to provide informed consent and operate a glucometer. Prior to the study, participants filled medical, lifestyle, and nutritional questionnaires. At connection week start, anthropometric, blood pressure and heart-rate measurements were taken by a CRA or a certified nurse, as well as a blood test. Glucose was measured for 7 days using the iPro2 CGM with Enlite sensors (Medtronic, MN, USA), independently calibrated with the Contour BGM (Bayer AG, Leverkusen, Germany) as required. During that week participants were instructed to record all daily activities, including standardized and real-life meals, in real-time using their smartphones; meals were recorded with exact components and weights. Full inclusion and exclusion criteria are detailed in [Supplemental Experimental Procedures](#). Questionnaires used can be found in [Data S1](#).

Standardized Meals

Participants were given standardized meals (glucose, bread, bread and butter, bread and chocolate, and fructose), calculated to have 50 g of available carbohydrates. Participants were instructed to consume these meals immediately after their night fast, not to modify the meal, and to refrain from eating or performing strenuous physical activity before, and for 2 hr following consumption.

Stool Sample Collection

Participants sampled their stool following detailed printed instructions. Sampling was done using a swab ($n = 776$) or both a swab and an OMNIgene-GUT (OMR-200; DNA Genotek) stool collection kit ($n = 413$, relative abundances (RA) for the same person are highly correlated ($R = 0.99 p < 10^{-10}$) between swabs and OMNIgene-GUT collection methods). Collected samples were immediately stored in a home freezer (-20°C), and transferred in a provided cooler to our facilities where it was stored at -80°C (-20°C for OMNIgene-GUT kits) until DNA extraction. All samples were taken within 3 days of connection week start.

Genomic DNA Extraction and Filtering

Genomic DNA was purified using PowerMag Soil DNA isolation kit (MoBio) optimized for Tecan automated platform. For shotgun sequencing, 100 ng of purified DNA was sheared with a Covaris E220X sonicator. Illumina compatible libraries were prepared as described (Suez et al., 2014). For 16S rRNA sequencing, PCR amplification of the V3/4 region using the 515F/806R 16S

(D) For *Bifidobacterium adolescentis*, which decreased significantly following the "good" diet interventions (see panel C), shown is the average and standard deviation of the (log) fold change of all participants in each day of the "good" (top) diet week relative to days 0–3 of the "good" week. Same for the "bad" diet week (bottom) in which *B. adolescentis* increases significantly (see panel C). Grey lines show fold changes (log) in individual participants.

(E) As in (D), for *Roseburia inulinivorans*.

rRNA gene primers was performed followed by 500 bp paired-end sequencing (Illumina MiSeq).

Microbial Analysis

We used USearch8.0 (Edgar, 2013) to obtain RA from 16S rRNA reads. We filtered metagenomic reads containing Illumina adapters, filtered low quality reads and trimmed low quality read edges. We detected host DNA by mapping with GEM (Marco-Sola et al., 2012) to the Human genome with inclusive parameters, and removed those reads. We obtained RA from metagenomic sequencing via MetaPhlAn2 (Truong et al., 2015) with default parameters. We assigned length-normalized RA of genes, obtained by similar mapping with GEM to the reference catalog of (Li et al., 2014), to KEGG Orthology (KO) entries (Kanehisa and Goto, 2000), and these were then normalized to a sum of 1. We calculated RA of KEGG modules and pathways by summation. We considered only samples with >10K reads of 16S rRNA, and >10 M metagenomic reads (>1.5 M for daily samples in diet intervention cohort).

Associating PPGRs with Risk Factors and Microbiome Profile

We calculated the median PPGR to standardized meals for each participant who consumed at least four of the standardized meals and correlated it with clinical parameters (Pearson). We also calculated the mean PPGR of replicates of each standardized meal (if performed) and correlated (Pearson) these values with (a) blood tests; (b) anthropometric measurements; (c) 16S rRNA RA at the species to phylum levels; (d) MetaPhlAn tag-level RA; and (e) RA of KEGG genes. We capped RA at a minimum of 1e-4 (16S rRNA), 1e-5 (MetaPhlAn) and 2e-7 (KEGG gene). For 16S rRNA analysis we removed taxa present in less than 20% of participants. Correlations on RAs were performed in logspace.

Enrichment analysis of higher phylogenetic levels (d) and KEGG pathways and modules (e) was performed by Mann-Whitney *U*-test between $-\log(p \text{ value}) * \text{sign}(R)$ of above correlations (d, e) of tags or genes contained in the higher order groups and $-\log(p \text{ value}) * \text{sign}(R)$ of the correlations of the rest of the tags or genes.

FDR Correction

FDR was employed at the rate of 0.15, per tested variable (e.g., glucose standardized PPGR) per association test (e.g., with blood tests) for analyses in Figure 2G and Figure S4; per phylogenetic level in Figure 6 and Figure S7; and on the entire association matrix in Figure 4G.

Meal Preprocessing

We merged meals logged less than 30 min apart and removed meals logged within 90 min of other meals. We also removed very small (<15 g and <70 Calories) meals and meals with very large (>1 kg) components, meals with incomplete logging and meals consumed at the first and last 12 hr of the connection week.

PPGR Predictor

Microbiome derived features were selected according to number of estimators using them in an additional predictor run on training data. For detailed feature list see *Supplemental Experimental Procedures*. We predicted PPGRs using stochastic gradient boosting regression, such that 80% of the samples and 40% of the features were randomly sampled for each estimator. The depth of the tree at each estimator was not limited, but leaves were restricted to have at least 60 instances (meals). We used 4000 estimators with a learning rate of 0.002.

Microbiome Changes during Dietary Intervention

We determined the significantly changing taxa of each participant by a *Z* test of fold-change in RA between the beginning and end of each intervention week against a null hypothesis of no change and standard deviation calculated from at least 25-fold changes across the first profiling week (no intervention) of corresponding taxa from all participants with similar initial RA. We checked whether a change was consistent across the cohort for each taxa by performing Mann-Whitney *U*-test between the *Z* statistics of the "good" intervention weeks and those of the "bad" intervention weeks across all participants.

A detailed description of methods used in this paper can be found in the *Supplemental Experimental Procedures*.

ACCESSION NUMBERS

The accession number for the data reported in this paper is ENA: PRJEB11532.

SUPPLEMENTAL INFORMATION

Supplemental Information includes Supplemental Experimental Procedures, seven figures, one table and one dataset and can be found with this article online at <http://dx.doi.org/10.1016/j.cell.2015.11.001>.

AUTHOR CONTRIBUTIONS

T.K. and D.Z. conceived the project, designed and conducted all analyses, interpreted the results, wrote the manuscript and are listed in random order. D.R. conceived and directed the dietary intervention (DI) study and designed and conducted analyses. T.K., D.Z., and A.W. designed protocols and supervised data collection. N.Z., D.I., Z.H., and E.E. coordinated and supervised clinical aspects of data collection. T.K., D.Z., N.Z. and D.I. equally contributed to this work. A.W. conceived the project, developed protocols, directed and performed sample sequencing. M.R. and O.B.-Y. supervised the DI study. O.B.-Y. conducted analyses and wrote the manuscript. D.L. conducted analyses, interpreted results and advised nutritional decisions. T.A.-S. and M.L.-P. developed protocols and together with E.M. performed metagenomic extraction and sequencing. N.Z., J.S., J.A.M., G.Z.-S., L.D., and M.P.-F. developed protocols and performed 16S sequencing. G.M., N.K. and R.B. coordinated and designed data collection. Z.H. conceived the project and provided infrastructure. E.E. and E.S. conceived and directed the project and analyses, designed data collection protocols, designed and conducted the analyses, interpreted the results, and wrote the manuscript.

ACKNOWLEDGMENTS

We thank the Segal and Elinav group members for fruitful discussions; Keren Segal, Yuval Dor, Tali Raveh-Sadka, Michal Levo, and Leeat Keren for fruitful discussions and critical insights to the manuscript; Guy Raz and Ran Chen for website development; Shira Zelber-Sagi for discussions; and Noya Horowitz for writing and submitting documents for review by IRBs. This research was supported by the Weizmann Institute of Science. T.K., D.Z., and D.R. are supported by the Ministry of Science, Technology, and Space, Israel. T.K. is supported by the Foukes Foundation. E.E. is supported by Yael and Rami Ungar, Israel; Leona M. and Harry B. Helmsley Charitable Trust; the Gurwin Family Fund for Scientific Research; Crown Endowment Fund for Immunological Research; estate of Jack Gitlitz; estate of Lydia Hershkovich; the Benoziyo Endowment Fund for the Advancement of Science; John L. and Vera Schwartz, Pacific Palisades; Alan Markovitz, Canada; Cynthia Adelson, Canada; estate of Samuel and Alwyn J. Weber; Mr. and Mrs. Donald L. Schwarz, Sherman Oaks; grants funded by the European Research Council (ERC); the Israel Science Foundation (ISF); E.E. is the incumbent of the Rina Gudinski Career Development Chair. E.S. is supported by a research grant from Jack N. Halpern, and Mr. and Mrs. Donald L. Schwarz and by grants from the ERC and the ISF.

Received: October 5, 2015

Revised: October 29, 2015

Accepted: October 30, 2015

Published: November 19, 2015

REFERENCES

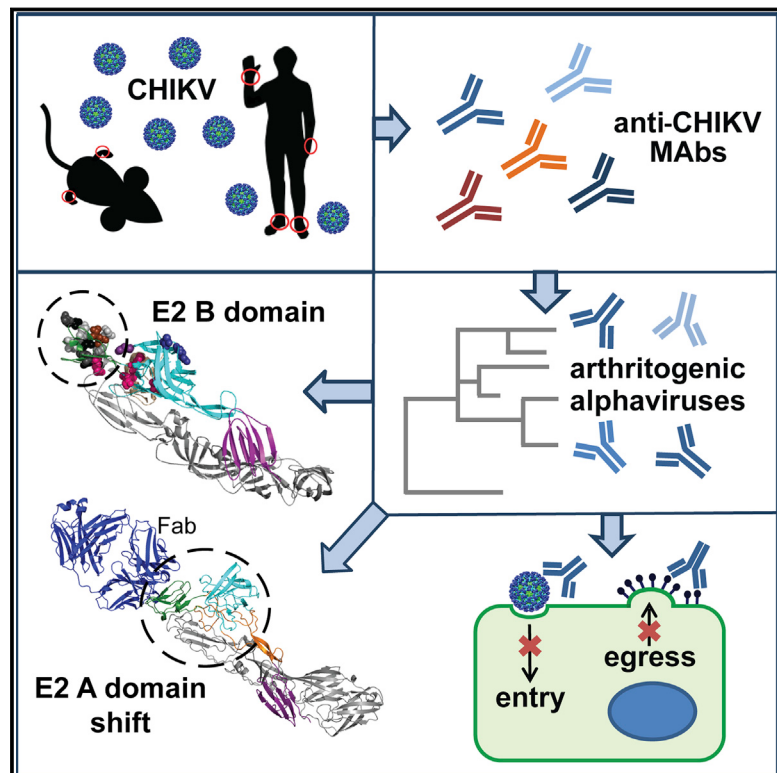
- American Diabetes Association (2015a). (5) Prevention or delay of type 2 diabetes. *Diabetes Care* 38 (Suppl), S31–S32.
- American Diabetes Association (2015b). (4) Foundations of care: education, nutrition, physical activity, smoking cessation, psychosocial care, and immunization. *Diabetes Care* 38 (Suppl), S20–S30.

- Atkinson, F.S., Foster-Powell, K., and Brand-Miller, J.C. (2008). International tables of glycemic index and glycemic load values: 2008. *Diabetes Care* 31, 2281–2283.
- Bailey, T.S., Ahmann, A., Brazg, R., Christiansen, M., Garg, S., Watkins, E., Welsh, J.B., and Lee, S.W. (2014). Accuracy and acceptability of the 6-day Enlite continuous subcutaneous glucose sensor. *Diabetes Technol. Ther.* 16, 277–283.
- Bansal, N. (2015). Prediabetes diagnosis and treatment: A review. *World J. Diabetes* 6, 296–303.
- Bao, J., Gilbertson, H.R., Gray, R., Munns, D., Howard, G., Petocz, P., Colagiuri, S., and Brand-Miller, J.C. (2011). Improving the estimation of mealtime insulin dose in adults with type 1 diabetes: the Normal Insulin Demand for Dose Adjustment (NIDDA) study. *Diabetes Care* 34, 2146–2151.
- Blaak, E.E., Antoine, J.-M., Benton, D., Björck, I., Bozzetto, L., Brouns, F., Diamant, M., Dye, L., Hulshof, T., Holst, J.V., et al. (2012). Impact of postprandial glycaemia on health and prevention of disease. *Obes. Rev.* 13, 923–984.
- Carpenter, D., Dhar, S., Mitchell, L.M., Fu, B., Tyson, J., Shwan, N.A.A., Yang, F., Thomas, M.G., and Armour, J.A.L. (2015). Obesity, starch digestion and amylase: association between copy number variants at human salivary (AMY1) and pancreatic (AMY2) amylase genes. *Hum. Mol. Genet.* 24, 3472–3480.
- Cavalot, F., Pagliarino, A., Valle, M., Di Martino, L., Bonomo, K., Massucco, P., Anfossi, G., and Trovati, M. (2011). Postprandial blood glucose predicts cardiovascular events and all-cause mortality in type 2 diabetes in a 14-year follow-up: lessons from the San Luigi Gonzaga Diabetes Study. *Diabetes Care* 34, 2237–2243.
- Conn, J.W., and Newburgh, L.H. (1936). The glycemic response to isoglycemic quantities of protein and carbohydrate. *J. Clin. Invest.* 15, 665–671.
- Cunningham, K.M., and Read, N.W. (1989). The effect of incorporating fat into different components of a meal on gastric emptying and postprandial blood glucose and insulin responses. *Br. J. Nutr.* 61, 285–290.
- David, L.A., Maurice, C.F., Carmody, R.N., Gootenberg, D.B., Button, J.E., Wolfe, B.E., Ling, A.V., Devlin, A.S., Varma, Y., Fischbach, M.A., et al. (2014). Diet rapidly and reproducibly alters the human gut microbiome. *Nature* 505, 559–563.
- Dodd, H., Williams, S., Brown, R., and Venn, B. (2011). Calculating meal glycemic index by using measured and published food values compared with directly measured meal glycemic index. *Am. J. Clin. Nutr.* 94, 992–996.
- Duncan, S.H., Belenguer, A., Holtrop, G., Johnstone, A.M., Flint, H.J., and Lobley, G.E. (2007). Reduced dietary intake of carbohydrates by obese subjects results in decreased concentrations of butyrate and butyrate-producing bacteria in feces. *Appl. Environ. Microbiol.* 73, 1073–1078.
- Dunstan, D.W., Kingwell, B.A., Larsen, R., Healy, G.N., Cerin, E., Hamilton, M.T., Shaw, J.E., Bertovic, D.A., Zimmet, P.Z., Salmon, J., and Owen, N. (2012). Breaking up prolonged sitting reduces postprandial glucose and insulin responses. *Diabetes Care* 35, 976–983.
- Edgar, R.C. (2013). UPARSE: highly accurate OTU sequences from microbial amplicon reads. *Nat. Methods* 10, 996–998.
- Everard, A., Lazarevic, V., Derrien, M., Girard, M., Muccioli, G.G., Neyrinck, A.M., Possemiers, S., Van Holle, A., François, P., de Vos, W.M., et al. (2011). Responses of gut microbiota and glucose and lipid metabolism to prebiotics in genetic obese and diet-induced leptin-resistant mice. *Diabetes* 60, 2775–2786.
- Everard, A., Lazarevic, V., Gaia, N., Johansson, M., Ståhlman, M., Backhed, F., Delzenne, N.M., Schrenzel, J., François, P., and Cani, P.D. (2014). Microbiome of prebiotic-treated mice reveals novel targets involved in host response during obesity. *ISME J.* 8, 2116–2130.
- Foster-Powell, K., Holt, S.H.A., and Brand-Miller, J.C. (2002). International table of glycemic index and glycemic load values: 2002. *Am. J. Clin. Nutr.* 76, 5–56.
- Friedman, J.H. (2001). Greedy Function Approximation: A Gradient Boosting Machine. *Ann. Stat.* 29, 1189–1232.
- Gallwitz, B. (2009). Implications of postprandial glucose and weight control in people with type 2 diabetes: understanding and implementing the International Diabetes Federation guidelines. *Diabetes Care* 32 (Suppl 2), S322–S325.
- Gibbs, E.M., Stock, J.L., McCoid, S.C., Stukenbrok, H.A., Pessin, J.E., Stevenson, R.W., Milici, A.J., and McNeish, J.D. (1995). Glycemic improvement in diabetic db/db mice by overexpression of the human insulin-regulatable glucose transporter (GLUT4). *J. Clin. Invest.* 95, 1512–1518.
- Greenwood, D.C., Threapleton, D.E., Evans, C.E.L., Cleghorn, C.L., Nykjaer, C., Woodhead, C., and Burley, V.J. (2013). Glycemic index, glycemic load, carbohydrates, and type 2 diabetes: systematic review and dose-response meta-analysis of prospective studies. *Diabetes Care* 36, 4166–4171.
- Grundy, S.M. (2012). Pre-diabetes, metabolic syndrome, and cardiovascular risk. *J. Am. Coll. Cardiol.* 59, 635–643.
- Hastie, T., Tibshirani, R., and Friedman, J. (2008). *The Elements of Statistical Learning: Data Mining, Inference and Prediction* (Stanford: Springer).
- Himsworth, H.P. (1934). Dietetic factors influencing the glucose tolerance and the activity of insulin. *J. Physiol.* 81, 29–48.
- Human Microbiome Project Consortium (2012). Structure, function and diversity of the healthy human microbiome. *Nature* 486, 207–214.
- Israeli Center for Disease Control (2014). *Health 2013* (Jerusalem: Israeli Ministry of Health).
- Jenkins, D.J., Wolever, T.M., Taylor, R.H., Barker, H., Fielden, H., Baldwin, J.M., Bowling, A.C., Newman, H.C., Jenkins, A.L., and Goff, D.V. (1981). Glycemic index of foods: a physiological basis for carbohydrate exchange. *Am. J. Clin. Nutr.* 34, 362–366.
- Kanehisa, M., and Goto, S. (2000). KEGG: kyoto encyclopedia of genes and genomes. *Nucleic Acids Res.* 28, 27–30.
- Karlsson, F.H., Tremaroli, V., Nookaew, I., Bergström, G., Behre, C.J., Fagerberg, B., Nielsen, J., and Bäckhed, F. (2013). Gut metagenome in European women with normal, impaired and diabetic glucose control. *Nature* 498, 99–103.
- Korem, T., Zeevi, D., Suez, J., Weinberger, A., Avnit-Sagi, T., Pompan-Lotan, M., Matot, E., Jona, G., Harmelin, A., Cohen, N., et al. (2015). Growth dynamics of gut microbiota in health and disease inferred from single metagenomic samples. *Science* 349, 1101–1106.
- Kristo, A.S., Matthan, N.R., and Lichtenstein, A.H. (2013). Effect of diets differing in glycemic index and glycemic load on cardiovascular risk factors: review of randomized controlled-feeding trials. *Nutrients* 5, 1071–1080.
- Lamkin, D.M., Spitz, D.R., Shahzad, M.M.K., Zimmerman, B., Lenihan, D.J., Degeest, K., Lubaroff, D.M., Shinn, E.H., Sood, A.K., and Lutgendorf, S.K. (2009). Glucose as a prognostic factor in ovarian carcinoma. *Cancer* 115, 1021–1027.
- Le Chatelier, E., Nielsen, T., Qin, J., Prifti, E., Hildebrand, F., Falony, G., Almeida, M., Arumugam, M., Batto, J.-M., Kennedy, S., et al.; MetaHIT consortium (2013). Richness of human gut microbiome correlates with metabolic markers. *Nature* 500, 541–546.
- Li, J., Jia, H., Cai, X., Zhong, H., Feng, Q., Sunagawa, S., Arumugam, M., Kultima, J.R., Prifti, E., Nielsen, T., et al.; MetaHIT Consortium; MetaHIT Consortium (2014). An integrated catalog of reference genes in the human gut microbiome. *Nat. Biotechnol.* 32, 834–841.
- Marco-Sola, S., Sammeth, M., Guigó, R., and Ribeca, P. (2012). The GEM mapper: fast, accurate and versatile alignment by filtration. *Nat. Methods* 9, 1185–1188.
- Martínez, I., Lattimer, J.M., Hubach, K.L., Case, J.A., Yang, J., Weber, C.G., Louk, J.A., Rose, D.J., Kyureghian, G., Peterson, D.A., et al. (2013). Gut microbiome composition is linked to whole grain-induced immunological improvements. *ISME J.* 7, 269–280.
- Nathan, D.M., Davidson, M.B., DeFronzo, R.A., Heine, R.J., Henry, R.R., Pratley, R., and Zinman, B.; American Diabetes Association (2007). Impaired fasting glucose and impaired glucose tolerance: implications for care. *Diabetes Care* 30, 753–759.
- Nielsen, H.B., Almeida, M., Juncker, A.S., Rasmussen, S., Li, J., Sunagawa, S., Plichta, D.R., Gautier, L., Pedersen, A.G., Le Chatelier, E., et al.; MetaHIT

- Consortium; MetaHIT Consortium (2014). Identification and assembly of genomes and genetic elements in complex metagenomic samples without using reference genomes. *Nat. Biotechnol.* 32, 822–828.
- Nishida, T., Tsuji, S., Tsuji, M., Arimitsu, S., Haruna, Y., Imano, E., Suzuki, M., Kanda, T., Kawano, S., Hiramatsu, N., et al. (2006). Oral glucose tolerance test predicts prognosis of patients with liver cirrhosis. *Am. J. Gastroenterol.* 101, 70–75.
- Qin, J., Li, Y., Cai, Z., Li, S., Zhu, J., Zhang, F., Liang, S., Zhang, W., Guan, Y., Shen, D., et al. (2012). A metagenome-wide association study of gut microbiota in type 2 diabetes. *Nature* 490, 55–60.
- Riccardi, G., and Rivelles, A.A. (2000). Dietary treatment of the metabolic syndrome—the optimal diet. *Br. J. Nutr.* 83 (Suppl 1), S143–S148.
- Ridaura, V.K., Faith, J.J., Rey, F.E., Cheng, J., Duncan, A.E., Kau, A.L., Griffin, N.W., Lombard, V., Henrissat, B., Bain, J.R., et al. (2013). Gut microbiota from twins discordant for obesity modulate metabolism in mice. *Science* 341, 1241214.
- Sandkvist, M. (2001). Type II secretion and pathogenesis. *Infect. Immun.* 69, 3523–3535.
- Santacruz, A., Marcos, A., Wärnberg, J., Martí, A., Martin-Matillas, M., Camppoy, C., Moreno, L.A., Veiga, O., Redondo-Figuero, C., Garagorri, J.M., et al.; EVASYON Study Group (2009). Interplay between weight loss and gut microbiota composition in overweight adolescents. *Obesity* (Silver Spring) 17, 1906–1915.
- Schwingshackl, L., and Hoffmann, G. (2013). Long-term effects of low glycemic index/load vs. high glycemic index/load diets on parameters of obesity and obesity-associated risks: a systematic review and meta-analysis. *Nutr. Metab. Cardiovasc. Dis.* 23, 699–706.
- Suez, J., Korem, T., Zeevi, D., Zilberman-Schapira, G., Thaiss, C.A., Maza, O., Israeli, D., Zmora, N., Gilad, S., Weinberger, A., et al. (2014). Artificial sweeteners induce glucose intolerance by altering the gut microbiota. *Nature* 514, 181–186.
- Truong, D.T., Franzosa, E.A., Tickle, T.L., Scholz, M., Weingart, G., Pasolli, E., Tett, A., Huttenhower, C., and Segata, N. (2015). MetaPhlAn2 for enhanced metagenomic taxonomic profiling. *Nat. Methods* 12, 902–903.
- Turnbaugh, P.J., Ley, R.E., Mahowald, M.A., Magrini, V., Mardis, E.R., and Gordon, J.I. (2006). An obesity-associated gut microbiome with increased capacity for energy harvest. *Nature* 444, 1027–1031.
- Turnbaugh, P.J., Hamady, M., Yatsunenko, T., Cantarel, B.L., Duncan, A., Ley, R.E., Sogin, M.L., Jones, W.J., Roe, B.A., Affourtit, J.P., et al. (2009). A core gut microbiome in obese and lean twins. *Nature* 457, 480–484.
- Vega-López, S., Ausman, L.M., Griffith, J.L., and Lichtenstein, A.H. (2007). Interindividual variability and intra-individual reproducibility of glycemic index values for commercial white bread. *Diabetes Care* 30, 1412–1417.
- Vrolix, R., and Mensink, R.P. (2010). Variability of the glycemic response to single food products in healthy subjects. *Contemp. Clin. Trials* 31, 5–11.
- Wolever, T.M., and Jenkins, D.J. (1986). The use of the glycemic index in predicting the blood glucose response to mixed meals. *Am. J. Clin. Nutr.* 43, 167–172.
- World Health Organization (2008). Global Health Observatory Data Repository (Disease and Injury Country Estimates).
- Wu, G.D., Chen, J., Hoffmann, C., Bittinger, K., Chen, Y.-Y., Keilbaugh, S.A., Bewtra, M., Knights, D., Walters, W.A., Knight, R., et al. (2011). Linking long-term dietary patterns with gut microbial enterotypes. *Science* 334, 105–108.
- Xiao, S., Fei, N., Pang, X., Shen, J., Wang, L., Zhang, B., Zhang, M., Zhang, X., Zhang, C., Li, M., et al. (2014). A gut microbiota-targeted dietary intervention for amelioration of chronic inflammation underlying metabolic syndrome. *FEMS Microbiol. Ecol.* 87, 357–367.
- Zhang, X., Shen, D., Fang, Z., Jie, Z., Qiu, X., Zhang, C., Chen, Y., and Ji, L. (2013). Human gut microbiota changes reveal the progression of glucose intolerance. *PLoS ONE* 8, e71108.

Broadly Neutralizing Alphavirus Antibodies Bind an Epitope on E2 and Inhibit Entry and Egress

Graphical Abstract



Authors

Julie M. Fox, Feng Long,
Melissa A. Edeling, ..., Daved H. Fremont,
Michael G. Rossmann,
Michael S. Diamond

Correspondence

diamond@wusm.wustl.edu

In Brief

A class of broadly neutralizing monoclonal antibodies identified here protects against infection and disease *in vivo* against multiple alphaviruses, including chikungunya. These antibodies bind a discrete epitope on the alphavirus E2 glycoprotein, block viral entry and egress, and allow cross-linking of adjacent E2 protein spikes, suggesting avenues for possible vaccine- or antibody-based therapeutic development against multiple alphaviruses.

Accession Numbers

5ANY, EMD-3144

Highlights

- Broadly neutralizing MAbs bind an epitope in the B domain of alphavirus E2 protein
- Broadly neutralizing MAbs protect *in vivo* against infection by multiple alphaviruses
- B domain MAb binding re-positions the A domain and cross-links adjacent E2 spikes
- MAbs that cross-neutralize alphavirus infection block viral entry and egress steps

Broadly Neutralizing Alphavirus Antibodies Bind an Epitope on E2 and Inhibit Entry and Egress

Julie M. Fox,¹ Feng Long,⁵ Melissa A. Edeling,² Hueylie Lin,¹ Mareike K.S. van Duijl-Richter,⁶ Rachel H. Fong,⁷ Kristen M. Kahle,⁷ Jolanda M. Smit,⁶ Jing Jin,⁸ Graham Simmons,⁸ Benjamin J. Doranz,⁷ James E. Crowe, Jr.,⁹ Daved H. Fremont,² Michael G. Rossmann,⁵ and Michael S. Diamond^{1,2,3,4,*}

¹Department of Medicine

²Department of Pathology and Immunology

³Department of Molecular Microbiology

⁴Center for Human Immunology and Immunotherapy Programs

Washington University School of Medicine, St. Louis, MO 63110, USA

⁵Department of Biological Sciences, Purdue University, West Lafayette, IN 47907, USA

⁶University of Groningen and University Medical Center Groningen, 9713 GZ Groningen, the Netherlands

⁷Integral Molecular, Inc., Philadelphia, PA 19104, USA

⁸Blood Systems Research Institute, San Francisco, CA 94118, USA

⁹Departments of Pediatrics, Pathology, Microbiology, and Immunology and the Vanderbilt Vaccine Center, Vanderbilt University, Nashville, TN 37235, USA

*Correspondence: diamond@wusm.wustl.edu

<http://dx.doi.org/10.1016/j.cell.2015.10.050>

SUMMARY

We screened a panel of mouse and human monoclonal antibodies (MAbs) against chikungunya virus and identified several with inhibitory activity against multiple alphaviruses. Passive transfer of broadly neutralizing MAbs protected mice against infection by chikungunya, Mayaro, and O'nyong'nyong alphaviruses. Using alanine-scanning mutagenesis, loss-of-function recombinant proteins and viruses, and multiple functional assays, we determined that broadly neutralizing MAbs block multiple steps in the viral lifecycle, including entry and egress, and bind to a conserved epitope on the B domain of the E2 glycoprotein. A 16 Å resolution cryo-electron microscopy structure of a Fab fragment bound to CHIKV E2 B domain provided an explanation for its neutralizing activity. Binding to the B domain was associated with repositioning of the A domain of E2 that enabled cross-linking of neighboring spikes. Our results suggest that B domain antigenic determinants could be targeted for vaccine or antibody therapeutic development against multiple alphaviruses of global concern.

INTRODUCTION

Alphaviruses are arthropod-transmitted single-stranded positive-sense-enveloped viruses of the *Togaviridae* family and cause disease worldwide. The two surface glycoproteins on the mature virion, E2 and E1, facilitate binding and entry through receptor-mediated endocytosis and low-pH-mediated fusion within endosomes (Lescar et al., 2001; Smith et al., 1995). Alphavirus virions have T = 4 quasi-icosahedral symmetry, with 240

copies of the E2-E1 heterodimer assembling into 80 trimeric spikes on the viral surface (Cheng et al., 1995). Twenty of these spikes ("i3") are coincident with the icosahedral 3-fold axes, and 60 are in general positions at quasi 3-fold axes ("q3"). X-ray crystallographic structures have been determined of the E1 glycoprotein, the p62-E1 precursor, the E2-E1 heterodimer, and the (E1-E2)₃ trimer (Lescar et al., 2001; Li et al., 2010; Roussel et al., 2006; Voss et al., 2010). The mature E2 protein contains three domains: an A domain, which is located centrally on the surface of the spike and possesses the putative receptor binding site; the B domain, located on the distal end of the spike, covering the fusion loop on E1; and the C domain, at the proximal end of the spike. The E1 protein is a type II membrane fusion protein containing three β-barrel domains. Domain I is located spatially between domains II and III, with the fusion peptide lying at the distal end of domain II (Lescar et al., 2001; Voss et al., 2010). The E1 protein lies at the base of the trimeric spike with E2 positioned on top of it.

Chikungunya virus (CHIKV) is transmitted to humans by *Aedes* species of mosquitoes and causes a debilitating infection characterized by fever, rash, myositis, and arthritis, with joint disease lasting in some individuals for several years (Schilte et al., 2013). CHIKV historically caused outbreaks in Africa and Asia. In 2013, transmission of CHIKV occurred in the Western Hemisphere, and in just 18 months, CHIKV has caused more than 1.4 million cases in the Americas in more than 40 countries, including locally acquired infections in Florida (Kendrick et al., 2014). In comparison, other arthritogenic alphaviruses (e.g., Ross River [RRV], Semliki Forest [SFV], Mayaro [MAYV], and Sindbis [SINV] viruses) circulate with more limited global distribution, with outbreaks in Oceania, Africa, and South America.

Although currently there are no available licensed vaccines or therapies for CHIKV or any other alphavirus, studies have demonstrated the importance of antibody-mediated protection (Kam et al., 2012; Lum et al., 2013). Passive transfer of γ-globulin purified from the plasma of CHIKV-immune patients to mice

Table 1. Cross-Reactivity of Mouse and Human MAbs against Different Alphaviruses^a

Antibody	CHIKV	ONNV	RRV	MAYV	SFV	UNAV	BEBV	GETV	MIDV	BFV
% E2 Identity	83.0	56.6	56.2	57.6	54.5	56.4	54.3	51.3	41.8	
CHK-48	++	++		++	++	++	++			
CHK-65	++			++	++	++				
CHK-77	++	++		++	++	++	++			
CHK-88	++			++	++	++	++			
CHK-96	++	++					++	++		
CHK-98	++			++			++			
CHK-105	++					++		++		
CHK-124	++			++	++	++	++	++		
CHK-187	++	++	++	++	++	++	++	++		
CHK-265	++	++	++	++	++	++	++	++		
I19	++	++	++	++				++	++	++
2C2	++	++	++	++				++		
2D12	++	++	++	++	++	++	++	++		
2H1	++	++		++						
4B8	++	++				++				
5F10	++	++		++		++				
8I4	++	++	++	++		++	++			
9D14	++	++	++	++	++	++	++	++	++	++

CHIKV, Chikungunya virus; ONNV, O'nyong'nyong virus; RRV, Ross River virus; SFV, Semliki Forest virus; MAYV, Mayaro virus; UNAV, Una virus; GETV, Getah virus; BEBV, Bebaru virus; MIDV, Middelburg virus; and BFV, Barmah Forest virus. See also Figures S1 and S2.

^a“++” denotes positive staining, and an absence of a symbol denotes negative staining by flow cytometry on infected cells.

prevented mortality following a lethal CHIKV infection (Couderc et al., 2009). Analogously, monoclonal antibodies (MAbs) neutralize CHIKV infection *in vitro* and protect against disease in mice and non-human primates (Fong et al., 2014; Fric et al., 2013; Goh et al., 2013; Pal et al., 2013, 2014; Smith et al., 2015).

One goal of vaccine and therapeutic efforts against viruses is the development of broadly neutralizing antibodies that inhibit most strains within a genetically diverse virus family. Broadly neutralizing MAbs have been described for human immunodeficiency (HIV), influenza A (IAV), dengue (DENV), and hepatitis C (HCV) viruses (reviewed in Corti and Lanzavecchia, 2013). Although broadly neutralizing MAbs against alphaviruses have not been described, polyclonal antibodies (induced by a CHIKV vaccine candidate) protected against O'nyong'nyong virus (ONNV) infection (Partidos et al., 2012) and convalescent serum from RRV-infected mice protected against CHIKV pathogenesis (Gardner et al., 2010). Earlier reports described cross-protection between different alphaviruses using hyperimmune serum (Wust et al., 1987). These studies suggest that conserved epitopes exist across different alphaviruses that are recognized by protective antibodies.

We screened a panel of murine and human MAbs against CHIKV (Pal et al., 2013; Smith et al., 2015) for neutralization of different alphaviruses. We identified ten MAbs that neutralized at least two different alphaviruses and showed that these MAbs blocked multiple steps in the viral lifecycle, including entry and egress. Two broadly neutralizing MAbs, CHK-187 and CHK-265, protected *in vivo* against CHIKV, ONNV, and MAYV. Ge-

netic analyses established that broadly neutralizing anti-alphavirus MAbs recognized an epitope centered on the B domain of the E2 protein. Cryo-electron microscopic studies showed that binding of CHK-265 to the B domain on CHIKV was associated with repositioning of the A domain away from its native position in the E2-E1 heterodimer, which facilitated interaction with an edge of the A domain and cross-linking of adjacent E2 protein spikes. Overall, these studies describe a class of broadly neutralizing antibodies with protective activity that inhibit entry and egress of distantly related viruses within the alphavirus genus.

RESULTS

Anti-CHIKV MAbs Cross-Neutralize Related Arthritogenic Alphaviruses

Previously, we identified a panel of neutralizing mouse and human MAbs that inhibited infection of multiple CHIKV strains (Pal et al., 2013; Smith et al., 2015). As a first step toward evaluating whether MAbs against CHIKV had inhibitory activity against distinct alphaviruses with envelope protein amino acid identities ranging from 42.2% to 86.3% (Figure S1), we assessed immunoreactivity by flow cytometry (Figure S2). From the panel of 60 neutralizing anti-CHIKV MAbs, ten mouse MAbs and eight human MAbs bound to three or more different viruses (Table 1). However, these cross-reactive MAbs did not bind to cells infected with Venezuelan equine encephalitis virus (data not shown), which is more divergent (45.3% amino acid identity with CHIKV).

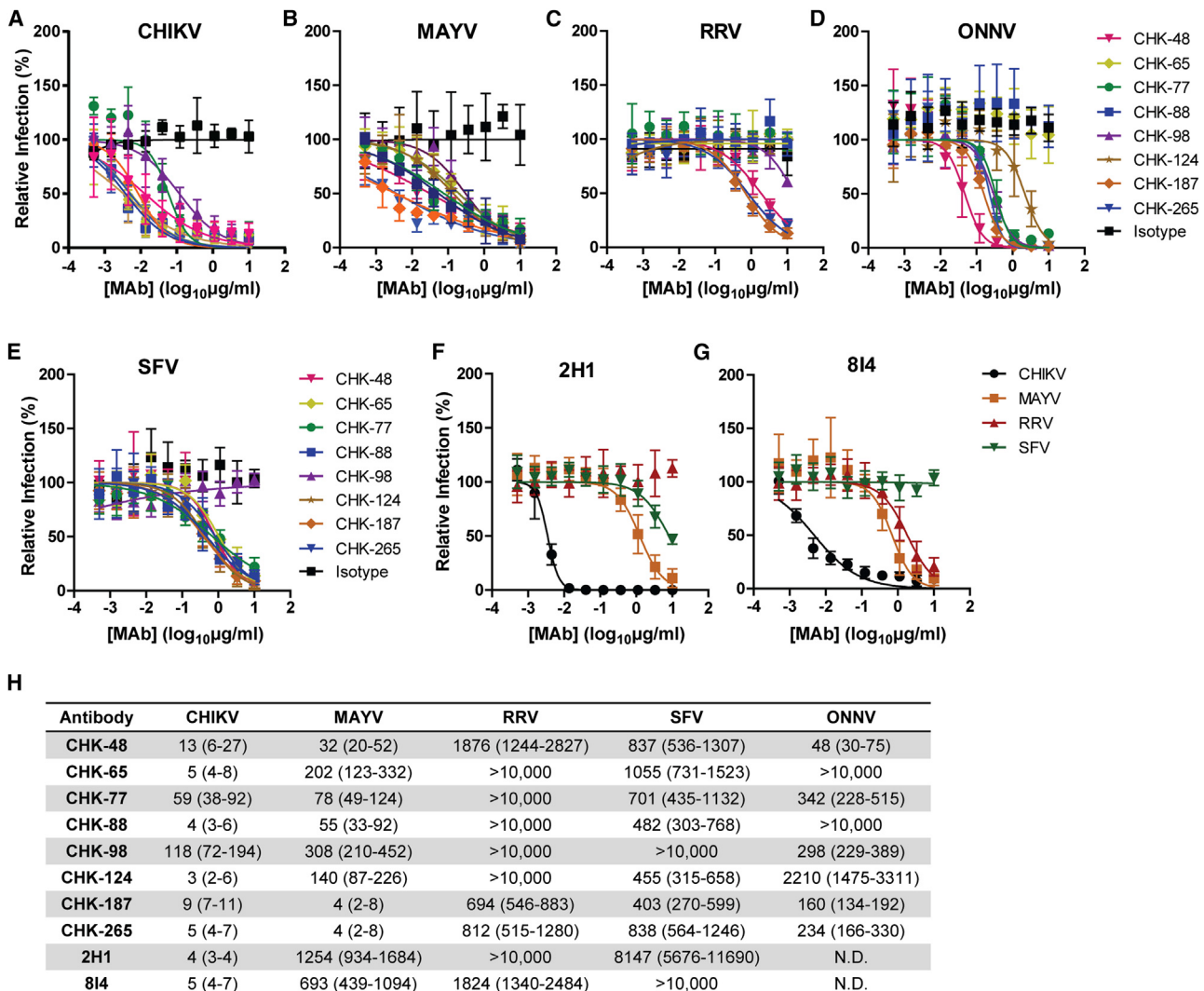


Figure 1. Murine and Human Anti-CHIKV Mabs Neutralize Infection of MAYV, RRV, ONNV, and SFV

(A–G) MAbs were incubated with 10^2 FFU of (A, F, G) CHIKV, (B, F, G) Mayaro, (C, F, G) Ross River, (D) O'nyong'nyong, or (E, F, G) Semliki Forest viruses for 1 hr at 37°C followed by addition of MAb-virus mixture to Vero cells for 18 hr. Virally infected foci were stained and counted. Wells containing MAb were compared to wells containing no MAb to determine the relative infection. DENV1-E98 was included as an isotype control MAb.

(H). EC₅₀ values were determined by non-linear regression and are shown as ng/ml (95% CI). Each graph represents the mean and standard deviation (SD) from at least two independent experiments.

See also Figure S1.

We evaluated the neutralization potential of the cross-reactive MAbs against alphaviruses that are closely (ONNV) or distantly (MAYV, RRV, and SFV) related to CHIKV. As anticipated, each of the MAbs neutralized CHIKV infection efficiently (Figures 1A and 1H), as reported previously (Pal et al., 2013; Smith et al., 2015). Of the ten cross-reactive mouse MAbs tested, eight neutralized MAYV, seven neutralized SFV, six neutralized ONNV, and three neutralized RRV (Figures 1B–1E and 1H). Unexpectedly, cross-neutralization of MAYV was greater than ONNV even though the latter virus is more closely related to CHIKV (Figure S1). Three MAbs (CHK-48, CHK-187, and CHK-265) neutralized all alphaviruses tested, with CHK-187 and CHK-265 showing the greatest potency (Figure 1H). Of the eight cross-

reactive human MAbs tested, only two (2H1 and 8I4) cross-neutralized MAYV, RRV, and/or SFV (Figure 1F and 1G). The sequences of human MAb 8I4 antibody variable genes were conventional; it used the most commonly expressed V_H gene (V_H3-23), had a high level of identity with germline sequences (99% [278 of 282 nucleotides] with V_H3-23*04 and 90% [45 of 50 nucleotides] with JH5*02), and had an HCDR3 length of 18.

Broadly Neutralizing MAbs Protect In Vivo against Multiple Alphaviruses

We assessed the efficacy of CHK-187 and CHK-265 in vivo against CHIKV using an arthritis model in wild-type (WT) mice (Morrison et al., 2011). A single 100 µg dose of CHK-187,

CHK-265, or an isotype control MAb was administered 1 day prior to infection with 10^3 FFU of CHIKV in the footpad. Treatment with CHK-187 or CHK-265 reduced ankle joint swelling to nearly baseline at 3 days after infection when compared to the isotype control MAb (Figure 2A). CHK-187 diminished the CHIKV burden in the ipsilateral ankle and prevented virus dissemination, whereas CHK-265 reduced spread to the contralateral ankle joint (Figure 2B).

Since the greatest cross-neutralization by CHK-265 or CHK-187 was against MAYV, we assessed the protective efficacy of these two MAbs in vivo against MAYV infection. To do this, we developed a new arthritis model of MAYV in WT mice. After inoculation with 10^3 FFU of MAYV, mice developed joint swelling, similar to that observed after CHIKV infection. Using this model, 100 µg of CHK-265, CHK-187, or an isotype control MAb was administered 1 day prior to infection, and ankle size was measured. Additionally, serum, spleen, quadriceps muscle, and ankles were collected on day 3 after infection. Treatment with CHK-265 or CHK-187 reduced joint swelling compared to isotype control MAb-treated animals (Figure 2C). The reduced disease correlated with decreased viral burden, as CHK-187 diminished viral load in the spleen, muscle, and contralateral ankle (Figure 2D). Remarkably, CHK-265 completely protected against MAYV infection, with no detectable virus at the site of inoculation or in any other tissue analyzed.

As an additional test, we evaluated the efficacy of CHK-265 and CHK-187 against ONNV infection. Since ONNV does not replicate extensively in WT mice (Seymour et al., 2013), we developed an arthritis model in *Ifnar*^{-/-} immunodeficient mice. After infection with ONNV, *Ifnar*^{-/-} mice developed ankle swelling and hind limb weakness, with variable rates of recovery. All mice receiving the isotype control MAb developed joint swelling and limb weakness. In contrast, mice receiving CHK-187 or CHK-265 showed minimal clinical disease (Figure 2E), reduced joint swelling from day 5 through day 14 after infection (Figure 2F), and greater weight gain (Figure 2G). To confirm that reduced disease was linked to decreased ONNV infection, we measured viral burden in the spleen, quadriceps muscles, and ankles 5 days after infection. CHK-187 reduced ONNV infection in the ipsilateral foot as well as at distant sites compared to isotype control MAb-treated animals (Figure 2H). CHK-265 limited ONNV spread to the contralateral joint and muscle. Thus, at least two broadly neutralizing MAbs can protect against infection and disease caused by multiple arthritogenic alphaviruses.

Cross-Protective MAbs Map to the B Domain of the E2 Glycoprotein

The binding sites of broadly neutralizing mouse and human MAbs were mapped by alanine-scanning mutagenesis and mammalian cell display (Davidson and Doranz, 2014) of the E2, 6K, and E1 proteins (Figure S3). All cross-neutralizing MAbs bound primarily to sites within the B domain of the E2 protein (Figures 3A and 3B). Eight amino acids (Q184, S185, I190, V197, Y199, G209, L210, I217) emerged as critical for binding (Figure 3A and 3B). These residues are highly conserved across CHIKV E2 proteins, as determined by alignment of 415 genome sequences (<http://www.viprbc.org>) (Figure 3C). Variation was

detected only at amino acid position 210 on E2, with leucine in 386 of 415 sequences, glutamine in 28 of 415 sequences, and threonine in 1 of 415 sequences. Alignment of other arthritogenic alphaviruses with CHIKV showed that I190, Y199, G209, and I217 are conserved, whereas Q184, S185, V197, and L210 are divergent, particularly in RRV (Figure 3A).

To corroborate the alanine-scanning mapping results, we introduced amino acid substitutions into CHIKV E2 ectodomain and generated recombinant proteins in *E. coli* (Pal et al., 2013) for binding studies (Figures 4A–4J). Amino acids in CHIKV E2 B domain were changed to the corresponding amino acids in RRV (Q184T, S185A, V192A, N193G) to previously defined escape mutations (G209E, L210P, K215E, K233E) against other neutralizing mouse MAbs or to residues (R68A and D250A) in the E2 A domain that showed loss of binding to other human MAbs (Pal et al., 2013; Smith et al., 2015). Binding of CHK-84, which maps to the A domain (data not shown), was not altered by any of the mutations, suggesting that the recombinant proteins folded correctly (Figure 4D). The majority of the E2 protein residues identified by alanine-scanning mutagenesis as part of the epitope (Figure 3A) were confirmed, and additional substitutions (e.g., Q184T, G209E, and L210P) that disrupted binding were detected. Binding of all cross-neutralizing MAbs tested was affected to varying levels by mutations at Q184, G209, and L210 (Figures 4A–4J). Mutation at S185 also was associated with loss of binding of several broadly neutralizing MAbs (Figures 4B, 4C, 4E, 4G, and 4H). These residues all are located within or immediately adjacent to the cryo-EM-determined footprint of CHK-265 (see structural analysis in Figure 5D) and thus comprise an epitope for broadly neutralizing MAbs.

When CHK-48, CHK-65, CHK-77, CHK-88, CHK-124, CHK-265, and 8I4 were tested for inhibition of RRV infection, they were poorly (CHK-65, CHK-77, CHK-88, and CHK-124), weakly (CHK-48 and 8I4), or only moderately (CHK-265) neutralizing (Figures 1C and 1H). To explore whether virus-specific amino acid differences in the epitope explained the reduced neutralization of RRV, we changed two residues in the E2 protein of the RRV cDNA clone to the corresponding CHIKV residues (184 [T → Q] and 185 [A → S]). The introduction of the two CHIKV amino acids into RRV resulted in improved binding and neutralization of RRV by CHK-48, CHK-65, CHK-77, CHK-88, CHK-124, CHK-187, and CHK-265 (Figures S4 and 4K–4Q). Engineering of two other CHIKV residues into RRV (192 [A → V] and 193 [G → N]) also improved binding (Figure S4) and neutralization (Figure 4R) of MAb CHK-98, which mapped to residues 189, 191, 192, and 193 in the B domain (Figure 3A).

Binding of B Domain MAbs Is Coincident with Structural Rearrangement of CHIKV E2

We determined the structure of CHIKV virions in complex with Fab fragments of CHK-265 by cryo-electron microscopy (cryo-EM) at ~ 16 Å resolution (Figure 5A). Three Fab molecules were bound to each of the q3 and i3 trimeric spikes within the 60 icosahedral asymmetric units. Unexpectedly, the virus density remaining after subtraction of the fitted CHK-265 Fab density could not be interpreted by fitting of the crystal structure of the E1-E2 heterodimer (Voss et al., 2010) (Figures S5A and S5B). Visual inspection suggested that the A and B domains in the

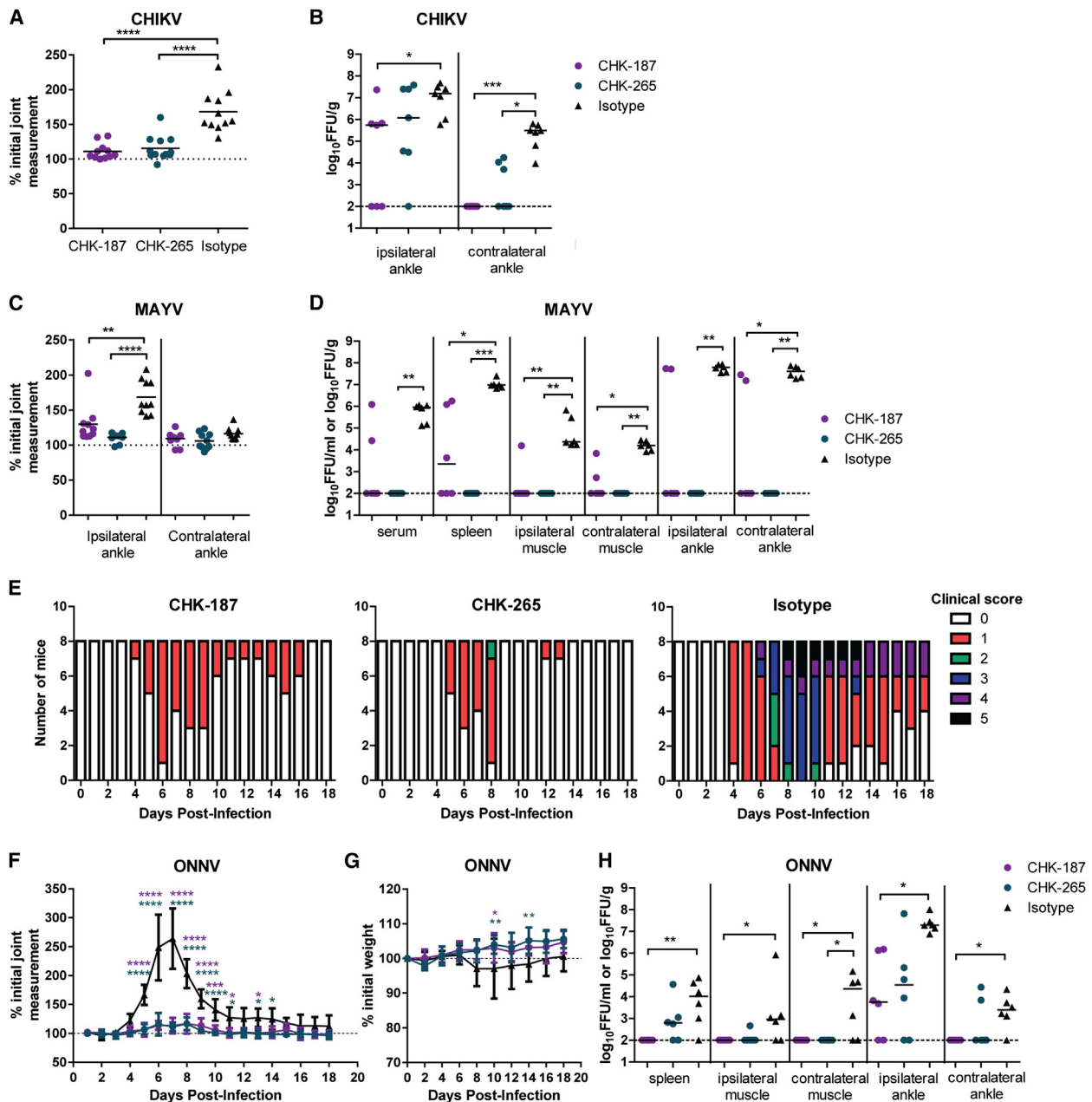


Figure 2. CHIK-187 or CHIK-265 Protect against Alphavirus Disease and Dissemination In Vivo

(A–D) Four-week-old WT mice were pretreated with 100 µg of CHIK-187, CHIK-265, or WNV E60 (isotype control) MAb 1 day prior to inoculation with 10³ FFU of (A, B) CHIKV or (C, D) MAYV in the footpad. (A and C) Footpad swelling (width × height) in the ipsilateral and/or contralateral joint was measured prior to and 3 days following inoculation (n = 10 to 12). (B and D) Viral load was determined in indicated tissues 3 days following inoculation (n = 6–7).

(E–H) Six- to seven-week-old *Ifnar*^{−/−} mice were administered MAbs as described above 1 day prior to inoculation with 10 FFU of ONNV in the footpad. (E) Mice (n = 8) were monitored for 18 days, and disease was scored as described in the [Supplemental Experimental Procedures](#) section. (F) Footpad swelling in the ipsilateral foot was followed during the course of infection (n = 8). (G) Weight was monitored each day and normalized to starting weight (n = 8). (H) The indicated tissues were collected 5 days after infection, and viral load was determined (n = 6).

For clinical measurements (panels A, C, F, and G), the mean and SD are shown, with the dashed line indicating the baseline prior to infection. For (A) and (C), statistical significance was determined by a one-way ANOVA with a Bonferroni post hoc test. For (F) and (G), statistical significance was determined by a two-way ANOVA with a Bonferroni post hoc test adjusting for repeated measures. For viral titers (B, D, and H), the median value is shown with the limit of sensitivity of the assay displayed as a dashed line. Statistical significance was determined by a Kruskal-Wallis with a Dunn's post hoc test. Each graph represents data obtained from at least two independent experiments (*p < 0.05, **p < 0.01, ***p < 0.001, ****p < 0.0001).

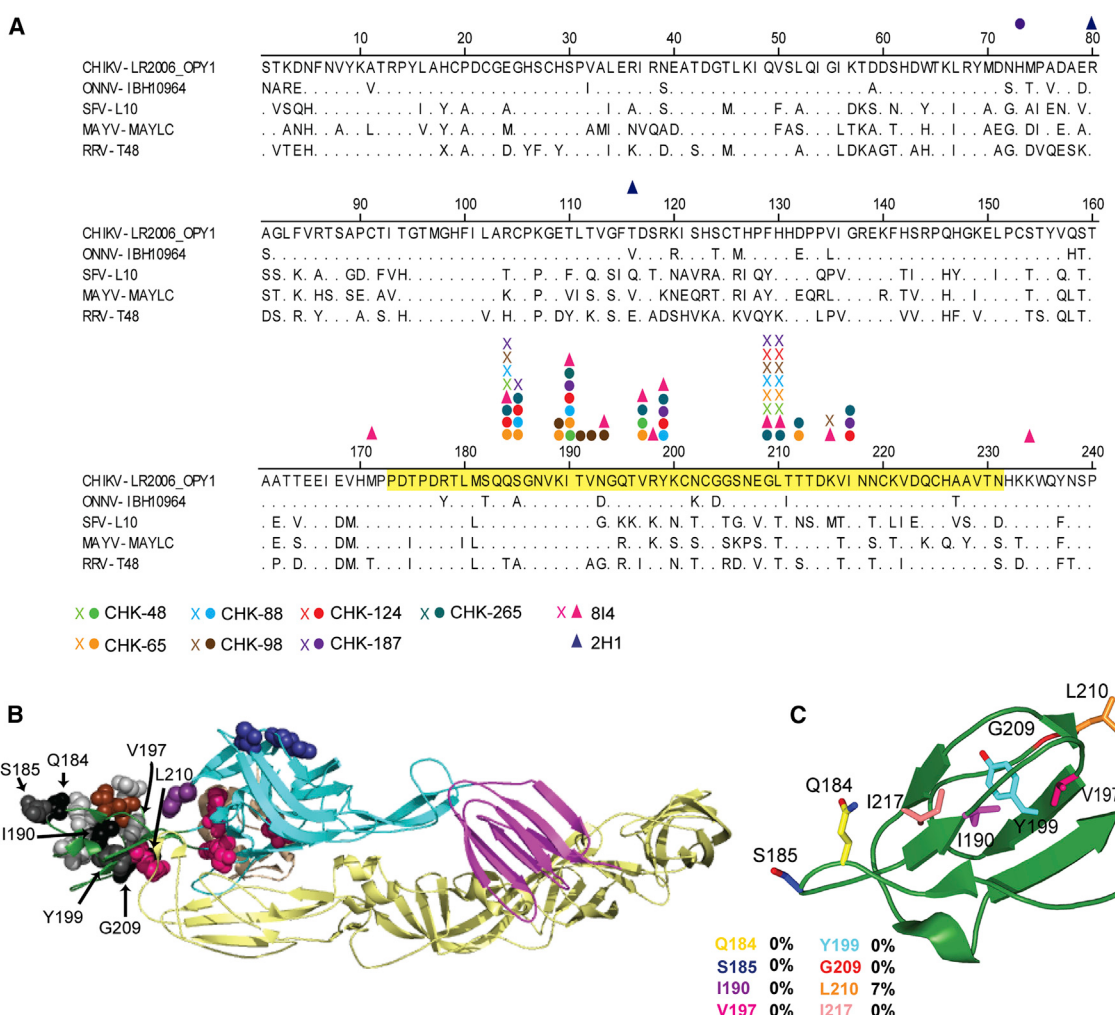


Figure 3. Broadly Neutralizing MAbs Map to Domain B of the E2 Protein

(A) CHIKV, ONNV, SFV, MAYV, and RRV were aligned using MegaAlign (DNA Star) with strain names following the virus. The B domain of CHIKV is highlighted in yellow. Residues mapped by alanine-scanning mutagenesis (see Figure S3) are in solid colored circles (mouse MAbs) or triangles (human MAbs). Additional residues identified as critical for MAb binding to the recombinant CHIKV E2 protein (Figure 4) are shown as an "X" in the MAb color.

(B) Mapped residues are shown as spheres on the CHIKV p62-E1 structure using PyMOL (PDB 3N42). Residues identified for a single MAb are indicated with a colored sphere corresponding to the MAb color in (A). Residues important for binding of multiple MAbs are colored in increasing shades of gray (light gray, 2–3 MAbs; medium gray, 4 MAbs; dark gray, 5 MAbs; and black, 7–8 MAbs). Residues identified for ≥4 MAbs are indicated on the E2 structure by an arrow. E1 is shown in yellow and E3 in tan. E2-A is in cyan, E2-B in dark green, and E2-C in purple.

(C) Blow-up of E2 B domain with key residues (≥3 MAbs with loss of binding) shown as sticks using Pymol (PDB: 3N42). The percent variation of amino acids in CHIKV strains is indicated to the right of the residue and was determined by aligning 415 different CHIKV E2 protein sequences.

See also Figure S3.

heterodimer had undergone substantial conformational change. To define this change, the A and B domains were removed from the crystal structure before fitting the remainder of the modified E1-E2 dimer, and then the A and B domains were fitted manually into the density using EMfit to maximize the average densities for each domain (Rossmann et al., 2001) (Table S3). This process showed that the position and orientation of the B domain had moved further over the fusion loop in domain II of E1 protein. In addition, the A domain had undergone a large repositioning (a translation of 21 Å and rotation of 71°) around the domain II of E1 (Figures 5B and S5C–S5E and Movies S1 and S2). In this

new position, CHK-265 Fab binds the B domain on one spike and contacts the A domain on a neighboring spike, effectively cross-linking the spikes on the virion surface (Figure 5C and Movie S3); each q3 spike is linked to two neighboring q3 spikes and one i3 spike, and each i3 spike is linked to three neighboring q3 spikes. The C termini of the constant domains of Fab molecules that are bound to neighboring spikes make contacts with each other across quasi 2-fold axes in a manner consistent with the T4 quasi symmetry surface lattice. This result suggests that the intact CHK-265 IgG might be able to bind and cross-link many of the spikes together. The interface between CHK-265

and the virus consists of 19 residues in the B domain and 4 in the A domain (Figure 5D and Table S4). The cryo-EM-determined footprint of CHK-265 on the B domain (amino acids 180–220) is consistent with the identified loss- or gain-of-binding residues (e.g., Q184, S185, V192, N193, G209, and L210) from the mutagenesis-based strategies described above.

Broadly Neutralizing MAbs Inhibit Both Viral Entry and Egress

We evaluated the mechanism of inhibition for two broadly neutralizing MAbs, CHK-187 and CHK-265. Inhibition of viral attachment was assessed by pre-incubating CHK-187, CHK-265, or an isotype control MAb with CHIKV and then adding the mixture to cells at 4°C. CHK-187 and CHK-265 did not block viral attachment any more strongly than did the isotype control MAb (Figure 6A). Entry blockade was tested by pre-incubating CHIKV with CHK-187, CHK-265, or with the isotype control MAb and then allowing it to bind to cells at 37°C. One hour later, unbound virus and MAb were removed by extensive washing, and infectivity was assessed 18 hr later. Exposing CHIKV to CHK-187 and CHK-265 only at the time of entry resulted in neutralization that was comparable to when MAbs were maintained throughout infection, suggesting that entry blockade is a dominant mode of inhibition (Figure 6B). To determine whether MAb valency affected entry blockade, studies were repeated with Fab fragments. The Fab fragments were somewhat less potent (5- to 10-fold) than their IgG counterparts (Figure 6B). Saturating amounts of either CHK-187 or CHK-265 Fab fragments could not inhibit infection completely and resulted in a substantial neutralization-resistant fraction. This result suggests that, while monovalent binding of B domain MAbs can inhibit the entry step of infection, bivalent binding is required for complete neutralization.

Since CHK-187 and CHK-265 blocked at a post-attachment entry step, we tested whether they inhibited fusogenic activity using a liposomal fusion assay (Smit et al., 1999). Pyrene-labeled CHIKV was incubated with MAbs and mixed with liposomes, and a low-pH (5.1) buffer was added to trigger fusion. In contrast to results with potently neutralizing type-specific MAbs that bind preferentially to the A domain and completely block fusion (Pal et al., 2013), the cross-neutralizing B domain MAbs showed variable inhibition: fusion was blocked weakly (~20%) by CHK-187, moderately (~60%) by CHK-265, and more strongly (~80%) by CHK-88, although none inhibited completely (Figure 6C).

We next evaluated whether B domain MAbs also could block viral egress, presumably by inhibiting assembly or budding from the plasma membrane. Cells were inoculated with CHIKV and then washed extensively to remove free virus. Subsequently, CHK-187, CHK-265, or isotype control MAb was added, and viral RNA was analyzed from supernatants harvested at 1 or 6 hr; 6 hr corresponds to the initial round of virion secretion. Addition of CHK-187 or CHK-265 reduced the amount of CHIKV RNA in the supernatant compared to cells treated with the isotype control MAb (Figure 6D). Fab fragments of CHK-187 or CHK-265 were less potent than intact IgG, suggesting that cross-linking of E2 proteins on the cell or virion surface might contribute to blockade of egress (Figure 6E). To confirm these results, we transfected CHIKV RNA directly into cells, then added CHK-

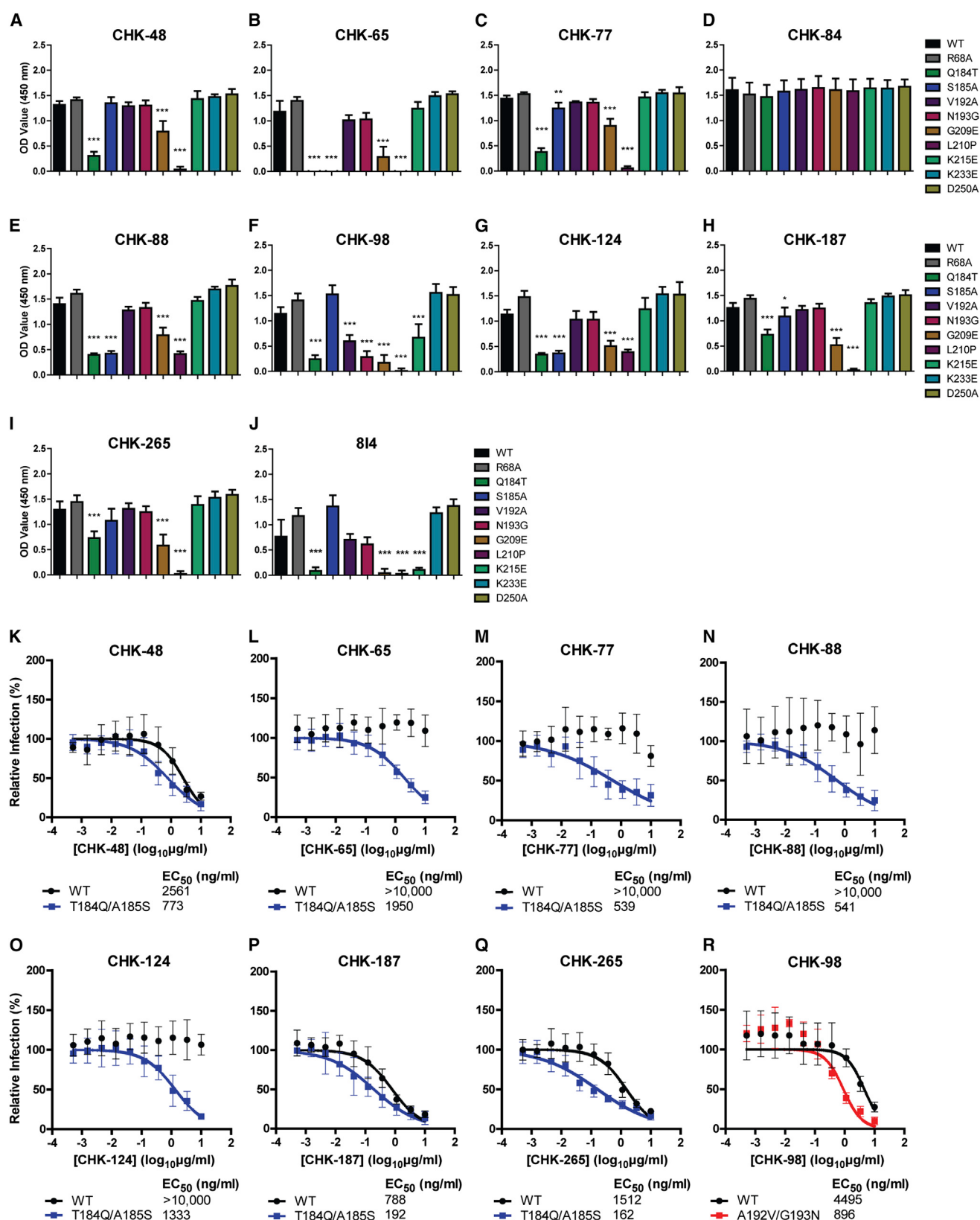
187, CHK-265, or isotype control MAb, and monitored accumulation of RNase-A-resistant encapsidated CHIKV RNA in the cells and supernatant. CHK-187 and CHK-265 had equivalent levels of intracellular viral RNA but had reduced accumulation of viral RNA in the supernatant compared to the isotype control MAb at 24 hr (Figure 6F). Finally, we determined the relative contribution of entry and egress blockade to cross-neutralization of MAYV. CHK-187 or CHK-265 inhibited MAYV infection at the entry (Figure 6G) and egress (Figure 6H) steps, although the effects on egress were less than that observed with CHIKV. Taken together, these results indicate that, while broadly neutralizing MAbs can inhibit multiple steps (including fusion and egress) in the alphavirus lifecycle, they preferentially cross-neutralize infection by blocking entry at a post-attachment pre-fusion step.

DISCUSSION

This study describes a panel of broadly neutralizing MAbs against multiple and distantly related arthritogenic alphaviruses. We identified ten mouse and human cross-neutralizing MAbs and showed that two of these MAbs protected *in vivo* against infection with homologous and heterologous alphaviruses. A conserved epitope in the B domain of the E2 protein contributed to the recognition of these broadly neutralizing MAbs. Structural analysis of CHIKV complexed with CHK-265 showed a large conformational change in the A domain of E2. Mechanistically, the B domain MAbs blocked CHIKV infection at both viral entry and egress steps, although the cross-neutralizing activity was due primarily to inhibition of entry. Collectively, these results describe a class of broadly neutralizing MAbs with substantive inhibitory activity against different members of the alphavirus genus.

We detected a larger number of broadly neutralizing mouse compared to human MAbs. While this could reflect a sampling bias of a small number of mice and a single human (Smith et al., 2015), it could suggest that the epitope repertoire is different between the species, as has been observed with antibodies against other viruses. In contrast to individuals who develop broadly neutralizing antibodies to HIV through constant exposure to the escaping viral envelope protein and extensive somatic hypermutation over time (Doria-Rose et al., 2014), sequencing of 814, the broadly neutralizing anti-alphavirus human MAb, revealed no evidence of such selection. Thus, selection for clones with specific and extensive somatic mutations, as required for HIV envelope protein antigens (Dosenovic et al., 2015), may not be required to elicit broadly neutralizing antibodies against alphaviruses.

Although CHK-187 and CHK-265 neutralized infection of CHIKV and MAYV equivalently in cell culture, greater protection in mice was observed against MAYV compared to CHIKV. The phenomenon in which an antibody raised against one virus protects to greater levels against a related virus was observed previously with flaviviruses. MAbs recognizing the conserved fusion loop of WNV E protein provided greater protection against DENV than WNV (Oliphant et al., 2006; Williams et al., 2013). In contrast to CHK-187 and CHK-265, the flavivirus-specific fusion loop-specific MAbs showed greater neutralizing activity in cell culture against DENV than WNV. The differences in protection *in vivo*



(legend on next page)

between CHIKV and MAYV with the same MAbs having equal neutralizing activity could reflect differences in tropism, pathogenesis, or propensity for accumulation of escape mutations with sustained virulence. Alternatively, the impact of effector functions (e.g., complement or antibody-dependent cellular cytotoxicity) on control of the different viruses could vary between models; these factors could be relevant especially for MAbs that block egress and bind to E1 or E2 proteins on the surface of infected cells.

Of the arthritogenic alphaviruses tested in this study, RRV had the greatest divergence in B domain sequence from CHIKV and, accordingly, was neutralized least efficiently by anti-CHIKV MAbs. MAbs that localize to the B domain on E2 of RRV have been reported to have neutralizing activity (Davies et al., 2000; Vrati et al., 1988), although their capacity for cross-neutralization was not assessed. Based on loss-of-binding studies with variant CHIKV E2 proteins, several key residues (Q184, S185, V192, N193, G209, and L210), all close to or within the cryo-EM determined footprint of CHK-265, contributed to the binding of broadly neutralizing anti-alphavirus MAbs. Four of these residues differed in RRV and, accordingly, substitution of the CHIKV amino acids at corresponding positions into RRV resulted in a gain-of-neutralization phenotype. Since RRV and CHIKV currently do not circulate in the same endemic regions, it seems unlikely that RRV evolved these changes to evade pre-existing immunity against CHIKV.

Our findings with B domain MAbs may be relevant in the context of vaccination, as cross-neutralization of different alphaviruses by polyclonal antibodies has been observed. Cross-protection by anti-RRV serum against CHIKV infection and anti-CHIKV serum against ONNV infection was reported in mice (Gardner et al., 2010; Partidos et al., 2012). However, serum or MAbs derived from ONNV-infected animals or humans weakly neutralized CHIKV (Blackburn et al., 1995; Porterfield, 1961). Future genetic analysis paired with reagents that deplete cross-neutralizing B domain antibodies in serum is needed to explain fully the basis for the directionality of inhibition of polyclonal serum of different alphaviruses.

Cryo-EM structures of several alphaviruses have shown that the B domain has a lower electron density, implying that its position varies by roughly 4 Å relative to the best average orientation of the icosahedral symmetry axes (Porta et al., 2014; Sun et al., 2013). Similarly, the B domain is disordered in the low-pH crystal structure of CHIKV trimeric spikes (Li et al., 2010) and has a high “temperature” factor in the crystal structure of the CHIKV E2-E1 heterodimer (Voss et al., 2010). This structural feature is important because the fusion loop on domain II of the E1 protein is hidden under the B domain to prevent adventitious fusion. Thus, the capacity for the B domain to move likely is

required for the fusogenic activity of the CHIKV. In the cryo-EM map of CHIKV complexed with CHK-265, the B domain had an electron density height equal to the other glycoprotein domains in all four quasi-equivalent positions within the icosahedral asymmetric unit. This configuration likely occurs because the Fab fragment bridges the normally flexible B domain to a second contact site in the more stable A domain. With the B domains tethered, it is more difficult for the fusion loops in E1 to be exposed, which might explain the observed partial inhibition of viral fusion. Another unusual feature of the cryo-EM map is that domain I of E1 has lower density than the other domains, implying a greater flexibility. This domain connects domain II to domain III of E1 that forms the base of the spike. A flexible domain I might result in a floppy trimeric spike, which could impair entry functions of the virus.

In a previous study with Fab fragments of four different MAbs bound to CHIKV-like particles, binding did not cause major conformational changes to the structure of the virus (Sun et al., 2013). These antibodies bound primarily to the A domain of E2. In contrast, CHK-265 Fab binding is centered in the B domain and is coincident with large conformational changes. The cryo-EM analysis of the CHK-265-virion complex showed that although the orientation of the A domain is changed radically, the putative receptor binding site (Sun et al., 2013) remains accessible. This finding is consistent with the observation that CHIKV can attach efficiently to cells in the presence of CHK-265. Binding of CHK-265 induced a conformational shift of the four quasi T-4 related A domains to sites between neighboring spikes, consistent with the T = 4 quasi-symmetry. Although mutagenesis studies did not identify residues in the A domain that resulted in loss of binding of CHK-265, amino acid H73 in domain A of E2 contributed to the binding of the broadly neutralizing MAb CHK-187. This residue is present in the cryo-EM-determined binding footprint of CHK-265.

Vaccine- and antibody-based therapy efforts against HIV, IAV, and DENV have focused on the induction or generation of neutralizing antibodies that target most strains of a virus within a given genus. These broadly neutralizing antibodies function by binding to conserved glycans, receptor-binding domains, stem regions, or dimer and trimer contacts of the envelope glycoproteins (Corti and Lanzavecchia, 2013). Our description of a class of MAbs that induces marked structural changes in the virion, inhibits infection at multiple steps in the viral lifecycle, and protects *in vivo* against disease pathogenesis by multiple alphaviruses suggests that targeting of the B domain on E2 could serve as a strategy for the development of vaccines with utility against CHIKV and several related viruses of global concern.

Figure 4. Mutation of Domain B Residues Eliminates Binding to CHIKV E2 and Enhances Neutralization of RRV

(A–J) Mutations were introduced into the CHIKV E2 ectodomain, and binding was determined by ELISA. Significant reduction compared to the WT E2 protein was determined by a one-way ANOVA with Dunnett's multiple comparison tests (*p < 0.05, **p < 0.01, ***p < 0.001). (K–R) Serial dilutions of MAbs were incubated with 10² FFU of RRV-WT, RRV-T184Q/A185S, or RRV-A192V/G193N for 1 hr at 37°C followed by addition of MAb-virus mixture to Vero cells for 18 hr. Cells were fixed, and virally infected foci were stained. Wells containing MAb were compared to wells containing no MAb to determine the relative infection. EC₅₀ values are shown as ng/ml. Each graph shows the mean and SD from two to three independent experiments performed in duplicate.

See also Figure S4.

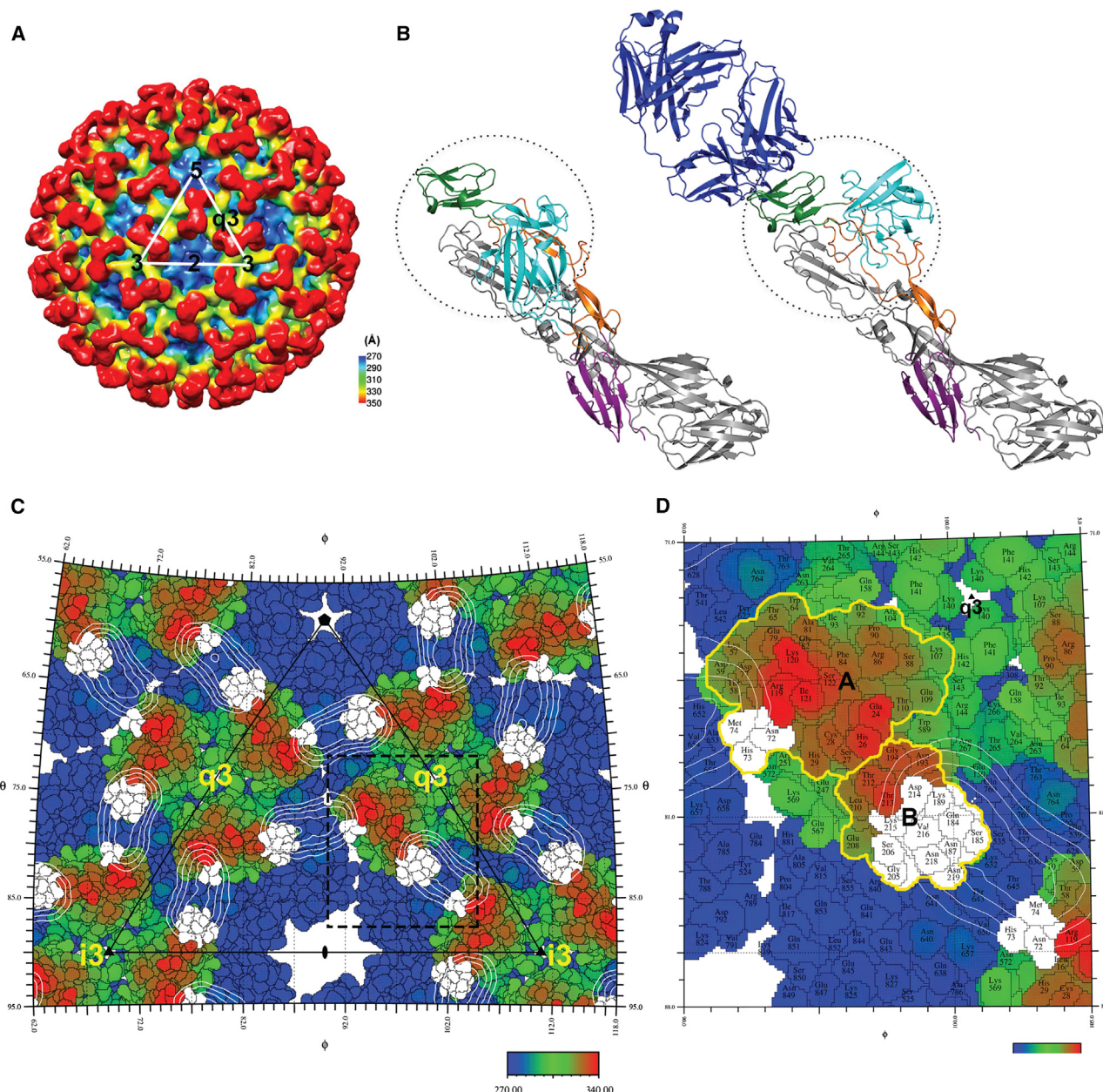


Figure 5. CHK-265 Binding to CHIKV Results in Repositioning of the E2 A Domain

(A) Cryo-EM reconstruction of CHIKV 181/25 in complex with CHK-265 Fab fragments. The triangle represents one icosahedral asymmetric unit. The colors indicate the radial distance in Å from the center of the virus, as shown on the scale bar.

(B) (Left) Structure of the E1-E2 heterodimer (PDB: 3N42). (Right) Structure of the E1-E2 heterodimer with the bound Fab molecule, as observed in the cryo-EM complex of the virus with CHK-265. The CHK-265 Fab molecule is colored blue, and the CHIKV E1-E2 heterodimer (PDB: 3N42) is colored with E1 in gray, E2-A in cyan, E2-B in green, E2-C in purple, and the E2-β-ribbon in orange. The left and right ribbon structures are oriented to place the lower parts of these figures (E1 and domain E2-C) into the same orientation. The E2 A and E2 B domains are circled, showing the difference in their conformations.

(C) Roadmap showing footprint of CHK-265 Fab projected onto the surface of CHIKV. The projections are colored according to the radial distance of the surface from the center of the virus, as shown in the scale bar. The white contours are the radial projections of the bound Fab molecules onto the surface of the virus. The black triangle denotes the boundary of an icosahedral asymmetric unit. The 5-fold, 3-fold, and 2-fold icosahedral axes are indicated by a small black pentagon, triangle, and oval symbol, respectively. The residues in the Fab footprints are shown in white. Each Fab footprint bridges separate trimers with the variable portion of the Fab binding to the E2-B domain on one spike and the E2-A domain on a neighboring spike.

(D) Enlargement of a part of the q3 spike shown on the right in (C). The A and B domains of E2 are outlined in yellow. Individual surface amino acids are labeled and outlined in black. To differentiate residues in E1 from those in E2, a value of 500 arbitrarily was added to the E1 residue numbers. The roadmaps were created by the program RIVEM (Xiao and Rossmann, 2007).

See also Figure S5, Table S3 and S4, and Movies S1, S2, and S3.

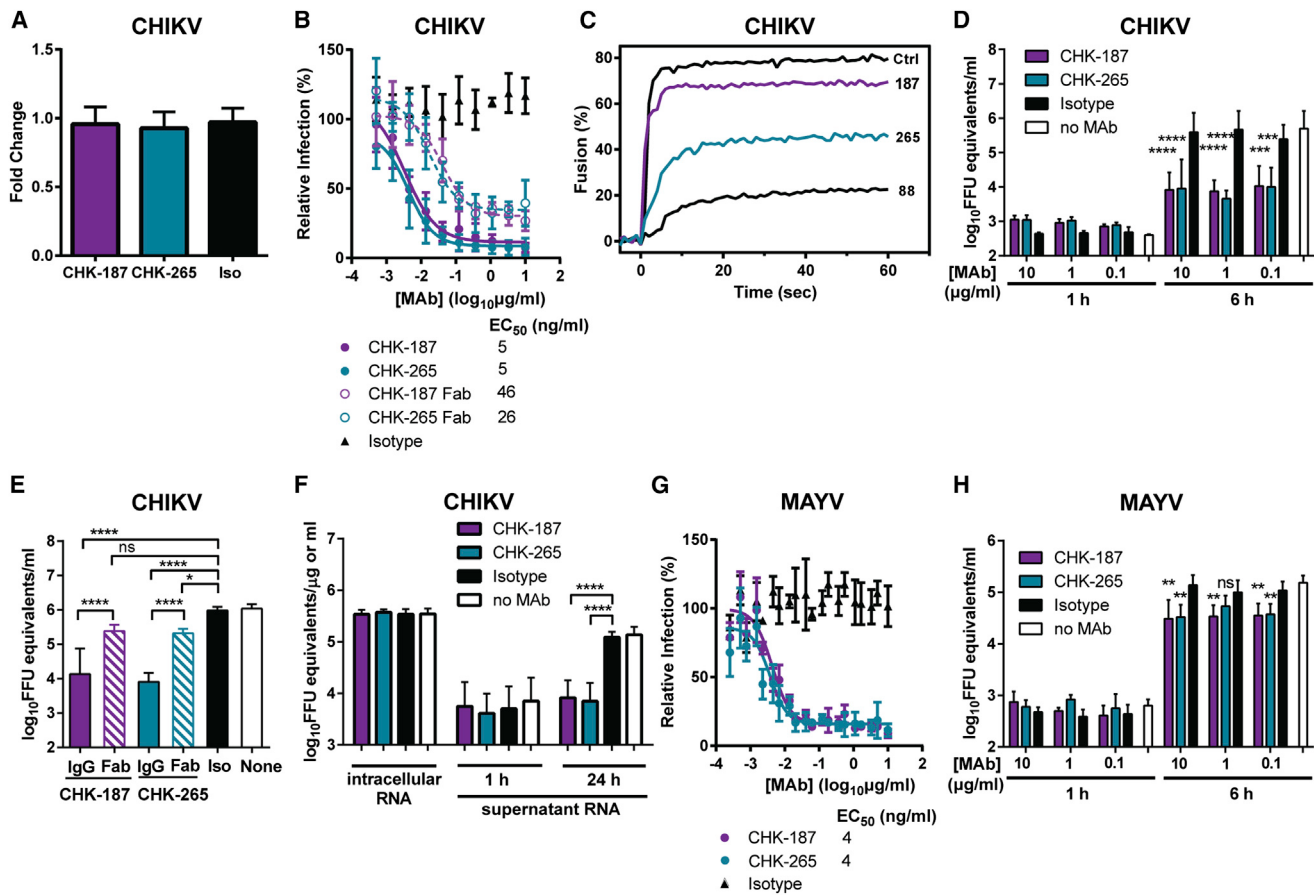


Figure 6. Broadly Neutralizing Anti-CHIKV MAbs Block Steps in Viral Entry and Egress

(A–F) Mechanism of action studies with CHIKV. (A) Attachment blockade. CHIKV was incubated with CHIK-187, CHIK-265, or isotype control MAb (Iso; WNV E60) for 1 hr, added to chilled Vero cells for 1 hr at 4°C, and washed extensively, and bound CHIKV viral RNA was measured. RNA levels are normalized to a no MAb treatment control. (B) Entry blockade. 10² FFU of CHIKV were incubated with indicated MAbs or Fabs at 37°C for 1 hr, added to Vero cells for 1 hr at 37°C, washed extensively, overlaid with methylcellulose, and fixed 18 hr later. Wells containing MAb were compared to wells containing no MAb to determine the relative infection. (C) Fusion blockade. Pyrene-labeled CHIKV was incubated with 1.5 µg/ml of the indicated MAbs and mixed with liposomes at 37°C, and fusion was triggered with a low-pH (5.1) buffer. The percent fusion was measured over time compared to a no MAb control. (D–F) Egress blockade. Vero cells were inoculated with (D, E) CHIKV for 2 hr at 37°C and rinsed extensively, and medium containing (D, E) IgG or (E) Fab fragments (10 µg/ml) and 25 mM NH₄Cl was added back. Supernatant was collected 1 or 6 hr later, the latter of which corresponds to the first round of virion production, and was analyzed for CHIKV viral RNA. (F) BHK21 cells were transfected with CHIKV RNA and rinsed extensively, and medium containing 10 µg/ml IgG and 25 mM NH₄Cl was added. Cells and supernatants were collected 1 or 24 hr later, treated with RNase A at 37°C to degrade unencapsidated RNA, and analyzed for CHIKV viral RNA. See Figure S6 for additional controls.

(G and H) Mechanism of action studies with MAYV. (G) Entry blockade. Studies were performed as described above in (B) using 10² FFU of MAYV. (H) Egress blockade. Studies were performed as described above in (D) using MAYV at an MOI of 1 and analyzed for MAYV viral RNA.

Graphs in this figure show the mean and SD of two or three independent experiments performed in triplicate or duplicate. EC₅₀ values for entry blockade are shown as ng/ml and were determined by non-linear regression. Statistical significance for the egress blockade assay was determined using a one-way ANOVA with a Bonferroni post hoc test at each MAb concentration and time point (*p < 0.05, **p < 0.01, ***p < 0.001, ****p < 0.0001).

EXPERIMENTAL PROCEDURES

Antibodies, Cell Culture, and Viruses

Mouse and human MAbs against CHIKV were reported previously (Pal et al., 2013; Smith et al., 2015) and were purified by Protein A Sepharose and S200 size-exclusion chromatography. Purified CHIK-265 and CHIK-187 were digested with papain (Pierce) to generate Fab fragments and were collected in the flow-through after passage over a Protein A Sepharose column. Vero, BHK21, and C6/36 cells were cultured as described (Pal et al., 2013). CHIKV (La Reunion OPY1 p142) and RRV (T48) were the gifts of S. Higgs (Kansas State University) and R. Kuhn (Purdue University), respectively, and were produced from infectious cDNA clones (Morrison et al., 2006; Tsetsarkin et al., 2006). MAYV

(BeH407), ONNV (MP30), SFV (Kumba), BEBV (MM 2354), MIDV (30037), GETV (AMM-2021), UNAV (CoAr2380), and BFV (K10521) were provided by the World Reference Center for Arboviruses and propagated in Vero cells.

Focus Reduction Neutralization Assay

Focus reduction neutralization tests (FRNT) were performed as described (Pal et al., 2013). Additional details are reported in the Supplemental Experimental Procedures.

Mouse Studies

Experiments were carried out in accordance with the recommendations in the Guide for the Care and Use of Laboratory Animals of the National Institutes of

Health after approval by the Institutional Animal Care and Use Committee at the Washington University School of Medicine. MAbs CHK-187 or CHK-265 or isotype control MAb WNV E60 (100 µg in PBS, 6 mg/kg) were administered to 4-week-old WT C57BL/6 mice or 6- to 7-week old *Ifnar*^{-/-} mice by intraperitoneal injection 1 day prior to infection. WT mice were infected subcutaneously in the footpad with CHIKV or MAYV. *Ifnar*^{-/-} mice were inoculated in the footpad with ONNV. Animals were scored daily using a modified clinical disease scale created for RRV (Morrison et al., 2006). Additional information is in the *Supplemental Experimental Procedures*.

Mutagenesis of CHIKV E2 and ELISA

Amino acid substitutions were introduced into the CHIKV E2 ectodomain (residues S1-E361) using Quikchange II mutagenesis (Aligent) and the primers listed in *Table S1*. Mutations were confirmed by direct sequencing of plasmid DNA. MAb binding to CHIKV WT or mutant E2 proteins was assessed by ELISA. Detailed protocols are described in the *Supplemental Experimental Procedures*.

Mutagenesis of RRV Infectious Clone

A double mutation at positions 192(A→V) and 193(G→N) of the E2 gene was introduced into the pPRR64 cDNA clone of RRV by Quikchange II mutagenesis (Aligent). Double mutations at positions 184(T→Q) and 185(A→S) of the E2 gene were engineered using Phusion high-fidelity DNA polymerase (New England BioLabs). The mutagenesis primers are listed in *Table S1*. Mutations were confirmed by sequencing with separate primers (*Table S2*). WT and mutant RRV were produced after plasmid linearization, in vitro transcription, and electroporation into BHK21 cells. Additional details of RRV mutagenesis are provided in the *Supplemental Experimental Procedures*.

Cryo-EM Reconstruction of CHK-265 in Complex with CHIKV

Purified CHK-265 Fab molecules (5 mg/ml) were mixed with purified and concentrated CHIKV (181/25) in 2:1 (Fab:E2) molar ratio and incubated on ice for 30 min. Samples were flash frozen on holey carbon grids (Ted Pella) in liquid ethane using Cryo-plunge 3 (CP3) in a biosafety cabinet. CCD images of the CHIKV-Fab complex were recorded under low-dose conditions (~22 e/Å²) using a FEI Titan Krios electron microscope operated at 300 kV and 47,000× magnification. All cryo-EM images were collected at about 1.5–3 µm below the focus level. A total of 5,828 particles was selected manually with the e2boxer program in the EMAN2 suite (Kimoto et al., 2003; Tang et al., 2007). Contrast levels of micrographs were corrected using the ctifit program in EMAN (Ludtke et al., 1999; Tang et al., 2007). Additional information about the purification of CHIKV and CHK-265 Fabs and the cryo-EM model generation is described in the *Supplemental Experimental Procedures*.

Mechanistic Analyses of MAb Inhibition

(a) For virus attachment inhibition assays, MAbs were incubated with CHIKV at 37°C, chilled, and added to pre-cooled Vero cells. Cells were extensively rinsed, and bound RNA was extracted from the cells and measured by qRT-PCR. (b) For entry inhibition assays, MAbs or Fabs were incubated with virus at 37°C, added to Vero cells, and after extensive rinsing, processed as described for the FRNT assay. (c) Liposomal fusion inhibition assays were performed as described (Pal et al., 2013). (d) For egress inhibition assays, Vero and BHK21 cells were infected with virus or transfected with viral RNA, respectively. Cells were rinsed extensively, and MAbs or Fabs were added in medium containing NH₄Cl. Viral RNA was quantified from supernatant or cells. Detailed protocols are described in the *Supplemental Experimental Procedures*.

ACCESSION NUMBERS

The cryo-EM density map of CHIKV in complex with CHK-265 Fab fragments was deposited with the EM Data Bank under accession number EMD: EMD-3144. The coordinates of the fitted structural models of CHK-265 Fab and E1-E2 were deposited with the Protein Data Bank under accession number PDB: 5ANY.

SUPPLEMENTAL INFORMATION

Supplemental Information includes Supplemental Experimental Procedures, six figures, four tables, and three movies and can be found with this article online at <http://dx.doi.org/10.1016/j.cell.2015.10.050>.

AUTHOR CONTRIBUTIONS

J.M.F., F.L., H.L., M.K.S.v.D.-R., R.H.F., and K.M.K. performed the experiments. J.M.F., F.L., H.L., M.K.S.v.D.-R., K.M.K., J.M.S., B.J.D., M.A.E., J.E.C., D.H.F., M.G.R., and M.S.D. designed the experiments and analyzed the data. M.A.E., J.E.C., J.J., and G.S. contributed key reagents and methodology. J.M.F., F.L., J.E.C., M.G.R., and M.S.D. wrote the first draft of the manuscript, and all authors provided editorial suggestions and criticisms.

ACKNOWLEDGMENTS

This work was supported by National Institutes of Health (NIH) grants R01 AI095366 (M.G.R.), R01 AI089591 (M.S.D.), HHSN272200900055C (B.J.D.), T32 AI007172 (J.M.F.), and R01 AI114816 (J.E.C. and M.S.D.); the Dutch Organization for Scientific Research (NWO—Earth and Life Sciences) (J.M.S.); the University Medical Center Groningen (M.K.S.v.D.-R.); and a NRSA-Infectious Diseases training grant (J.M.F.). The authors thank S. Johnson (MacroGenics) and G. Sapparapu (Vanderbilt University) for providing purified MAbs, R. Tesch for providing many of the alphaviruses used in this study, P. Pal for the initial cross-reactivity studies, and K. O'Brien and N. DiStasio for technical assistance with mutant E2 protein production and epitope mapping. J.E.C. and M.S.D. have been consultants for Sanofi-Pasteur, which has an agreement with Vanderbilt University to evaluate antibody-based therapeutics against CHIKV. R.H.F., K.M.K., and B.J.D. are employees of Integral Molecular, and B.J.D. is a shareholder of Integral Molecular.

Received: July 30, 2015

Revised: September 18, 2015

Accepted: October 19, 2015

Published: November 5, 2015

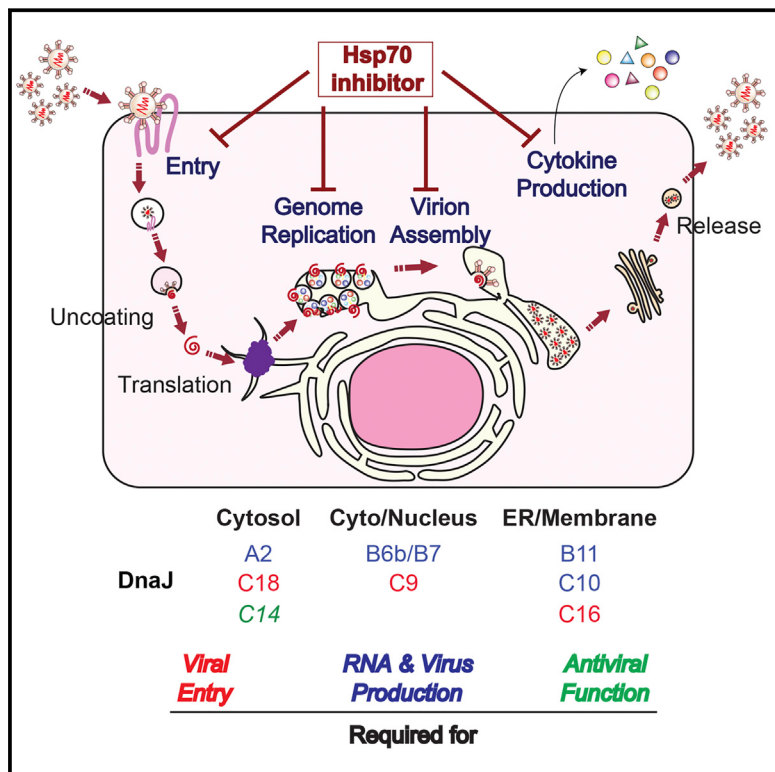
REFERENCES

- Blackburn, N.K., Besselaar, T.G., and Gibson, G. (1995). Antigenic relationship between chikungunya virus strains and o'nyong nyong virus using monoclonal antibodies. *Res. Virol.* **146**, 69–73.
- Cheng, R.H., Kuhn, R.J., Olson, N.H., Rossmann, M.G., Choi, H.K., Smith, T.J., and Baker, T.S. (1995). Nucleocapsid and glycoprotein organization in an enveloped virus. *Cell* **80**, 621–630.
- Corti, D., and Lanzavecchia, A. (2013). Broadly neutralizing antiviral antibodies. *Annu. Rev. Immunol.* **31**, 705–742.
- Couderc, T., Khandoudi, N., Grandadam, M., Visse, C., Gangneux, N., Bagot, S., Prost, J.F., and Lecuit, M. (2009). Prophylaxis and therapy for Chikungunya virus infection. *J. Infect. Dis.* **200**, 516–523.
- Davidson, E., and Doranz, B.J. (2014). A high-throughput shotgun mutagenesis approach to mapping B-cell antibody epitopes. *Immunology* **143**, 13–20.
- Davies, J.M., Cai, Y.P., Weir, R.C., and Rowley, M.J. (2000). Characterization of epitopes for virus-neutralizing monoclonal antibodies to Ross River virus E2 using phage-displayed random peptide libraries. *Virology* **275**, 67–76.
- Doria-Rose, N.A., Schramm, C.A., Gorman, J., Moore, P.L., Bhiman, J.N., DeKosky, B.J., Ernandes, M.J., Georgiev, I.S., Kim, H.J., Pancera, M., et al.; NISC Comparative Sequencing Program (2014). Developmental pathway for potent V1V2-directed HIV-neutralizing antibodies. *Nature* **509**, 55–62.
- Dosenovic, P., von Boehmer, L., Escolano, A., Jardine, J., Freund, N.T., Gitlin, A.D., McGuire, A.T., Kulp, D.W., Oliveira, T., Scharf, L., et al. (2015). Immunization for HIV-1 Broadly Neutralizing Antibodies in Human Ig Knockin Mice. *Cell* **161**, 1505–1515.
- Fong, R.H., Banik, S.S., Mattia, K., Barnes, T., Tucker, D., Liss, N., Lu, K., Selvarajah, S., Srinivasan, S., Mabila, M., et al. (2014). Exposure of epitope

- residues on the outer face of the chikungunya virus envelope trimer determines antibody neutralizing efficacy. *J. Virol.* 88, 14364–14379.
- Fric, J., Bertin-Maghit, S., Wang, C.I., Nardin, A., and Warter, L. (2013). Use of human monoclonal antibodies to treat Chikungunya virus infection. *J. Infect. Dis.* 207, 319–322.
- Gardner, J., Anraku, I., Le, T.T., Larcher, T., Major, L., Roques, P., Schroder, W.A., Higgs, S., and Suhrbier, A. (2010). Chikungunya virus arthritis in adult wild-type mice. *J. Virol.* 84, 8021–8032.
- Goh, L.Y., Hobson-Peters, J., Prow, N.A., Gardner, J., Bielefeldt-Ohmann, H., Pyke, A.T., Suhrbier, A., and Hall, R.A. (2013). Neutralizing monoclonal antibodies to the E2 protein of chikungunya virus protects against disease in a mouse model. *Clin. Immunol.* 149, 487–497.
- Kam, Y.W., Lum, F.M., Teo, T.H., Lee, W.W., Simarmata, D., Harjanto, S., Chua, C.L., Chan, Y.F., Wee, J.K., Chow, A., et al. (2012). Early neutralizing IgG response to Chikungunya virus in infected patients targets a dominant linear epitope on the E2 glycoprotein. *EMBO Mol. Med.* 4, 330–343.
- Kendrick, K., Stanek, D., and Blackmore, C.; Centers for Disease Control and Prevention (CDC) (2014). Notes from the field: Transmission of chikungunya virus in the continental United States—Florida, 2014. *MMWR Morb. Mortal. Wkly. Rep.* 63, 1137.
- Kimoto, K., Ishizuka, K., Tanaka, N., and Matsui, Y. (2003). Practical procedure for coma-free alignment using caustic figure. *Ultramicroscopy* 96, 219–227.
- Lescar, J., Roussel, A., Wien, M.W., Navaza, J., Fuller, S.D., Wengler, G., Wengler, G., and Rey, F.A. (2001). The Fusion glycoprotein shell of Semliki Forest virus: an icosahedral assembly primed for fusogenic activation at endosomal pH. *Cell* 105, 137–148.
- Li, L., Jose, J., Xiang, Y., Kuhn, R.J., and Rossmann, M.G. (2010). Structural changes of envelope proteins during alphavirus fusion. *Nature* 468, 705–708.
- Ludtke, S.J., Baldwin, P.R., and Chiu, W. (1999). EMAN: semiautomated software for high-resolution single-particle reconstructions. *J. Struct. Biol.* 128, 82–97.
- Lum, F.M., Teo, T.H., Lee, W.W., Kam, Y.W., Rénia, L., and Ng, L.F. (2013). An essential role of antibodies in the control of Chikungunya virus infection. *J. Immunol.* 190, 6295–6302.
- Morrison, T.E., Whitmore, A.C., Shabman, R.S., Lidbury, B.A., Mahalingam, S., and Heise, M.T. (2006). Characterization of Ross River virus tropism and virus-induced inflammation in a mouse model of viral arthritis and myositis. *J. Virol.* 80, 737–749.
- Morrison, T.E., Oko, L., Montgomery, S.A., Whitmore, A.C., Lotstein, A.R., Gunn, B.M., Elmore, S.A., and Heise, M.T. (2011). A mouse model of chikungunya virus-induced musculoskeletal inflammatory disease: evidence of arthritis, tenosynovitis, myositis, and persistence. *Am. J. Pathol.* 178, 32–40.
- Oliphant, T., Nybakken, G.E., Engle, M., Xu, Q., Nelson, C.A., Sukupolvi-Petty, S., Marri, A., Lachmi, B.E., Olshevsky, U., Fremont, D.H., et al. (2006). Antibody recognition and neutralization determinants on domains I and II of West Nile Virus envelope protein. *J. Virol.* 80, 12149–12159.
- Pal, P., Dowd, K.A., Brien, J.D., Edeling, M.A., Gorlatov, S., Johnson, S., Lee, I., Akahata, W., Nabel, G.J., Richter, M.K., et al. (2013). Development of a highly protective combination monoclonal antibody therapy against Chikungunya virus. *PLoS Pathog.* 9, e1003312.
- Pal, P., Fox, J.M., Hawman, D.W., Huang, Y.J., Messaoudi, I., Kreklywich, C., Denton, M., Legasse, A.W., Smith, P.P., Johnson, S., et al. (2014). Chikungunya viruses that escape monoclonal antibody therapy are clinically attenuated, stable, and not purified in mosquitoes. *J. Virol.* 88, 8213–8226.
- Partidos, C.D., Paykel, J., Weger, J., Borland, E.M., Powers, A.M., Seymour, R., Weaver, S.C., Stinchcomb, D.T., and Osorio, J.E. (2012). Cross-protective immunity against o'nyong-nyong virus afforded by a novel recombinant chikungunya vaccine. *Vaccine* 30, 4638–4643.
- Porta, J., Jose, J., Roehrig, J.T., Blair, C.D., Kuhn, R.J., and Rossmann, M.G. (2014). Locking and blocking the viral landscape of an alphavirus with neutralizing antibodies. *J. Virol.* 88, 9616–9623.
- Porterfield, J.S. (1961). Cross-neutralization studies with group A arthropod-borne viruses. *Bull. World Health Organ.* 24, 735–741.
- Rossmann, M.G., Bernal, R., and Pletnev, S.V. (2001). Combining electron microscopic with x-ray crystallographic structures. *J. Struct. Biol.* 136, 190–200.
- Roussel, A., Lescar, J., Vaney, M.C., Wengler, G., Wengler, G., and Rey, F.A. (2006). Structure and interactions at the viral surface of the envelope protein E1 of Semliki Forest virus. *Structure* 14, 75–86.
- Schilte, C., Staikowsky, F., Couderc, T., Madec, Y., Carpentier, F., Kassab, S., Albert, M.L., Lecuit, M., and Michault, A. (2013). Chikungunya virus-associated long-term arthralgia: a 36-month prospective longitudinal study. *PLoS Negl. Trop. Dis.* 7, e2137.
- Seymour, R.L., Rossi, S.L., Bergren, N.A., Plante, K.S., and Weaver, S.C. (2013). The role of innate versus adaptive immune responses in a mouse model of O'nyong-nyong virus infection. *Am. J. Trop. Med. Hyg.* 88, 1170–1179.
- Smit, J.M., Bittman, R., and Wilschut, J. (1999). Low-pH-dependent fusion of Sindbis virus with receptor-free cholesterol- and sphingolipid-containing liposomes. *J. Virol.* 73, 8476–8484.
- Smith, T.J., Cheng, R.H., Olson, N.H., Peterson, P., Chase, E., Kuhn, R.J., and Baker, T.S. (1995). Putative receptor binding sites on alphaviruses as visualized by cryoelectron microscopy. *Proc. Natl. Acad. Sci. USA* 92, 10648–10652.
- Smith, S.A., Silva, L.A., Fox, J.M., Flyak, A.I., Kose, N., Sapparapu, G., Khomadiak, S., Ashbrook, A.W., Kahle, K.M., Fong, R.H., et al. (2015). Isolation and Characterization of Broad and Ultrapotent Human Monoclonal Antibodies with Therapeutic Activity against Chikungunya Virus. *Cell Host Microbe* 18, 86–95.
- Sun, S., Xiang, Y., Akahata, W., Holdaway, H., Pal, P., Zhang, X., Diamond, M.S., Nabel, G.J., and Rossmann, M.G. (2013). Structural analyses at pseudo atomic resolution of Chikungunya virus and antibodies show mechanisms of neutralization. *eLife* 2, e00435.
- Tang, G., Peng, L., Baldwin, P.R., Mann, D.S., Jiang, W., Rees, I., and Ludtke, S.J. (2007). EMAN2: an extensible image processing suite for electron microscopy. *J. Struct. Biol.* 157, 38–46.
- Tsetsarkin, K., Higgs, S., McGee, C.E., De Lamballerie, X., Charrel, R.N., and Vanlandingham, D.L. (2006). Infectious clones of Chikungunya virus (La Réunion isolate) for vector competence studies. *Vector Borne Zoonotic Dis.* 6, 325–337.
- Voss, J.E., Vaney, M.C., Duquerroy, S., Vonrhein, C., Girard-Blanc, C., Crublet, E., Thompson, A., Bricogne, G., and Rey, F.A. (2010). Glycoprotein organization of Chikungunya virus particles revealed by X-ray crystallography. *Nature* 468, 709–712.
- Vrati, S., Fernon, C.A., Dalgarno, L., and Weir, R.C. (1988). Location of a major antigenic site involved in Ross River virus neutralization. *Virology* 162, 346–353.
- Williams, K.L., Sukupolvi-Petty, S., Beltramello, M., Johnson, S., Sallusto, F., Lanzavecchia, A., Diamond, M.S., and Harris, E. (2013). Therapeutic efficacy of antibodies lacking Fc γ receptor binding against lethal dengue virus infection is due to neutralizing potency and blocking of enhancing antibodies [corrected]. *PLoS Pathog.* 9, e1003157.
- Wust, C.J., Crombie, R., and Brown, A. (1987). Passive protection across subgroups of alphaviruses by hyperimmune non-cross-neutralizing anti-Sindbis serum. *Proc. Soc. Exp. Biol. Med.* 184, 56–63.
- Xiao, C., and Rossmann, M.G. (2007). Interpretation of electron density with stereographic roadmap projections. *J. Struct. Biol.* 158, 182–187.

Defining Hsp70 Subnetworks in Dengue Virus Replication Reveals Key Vulnerability in Flavivirus Infection

Graphical Abstract



Authors

Shuhei Taguwa, Kevin Maringer,
Xiaokai Li, ..., Raul Andino,
Ana Fernandez-Sesma, Judith Frydman

Correspondence

jfrydman@stanford.edu

In Brief

Dengue virus infects almost 400 million people annually with no treatment or vaccine. Hsp70/DnaJ chaperone network components are found to be required at distinct steps of dengue viral life cycle, with compounds that allosterically modulate Hsp70 showing potent antiviral activity against dengue and other flavivirus pathogens.

Highlights

- The Hsp70 chaperone network mediates distinct steps of the dengue virus life cycle
- DENV cycle requires Hsp70 for viral entry, RNA replication, and virion production
- Hsp70 function at each step of DENV cycle is specified by different DNAJ proteins
- Drug inhibitor of Hsp70 potently blocks DENV infection in human and mosquito cells

Defining Hsp70 Subnetworks in Dengue Virus Replication Reveals Key Vulnerability in Flavivirus Infection

Shuhei Taguwa,¹ Kevin Maringer,^{2,5} Xiaokai Li,³ Dabeiba Bernal-Rubio,² Jennifer N. Rauch,³ Jason E. Gestwicki,³ Raul Andino,⁴ Ana Fernandez-Sesma,² and Judith Frydman^{1,*}

¹Department of Biology and Genetics, Stanford University, Stanford, CA 94305, USA

²Department of Microbiology, Icahn School of Medicine at Mount Sinai, New York, NY 10029, USA

³Department of Pharmaceutical Chemistry University of California at San Francisco, San Francisco, CA 94158, USA

⁴Department of Microbiology and Immunology, University of California at San Francisco, San Francisco, CA 94158, USA

⁵School of Cellular and Molecular Medicine, University of Bristol, Bristol, BS8 1TD, UK

*Correspondence: jfrydman@stanford.edu

<http://dx.doi.org/10.1016/j.cell.2015.10.046>

SUMMARY

Viral protein homeostasis depends entirely on the machinery of the infected cell. Accordingly, viruses can illuminate the interplay between cellular proteostasis components and their distinct substrates. Here, we define how the Hsp70 chaperone network mediates the dengue virus life cycle. Cytosolic Hsp70 isoforms are required at distinct steps of the viral cycle, including entry, RNA replication, and virion biogenesis. Hsp70 function at each step is specified by nine distinct DNAJ cofactors. Of these, DnaJB11 relocates to virus-induced replication complexes to promote RNA synthesis, while DnaJB6 associates with capsid protein and facilitates virion biogenesis. Importantly, an allosteric Hsp70 inhibitor, JG40, potently blocks infection of different dengue serotypes in human primary blood cells without eliciting viral resistance or exerting toxicity to the host cells. JG40 also blocks replication of other medically-important flaviviruses including yellow fever, West Nile and Japanese encephalitis viruses. Thus, targeting host Hsp70 subnetworks provides a path for broad-spectrum antivirals.

INTRODUCTION

A third of the world population is at risk of infection with the mosquito-borne dengue virus (DENV) (Bhatt et al., 2013; Shepard et al., 2014), with an estimated 390 million infections annually (Bhatt et al., 2013). Any of four serotypes causes a range of severe diseases; dengue fever (DF) is a debilitating acute flu-like illness, while dengue hemorrhagic fever (DHF) and dengue shock syndrome (DSS), with about 500,000 cases annually, are life-threatening diseases typified by vascular leakage and circulatory shock (Halstead, 2007) (Bhatt et al., 2013). DENV's major in vivo targets in humans are myeloid cells, including dendritic cells (DCs) and macrophages (Schmid et al., 2014). The dysregulated overproduction of cytokines and chemokines during DENV infection is thought to contribute to the increased vascular

permeability, disruption of the coagulation system and shock associated with DHF/DSS (Rothman, 2011). Despite its burden on global health, no specific antivirals or vaccines are licensed for human use (Lim et al., 2013).

DENV belongs to the genus *Flavivirus* of the family *Flaviviridae*, comprising other clinically relevant arthropod-borne viruses such as yellow fever virus (YFV), West Nile virus (WNV), Japanese encephalitis virus (JEV) and tick-borne encephalitis virus (TBEV) (Lindenbach et al., 2007). Flaviviruses have a capped positive-sense single-stranded RNA genome of ~11 kb that encodes a single polyprotein, which is co- and post-translationally cleaved by host and viral proteases into three structural (capsid, prM, and E) and seven non-structural (NS1, NS2A/B, NS3, NS4A/B, and NS5) proteins (Apte-Sengupta et al., 2014; Lindenbach et al., 2007). Capsid encapsidates the genomic RNA and is then enveloped by membranes containing prM and E to produce progeny virions (Perera and Kuhn, 2008). The non-structural proteins are involved in viral replication and modulate the host cell environment by, for example, remodeling cellular membranes or inhibiting immune responses (Rothman, 2011; Rodriguez-Madroz et al., 2010).

Like all RNA viruses, flaviviruses are dependent on the host cell machinery for replication. With only ten proteins, DENV completely remodels the cell and generates an ER-derived membranous web (Junjhon et al., 2014; Welsch et al., 2009), where viral replication complexes are assembled. DENV proteins also associate with lipid droplets (LD) (Figure 1A) (Samsa et al., 2009). The ability of such a small genome to remodel the cell is linked to the structural and functional complexity of DENV proteins (Perera and Kuhn, 2008). This, in turn, presents a challenge to viral protein folding and assembly. Indeed, many viruses depend on host molecular chaperones for folding and proteostasis (Mayer, 2005; Nagy and Pogany, 2012). Chaperones are reported to facilitate flavivirus replication; ER chaperones associate with DENV E (Limjindaporn et al., 2009), and Hsp70 protects JEV NS3 and NS5 from degradation (Ye et al., 2013). However, the interplay between chaperone networks and the viral life cycle remains unclear. The structural complexity and accumulation to high levels of viral proteins may make viruses hyper-dependent on chaperones, and vulnerable to their inhibition (Neckers and Tatu, 2008; Geller et al., 2012). Pharmacological chaperone inhibitors are emerging as promising cancer

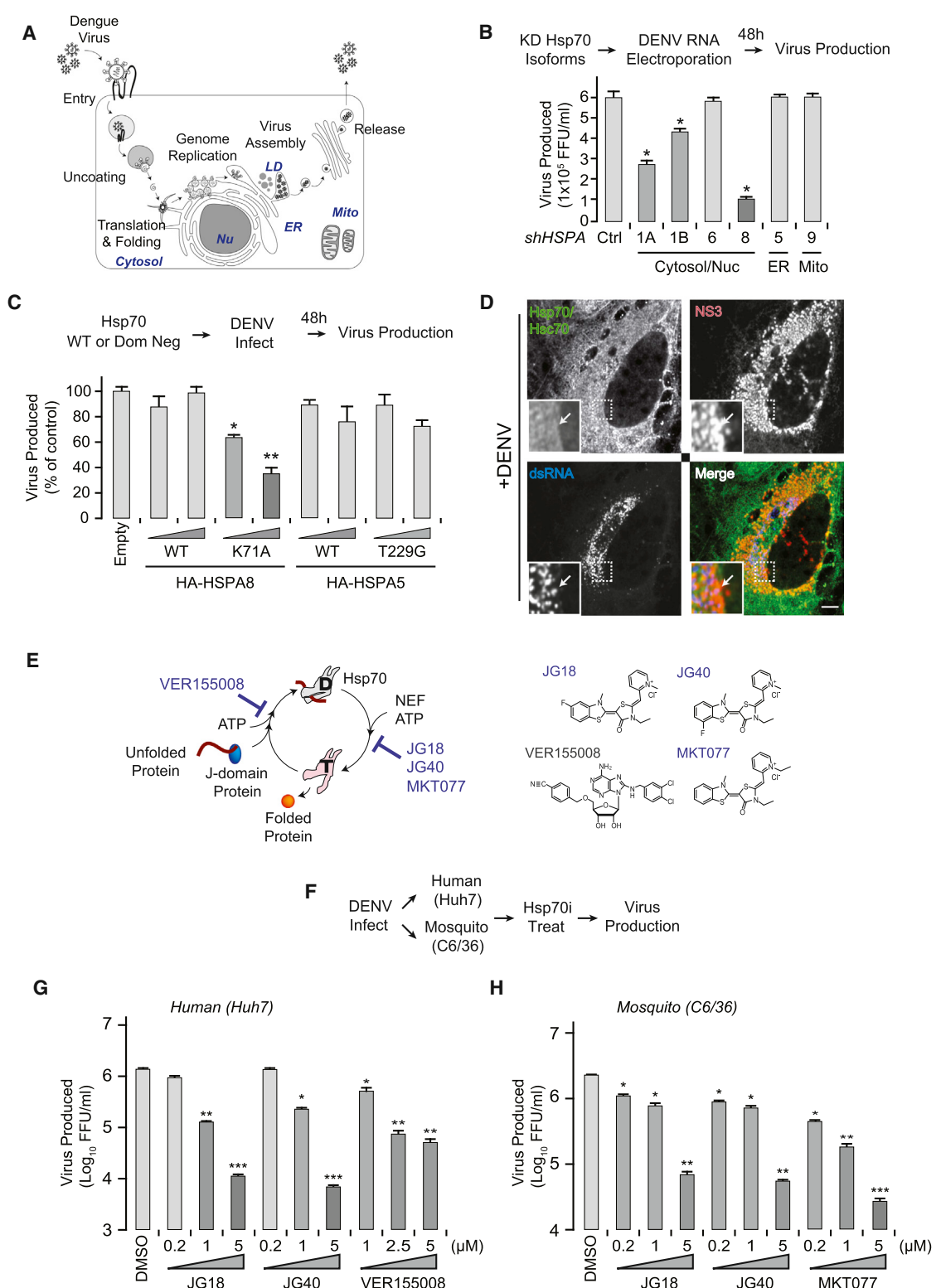


Figure 1. Cytosolic Hsp70 Isoforms Are Required for DENV Life Cycle

(A) DENV life cycle highlighting major steps and their subcellular localization. Nu, nucleus; LD, lipid droplet; Mito, mitochondria, ER; endoplasmic reticulum. (B) Depletion of cytosolic Hsp70 isoforms reduces DENV replication. In vitro transcribed DENV RNA introduced by electroporation; 48 hr post-infection (hpi), supernatants were harvested and extracellular virus titrated by focus forming assay (FFA). Ctrl: shRNA against luciferase as a control.

(legend continued on next page)

therapies, particularly Hsp90 inhibitors (Neckers and Tatu, 2008; Trepel et al., 2010). A number of viruses are also sensitive to Hsp90 inhibitors (Geller et al., 2012), without evolving drug-resistant viral escape variants (Geller et al., 2013; Geller et al., 2007). Since drug resistance is a major stumbling block in antiviral treatment (De Clercq, 2007), the potential inability of viruses to become chaperone-independent makes chaperones attractive antiviral drug targets.

We have a limited understanding of the chaperone network architecture and its relationship to the organization of the cell (Hartl et al., 2011). One hallmark of the evolution of the chaperone machinery is the progressive diversification of chaperone isoforms and cofactors (Powers and Balch, 2013). In bacteria there is one Hsp70 chaperone and one Hsp70 cofactor, DnaJ, while in humans there are 13 Hsp70s and over 45 DNAJ-like proteins (Kampinga and Craig, 2010; Powers and Balch, 2013). This diversification may allow more nuanced regulation of chaperone activity in an increasingly complex proteome. Understanding how chaperone systems facilitate a complex phenotype like viral infection could provide a window into the functional specialization of chaperone isoforms. Here, we address the role of Hsp70 chaperones and their DnaJ cofactors in the DENV life cycle. We find that cytosolic Hsp70s, assisted by distinctly localized DnaJ's, are required at multiple steps of the viral life cycle. Importantly, Hsp70 provides a susceptible node for antiviral Hsp70 inhibitors, with negligible toxicity and no resistance. Hsp70 inhibitors block the replication of diverse DENV serotypes and other flaviviruses (WNV, YFV, TBEV). The multifaceted roles of Hsp70 subnetworks in flavivirus infection may provide the basis for broad-spectrum, resistance-free antivirals for a range of human diseases.

RESULTS

Hsp70 Is Required for DENV Infection of Human and Mosquito Cells

To explore the involvement of Hsp70 in the DENV lifecycle (Figure 1A), we established six Hsp70 isoform-specific shRNA knockdown (KD) cell lines (Figure S1A) and confirmed reduction of mRNA (50%–80%, Figure S1A) and protein (50%–95%, Figure S1B). While reductions in some Hsp70 isoforms upregulated others, Hsp90 immunoblot confirmed that a general stress response was not induced (Figure S1B). Depletion of cytosolic HSPA1A, 1B and 8, (also called Hsp70-1A, 1B and Hsc70, respectively) significantly reduced DENV infectious particle production (Figure 1B). In contrast, depletion of ER-resident Hsp70 HSPA5 (BiP) or mitochondrial Hsp70 HSPA9 had no effect on DENV (Figure 1B). KD of all cytosolic isoforms caused similar re-

ductions in viral RNA (vRNA) levels (Figure S1C) but HSPA8 had the most dramatic effect on virion production (Figure 1B). Furthermore, overexpression of dominant-negative cytosolic Hsc70, mutated in the ATPase active site (HSPA8 K71A) (O'Brien et al., 1996), significantly and dose dependently reduced vRNA replication and virion production (Figure 1C, S1D). In contrast, dominant-negative BiP (HSPA5 T229G) had no effect. Immunofluorescence analysis showed that cytosolic Hsp70s, while ubiquitous, were concentrated in viral replication complexes containing double-stranded RNA (dsRNA) and NS3 (Figure 1D; see S1E for uninfected control).

To overcome the confounding effects of functional redundancy between Hsp70 isoforms we employed a chemical biology approach. Hsp70 is a weak ATPase regulated by several sets of cellular cofactors (Figure 1E) (Hartl et al., 2011). DnaJ-like proteins contain a J-domain that binds Hsp70 and promotes ATP hydrolysis, stabilizing the substrate-Hsp70 complex. Many DnaJ homologs also have domains that help deliver substrate proteins to Hsp70. Nucleotide exchange factors (NEFs) promote the release of Hsp70-bound substrates. Chemical modulators that interfere with these enzymatic activities and protein-protein interactions have been developed (Assimon et al., 2013). One class of molecules, exemplified by VER155008, competes with ATP for Hsp70 binding (Williamson et al., 2009), while MKT077 and its analogs target Hsp70-NEF interactions (Figure 1E) (Assimon et al., 2013; Li et al., 2015; Li et al., 2013). We used both VER155008 and MKT077 and two improved MKT077 analogs, JG18 and JG40 (Figure 1E). Of note, MKT077 analogs act similarly to the Hsp70 mutant K71A, since both stabilize Hsp70-substrate interactions by blocking NEF binding (Wang et al., 2013). The binding site of MKT077 analogs is known and conserved across eukaryotes and all Hsp70 isoforms (Assimon et al., 2013), thus the compounds function in both natural DENV hosts, humans, and mosquitoes (Figures 1F–1H). Indeed, JG18, JG40, and VER155008 dose dependently blocked DENV propagation in human (Huh7) cells (Figure 1G), while MKT077, JG18, and JG40 suppressed DENV in mosquito (C6/36) cells (Figure 1H). The fact that these chemically distinct compounds block DENV propagation is strong evidence for a role for Hsp70 in DENV replication. Furthermore, the structurally similar but inactive JG18 and JG40 derivatives JG19 and JG28 did not suppress DENV propagation (Figure S1F). Thus, both genetic (Hsc70 K71A) and chemical (JG40, JG18) disruption of Hsp70-NEF function inhibited DENV replication, demonstrating the selectivity of the compounds and supporting a role for Hsp70 in DENV replication.

We next focused on the second-generation, metabolically stable MKT077 analogs, JG18 and JG40 (Li et al., 2013). A concern

(C) Overexpression of dominant-negative cytosolic Hsp70 but not ER Hsp70 BiP reduces DENV propagation. Wild-type (WT) or dominant negatives (K71A or T229G) of cytosolic (HSPA8) or ER (BiP) Hsp70 were transduced into Huh7 cells. Transfected cells were infected with DENV2 at MOI 0.5 and extracellular virus quantified 36 hpi by FFA.

(D) Hsc70/Hsp70 co-localizes with DENV replication compartments. Huh7 cells infected with DENV2 were stained at 48 hpi with a pan cytosolic Hsc70/Hsp70 antibody (green), dsRNA (blue) and NS3 (red), marking viral replication sites. Scale bar, 10 μm

(E) Hsp70 chaperone and ATPase cycle is regulated by co-chaperone cofactors and targeted by inhibitors. Hsp70 inhibitors used here: VER15508 blocks ATP binding to Hsp70. JG18, JG40 and MKT077 block binding of Hsp70 to Nucleotide Exchange Factors (NEF).

(F–H) Hsp70 inhibitors suppress DENV propagation in human and mosquito cells in a dose dependent manner. (F) Experimental design: Huh7 (G) and C6/36 (H) cells infected with DENV2 at MOI 0.5 for 1 hr, and inhibitors added for 36 hr (Huh7 cells) or 48 hr (C6/36 cells). Extracellular virus: determined by FFA. All data are expressed as means ± SD of three independent experiments each carried out in triplicate. *p < 0.01, **p < 0.005.

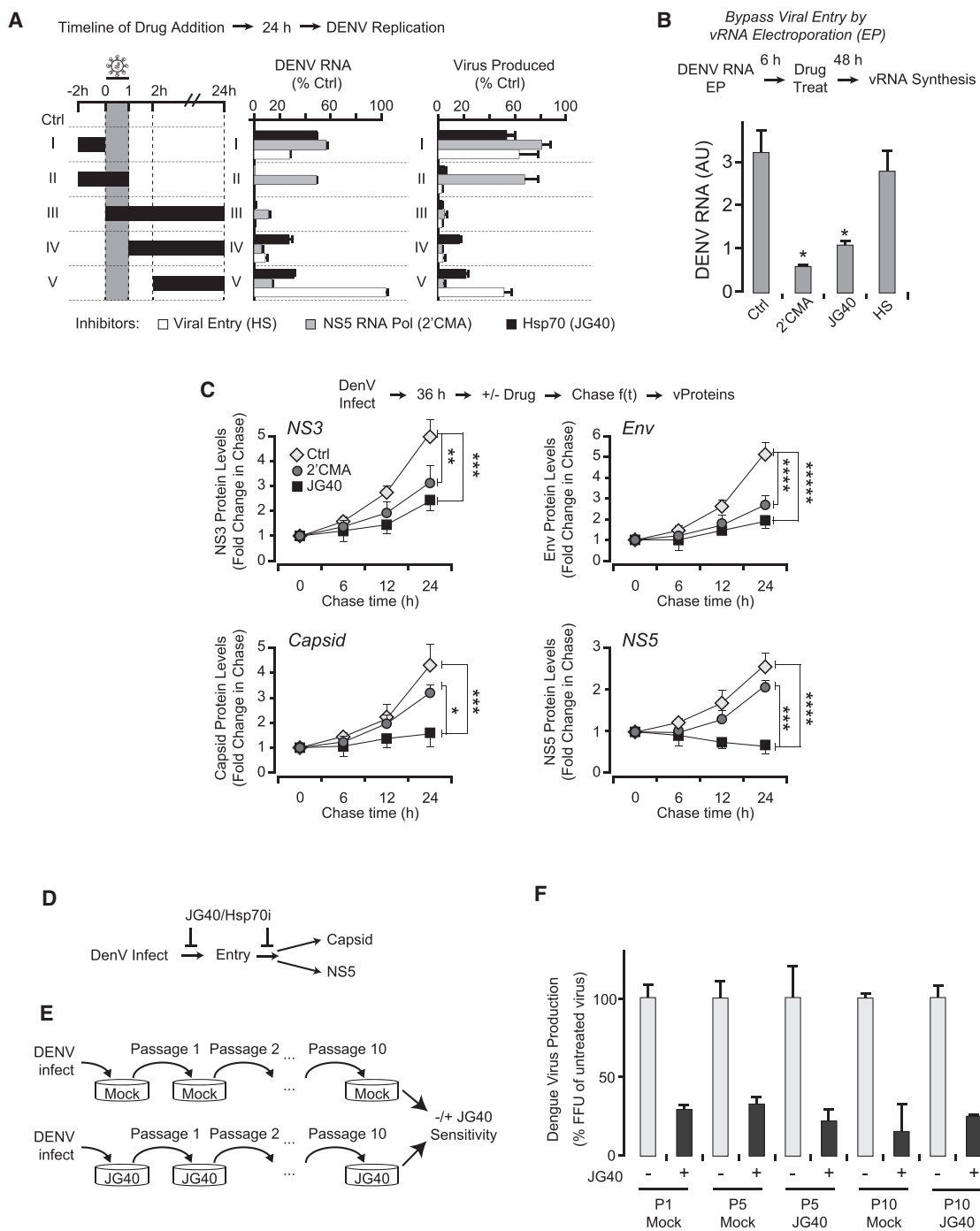


Figure 2. Hsp70s Facilitate Multiple Steps in the DENV Viral Life Cycle

(A) Hsp70 inhibition blocks viral entry and post-entry steps. Time course of drug-addition experiment vis-a-vis DENV infection compared JG40 (Hsp70i); entry inhibitor heparin (HP) and NS5 polymerase inhibitor (2'CMA). Huh7 cells infected with DENV2 at MOI 0.5. Intracellular DENV RNA and extracellular viral production: measured by qRT-PCR and FFA, respectively.

(B) JG40-treatment suppresses DENV replication post-entry. DENV RNA electroporated into Huh7 cells and inhibitors added 6 hpi. After 48 hr, intracellular vRNA was quantified by qRT-PCR.

(C) Hsp70 inhibition decreases DENV capsid and NS5 protein levels. Huh7 cells infected with DENV2 at MOI 0.5 for 36 hr. Inhibitors were then added and cells harvested as indicated. The levels of viral and host proteins during treatment were assessed by immunoblot using IR fluorescence on a Li-Cor Odyssey System (see Fig.S2F-S2G). (D) Hsp70 functions at different steps in the DENV lifecycle suggesting low chances of viral resistance to the drug.

(legend continued on next page)

with Hsp70 inhibitors is that they may block essential chaperone functions, leading to host cell toxicity. However, allosteric inhibitors of the Hsp70-NEF complex are surprisingly non-toxic in normal fibroblasts and animals (Assimon et al., 2013; Li et al., 2015; Li et al., 2013), likely because they leave other chaperone functions intact. Consistent with the idea that viral infection creates a hyper-dependence on distinct chaperone activities compared to host proteostasis, neither JG18 nor JG40 was toxic to host cells at concentrations that inhibit viral replication, as measured by the complementary MTT and LDH release assays (Figure S1G).

Hsp70 Acts at Multiple Steps in the DENV Infectious Cycle

The activity of Hsp70 inhibitors on DENV replication was comparable to a previously described NS5 polymerase inhibitor, 2'C-methyladenosine (2'CMA; Figures S2A–S2E). Hsp70 inhibitors and 2'CMA suppressed vRNA synthesis (Figures S2A and S2B) and viral protein expression (vProtein; Figure S2C) in human and mosquito cells. To dissect which steps in the viral life cycle require Hsp70 in human cells, we performed an order-of-addition experiment using JG40, 2'CMA, and the entry inhibitor heparin (HP). As expected, HP only blocked vRNA replication and viral production (Figure 2A, series I–IV) when added prior to or concurrently with DENV infection (Figure 2A, series V). In contrast, 2'CMA was effective only when added concurrently with or after infection (Figure 2A, series III–V). JG40 inhibits DENV production and vRNA replication in any of these treatment regimes, indicating that Hsp70 is required both at entry and for post-entry steps (Figure 2A, series I–V). To bypass viral entry, we directly electroporated *in vitro* transcribed genomic vRNA into Huh7 cells in the presence of these various compounds. As expected, HP no longer inhibited viral replication, but both 2'CMA and JG40 inhibited vRNA production to a similar extent (Figure 2B). Thus, Hsp70 is required for both entry and post-entry steps of the viral life cycle.

A drug-chase experiment in infected cells next examined whether Hsp70 inhibitors specifically affect individual DENV proteins. Huh7 cells were infected with DENV for 36 hr; then either 2'CMA, JG40, or vehicle were added and the level of viral RNA and proteins examined during a 24 hr time course. Both 2'CMA and JG40 blocked vRNA production to a similar degree, and no new vRNA was synthesized during the chase (Figure S2A, 4F). Both drugs also decreased the expression of cytosolic and ER viral proteins (Figure 2C, S2F and S2G; see Experimental Procedures). All DENV proteins are translated in an equimolar ratio as a single polyprotein, but their steady-state levels are also determined by their half-life. For a given protein, the ratio between 2'CMA and JG40 treatment should reveal which proteins are further destabilized by Hsp70 inhibition, a hallmark of an Hsp70 substrate. The levels of cytosolic NS3 and membrane-bound E, prM, NS2B, and NS4B all decreased to a similar extent

upon 2'CMA or JG40 treatment (Figure 2C, S2G). In contrast, JG40 disproportionately reduced the levels of NS5 and capsid (Figure 2C, S2G). This is not due to positional effects on translation, since the capsid is the most N-terminal protein in the polyprotein and NS5 the most C-terminal. Thus, Hsp70 is required for folding and/or stabilization of capsid and NS5, suggesting these proteins are Hsp70 substrates (Figure 2D).

Dengue Virus Cannot Develop Resistance to Small Molecule Inhibitors of Hsp70

The mutational plasticity of viruses allows them to escape from most antiviral drugs targeting viral and even host factors (Dowd et al., 2014; Lauring et al., 2013). The spread of resistant viruses then renders drugs completely or partially ineffective. To determine if DENV can escape treatment with Hsp70 inhibitors, we serially passaged DENV in the presence of 2'CMA (Figure S2D) or 3 μM JG40 (Figure 1G). At each passage, the drug-sensitivity of the untreated and compound-passaged virus was tested in the presence of JG40 or 2'CMA (Figure 2E, S2H). Even after ten passages in the presence of JG40, the virus remained as sensitive to JG40 as untreated or parental virus (Figure 2F) while virus passaged in 2'CMA developed significant resistance against 2'CMA by passage 10 (Figure S2H). Similar results were obtained in at least three independent biological replicates (data not shown). These results, together with the low toxicity of JG40 in human cells, suggest Hsp70 inhibitors could provide an antiviral treatment against DENV replication that exhibit reduced emergence of drug resistant variants.

Cytosolic Hsp70 Is Required for NS5 Stability and Its Polymerase Function

To examine whether the observed decrease in NS5 upon Hsp70 inhibition is due to proteasomal degradation, cells infected with DENV for 36 hr were treated with JG40 for an additional 12 hr with or without the proteasome inhibitor MG132 (Figure 3A). Indeed, the JG40-induced reduction in NS5 was abrogated by proteasome inhibition (Figure 3A). Furthermore, Hsp70 appears to act directly on NS5 in the absence of other viral proteins, as transfected HA-NS5 was also degraded upon addition of JG40 in a proteasome-dependent manner (Figure 3B). NS5 also co-immunoprecipitated with Hsp70 (Figure 3C). Even though MG132 abrogated the JG40-induced NS5 reduction (Figures 3A and 3B), restoring NS5 levels did not rescue vRNA synthesis or virus production (Figure 3D). Since MG132 does not block DENV replication under the conditions of the experiment, it appears that Hsp70 is not only required for NS5 stability, but also for the acquisition of its folded, functional state. To test this, we isolated active crude replication complexes (RCs) from DENV-infected cells. These RCs produce vRNA in an NS5-dependent manner (Figure 3E), allowing us to examine the effect of JG40 on the activity of NS5 that has already folded and assembled into the large multi-component replication complex.

(E) Serial passaging of DENV in JG40 to test development of drug resistance. At each passage, Huh7 cells were infected with DENV2 at an MOI of 0.5 in the presence or absence of JG40. Virus produced in each passage served as input in the next passage in the absence (Mock) or presence (JG40) of drug.

(F) DENV remains JG40-sensitive following serial passage in the presence of JG40. JG40 sensitivity for the indicated virus passages obtained as above. Extracellular virus produced in the presence or absence of JG40 was quantified by FFU assay 36 hpi.

All data are expressed as mean ± SD of three independent experiments. *p < 0.05, **p < 0.01, ***p < 0.005, ****p < 0.001, *****p < 0.0005.

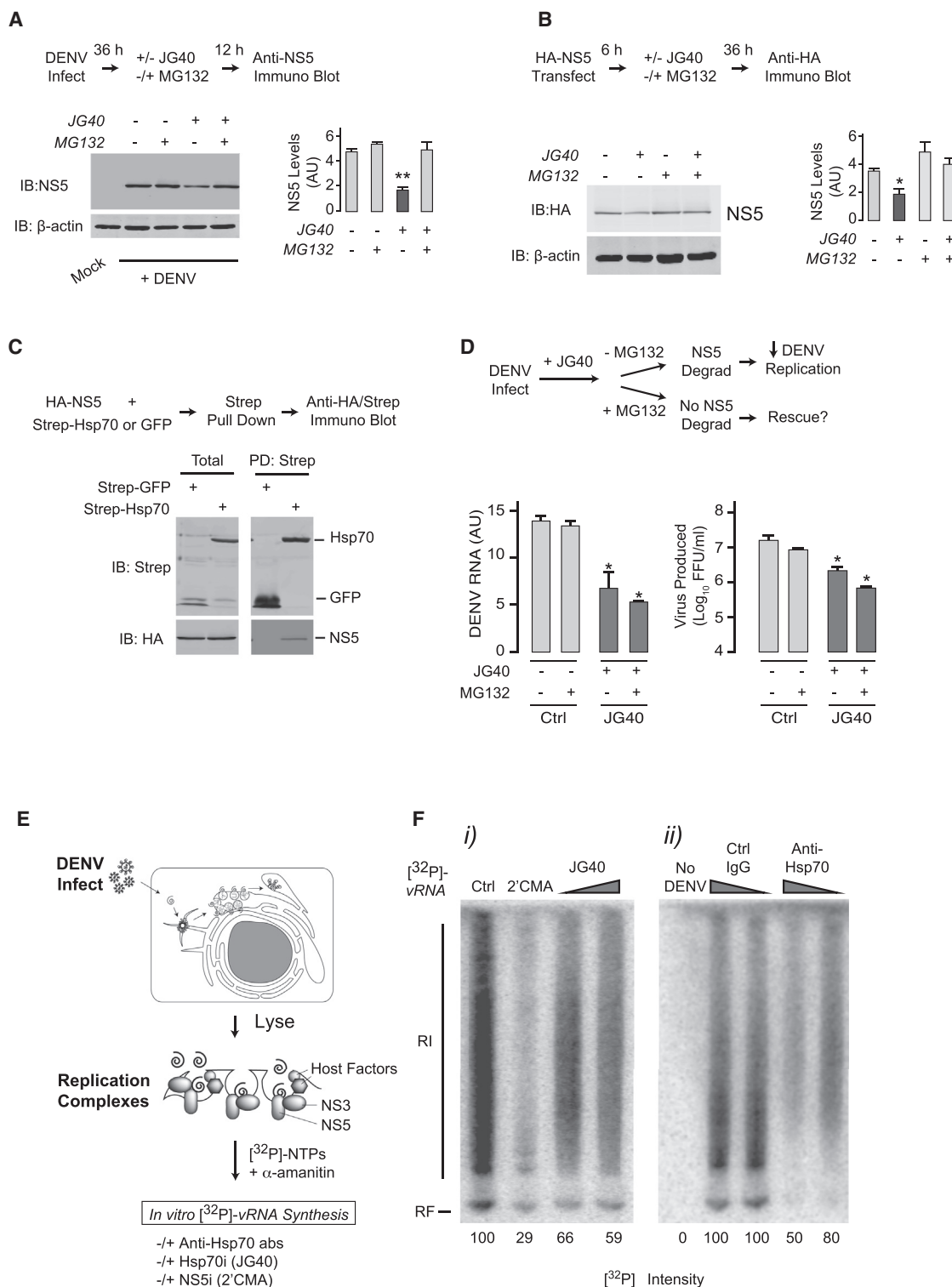


Figure 3. Hsp70 Required for Polymerase NS5 Biogenesis and Function

(A) Hsp70 inhibition leads to proteasomal degradation of NS5. Huh7 cells were infected with DENV2 at MOI 0.5. At 36 hpi, JG40 was added with or without proteasome inhibitor MG132 for an additional 12 hr. Immunoblot analysis (left panel) and quantification (right panel) show that JG40-induced NS5 decrease is rescued by MG132.

(legend continued on next page)

α -amanitin was added to inhibit host RNA polymerase, and DENV vRNA synthesis monitored by incorporation of radioactive ^{32}P -nucleotides into dsRNA duplexes (replicative form; RF) and replication intermediates (RI) (Figure 3F). No radioactive species were detected using uninfected cells (no DENV, Figure 3F, ii), confirming their dependence on DENV RCs. As expected, the NS5 inhibitor 2'CMA blocked production of vRNA species (Figure 3F, i). Of note, JG40 also caused a reduction in vRNA synthesis (Figure 3F, i), and incubating the RCs with anti-Hsp70 antibodies blocked vRNA production in a concentration-dependent manner (Figure 3F, ii). We conclude that the large 100 kDa protein NS5 is a direct substrate of Hsp70, which is required for both stabilizing NS5 and for continued NS5 activity after replication complexes assemble.

Hsp70 Associates with Capsid Protein and Promotes Virus Production

A parallel analysis of the role of Hsp70 in capsid stability showed MG132 did not fully restore the drop in capsid levels observed with JG40 (Figure 4A). Since capsid associates with LDs (Samsa et al., 2009) and vesicles, we considered lysosomal degradation as an alternative degradation route. Despite the confounding fact that the lysosome inhibitor concanamycin A (CM) reduces overall DENV replication (not shown), co-incubation of JG40 with CM did partially restore capsid levels. We also observed an additive effect of blocking both proteasomal and lysosomal degradation (Figure 4A). JG40 also reduced levels of transfected HA-capsid, circumventing the effect of these inhibitors on DENV replication (Figure 4B). This reduction was partially abrogated by independent treatment with MG132 and CM, and additively blocked when both pathways were inhibited (Figure 4B). Thus, JG40 induces capsid degradation via proteasomal and lysosomal routes.

Hsp70 also associated with capsid in co-immunoprecipitation experiments (Figure 4C). Immunofluorescence analysis demonstrated that, as reported (Balinsky et al., 2013; Samsa et al., 2009), some of the capsid pool is directed to nucleoli, and in the cytoplasm capsid associates with LDs and nearby vesicles, forming puncta and ring-like structures distinct from sites containing viral dsRNA (Figures 4D and S3). We therefore questioned whether Hsp70 is required for the assembly of viral particles. 2'CMA or JG40 were used to inhibit vRNA production 36 hpi to compare the effect of the drugs on encapsidation of preexisting vRNA (Figure 4E). Both inhibitors rapidly blocked vRNA synthesis to a similar extent (Figure 4F), but had very different effects on the accumulation of intracellular (Figure 4G) and extracellular

infectious virus (Figure 4H). Cells treated with 2'CMA continue to produce viral particles and secrete them into the medium for at least 24 hr post-treatment. This suggests that by 36 hpi, DENV-infected cells contain sufficient vRNA and proteins to support the assembly of new virus particles. In contrast, JG40 treatment did reduce intracellular and extracellular virus accumulation, suggesting Hsp70 plays an additional role in virion biogenesis.

Selected J-Domain Proteins Are Required for DENV Replication

How and why chaperones select their substrates *in vivo* is an important and poorly understood question. Substrate selection and stable binding to Hsp70 is thought to rely on DNAJ proteins (Figure 5A), which in humans constitute the largest and most diverse sub-group of chaperones. All DNAJs contain a J-domain and additional domains confer distinct subcellular localization and recruitment to specific complexes. Depending on their additional domains, DNAJs are classified into three types: type I, also called DNAJA; Type II, or DNAJB; and Type III, or DNAJC (Kampinga and Craig, 2010). The diversification of J-domain proteins likely underlies the multifaceted regulation of Hsp70, however, few examples exist of the division of labor among different DNAJs.

To test if the distinct function of Hsp70 in the DENV life cycle is driven by different DNAJ proteins, we conducted a comprehensive screen using two or three shRNAs per J-domain protein in human cells. Thirty-five of the KD cells were viable (Figure 5A, S4A, S4B), and KD of DNAJs affecting DENV replication was confirmed by qRT-PCR and immunoblot (Figures 5B and 5C). DENV infection was significantly reduced upon depletion of eight DNAJ proteins (Figure 5A, S4A), and enhanced upon depletion of the known DENV restriction factor DnaJC14 (Yi et al., 2011). Following electroporation of vRNA, four of the DNAJ proteins no longer inhibited infectious virion production, suggesting they participate in viral entry (Figure 5D-F). In contrast, five DNAJs still inhibited DENV particle production (Figure 5D) and vRNA synthesis (Figure 5E), which we independently confirmed using enzymatically-produced esiRNAs (Figure S4C). The distinction between DNAJs required in entry versus post-entry steps was also confirmed by immunoblot for viral proteins following vRNA electroporation (Figure 5F). The DNAJ proteins required for DENV replication exhibit distinct domain structures and subcellular localizations (Figure S4D) (Kampinga and Craig, 2010). Those involved in entry include DnaJC9, reportedly nuclear localized, as well as the membrane-anchored DnaJC16

(B) Hsp70 inhibition directly leads to proteasomal degradation of NS5. 293T cells transfected with HA-NS5 were treated with JG40 with or without proteasome inhibitor MG132 for 36 hr and analyzed as in (A).

(C) Hsp70 physically associates with NS5. Strep-tagged Hsp70 or a GFP control were expressed together with HA-tagged NS5 in 293T cells, and their association assessed by coimmunoprecipitation and immunoblot. Total: represents 20% of the IP input.

(D) Rescue of NS5 levels by MG132 is not enough to restore DENV RNA replication and viral progeny production. NS5 degradation was blocked as in Figure 3A, and levels of intracellular viral RNA and extracellular virus production measured by qRT-PCR (left panel) and FFA (right panel), respectively.

(A, B and C) Data are expressed as mean \pm SD of three independent experiments. * $p < 0.05$. ** $p < 0.01$

(E) In vitro RNA replication assay to test the effect of Hsp70 inhibition on activity of preassembled, folded DENV replication complexes. Crude replication complexes were harvested from infected cells 48 hpi, and processed as described.

(F) Hsp70 is required for NS5 polymerase activity. [^{32}P]-vRNA synthesized *in vitro* in isolated replication complexes in the presence of NS5 or Hsp70 inhibitors (i) or following addition of control or anti-Hsp70 antibody (ii). No vRNA is synthesized in extracts from uninfected cells. The data shown are representative of three independent experiments.

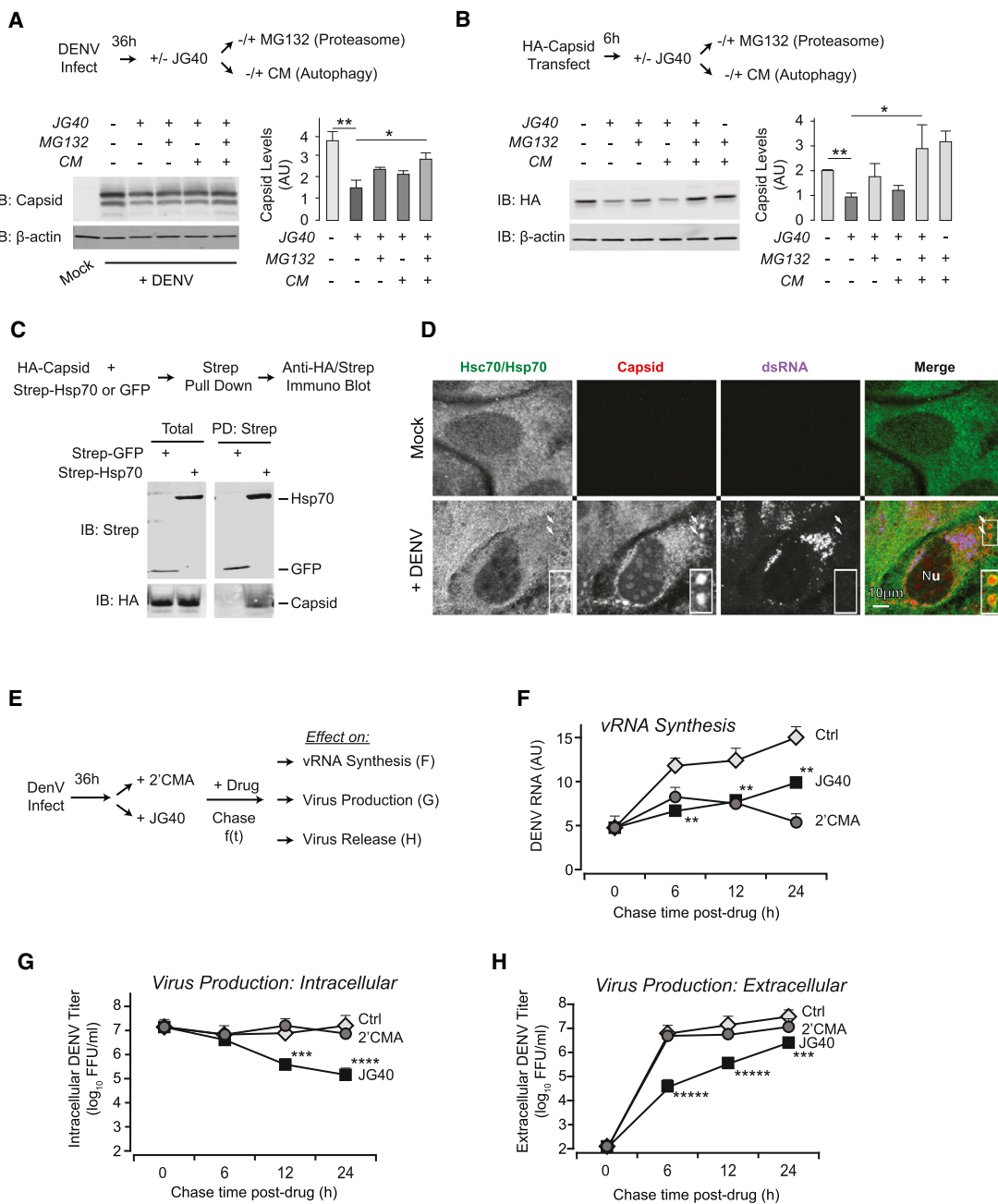


Figure 4. Hsp70 Interacts with Capsid and Participates in Virion Production

(A and B) JG40 treatment leads to capsid degradation through proteasome- and autophagy-dependent pathways. (A) Huh7 cells were infected with DENV2 at MOI 0.5. At 36 hpi, JG40 was added with or without proteasome inhibitor MG132 and/or lysosomal inhibitor CM for an additional 12 hr. Immunoblot analysis (left panel) and quantification (right panel) show that the JG40-induced decrease in NS5 is rescued by MG132.

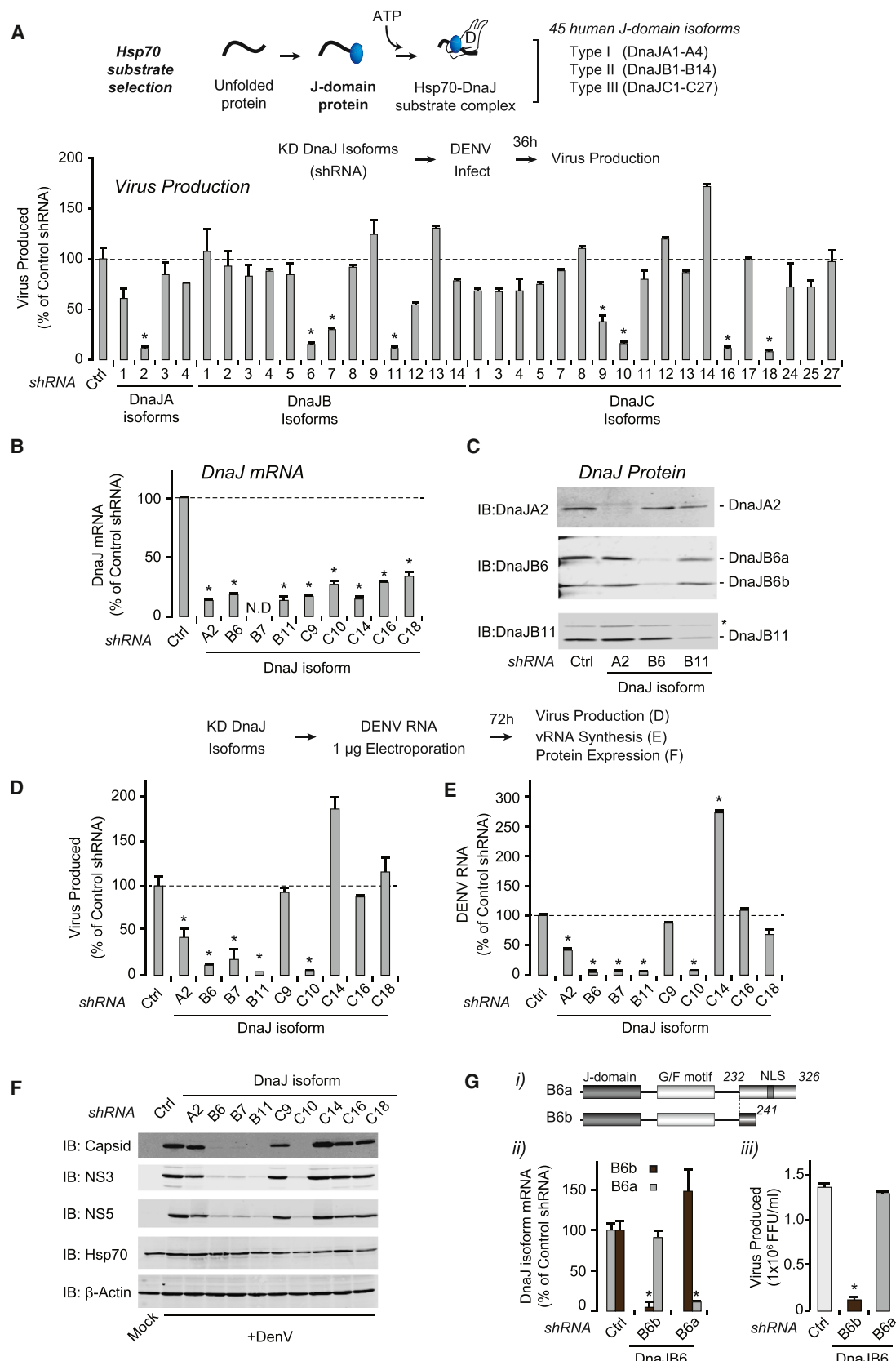
(B) 293T cells expressing HA-capsid were treated with JG40 with or without MG132 and/or CM for 36 hr and analyzed as in (A).

(C) Hsp70 physically associates with capsid. Strep-tagged Hsp70 or a GFP control were expressed together with HA-tagged capsid in 293T cells, and their association assessed by coimmunoprecipitation and immunoblot.

(D) Hsp70 co-localizes with capsid in infected cells. Huh7 cells infected with DENV2 were immunostained for Hsc70/Hsp70 (green), dsRNA (blue) and capsid (red) 48 hpi. Insets: ring-shaped structures formed by capsid due to its association with LD and vesicles. Scale bar, 10 μm

(E–H) Hsp70 is required for infectious viral particle production. (E) Scheme of drug-chase experiment comparing the effect of the NS5 inhibitor (2'CMA) and the Hsp70i JG40 on vRNA production and virion production. Huh7 cells infected with DENV2 at MOI 0.5 were treated at 36 hpi with 3 μM 2'CMA or 3 μM JG40 and levels of intracellular DENV RNA was measured by qRT-PCR (F); intra- and extracellular virion levels (G and H) were measured by FFA. Data are expressed as mean ± SD of three independent experiments.

*p < 0.05, **p < 0.01, ***p < 0.005, ****p < 0.001, *****p < 0.0005.



(legend on next page)

and DnaJC18, which expose the J-domain into the cytosol. Post-entry steps require DnaJA2, DnaJB6, DnaJB7, DnaJB11, and DnaJC10. The cytosolic DnaJA2 significantly inhibited virus production and vRNA synthesis, with only a minor impact on viral proteins. The closely related DnaJA1 and DnaJA3 had little or no effect on DENV replication, indicating that related isoforms can have different substrate specificities. DnaJC10, a luminal ER chaperone (Kampinga and Craig, 2010), may participate in folding ER-bound DENV proteins, or alternatively, host proteins required for DENV replication. Membrane-anchored DnaJB11 is also ER localized (Kampinga and Craig, 2010). DnaJB6 exists as two alternatively spliced isoforms: DnaJB6a is predominantly nuclear and DnaJB6b is nuclear/cytoplasmic (Figure 5G, i). We used shRNAs to selectively KD these splice-variants (Figure 5G, ii, S4E). DENV RNA replication, protein expression, and virion production were all significantly reduced in DnaJB6b KD cells but unaffected by DnaJB6a KD (Figures 5G, iii, S4E and S4F). Thus, closely related DnaJs, and even splice-variants, have divergent specificities and functions. We conclude that the distributed action of DNAJ cofactors localized in distinct cellular compartments orchestrates the many processes leading to productive DENV infection.

Distinct Roles of DnaJB11 and DnaJB6b in DENV Replication

We next focused on DnaJB11 and DnaJB6b, since their KD resulted in strong post-entry effects. To distinguish between a role in vRNA synthesis and viral particle assembly, we electroporated an excess of vRNA into cells depleted of DnaJB6b or DnaJB11. This incoming vRNA should provide enough template for viral protein synthesis and biogenesis, reducing the requirement for vRNA synthesis (Figure 6A). Depletion of DnaJB6b and DnaJB11 resulted in comparable reductions in vProtein (Figure 6A, i) and vRNA (Figure 6A, ii). However, viral particle production was virtually unaffected in DnaJB11-depleted cells, suggesting that significant reductions in vRNA and vProtein levels can have only modest effects on the output of viral particles. In contrast, DnaJB6b depletion significantly reduced infectious particle release (Figure 6A, iii). Therefore, DnaJB6b participates in viral particle biogenesis, while DnaJB11 is not required if sufficient vRNA and vProteins are present.

The observed reduction in viral infectivity upon DnaJB6 KD could be due to reduced particle production or impaired particle maturation. These possibilities make distinct predictions as to how DnaJB6 KD affects the ratio of infectious versus total virions (Figure S5A). To address this, we quantified vRNA genomes from equivalent amounts of focus forming units (FFUs) from the super-

nants of infected DnaJB6 KD or control cells. A reduction in infectivity would predict that more viral particles, i.e., more RNA genomes, will be required for the same number of FFU in DnaJB6 KD cells. This was not the case (Figure S5A), confirming that DnaJB6 is required for viral particle production itself.

Immunofluorescence analysis using confocal microscopy and super-resolution stochastic optical reconstruction microscopy (STORM) (Figures 6B, 6C, and S5B) indicated that DnaJB11 is distributed throughout the cell, co-localizing with the ER, in uninfected cells. Upon infection, DnaJB11 was additionally enriched in dsRNA-containing DENV replication complexes (Figures 6B, 6C, and S5B.). Immunoprecipitation of DnaJB11 followed by RT-PCR analysis (Figure 6D) confirmed that both positive and negative vRNA strands associate with DnaJB11, probably in DENV replication complexes.

Since DnaJB6b is cytosolic and facilitates viral particle biogenesis, we tested its association with capsid, the cytosolic component of virions. DnaJB6b co-immunoprecipitated with transfected HA-capsid (Figure 6E). In DENV-infected cells, capsid was distributed throughout the cell and displayed a previously-described association with LDs (white arrow, shown in inset) and other vesicular structures (Figure 6F) (Samsa et al., 2009). While DnaJB6 localized to the cytosol and nucleus in uninfected cells (Figures 6F and S5C), DnaJB6 co-localized with capsid on vesicular structures and on the surface of LDs after infection, and the proportion of nuclear DnaJB6 was slightly reduced. These results suggest that DnaJB6 associates with capsid to facilitate viral particle biogenesis. To test whether DnaJB6b acts only through Hsp70, we employed two mutations known to disrupt different aspects of DnaJB6b activity (Figure 6G, i). The Hsp70 recruitment ability of DnaJB6 was disrupted by replacing its J-domain HPD motif with an AAA sequence. DnaJB6 is mutated in inherited myofibrillar myopathy and limb-girdle muscular dystrophy (Stein et al., 2014), and we also tested the effect of a disease-linked DnaJB6b mutation on DENV replication (Figures 6G and S5D, F93L). In DnaJ-depleted cells, only wild-type (WT) DnaJB6b fully restored viral production (Figure 6G, i–iii, and S5D). However, the HPD-AAA mutation, but not the F93L mutation, had a modest effect in restoring vRNA synthesis (Figure 6G, ii). Thus, the interaction of DnaJB6b with Hsp70 is important to promote viral particle biogenesis, though DnaJB6b may also possess intrinsic chaperone activity.

JG40 Inhibits the Replication of Divergent Flaviviruses in Human Dendritic Cells

Primary human monocyte-derived dendritic cells (MDDCs) are an established ex vivo model system for DENV (Figure 7A) (Aguirre

Figure 5. A Subset of Human DNAJ Co-chaperones Is Required for the DENV Life Cycle

(A) Screen for human DNAJ involvement in DENV replication. Forty-five human DNAJs were tested for effect on DENV by KD using three different shRNAs. Indicated DNAJ-KD cells were established as for Hsp70s in Figure 1, and infected with DENV2 for 36 hr. Extracellular virus production was measured by FFA. Ctrl: shRNA against luciferase.

(B and C) Validation of KD of different DNAJ isoforms by assessing mRNA levels (B) and DNAJ protein (C).

(D–F) Identification of DNAJs involved in post-entry stages of the DENV life cycle. DENV vRNA was electroporated into DNAJ-KD cells. Extracellular viral infectivity (D); intracellular viral RNA (E) and viral proteins (F) were measured after 72 hr, by FFA, qRT-PCR and immunoblotting, respectively.

(G) Isoform DnaJB6b is required for DENV propagation. (i) Splicing creates DnaJB6 variants. KD cells were established for each variant, and infected with DENV2 for 36 hr. The levels of each variant transcript (ii) and extracellular viral production (iii) were measured by qRT-PCR with variant-specific primers and FFA, respectively. Data are representative of three independent experiments and expressed as mean ± SD of triplicates. *p < 0.01.

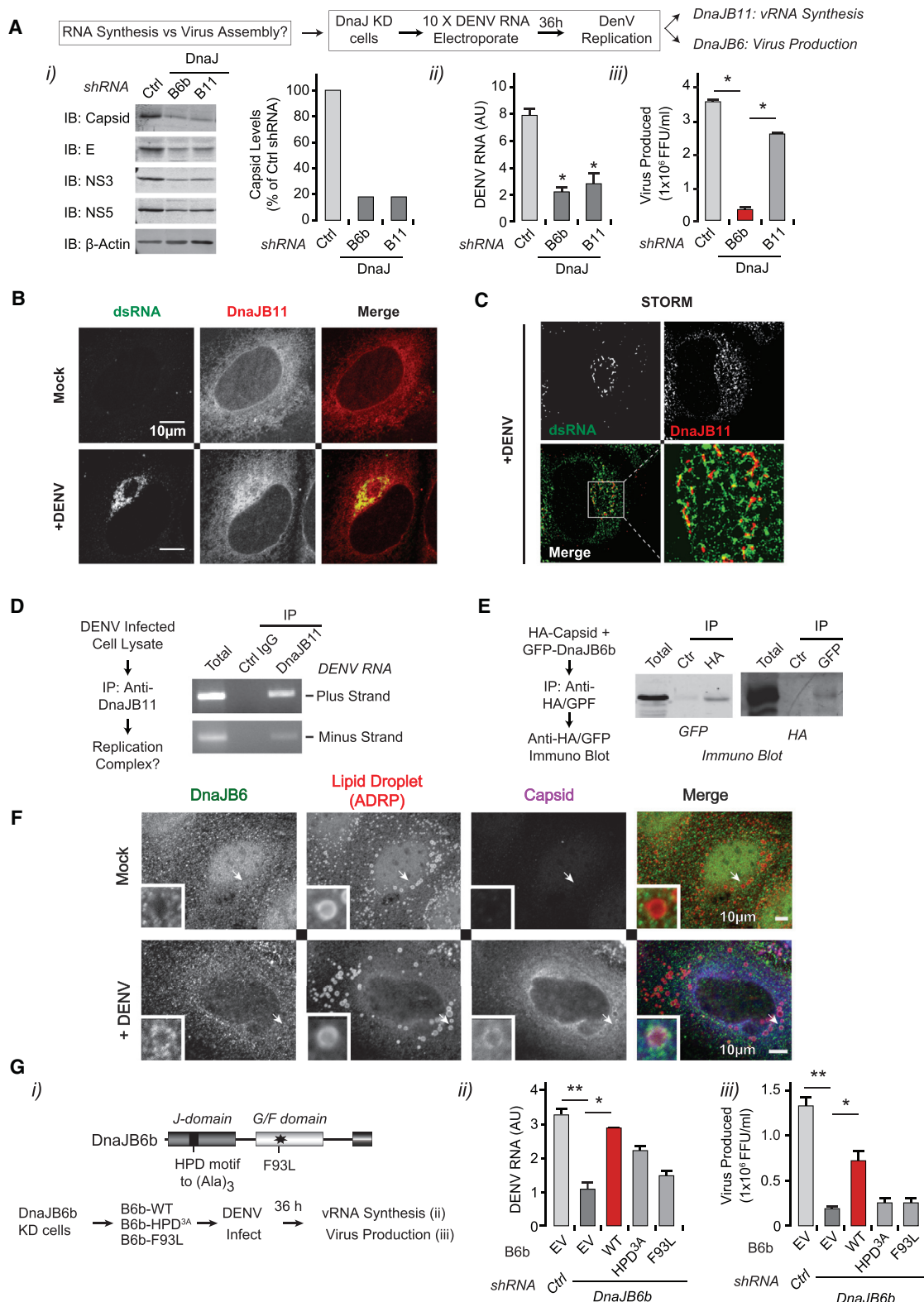


Figure 6. Spatial and Functional Diversity of DNAJs in DENV Propagation

(A) Introduction of excess DENV RNA by electroporation rescues DENV production in DnaJB11-KD, but not in DnaJB6-KD cells. Intracellular proteins (i), viral RNA (ii), and extracellular viral infectivity (iii) were measured by immunoblot, qRT-PCR, and FFA, respectively, at 36 hpi. *p < 0.05

(legend continued on next page)

et al., 2012; Rodriguez-Madoz et al., 2010), allowing us to examine the therapeutic potential of Hsp70 inhibitors (Figures 7 and S6). JG40 dose-dependently inhibited DENV2 replication, to undetectable levels at 5 μ M (Figure 7C) but did not reduce MDDC viability at these concentrations (Figure 7B). JG40 also reduced vRNA accumulation (Figure S6A). JG40's higher potency in primary MDDCs compared to Huh7 cells is interesting, since transformed cells have disregulated chaperone activity, making primary cells more responsive to chaperone inhibition (Trepel et al., 2010). The therapeutic window for antiviral use of chaperone modulators is also greater in primary cells (Geller et al., 2013; Geller et al., 2007). JG40 also inhibited DENV4, the most divergent of the four DENV serotypes (Figures 7C and S6A). We next examined the antiviral effects of JG40 on the flaviviruses WNV (strain Kunjin; KUNV), YFV, and the TBEV model Langat virus (LGTV). All three viruses were dose-dependently inhibited by JG40 (Figures 7D, S6A, and S6B), and in all cases infectious virus was undetectable with 5 μ M JG40 (Figure 7D). JG40 is therefore a broad spectrum antiviral active against distantly related flaviviruses, many of which have limited treatment options.

Effects of JG40 on Cytokine and Chemokine Induction in DENV-Infected MDDCs

An ideal dengue therapy should attenuate the overproduction of cytokines and chemokines associated with DHF/DSS as well as viral replication. We therefore measured the effect of JG40 on relevant cytokines and chemokines produced during DENV2 or DENV4 infection in MDDCs (Figures 7E and S6C). The pro-inflammatory cytokines TNF- α , IL-6, and IL-1 β induce fever and may cause vascular permeability during DENV infection; the chemokine RANTES is involved in leukocyte recruitment, and type I interferon (IFN) is involved in viral clearance but also contributes to the "flu-like" symptoms of dengue disease (Charo and Ransohoff, 2006; Rothman, 2011). As we showed previously, DENV2 does not induce type I IFN, and transiently induces pro-inflammatory cytokines and chemokines (Figure S6C) (Aguirre et al., 2012; Rodriguez-Madoz et al., 2010). In contrast, DENV4 induced higher levels of chemokines and pro-inflammatory cytokines (Figures 7E and S6C), perhaps due to intrinsic viral differences or due to higher replication levels (Figure 7C). JG40 dose-dependently reduced the induction of IFN- α , TNF- α , RANTES, IL-1 β , and IL-6 in DENV4-infected MDDCs (Figure 7E). However, macrophage inflammatory protein 1 β (MIP-1 β), involved in leukocyte recruitment (Charo and Ransohoff, 2006), was unaffected (Figure S6C), indicating that JG40 does not grossly alter the ability of DCs to induce and secrete proteins.

In principle, the effects of JG40 on cytokine and chemokine production may stem from the inhibitor's effects on viral replication, and the resultant reduction in immunostimulatory pathogen-associated molecular patterns (PAMPs). However, when we directly stimulated MDDCs with the dsRNA mimic poly(I:C) without viral infection, JG40 still reduced TNF- α and RANTES induction, while IFN- α was unaffected (Figures 7F and S6D). Thus, JG40 directly modulates the production of a subset of cytokines independently of its effects on viral replication.

DISCUSSION

Due to their small genomes, RNA viruses rely on the host machinery to support their life cycle, providing a window into fundamental cellular processes. Here we examined the role of the complex Hsp70 chaperone network, central to protein homeostasis, in DENV replication. We find that distinct Hsp70 isoforms and their DnaJ cofactors orchestrate the proteostatic control of specific steps in the DENV life cycle. Distinct steps in DENV replication require different DNAJ Hsp70-cofactors localized to distinct cellular compartments. Our data illustrate how a non-specific chaperone like Hsp70 acquires functional and sub-cellular specificity through the action of DNAJ cofactors. Furthermore, compounds targeting Hsp70 appear to be promising antivirals, for several reasons. First, due to the dependence on Hsp70 at various steps of the viral life cycle, DENV cannot escape these drugs. Second, because these compounds allosterically modulate Hsp70 rather than fully block its activity, they exhibit negligible toxicity at concentrations that completely block virus production. This favorable therapeutic window likely arises from the chaperone-hyperdependence of the virus. Most excitingly, these compounds are effective against different DENV serotypes and diverse flaviviruses. Importantly, they also decrease the virally-induced release of inflammatory cytokines that contribute to severe dengue disease. The effectiveness of antivirals is severely limited by the emergence and spread of resistance (Lipsitch et al., 2007). However, so far no viral resistance has been observed for three unrelated viruses treated with inhibitors of two different chaperones, Hsp90 and Hsp70. This unique property of targeting viral proteostasis may close a gap in antiviral drug development.

Multiple DNAJs Facilitate Distinct Steps of the DENV Replication Cycle

The Hsp70 network has become progressively diversified in evolution (Powers and Balch, 2013). Our work on one simple

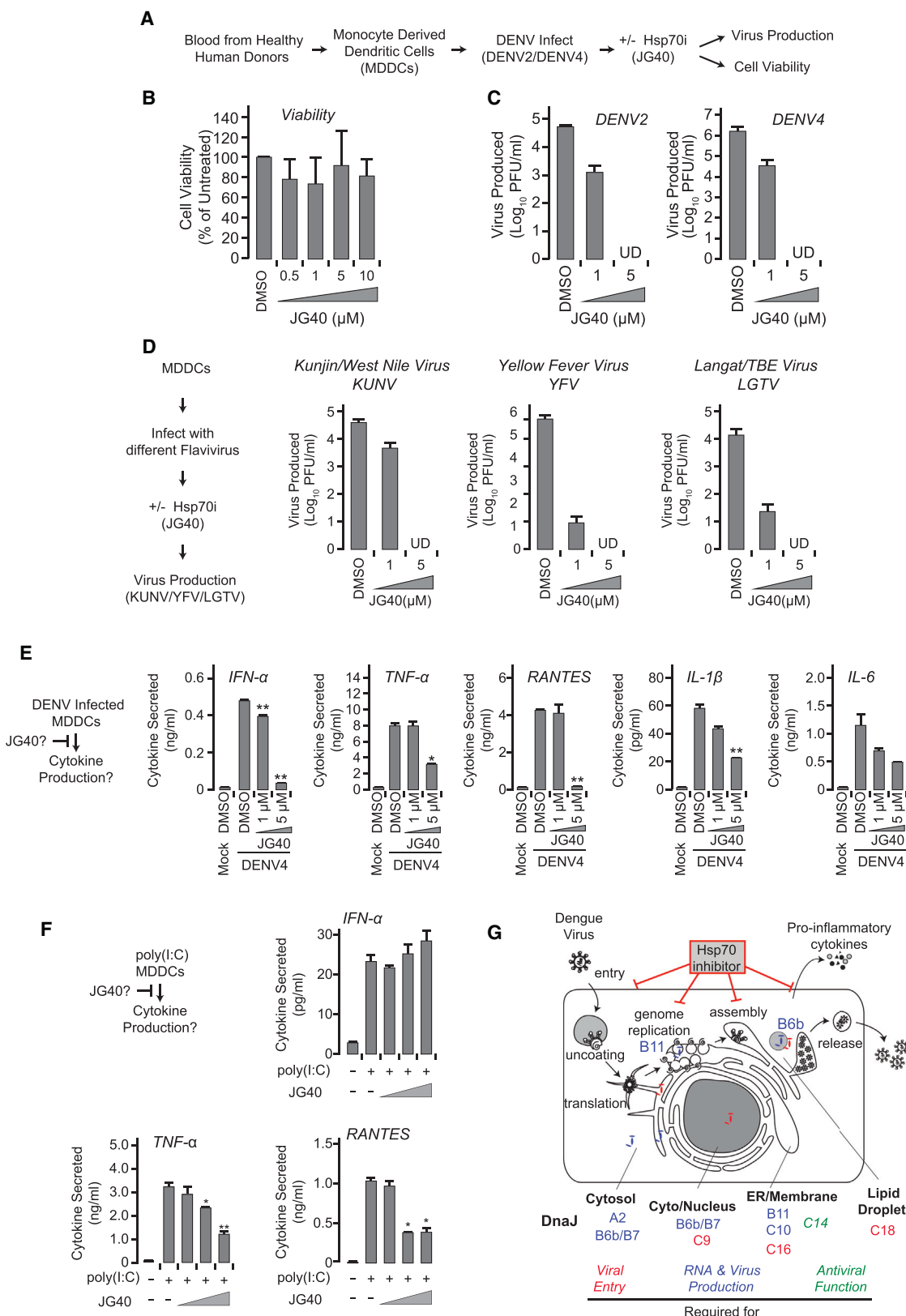
(B and C) DnaJB11 relocates to DENV replication sites. Uninfected Huh7 cells or cells infected with DENV2 for 48 hr were immunostained for DnaJB11 (red) and dsRNA (green) and imaged using confocal microscopy (B) and super-resolution microscopy by STORM (C). Scale bar, 10 μ m

(D) DnaJB11 physically associates with DENV vRNA. DENV-infected cell lysates were subjected to immunoprecipitation with DnaJB11 antibodies. vRNA was extracted and positive strand and negative strand detected by RT-PCR.

(E) DnaJB6b associates with capsid in the absence of infection. GFP-tagged DnaJB6b or GFP were overexpressed together with HA-tagged capsid in 293T cells and association measured by immunoprecipitation and immunoblot.

(F) DnaJB6 co-localizes with capsid in infected cells. Uninfected Huh7 cells or cells infected with DENV2 for 48 hr were immunostained for DnaJB6 (green), ADRP (a marker of lipid droplets; red) and capsid (blue). Inset: magnification of capsid containing cellular structure. Scale bar, 10 μ m

(G) Wild-Type DnaJB6b, but not its mutants can rescue the reduced DENV propagation in DnaJB6b KD cells. (i) DnaJB6b domain structure and position of HDP-AAA mutation, disrupting Hsp70 binding, and disease associated F39L mutation. DnaJB6b or its mutants were transfected into KD cells 48 hr prior to infection with DENV2 at MOI 0.5. At 36 hpi, intracellular viral RNA (ii) and extracellular virus production (iii) were measured as described. Data are representative of three independent experiments and expressed as mean \pm SD of triplicate. *p < 0.05, **p < 0.01.



(legend on next page)

“organism” that uses the protein folding machinery provides insight into the division of labor and connectivity of the many DNAJs and Hsp70s in human cells. It is striking how many DNAJs are involved in viral replication. Nine DNAJs have strong effects upon depletion, while others, such as DNAJC25 or DNAJC13, have smaller but reproducible effects. As we observed strong effects with single-gene depletions, there must be limited redundancy among these DNAJ isoforms. Some DNAJs, e.g., DNAJB11, were reorganized upon infection (Figure 6) while others, e.g., DNAJA2, were not (data not shown). Future studies should clarify whether DENV actively remodels chaperone localization or whether the high levels of viral substrates concentrate their binding factors.

Our data indicate a role for Hsp70 and a subset of DNAJs in viral entry, and a direct role for Hsp70 and DNAJB11 in viral RNA synthesis and for Hsp70 and DNAJB6 in virion production. Hsp70 is not only required for folding and assembly but also for function of the active replication complex. Interestingly, DNAJB6 is important in the regulation of protein aggregation diseases (Hageman et al., 2010), suggesting this chaperone may function to regulate protein assembly processes. While these DNAJs have a direct role in viral proteostasis, at least some DNAJs may participate in host processes required by DENV.

Therapeutic Potential of Hsp70 Inhibitors as Pan-Flavivirus Antivirals

The Hsp70 inhibitor used here, JG40, caused over four logs reduction in DENV2 and DENV4 replication in MDDCs, with negligible toxicity to host cells. Since MDDCs closely model human physiology and disease, these reductions may more accurately reflect the dependence of DENV on the cellular protein folding machinery during human infection than cell lines. In addition, JG40 suppressed the production of proinflammatory cytokines and chemokines, suggesting that Hsp70 inhibitors might benefit patients both by directly inhibiting DENV replication, and by reducing the production of cytokines contributing to severe dengue disease. The comparison of JG40 with the specific NS5 inhibitor 2'CMA is informative for designing antiviral strategies. While 2'CMA is more specific and potent in inhibiting vRNA production, the infected cell makes sufficient precursors to continue new virus production long after inhibitor addition. In contrast, JG40 simultaneously inhibits replication of viral RNA and packaging of viral particles, increasing its effectiveness.

One exciting finding is that JG40 is effective against a diverse set of mosquito- and tick-borne flaviviruses that cause severe human disease (Figures 7 and S6). Our experimental design in primary human cells only measured post-entry effects, thus these compounds might be even more effective *in vivo* as viral entry would additionally be targeted. Future research should further compare the chaperone requirements of different flaviviruses at all stages of their life cycles.

Hsp70 inhibitors may represent a novel class of broadly-acting antivirals to treat diverse flavivirus infections for which there are no specific approved treatments. Considering their pan-flavivirus specificity alongside the lack of observed resistance, such compounds could become an important tool for reducing the worldwide human disease burden caused by these diverse viruses.

EXPERIMENTAL PROCEDURES

Infectious cDNA clone pD2/IC-30P-A of DENV2 (strain 16681) (from CDC [Butrapet et al., 2000]) was used to *in vitro* transcribe vRNA that was electroporated into Huh7 cells to produce infectious DENV2. Kunjin virus (KUNV) and Langat virus (LGT) were kindly provided by Dr. Jean Lim (Icahn School of Medicine at Mount Sinai, NY, USA). DENV and yellow fever virus (YFV) stocks were prepared in Huh7 and C6/36 cells; KUNV and LGTV stocks were prepared on Vero cells. Virus titrations were carried out using the methylcellulose overlay method as described in *Supplemental Experimental Procedures*.

Cells were maintained at 37°C (Huh7) or 32°C (C6/36). MDDCs were generated from healthy human blood donors (New York Blood Center, NY, USA) as described (Rodriguez-Madoz et al., 2010). qRT-PCR quantification of purified RNA was performed using primers specified in Table S1. Transcripts were normalized to GAPDH or Rps11 mRNA (human) or 18S rRNA (mosquito). Viral genome equivalents were quantified using +ssRNA virus-specific standards. Each experiment was independently performed at least three times and each time was performed in triplicate.

Extracellular secreted cytokines were quantified using a customized multiplex ELISA (Millipore, Billerica, MA, USA) as per manufacturer's instructions.

Plasmid transfections, immunoprecipitations, immunoblots, isolation of DENV replication complexes, and *in vitro* DENV replication assay and other biochemical analyses were performed as described in the *Supplemental Experimental Procedures*. For immunofluorescence, cells cultured on glass slides were incubated with the relevant primary and secondary antibodies and imaged by confocal microscope and stochastic reconstruction microscopy (STORM) as described in *Supplemental Experimental Procedures*.

Statistical significance was determined using two-tailed Student's *t* test analysis for samples of equal variance, with sequentially rejective Bonferroni correction where appropriate. Significance levels are as stated in the figure legends.

Figure 7. JG40 Inhibits the Replication of DENV and Other Flaviviruses in Primary Human MDDCs and Modulates Cytokine Induction during DENV Infection

(A–C) JG40 potently inhibits different DENV serotypes at concentrations without toxicity to the host cell. (A) Effects of JG40 in primary human MDDCs at 36 hr post-treatment. (B) Host toxicity of JG40 was determined by LDH release into the culture supernatant. Differences are not statistically significant. (C) MDDCs infected with DENV2 or DENV4 at MOI 0.5 and subsequently treated with JG40 for 36 hr. The level of extracellular viral infectivity was measured by plaque assay. UD, undetectable. Data are the mean of three independent donors, expressed as mean \pm SD.

(D) Broad Spectrum action of JG40 inhibiting the replication of diverse flaviviruses. MDDCs were infected with KUNV, YFV or LGTV at MOI 0.5 and subsequently treated with JG40 for 36 hr. The level of extracellular viral infectivity was measured by plaque assay. UD, undetectable. Data are the mean of three independent donors, expressed as mean \pm SD.

(E) JG40 can suppress cytokine induction during DENV infection. Human MDDCs were infected with DENV4 (MOI 0.5) and subsequently treated with JG40 for 36 hr. Cytokine levels in the culture supernatant were measured by ELISA. * p < 0.05, ** p < 0.01. One representative donor of three shown.

(F) JG40 directly affects the production or secretion of a subset of cytokines. Human MDDCs were treated with increasing amounts (0, 1, 5, or 10 μ M) of JG40, and subsequently transfected with 5 μ g/ml poly(I:C). Cytokine induction was measured by ELISA. * p < 0.05, ** p < 0.01 (one-tailed Student's *t* test with Bonferroni correction). One representative donor of three shown.

(G) Role of the Hsp70/DNAJ network at various steps in the DENV life cycle, highlighting the therapeutic potential of Hsp70 inhibitors (see text for details).

SUPPLEMENTAL INFORMATION

Supplemental Information includes Supplemental Experimental Procedures, six figures, and one table and can be found with this article online at <http://dx.doi.org/10.1016/j.cell.2015.10.046>.

AUTHOR CONTRIBUTION

S.T. and J.F. conceived the project; S.T., R.A., and J.F. designed and interpreted experiments in tissue culture. S.T. performed all experiments in cultured cells. K.M. and A.F.-S. designed and interpreted MDDC experiments; D.B.-R. isolated and differentiated MDDCs. X.L., J.N.R., and J.E.G. synthesized and characterized Hsp70 inhibitors. S.T., K.M., R.A., A.F.-S. and J.F. wrote the manuscript. All authors contributed to preparation of the manuscript.

ACKNOWLEDGMENTS

We thank L. Nguyen for technical assistance and Drs. P. Dolan and A. Gamarnik for helpful discussions. This work was supported by a contract from DARPA Prophecy to R.A., J.F., and A.F.-S.; NIH grants R01AI073450 to A.F.-S. and R01NS059690 to J.E.G.; Wellcome Trust grant 096062 to K.M. and Fellowships from the Naito Foundation and Uehara Memorial Foundation to S.T.

Received: March 6, 2015

Revised: August 25, 2015

Accepted: October 16, 2015

Published: November 12, 2015

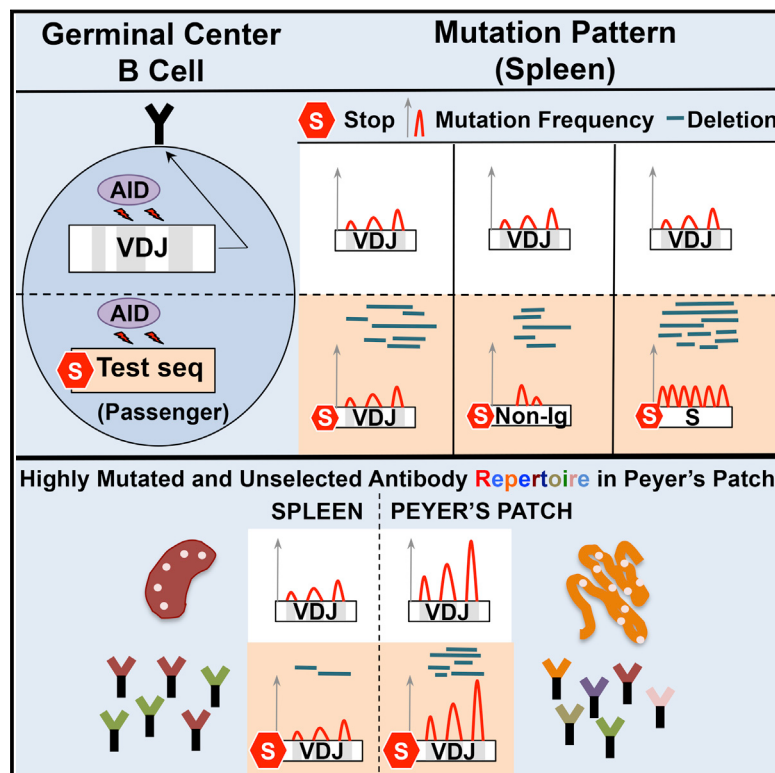
REFERENCES

- Aguirre, S., Maestre, A.M., Pagni, S., Patel, J.R., Savage, T., Gutman, D., Maringer, K., Bernal-Rubio, D., Shabman, R.S., Simon, V., et al. (2012). DENy inhibits type I IFN production in infected cells by cleaving human STING. *PLoS Pathog.* 8, e1002934.
- Apte-Sengupta, S., Sirohi, D., and Kuhn, R.J. (2014). Coupling of replication and assembly in flaviviruses. *Curr. Opin. Virol.* 9, 134–142.
- Assimon, V.A., Gillies, A.T., Rauch, J.N., and Gestwicki, J.E. (2013). Hsp70 protein complexes as drug targets. *Curr. Pharm. Des.* 19, 404–417.
- Balinsky, C.A., Schmeisser, H., Ganesan, S., Singh, K., Pierson, T.C., and Zoon, K.C. (2013). Nucleolin interacts with the dengue virus capsid protein and plays a role in formation of infectious virus particles. *J. Virol.* 87, 13094–13106.
- Bhatt, S., Gething, P.W., Brady, O.J., Messina, J.P., Farlow, A.W., Moyes, C.L., Drake, J.M., Brownstein, J.S., Hoen, A.G., Sankoh, O., et al. (2013). The global distribution and burden of dengue. *Nature* 496, 504–507.
- Butrapet, S., Huang, C.Y., Pierro, D.J., Bhamarapratvi, N., Gubler, D.J., and Kinney, R.M. (2000). Attenuation markers of a candidate dengue type 2 vaccine virus, strain 16681 (PDK-53), are defined by mutations in the 5' noncoding region and nonstructural proteins 1 and 3. *J. Virol.* 74, 3011–3019.
- Charo, I.F., and Ransohoff, R.M. (2006). The many roles of chemokines and chemokine receptors in inflammation. *N. Engl. J. Med.* 354, 610–621.
- De Clercq, E. (2007). Three decades of antiviral drugs. *Nat. Rev. Drug Discov.* 6, 941.
- Dowd, K.A., Mukherjee, S., Kuhn, R.J., and Pierson, T.C. (2014). Combined effects of the structural heterogeneity and dynamics of flaviviruses on antibody recognition. *J. Virol.* 88, 11726–11737.
- Geller, R., Andino, R., and Frydman, J. (2013). Hsp90 inhibitors exhibit resistance-free antiviral activity against respiratory syncytial virus. *PLoS ONE* 8, e56762.
- Geller, R., Taguwa, S., and Frydman, J. (2012). Broad action of Hsp90 as a host chaperone required for viral replication. *Biochim. Biophys. Acta* 1823, 698–706.
- Geller, R., Vignuzzi, M., Andino, R., and Frydman, J. (2007). Evolutionary constraints on chaperone-mediated folding provide an antiviral approach refractory to development of drug resistance. *Genes Dev.* 21, 195–205.
- Hageman, J., Rujano, M.A., van Waarde, M.A., Kakkar, V., Dirks, R.P., Govorukhina, N., Oosterveld-Hut, H.M., Lubsen, N.H., and Kampinga, H.H. (2010). A DNAJB chaperone subfamily with HDAC-dependent activities suppresses toxic protein aggregation. *Mol. Cell* 37, 355–369.
- Halstead, S.B. (2007). Dengue. *Lancet* 370, 1644–1652.
- Hartl, F.U., Bracher, A., and Hayer-Hartl, M. (2011). Molecular chaperones in protein folding and proteostasis. *Nature* 475, 324–332.
- Junjhon, J., Pennington, J.G., Edwards, T.J., Perera, R., Lanman, J., and Kuhn, R.J. (2014). Ultrastructural characterization and three-dimensional architecture of replication sites in dengue virus-infected mosquito cells. *J. Virol.* 88, 4687–4697.
- Kampinga, H.H., and Craig, E.A. (2010). The HSP70 chaperone machinery: J proteins as drivers of functional specificity. *Nat. Rev. Mol. Cell Biol.* 11, 579–592.
- Lauring, A.S., Frydman, J., and Andino, R. (2013). The role of mutational robustness in RNA virus evolution. *Nat. Rev. Microbiol.* 11, 327–336.
- Li, X., Colvin, T., Rauch, J.N., Acosta-Alvear, D., Kampmann, M., Dunyak, B., Hann, B., Aftab, B.T., Murnane, M., Cho, M., et al. (2015). Validation of the Hsp70-Bag3 protein-protein interaction as a potential therapeutic target in cancer. *Mol. Cancer Ther.* 14, 642–648.
- Li, X., Srinivasan, S.R., Connarn, J., Ahmad, A., Young, Z.T., Kabza, A.M., Zuideweg, E.R., Sun, D., and Gestwicki, J.E. (2013). Analogs of the Allosteric Heat Shock Protein 70 (Hsp70) Inhibitor, MKT-077, as Anti-Cancer Agents. *ACS Med. Chem. Lett.* 4, 4.
- Lim, S.P., Wang, Q.Y., Noble, C.G., Chen, Y.L., Dong, H., Zou, B., Yokokawa, F., Nilar, S., Smith, P., Beer, D., et al. (2013). Ten years of dengue drug discovery: progress and prospects. *Antiviral Res.* 100, 500–519.
- Limjindaporn, T., Wongwiwat, W., Noisakran, S., Srisawat, C., Netsawang, J., Puttikhunt, C., Kasinrerk, W., Avirutnan, P., Thiemmeca, S., Sriburi, R., et al. (2009). Interaction of dengue virus envelope protein with endoplasmic reticulum-resident chaperones facilitates dengue virus production. *Biochem. Biophys. Res. Commun.* 379, 196–200.
- Lindenbach, B.D., Thiel, H.J., and Rice, C.M. (2007). Flaviviridae: the viruses and their replication. *Fields Virology*, Fifth Edition (Lippincott Williams & Wilkins), pp. 1101–1152.
- Lipsitch, M., Cohen, T., Murray, M., and Levin, B.R. (2007). Antiviral resistance and the control of pandemic influenza. *PLoS Med.* 4, e15.
- Mayer, M.P. (2005). Recruitment of Hsp70 chaperones: a crucial part of viral survival strategies. *Rev. Physiol. Biochem. Pharmacol.* 153, 1–46.
- Nagy, P.D., and Pogany, J. (2012). The dependence of viral RNA replication on co-opted host factors. *Nat. Rev. Microbiol.* 10, 137–149.
- Neckers, L., and Tatu, U. (2008). Molecular chaperones in pathogen virulence: emerging new targets for therapy. *Cell Host Microbe* 4, 519–527.
- O'Brien, M.C., Flaherty, K.M., and McKay, D.B. (1996). Lysine 71 of the chaperone protein Hsc70 is essential for ATP hydrolysis. *J. Biol. Chem.* 271, 15874–15878.
- Perera, R., and Kuhn, R.J. (2008). Structural proteomics of dengue virus. *Curr. Opin. Microbiol.* 11, 369–377.
- Powers, E.T., and Balch, W.E. (2013). Diversity in the origins of proteostasis networks—a driver for protein function in evolution. *Nat. Rev. Mol. Cell Biol.* 14, 237–248.
- Rodriguez-Madoz, J.R., Belicha-Villanueva, A., Bernal-Rubio, D., Ashour, J., Ayllon, J., and Fernandez-Sesma, A. (2010). Inhibition of the type I interferon response in human dendritic cells by dengue virus infection requires a catalytically active NS2B3 complex. *J. Virol.* 84, 9760–9774.
- Rothman, A.L. (2011). Immunity to dengue virus: a tale of original antigenic sin and tropical cytokine storms. *Nat. Rev. Immunol.* 11, 532–543.
- Samsa, M.M., Mondotte, J.A., Iglesias, N.G., Assunção-Miranda, I., Barbosa-Lima, G., Da Poian, A.T., Bozza, P.T., and Gamarnik, A.V. (2009). Dengue virus

- capsid protein usurps lipid droplets for viral particle formation. *PLoS Pathog.* 5, e1000632.
- Schmid, M.A., Diamond, M.S., and Harris, E. (2014). Dendritic cells in dengue virus infection: targets of virus replication and mediators of immunity. *Front. Immunol.* 5, 647.
- Shepard, D.S., Undurraga, E.A., Betancourt-Cravioto, M., Guzmán, M.G., Halstead, S.B., Harris, E., Mudin, R.N., Murray, K.O., Tapia-Conyer, R., and Gubler, D.J. (2014). Approaches to refining estimates of global burden and economics of dengue. *PLoS Negl. Trop. Dis.* 8, e3306.
- Stein, K.C., Bengoechea, R., Harms, M.B., Weihl, C.C., and True, H.L. (2014). Myopathy-causing mutations in an HSP40 chaperone disrupt processing of specific client conformers. *J. Biol. Chem.* 289, 21120–21130.
- Trepel, J., Mollapour, M., Giaccone, G., and Neckers, L. (2010). Targeting the dynamic HSP90 complex in cancer. *Nat. Rev. Cancer* 10, 537–549.
- Wang, A.M., Miyata, Y., Klinedinst, S., Peng, H.M., Chua, J.P., Komiyama, T., Li, X., Morishima, Y., Merry, D.E., Pratt, W.B., et al. (2013). Activation of Hsp70 reduces neurotoxicity by promoting polyglutamine protein degradation. *Nat. Chem. Biol.* 9, 112–118.
- Welsch, S., Miller, S., Romero-Brey, I., Merz, A., Bleck, C.K., Walther, P., Fuller, S.D., Antony, C., Krijnse-Locker, J., and Bartenschlager, R. (2009). Composition and three-dimensional architecture of the dengue virus replication and assembly sites. *Cell Host Microbe* 5, 365–375.
- Williamson, D.S., Borgognoni, J., Clay, A., Daniels, Z., Dokurno, P., Drysdale, M.J., Foloppe, N., Francis, G.L., Graham, C.J., Howes, R., et al. (2009). Novel adenosine-derived inhibitors of 70 kDa heat shock protein, discovered through structure-based design. *J. Med. Chem.* 52, 1510–1513.
- Ye, J., Chen, Z., Zhang, B., Miao, H., Zohaib, A., Xu, Q., Chen, H., and Cao, S. (2013). Heat shock protein 70 is associated with replicase complex of Japanese encephalitis virus and positively regulates viral genome replication. *PLoS ONE* 8, e75188.
- Yi, Z., Sperzel, L., Nürnberger, C., Bredenbeek, P.J., Lubick, K.J., Best, S.M., Stoyanov, C.T., Law, L.M., Yuan, Z., Rice, C.M., and MacDonald, M.R. (2011). Identification and characterization of the host protein DNAJC14 as a broadly active flavivirus replication modulator. *PLoS Pathog.* 7, e1001255.

Sequence-Intrinsic Mechanisms that Target AID Mutational Outcomes on Antibody Genes

Graphical Abstract



Authors

Leng-Siew Yeap, Joyce K. Hwang, Zhou Du, ..., Thomas B. Kepler, Jing H. Wang, Frederick W. Alt

Correspondence

alt@enders.tch.harvard.edu

In Brief

An *in vivo* passenger assay elucidates the role of DNA substrate sequences in AID-initiated antibody diversification. Gut-associated B lymphocytes provide a reservoir of highly diversified and unselected antibodies.

Highlights

- V exons and non-Ig sequences are similarly targeted for SHMs and DSBs
- The V exon location is privileged for SHM
- CSR-activated B cells in culture undergo SHM of AID hotspot targets in V exons
- Pre-selection BCR repertoires are expanded by SHM in Peyer's patch B cells

Sequence-Intrinsic Mechanisms that Target AID Mutational Outcomes on Antibody Genes

Leng-Siew Yeap,^{1,4} Joyce K. Hwang,^{1,4} Zhou Du,¹ Robin M. Meyers,¹ Fei-Long Meng,¹ Agnè Jakubauskaité,¹ Mengyuan Liu,¹ Vinidhra Mani,¹ Donna Neuberg,² Thomas B. Kepler,³ Jing H. Wang,^{1,5,6} and Frederick W. Alt^{1,5,*}

¹Howard Hughes Medical Institute, Program in Cellular and Molecular Medicine at Boston Children's Hospital, and Department of Genetics, Harvard Medical School, 300 Longwood Avenue, Boston, MA 02115, USA

²Department of Biostatistics and Computational Biology, Dana-Farber Cancer Institute, Boston, MA 02215, USA

³Department of Microbiology, Boston University School of Medicine, Boston, MA 02215, USA

⁴Co-first author

⁵Co-senior author

⁶Present address: Department of Immunology and Microbiology, University of Colorado Anschutz Medical Campus, Aurora, CO 80045, USA

*Correspondence: alt@enders.tch.harvard.edu

<http://dx.doi.org/10.1016/j.cell.2015.10.042>

SUMMARY

In activated B lymphocytes, AID initiates antibody variable (V) exon somatic hypermutation (SHM) for affinity maturation in germinal centers (GCs) and IgH switch (S) region DNA breaks (DSBs) for class-switch recombination (CSR). To resolve long-standing questions, we have developed an *in vivo* assay to study AID targeting of passenger sequences replacing a V exon. First, we find AID targets SHM hot-spots within V exon and S region passengers at similar frequencies and that the normal SHM process frequently generates deletions, indicating that SHM and CSR employ the same mechanism. Second, AID mutates targets in diverse non-Ig passengers in GC B cells at levels similar to those of V exons, definitively establishing the V exon location as “privileged” for SHM. Finally, Peyer’s patch GC B cells generate a reservoir of V exons that are highly mutated before selection for affinity maturation. We discuss the implications of these findings for harnessing antibody diversification mechanisms.

INTRODUCTION

Antibodies are the secreted form of B cell antigen receptors (BCRs), the basic subunit of which is a pair of identical immunoglobulin (Ig) heavy (IgH) and light (IgL) chains. N-terminal regions of IgH and IgL chains provide the antigen-binding variable (“V”) region of antibodies. Ig V regions are encoded by exons (“V exons”) assembled by V(D)J recombination during bone marrow B cell development. V(D)J recombination creates diverse antibody repertoires by assembling multitudes of different germline V, D, and J combinations and by diversifying junctions between these segments through nucleotide deletions and insertions (Alt et al., 2013). V exons contain three highly variable domains termed complementarity-determining regions (CDRs), which en-

code antigen-contact sites and determine binding specificity (Di Noia and Neuberger, 2007). CDR1 and CDR2 are encoded by germline V segments, whereas CDR3 is encoded by V(D)J junctional regions and therefore has the greatest diversity (Hwang et al., 2015). Conserved framework regions (FWRs) between CDRs impart antibody structure. Due to junctional diversity, about two-thirds of V exons are assembled out of frame and do not encode proteins. These “non-productive” V exons are often present in B cells in which the other IgH (and/or IgL) locus is productively rearranged and supports development (Mostoslavsky et al., 2004).

The mouse expresses different antibody classes determined by expressed IgH constant regions exons (C_Hs). The first developmentally expressed C_H (C_H) generates primary B cells expressing IgM. Newly generated IgM-expressing B cells migrate to peripheral lymphoid organs, where, upon antigen activation, they further diversify primary antibody V exon repertoires by somatic hypermutation (SHM) and change expressed C_H antibody effector functions via IgH class-switch recombination (CSR) (Hwang et al., 2015). SHM occurs in response to antigen-dependent B cell activation in specialized lymphoid structures termed germinal centers (GCs) (Victora and Nussenzweig, 2012). SHM mainly introduces point mutations into V exons (Di Noia and Neuberger, 2007). GC B cells with SHMs that result in increased BCR antigen-binding affinity are positively selected, leading to affinity maturation, and those that decrease BCR affinity or cause loss of BCR expression are negatively selected (Di Noia and Neuberger, 2007; Victora and Nussenzweig, 2012). IgH CSR occurs within or outside GCs and can be activated in cultured IgM-expressing primary B cells (Stavnezer et al., 2008). During CSR, DNA double-strand breaks (DSBs) are introduced into long, repetitive switch (S) regions that precede C_H (S_H) and each downstream C_H. Joining a donor S_H DSB to a downstream acceptor S region DSB mediates CSR to IgG, IgE, or IgA (Hwang et al., 2015).

Both V exon SHM and IgH CSR are initiated by activation-induced cytidine deaminase (AID) (Muramatsu et al., 2000), an enzyme that deaminates cytosines (C) to uridines (U) in single-stranded DNA. AID is targeted transcriptionally to V exons and S regions, where it acts on both DNA strands (Alt et al., 2013).

Co-opted base excision repair (BER) or mismatch repair (MMR) factors convert AID-initiated lesions into mutational or DSB outcomes (Di Noia and Neuberger, 2007; Peled et al., 2008). Uridine/guanine (U/G) mismatches, which are the result of AID activity, are converted to transition or transversion mutations at initiating C/G residues by replication over uracils or over an abasic site upon uracil removal by BER (Di Noia and Neuberger, 2007). MMR also generates transition or transversion mutations and extends SHM to flanking adenine/thymidine (A/T) residues by error prone DNA polymerase activity following excision of DNA patches around AID-generated uracils (Peled et al., 2008). DSBs can be generated by BER in the form of adjacent nicks on both DNA strands or by MMR in the form of overlapping gaps (Saribasak and Gearhart, 2012; Chahwan et al., 2012). AID preferentially deaminates cytidines in short RGYW ($R = A/G$, $Y = C/T$, $W = A/T$) or related motifs (Liu and Schatz, 2009; Hackney et al., 2009). Compared to the genome, such motifs are mildly enriched in certain V exons (Hackney et al., 2009). AGCT, a canonical RGYW motif, occurs at high density in the core of long, highly repetitive mammalian S regions, where its palindromic sequence provides AID substrates on both DNA strands (Han et al., 2011; Zarrin et al., 2004). However, AID-targeting patterns on core S regions have not been measured due to the repetitive S region nature.

While transcription targets AID to different S regions (Alt et al., 2013), mechanisms that differentially target AID to sequences within a V exon or between V exons and S regions have remained enigmatic. AID targets both productive and non-productive V exons during SHM at high frequency (10^{-3} mutations per base pair) (Odegard and Schatz, 2006). Within V exons, SHMs are focused at RGYW motifs in CDRs of both productive and non-productive alleles (Di Noia and Neuberger, 2007; Dörner et al., 1997; Betz et al., 1993a, 1993b; Wei et al., 2015). RGYW motifs do not appear sufficient for targeting, since identical motifs mutate less frequently in FWRs (Dörner et al., 1997; Wei et al., 2015). In this regard, non-Ig sequences driven by Ig promoters and enhancers in transgenes can, in some cases, undergo substantial SHM (Yélamos et al., 1995). However, as such transgene results are variable and could reflect influences of integration site and copy number, they have not generally been considered to represent normal SHM processes (Yang and Schatz, 2007; Maul and Gearhart, 2010a). Thus, the question of what mechanisms enable high AID targeting within V exons and within CDRs, in particular, has remained an enigma.

Another AID-targeting enigma comes from findings that B cells or B cell lines activated in culture to undergo robust CSR have not been found to undergo SHM of adjacent, transcribed V exons (Nagaoka et al., 2002; Maul et al., 2014; Liu and Schatz, 2009). Such findings led to the conclusion that differential mechanisms target AID to V exons versus S regions (Maul and Gearhart, 2010b; Storb, 2014). While such mechanisms have been elusive, one postulate is that these activities involve differential activation of CSR versus SHM factors by AID (Muramatsu et al., 2007). V exon SHM is considered to predominantly involve point mutations (Di Noia and Neuberger, 2007) and rarely lead to DSBs (Betz et al., 1993a). Estimates of the frequency of V exon DSBs have been highly variable, likely due to the limited number of sequences analyzed (Goossens et al., 1998; Betz et al., 1993a,

1993b; Bross et al., 2000; Briney et al., 2012). Thus, the question of whether AID specifically mediates point mutation during SHM and DSBs during CSR via distinct mechanisms has remained unresolved. Correspondingly, whether or not most V exon DSBs are directly linked to AID-initiated SHM remains an important question, given that deletions (and related insertions) can contribute to antibody specificity, for example in certain extensively mutated anti-HIV-1 broadly neutralizing antibodies (bnAb) (Wu et al., 2011; Mascola and Haynes, 2013; Kepler et al., 2014).

Intestinal Peyer's patch (PP) GCs are chronically present in mice in the absence of specific immunization due to continual stimulation by commensals and gut antigens (Casola et al., 2004). Correspondingly, PP GC B cells with V_λ exon SHMs are found robustly in BCR-deficient mice that express the Epstein Barr Virus protein LMP2a as a BCR signaling surrogate, indicating that SHM occurs in PP GC B cells in the absence of BCR engagement with antigen (Casola et al., 2004). In this regard, intestinal B cell development and primary antibody diversification occurs in sheep, cattle, pigs, chicken, and rabbits (Lanning and Knight, 2005) and has also been implicated in the mouse (Wesemann et al., 2013). Thus, it is conceivable that mouse PP GCs, beyond initiating antigen-specific responses, may also undergo SHM via antigen-independent stimulation to further expand primary BCR repertoires (Lanning and Knight, 2005; Casola et al., 2004). However, the degree to which SHMs are selected by specific antigens in V exon repertoires of PP GC B cells that express a functional BCR has not been addressed.

To elucidate roles of V(D)J exon and S region sequences in AID-targeting and DSB versus mutational outcomes in mouse GC B and CSR-activated B cells, we developed an efficient approach to measure AID activity on a fixed "productive" *IgH* V(D)J exon allele, versus an array of test sequences driven by the same promoter on the other "passenger" allele. This approach has provided unanticipated insight into long-standing questions regarding AID targeting and outcome during SHM and CSR.

RESULTS

A V(D)J Replacement Passenger Allele System

We developed an efficient V(D)J passenger allele system to test the influence of substrate sequences on AID targeting and the outcome of such activity in mouse GC B cells or CSR-activated cultured B cells (Figures 1A and S1A). For this approach, we generated an embryonic stem (ES) cell line with a productive pre-assembled V(D)J allele encoding the *IgH* V region of the 4-hydroxy-3-nitrophenylacetyl (NP)-binding B1-8 antibody (VB1-8) inserted in place of the four *IgH* J_H segments (Sonoda et al., 1997). On the other "passenger" *IgH* allele of these "VB1-8" ES cells, we inserted a puromycin-resistance cassette in place of the four J_H s. To generate VB1-8 ES cells with different test passenger sequences, we replaced the inserted puromycin-resistance cassette with a "passenger" cassette, which consisted of a VB1-8 promoter and leader sequence containing a translation termination codon, followed by test sequences (Figure 1A, bottom). Thus, as the passenger test sequences cannot encode proteins, their SHM patterns

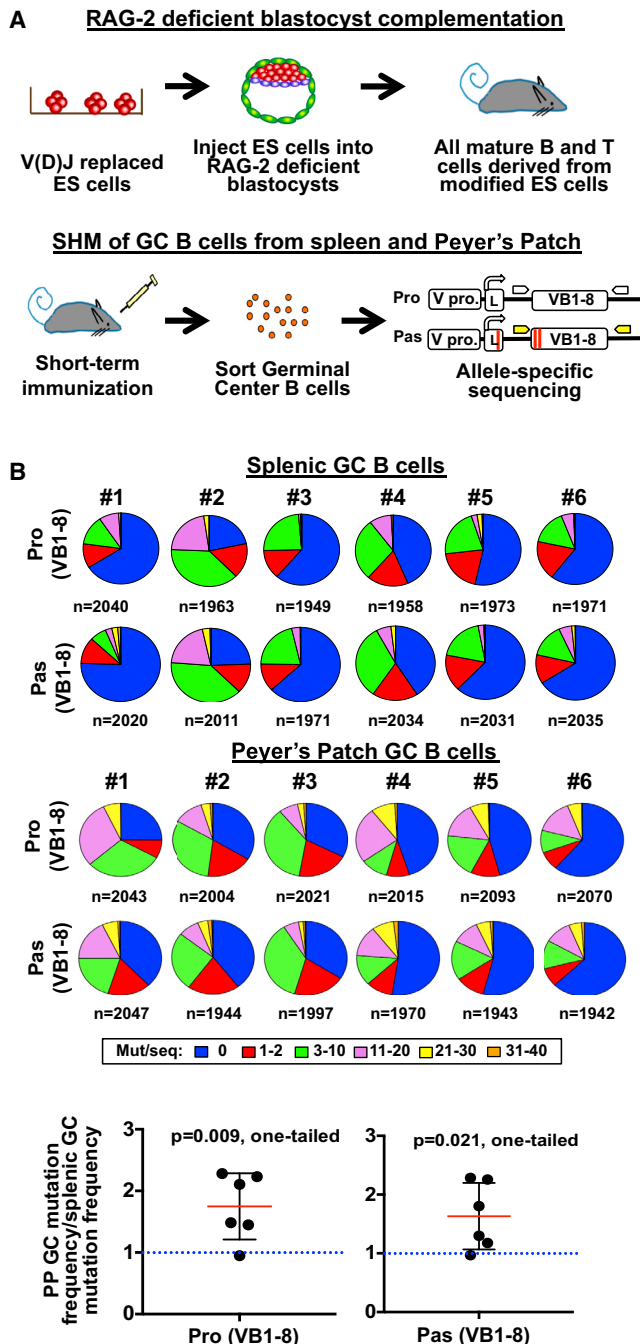


Figure 1. V(D)J Replacement Passenger Allele System

(A) Top: RDBC generates chimeric mice whose mature B cells carry a fixed VB1-8-productive allele and test sequences in the V(D)J passenger allele. Bottom: assay of SHM of GC B cells from spleen and PP of immunized mice. Pro, pas, V pro, and L represent productive allele, passenger allele, V promoter, and leader sequence, respectively. Red lines across the leader sequence and VB1-8 in the passenger allele represent a termination codon and two nucleotide changes from productive VB1-8, respectively.

(B) Pie charts showing the proportion of sequences that have the indicated number of mutations per sequence in productive and passenger VB1-8 alleles from splenic GC B cells (top) and PP GC B cells (middle) of six independent mice. The total number of sequence reads from each mouse is indicated below

are not biased by antigen-specific B cell selection forces. VB1-8/pasenger ES clones are used for RAG-2-deficient blastocyst complementation (“RDBC;” [Chen et al., 1993](#)) to generate chimeric mice in which all peripheral lymphocytes are derived from the injected ES cells ([Figure 1A, top](#)). We induce SHM in splenic GC B cells of VB1-8/pasenger chimeras by short-term immunization (10 days) with NP-chicken gamma globulin (NP-CGG) or other immunogens to activate GC formation in the absence of appreciable antigen-specific B cell selection ([Weiss et al., 1992](#)). Following immunization, we purify GC B cells from spleens and PP of individual RDBC chimeras and amplify their productive VB1-8 and the passenger allele sequences via allele-specific primers, sequence the products via next-generation high-throughput sequencing, and assay them for SHMs ([Figure 1A, bottom](#); [Figure S1B](#)).

Mutation Profiles of Productive and Passenger VB1-8 Alleles in Splenic GC B Cells

To validate the RDBC-based VB1-8/pasenger approach, we assayed a bona fide VB1-8 sequence as a passenger ([Figure 1A, bottom](#)). Given the essentially identical sequence and transcription control elements, we expected a similar frequency and pattern of SHMs in productive and passenger alleles of splenic GC B cells under non-selective immunization conditions. For analysis, we compared mutations per sequence in productive and passenger alleles from six different chimeras by breaking them into six different mutation strata, ranging from 0 to 31–40 mutations/sequence and using pie charts to visualize overall SHM levels for each mouse ([Figures 1B and S1C](#)). Both productive and passenger VB1-8 alleles were mutated substantially in splenic GC B cells ([Figure 1B, top](#)), with levels far above background ([Figures S1D and S1E](#); [Table S1](#)). While overall SHM levels varied between different chimeras, productive and passenger VB1-8 alleles in splenic GC B cells of a given chimera had very similar SHM levels ([Figure 1B, top](#); [Figure S1F, left](#)). Moreover, productive and passenger VB1-8 alleles in GC B cells from given chimeras had remarkably similar distributions of sequences across the six tested SHM strata ([Figure 1B, top](#)).

Kinetic Analysis of Hotspot Mutations with Increasing Mutation Frequency

One of our major goals was to test for AID target hotspots in various passenger sequences by assaying for them in sequences with low to high mutation levels. In this regard, duplicate mutations that arise from independent targeting events at hotspots when mutation levels are low may be difficult to distinguish from PCR repeats and, therefore, difficult to capture by standard SHM analyses that exclude duplicates (e.g., [Rada et al., 2004](#)). To counter this limitation, we developed an analysis

each pie chart. Bottom: ratios of the mutation frequencies of PP GC B cells to mutation frequencies of splenic GC B cells (calculated within each mouse), for productive VB1-8 (left) and passenger VB1-8 alleles (right). Ratios were calculated for each of the six mice separately and displayed as the mean \pm SD of the six mice. One-sample Student’s t test was performed to test for the significance of the difference of the mean from a hypothetical mean of 1.0 (labeled in blue dotted line). A one-tailed p value is shown. See also [Figure S1](#) and [Table S1](#).

strategy that includes duplicates, but controls for PCR repeats by analyzing 5 to 6 independent mouse replicates for each experiment and then averaging mutation frequency of each nucleotide across replicates. In addition, comparing the mutation pattern of sequences in low to high strata allowed us to visualize hotspot emergence and ongoing accumulation and thus served as a surrogate SHM kinetic analysis. For ease of presentation, we present such “kinetic” analyses for productive and passenger alleles in three representative bins (Figure 2A). The stratification of sequences into narrower bins gives similar results and conclusions (Figure S2A, left).

Combined analyses of sequence reads revealed three robust hotspots in both productive and passenger VB1-8 alleles, including the two C nucleotides on opposite DNA strands of the AGCT motif in CDR3 (positions 454 and 455) and a C in an RGYW (AGCA) motif in CDR2 (position 337) (Figure S2B, top). These hotspots were apparent at low SHM levels (1–2 mutations/sequence) and further accumulated in sequences with intermediate (3–10 mutations/sequence) and high (11–30 mutations/sequence) SHM levels. In the latter, they were mutated in 40%–60% of sequences (Figure 2A). AGCT motifs in FWR1 and FW3, and certain RGYW motifs in CDR2 and CDR3, were lower level hotspots in both productive and passenger alleles, which was evident at intermediate mutation levels and more so in highly mutated sequences, reaching mutation in 20%–40% of sequences (Figure 2A). Within all productive and passenger sequences with high SHM levels, AGCT and RGYW motifs contributed the most residues with mutations well above background; those above background in non-RGYW motifs tended to occur adjacent to CDRs, where they may have, in part, resulted from SHM spreading from initiating G/C base pairs (bp) (Figure 2A). Finally, the SHM frequency at each base pair of the productive allele was highly correlated with that of the passenger allele at each strata (Pearson correlation, $r = 0.75\text{--}0.87$) (Figure S2C). Overall, these findings support a “hierarchical” SHM process by which mutations are targeted preferentially to a few preferred CDR hotspot motifs, followed by accumulation of mutations in other AID target motifs sites and eventually in non-RGYW sequences that in part represent SHM spreading to other sites.

Peyer's Patches GC B Cells Contain Highly Mutated, but Unselected, BCR Repertoire

We also examined the VB1-8 productive and passenger alleles in purified PP GC B cells from the same short-term immunized chimeras described above. Again, productive and passenger VB1-8 alleles in PP GC B cells of a given chimera had very similar overall SHM levels (Figures 1B, middle; Figure S1F, left). A major difference between SHM of productive and passenger VB1-8 sequences between splenic and PP GC B cells was that the frequency of SHMs on each was substantially higher in PP GC B cells than in splenic B cells (Figure 1B, bottom). PP GC B cells also had a significantly greater percentage of highly mutated sequences (>20 mutations per sequence) than did splenic GC B cells (Figure S1F, right). Notably, despite having accumulated higher levels of SHMs, PP GC B cells exhibited very similar SHM patterns to those of splenic GC B cells on both productive and passenger alleles (Figures 2B and S2A, right; Figure S2B, bottom). In particular, productive and passenger alleles in PP

GC B cells had the same major and lower level hotspots (Figure 2B) with the only minor difference being a slight dampening of the more major hotspot levels on passenger versus productive allele sequences (Figure 2B), which may reflect loss of some via AID-initiated deletions (see below). Nevertheless, in PP GC B cells there were high correlations between the mutation frequencies at each base pair across each strata when comparing productive alleles to the passenger alleles (Pearson correlation, $r = 0.71\text{--}0.85$) (Figure S2D), or when comparing the productive allele on PP GC B cells to the productive allele in splenic GC B cells (Pearson correlation, $r = 0.80\text{--}0.90$) (Figure S2E). Thus, in both splenic and PP GC B cells, SHM patterns reflect preferred sites of AID activity on the VB1-8 sequence rather than selection for a specific response. PP GC B cells of four unimmunized mice showed similar hotspots and highly correlated SHM profiles (Figures S1C, S2F, and S2G). These findings suggest that the BCR repertoire of PP GC B cells may reflect SHM activity on a germline V(D)J repertoire in the absence of antigen selection.

Regions that Are Highly Targeted for SHM Are Also Highly Targeted for DSBs

We found deletions on average in about 8% of splenic and 19% of PP GC B cell mutated passenger allele sequences, but only in about 2% of the corresponding productive sequences (Figures 3A and 3B; Table S2A). Given that VB1-8 passenger and productive alleles accumulated SHMs similarly, the relative absence of deletions in productive alleles likely represents negative cellular selection against B cells with BCR-inactivating deletions. We also did similar analysis of unique (excluding duplicates) sequences and reached the same conclusions (Figures S3A and S3B; Table S2B). For both splenic and PP GC passenger VB1-8 sequences, deletion frequency was directly related to SHM frequency as sequences with higher levels of mutations had higher levels of deletions (Figures S3C and S3D). In this regard, many unique deletions in passenger VB1-8 alleles (Figures 3C and 3D) (and productive alleles; Figures S3E and S3F) had endpoints that occurred in and around VB1-8 CDR sequences, the sites that harbor the highest SHM levels (Figure 2). The location of deletions endpoints versus SHMs along VB1-8 passenger sequences was highly correlated for both splenic GC B cell sequences (Figure 3E) and PP GC B cell sequences (Figure 3F). Thus, AID targeting for SHMs in VB1-8 frequently generated DSBs that were the precursors for deletions. Finally, we found very low levels of insertions in the assayed VB1-8 productive and passenger allele sequences (Figures S3G and S3H).

Non-Ig Sequences Target as Robust SHM as V Exons

To address the question of whether high-level SHM targeting is unique to V exon CDR sequences, we assayed SHM activity on two non-Ig passenger allele substrates, an *Escherichia coli* *gpt* gene (Figures 4 and S4) and a human β -*globin* gene (Figures 5 and S5), and compared SHM frequency on each passenger to that of its corresponding productive VB1-8 allele. These non-Ig sequence passengers were matched to the VB1-8 sequence in size (360 bp) and also contained similar densities of AID-targeting motifs (23 RGYWs in the *gpt* sequence and 30 RGYWs in the β -*globin* sequence, compared to 31 RGYWs in the VB1-8 sequence). Both bacterial *gpt* and β -*globin* passengers undergo

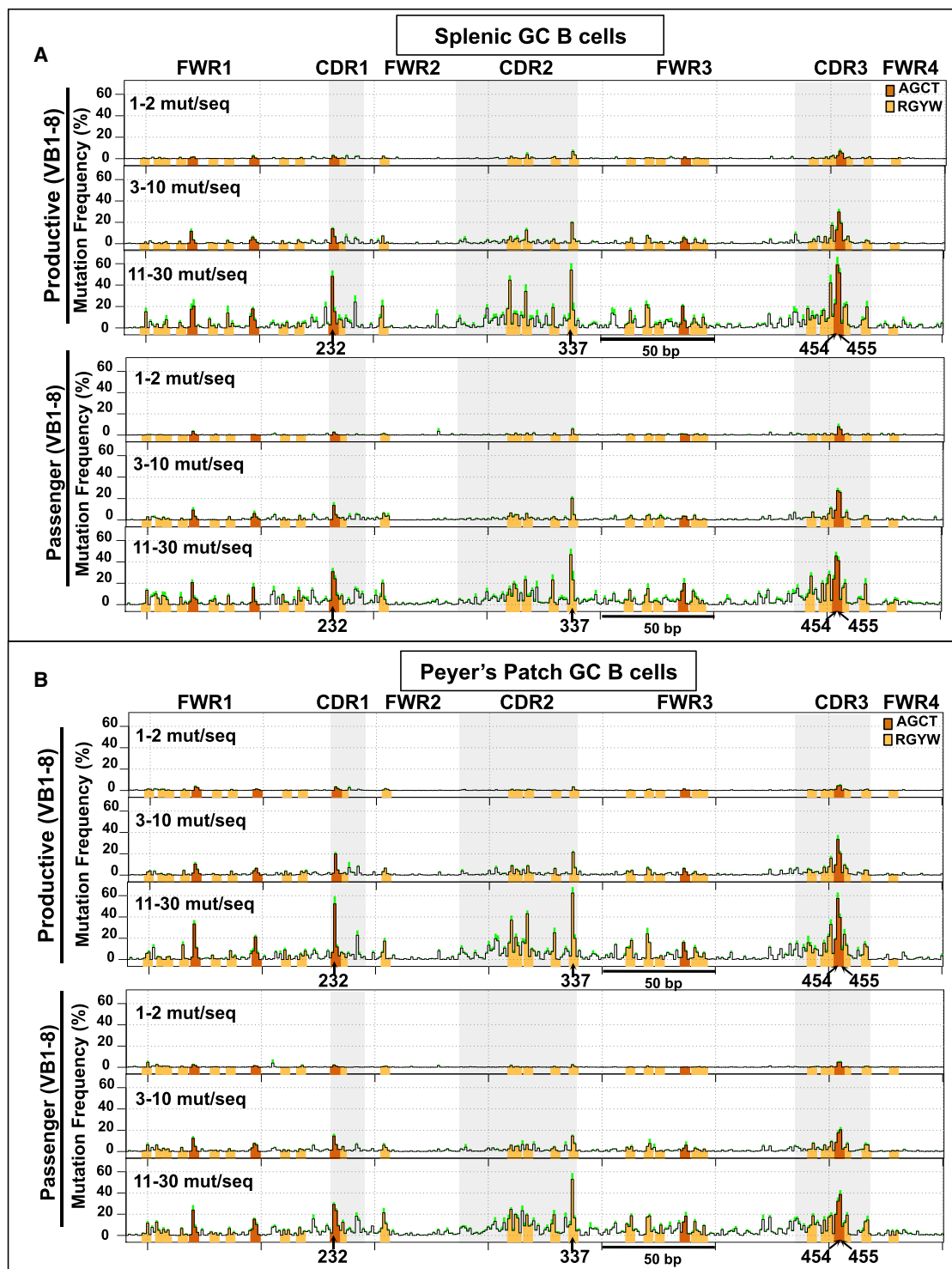


Figure 2. SHM Profiles of VB1-8 Productive and Passenger Alleles

(A and B) Map of mutations (SHM profile) on the VB1-8 productive and passenger allele sequences in (A) splenic and (B) PP GC B cells. The y axis indicates the mutation frequency at each nucleotide plotted as the mean percent of sequences in the indicated strata that contain a mutation at the indicated nucleotide \pm SEM (green shading indicates top error bar) from six independent mice. Orange and yellow bars mark the positions of AGCT and other RGYW motifs, respectively. See also Figure S2.

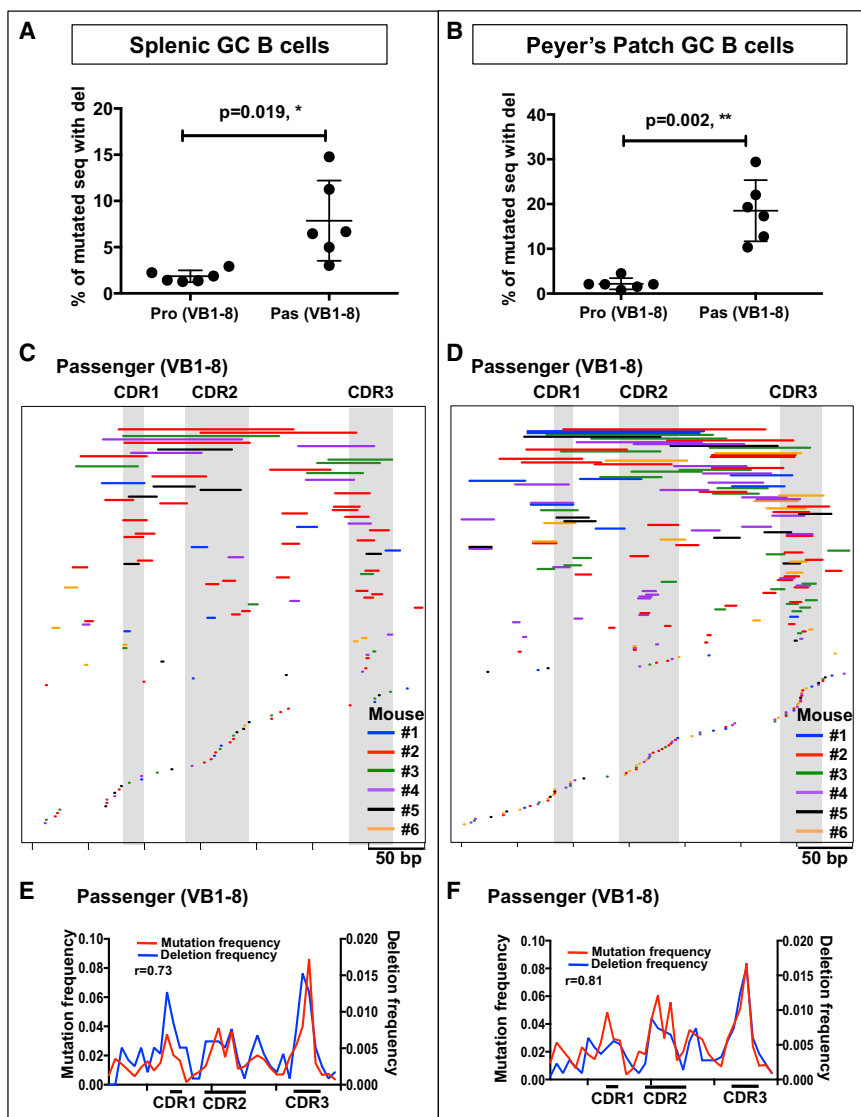


Figure 3. Deletions in VB1-8 Passenger Allele

(A and B) Deletion frequency, calculated as the percent of all mutated sequences that contain deletions of VB1-8-productive and passenger alleles in (A) splenic and (B) PP GC B cells. Data are represented as mean \pm SD from six mice. Two-tailed, paired t test p values are indicated.

(C and D) Map of unique deletions in VB1-8 passenger allele from (C) splenic and (D) PP GC B cells. Deletions are represented by lines whose start and end indicate the start and end of the deletion. Deletions from each of the six mice are displayed with a line of a different color.

(E and F) The location of SHMs compared to the location of deletion endpoints. The Pearson correlation coefficient (r) between SHM frequency and deletion (endpoint) frequency of each bin in (E) splenic and (F) PP GC B cells is indicated.

See also Figure S3 and Table S2.

strata (Figures S4D, S4E, S5D, and S5E). As for VB1-8 passengers, SHM patterns in splenic GC B cells and PP GC B cell sequence were very similar, despite the latter accumulating higher levels of mutations (Figures 4C, 4D, 5C, 5D, S4D, S4E, S5D, and S5E). Also, like the VB1-8 passenger, *gpt* and β -globin passenger sequences underwent substantial levels of deletions (Figures S4F, S4G, S5F, and S5G), with endpoints highly correlated with the location of SHMs (Figures S4H, S4I, S5H, and S5I).

SHM Profile of S Regions in GC B Cells

Analyses of SHM patterns of core mouse S regions have been hindered by their highly repetitive sequence (Rouaud et al., 2013). We circumvented this limita-

tion by using a 756-bp truncation of S_{μ} , which includes 426 bp of the S_{μ} core as a passenger, in both direct and inverted orientations ("c S_{μ} " and "in S_{μ} ," respectively; Figure 6A). For analyses, the c S_{μ} and in S_{μ} passengers were sequenced by Sanger method, since we could not optimize high-throughput sequencing through these highly repetitive sequences. Given the more limited number of reads obtained by this approach, we focused on SHM patterns, by pooling reads from six mice and plotting for unique sequences the total number of mutations at each base pair. For both c S_{μ} and in S_{μ} passengers, each of the densely packed S region AGCT motifs are SHM hotspots in both PP GC B cells (Figures 6B, S6A, and S6B) and splenic GC B cells (Figure S6C). The symmetrical AID targeting of SHMs of cytidines within AGCT palindromes in both transcriptional directions likely facilitates S region DSBs as proposed (Di Noia and Neuberger, 2007). Further supporting the importance of the AGCTs to DSB formation, the great majority of deletions in passenger c S_{μ} and in S_{μ} sequences map to regions

of AGCTs (Figures 6C, 6D, S6C, and S6D). In addition, the distribution of SHMs in the S region of the productive V(D)J allele was very similar to that of the passenger c S_{μ} and in S_{μ} sequences (Figures 6E, 6F, S6E, and S6F). The distribution of SHMs in the S region of the productive V(D)J allele was very similar to that of the passenger c S_{μ} and in S_{μ} sequences (Figures 6E, 6F, S6E, and S6F). The distribution of SHMs in the S region of the productive V(D)J allele was very similar to that of the passenger c S_{μ} and in S_{μ} sequences (Figures 6E, 6F, S6E, and S6F).

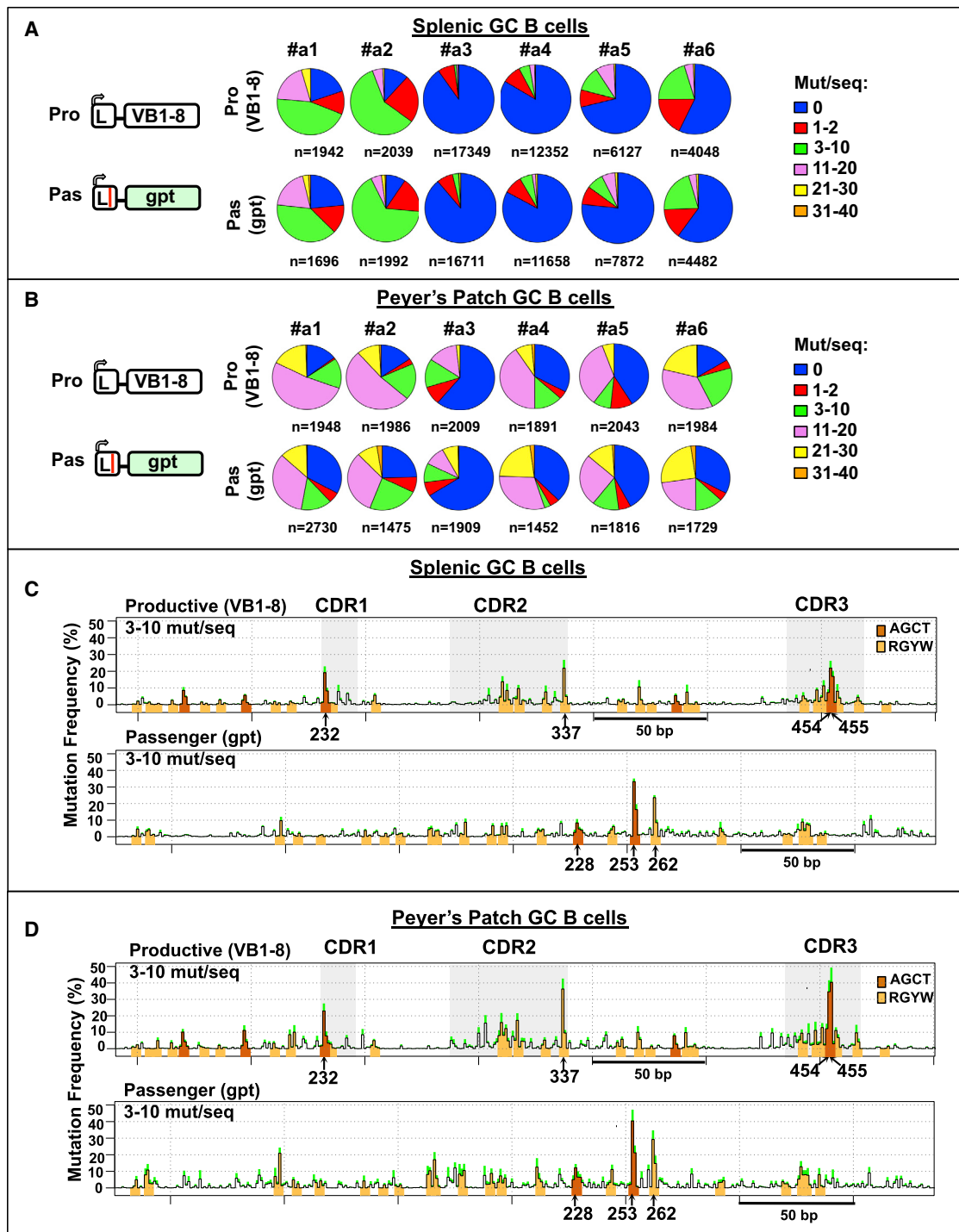


Figure 4. *E. coli* gpt Sequence Mutates as Frequently as VB1-8 Sequence

(A and B) Left: schematic of productive VB1-8 and passenger gpt alleles. Middle: pie charts showing the proportion of sequences that have the indicated (see legend, right) number of mutations per sequence in productive VB1-8 and passenger gpt allele from (A) splenic and (B) PP GC B cells of six independent mice. (C and D) SHM profiles of productive VB1-8 and passenger gpt allele from (C) splenic and (D) PP GC B cells from six mice. The y axis and other details are as described for Figure 2. Data from mutation strata 3–10 mutation/sequence are shown.

See also Figure S4.

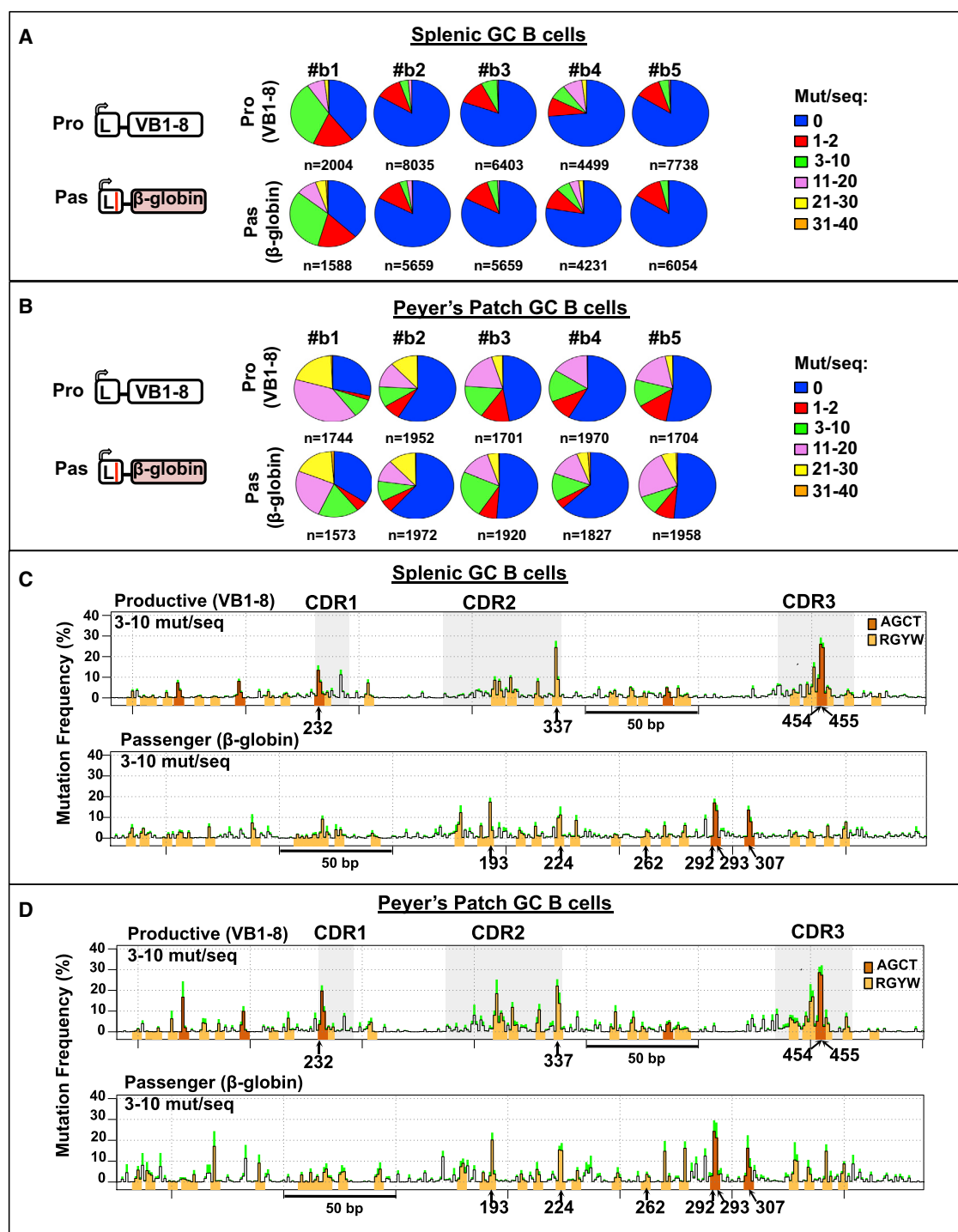


Figure 5. Human β -globin Sequence Mutates as Frequently as VB1-8 Sequence

(A and B) Left: schematic of productive VB1-8 and passenger β -globin alleles. Middle: pie charts showing the proportion of sequences that have the indicated (see legend, right) number of mutations per sequence in productive VB1-8 and passenger β -globin allele from (A) splenic and (B) PP GC B cells of five independent mice.

(C and D) SHM profiles of productive VB1-8 and passenger β -globin allele from (C) splenic and (D) PP GC B cells from five mice. The y axis and other details are as described for Figure 2. Data from mutation strata 3-10 mutation/sequence are shown.

See also Figure S5.

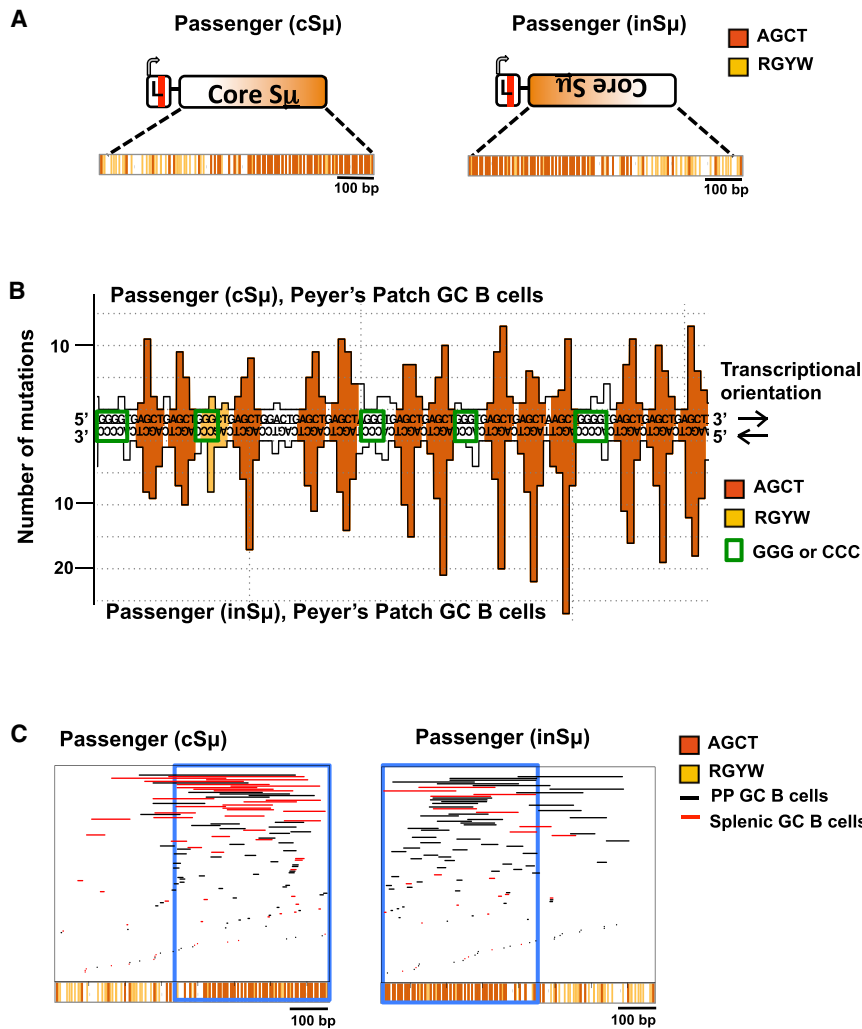


Figure 6. SHM Profiles and Deletion Maps of Switch Regions

(A) Schematic of passenger core $S\mu$ ($c\mu$) (left) and inverted $S\mu$ ($in\mu$) (right) alleles.

(B) Excerpt of SHM pattern of $c\mu$ (top) and $in\mu$ (bottom) passengers from PP GC B cells. The y axis indicates the total number of mutations. The green open boxes show the positions of G-stretches and C-stretches on $c\mu$ and $in\mu$ alleles, respectively.

(C) Location of unique deletions in passenger $c\mu$ (left) and $in\mu$ alleles (right). Deletions from splenic GC B cells are depicted with red lines and from PP GC B cells with black lines. For (B) and (C), the data are pooled from six mice. See also Figure S6.

of high AGCT density which occur on opposite ends of the $c\mu$ and $in\mu$ passenger sequences (Figures 6C, S6D, and S6E). Finally, intervening G/C-rich stretches between AGCT hotspots are rarely SHM targets in the passenger sequences (Figures 6B and S6C). As these G/C stretches are highly conserved in mammalian S regions, our findings suggest that they may provide functions other than serving as targets for AID-initiated lesions.

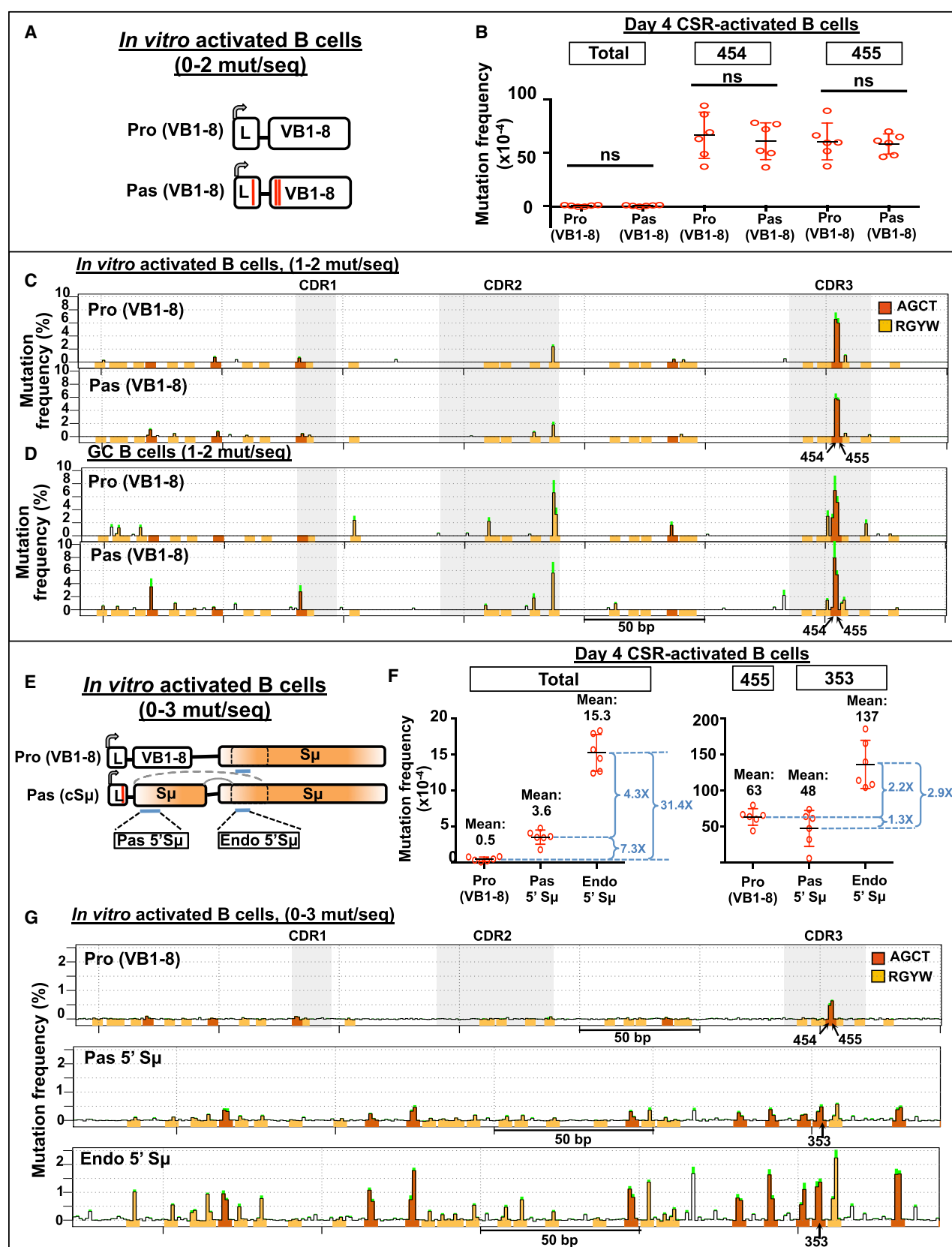
SHM of V Region in B Cells Activated in Culture

While S regions are AID targets in both GC and CSR-activated B cells in culture, V exons reportedly are targeted by AID only in GC B cells (Storb, 2014; Nagaoka et al., 2002; Maul et al., 2014), leading to the lingering question of how AID is targeted to S regions, but not adjacent IgH V exons, given that both are transcribed (Storb, 2014). We re-evaluated this notion, now with the insight that SHMs of VB1-8 in GC B cell sequences with low SHM levels concentrate in two CDR3 AGCT hotspots (positions 454 and 455). Consistent with prior findings, SHM along the length of productive and passenger VB1-8 sequences is close to assay background in B cells stimulated in culture for 4 days with

α CD40 plus IL-4 to induce CSR to $S\gamma 1$ and $S\epsilon$ (Figures 7A, 7B, and S7A–S7C). However, examination of SHM at VB1-8 hotspot nucleotides 454 and 455 of productive and passenger VB1-8 alleles in CSR-activated B cells reveals that they undergo readily detectable and similar levels of SHM (Figure 7B) and deletions (Figures S7D–S7H). Indeed, comparison of SHM profiles of productive and passenger VB1-8 alleles of CSR-activated B cells with those of GC B cell sequences with similarly low SHM levels (1–2 mutations/sequence), reveals highly similar profiles and extent of hotspot nucleotide 454 and 455 mutation (Figures 7C and 7D).

To compare mutation frequencies of hotspots in VB1-8 to those in S regions, we assayed day 4 CSR-activated B cells

that harbored a productive VB1-8 and a passenger $S\mu$. For these analyses, we sequenced a portion of passenger $c\mu$ amenable to high-throughput analysis ("Pas 5' $S\mu$ ") and also the same portion of the endogenous $S\mu$ ("Endo 5' $S\mu$ ") (Figure 7E). The overall mutation frequency of the Pas 5' $S\mu$ was much greater (more than 7-fold) than that of the productive VB1-8 exon (Figures 7F, left; Figures S7I–S7K). However, comparison of the SHM level of VB1-8 nucleotide 455 to that of a representative S region AGCT hotspot at nucleotide 353 revealed them to be quite similar (Figure 7F, right). Thus, the increased frequency of overall SHM of Pas 5' $S\mu$ compared to that of VB1-8 is generated by the much larger number of AGCT (and related) hotspots in Pas 5' $S\mu$, rather than increased AID-activity at a given hotspot (Figure 7G). Notably, the endogenous 5' $S\mu$ sequence undergoes SHM at AGCT hotspots at somewhat increased levels (approximately 3-fold) compared to that of AGCT motifs in the Pas 5' $S\mu$ (Figure 7F, right; Figure 7G). This increase could result from different transcriptional promoters and/or effects of having an adjacent full-length S region that could influence AID recruitment via transcription-associated mechanisms and/or by promoting longer stable R loops that increase AID access. Finally, $c\mu$



(legend on next page)

passenger sequences undergo internal deletions (Figures S7L–S7P) and support robust CSR-like events to Se in about 20% of the day 4 activated B cells (Figures S7Q and S7R). As Sanger sequencing in GC B cells indicated that SHM frequency 5' S μ AGCT hotspots were similar to that of such hotspots across core S μ (Figure S6A), we concluded that relatively low SHM levels of individual AGCT motifs in cS μ collectively are sufficient to drive CSR.

DISCUSSION

We describe a rapid passenger allele approach to test intrinsic capacity and preferences of AID to induce SHMs and DSBs within test sequences that replace a non-productive IgH V exon. A key feature of the approach is lack of cellular selection for or against mutations and deletions, enabling insights into roles of substrate sequences in AID-targeting. In this regard, the assay uses short immunization protocols that do not activate affinity maturation; thus, SHM patterns on identical productive and passenger V exon sequences in GC B cells are remarkably similar, both in extent and detail. This assay feature allows use of the same productive allele to standardize overall SHM experienced by different passengers in different experiments. Additional assay innovations include retaining all recovered sequences for analysis and relying on multiple biological replicates to validate conclusions, allowing detection of AID hotspots even at low overall SHM levels, such as those early in an immune response or the previously unappreciated V exon SHMs in cultured CSR-activated B cells. Also, by dividing recovered sequences into mutational strata, we can estimate relative mutational kinetics at which SHMs of a particular nucleotide appear, revealing early and late hotspots, as well as “spreading” of SHMs from CDR hotspots to adjacent regions. This overall approach allowed us to address long-standing questions in the SHM and CSR field (see below). Finally, many of these powerful assay features could be extended to dissect contributions of sequence-intrinsic AID targeting to affinity maturation and antibody responses by using an antigen-specific productive V(D)J exon and a matched passenger V(D)J exons in the context of longer term immunizations.

Mechanisms that Target SHM Activity

We addressed the long-standing question of whether V exon sequences are required to recruit high-level SHM activity. Our

studies reveal that single-copy bacterial *gpt* and human β -*globin* sequences in the endogenous V exon location have overall SHM frequencies similar to V exons and that some of their AID target motifs mutate at similar frequencies as the same motifs in V exon CDR sequences. These findings prove that high level SHM targeting in GC B cells is not specific to V exons, or even CDR sequences; establishing definitively that the V exon location is privileged for SHM. Mechanisms that make V exon location privileged for AID targeting may involve linked enhancers (Odegard and Schatz, 2006; Buerstedde et al., 2014; Rouaud et al., 2013), adjacent AID recruitment motifs (Storb, 2014), or transcriptional-related mechanisms, such as convergent sense/antisense transcription (Meng et al., 2014). SHM versus CSR specific AID-targeting factors were hypothesized based on the notion that V exons do not undergo SHM in CSR-activated B cells (Muramatsu et al., 2007); however, our finding that V exons are targeted for SHM in CSR-activated B cells obviates a strict requirement for such factors (see below).

It has generally been thought that CDRs are highly evolved to target high SHM levels (e.g., Wei et al., 2015). Consistent with this notion, AGCT or AGCA motifs in the V(D)J exon CDRs are hotspots, while the same motifs in FWRs are not (Figure 2). However, we found similar examples in the bacterial *gpt* sequence, where one AGCT (position 253) was as strong a hotspot as those in VB1-8 CDRs, while another was not (position 228) (Figures 4C and 4D). Likewise, in the β -*globin* sequence, AACC at position 193 was a major hotspot, but the identical motif at position 262 was not (Figures 5C and 5D). Thus, the elements that can enhance SHM at CDRs and/or suppress SHM at FWRs are not specialized to V exons or to CDR sequences. Such relatively recurrent hotspot sequence combinations are likely evolutionarily selected for in CDRs and against in FWRs. In ongoing studies, we are using the passenger system to test additional sequence combinations flanking AGCT hotspots within otherwise randomized synthetic sequences to ultimately elucidate sequences that define an AID hotspot in the V exon location.

SHMs and DSBs Are Targeted by the Same Mechanism

We now show that deletions occur frequently on highly mutated V(D)J exons as part of a normal SHM process. In this regard, we demonstrate a clear and direct relationship between SHM activity and DSB activity on a V exon, with the highest density and the majority of deletion endpoints focused at locations of highest level SHM (e.g., at AGCTs within CDR sequences). In addition,

Figure 7. SHM of the V Exon and S Region in B Cells Activated in Culture

- (A) Naive B cells of VB1-8 passenger mice were stimulated in culture for 4 days with α CD40 and IL4.
- (B) Mutation frequency of total nucleotides, nucleotide 454 and 455 of VB1-8 productive and passenger alleles at day 4. All sequences that have 0–2 mutations per sequence were included in the analysis. An unpaired t test was performed.
- (C and D) SHM profiles of matched VB1-8-productive and passenger alleles in sequences that contain 1–2 mutations/sequence from (C) day 4 CSR-activated B cells and (D) splenic GC B cells shown in Figure 2A. Peaks that have a SD greater than the mean were excluded.
- (E) Naive B cells of cS μ passenger mice were stimulated in culture for 4 days with α CD40 and IL4. The 5' region immediately upstream of the core in passenger S μ (Pas 5' S μ) and endogenous S μ (Endo 5' S μ), indicated in blue lines, was analyzed.
- (F) Mutation frequency over the entire indicated allele/region (left) and at individual nucleotides indicated (right). All sequences that have 0–3 mutations/sequence were included in the analysis. The mean values and fold change between each mean are indicated.
- (G) SHM profiles of VB1-8-productive allele, Pas 5' S μ , and Endo 5' S μ of data shown in (F). For (B) and (F), data represent mean \pm SD of six independent stimulations of cells from six independent mice. For (C), (D), and (G), data represent mean frequency \pm SEM of six independent mice. The y axis and other details are as described for Figure 2. For (B), (C), (F), and (G), data shown are mutation frequency at day 4 after subtraction of mutation frequency at day 0. See also Figure S7.

we found that this same relationship holds for non-Ig passenger sequences. Taken together, our findings reveal that DSB generation within V(D)J exons is a common and normal outcome of SHM activity. These findings answer a long-standing question in the vaccine field regarding how bnAbs with Ig chains encoded by V exons harboring deletions arise by showing that specialized mechanisms are not necessary. Our findings that highly mutated PP GC B cells contain abundant V exon deletions offers the potential of developing new strategies to elicit such antibodies (see below).

Features that Optimize S Region Sequences for CSR

By using a passenger S_{μ} region, we are able to view in-depth the SHM and DSB (deletion) pattern of core S regions. Mammalian S_{μ} contained large numbers of densely packed repeats closely related to the sequence GGGGTGAGCT. Strikingly, within such core S_{μ} repeats, Cs on both strands of the canonical AGCT hotspot duplexes were robustly targeted in both transcriptional orientations in GC B cells. In this regard, DSBs/deletions in passenger core S_{μ} were highly enriched in regions of high AGCT density, independent of transcriptional orientation, providing direct support for the model that the high density of these palindromic targets allows generation of closely spaced AID-initiated lesions on both strands that then promote DSBs (Di Noia and Neuberger, 2007). Notably, however, we found little or no targeting of Cs in S_{μ} passengers that occurred opposite the conserved template strand S_{μ} repeat G-stretches, even if S_{μ} transcriptional orientation was reversed. This latter finding is consistent with adjunct functions, perhaps in AID recruitment via R-loops (Shinkura et al., 2003), RNA-mediated mechanisms (Zheng et al., 2015), and/or potential roles in S region synapsis (Maizels and Gray, 2013).

Prior studies concluded that V exons are not SHM targets in B cell activated in culture. Consistent with this notion, we found the passenger S_{μ} had an approximately 7-fold greater overall mutation frequency than the V exon in CSR-activated B cells. However, AGCT hotspot motifs in V exons and S region passengers were targeted at similar levels in these cells with the increased overall SHM frequency of the S region passenger reflecting a greater number of AGCT hotspots. Indeed, endogenous S_{μ} region AGCT motifs are targeted only about 2-fold more frequently than AGCT hotspots in passenger V exons. Notably, the pattern and extent of V exon hotspot mutations in CSR-activated B cells was similar to that of GC B cells early in the process of SHM accumulation. Thus, we suggest that SHM is limited in CSR-activated B cells because they have not been exposed to sufficient AID-activity, due to AID levels, length of exposure, or both. Still, S_{μ} passengers, while having similarly low-level SHM at AID hotspot motifs as GC B cells early in the process, were targeted for sufficient DSBs to promote relatively robust joining to downstream S region sequences in a CSR-like process. Thus, the great abundance of palindromic AGCT hotspots make S regions highly sensitive substrates for generating CSR-initiating DSBs at relatively low-level AID exposure. Accordingly, the limited number of highly targeted AGCT motifs in the V exon results in fewer deletions/DSBs in the V exon compared to the S region. Based on our findings, we propose that ability of S regions to undergo DSBs with limited AID exposure evolved to allow efficient IgH

CSR, without generating substantial SHM of adjacent V exons that could affect antibody affinity or specificity.

Implications for Generation of Highly Mutated Antibodies during an Immune Response

Microbial antigens promote formation of PP GCs and IgL V exon SHM without immunization (González-Fernández and Milstein, 1993) and even in the absence of antigen recognition via IgH or IgL chains in the context of a BCR (Casola et al., 2004). The latter studies led to the hypothesis that chronic activation of PP GC B cells expands primary V(D)J recombination-generated antibody repertoires via extensive SHM in the absence of antigenic engagement of BCR (Casola et al., 2004). Our studies support this hypothesis by showing that productive and passenger IgH VB1-8 alleles in PP GC B cells undergo similarly high levels and specific patterns of SHMs, with the same set of major hotspots that reflect preferred AID SHM targets. Indeed, under short-term immunization conditions, SHM patterns of VB1-8 productive and passenger sequences were highly similar between splenic and PP GC B cells. Moreover, each Ig or non-Ig passenger, respectively, had similar SHM and deletion patterns in splenic versus PP GC B cells, except that levels were higher in the latter. Notably, primary hotspots in PP GC B cell productive and passenger alleles become saturated at high SHM levels, with additional SHMs accumulating in secondary hotspots or non-hotspot regions, allowing further diversification that might be enhanced by primary hotspot saturation. While our current studies do not assay for theoretical contributions of endogenous IgL chains, they clearly show that PP GC B cells harbor a diverse IgH VB1-8 repertoire via high-level SHM in the absence of obvious selection. This process could generate B cell lineages that provide V exons with high levels of mutations and deletions as substrates for further mutation and selection via antigen-specific responses, providing greater diversity for additional mutational and selective forces. Our findings, coupled with prior findings (Casola et al., 2004), raise the possibility of tapping the highly mutated PP GC B cell antibody reservoir as an approach to elicit anti-HIV1 bnAbs or other antibodies with abundant SHMs and/or deletions.

EXPERIMENTAL PROCEDURES

Generation of Targeted ES Cells

An ES cell line containing a VB1-8-productive allele (Sonoda et al., 1997) and a puromycin cassette in place of the V(D)J exon on the other allele was generated. ES cell lines containing passenger alleles were generated by replacing the puromycin cassette with the respective passenger sequences (see the *Supplemental Experimental Procedures* for details). Chimeric mice were generated by RAG-2 blastocyst complementation (Chen et al., 1993).

Assays for SHM

GC B cells from spleen and PP were collected from 8- to 12-week-old mice immunized with NP-CGG (N-5055A; Biosearch Technologies) for 10 days. GC B cells were isolated from PPs and spleens of chimeras by flow cytometry sorting of cells that are B220+ and Peanut Agglutinin (PNA) hi. B220+ PNA lo cells were also collected during each sort and (along with ES cell DNA) served as negative controls for SHM. For SHM analysis of CSR-activated B cells *in vitro*, naive B cells collected from the spleen of 6- to 8-week-old mice were stimulated with α CD40 and IL4 for 4 days (see the *Supplemental Experimental Procedures* for details).

PCR and Sequencing

The productive and passenger alleles were amplified in separate PCR reactions using allele-specific primers. The products were sequenced by 2 × 250 bp Illumina MiSeq high-throughput sequencing (Illumina) or Sanger sequencing systems, where indicated in the text. For Illumina high-throughput sequencing, sequencing adapters and barcodes were added to the end of DNA fragments by a second round of PCR (see the *Supplemental Experimental Procedures* for details).

Data Analysis

A custom pipeline was used to process the sequencing data and to call mutations. To compare the location of deletion endpoints versus SHMs along passenger sequences, we measured the frequency of each within 10-bp bins and calculated the Pearson correlation (*r*) between deletion endpoint frequency and mutation frequency (see the *Supplemental Experimental Procedures* for details). Statistical analysis is as stated in the figure legends.

ACCESSION NUMBERS

The accession number for the next-generation sequencing data reported in this paper has been uploaded to the NCBI Sequence Read Archive: SRP061422.

SUPPLEMENTAL INFORMATION

Supplemental Information includes Supplemental Experimental Procedures, seven figures, and two tables and can be found with this article online at <http://dx.doi.org/10.1016/j.cell.2015.10.042>.

AUTHOR CONTRIBUTIONS

L.S.Y., J.K.H., J.H.W., and F.W.A. designed the study. L.S.Y., J.K.H., F.-L.M., A.J., M.L., V.M., and J.H.W. performed the experiments. Z.D. and R.M.M. performed bioinformatics analyses, and R.M.M. designed the SHM pipeline. L.S.Y., J.K.H., J.H.W., Z.D., and F.W.A. analyzed and interpreted the data. D.N. and T.B.K. advised on statistical analysis and various other aspects of data analysis. L.S.Y., J.K.H., Z.D., R.M.M., and F.W.A. designed the figures. L.S.Y., J.K.H., and F.W.A. drafted the manuscript, and L.S.Y., J.K.H., Z.D., R.M.M., T.B.K., J.H.W., and F.W.A. polished the manuscript.

ACKNOWLEDGMENTS

The authors thank Dr. Kefei Yu for the RMCE exchange plasmid, Klaus Rajewsky for the J_H targeting construct, Pei-Yi Huang and Yuko Fujiwara for generating the chimeras, Kenneth Ketman and Natasha Barteneva for help with FACS sorting, and Garnett Kelsoe for helpful discussions. This work was supported by NIH grants (R01AI077595 and CHAVI-ID 5UM1AI100645 to F.W.A.; R21AI110777-01A1, R21CA184707-01A1, and R01CA166325-01A1 to J.H.W.). J.K.H. was supported by an NIH grant (F30AI114179-01A1). D.N. is supported by a Dana Farber/Harvard Cancer Center Core Grant (5P30 CA06516). J.H.W. is also supported by a Boettcher Foundation Webb-Waring Biomedical Research Award, an American Society of Hematology Scholar Award, and the Cancer League of Colorado. F.W.A. is an investigator and Z.D. is a postdoctoral fellow of the Howard Hughes Medical Institute. L.S.Y. was a Cancer Research Institute postdoctoral fellow, and F.-L.M. is a Lymphoma Research Foundation postdoctoral fellow.

Received: July 21, 2015

Revised: September 1, 2015

Accepted: October 13, 2015

Published: November 12, 2015

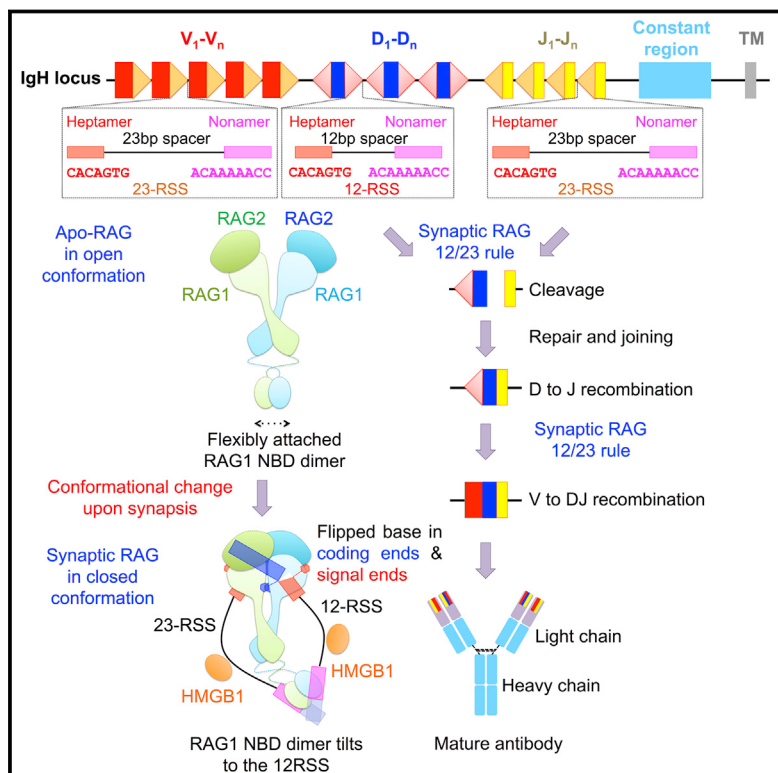
REFERENCES

- Alt, F.W., Zhang, Y., Meng, F.L., Guo, C., and Schwer, B. (2013). Mechanisms of programmed DNA lesions and genomic instability in the immune system. *Cell* 152, 417–429.
- Betz, A.G., Neuberger, M.S., and Milstein, C. (1993a). Discriminating intrinsic and antigen-selected mutational hotspots in immunoglobulin V genes. *Immunol. Today* 14, 405–411.
- Betz, A.G., Rada, C., Pannell, R., Milstein, C., and Neuberger, M.S. (1993b). Passenger transgenes reveal intrinsic specificity of the antibody hypermutation mechanism: clustering, polarity, and specific hot spots. *Proc. Natl. Acad. Sci. USA* 90, 2385–2388.
- Briney, B.S., Willis, J.R., and Crowe, J.E., Jr. (2012). Location and length distribution of somatic hypermutation-associated DNA insertions and deletions reveals regions of antibody structural plasticity. *Genes Immun.* 13, 523–529.
- Bross, L., Fukita, Y., McBlane, F., Démolière, C., Rajewsky, K., and Jacobs, H. (2000). DNA double-strand breaks in immunoglobulin genes undergoing somatic hypermutation. *Immunity* 13, 589–597.
- Buerstedde, J.M., Alinikula, J., Arakawa, H., McDonald, J.J., and Schatz, D.G. (2014). Targeting of somatic hypermutation by immunoglobulin enhancer and enhancer-like sequences. *PLoS Biol.* 12, e1001831.
- Casola, S., Otipoby, K.L., Alimzhanov, M., Humme, S., Uttersprot, N., Kutok, J.L., Carroll, M.C., and Rajewsky, K. (2004). B cell receptor signal strength determines B cell fate. *Nat. Immunol.* 5, 317–327.
- Chahwan, R., Edelmann, W., Scharff, M.D., and Roa, S. (2012). AIDing antibody diversity by error-prone mismatch repair. *Semin. Immunol.* 24, 293–300.
- Chen, J., Lansford, R., Stewart, V., Young, F., and Alt, F.W. (1993). RAG-2-deficient blastocyst complementation: an assay of gene function in lymphocyte development. *Proc. Natl. Acad. Sci. USA* 90, 4528–4532.
- Di Noia, J.M., and Neuberger, M.S. (2007). Molecular mechanisms of antibody somatic hypermutation. *Annu. Rev. Biochem.* 76, 1–22.
- Dörner, T., Brezinschek, H.P., Brezinschek, R.I., Foster, S.J., Domiaty-Saad, R., and Lipsky, P.E. (1997). Analysis of the frequency and pattern of somatic mutations within nonproductively rearranged human variable heavy chain genes. *J. Immunol.* 158, 2779–2789.
- González-Fernández, A., and Milstein, C. (1993). Analysis of somatic hypermutation in mouse Peyer's patches using immunoglobulin κ light-chain transgenes. *Proc. Natl. Acad. Sci. USA* 90, 9862–9866.
- Goossens, T., Klein, U., and Küppers, R. (1998). Frequent occurrence of deletions and duplications during somatic hypermutation: implications for oncogene translocations and heavy chain disease. *Proc. Natl. Acad. Sci. USA* 95, 2463–2468.
- Hackney, J.A., Misaghi, S., Senger, K., Garris, C., Sun, Y., Lorenzo, M.N., and Zarrin, A.A. (2009). DNA targets of AID evolutionary link between antibody somatic hypermutation and class switch recombination. *Adv. Immunol.* 101, 163–189.
- Han, L., Masani, S., and Yu, K. (2011). Overlapping activation-induced cytidine deaminase hotspot motifs in Ig class-switch recombination. *Proc. Natl. Acad. Sci. USA* 108, 11584–11589.
- Hwang, J.K., Alt, F.W., and Yeap, L.S. (2015). Related mechanisms of antibody somatic hypermutation and class switch recombination. *Microbiol. Spectr.* 3(1) <http://dx.doi.org/10.1128/microbiolspec.MDNA3-0037-2014>, MDNA3-0037-2014.
- Kepler, T.B., Liao, H.X., Alam, S.M., Bhaskarabhatla, R., Zhang, R., Yandava, C., Stewart, S., Anasti, K., Kelsoe, G., Parks, R., et al. (2014). Immunoglobulin gene insertions and deletions in the affinity maturation of HIV-1 broadly reactive neutralizing antibodies. *Cell Host Microbe* 16, 304–313.
- Lanning, D.K., and Knight, K.L. (2005). Intestinal bacteria and development of the antibody repertoire. *Discov. Med.* 5, 393–398.
- Liu, M., and Schatz, D.G. (2009). Balancing AID and DNA repair during somatic hypermutation. *Trends Immunol.* 30, 173–181.
- Maizels, N., and Gray, L.T. (2013). The G4 genome. *PLoS Genet.* 9, e1003468.
- Mascola, J.R., and Haynes, B.F. (2013). HIV-1 neutralizing antibodies: understanding nature's pathways. *Immunol. Rev.* 254, 225–244.
- Maul, R.W., and Gearhart, P.J. (2010a). AID and somatic hypermutation. *Adv. Immunol.* 105, 159–191.

- Maul, R.W., and Gearhart, P.J. (2010b). Controlling somatic hypermutation in immunoglobulin variable and switch regions. *Immunol. Res.* 47, 113–122.
- Maul, R.W., Cao, Z., Venkataraman, L., Giorgetti, C.A., Press, J.L., Denizot, Y., Du, H., Sen, R., and Gearhart, P.J. (2014). Spt5 accumulation at variable genes distinguishes somatic hypermutation in germinal center B cells from ex vivo-activated cells. *J. Exp. Med.* 211, 2297–2306.
- Meng, F.L., Du, Z., Federation, A., Hu, J., Wang, Q., Kieffer-Kwon, K.R., Meyers, R.M., Amor, C., Wasserman, C.R., Neuberg, D., et al. (2014). Convergent transcription at intragenic super-enhancers targets AID-initiated genomic instability. *Cell* 159, 1538–1548.
- Mostoslavsky, R., Alt, F.W., and Rajewsky, K. (2004). The lingering enigma of the allelic exclusion mechanism. *Cell* 118, 539–544.
- Muramatsu, M., Kinoshita, K., Fagarasan, S., Yamada, S., Shinkai, Y., and Honjo, T. (2000). Class switch recombination and hypermutation require activation-induced cytidine deaminase (AID), a potential RNA editing enzyme. *Cell* 102, 553–563.
- Muramatsu, M., Nagaoka, H., Shinkura, R., Begum, N.A., and Honjo, T. (2007). Discovery of activation-induced cytidine deaminase, the engraver of antibody memory. *Adv. Immunol.* 94, 1–36.
- Nagaoka, H., Muramatsu, M., Yamamura, N., Kinoshita, K., and Honjo, T. (2002). Activation-induced deaminase (AID)-directed hypermutation in the immunoglobulin Smu region: implication of AID involvement in a common step of class switch recombination and somatic hypermutation. *J. Exp. Med.* 195, 529–534.
- Odegard, V.H., and Schatz, D.G. (2006). Targeting of somatic hypermutation. *Nat. Rev. Immunol.* 6, 573–583.
- Peled, J.U., Kuang, F.L., Iglesias-Ussel, M.D., Roa, S., Kalis, S.L., Goodman, M.F., and Scharff, M.D. (2008). The biochemistry of somatic hypermutation. *Annu. Rev. Immunol.* 26, 481–511.
- Rada, C., Di Noia, J.M., and Neuberger, M.S. (2004). Mismatch recognition and uracil excision provide complementary paths to both Ig switching and the A/T-focused phase of somatic mutation. *Mol. Cell* 16, 163–171.
- Rouaud, P., Vincent-Fabert, C., Saintamand, A., Fiancette, R., Marquet, M., Robert, I., Reina-San-Martin, B., Pinaud, E., Cogné, M., and Denizot, Y. (2013). The IgH 3' regulatory region controls somatic hypermutation in germinal center B cells. *J. Exp. Med.* 210, 1501–1507.
- Saribasak, H., and Gearhart, P.J. (2012). Does DNA repair occur during somatic hypermutation? *Semin. Immunol.* 24, 287–292.
- Shinkura, R., Tian, M., Smith, M., Chua, K., Fujiwara, Y., and Alt, F.W. (2003). The influence of transcriptional orientation on endogenous switch region function. *Nat. Immunol.* 4, 435–441.
- Sonoda, E., Pewzner-Jung, Y., Schwers, S., Taki, S., Jung, S., Eilat, D., and Rajewsky, K. (1997). B cell development under the condition of allelic inclusion. *Immunity* 6, 225–233.
- Stavnezer, J., Guikema, J.E., and Schrader, C.E. (2008). Mechanism and regulation of class switch recombination. *Annu. Rev. Immunol.* 26, 261–292.
- Storb, U. (2014). Why does somatic hypermutation by AID require transcription of its target genes? *Adv. Immunol.* 122, 253–277.
- Victora, G.D., and Nussenzweig, M.C. (2012). Germinal centers. *Annu. Rev. Immunol.* 30, 429–457.
- Wei, L., Chahwan, R., Wang, S., Wang, X., Pham, P.T., Goodman, M.F., Bergman, A., Scharff, M.D., and MacCarthy, T. (2015). Overlapping hotspots in CDRs are critical sites for V region diversification. *Proc. Natl. Acad. Sci. USA* 112, E728–E737.
- Weiss, U., Zeebelein, R., and Rajewsky, K. (1992). Accumulation of somatic mutants in the B cell compartment after primary immunization with a T cell-dependent antigen. *Eur. J. Immunol.* 22, 511–517.
- Wesemann, D.R., Portuguese, A.J., Meyers, R.M., Gallagher, M.P., Cluff-Jones, K., Magee, J.M., Panchakshari, R.A., Rodig, S.J., Kepler, T.B., and Alt, F.W. (2013). Microbial colonization influences early B-lineage development in the gut lamina propria. *Nature* 507, 112–115.
- Wu, X., Zhou, T., Zhu, J., Zhang, B., Georgiev, I., Wang, C., Chen, X., Longo, N.S., Louder, M., McKee, K., et al.; NISC Comparative Sequencing Program (2011). Focused evolution of HIV-1 neutralizing antibodies revealed by structures and deep sequencing. *Science* 333, 1593–1602.
- Yang, S.Y., and Schatz, D.G. (2007). Targeting of AID-mediated sequence diversification by cis-acting determinants. *Adv. Immunol.* 94, 109–125.
- Yélamos, J., Klix, N., Goyenechea, B., Lozano, F., Chui, Y.L., González Fernández, A., Pannell, R., Neuberger, M.S., and Milstein, C. (1995). Targeting of non-Ig sequences in place of the V segment by somatic hypermutation. *Nature* 376, 225–229.
- Zarrin, A.A., Alt, F.W., Chaudhuri, J., Stokes, N., Kaushal, D., Du Pasquier, L., and Tian, M. (2004). An evolutionarily conserved target motif for immunoglobulin class-switch recombination. *Nat. Immunol.* 5, 1275–1281.
- Zheng, S., Vuong, B.Q., Vaidyanathan, B., Lin, J.Y., Huang, F.T., and Chaudhuri, J. (2015). Non-coding RNA generated following lariat debranching mediates targeting of AID to DNA. *Cell* 161, 762–773.

Molecular Mechanism of V(D)J Recombination from Synaptic RAG1-RAG2 Complex Structures

Graphical Abstract



Highlights

- Cryo-EM structures of synaptic RAG complexes reveal a closed dimer conformation
- RAG cooperatively recognizes the RSSs with base flipping in the nicked signal end
- Distortion and base flipping in coding end DNA facilitate hairpin formation
- Induced asymmetry and HMGB1-induced RSS bending underlie the 12/23 rule

Authors

Heng Ru, Melissa G. Chambers,
Tian-Min Fu, Alexander B. Tong,
Maofu Liao, Hao Wu

Correspondence

maofu_liao@hms.harvard.edu (M.L.),
wu@crystal.harvard.edu (H.W.)

In Brief

Cryo-EM structures of synaptic RAG complexes reveal a recombination signal sequence (RSS)-induced closed conformation that enables catalytic activation and explain the molecular basis for the 12/23 rule, a dogma in which 12-RSS and 23-RSS flanking the V, D, and J segments are synapsed.

Accession Numbers

3JBX
3JBY
3JBW

Molecular Mechanism of V(D)J Recombination from Synaptic RAG1-RAG2 Complex Structures

Heng Ru,^{1,2} Melissa G. Chambers,³ Tian-Min Fu,^{1,2} Alexander B. Tong,^{1,2} Maofu Liao,^{3,*} and Hao Wu^{1,2,*}

¹Department of Biological Chemistry and Molecular Pharmacology, Harvard Medical School, Boston, MA 02115, USA

²Program in Cellular and Molecular Medicine, Boston Children's Hospital, Boston, MA 02115, USA

³Department of Cell Biology, Harvard Medical School, Boston, MA 02115, USA

*Correspondence: maofu_liao@hms.harvard.edu (M.L.), wu@crystal.harvard.edu (H.W.)

<http://dx.doi.org/10.1016/j.cell.2015.10.055>

SUMMARY

Diverse repertoires of antigen-receptor genes that result from combinatorial splicing of coding segments by V(D)J recombination are hallmarks of vertebrate immunity. The (RAG1-RAG2)₂ recombinase (RAG) recognizes recombination signal sequences (RSSs) containing a heptamer, a spacer of 12 or 23 base pairs, and a nonamer (12-RSS or 23-RSS) and introduces precise breaks at RSS-coding segment junctions. RAG forms synaptic complexes only with one 12-RSS and one 23-RSS, a dogma known as the 12/23 rule that governs the recombination fidelity. We report cryo-electron microscopy structures of synaptic RAG complexes at up to 3.4 Å resolution, which reveal a closed conformation with base flipping and base-specific recognition of RSSs. Distortion at RSS-coding segment junctions and base flipping in coding segments uncover the two-metal-ion catalytic mechanism. Induced asymmetry involving tilting of the nonamer-binding domain dimer of RAG1 upon binding of HMGB1-bent 12-RSS or 23-RSS underlies the molecular mechanism for the 12/23 rule.

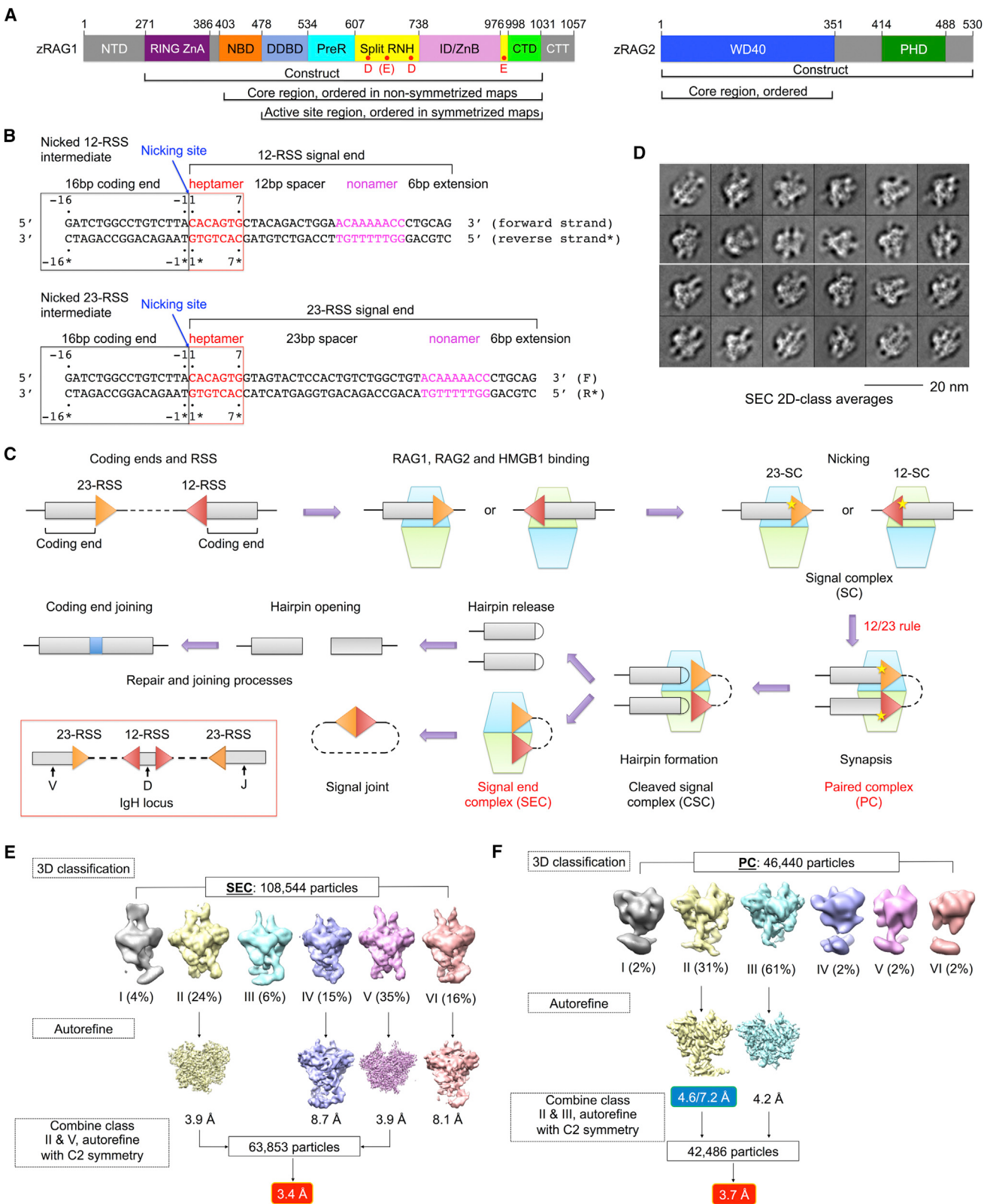
INTRODUCTION

For optimal host defense, jawed vertebrates have evolved an elegant combinatorial mechanism to generate large repertoires of antibody and antigen-receptor genes. The V(D)J recombination process cleaves and splices variable (V), diversity (D), and joining (J) non-contiguous immunoglobulin (Ig) segments in the genome (Fanning et al., 1996; Tonegawa, 1983). Ig heavy chains and T cell receptor (TCR) β chains are formed by sequential steps of D-J and V-DJ recombination, while Ig light chains and TCR α chains are generated by direct VJ recombination. The critical cleavage step in V(D)J recombination is executed by the lymphocyte-specific enzyme containing the multi-domain proteins recombination-activating gene 1 and 2 (RAG1 and RAG2) (Oettinger et al., 1990; Schatz et al., 1989) (Figure 1A). RAG recognizes specific recombination signal sequences (RSSs) flanking the 3' end of the V, D, and J segments, which are composed of a conserved heptamer, a spacer of either 12 or 23 base pairs

(bp), and a conserved nonamer (Akira et al., 1987; Ramsden et al., 1994) (Figures 1B and 1C). These RSSs are designated as 12-RSS or 23-RSS after the length of the spacer. Splicing can only occur between one gene coding segment flanked by a 12-RSS and another segment flanked by a 23-RSS, establishing the 12/23 rule (Schatz and Swanson, 2011). Because V, D, and J segments are flanked by different RSSs such as in the IgH locus (Figure 1C), the 12/23 rule helps to ensure recombination between V, D, and J, but not within homotypic gene segments.

The RAG complex catalyzes two consecutive reactions, nicking (strand cleavage) and hairpin formation (strand transfer), without dissociation. First, it binds either a 12-RSS substrate or a 23-RSS substrate and introduces a nick precisely at the junction between the coding segment and the RSS. Interactions with both the conserved heptamer and nonamer are required for optimal RAG activity because considerable sequence variation in endogenous RSSs substantially affects RAG binding affinity and recombination frequency (Schatz and Swanson, 2011). When a 12-RSS and a 23-RSS are bound to the same RAG, a synaptic, paired complex (PC) is formed (Figure 1C). Second, upon PC formation, the free 3'-hydroxyl released from the nicking step attacks the opposing strand to create a hairpin coding segment and a blunt signal end, generating the cleaved signal complex (CSC) (Figure 1C). Dissociation of gene segment hairpins results in a signal end complex (SEC) (Figure 1C). Proteins in the classical nonhomologous end joining (NHEJ) DNA repair pathway are recruited to the RAG complex to process and join the coding segments (Lieber, 2010). In vitro, high-mobility group (HMG) proteins such as HMGB1 have been shown to stimulate RAG's activity in DNA binding, nicking, and hairpin formation, presumably by inducing RSS bending (Schatz and Swanson, 2011).

Many RAG mutations have been identified in humans that are associated with a spectrum of genetic disorders ranging from severe combined immunodeficiency (SCID) to milder variants, such as Omenn syndrome (OS), RAG deficiency with γδ T cell expansion, granuloma formation, or maternofetal engraftment (Lee et al., 2014; Schatz and Swanson, 2011). Aberrant V(D)J recombination is an important mechanism responsible for chromosomal translocations in cancer and autoimmunity (Brandt and Roth, 2009). Despite extensive structural pursuits, the only known RAG structure in complex with DNA is that of the isolated nonamer-binding domain (NBD) dimer with a nonamer sequence (Yin et al., 2009). Here, we report cryo-electron microscopy



(legend on next page)

(cryo-EM) structures of the core RAG complex in the absence of DNA and in the presence of RSS intermediates and products. These structures, representing the apo-form, the nicked paired complex, and the cleaved signal end complex, capture snapshots in RAG-mediated catalysis with additional implications for mechanistically related transposases and integrases.

RESULTS

Cryo-EM Structure Determination

Previous biochemical studies on the RAG complex almost exclusively utilized the mouse recombinant proteins (Schatz and Swanson, 2011). To tackle the long-standing structural questions on RAG, we screened RAG1 and RAG2 from different vertebrate species using both insect and mammalian cell expression systems. We selected insect cell-expressed zebrafish RAG (zRAG) for further studies due to its higher expression level and favorable behavior in solution. We reconstituted the apo-RAG1-RAG2 complex (Apo-RAG) containing RAG1 (271–1031) and RAG2 (full-length) (Figure 1A), its complex with 12-RSS and 23-RSS signal ends (SEC) in the presence of Mg²⁺, and its complex with paired, nicked 12-RSS and 23-RSS intermediates (PC) in the presence of Ca²⁺, which was reported to inhibit RSS cleavage by RAG (Grundy et al., 2009) (Figure 1B). Consistently, our PC sample showed only nicked RSSs on a urea PAGE (Figure S1A). Human HMGB1, which is nearly identical with zebrafish HMGB1 (Figure S1B), was included in both SEC and PC reconstructions.

We collected cryo-EM images for the SEC and PC samples, and two-dimensional (2D) class averages showed a distribution of different views of the complex (Figures 1D and S1C). Cryo-EM structure determination using multiple rounds of three-dimensional (3D) classification and refinement resulted in a number of density maps, including 2-fold symmetrized Apo-RAG, PC, and SEC at 9.0, 3.7, and 3.4 Å resolutions, respectively, and non-symmetrized PC at an overall resolution of 4.6 Å with an NBD/nonamer region resolution of 7.2 Å (Figures 1E, 1F, S1D, and S1E). The Apo-RAG maps refined with and without applying symmetry appeared similar, supporting the validity of the 2-fold symmetry (Figure S1F). While the Apo-RAG adopts a similarly

open configuration as the mouse RAG1-RAG2 (mRAG1-RAG2) crystal structure (Kim et al., 2015), the SEC and PC complexes with DNA appear in a closed and more compact conformation (see below in Figure 3).

Atomic models were built into the 3.4 Å symmetrized SEC, 3.7 Å symmetrized PC, and 4.6 Å non-symmetrized PC maps using the crystal structures of the mRAG1-RAG2 complex (Kim et al., 2015) (PDB 4wwx) and the isolated nonamer-bound NBD dimer as references (Yin et al., 2009) (PDB 3gna), and refined (Table S1). The 9.0 Å resolution Apo-RAG map was first fitted with the refined RAG1-RAG2 monomer from SEC and later refitted directly with the mRAG1-RAG2 dimer from the crystal structure (Kim et al., 2015). Because the structures of SEC and PC reconstructions are largely identical, the cryo-EM particles were also grouped together to increase the data size and generated a structure at 3.3 Å resolution (Figures S1E, S1G, and S1H). These maps were used for cross-references in model building. The map/model Fourier shell correlation (FSC) curves and local resolution estimations are consistent with the gold-standard resolutions from FSC curves between half maps of split data (Figures S1D, S1E, and S2A–S2D).

Overview of PC and SEC Maps and Models

The cryo-EM maps revealed dimeric (RAG1-RAG2)₂ structures with DNA chains running through the entire lengths of the complexes (Figures 2A–2C, S2E, and S2F). The RAG1 and RAG2 densities lacked the N-terminal RING and the C-terminal plant homeodomain (PHD) in the constructs, respectively (Figure 1A), likely due to the flexibility of these domains relative to the core regions. For symmetrized PC and SEC, in which the NBD is largely invisible, the final models contain residues 480–1,029 of zRAG1 (the active site region in Figure 1A), residues 1–351 of zRAG2 (the core region in Figure 1A), and 124 and 116 nucleotides, respectively (Figures 2A, 2C, S2E, and S2F). The excellent superimposition of cryo-EM densities with the refined model is shown for representative regions of the SEC map (Figure 2D). For non-symmetrized PC, by tracing from the nonamer DNA in the superimposed, previous crystal structure of the nonamer-bound NBD dimer (Yin et al., 2009), we could unambiguously fit the DNA sequences in which all the nucleotides were counted for. The final

Figure 1. Cryo-EM Structure Determination

- (A) Domain organization of zebrafish RAG1 and RAG2 (zRAG1 and zRAG2). NTD, N-terminal domain; RING ZnA, RING domain and zinc finger A domain; NBD, nonamer binding domain; DDBD, dimerization and DNA binding domain; PreR, pre-RNase domain; RNH, RNase H-like domain; ID/ZnB, insertion domain/zinc binding domain B; CTD, C-terminal domain; CTT, C-terminal tail; WD40, WD40 repeat domain; and PHD, plant homeodomain. Approximate domain boundaries are shown by residue numbers. Potential active site residues are indicated as red dots in RNH.
- (B) Recombination signal sequences used in this study. Heptamer sequences (red) are numbered from 1 to 7 for the forward strand and from 1* to 7* for the reverse strand. Coding segment ends are numbered from –16 to –1 for the forward strand and from –16* to –1* for the reverse strand. The nicking site is between A-1 (coding end) and C1 (signal end) with a 3'-OH on the A-1.
- (C) Overview of V(D)J recombination. In the red box, RSSs flanking V, D, and J segments in the IgH locus are illustrated. The dimeric (RAG1-RAG2)₂ complex is shown as stacked cyan and lemon green trapezoids. Briefly, RAG binds a single RSS in the presence of HMGB1 to form a signal complex (SC), either 12-SC or 23-SC, which can undergo nicking at the coding end–signal end junction in the presence of Mg²⁺. Synapsis of one 12-RSS and one 23-RSS in the same RAG dimer forms the paired complex (PC), followed by generation of the cleaved signal complex with hairpin coding end and cleaved signal end. Hairpin release produces the signal end complex (SEC). Further processing by enzymes in the non-homologous end-joining DNA repair pathway results in ligation of the coding ends and circularization of the signal ends.
- (D) Representative 2D class averages of cryo-EM particles of the SEC.
- (E and F) Flow charts of cryo-EM structure determination for the SEC (E) and the PC (F). The two numbers in the blue box are the resolutions of the entire molecule and the NBD region only, respectively.

See also Figure S1.

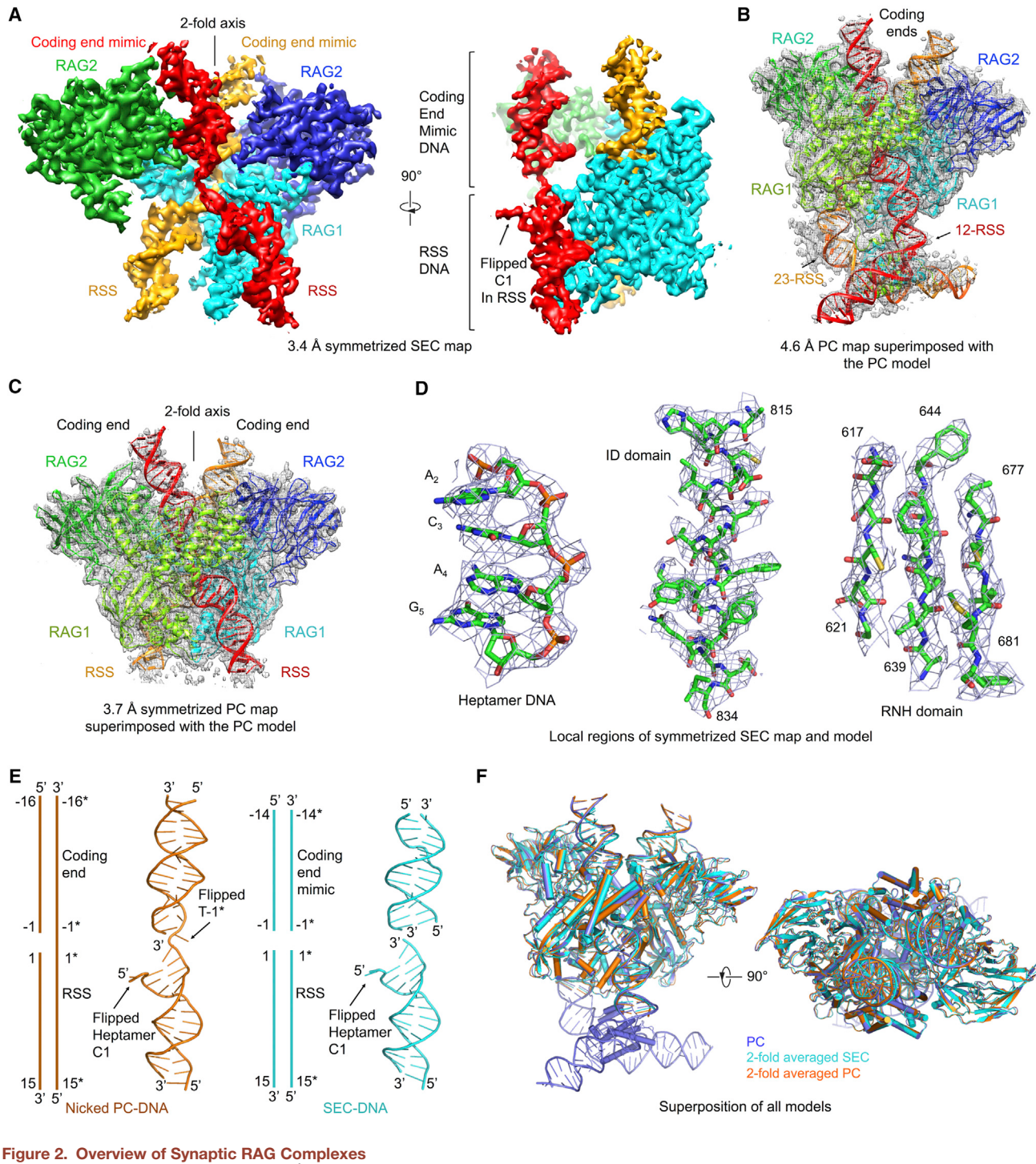


Figure 2. Overview of Synaptic RAG Complexes

(A) Orthogonal views of the symmetrized 3.4 Å resolution SEC map. One RAG1 is omitted in order to present the bound DNAs (red and orange) inside the protein clearly. For the side view, one RAG2 is also omitted to display the density for the flipped C1 base at the RSS.

(B and C) Atomic models superimposed with the non-symmetrized 4.6 Å resolution PC map (B) and the symmetrized 3.7 Å resolution PC map (C), respectively.

(D) Representative regions of the SEC map superimposed with the final model.

(E) Side-by-side comparison of the DNA models in symmetrized PC (orange) and SEC (cyan). Both schematic and ribbon models are shown. Locations of flipped bases are labeled.

(F) Orthogonal views of superimposed symmetrized SEC (cyan), symmetrized PC (orange), and non-symmetrized PC (slate) structures.

See also Figure S2.

model contains residues 408–1,029 of zRAG1 (the core region in **Figure 1A**), residues 1–351 of zRAG2, and the 222 nucleotides in the entire 12-RSS and 23-RSS intermediates (**Figure 2B** and **Movie S1**).

Although no coding end DNA was included in the preparation, the SEC map contains density above the active site that mimics the coding end DNA as seen in the PC (**Figures 2A** and **S2E**). We reasoned that the density comes from RSSs non-specifically bound to the coding end binding site. This is supported by the variation on the lengths and protruding angles of the DNA duplex bound at this site among the 3D classes of the SEC complex due to the different lengths of RSSs (34 bp and 45 bp) available for this interaction (**Figure 1E**). By contrast, the coding end DNA (16 bp) of the PC complex appears to protrude to a homogeneous length (**Figure 1F**). In the 3.4 Å symmetrized SEC map, 14 base pairs appear bound symmetrically and therefore visible at this coding end mimic. Similarly, in the crystal structure of the eukaryotic transposase Mos1, precleaved transposon signal ends mimicked non-specific interactions by the flanking DNA (Richardson et al., 2009).

Although nicked DNA and blunt-ended DNA are present in the PC and the SEC, respectively (**Figure 2E**), a superposition showed that the overall structures of PC and SEC are highly similar (**Figure 2F**). The only gross difference is the visible NBD dimer and the longer RSS in the non-symmetrized PC (**Figures 2B** and **2F**). The RAG protein dimer has a previously described Y shape (Kim et al., 2015). In non-symmetrized RAG/DNA complexes, this shape now resembles a butterfly with DNA chains at the top as antennas and DNA chains at the bottom that emphasize the tail (**Figure 3A**). This butterfly shape is also visible in some 2D averages of SEC and PC particles (**Figures 1D** and **S1C**). Because the 2-fold axis of the NBD dimer does not coincide with that of the RAG active site dimer and due to lack of symmetry at the bound 12-RSS and 23-RSS, symmetrized PC and SEC both lacked the butterfly tail (**Figures 2A** and **2C**). The active site regions of RAG1-RAG2 monomers in all RAG structures are highly conserved with pairwise RMSDs of ~0.6 Å. When compared with a RAG1-RAG2 monomer from the mRAG1-RAG2 crystal structure (Kim et al., 2015), the NBD of RAG1 in the PC exhibits a dramatically different orientation (**Figure 3B**). The NBD dimers alone align well with each other (**Figure 3C**), suggesting a rigid body movement of the NBD dimer upon DNA binding. When the NBD region was excluded, individual RAG1-RAG2 monomers in PC and SEC aligned separately with the crystal structure at pairwise RMSDs of ~1.5 Å (**Figure 3B**). Local differences, in particular near the active site, are apparent (see below), as also shown by changes in secondary structures (**Figures S3A** and **S3B**).

Closure of the RAG Dimer upon DNA Binding

The RAG1-RAG2 monomers have a highly conserved mode of dimerization in the DNA-bound complex structures as the dimers superimpose to pairwise root-mean-square deviations (RMSDs) of ~0.8 Å (**Figure 2F**). However, this conserved relative orientation between the RAG1-RAG2 monomers is dramatically different from that in the Apo-RAG (**Figure 3D**). Up to ~27 Å movements in C α positions are observed, which draw the two halves of the dimer closer together (**Figure 3D**). Consequently,

the Apo-RAG is much more open, as shown by the gap between the two subunits (**Figure S3C**), which is closed upon DNA binding (**Figure 3D**). Therefore, we refer to Apo-RAG as the open conformation and DNA-bound RAG complexes as the closed conformation (**Figure 3D**). We found that the crystal structure of mRAG1-RAG2 (Kim et al., 2015) fits well with the symmetrized Apo-RAG cryo-EM density (**Figure 3E**). These observations suggest that, although 12-RSS and 23-RSS were both present in washed crystals, the mRAG1-RAG2 complex was crystallized in an apo-form, explaining the lack of DNA density. The low resolution of the Apo-RAG cryo-EM structure also suggests a highly dynamic property in the absence of DNA interaction.

Extensive RSS-induced interactions are observed between RAG1 from one RAG monomer and RAG2 from the symmetric RAG monomer and between the two RAG1 subunits (**Figure 3F**), which are completely absent in Apo-RAG. The RAG1-RAG2 interaction is mostly mediated by polar contacts between the α 15 helix in RAG1 and the α 1 helix and the β 27– β 28 loop in RAG2 (**Figures 3F**, **S3A**, and **S3B**). The RAG1-RAG1 interaction is mediated by the β 4– β 5 loop, α 15, and the α 15– α 16 loop (**Figures 3F** and **S3A**). The β 4– β 5 loop is in the RNH domain, which is involved in RSS recognition and harbors the catalytic residues (see below). The interfacial residues in the closed conformation are largely conserved across species (**Figures S3A** and **S3B**). RAG disease mutations R841Q and R841W, equivalent to mutations on R860 in zRAG1, are associated with combined immune deficiency with granuloma and/or autoimmunity (Lee et al., 2014) (**Figure S3A** and **Table S2**). R860 resides on α 15 at the closed dimerization interface and likely participates in charged interactions with E627 in the β 4– β 5 loop of RAG1 and E334 in the β 27– β 28 loop of RAG2 (**Figures 3F** and **3G**). The β 4– β 5 loop of RAG1 and the β 27– β 28 loop in RAG2 are mostly disordered in Apo-RAG (**Figure 3G**). Because binding of each RSS requires both RAG1 monomers, the RSS interaction induces the dimer closure, may be sufficient to stabilize the closed formation, and is critically important for catalysis (**Figure 4**).

Cooperative RSS Recognition by RAG1 with Base Flipping

The RAG/DNA complex structures provide the first glimpse of RSS recognition at the heptamer. Because nearly identical RSS interactions are seen in the SEC and the PC (**Figure S4A**), we used the symmetrized SEC at 3.4 Å resolution for the structural description. The bound 12-RSS and 23-RSS are visible at the first 15 positions, suggesting that these positions of the RSSs are symmetrically arranged in the RAG dimer (**Figures 2E** and **S2E**). The first 12 positions of the RSS, including the heptamer and the first 5 positions of the spacer, form the region that directly contacts RAG. Consistently, the first 5 positions in the spacer of both 12-RSS and 23-RSS represent the most consecutively conserved spacer segments across genomes (Ramsden et al., 1994). Complementary electrostatics is displayed at the RSS-binding site of RAG1 (**Figure 4A**) with extensive sugar phosphate backbone contacts (**Figures S4B** and **S4C**).

An RSS is recognized by both subunits of RAG1 in the RAG dimer, with the beginning part mainly recognized by the insertion domain (ID) and RNase H-like domain (RNH) of one subunit and

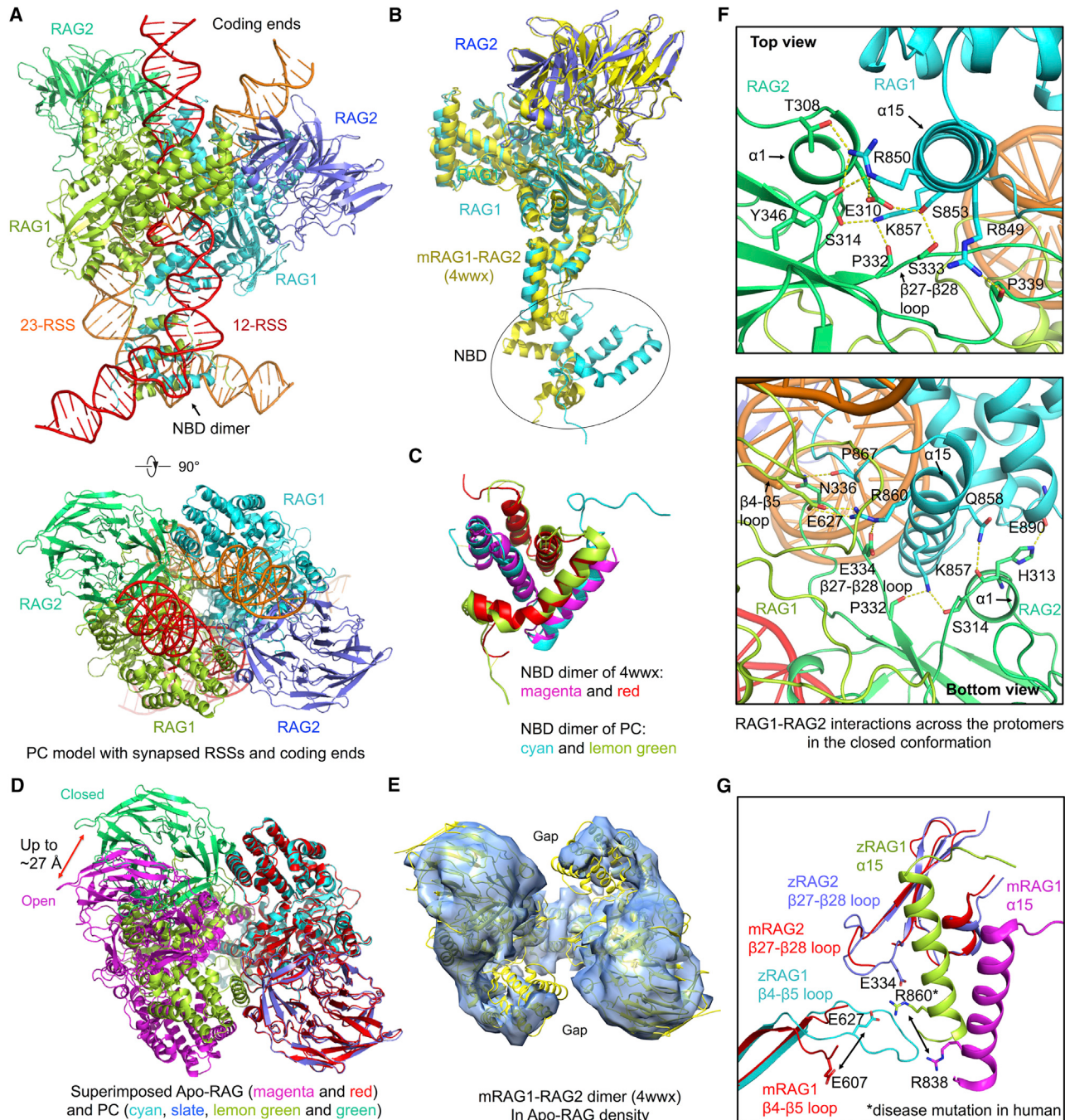


Figure 3. Open Conformation of Apo-RAG and Closed Conformation of Synaptic Complexes

- (A) Side and top views of RAG in complex with the complete 12-RSS and 23-RSS intermediates in the PC.
 - (B) Superimposition of RAG1-RAG2 monomers between the PC model (cyan and blue) and the crystal structure (PDB 4wwx, yellow).
 - (C) Superimposition of NBD dimers between the PC (cyan and lemon green) and the crystal structure (magenta and red, PDB: 4wwx).
 - (D) Top view of superimposed PC dimer in the closed conformation and Apo-RAG dimer in the open conformation. One RAG1-RAG2 monomer is aligned, and the difference in the location of the symmetric monomer is evident. The magnitude of displacement required to switch between the two conformations is indicated.
 - (E) Rigid body fit of the mRAG dimer crystal structure (yellow) in the 9.0 Å Apo-RAG map (light blue).
 - (F) Top and bottom views of the new interactions in the closed conformation between RAG1 of one monomer and RAG2 of the symmetric monomer and between two RAG1 subunits. Potential interactions are displayed as yellow dashed lines.
 - (G) The RAG1 β4-β5 loop and the RAG2 β27-β28 loop involved in interactions in the closed conformation are disordered in mRAG in the open conformation. A potential charged interaction is highlighted, including residue R860 that is equivalent to R841 mutated in human RAG patients.
- See also Figure S3.

the more distal part recognized by the RNH, dimerization and DNA binding domain (DDBD), and C-terminal domain (CTD) of the symmetric subunit (Figures 4B and 4C). The interactions are mostly at the minor groove of the RSS, with significant widening in this region (Figure 4D). Specific base contacts are restricted to the heptamer only. Multiple interactions are observed at the first three positions (Figure 4E), explaining the perfect sequence conservation of these nucleotides across genomes (Ramsden et al., 1994). Helices α 16 and α 23 (Figure S3A) of one RAG1 subunit interact with beginning positions of the heptamer at the major and minor grooves, respectively (Figures 4C, 4E, and 4F). The α 23- α 24 loop of the symmetric subunit recognizes bases at more distal positions of the heptamer at the minor groove (Figures 4C, 4E, 4G, and S4D).

Grafting a bound RSS to one RAG1 subunit in the apo-like mRAG crystal structure (Kim et al., 2015) shows that the symmetric RAG1 needs to pivot in order to interact with the RSS (Figure 4G), a movement that is also evident in the comparison between Apo-RAG and DNA-bound RAG conformations (Figure 3D). Upon the RSS binding-induced structural shift, the α 23- α 24 loop of the symmetric RAG1 moves in position to contact multiple bases at the minor groove (Figures 4E, 4G, and S4D). The β 4- β 5 loop of the RNH domain, which was disordered in the Apo-RAG crystal structure, becomes ordered and interacts with the RSS (Figure 4G) and contributes to the dimer closure (Figures 3F and 3G). Thus, binding of one RSS induces conformational changes in both RAG1 monomers, and this cooperativity might facilitate formation of the 12-RSS and 23-RSS paired complex. Notably, the catalytic residue E984 in the active site situates on α 23. Therefore, the binding of RSS may also induce catalytically competent conformations in RAG1 (see below in Figure 6).

A surprising observation is that the base of nucleotide C1 of the heptamer, which is either nicked or cleaved at this position in PC and SEC, flips out from the duplex (Figures 4E and 4H). It is recognized extensively by the region of α 18- α 19 in the ID of RAG1, including K912, P913, and R916 on the α 18 helix; S917 and T918 on the α 18- α 19 loop; and D923 on α 19 (Figures 4E and 4H). Multiple potential interactions are present at both the cytosine base and the ribose, putting a specific anchor at this position (Figure 4H). Inspection of the structure suggests that the base flipping is also necessary to avoid a clash with the closed conformation of RAG, which would have occurred if nicked C1 stayed in the duplex form (Figure 5A).

Distortion and Base Flipping in Coding End DNA Recognition

From an overview of the PC model containing nicked DNA, the RSS and the coding segment almost appear continuous. When a standard B-form DNA duplex is superimposed with the RSS, it extends into the coding end binding site (Figure 5A), suggesting that an intact RSS substrate with both coding DNA and RSS may bind in a similar fashion. However, as discussed above, the observed clash of the modeled duplex with RAG suggests that a RAG complex with an intact RSS substrate may be in a partially, instead of a fully closed, conformation. In addition to sharing structural features at the RSS-binding site, the nicked PC and the cleaved SEC structures possess similarities at the coding ends, with clearly defined electron densities (Figure 5B). Super-

position of the symmetrized PC and SEC structures shows that the PC coding end DNA is almost identical with the SEC coding end mimic, displaying only local deviations in the duplex positioning (Figure 2F).

Unlike RSS recognition, in which both RAG subunits of the dimer participate, each RAG1-RAG2 monomer interacts with one coding end DNA chain exclusively. The beginning of the coding end close to the active site interacts mostly with a highly positively charged patch on ID and RNH of RAG1, while the more distal part of the coding segments interacts with a highly positively charged patch on RAG2 (Figures 5C and 5D). Therefore, RAG2 is also important in DNA binding, a role that was not ascribed previously. The coding end DNA is recognized mostly by electrostatic interactions with few base pair interactions (Figures 5E, S5A, and S5D), which is consistent with lack of sequence conservation in the DNA.

In the nicked RSS intermediates in the PC, there is significant distortion in the DNA conformation at the junction between the RSS and the coding end, when the continuous strand of the DNA abruptly breaks off from the duplex trajectory (Figures 5A and 5B). The single-stranded junction essentially unwinds completely, and the terminal base T-1* of the coding end is flipped to the opposite side of the DNA chain (Figures 2E and 5B). This distortion places the scissile phosphate of T-1*, which is to be attacked by the free 3'-hydroxyl of A-1 for hairpin formation, to the already formed active site that generated the nicking at the opposing strand. A number of previous biochemical studies suggested that T-1* flips out of the coding end duplex during hairpin formation (Bischerour et al., 2009; Schatz and Swanson, 2011). Models for the mechanism of flipping led to proposals involving specific aromatic stacking, for example, by residues of mRAG1 equivalent to W915, Y957, W978, and F993 of zRAG1 (Schatz and Swanson, 2011).

Surprisingly, in the PC structure, the flipped base T-1* not only has no stacking interactions but also does not appear to form any specific polar interactions. Only van der Waals contacts to the M869 side chain and the aliphatic portion of the R870 side chain were observed (Figure 5F). The previously identified aromatic residues are located away from the T-1* nucleotide (Figures S5E-S5G). Only Y957 potentially interacts with the bound DNA at the phosphate group of A-1 (Figure 5F). The base of A-1 is stacked with the guanidinium group of R870 (Figure 5F). Instead of using base stacking, the position of the T-1* nucleotide is held by interactions at the ribose and the phosphate group, in particular, to R870 and H817 (Figure 5F). Because T-1* is a variable nucleotide at the coding end, it is reasonable that the conformation of the nucleotide is stabilized by interactions with the sugar phosphate backbone. The pocket for the flipped T-1* base locates near the 2-fold axis and is deep, highly solvent accessible, and able to accommodate larger bases such as purines (Figure 5G). Previously, an alternative model not involving aromatic stacking correctly predicted the accommodation of the flipped base in a non-specific pocket (Bischerour et al., 2009), as we observed here.

Metal Ion Binding and Catalytic Mechanisms

RAG1 contains a metal ion binding catalytic D(E)DE motif (D620, E684, D730 and E984) within the split RNH domain (Figure 1A)

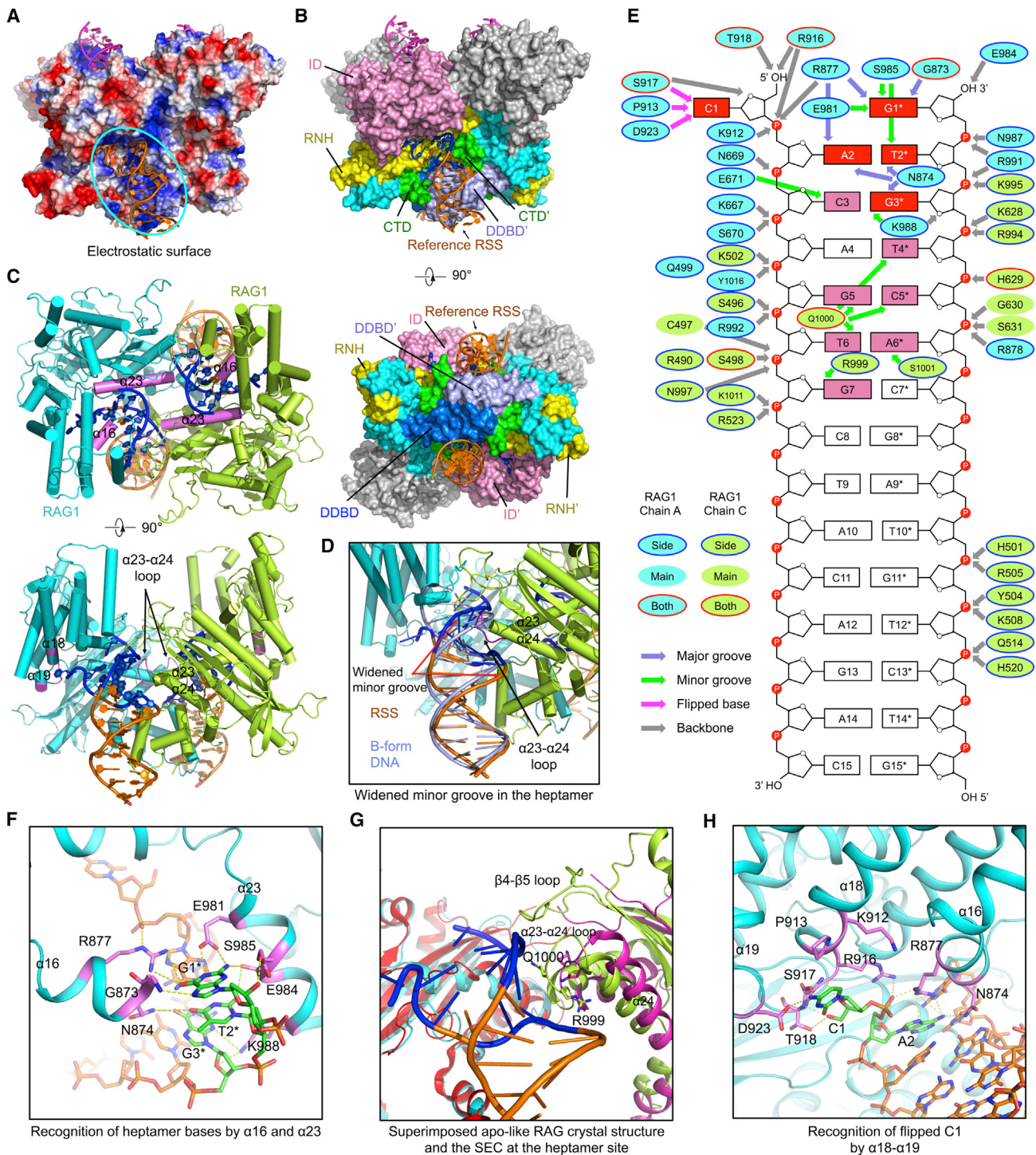


Figure 4. RSS Recognition at the Heptamer and the Spacer

(A) Electrostatic surface of the RAG dimer from the symmetrized SEC model with bound RSSs (orange) and coding end mimics (magenta) in ribbons. The cyan oval shows the RAG surface for one RSS.

(B) Side and bottom views of the RAG dimer displayed as molecular surfaces with bound DNAs displayed in ribbons. For the reference RSS, nucleotides with base recognition by RAG are highlighted in blue, whereas others are shown in orange. Domains involved in RSS interactions are colored as in Figure 1A, except that one DDBD at the bottom view is shown in blue to distinguish it from the neighboring DDBD. Two RAG2 molecules are shown in gray. A prime symbol is added to domain names for the symmetric subunit that interacts with the reference RSS.

(C) Top and side views of RAG1 regions (magenta) that are in contact with the heptamer DNA. RSSs are colored as in (B). RAG2 subunits are omitted.

(legend continued on next page)

and belongs to the DDE family recombinases (Montaño and Rice, 2011). We used Mg²⁺ (the catalytic ion) and Ca²⁺ (a replacement ion), respectively, in the reconstitution of the SEC and the PC. Cryo-EM difference density suggested the presence of at least two metal ions in these structures (sites A and B) (Figures 6A and S6A). The positions of A and B in the PC structure (Figures 6A–6C) and in the SEC structure (Figures 6D and 6E) are somewhat shifted, likely because the coding end mimic duplex is not an authentic intermediate in the reaction. When compared with the nicked DNA, the coding end mimic occupies a similar –1 nucleotide position but a completely different –1* nucleotide position (Figures 6E and 1B).

In the PC structure containing the authentic nicked RSS reaction intermediate, the metal ions A and B are jointly coordinated by the scissile phosphate of the flipped nucleotide T-1* and the D(E)DE motif. A and B are additionally coordinated by O3' of G1* and 3'-hydroxyl of A-1, which are, respectively, the leaving group and the attacking nucleophile in hairpin formation (Figure 6B). Therefore, while ion A stabilizes the leaving group and B activates the nucleophile, A and B together stabilize the pentacovalent intermediate (Figure 6C), poised for hairpin formation. The coordination environment of A and B in the PC is analogous to that in a substrate-bound RNase H structure but with switched roles of A and B (Nowotny et al., 2005) (Figure S6B). We propose that A and B oscillate their roles between the two RAG-catalyzed consecutive phosphoryl transfer reactions, the nicking step and the hairpin formation step, as similarly shown in other systems (Nowotny et al., 2005).

The catalytic D(E)DE motif appears to undergo significant conformational changes upon DNA binding. In the apo-like crystal structure of mRAG1-RAG2 (Kim et al., 2015), the D(E)DE motif residues are not properly positioned for metal ion coordination as seen in the PC structure (Figure 6F). Especially, the E962 (equivalent to zRAG1 E984) catalytic residue situates in a loop immediately preceding the α 23 helix. In SEC or PC, α 23 is much longer and E984 situates on α 23, with 3.2 Å distance away in the C α position from the equivalent E962 (Figure 6F). Of note, mRAG1 and zRAG1 have exactly the same sequence in the region around the α 23 helix (Figure S3A). Two cooperative interactions, one from α 23 of one RAG1 and the other from the α 23– α 24 loop of the symmetric RAG1 (Figure 4C), may be responsible for the coupled RSS binding-induced active site formation.

NBD Dimer Conformation and HMGB1-Induced RSS Bending

We used non-symmetrized PC structure to analyze the location of the NBD dimer and the highly bent conformations of bound 12-RSS and 23-RSS intermediates (Figure 7A). Similar observations were seen in the non-symmetrized reconstructions from merged datasets (Figure S1H). The coding segment, heptamer, and beginning of the spacer of an RSS are essentially 2-fold symmetric. Starting from the remainder of the spacer, the 12-RSS and 23-RSS each assume a different chain trajectory. While the 12-RSS spacer traverses about one turn as a DNA duplex, the 23-RSS spacer traverses about two turns, creating asymmetric conformations at the nonamer (Figure 7A). Both 12-RSS and 23-RSS duplexes are exceedingly bent, by ~60° for the 12-RSS and ~120° for the 23-RSS (Figures 7A and S7A). The bends occur most severely near the end of the spacer for the 12-RSS and near the middle of the spacer for the 23-RSS.

In non-symmetrized Apo-RAG map, no density is visible for the NBD region, suggesting that the NBD dimer is flexibly linked to the RAG active site dimer (Figure S1F). In the apo-like RAG crystal structure, the conformation of the NBD dimer may have been defined by crystal packing (Kim et al., 2015). The flexibility of the NBD dimer is evident even when it is bound to the nonamer DNA, as shown by conformational fluctuations in three superimposed reconstructions (Figures 7B, 1F, and S1H), which may allow ± 1 variation of the spacer lengths in both 12-RSS and 23-RSS in a minor population of recombination sites (Fanning et al., 1996). The flexibility may have also compromised the resolution of the NBD region to ~7.2 Å (Figures 1F and S1E). The dimeric NBD/nonamer complex in the PC aligns well with the previous crystal structure of the isolated NBD/nonamer complex (Yin et al., 2009) (Figure 7C), suggesting that the NBD dimer mostly oscillates as a rigid body. When the PC is superimposed with the apo-like RAG dimer using one of the RAG1-RAG2 monomers, the associated NBD dimer in the apo-like conformation needs to swing about 76° to reach the RSS-bound orientation (Figure 7D). The rotation moves the NBD closer to the 12-RSS but away from the 23-RSS.

Using known molar ratios of Apo-RAG and HMGB1 as standards, we showed by SDS-PAGE that our reconstituted PC sample contained one HMGB1 per RAG monomer (Figure 7E). This composition is different from that of a previously reconstituted SEC under a different condition, which showed one HMGB1 per RAG dimer (Grundy et al., 2009; Kim et al., 2015). HMGB1 contains two HMG boxes, each composed of a pair of helices

- (D) A bound RSS colored as in (B) superimposed with an ideal B-form DNA (light blue), showing the widening of the minor groove. The α 23– α 24 loop inserted into the minor groove of the RSS is highlighted in magenta.
- (E) Schematic depiction of the detailed interactions between RAG and the RSS. RAG1 residues from one and the symmetric subunits are displayed as cyan and lemon green ovals, respectively. These ovals are bounded in blue lines, no lines, and red lines, respectively, for side-chain, main-chain, and side- and main-chain interactions. Slate, green, magenta, and gray arrows indicate interactions at the major groove, minor groove, flipped base, and the backbone. Heptamer bases that have multiple contacts with RAG are highlighted in red, and those with a single contact are in pink.
- (F) Detailed interactions between RAG and the heptamer DNA. Direct base interactions are highlighted in magenta for the protein and in green for the bases. Potential interactions are displayed as yellow dashed lines.
- (G) Superimposed apo-like RAG crystal structure (magenta and red, PDB: 4wwx) and SEC (lemon green and cyan) at the heptamer-binding site. One RAG1 subunit (red and cyan) is aligned, showing the different orientations of the symmetric RAG1 (magenta and lemon green), especially at the β 4– β 5 loop that was disordered in the crystal structure, and the α 23– α 24 loop.
- (H) Detailed interactions between RAG and the flipped C1 of the heptamer DNA.
- See also Figure S4.

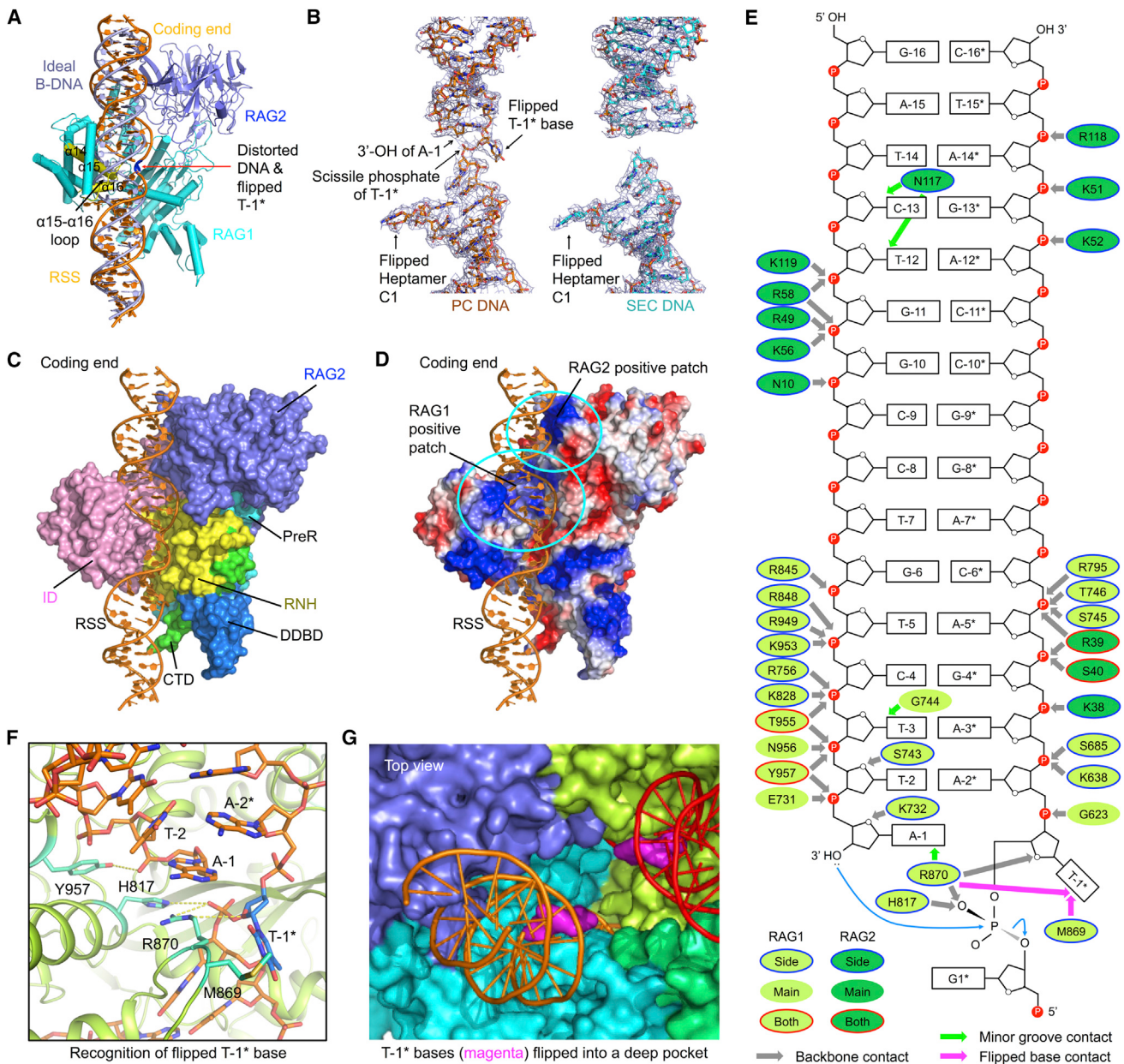


Figure 5. Interactions at the Coding Segment Ends

- (A) Superposition of an ideal B-form DNA (light blue) with the nicked RSS DNA (orange) from the symmetrized PC model. The distorted base T-1* is highlighted in blue. Parts of α_{14} , α_{16} , and the $\alpha_{15}-\alpha_{16}$ loop (yellow) of RAG1 clash with the B-form DNA.
- (B) Cryo-EM density maps superimposed with the final DNA models (show in sticks) in the symmetrized PC (orange) and SEC (cyan).
- (C) Side view of RAG/DNA interactions in the PC. Only one RAG1-RAG2 monomer is shown and displayed as a molecular surface. Nicked RSS intermediate (orange) is shown as ribbons. Domains in RAG1 involved in the interactions are colored as in Figure 1A.
- (D) Electrostatic surface of one RAG1-RAG2 monomer in the PC model. The cyan ovals denote the positively charged patches in RAG1 and RAG2, respectively.
- (E) Schematic depiction of the detailed interactions between RAG and the coding end in the PC. RAG1 and RAG2 residues are displayed as lemon green and green ovals, respectively. These ovals are bounded in blue lines, no lines, and red lines, respectively, for side-chain, main-chain, and side- and main-chain interactions. Green, magenta, and gray arrows indicate interactions at the minor groove, flipped base, and the backbone.
- (F) Detailed interactions at the flipped T-1* base in the nicked DNA intermediate. T-1* is highlighted in marine blue. Residues that have direct contacts with T-1* and nearby nucleotides are shown in cyan. Potential interactions are displayed as yellow dashed lines.
- (G) Top view of the flipped T-1* bases (magenta surfaces) in a deep pocket of the RAG dimer (surfaces in cyan, blue, lemon green, and green). The coding ends (orange and red) are shown as ribbons.

See also Figure S5.

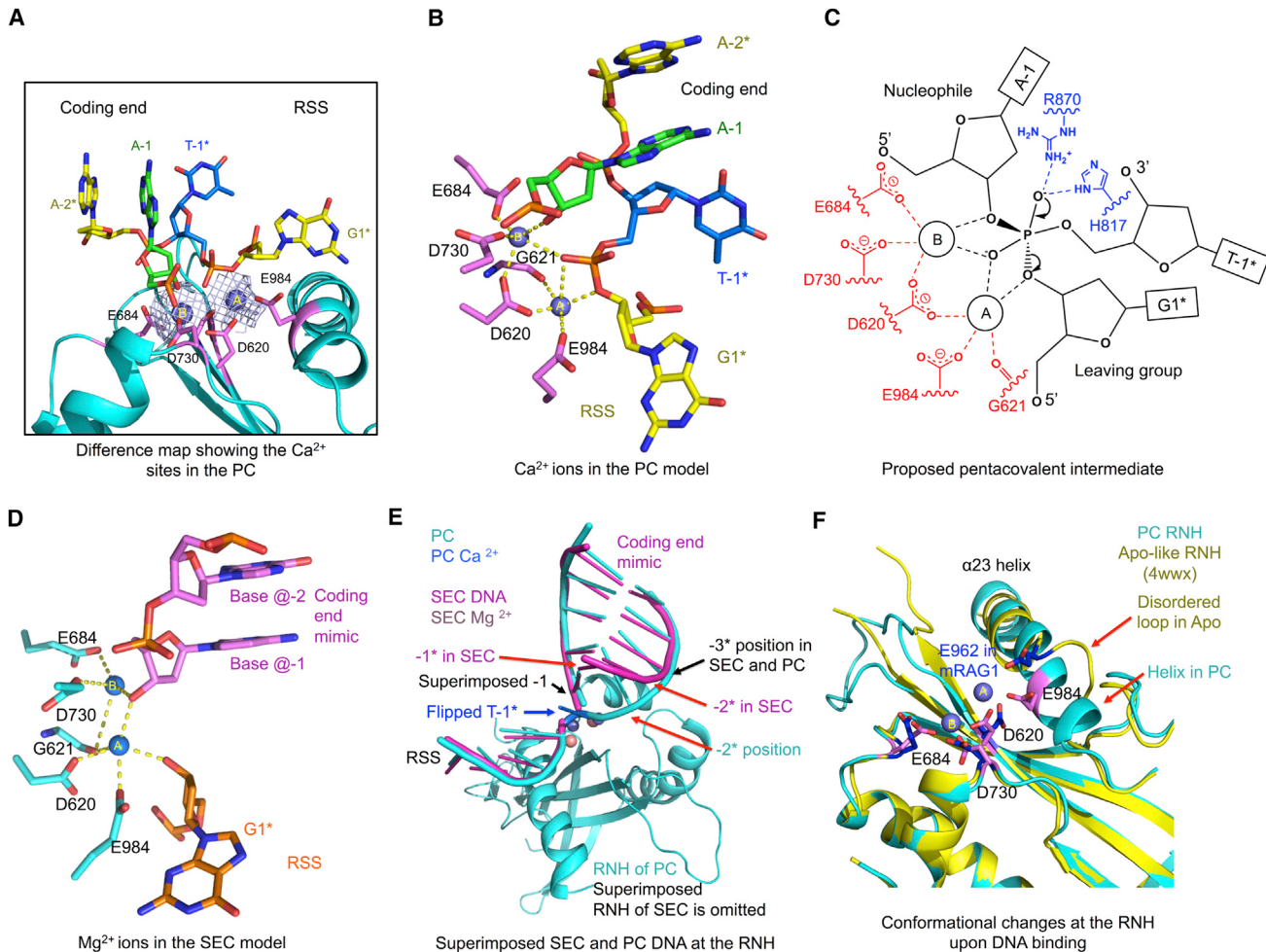


Figure 6. Two-Metal-Ion Catalysis and Conformational Remodeling

(A) Difference density between the PC cryo-EM map and the model without metal ions showing the proposed Ca^{2+} sites. Ca^{2+} sites A and B are shown as slate spheres and active site residues highlighted in magenta.

(B) Active site of the PC model around the Ca^{2+} sites (slate spheres, A and B). Ca^{2+} A and B are jointly coordinated by the scissile phosphate of the flipped nucleotide T-1* and D620. A is additionally coordinated by O3' of G1* (the leaving group), E984, and the carbonyl oxygen of G621, and B is coordinated by 3'-OH of A-1 (the nucleophile), E684, and D730. Potential coordination of the metal ions is displayed using yellow dashed lines.

(C) Proposed pentacovalent phosphate intermediate in two-metal-ion catalysis of hairpin formation by RAG.

(D) Active sites of the SEC models. Mg^{2+} ions in SEC are presented as blue spheres. Briefly, A is coordinated by five ligands, 3'-OH of G1*, 3'-OH of the non-specifically bound DNA, D620, E984, and the carbonyl oxygen of G621. B is coordinated by four ligands, 3'-OH of the non-specifically bound DNA, E684, D730, and the carbonyl oxygen of G621.

(E) Superimposed PC and SEC models at the RNH domain, showing the shifted metal ions, the aligned -1 nucleotides, and the different positions of the -1* nucleotides in PC and SEC.

(F) Superimposed active sites of the PC (cyan) and the apo-like mRAG crystal structure (PDB: 4wwx, yellow). The D(E)DE motif side chains are shown. The E984 residue changes by $\sim 3.2 \text{ \AA}$ in $\text{C}\alpha$ position from its location on a disordered loop in the apo-conformation to its location on α 23 in the PC. Active site residues in the PC and the crystal structure are highlighted in magenta and blue, respectively. Red arrows indicate regions of local conformational changes.

See also Figure S6.

and a long, slightly bent third helix, which interacts with DNA at the minor groove to generate bending (Stott et al., 2006) (PDB 2gzk). To determine if the PC cryo-EM density contained HMGB1, we displayed the map with the complete model superimposed. While one piece of unassigned density was revealed at the 12-RSS spacer, two were seen at the 23-RSS spacer (Figure 7F), suggesting that the former is bound with one HMG box and the latter with both HMG boxes in HMGB1.

The difference map between the cryo-EM reconstruction and the model clearly revealed densities with a two-cylinder shape at the 12-RSS and the 23-RSS that could be fitted with the pair of helices in an HMG box (Figure 7G). The fitting allowed positioning of one HMG box each to the 12-RSS and the 23-RSS (Figures 7G, 7H, and S7B). Although no clear density was apparent for the third helix of the HMG box bound to either 12-RSS or 23-RSS, the generated mode of DNA interaction is similar to that

(legend on next page)

in the NMR structure of the HMG/DNA complex (Stott et al., 2006) (Figures S7C and S7D), supporting the HMG/RSS model. The second piece of density at the 23-RSS was not sufficiently clear to enable direct HMG fitting. However, the distance between the two pieces of density is similar to the distance between the two HMG boxes in the NMR structure, suggesting that the second piece of density represents the second HMG box of the same bound HMGB1 molecule (Figures 7H and S7B). Because the spacer DNA of 12-RSS is short, it is likely that only one HMG box of HMGB1 is bound.

DISCUSSION

Induced Asymmetry as the Structural Basis for the 12/23 Rule of Recombination

Recognition of two different signal sequences is unique for RAG, as most other recombinases interact with and cleave a pair of identical signal sequences. Our cryo-EM structures suggest an induced asymmetry mechanism that requires flexibility of NBD dimer orientation and plasticity of RSS conformation in the execution of the 12/23 rule. An RSS must bind RAG using both the heptamer and the nonamer for optimal affinity and recombination efficiency. The interactions at the heptamer are symmetric and relatively fixed. When a 12-RSS is bound at both the heptamer and the nonamer in an HMGB1-bent conformation, the NBD dimer tilts toward the shorter 12-RSS, leaving the same NBD dimer with the ability to synapse with only a 23-RSS, also in an HMGB1-bent conformation. Conversely, when a 23-RSS is bound, the NBD dimer tilts away from the longer 23-RSS, leaving the same NBD dimer with the ability to combine with only a 12-RSS. Modeling a pair of 12-RSSs or a pair of 23-RSSs onto RAG showed that the supposed interaction sites on NBD and the RSS are ~40 Å

away (Figures S7E and S7F). Utilizing the spatial difference between the 12 bp and 23 bp spacers, it appears that nature has evolved one effective solution to RSS pairing to enable recombination fidelity. The synapsis of 12-RSS and 23-RSS also promotes effective chemical catalysis through coupled conformational changes at the active sites, further enhancing the 12/23 rule.

To contemplate whether other DNA sequences may also be paired by RAG, we used NBD dimer conformations in the apo-like crystal structure (Kim et al., 2015) and the PC as two possible extremes of NBD tilt angles. We then modeled hypothetical B-form RSS duplexes onto the RAG-bound RSSs by superimposing the heptamer regions (Figure S7G). This exercise suggests the possibility that, if the spacer lengths are varied, there may be additional ways of symmetrical and asymmetrical RSS synapsis, causing pathological DNA double-strand breaks and chromosomal translocations in cancer and autoimmunity, especially when facilitated by spatial proximity (Zhang et al., 2012). In cells, it is thus far unclear what causes bending of the spacer in an RSS to promote recombination. HMG proteins are abundant in the nucleus (Shirakata et al., 1991). Other nuclear proteins may also fulfill the function of RSS-bending, such as the TATA binding protein (TBP) that is known to dramatically bend DNA (Nikolov et al., 1996) (PDB: 1tgh) (Figure 7I).

RAG-Mediated Catalytic Pathway

We propose the following molecular mechanism in RAG-catalyzed cleavage phase of V(D)J recombination based on structures of Apo-RAG and synaptic complexes, as well as our conjecture on steps involving singly RSS-bound forms that still lack structural information (Figure 7J). First, our Apo-RAG structure shows a dynamic open conformation in the absence of RSS binding, with its NBD dimer flexibly attached to the RAG active

Figure 7. NBD Flexibility and RSS Bending by HMGB1 Underlie the 12/23 Rule

- (A) Surface representation of the non-symmetrized synaptic PC model in two orientations, with indicated bending at the 12-RSS and 23-RSS spacers. Color coding for regions of the RSSs is shown.
- (B) Superimposition of three non-symmetrized NBD-containing reconstructions at 4.6 Å, 4.2 Å, and 4.4 Å resolutions (Figures 1F and S1G) in gray, yellow, and salmon, respectively. The variable positions of RSS are indicated by the arrows in corresponding colors.
- (C) The crystal structure of the NBD/nonamer complex (PDB: 3gna, light blue for NBD and blue for DNA) is superimposed onto the synaptic PC model.
- (D) The NBD dimer in the synaptic RAG complex tilts to the direction of 12-RSS. Superposition of the RAG active site dimer of the PC with that of the apo-like RAG crystal structure (PDB: 4www, magenta and red) shows that the NBD dimer needs to swing by ~76° to accommodate the bound RSS.
- (E) Quantitative SDS-PAGE of the PC sample used for cryo-EM studies, showing the ratio of one HMGB1 per RAG monomer.
- (F) Superimposed non-symmetrized PC model and PC map filtered at 5.5 Å resolution. Extra densities along 12-RSS and 23-RSS are highlighted by magenta and purple ovals, for which HMG box1 and box2 were fit, respectively, in (G) and (H).
- (G) The difference density between the PC map and the PC model showed that the extra pieces of density in the magenta ovals in (F) could be fitted with residues 10–48 (a pair of helices) from the first HMG box of a tandem HMG box NMR structure (PDB: 2gzk) (Stott et al., 2006). Left, for 12-RSS; right, for 23-RSS.
- (H) Modeled PC/HMGB1 complex. One HMG box is bound at the 12-RSS, and both HMG boxes of an HMGB1 molecule are bound at the 23-RSS. The fitting of the second HMG box was done by superimposing the DNA in the NMR structure and the DNA in the region of the second piece of extra density. HMG box-bound DNA segments in the NMR structure (PDB 2gzk) (Stott et al., 2006) are shown in blue.
- (I) TBP causes similar bending in DNA as HMGB1. The TBP-DNA complex (PDB: 1tgh) was superimposed with 12-RSS and 23-RSS. Protein and DNA in the TBP-DNA complex are shown in magenta and blue, respectively.
- (J) Structure-derived insights on RAG-mediated cleavage pathway in V(D)J recombination. RAG1 (light green and light cyan), RAG2 (green and cyan), and HMGB1 (orange) are represented as cartoons. Coding ends, heptamers, nonamers, and 3' extension DNAs are shown by semi-transparent blue, red, magenta, and light slate rectangles, respectively. 12 and 23 bp spacers are shown as black lines. Briefly, without binding to an RSS, Apo-RAG is in an open conformation with the flexibly attached NBD dimer. When bound to either 12-RSS or 23-RSS intact DNA in the presence of HMGB1, a partially closed conformation of RAG may be induced. The NBD dimer is tilted through the interaction with either the 12-RSS or 23-RSS nonamer. Then a nick is produced at the junction between the coding end and the signal end, and the first base at the cleaved end of the heptamer is likely flipped out (red filled circle). Subsequent synapsis with a different RSS substrate leads to the formation of the PC, which assumes a fully closed conformation with a flipped base (blue filled circle) on the coding end of both nicked RSS intermediates. The coding ends are linked into hairpin DNA to form the CSC. NHEJ factors are recruited to dissociate the hairpin coding ends, leaving the SEC with only the bound signal ends.

See also Figure S7.

site dimer. Second, because both RAG monomers are required for binding of each RSS, we posit that, upon interaction with an intact RSS substrate, immediate closure of the RAG dimer may ensue to bring the RAG monomers closer together, forming the signal complex (SC). Because the closed conformation of synaptic complexes would have been in clash with an intact RSS substrate, we suspect that an SC may be in a partially closed conformation. Nicking at the RSS-coding end junction can proceed in the SC; however, we do not yet know the associated conformational changes and whether base flipping of C1 and T-1* in synaptic complexes occurs in singly RSS-bound forms. Third, due to dimerization-mediated cooperativity, binding and nicking at one active site of the RAG dimer likely enhances the binding affinity of the symmetric active site to another RSS substrate for formation of the synaptic PC, leading to further closure of the RAG dimer. Fourth, the nicked RSS in PC is severely distorted at the RSS-coding end junction with local unwinding and base flipping of both C1 and T-1*. This conformation, together with the bound metal ions, promotes hairpin formation at the coding end. Simultaneous dissociation of the hairpin coding ends in the presence of proper DNA repair proteins, ensures joining fidelity, and leads to formation of the SEC.

Insights into Human RAG Disease Mutations

Over 100 disease mutations on human RAG1 and RAG2 have been identified (Lee et al., 2014; Schatz and Swanson, 2011). Mapping these mutations onto the crystal structure of mRAG has previously identified those that destabilize the tertiary structure or interfere with the conserved quaternary interaction within the RAG1-RAG2 complex monomer (Kim et al., 2015). The RAG1 mutations R841W/Q may disrupt RSS-induced RAG dimer closure because the equivalent zebrafish residue R860 appears central in stabilizing the closed conformation (Figures 3F and 3G and Table S2). We found that quite a few RAG1 mutations are on residues directly involved in heptamer recognition in the synaptic complexes (Table S2), explaining their deleterious effects on the recombinase. Mutations on residues that participate in non-specific spacer DNA interaction and coding end DNA interaction are also present (Table S2). Interestingly, analysis on the characteristics of rearrangements by hypomorphic RAG mutants revealed occurrence of preferential use of certain gene segments, which generates qualitative differences in the patient T and B cell repertoire when compared with normal controls (Lee et al., 2014). We hypothesize that mutations on residues that directly interact with RSSs may alter the specificity of V(D)J recombination, making some RSSs better substrates than others and leading to the wide spectrum of the disease.

Implications on Other DDE Family Enzymes

Despite having different structural architectures, many transposases and integrases also belong to the DDE family recombinases and catalyze multi-step strand cleavage and strand transfer reactions (Montaño and Rice, 2011). In general, these enzymes excise an insertion element by binding and breaking the DNA at the flanking signal sequences. The cleaved signal sequences with the insertion element located in between are then bound and become ligated to a target DNA. Only limited structural information is available on these enzymes, likely due to their

fairly large size and complexity. Our RAG structures with DNA intermediates and products therefore provide insights into their mechanism of catalysis, especially for the excision step that bears a direct parallel to RAG-mediated cleavage. Specifically, cooperative conformational changes upon DNA synapsis, DNA distortion at the junction with the signal sequence, and based flipping at the nicked signal sequence may all be general features in transposases and integrases as well.

EXPERIMENTAL PROCEDURES

Cloning, Protein Expression, and Purification

The zRAG1 (271–1031) and full-length zRAG2 constructs containing N-terminal His-MBP tags were expressed using the Bac-to-Bac baculovirus-insect cell system. RAG1 was purified sequentially by amylose affinity, heparin, and size-exclusion chromatography, and RAG2 was purified by amylose affinity, anion exchange, and size-exclusion chromatography. The zRAG1-RAG2 complex was reconstituted by mixing zRAG1, zRAG2, and the H3K4Me3 peptide in a 1:1.2:1.2 molar ratio, followed by removal of the His-MBP tags and size-exclusion chromatography. C-terminally His-tagged HMGB1 was expressed in *E. coli* and purified using Ni-NTA affinity and size-exclusion chromatography. The DNAs were synthesized as oligos, annealed appropriately to generate nicked or cleaved RSSs, and purified by gel filtration. Synaptic RAG complexes were reconstituted by incubating the zRAG1-RAG2 complex, 12-RSS, 23-RSS, and HMGB1 in a 2:1:1:3 molar ratio in the presence of Ca²⁺ or Mg²⁺, followed by gel filtration.

Cryo-EM Data Acquisition, Image Processing, Model Building, and Refinement

Cryo-EM images were collected using an FEI TF30 Polara electron microscope and a Gatan K2 Summit direct electron detector in super-resolution counting mode. Simplified Application Managing Utilities for EM Labs (SAMUEL) scripts were used for image preprocessing, particle picking, 2D classification, and 3D initial model building. 3D classification and refinement were carried out in RELION (Scheres, 2012). All refinements follow the gold-standard procedure, in which two half datasets were refined independently. RELION “post-processing” was used to estimate resolution based on the Fourier shell correlation (FSC) = 0.143 criterion. The mRAG1-RAG2 complex (Kim et al., 2015) and the NBD-DNA complex structures (Yin et al., 2009) were used as starting points for model building. The atomic models were refined first in real space and then in reciprocal space using phase restraints, electron scattering factors, and artificial unit cells.

ACCESSION NUMBERS

The cryo-EM maps of symmetrized SEC, symmetrized PC, and non-symmetrized PC at 3.4 Å, 3.7 Å, and 4.6 Å resolutions, respectively, have been deposited in the EMDataBank under accession codes of EMD-6487, EMD-6488, and EMD-6489. The corresponding refined structural models have been deposited in the Protein Data Bank with PDB: 3JBX, 3JBY, and 3JBW, respectively. The cryo-EM maps of symmetrized Apo-RAG at 9.0 Å resolution and of symmetrized synaptic RAG at 3.3 Å resolution reconstructed from mixed PC and SEC particles have been deposited in the EMDataBank under accession codes of EMD-6490 and EMD-6491, respectively.

SUPPLEMENTAL INFORMATION

Supplemental Information includes Supplemental Experimental Procedures, seven figures, two tables, and one movie and can be found with this article online at <http://dx.doi.org/10.1016/j.cell.2015.10.055>.

AUTHOR CONTRIBUTIONS

H.R. and H.W. conceived the project. H.W. and H.R. designed the biochemical experiments. H.R. prepared Apo-RAG and all RAG complexes and performed

biochemical and initial negative-stain EM experiments. M.G.C. carried out negative-stain EM analysis and characterization of cryo-EM conditions. M.L. and M.G.C. performed cryo-EM data collection. M.L. carried out cryo-EM data processing. H.R. and H.W. performed model building and refinement. T.-M.F. helped with model building and refinement, and A.B.T. calculated FSC curves and local resolution distributions. H.W., H.R., and M.L. performed data analysis, result discussion, and interpretation. H.W., H.R., and M.L. wrote the manuscript.

ACKNOWLEDGMENTS

We thank Dr. Wei Mi for help with sample freezing for cryo-EM studies, Drs. Liron David and Maria Ericsson for help with negative-stain EM experiments, Drs. Yang Li and Wei Ding for suggestions on model building and refinement, and the support of the Cancer Research Institute Irvington Postdoctoral Fellowship (to H.R.).

Received: August 21, 2015

Revised: October 10, 2015

Accepted: October 20, 2015

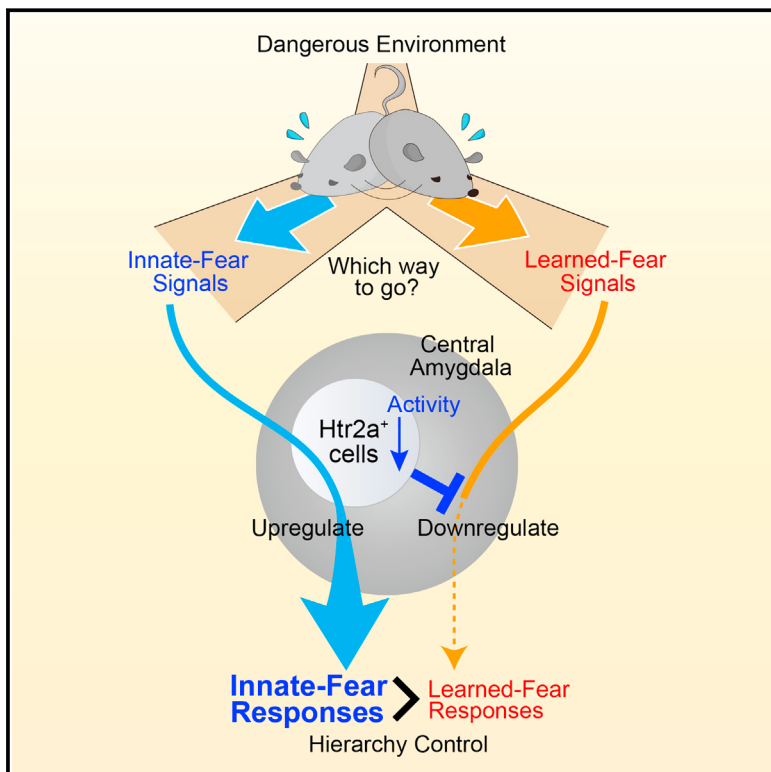
Published: November 5, 2015

REFERENCES

- Akira, S., Okazaki, K., and Sakano, H. (1987). Two pairs of recombination signals are sufficient to cause immunoglobulin V-(D)-J joining. *Science* 238, 1134–1138.
- Bischerour, J., Lu, C., Roth, D.B., and Chalmers, R. (2009). Base flipping in V(D)J recombination: insights into the mechanism of hairpin formation, the 12/23 rule, and the coordination of double-strand breaks. *Mol. Cell. Biol.* 29, 5889–5899.
- Brandt, V.L., and Roth, D.B. (2009). Recent insights into the formation of RAG-induced chromosomal translocations. *Adv. Exp. Med. Biol.* 650, 32–45.
- Fanning, L., Connor, A., Baetz, K., Ramsden, D., and Wu, G.E. (1996). Mouse RSS spacer sequences affect the rate of V(D)J recombination. *Immunogenetics* 44, 146–150.
- Grundy, G.J., Ramón-Maiques, S., Dimitriadis, E.K., Kotova, S., Biertümpfel, C., Heymann, J.B., Steven, A.C., Gellert, M., and Yang, W. (2009). Initial stages of V(D)J recombination: the organization of RAG1/2 and RSS DNA in the post-cleavage complex. *Mol. Cell* 35, 217–227.
- Kim, M.S., Lapkouski, M., Yang, W., and Gellert, M. (2015). Crystal structure of the V(D)J recombinase RAG1-RAG2. *Nature* 518, 507–511.
- Lee, Y.N., Frugoni, F., Dobbs, K., Walter, J.E., Giliani, S., Gennery, A.R., Al-Herz, W., Haddad, E., LeDeist, F., Bleesing, J.H., et al. (2014). A systematic analysis of recombination activity and genotype-phenotype correlation in human recombination-activating gene 1 deficiency. *J. Allergy Clin. Immunol.* 133, 1099–1108.
- Lieber, M.R. (2010). The mechanism of double-strand DNA break repair by the nonhomologous DNA end-joining pathway. *Annu. Rev. Biochem.* 79, 181–211.
- Montaño, S.P., and Rice, P.A. (2011). Moving DNA around: DNA transposition and retroviral integration. *Curr. Opin. Struct. Biol.* 21, 370–378.
- Nikolov, D.B., Chen, H., Halay, E.D., Hoffman, A., Roeder, R.G., and Burley, S.K. (1996). Crystal structure of a human TATA box-binding protein/TATA element complex. *Proc. Natl. Acad. Sci. USA* 93, 4862–4867.
- Nowotny, M., Gaidamakov, S.A., Crouch, R.J., and Yang, W. (2005). Crystal structures of RNase H bound to an RNA/DNA hybrid: substrate specificity and metal-dependent catalysis. *Cell* 121, 1005–1016.
- Oettinger, M.A., Schatz, D.G., Gorka, C., and Baltimore, D. (1990). RAG-1 and RAG-2, adjacent genes that synergistically activate V(D)J recombination. *Science* 248, 1517–1523.
- Ramsden, D.A., Baetz, K., and Wu, G.E. (1994). Conservation of sequence in recombination signal sequence spacers. *Nucleic Acids Res.* 22, 1785–1796.
- Richardson, J.M., Colloms, S.D., Finnegan, D.J., and Walkinshaw, M.D. (2009). Molecular architecture of the Mos1 paired-end complex: the structural basis of DNA transposition in a eukaryote. *Cell* 138, 1096–1108.
- Schatz, D.G., and Swanson, P.C. (2011). V(D)J recombination: mechanisms of initiation. *Annu. Rev. Genet.* 45, 167–202.
- Schatz, D.G., Oettinger, M.A., and Baltimore, D. (1989). The V(D)J recombination activating gene, RAG-1. *Cell* 59, 1035–1048.
- Scheres, S.H. (2012). RELION: implementation of a Bayesian approach to cryo-EM structure determination. *J. Struct. Biol.* 180, 519–530.
- Shirakata, M., Hüppi, K., Usuda, S., Okazaki, K., Yoshida, K., and Sakano, H. (1991). HMG1-related DNA-binding protein isolated with V-(D)-J recombination signal probes. *Mol. Cell. Biol.* 11, 4528–4536.
- Stott, K., Tang, G.S., Lee, K.B., and Thomas, J.O. (2006). Structure of a complex of tandem HMG boxes and DNA. *J. Mol. Biol.* 360, 90–104.
- Tonegawa, S. (1983). Somatic generation of antibody diversity. *Nature* 302, 575–581.
- Yin, F.F., Bailey, S., Innis, C.A., Ciubotaru, M., Kamtekar, S., Steitz, T.A., and Schatz, D.G. (2009). Structure of the RAG1 nonamer binding domain with DNA reveals a dimer that mediates DNA synapsis. *Nat. Struct. Mol. Biol.* 16, 499–508.
- Zhang, Y., McCord, R.P., Ho, Y.J., Lajoie, B.R., Hildebrand, D.G., Simon, A.C., Becker, M.S., Alt, F.W., and Dekker, J. (2012). Spatial organization of the mouse genome and its role in recurrent chromosomal translocations. *Cell* 148, 908–921.

Htr2a-Expressing Cells in the Central Amygdala Control the Hierarchy between Innate and Learned Fear

Graphical Abstract



Authors

Tomoko Isosaka, Tomohiko Matsuo,
Takashi Yamaguchi, Kazuo Funabiki,
Shigetada Nakanishi, Reiko Kobayakawa,
Ko Kobayakawa

Correspondence

kobayakr@hirakata.kmu.ac.jp (R.K.),
kobayakk@hirakata.kmu.ac.jp (K.K.)

In Brief

The integration of innate and learned information processing is fundamental to controlling behavior. A population of serotonin 2A receptor-expressing cells in the central amygdala acts as a hierarchy generator by prioritizing innate over learned fear.

Highlights

- A hierarchical relationship exists between innate- and learned-fear responses
- Innate but not learned-fear stimuli suppress the activity of CeA Htr2a⁺ cells
- CeA Htr2a⁺ cell inhibition up/downregulates innate/learned freezing, respectively
- CeA Htr2a⁺ cells act as a hierarchy generator prioritizing innate over learned fear

Htr2a-Expressing Cells in the Central Amygdala Control the Hierarchy between Innate and Learned Fear

Tomoko Isosaka,^{1,2} Tomohiko Matsuo,^{1,2} Takashi Yamaguchi,³ Kazuo Funabiki,³ Shigetada Nakanishi,³ Reiko Kobayakawa,^{1,2,*} and Ko Kobayakawa^{1,2,*}

¹Institute of Biomedical Science, Kansai Medical University, Osaka 573-1010, Japan

²Department of Functional Neuroscience, Osaka Bioscience Institute, Osaka 565-0874, Japan

³Department of Systems Biology, Osaka Bioscience Institute, Osaka 565-0874, Japan

*Correspondence: kobayakr@hirakata.kmu.ac.jp (R.K.), kobayakk@hirakata.kmu.ac.jp (K.K.)

<http://dx.doi.org/10.1016/j.cell.2015.10.047>

SUMMARY

Fear is induced by innate and learned mechanisms involving separate pathways. Here, we used an olfactory-mediated innate-fear versus learned-fear paradigm to investigate how these pathways are integrated. Notably, prior presentation of innate-fear stimuli inhibited learned-freezing response, but not vice versa. Whole-brain mapping and pharmacological screening indicated that serotonin-2A receptor (Htr2a)-expressing cells in the central amygdala (CeA) control both innate and learned freezing, but in opposing directions. In vivo fiber photometry analyses in freely moving mice indicated that innate but not learned-fear stimuli suppressed the activity of Htr2a-expressing CeA cells. Artificial inactivation of these cells upregulated innate-freezing response and downregulated learned-freezing response. Thus, Htr2a-expressing CeA cells serve as a hierarchy generator, prioritizing innate fear over learned fear.

INTRODUCTION

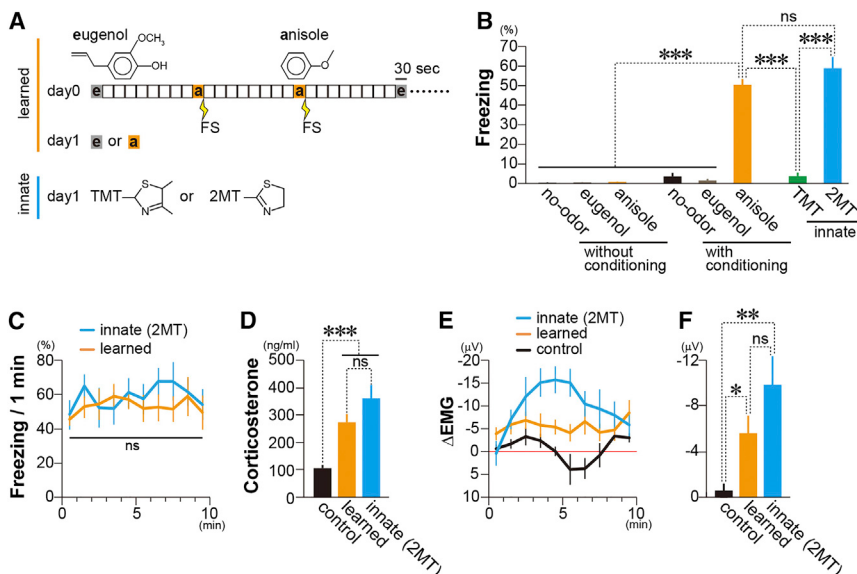
Behaviors are controlled by innate and learned mechanisms. How the brain determines the appropriate behavior when both innate and learned sensory inputs are simultaneously presented is of great interest. Fear is a powerful emotion that greatly influences behaviors across species and can be induced by both innate and learned sensory inputs (Gross and Canteras, 2012; LeDoux, 2012). Both types of fear can be experienced simultaneously, in situations such as exposure to dangerous natural environments, raising the possibility that the integration of information processed by innate- and learned-fear pathways contributes to the selection of appropriate behaviors to promote organism survival. However, the cellular and molecular mechanisms underlying this process are not clear.

Although various therapeutic interventions have been tested, a considerable number of people experience fear- and anxiety-related disorders, such as phobia, posttraumatic stress disorder,

and obsessive-compulsive disorder (Kessler et al., 2005; Dias et al., 2013). The pathogenesis and symptoms of these disorders are considered to be affected by innate and learned mechanisms (Rosen et al., 2008; Parsons and Ressler, 2013), but the precise contribution of each mechanism is still not understood. If innate and learned fears are controlled by synergistic mechanisms, administration of drugs that inhibit either fear mechanism is expected to alleviate advanced abnormal fear emotion. However, if both fears are controlled by antagonistic mechanisms, drugs that alleviate only one fear can aggravate the other fear, leading to paradoxical results. Thus, to formulate an effective drug discovery strategy, it is important to clarify the molecular targets that determine the relationship between innate and learned fears.

In mice, olfaction is the most important sensory system for detecting danger (Rottman and Snowdon, 1972; Apfelbach et al., 2005). Unlike other sensory systems, olfaction is unique in that different types of odorant molecules can induce either innate or learned-fear responses in mice. Thus, in this study, we focused on the olfactory system to clarify interaction mechanisms of innate- and learned-fear processing.

The amygdala is thought to be central to the mediation of both innate and learned fear. The amygdala consists of several subnuclei with distinct connections and functions. Like other sensory modalities, olfactory-mediated learned-fear information is conveyed to the lateral/basolateral amygdala (LA/BLA). Disruption of these nuclei affects learned-freezing behavior induced by olfaction (Cousens and Otto, 1998). Although it has not been reported for olfaction, auditory and visual conditioned information processed in the LA/BLA are then relayed to the CeA, which then regulates multiple fear responses (LeDoux, 2000; Davis, 2000; Maren and Quirk, 2004). 2,4,5-trimethyl-3-thiazoline (TMT) is a component of secretion products from the anogenital gland of foxes and induces innate-fear responses in mice through the main olfactory pathway (Vernet-Maury et al., 1984; Fendt et al., 2005; Kobayakawa et al., 2007). Presentation of TMT to mice upregulates the expression of immediate early genes (IEGs) in the medial amygdala (MeA) and the CeA (Day et al., 2004). Thus, among the subnuclei of the amygdala, the CeA is a candidate site involved in the interaction of olfactory-mediated innate- and learned-fear information. However, the cellular and molecular targets in the CeA underlying this interaction are not known.



(E and F) The temporal changes (E) and the mean (F) of delta neck electromyography (Δ EMG) are shown for control odor (a spice odor, eugenol), learned-freezing-inducing, and innate-freezing-inducing (2MT) odorants. The mean EMG value prior to odor presentation was set to 0. (B, D, and F) One-way ANOVA followed by Bonferroni correction. (C) Unpaired t test. Data are means \pm SEM. * p < 0.05; ** p < 0.01; *** p < 0.001; ns, p > 0.05.

To clarify the relationship and potential integration mechanisms between innate- and learned-fear information processing, we developed an olfactory-mediated innate-fear versus learned-fear paradigm and established an anatomical, molecular, and cellular framework for the integration of innate- versus learned-fear information.

RESULTS

Induction of Innate- and Learned-Freezing Behavior by Olfaction

Freezing is a characteristic behavior that is closely linked to fear in mice and other species. It can be measured as the ratio of immobile time during a test period and is widely used as a quantitative marker for fear in various experimental paradigms (Blanchard and Blanchard, 1969; Bouton and Bolles, 1980; Bolles and Fanselow, 1980). A learned-freezing response is easily induced by pairing a neutral odorant with electric foot shocks (Figures 1A and 1B). Although the odorant-mediated induction of a potent innate-freezing response, comparable to that induced in learned freezing, was previously considered difficult, we recently developed potent innate-freezing inducers termed thiazoline-related fear odors (tFOs) (Kobayakawa and Kobayakawa, 2011) that enabled us to overcome this challenge. TMT is a widely used odorant molecule that induces innate-fear responses in rodents (Fendt et al., 2005; Takahashi et al., 2005). However, the level of innate-freezing response it induces is extremely weak compared to that induced in the learned-fear condition (Figures 1A and 1B) (Morrow et al., 2000; McGregor et al., 2002). tFOs were developed by optimization of the chemical structure of TMT. From our tFO catalog, we selected 2-methyl-2-thiazoline (2MT), which induces a level of freezing comparable to that induced in the learned condition (Figures 1A and 1B).

First, we used several fear indices to confirm whether 2MT actually induces fear responses comparable to those induced in the learned-fear condition. There were no significant differences in temporal patterns between the two freezing behaviors (Figure 1C). In addition to inducing freezing behavior, increases in plasma concentration of stress hormones and decreases in neck electromyography are used as fear indices (Steenland and Zhuo, 2009; Armario et al., 2012). Again, no significant differences were observed between 2MT-induced innate-fear and learned-fear conditions in terms of these fear indices (Figures 1D–1F). From these results, we concluded that 2MT induces innate-fear responses that are comparable to the learned-fear condition in terms of behavioral and physiological aspects. Thus, utilizing 2MT enabled us to fulfill the ideal experimental conditions for comparing the nature of innate and learned fear, in which both fear responses are induced by the same sensory modality and accompanied by the same behavior.

The Innate-Fear Response Is Prioritized over the Learned-Fear Response

Even under high-risk conditions, where innate- and learned-fear signals exist simultaneously, starving wild animals have to keep exploring to find food for survival. We reconstructed similar situations using two different behavior tests and explored the mutual effects of innate- and learned-fear inputs on behavioral outputs (Figure 2). Mice were classified into three groups. Food pellets were placed at both ends of two isles of a Y-maze, and either an innate-fear-inducing odorant or a learned-fear-inducing odorant, which had previously been linked to electric foot shocks, was presented in one aisle for the first and second groups, respectively. Then, food-deprived mice were placed at the maze entrance. Under these conditions, eating behavior

Figure 1. Odor-Induced Innate- and Learned-Freezing Behavior

(A) Induction methods of innate- and learned-freezing responses. Learned freezing was induced as follows: On day 0, eugenol (e) or anisole (a) was randomly presented for 30 s with a 4 min interval, and at the end of anisole presentation, electric foot shocks (FS) were delivered to mice. On day 1, eugenol or anisole was presented to the mice. For induction of innate freezing, TMT or 2MT was presented on day 1.

(B) The mean percentage of time spent freezing is shown for the no-odor control, eugenol, and anisole, with or without conditioning, and for innate-fear-inducing odorants (TMT and 2MT). Anisole previously paired with foot shocks and 2MT presentation induced robust freezing behavior.

(C) Temporal analyses of 2MT-induced innate- and learned-freezing responses indicate that the two freezing behaviors are indistinguishable.

(D) The mean levels of plasma corticosterone induced by no-odor (control), learned-freezing-inducing, and innate-freezing-inducing (2MT) odorants.

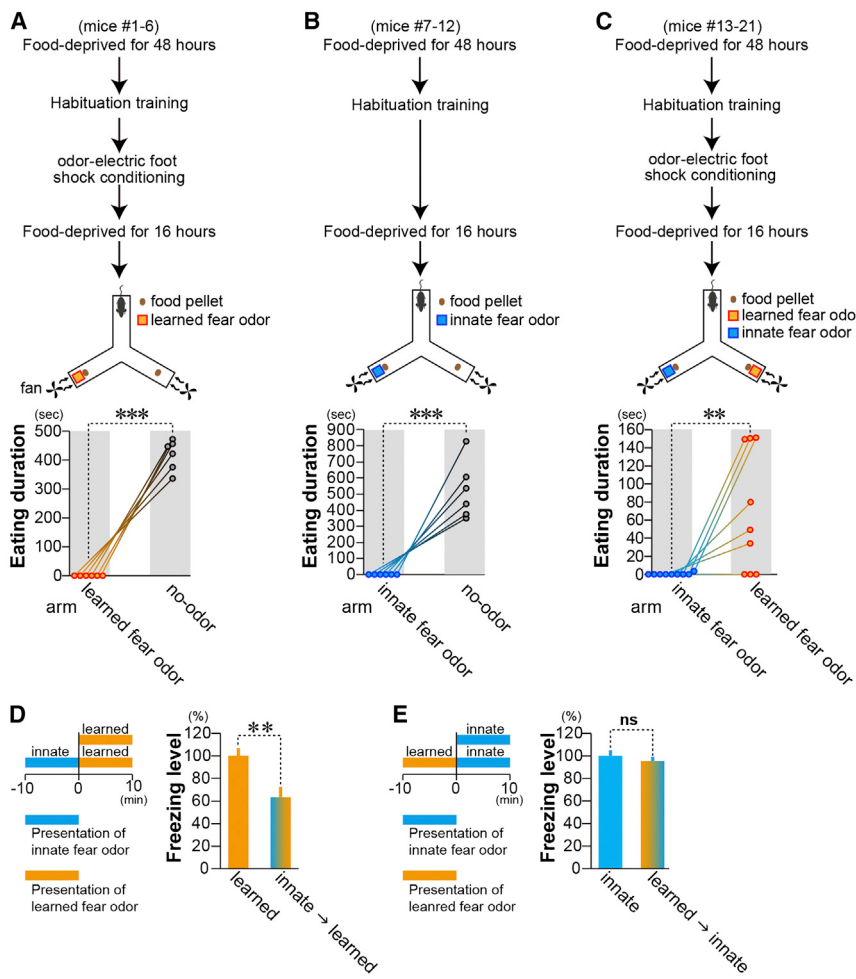


Figure 2. Hierarchical and Antagonistic Relationships between Innate- and Learned-Fear Responses

(A–C) Timelines of Y-maze experiments are shown in upper panels. Time spent eating by the individual mouse in each aisle is plotted (lower panels). Data points for the same individual are linked by a line.

(D and E) The mean percentages of time spent in learned freezing with and without prior induction of innate freezing (D) and spent in innate freezing with and without prior induction of learned freezing (E) are shown. The levels of freezing without prior induction of the other type of freezing were set at 100%. The experimental procedures are also shown in the left panels.

(A–C) Paired t test. (D and E) Unpaired t test. Data are means + SEM. **p < 0.01; ***p < 0.001; ns, p > 0.05.

Serotonin 2A Receptors in the Central Amygdala Have Opposite Effects on Innate and Learned Freezing

We next aimed to clarify the cellular and molecular bases of this hierarchical control mechanism. To identify candidate molecules involved in the hierarchical control of innate- and learned-freezing responses, various antipsychotropic agents that affect different neurotransmitter systems were injected intraperitoneally (IP) in mice, and their effects on innate- and learned-freezing responses were analyzed (Figure 3A).

Notably, injection of the atypical antipsychotic risperidone led to significantly downregulated learned freezing and significantly upregulated innate-freezing responses. The serotonin 2A receptor (Htr2a; Roth et al., 1998) is the major antagonistic target of risperidone, but the drug also affects the dopamine D2 receptor and other molecules, although with lower affinities (Binding DB: <http://bindingdb.org/bind/index.jsp>). Thus, we also analyzed the effects of IP injection of the Htr2a-selective antagonist glemserin (Dudley et al., 1988) and observed the same results as those induced by risperidone (Figure 3B). This indicates that Htr2a controls both innate and learned freezing, but in opposing directions.

Next, a putative interaction site for innate- and learned-fear pathways was selected by whole-brain activity mapping of innate and learned freezing using mRNA expression levels of the immediate-early genes (IEGs) *arc* and *c-fos* as neuronal activity markers. We found that IEG expression levels were markedly upregulated in several brain regions, including the amygdala, extended amygdala, lateral septum, and hypothalamus during both innate and learned freezing.

In this study, we focused on the amygdala because it is the area most implicated in the processing of fear (LeDoux, 2000; Maren and Quirk, 2004). The amygdala is subdivided into anatomically

was completely suppressed in mice in both aisles in which a fear-inducing odorant was presented but not in the odor-free aisle (Figures 2A and 2B). For the third group, the learned-fear-inducing odorant that had previously been linked to electric shocks was presented in one aisle and the innate-fear-inducing odorant was presented in the other. Under this condition, we observed eating behavior in the aisle where the learned-fear-inducing odorant was presented, but this behavior was almost fully suppressed in the aisle where the innate-fear-inducing odorant was presented (Figure 2C). These results indicate that innate fear is prioritized over learned fear, at least under this condition.

Our findings also suggest that innate-fear-inducing odorants might suppress learned-fear behavior. To examine this possibility, we analyzed the effects of the sequential presentation of innate- and learned-fear-inducing odorants. Interestingly, prior presentation of an innate-fear-inducing odorant significantly decreased the learned-freezing response (Figure 2D). Conversely, prior induction of learned freezing did not affect the innate-freezing response (Figure 2E). These results suggest that the behavioral response to the presence of innate- and learned-fear stimuli is controlled through a hierarchical relationship in which innate fear predominates.

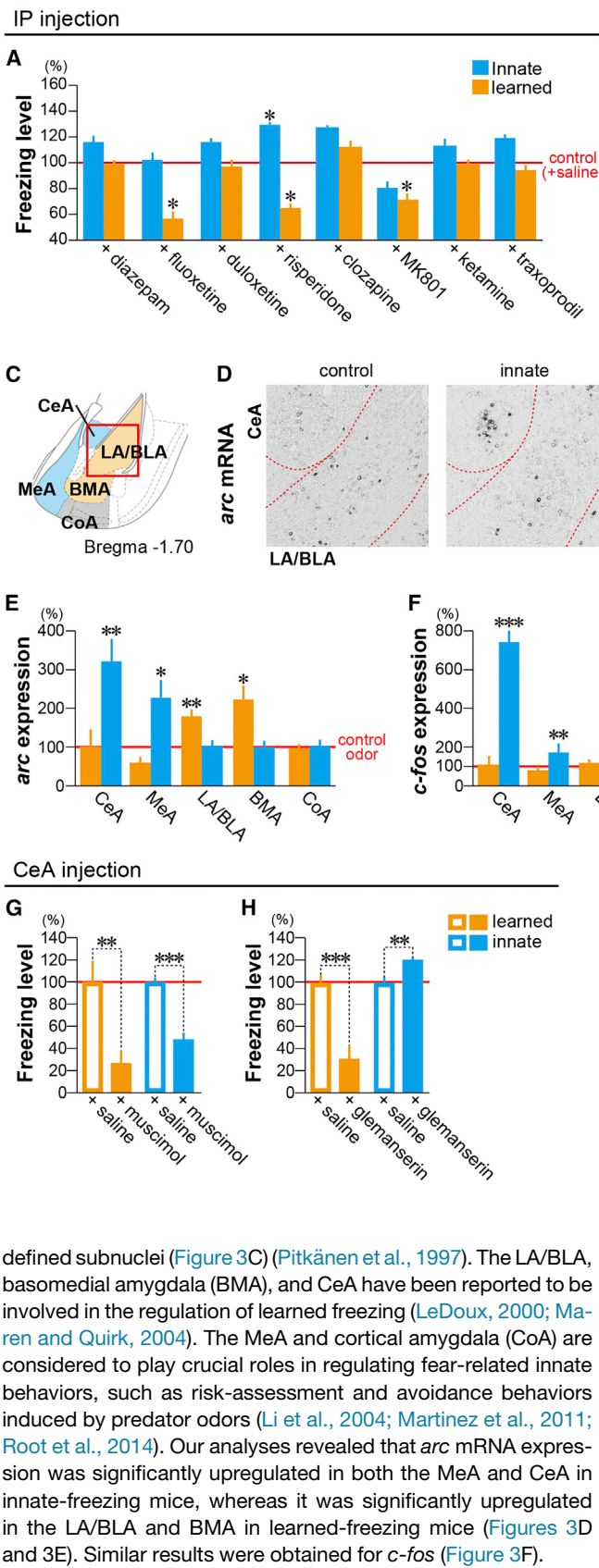


Figure 3. Screening for Molecules and Target Sites Involved in Differential Regulation of Innate and Learned Freezing

(A) The effect of intraperitoneal (IP) injection of psychotropics compared with that of saline (control value set at 100%) are shown for innate (blue) and learned (orange) freezing.

(B) The effect of IP injection of glemanserin compared with that of saline (control value set at 100%) is shown for innate (blue) and learned (orange) freezing.

(C) Schematic illustration of the structural organization of the amygdala. Blue and orange shaded areas represent areas in which *arc* mRNA was upregulated in the innate- and learned-freezing conditions, respectively.

(D) Representative images of *in situ* hybridization of *arc* mRNA following exposure to control, innate-, or learned-fear-inducing odorants. Scale bar, 200 μ m.

(E and F) Levels of *arc* (E) and *c-fos* (F) mRNA following exposure to innate (blue) and learned (orange) fear-inducing odorants, as compared to control odorant (control values set at 100%).

(G and H) The CeA was infused with muscimol (G) or glemanserin (H), and the freezing levels were compared to the level seen in saline-infusion controls (control values set at 100%) for innate (blue) and learned (orange) freezing.

(A) One-way ANOVA and unpaired t test. (B, G, and H) Unpaired t test. (E and F) One-way ANOVA followed by Bonferroni correction. Data are means + SEM. * $p < 0.05$; ** $p < 0.01$; *** $p < 0.001$. See also Figure S1.

Previous studies have also shown that IEGs are not upregulated in the CeA during the learned-freezing condition (Pezzone et al., 1992; Campeau et al., 1997). Nevertheless, it is widely accepted that the CeA regulates the expression of learned freezing (Medina et al., 2002). Electric ablation of the CeA decreases secretion of adrenocorticotrophic hormone (ACTH) that is induced by forced immobilization stress (Beaulieu et al., 1986) and decreases tone-enhanced excitability of the nictitating membrane response (Weisz et al., 1992). These results indicate that the CeA also contributes to the regulation of innate responses induced by various fear-related stimuli. In this study, we first confirmed the possibility that the CeA regulates both innate- and learned-freezing behavior induced by olfaction. Stereotaxic injection of muscimol, a gamma-aminobutyric acid (GABA)-A receptor agonist, into the CeA significantly downregulated both innate and learned freezing, indicating that the CeA is involved in controlling both behaviors (Figures 3G and S1A). This result suggests that the CeA potentially works as an integrator of odor-induced innate- and learned-fear information.

tating membrane response (Weisz et al., 1992). These results indicate that the CeA also contributes to the regulation of innate responses induced by various fear-related stimuli. In this study, we first confirmed the possibility that the CeA regulates both innate- and learned-freezing behavior induced by olfaction. Stereotaxic injection of muscimol, a gamma-aminobutyric acid (GABA)-A receptor agonist, into the CeA significantly downregulated both innate and learned freezing, indicating that the CeA is involved in controlling both behaviors (Figures 3G and S1A). This result suggests that the CeA potentially works as an integrator of odor-induced innate- and learned-fear information.

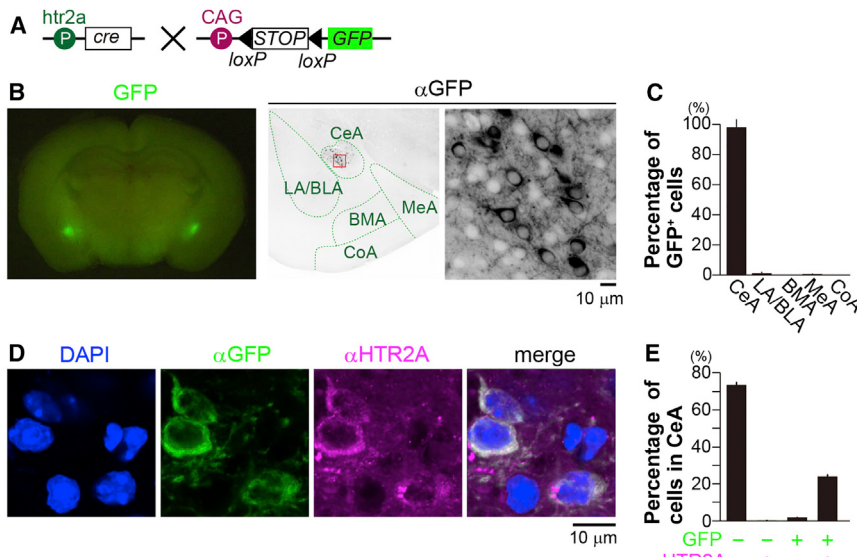


Figure 4. Expression Analysis of Cre in Htr2a-Cre BAC Transgenic Mice

(A) Strategy for selective labeling of CeA Htr2a⁺ cells using *Htr2a-Cre* and *floxed-GFP* mice. (B and C) Transgene expression, visualized by GFP immunofluorescent labeling, is shown (B). A low-magnification view is shown in the left panel. The area in the red box in the middle panel is enlarged in the right panel. The percentage of GFP⁺ cells in amygdala subnuclei is shown (C). (D and E) Transgene expression was compared with endogenous HTR2A expression detected by anti-HTR2A antibodies (D). Quantifications of the HTR2A[±] and GFP[±] cells are shown (E). Data are means + SEM. Scale bars, 10 μm. See also Figure S2.

Next, we analyzed the function of the Htr2a receptor in the CeA for induction of innate- and learned-freezing behavior. Stereotaxic injection of glemanserin into the CeA significantly downregulated the learned-freezing and upregulated the innate-freezing response (Figures 3H and S1B). This suggests the possibility that the CeA is one of the major target sites for the differential control of innate and learned freezing mediated by Htr2a. However, it is difficult to confirm that neuronal inactivation is limited to the CeA using pharmacological methods. To overcome this challenge, we utilized Cre/loxP technology to manipulate Htr2a-expressing cells in the CeA (CeA Htr2a⁺ cells).

Induction of Cre Gene Expression in CeA Htr2a⁺ Cells

In many biological contexts, Htr2a increases neural activities by coupling with Gq (Roth et al., 1998). Therefore, injection of glemanserin is likely to decrease the activity of Htr2a-expressing neurons. Thus, it is possible that inactivation of CeA Htr2a⁺ cells upregulates the innate-freezing response and downregulates the learned-freezing response. To test this hypothesis at the cellular level, we obtained *Htr2a-Cre* BAC transgenic mice (GENSAT, line KM208) in which Cre is selectively expressed in the CeA. We crossed *Htr2a-Cre* mice with floxed green fluorescent protein (GFP) mice to confirm Cre expression (Figure 4A). GFP signals were detected in the CeA, but not in the LA/BLA, BMA, MeA, or CoA (Figures 4B and 4C). GFP expression was compared with that of endogenous HTR2A using anti-HTR2A antibodies. Almost all GFP-positive cells were also HTR2A-positive, and almost all GFP-negative CeA cells were HTR2A-negative (Figures 4D and 4E). Therefore, Cre expression correctly recapitulated the pattern of endogenous Htr2a in the CeA. Detailed anatomical analyses indicated that CeA Htr2a⁺ cells were mainly located in the CeL, and the majority of these cells co-expressed somatostatin (SOM) but not protein kinase C-δ (PKCδ) (Figure S2).

Innate- but Not Learned-Fear Stimuli Suppress the Activity of CeA Htr2a⁺ Cells

To monitor the neuronal activity of CeA Htr2a⁺ cells in parallel with the behavioral

response in mice, *in vivo* photometry using a fiber-bundle probe was performed in freely moving mice (Goto et al., 2015). *Htr2a-Cre* mice were injected with a Cre-dependent adeno-associated virus (AAV) encoding GCaMP6. At 3 weeks after injection, a fiber-bundle probe was stereotactically implanted above the CeA to monitor the GCaMP6 signal in the CeA (Figures 5A and 5B). GCaMP6 transients were occasionally observed without odor presentation, but these were absent in mice without AAV infection (Figure 5C). GCaMP6 transients were significantly reduced in the innate-freezing condition compared to the no-odor condition, but they were not significantly changed in the learned-freezing condition (Figures 5C, 5D, 5F, and 5G). Freezing levels were not significantly different between the innate- and learned-fear conditions in the photometry sessions analyzed (Figure 5E), suggesting that the observed difference in GCaMP6 transients was not due to motion artifacts. Glemanserin administration reduced GCaMP6 transients (Figures 5H and 5I), confirming that neuronal activity in CeA Htr2a⁺ cells is controlled by Htr2a. These results, combined with our pharmacological analysis (Figure 3H), indicate that the activity of CeA Htr2a⁺ neurons is downregulated by innate-fear-inducing odors, which would result in upregulation of the innate-freezing response and downregulation of the learned-freezing response.

Pharmacogenetic and Optogenetic Regulation of CeA Htr2a⁺ Cells

To confirm the possibility described above, we utilized designer receptors exclusively activated by a designer drug (DREADD) (Alexander et al., 2009) to artificially control the activity of CeA Htr2a⁺ cells. A Cre-dependent AAV encoding hM3Dq (a chemogenetic activator) fused with mCherry (AAV-DIO-hM3Dq), or hM4Di (a chemogenetic silencer) fused with mCherry (AAV-DIO-hM4Di), was injected into the bilateral CeA of the *Htr2a-Cre* transgenic mice and control (*Htr2a-Cre*⁻) mice (Figure 6A). At 3 weeks after injection, the respective hM4Di-mCherry and hM3Dq-mCherry expression was detected in the CeA of

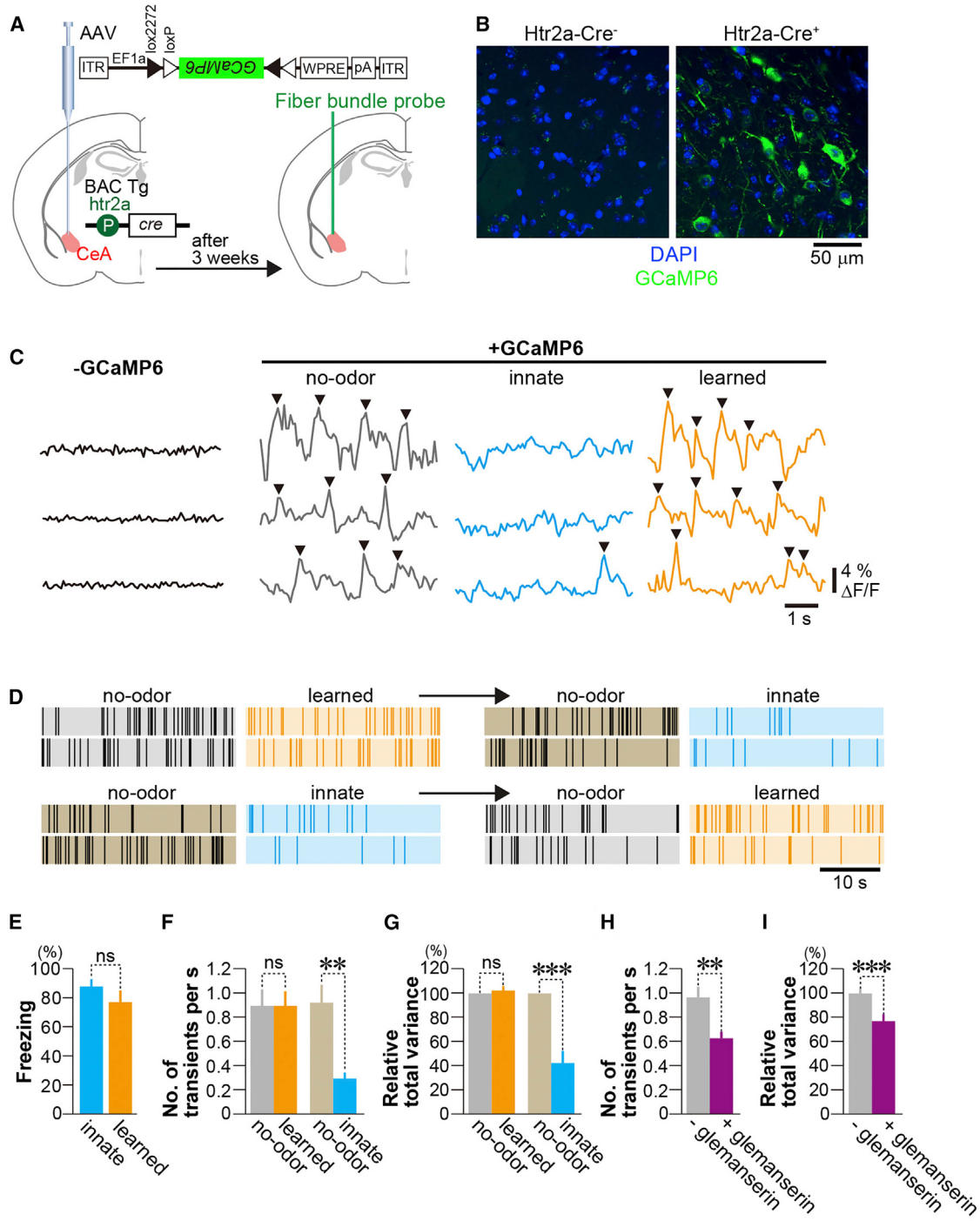


Figure 5. In Vivo Imaging of CeA Htr2a⁺ Cells in Freely Moving Mice

(A) Experimental design of in vivo fiber photometry assays.

(B) Representative images of GCaMP6 expression in the CeA of control (*Htr2a-Cre*⁻) and *Htr2a-Cre*⁺ mice are shown. GCaMP6 signals were detected only in the *Htr2a-Cre*⁺ mice. Scale bar, 50 μm.

(C) Examples of GCaMP6 fluorescence following exposure to innate- and learned-fear-inducing odorants. Mice without adeno-associated virus (AAV) infection (-GCaMP6) and no-odor control are also shown. Arrowheads indicate GCaMP transients that exceeded the arbitrary threshold (4% ΔF/F).

(D) Representative raster plots of GCaMP6 transients following exposure to innate- and learned-fear-inducing odorants. Two individuals first presented with the learned-fear-inducing odorant (upper panels) and two individuals first presented with the innate-fear-inducing odorant (lower panels) are shown.

(E) Levels of freezing during transient measurement induced by innate- and learned-fear-inducing odorants are shown.

(legend continued on next page)

Htr2a-Cre⁺ mice but not in that of *Htr2a-Cre⁻* mice (Figure 6B). In vivo photometry demonstrated that GCaMP6 transients in the CeA Htr2a⁺ cells were significantly reduced by IP injection of clozapine-N-oxide (CNO) in AAV-DIO-hM4Di-treated mice (Figure 6C), indicating that this treatment artificially downregulates the neuronal activity of CeA Htr2a⁺ cells as expected.

Following IP injection of CNO in AAV-DIO-hM4Di-treated mice, the innate-freezing response was significantly upregulated and the learned-freezing response was significantly downregulated in *Htr2a-Cre⁺* mice compared to *Htr2a-Cre⁻* mice (Figure 6D). These results are consistent with our pharmacological experiments (Figure 3H). On the other hand, IP injection of CNO into AAV-DIO-hM3Dq-treated mice significantly downregulated innate freezing but did not affect learned freezing (Figure 6E).

The opposing effects of CeA Htr2a⁺ cells on innate and learned freezing were further confirmed using optogenetic methods (Boyden et al., 2005). A Cre-dependent AAV encoding archaerhodopsin (eArch3.0) fused with enhanced yellow fluorescent protein (EYFP), or channelrhodopsin (hChR2(H134R)) fused with EYFP, was injected into the bilateral CeA of the *Htr2a-Cre* transgenic mice and control (*Htr2a-Cre⁻*) mice (Figure 6F). At 3 weeks after injection, eArch3.0-EYFP and hChR2-EYFP expressions were detected in the CeA of *Htr2a-Cre⁺* mice but not in that of *Htr2a-Cre⁻* mice (Figure 6G). Next, we investigated the effects on innate- and learned-freezing behaviors by optogenetic alteration of the activity of CeA Htr2a⁺ cells. Levels of odor-induced innate- and learned-freezing behaviors before and during light stimulation were compared. Following artificial inactivation of CeA Htr2a⁺ cells by light stimulation of eArch3.0, upregulation of the innate-freezing response and downregulation of the learned-freezing response in *Htr2a-Cre⁺* transgenic mice compared to *Htr2a-Cre⁻* mice were observed (Figure 6H). On the other hand, artificial activation of CeA Htr2a⁺ cells by light stimulation of ChR2 significantly downregulated innate freezing but did not affect learned freezing (Figure 6I). Our pharmacological, pharmacogenetic, and optogenetic analyses confirmed that artificial inactivation of CeA Htr2a⁺ cells upregulates innate freezing and, in parallel, downregulates learned freezing.

Unlike innate-fear-inducing odors, learned-fear-inducing odors did not influence CeA Htr2a⁺ cell activity (Figures 5F and 5G). Moreover, pharmacogenetic activation of hM3Dq as well as optogenetic stimulation of ChR2 in CeA Htr2a⁺ cells did not upregulate learned freezing; thus, hierarchical control between innate and learned freezing mediated by CeA Htr2a⁺ cells is asymmetric. This can contribute to stabilizing the one-way hierarchical control of innate-fear over learned-fear responses, which may determine the behavior of mice in dangerous situations.

We next confirmed whether CeA Htr2a⁺ cells actually contribute to regulation of the hierarchical relationship between the innate- and learned-fear responses, rather than just regulating innate- and learned-freezing behavior. As we have shown

in Figure 2D, prior presentation of innate-fear stimuli suppressed the learned-fear response. Presentation of innate-fear stimuli downregulated the activity of CeA Htr2a⁺ cells (Figures 5C, 5D, 5F, and 5G). If this inactivation contributes to determining the hierarchical relationship between innate and learned fear, artificial activation of CeA Htr2a⁺ cells during the presentation of innate-fear stimuli may affect the suppressing effect on learned-freezing behavior by prior presentation of innate-fear stimuli. To test this concept, CeA Htr2a⁺ cells were artificially activated by pharmacogenetic and optogenetic methods. Interestingly and importantly, artificial activation of CeA Htr2a⁺ cells by hM3Dq, as well as ChR2, clearly reversed the suppressing effect (Figures 6J and 6K). These results indicate that the effect of prior presentation of innate-fear stimuli on learned-fear responses can be bidirectionally controlled by CeA Htr2a⁺ cells. Thus, CeA Htr2a⁺ cells do not merely influence innate- and learned-fear responses in opposite directions but control the hierarchy and relationship between innate- and learned-fear responses.

Odor-Induced Innate- and Learned-Freezing Behaviors Are Regulated in Distinct Subnuclei in the Periaqueductal Gray

Opposite directional control of innate and learned freezing (upregulation of innate freezing in parallel with downregulation of learned freezing) may imply that both freezing behaviors are regulated by separate neuronal mechanisms. Learned-freezing behaviors are controlled by the ventral periaqueductal gray (vPAG) (LeDoux et al., 1988; De Oca et al., 1998; Vianna et al., 2001; Gross and Canteras, 2012; LeDoux, 2012). On the contrary, the dorsal periaqueductal gray (dPAG) regulates innate-avoidance and risk-assessment behaviors induced by presentation of predator animals (Aguiar and Guimarães, 2009; Sukikara et al., 2010; Silva et al., 2013). Furthermore, electrical stimulation of the dPAG induces freezing behavior (Vianna et al., 2001). Thus, it is possible that innate- and learned-freezing behaviors are separately controlled by the dPAG and vPAG, respectively. To confirm this possibility, induction of IEG expression in the PAG was analyzed in mice after induction of either innate- or learned-freezing behavior. In the dPAG, arc mRNA expression was significantly upregulated in the innate-freezing condition but not in the learned-freezing condition. In contrast, in the vPAG, c-fos mRNA expression was significantly upregulated in the learned-freezing condition but not in the innate-freezing condition (Figure S3). Stereotaxic injection of muscimol into the dPAG significantly downregulated innate-freezing behavior but not learned-freezing behavior (Figures S4A and S4B), whereas such an injection into the vPAG significantly downregulated learned-freezing behavior but not innate-freezing behavior (Figures S4C and S4D). These results indicate that odor-induced innate- and learned-freezing behaviors are separately controlled by the dPAG and vPAG, respectively.

We examined whether artificial inactivation of CeA Htr2a⁺ cells affects IEG expression in the dPAG and vPAG in parallel with

(F–I) Changes in GCaMP6 transients (F and H) and in the mean total variance in the trace of GCaMP transients (G and I) induced by innate- and learned-fear-inducing odors (F and G) and by IP injection of glemanserin (H and I) are shown. The mean total variances in control sessions (no-odor) prior to odor presentation were set at 100%.

(E–I) Unpaired t test. Data are means ± SEM. **p < 0.01; ***p < 0.001; ns, p > 0.05.

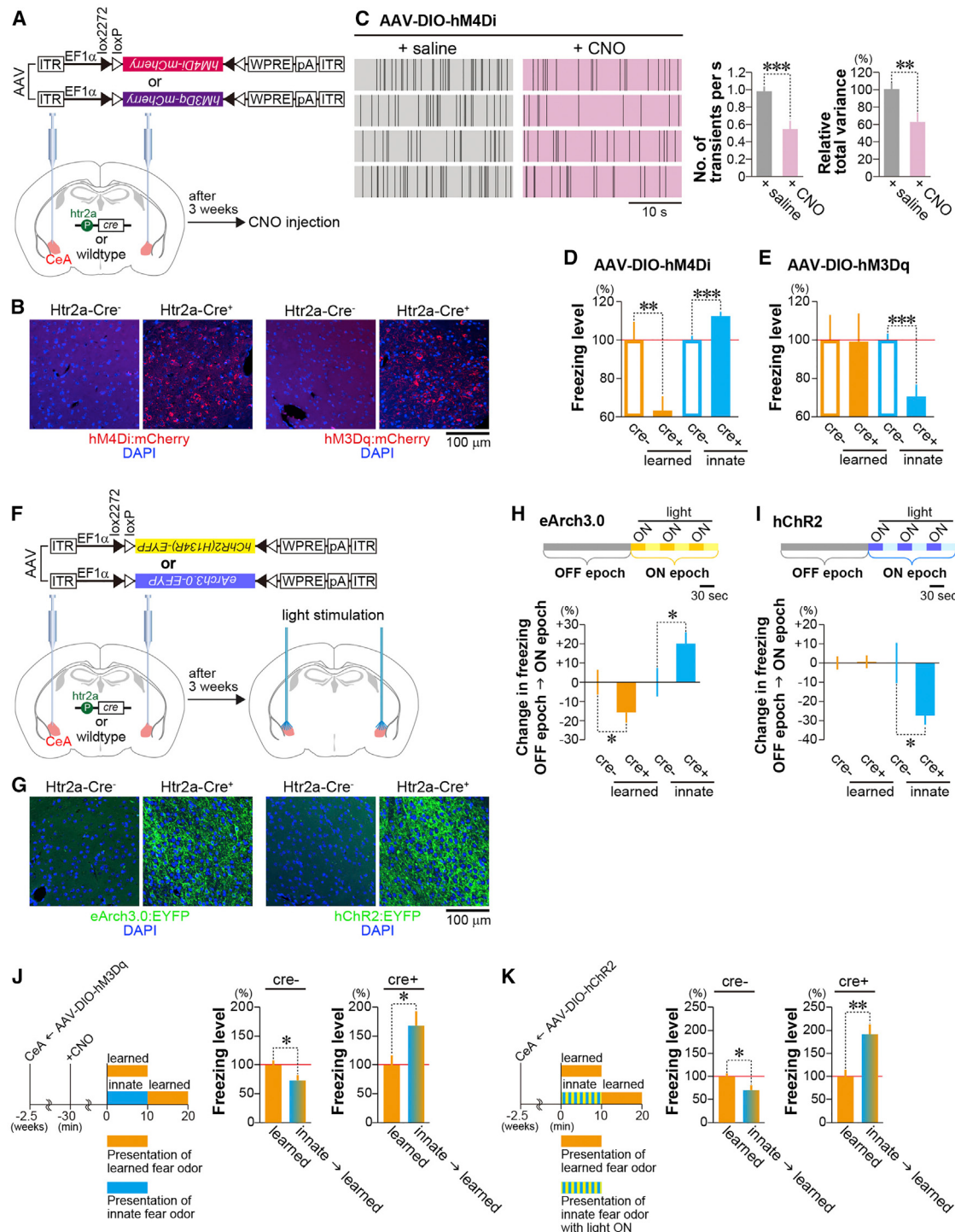


Figure 6. Chemogenetic and Optogenetic Manipulation of CeA Htr2a⁺ Cells

(A) Experimental design of the chemogenetic activation and silencing of CeA Htr2a⁺ cells.

(B) Representative images of hM4Di-mCherry and hM3Dq-mCherry expression in the CeA of control (*Htr2a-Cre*⁻) and *Htr2a-Cre*⁺ mice are shown.

(C) Representative raster plots (left), number of GCaMP6 transients (middle), and the mean total variance in the trace of GCaMP transients (right) induced by IP injection of saline and CNO in hM4Di-infected mice.

(D and E) Levels of freezing following exposure to innate- and learned-fear-inducing odors are shown for hM4Di inhibition (D) and hM3Dq activation (E). The mean percentage of freezing in control mice (cre⁻) following exposure to either the innate- or learned-fear-inducing odorant was set at 100%.

(F) Experimental design of the optogenetic activation and silencing of CeA Htr2a⁺ cells.

(legend continued on next page)

controlling innate- and learned-freezing behaviors in opposite directions (Figure 7A). Upregulation of *arc* expression in the dPAG induced by an innate-fear-inducing odorant was further increased by selective inhibition of CeA Htr2a⁺ cells using hM4Di. In contrast, upregulation of *c-fos* expression in the vPAG by a learned-fear-inducing odorant was inhibited by selective inhibition of CeA Htr2a⁺ cells using hM4Di (Figures 7B–7D).

Collectively, our results indicate that innate-fear-inducing odorants inactivate CeA Htr2a⁺ cells. Inactivation of these cells led to an increase of the innate-freezing response and IEG expression in the dPAG and a decrease of the learned-freezing response and IEG expression in the vPAG. Thus, CeA Htr2a⁺ cells regulate the antagonistic and hierarchical relationship between innate- and learned-freezing responses, in which the innate-freezing response predominates (Figure 7E).

Discussion

It is widely accepted that innate and learned fears are regulated by distinct neural pathways (Gross and Canteras, 2012; LeDoux, 2012), but potential interactions between these pathways are still unclear. In this study, we illustrated that innate-fear-inducing odorants suppress learned-fear response via the activity of CeA Htr2a⁺ cells. Although our finding of a hierarchical relationship between innate- and learned-fear responses was unexpected, this mechanism does seem advantageous for organism survival. It is conceivable that animals experience the two types of fear simultaneously in the natural environment and are forced to prioritize their response to one type of fear over the other (for example, when they have to explore dangerous environments for food). We modeled this scenario experimentally in this study as described in Figure 2C. Innate fear is induced by conserved dangers among species and is acquired over the course of evolution. In contrast, learned fear is acquired in response to an individual's fearful experiences and is therefore mutable. Thus, it is reasonable that innate fear has priority over learned fear if the risk levels of both fears are comparable, and our data support this idea.

The amygdala is proposed to work as a switchboard for separating innate- and learned-fear information into adjacent subnuclei connecting to different downstream pathways that induce distinct behavioral and physiological responses (Gross and Canteras, 2012; LeDoux, 2012). Contrary to this idea, we propose that the CeA works as an integrator for innate- and learned-fear information. It is widely accepted that the CeA contributes to the regulation of learned-freezing responses (LeDoux, 2000; Davis, 2000; Maren and Quirk, 2004); however, the function of the CeA in regulating innate-freezing responses has not been directly clarified. Our pharmacological, pharmacogenetic, and optogenetic experiments clearly show that CeA Htr2a⁺ cells

regulate the innate-freezing response. Moreover, we showed that CeA Htr2a⁺ cells regulate both innate- and learned-freezing responses, in opposite directions, which contributes to establishing the hierarchical relationship in which the innate-fear response predominates over the learned-fear response.

It has been reported that olfactory-mediated innate-fear information is conveyed to the MeA and CoA to regulate fear responses (Li et al., 2004; Martinez et al., 2011; Root et al., 2014). However, the pathway conveying olfactory information to the CeA is not known. In this study, we demonstrated that inactivation of CeA Htr2a⁺ cells by innate-fear information is a key process for determining the hierarchical relationship between innate- and learned-fear responses. To further confirm this idea, it is important to clarify the afferent pathway that conveys olfactory fear information to CeA Htr2a⁺ cells. We also demonstrated that innate- and learned-freezing responses are separately processed in the dPAG and vPAG, respectively. Artificial inactivation of CeA Htr2a⁺ cells inhibits upregulation of IEG expression in the vPAG induced by learned-fear odors, indicating that the vPAG is a downstream target of CeA Htr2a⁺ cells. However, in this study we did not clarify anatomical connections of the CeA Htr2a⁺ cells.

The majority of CeA Htr2a⁺ cells are located in the lateral subnucleus of the CeA (CeL) (Figure S2A). In the CeL, two distinct cell populations (SOM⁺ and PKC δ ⁺) have been reported to regulate learned-freezing behavior in opposing directions. Histological analyses indicated that the majority of CeA Htr2a⁺ cells were also SOM⁺ (Figure S2B). Inactivation of CeL SOM⁺ cells has been reported to downregulate learned-freezing behavior (Li et al., 2013). Thus, it is suggested that suppression of learned-freezing behavior by the CeL Htr2a⁺ cells is at least partly mediated by CeL SOM⁺ cells. We also clarified that a considerable number of *c-fos*⁺ cells induced by innate-fear input in the CeL were PKC δ ⁺ (Figure S2D). Inactivation of CeL PKC δ ⁺ cells has been reported to upregulate learned-freezing behavior, and, inversely, activation of these cells inhibits PAG-projecting CeM cells, which may then downregulate learned-freezing behavior (Haubensak et al., 2010). If this is the case, it is likely that innate-fear input suppresses learned-freezing behavior via activation of *c-fos*/PKC δ double-positive cells. In summary, suppression of learned-freezing behavior by innate-fear input may be mediated by two distinct cell populations (SOM⁺ and PKC δ ⁺) in the CeL, which are reported to regulate learned-freezing behavior (Figure S5).

The CeL PKC δ ⁺ cells connect with CeM PAG-projecting output neurons, whereas CeL SOM⁺ cells directly connect with the PAG (Haubensak et al., 2010; Penzo et al., 2014). These indirect and direct connections to the PAG may contribute to

(G) Representative images of eArch3.0-EYFP and hChR2-EYFP expression in the CeA of control (*Htr2a-Cre*⁻) and *Htr2a-Cre*⁺ mice are shown.

(H and I) Timelines of the experiments are shown in the upper panel. After odor presentation, freezing behavior in the 3 min light-OFF epoch and the subsequent light-ON epoch (3 times repeat of 30 s light ON, with 30 s interval) was measured. Delta freezing was calculated by subtracting freezing rate during light-OFF epochs from those during light-ON epoch. The mean delta freezing are indicated in bar graphs for eArch3.0 stimulation (H) and ChR2 stimulation (I). The mean delta freezing in control mice (*cre*⁻) was set at 0%.

(J and K) Timelines of the experiments are shown in the left panels. The mean percentages of time spent in learned freezing with and without prior induction of innate freezing were analyzed for hM3Dq (J) and ChR2 (K) activation of CeA Htr2a⁺ cells (*Htr2a-Cre*⁺) and control (*Htr2a-Cre*⁻). The levels of freezing without prior induction of innate freezing were set at 100%.

(C–E, and H–K) Unpaired t test. Data are presented as means + SEM. *p < 0.05; **p < 0.01; ***p < 0.001. Scale bars, 100 μ m.

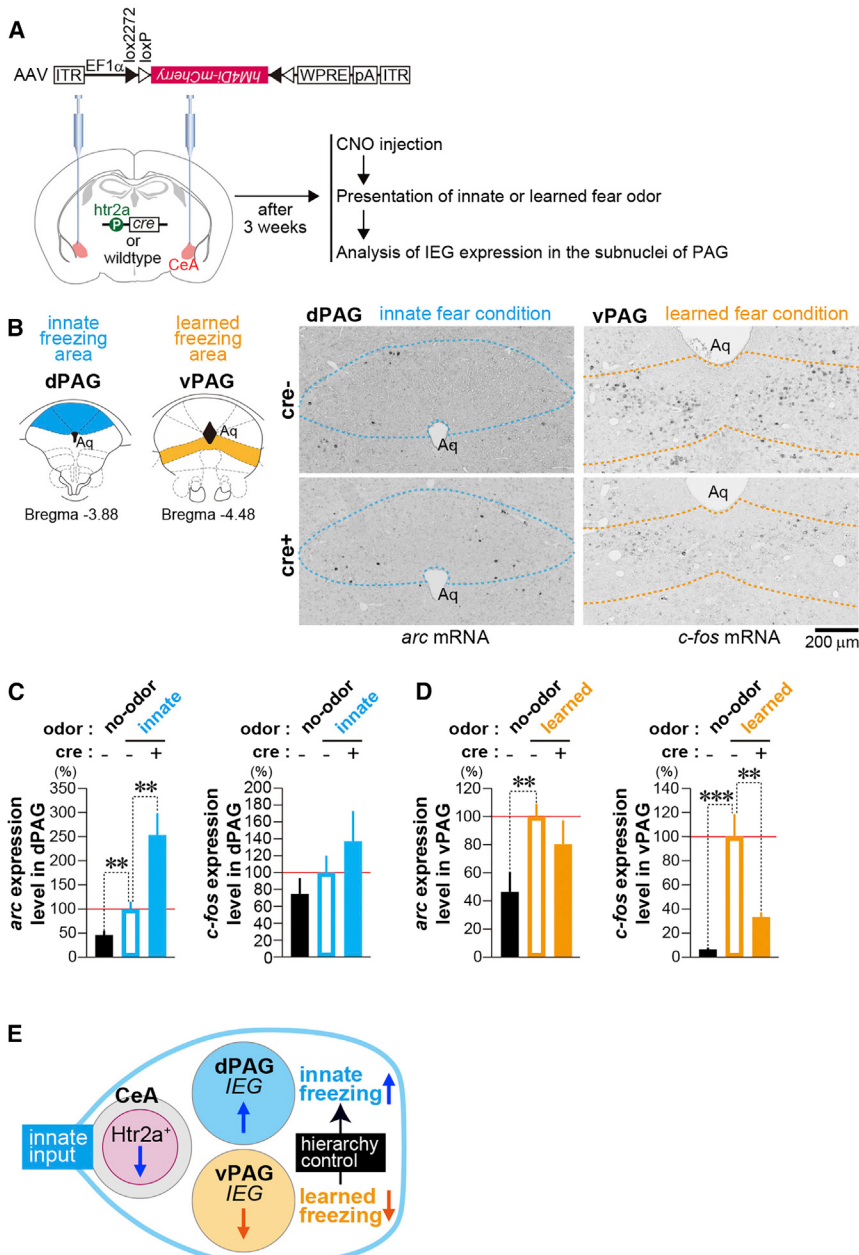


Figure 7. Effect of Artificial Inactivation of CeA Htr2a⁺ Cells on IEG Expression in the Subnuclei of the PAG

(A) Design of the experiment. At 3 weeks after injection of a cre-dependent AAV-encoding hM4Di-mCherry to the CeA, CNO was intraperitoneally injected, and IEG expression in the subnuclei of the PAG induced by innate- or learned-fear odors was analyzed.

(B) IEG expression in the dorsal PAG (dPAG, blue area) and ventral PAG (vPAG, orange area) was analyzed with and without artificial inactivation of CeA Htr2a⁺ cells following exposure to innate-fear-inducing and learned-fear-inducing odorants, respectively. Representative images of *arc* mRNA in the dPAG (left) and *c-fos* mRNA in the vPAG (right) following exposure to innate- and learned-fear-inducing odorants with (cre⁺) and without (cre⁻) hM4Di silencing of CeA Htr2a⁺ cells are shown. Scale bar, 200 μ m.

(C and D) Levels of *arc* and *c-fos* mRNA in the dPAG (C) and in the vPAG (D) compared to the no-odor control following exposure to innate-fear-inducing odorants (C) and learned-fear-inducing odorants (D) with (cre⁺) and without (cre⁻) hM4Di silencing of CeA Htr2a⁺ cells are shown. The levels of mRNA following exposure to innate-fear-inducing odorant (C) and learned-fear-inducing odorant (D) without hM4Di silencing were set at 100%.

(E) Model of hierarchical control of innate- and learned-freezing responses by CeA Htr2a⁺ cells. (C and D) One-way ANOVA followed by Bonferroni correction. Data are presented as means \pm SEM. **p < 0.01; ***p < 0.001. See also Figures S3 and S4.

suppress learned-freezing behavior by CeA Htr2a⁺ cells. We showed that the dPAG contributes to regulating odor-induced innate- but not learned-freezing behavior (Figures S3 and S4). Moreover, artificial inactivation of CeA Htr2a⁺ cells upregulated odor-induced innate-freezing behavior (Figures 6D and 6H) and *arc* mRNA expression in the dPAG (Figure 7C). These data suggest that CeA Htr2a⁺ cells control innate-freezing behavior through the dPAG. However, the anatomical connection between CeA Htr2a⁺ cells and dPAG is still unclear. Innate-fear responses are controlled by the medial amygdala-hypothalamus-dPAG pathway (Gross and Canteras, 2012). It may be possible that CeA Htr2a⁺ cells control innate-freezing behavior via this pathway.

The BLA is proposed to connect the processing of unconditioned stimuli (US) and conditioned stimuli (CS) (Le Doux, 2000; Davis, 2000; Maren and Quirk, 2004). US induce *c-fos* expression in the BLA, and these *c-fos*⁺ cells contribute to regulation of learned-freezing behavior (Gore et al., 2015). Thus, in the BLA, innate- and learned-fear circuits are synergistically integrated to form conditioned fear memory. In contrast, in the CeA, innate sensory inputs have an antagonistic effect on learned-fear responses to determine the behavioral hierarchy. Thus, there are two distinct modes for integration between innate- and learned-fear information processing: synergistic and antagonistic. These modes are separately regulated in the different subnuclei in the amygdala.

Our finding that innate fear affects learned fear antagonistically, but not synergistically, provides new insight not only for understanding the emotion of fear but also for the development of psychotropic medications. For instance, our data indicate that Htr2a antagonists, such as risperidone, which can alleviate learned fear, may in turn aggravate innate fear. Accordingly, our results suggest that it is important to dissect and analyze

the contribution of innate and learned systems in mental disorders and identify appropriate molecules for their treatment.

EXPERIMENTAL PROCEDURES

Mice

Male C57BL/6NCr mice were purchased from Japan SLC, Inc. The *Htr2a-Cre* BAC transgenic line (STOCK Tg[Htr2a-cre] KM208Gsat/Mmucl) was imported from the Mutant Mouse Regional Resource Center. Rosa-CAG-LSL-GCaMP3-WPRE mice (stock number 14538) were purchased from The Jackson Laboratory to monitor Cre recombination; these are referred to as *floxed-GFP* mice in this study. All animals were maintained on a 12 hr light–dark schedule (lights on at 7:00 a.m.) with food and water available ad libitum at the Osaka Bioscience Institute and Kansai Medical University animal house. Mice were 9–13 weeks old at the start of testing. All tests were performed between 9:00 a.m. and 7:00 p.m. The protocols used for all animal experiments in this study were approved by the Animal Research Committee of the Osaka Bioscience Institute and Kansai Medical University.

Viral Production

AAV expression vectors were created by subcloning GCaMP6 (Ohkura et al., 2012) into the Ascl-Nhel site of pAAV-EF1a-DIO-hChR2(C128S/D156A)-EYFP vector (Addgene #35503). The resulting AAV-EF1a-DIO-GCaMP6 construct was packaged and serotyped as described previously (Hikida et al., 2010). AAVs expressing hM4Di (AAV-EF1 α -DIO-hM4Di-mCherry), hM3Dq (AAV-EF1 α -DIO-hM3Dq-mCherry), ChR2 (AAV-EF1 α -DIO-hChR2(H134R)-eYFP), or Arch (AAV-EF1 α -DIO-eArch3.0 -eYFP) were obtained from the UNC Vector Core Facilities (Chapel Hill, NC, USA).

Freezing-Behavior Analysis

For analyses of freezing behavior induced by innate (2MT or TMT) or learned (anisole, previously paired with electric foot shocks) fear-inducing odors, mice were individually placed in a test cage (28 × 18 × 13.5 cm) and habituated for 10 min. Each subject received test odor presentations for 10 min. Each odorant (271 μ mol) was pipetted onto a filter paper (2 × 2 cm). For the no-odor control condition, a plain filter paper was presented.

Odor presentation was performed in the chemical fume hood. Mouse behavior was recorded and quantified using a video-based measurement system (Freeze Frame2, Actimetrics). The mice were considered to freeze if movement was not detected for 2 s.

Further methods, including behavioral assays, in vivo fiber photometry, and histological procedures, can be found in *Supplemental Experimental Procedures*.

SUPPLEMENTAL INFORMATION

Supplemental Information includes Supplemental Experimental Procedures and five figures and can be found with this article online at <http://dx.doi.org/10.1016/j.cell.2015.10.047>.

AUTHOR CONTRIBUTIONS

K.K. designed the experiments. T.I., R.K., and K.K. performed most of the experiments. T.M. performed most of the histological analyses. T.I., T.Y., K.F., and S.N. performed in vivo photometry. K.K., R.K., and T.I. analyzed the data. The manuscript was written by K.K., R.K., and T.I. All authors discussed the results and commented on the manuscript.

ACKNOWLEDGMENTS

We are grateful to F. Kato for critical comments on the manuscript. We are grateful to H. Tada and A. Kishi for many suggestions regarding the pharmacological analysis. We thank T. Kitsukawa for the *c-fos* plasmid. We thank H. Takebayashi for *jun-b*, *nr4a1*, *egr1*, *egr3*, *fosB*, *c-jun*, and *npas4* plasmids. We thank A. Teratani, N. Hayashi, T. Iida, and S. Kobayashi for technical assistance. This work was supported by the following foundations: the PRESTO

program of the Japan Science and Technology Agency; the Strategic Research Program for Brain Sciences of the Ministry of Education, Culture, Sports, Science, and Technology (MEXT) of Japan; the Program for Promotion of Basic and Applied Research for Innovations in Bio-oriented Industry; and the Takeda Science Foundation.

Received: April 3, 2015

Revised: August 3, 2015

Accepted: October 9, 2015

Published: November 19, 2015

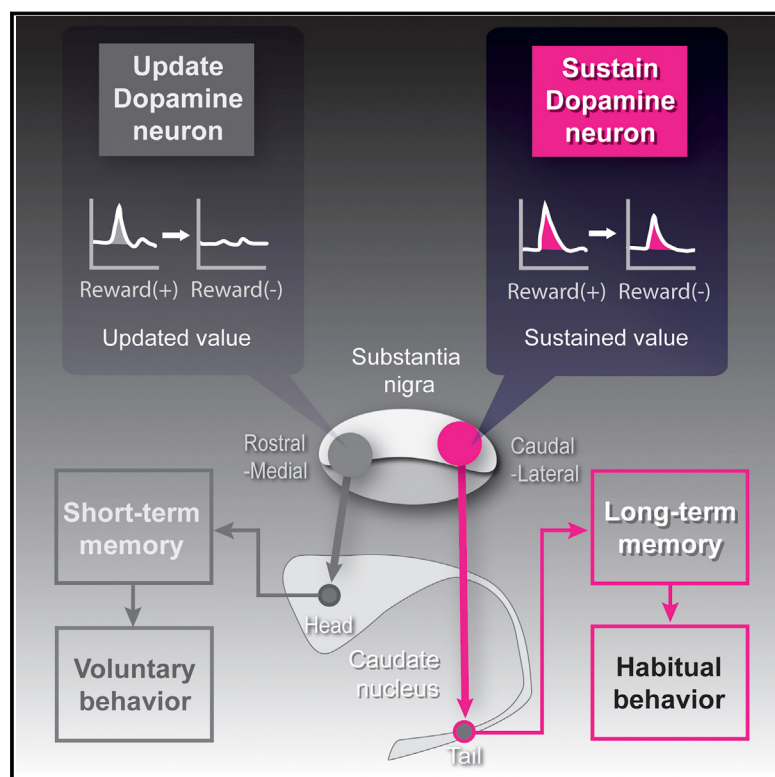
REFERENCES

- Aguiar, D.C., and Guimarães, F.S. (2009). Blockade of NMDA receptors and nitric oxide synthesis in the dorsolateral periaqueductal gray attenuates behavioral and cellular responses of rats exposed to a live predator. *J. Neurosci. Res.* 87, 2418–2429.
- Alexander, G.M., Rogan, S.C., Abbas, A.I., Armbruster, B.N., Pei, Y., Allen, J.A., Nonneman, R.J., Hartmann, J., Moy, S.S., Nicolelis, M.A., et al. (2009). Remote control of neuronal activity in transgenic mice expressing evolved G protein-coupled receptors. *Neuron* 63, 27–39.
- Apfelbach, R., Blanchard, C.D., Blanchard, R.J., Hayes, R.A., and McGregor, I.S. (2005). The effects of predator odors in mammalian prey species: a review of field and laboratory studies. *Neurosci. Biobehav. Rev.* 29, 1123–1144.
- Armario, A., Daviu, N., Muñoz-Abellán, C., Rabasa, C., Fuentes, S., Belda, X., Gagliano, H., and Nadal, R. (2012). What can we know from pituitary-adrenal hormones about the nature and consequences of exposure to emotional stressors? *Cell. Mol. Neurobiol.* 32, 749–758.
- Beaulieu, S., Di Paolo, T., and Barden, N. (1986). Control of ACTH secretion by the central nucleus of the amygdala: implication of the serotonergic system and its relevance to the glucocorticoid delayed negative feedback mechanism. *Neuroendocrinol.* 44, 247–254.
- Blanchard, R.J., and Blanchard, D.C. (1969). Passive and active reactions to fear-eliciting stimuli. *J. Comp. Physiol. Psychol.* 68, 129–135.
- Bolles, R.C., and Fanselow, M.S. (1980). A perceptual-defensive-recuperative model of fear and pain. *Behav. Brain Sci.* 3, 291–301.
- Bouton, M.E., and Bolles, R.C. (1980). Conditioned fear assessed by freezing and by the suppression of three different baselines. *Anim. Learn. Behav.* 8, 429–434.
- Boyden, E.S., Zhang, F., Bamberg, E., Nagel, G., and Deisseroth, K. (2005). Millisecond-timescale, genetically targeted optical control of neural activity. *Nat. Neurosci.* 8, 1263–1268.
- Campeau, S., Falls, W.A., Cullinan, W.E., Helmreich, D.L., Davis, M., and Watson, S.J. (1997). Elicitation and reduction of fear: behavioural and neuroendocrine indices and brain induction of the immediate-early gene *c-fos*. *Neuroscience* 78, 1087–1104.
- Cousens, G., and Otto, T. (1998). Both pre- and posttraining excitotoxic lesions of the basolateral amygdala abolish the expression of olfactory and contextual fear conditioning. *Behav. Neurosci.* 112, 1092–1103.
- Davis, M. (2000). The role of the amygdala in conditioned and unconditioned fear and anxiety. In *The Amygdala*, J.P. Aggleton, ed. (Oxford: Oxford University Press), pp. 213–288.
- Day, H.E., Masini, C.V., and Campeau, S. (2004). The pattern of brain *c-fos* mRNA induced by a component of fox odor, 2,5-dihydro-2,4,5-trimethylthiazoline (TMT), in rats, suggests both systemic and processive stress characteristics. *Brain Res.* 1025, 139–151.
- De Oca, B.M., DeCola, J.P., Maren, S., and Fanselow, M.S. (1998). Distinct regions of the periaqueductal gray are involved in the acquisition and expression of defensive responses. *J. Neurosci.* 18, 3426–3432.
- Dias, B.G., Banerjee, S.B., Goodman, J.V., and Ressler, K.J. (2013). Towards new approaches to disorders of fear and anxiety. *Curr. Opin. Neurobiol.* 23, 346–352.
- Dudley, M.W., Wiech, N.L., Miller, F.P., Carr, A.A., Cheng, H.C., Roebel, L.E., Doherty, N.S., Yamamura, H.I., Ursillo, R.C., and Palfreyman, M.G. (1988).

- Pharmacological effects of MDL 11,939: A selective, centrally acting antagonist of 5-HT₂ receptors. *Drug Dev. Res.* **13**, 29–43.
- Fendt, M., Endres, T., Lowry, C.A., Apfelbach, R., and McGregor, I.S. (2005). TMT-induced autonomic and behavioral changes and the neural basis of its processing. *Neurosci. Biobehav. Rev.* **29**, 1145–1156.
- Gore, F., Schwartz, E.C., Brangers, B.C., Aladi, S., Stujenske, J.M., Likhtik, E., Russo, M.J., Gordon, J.A., Salzman, C.D., and Axel, R. (2015). Neural representations of unconditioned stimuli in basolateral amygdala mediate innate and learned responses. *Cell* **162**, 134–145.
- Goto, A., Nakahara, I., Yamaguchi, T., Kamioka, Y., Sumiyama, K., Matsuda, M., Nakanishi, S., and Funabiki, K. (2015). Circuit-dependent striatal PKA and ERK signaling underlies rapid behavioral shift in mating reaction of male mice. *Proc. Natl. Acad. Sci. USA* **112**, 6718–6723.
- Gross, C.T., and Canteras, N.S. (2012). The many paths to fear. *Nat. Rev. Neurosci.* **13**, 651–658.
- Haubensak, W., Kunwar, P.S., Cai, H., Ciocchi, S., Wall, N.R., Ponnusamy, R., Biag, J., Dong, H.W., Deisseroth, K., Callaway, E.M., et al. (2010). Genetic dissection of an amygdala microcircuit that gates conditioned fear. *Nature* **468**, 270–276.
- Hikida, T., Kimura, K., Wada, N., Funabiki, K., and Nakanishi, S. (2010). Distinct roles of synaptic transmission in direct and indirect striatal pathways to reward and aversive behavior. *Neuron* **66**, 896–907.
- Kessler, R.C., Berglund, P., Demler, O., Jin, R., Merikangas, K.R., and Walters, E.E. (2005). Lifetime prevalence and age-of-onset distributions of DSM-IV disorders in the National Comorbidity Survey Replication. *Arch. Gen. Psychiatry* **62**, 593–602.
- Kobayakawa, K., and Kobayakawa, R. (2011). Animal Repellents. U.S. Patent WO 2011096575A1.
- Kobayakawa, K., Kobayakawa, R., Matsumoto, H., Oka, Y., Imai, T., Ikawa, M., Okabe, M., Ikeda, T., Itohara, S., Kikusui, T., et al. (2007). Innate versus learned odour processing in the mouse olfactory bulb. *Nature* **450**, 503–508.
- LeDoux, J.E. (2000). Emotion circuits in the brain. *Annu. Rev. Neurosci.* **23**, 155–184.
- LeDoux, J. (2012). Rethinking the emotional brain. *Neuron* **73**, 653–676.
- LeDoux, J.E., Iwata, J., Cicchetti, P., and Reis, D.J. (1988). Different projections of the central amygdaloid nucleus mediate autonomic and behavioral correlates of conditioned fear. *J. Neurosci.* **8**, 2517–2529.
- Li, C.I., Maglinao, T.L., and Takahashi, L.K. (2004). Medial amygdala modulation of predator odor-induced unconditioned fear in the rat. *Behav. Neurosci.* **118**, 324–332.
- Li, H., Penzo, M.A., Taniguchi, H., Kopec, C.D., Huang, Z.J., and Li, B. (2013). Experience-dependent modification of a central amygdala fear circuit. *Nat. Neurosci.* **16**, 332–339.
- Maren, S., and Quirk, G.J. (2004). Neuronal signalling of fear memory. *Nat. Rev. Neurosci.* **5**, 844–852.
- Martinez, R.C., Carvalho-Netto, E.F., Ribeiro-Barbosa, E.R., Baldo, M.V., and Canteras, N.S. (2011). Amygdalar roles during exposure to a live predator and to a predator-associated context. *Neuroscience* **172**, 314–328.
- McGregor, I.S., Schrama, L., Ambermoon, P., and Dielenberg, R.A. (2002). Not all ‘predator odours’ are equal: cat odour but not 2,4,5 trimethylthiazoline (TMT; fox odour) elicits specific defensive behaviours in rats. *Behav. Brain Res.* **129**, 1–16.
- Medina, J.F., Repa, J.C., Mauk, M.D., and LeDoux, J.E. (2002). Parallels between cerebellum- and amygdala-dependent conditioning. *Nat. Rev. Neurosci.* **3**, 122–131.
- Morgan, J.I., and Curran, T. (1991). Stimulus-transcription coupling in the nervous system: involvement of the inducible proto-oncogenes fos and jun. *Annu. Rev. Neurosci.* **14**, 421–451.
- Morrow, B.A., Redmond, A.J., Roth, R.H., and Elsworth, J.D. (2000). The predator odor, TMT, displays a unique, stress-like pattern of dopaminergic and endocrinological activation in the rat. *Brain Res.* **864**, 146–151.
- Ohkura, M., Sasaki, T., Sadakari, J., Gengyo-Ando, K., Kagawa-Nagamura, Y., Kobayashi, C., Ikegaya, Y., and Nakai, J. (2012). Genetically encoded green fluorescent Ca²⁺ indicators with improved detectability for neuronal Ca²⁺ signals. *PLoS ONE* **7**, e51286.
- Parsons, R.G., and Ressler, K.J. (2013). Implications of memory modulation for post-traumatic stress and fear disorders. *Nat. Neurosci.* **16**, 146–153.
- Penzo, M.A., Robert, V., and Li, B. (2014). Fear conditioning potentiates synaptic transmission onto long-range projection neurons in the lateral subdivision of central amygdala. *J. Neurosci.* **34**, 2432–2437.
- Pezzone, M.A., Lee, W.S., Hoffman, G.E., and Rabin, B.S. (1992). Induction of c-Fos immunoreactivity in the rat forebrain by conditioned and unconditioned aversive stimuli. *Brain Res.* **597**, 41–50.
- Pitkänen, A., Savander, V., and LeDoux, J.E. (1997). Organization of intra-amygdaloid circuitries in the rat: an emerging framework for understanding functions of the amygdala. *Trends Neurosci.* **20**, 517–523.
- Root, C.M., Denny, C.A., Hen, R., and Axel, R. (2014). The participation of cortical amygdala in innate, odour-driven behaviour. *Nature* **515**, 269–273.
- Rosen, J.B., Pagani, J.H., Rolla, K.L., and Davis, C. (2008). Analysis of behavioral constraints and the neuroanatomy of fear to the predator odor trimethylthiazoline: a model for animal phobias. *Neurosci. Biobehav. Rev.* **32**, 1267–1276.
- Roth, B.L., Willins, D.L., Kristiansen, K., and Kroese, W.K. (1998). 5-Hydroxytryptamine2-family receptors (5-hydroxytryptamine2A, 5-hydroxytryptamine2B, 5-hydroxytryptamine2C): where structure meets function. *Pharmacol. Ther.* **79**, 231–257.
- Rottman, S.J., and Snowdon, C.T. (1972). Demonstration and analysis of an alarm pheromone in mice. *J. Comp. Physiol. Psychol.* **81**, 483–490.
- Silva, B.A., Mattucci, C., Krzywkowski, P., Murana, E., Illarionova, A., Grinevich, V., Canteras, N.S., Ragozzino, D., and Gross, C.T. (2013). Independent hypothalamic circuits for social and predator fear. *Nat. Neurosci.* **16**, 1731–1733.
- Steenland, H.W., and Zhuo, M. (2009). Neck electromyography is an effective measure of fear behavior. *J. Neurosci. Methods* **177**, 355–360.
- Sukikara, M.H., Mota-Ortiz, S.R., Baldo, M.V., Felicio, L.F., and Canteras, N.S. (2010). The periaqueductal gray and its potential role in maternal behavior inhibition in response to predatory threats. *Behav. Brain Res.* **209**, 226–233.
- Takahashi, L.K., Nakashima, B.R., Hong, H., and Watanabe, K. (2005). The smell of danger: a behavioral and neural analysis of predator odor-induced fear. *Neurosci. Biobehav. Rev.* **29**, 1157–1167.
- Vernet-Maury, E., Polak, E.H., and Demael, A. (1984). Structure-activity relationship of stress-inducing odorants in the rat. *J. Chem. Ecol.* **10**, 1007–1018.
- Vianna, D.M., Graeff, F.G., Landeira-Fernandez, J., and Brandão, M.L. (2001). Lesion of the ventral periaqueductal gray reduces conditioned fear but does not change freezing induced by stimulation of the dorsal periaqueductal gray. *Learn. Mem.* **8**, 164–169.
- Weisz, D.J., Harden, D.G., and Xiang, Z. (1992). Effects of amygdala lesions on reflex facilitation and conditioned response acquisition during nictitating membrane response conditioning in rabbit. *Behav. Neurosci.* **106**, 262–273.

Dopamine Neurons Encoding Long-Term Memory of Object Value for Habitual Behavior

Graphical Abstract



Authors

Hyoung F. Kim, Ali Ghazizadeh, Okihide Hikosaka

Correspondence

hyoung.f.kim@gmail.com

In Brief

A population of dopamine neurons in the basal ganglia is involved in learning and sustaining habitual behavior in monkeys, providing a possible neural framework for the dysfunction in performing daily routines in Parkinson's disease.

Highlights

- Dopamine neurons with a unique function were found in monkey substantia nigra
- They retain past-learned reward values stably and promote habitual behavior
- This mechanism guides gaze and attention automatically to valuable objects
- The behavior is achieved by a local circuit between substantia nigra and caudate tail

Dopamine Neurons Encoding Long-Term Memory of Object Value for Habitual Behavior

Hyoung F. Kim,^{1,2,3,*} Ali Ghazizadeh,¹ and Okihide Hikosaka^{1,4}

¹Laboratory of Sensorimotor Research, National Eye Institute, National Institutes of Health, Bethesda, MD 20892, USA

²Center for Neuroscience Imaging Research (CNIR), Institute for Basic Science (IBS), Suwon 440-746, Republic of Korea

³Department of Biomedical Engineering, Sungkyunkwan University, Suwon 440-746, Republic of Korea

⁴Intramural Research Program, National Institute on Drug Abuse, National Institutes of Health, Bethesda, MD 20892, USA

*Correspondence: hyoung.f.kim@gmail.com

<http://dx.doi.org/10.1016/j.cell.2015.10.063>

SUMMARY

Dopamine neurons promote learning by processing recent changes in reward values, such that reward may be maximized. However, such a flexible signal is not suitable for habitual behaviors that are sustained regardless of recent changes in reward outcome. We discovered a type of dopamine neuron in the monkey substantia nigra pars compacta (SNc) that retains past learned reward values stably. After reward values of visual objects are learned, these neurons continue to respond differentially to the objects, even when reward is not expected. Responses are strengthened by repeated learning and are evoked upon presentation of the objects long after learning is completed. These “sustain-type” dopamine neurons are confined to the caudal-lateral SNc and project to the caudate tail, which encodes long-term value memories of visual objects and guides gaze automatically to stably valued objects. This population of dopamine neurons thus selectively promotes learning and retention of habitual behavior.

INTRODUCTION

Dopamine (DA) neurons are sensitive to reward value that is different from predicted, the signal often called reward prediction error (RPE) (Schultz et al., 1997). Positive or negative RPE is used to facilitate or inhibit, respectively, behavior associated with the reward until a desirable behavior is chosen (Sutton, 1988). However, reward-seeking behavior changes as it progresses. Initially, behavior changes flexibly depending on recent reward outcomes (goal-directed), but once a desirable pattern is acquired, it is maintained stably regardless of reward outcomes (habit) (Balleine and Dickinson, 1998; Graybiel, 2008; Seger and Spiering, 2011). The RPE-based DA signal would thus be suitable for acquiring goal-directed behavior but not for sustaining habits. Then, how can a habit be sustained?

It has been suggested that goal-directed behavior and habits are controlled by separate mechanisms, especially separate circuits in the basal ganglia: dorsomedial versus dorsolateral stria-

tum in rodents (Yin and Knowlton, 2006) and rostral versus caudal striatum in monkeys (Hikosaka et al., 1999) and humans (Balleine and O'Doherty, 2010; Lehéricy et al., 2005). Notably, all of these striatal areas are heavily innervated by DA neurons (Richfield et al., 1987). Furthermore, we recently found that a distinct group of DA neurons selectively project to the tail of the caudate nucleus (CDt), part of the caudal striatum, which has a critical role in habitual visual-oculomotor behavior (Fernandez-Ruiz et al., 2001; Kim and Hikosaka, 2013; Kim et al., 2014; Yamamoto et al., 2013).

This raises a question. Are the CDt-projecting DA neurons involved in habitual visual-oculomotor behavior? To answer this question, we let monkeys experience many visual objects in two contexts sequentially: (1) each object associated with a high or low reward value consistently and repeatedly (learning context), and (2) the same objects with no contingent reward feedback (habitual context). We found that a spatially localized group of DA neurons acquired object value signals without encoding RPE in the learning context and then continued to respond to the objects differentially by their past-learned values in the habitual context. These DA neurons projected to CDt, suggesting that they play a critical role in learning and sustaining habitual visual-oculomotor behavior.

RESULTS

Habitual Visual-Oculomotor Behavior Caused by Object-Value Learning

We used computer-generated fractals for experimental objects, half of them associated with a reward (high-valued) and the other half with no reward (low-valued) (Figure 1A). Our experiments consisted of two steps: (1) object-reward association (learning), and (2) behavior and neuronal encoding of object values (testing) (Figure 1B). In the learning procedure, the monkey made a saccade to the presented object, which was followed by a liquid reward or no reward depending on the presented object (Figure 1C). In each learning session, the object was chosen pseudo-randomly from a set of eight objects (each row in Figure 1A). Monkeys developed the difference in target acquisition time gradually across the trials in the first learning session (Figure 1D), indicating that the saccade was controlled by the expected reward outcome.

To test habitual behavior, we let the monkey freely look at the value-learned objects with no reward outcome (free viewing

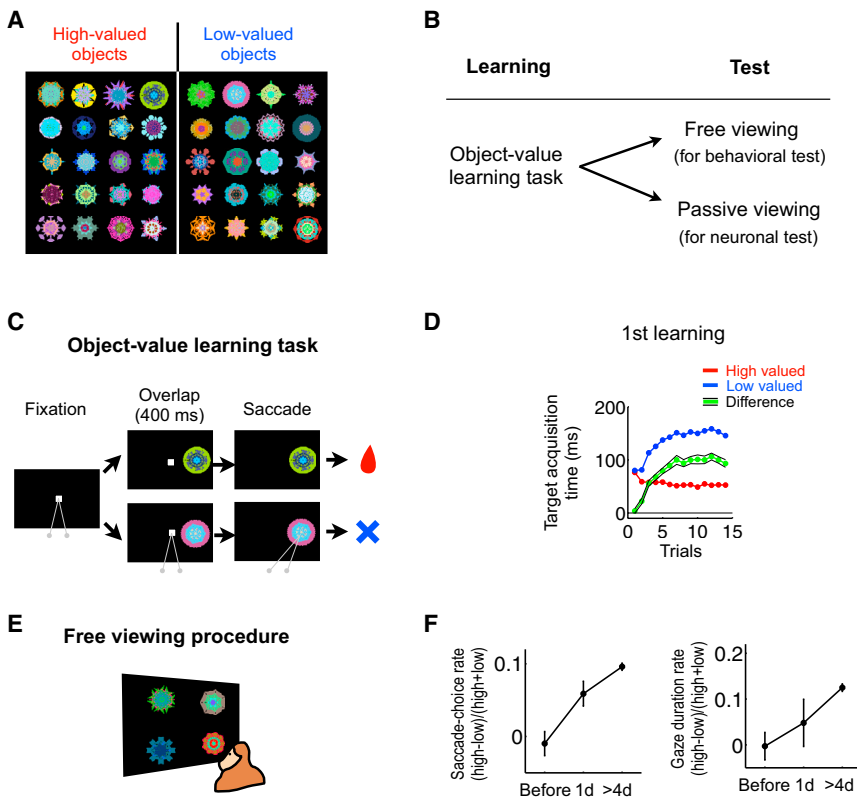


Figure 1. Object-Value Learning and Habitual Visual-Oculomotor Behavior

(A) Fractal objects, each consistently associated with a reward (high-valued) or no reward (low valued). Monkey PK and DW learned 440 and 840 fractals respectively, among which 56 and 376 were long-term learned (>4 days).

(B) Learning and testing procedures.

(C) Object-value learning task. A fractal object was presented at a neurons' preferred position, and the monkey made a saccade to it after the central fixation dot turned off. This was followed by a reward if the object was high-valued (top) or no reward if the object was low-valued (bottom). A set of eight objects (as in A) was used in each learning session.

(D) Behavioral changes during learning. Mean target acquisition time (time after the fixation dot disappeared until the gaze reached the object) is plotted against the number of trials for each object during the first learning ($n = 107$). Data are shown separately for high-valued objects (red) and low-valued objects (blue). Green line indicates the difference of target acquisition time between the high- and low-valued objects (mean \pm SE).

(E) Free viewing procedure to test behavioral changes after learning. Four fractal objects among one set of eight objects were chosen pseudorandomly and presented simultaneously. Monkeys were free to look at the objects (or look elsewhere) for 2 s without reward feedback.

(F) Increase in gaze bias during free viewing after repeated learning. The saccade-choice rate (left) and gazing duration rate (right) are plotted before learning (before, $n = 42$); after 1 day learning (1d, $n = 22$); after more than 4 days learning (>4d, $n = 316$). See also Figure S1.

procedure) (Figure 1E). When the previously learned objects were presented, monkeys looked at high-valued objects more frequently with longer durations than low-valued objects, even though no reward was given. The gaze bias became stronger after repeated learning (Figure 1F). Once established, the gaze bias occurred each time the free viewing was tested without further learning, confirming previous studies (Kim and Hikosaka, 2013; Yasuda et al., 2012). Although the gaze bias declined initially, it showed no further decrease, even though monkeys viewed the learned objects many times without contingent reward outcomes (i.e., free viewing or passive viewing) (Figure S1). This extinction-resistant gaze bias would be regarded as a habitual visual-oculomotor behavior, although we did not apply “devaluation,” a common procedure to characterize habits (Balleine and Dickinson, 1998).

Two Types of Dopamine Neurons Updating and Sustaining Object Values

To test if DA neurons encode object values habitually, we recorded from presumed DA neurons in SNc during the two steps: learning and testing (Figure 1B). Figure 2 shows the activity of two example neurons. They fired slowly with long duration spikes (Figures 2C and 2F), which is distinct from GABAergic neurons in the substantia nigra pars reticulata (SNr) (Schultz, 1986). As the first step (learning), we recorded their activity while the monkey

was looking at novel fractal objects with or without reward (Figures 2A, 2C, and 2F). Both neurons responded to these objects differentially, more excited by high-valued objects (Figures 2D and 2G), consistent with previous reports (Tobler et al., 2005). Such value-differential responses developed gradually (Figures S2A and S2C), as the difference in target acquisition time developed (Figure 1D).

However, the two neurons behaved differently in the second step (testing). The learned objects were presented sequentially while the monkey was fixating at the center (passive viewing task, Figure 2B). Unlike the learning procedure, each object presentation induced no increase or decrease of the expected reward value. Neuron #1 stopped responding to the previously learned objects (Figure 2E), reflecting the lack of reward contingency. In contrast, neuron #2 continued to respond to the objects differentially (Figure 2H). In short, neuron #1 updated object values flexibly based on immediate reward expectation (update-type), whereas neuron #2 sustained object values stably based on past experience (sustain-type).

We recorded activity of 133 presumed DA neurons and found 69 neurons that encoded object values in two monkeys. In the passive viewing task, 45 neurons showed value-differential responses (sustain-type), and 24 neurons showed no response (update-type) ($p < 0.05$, Wilcoxon rank-sum test). Their average activity is shown in Figure 3.

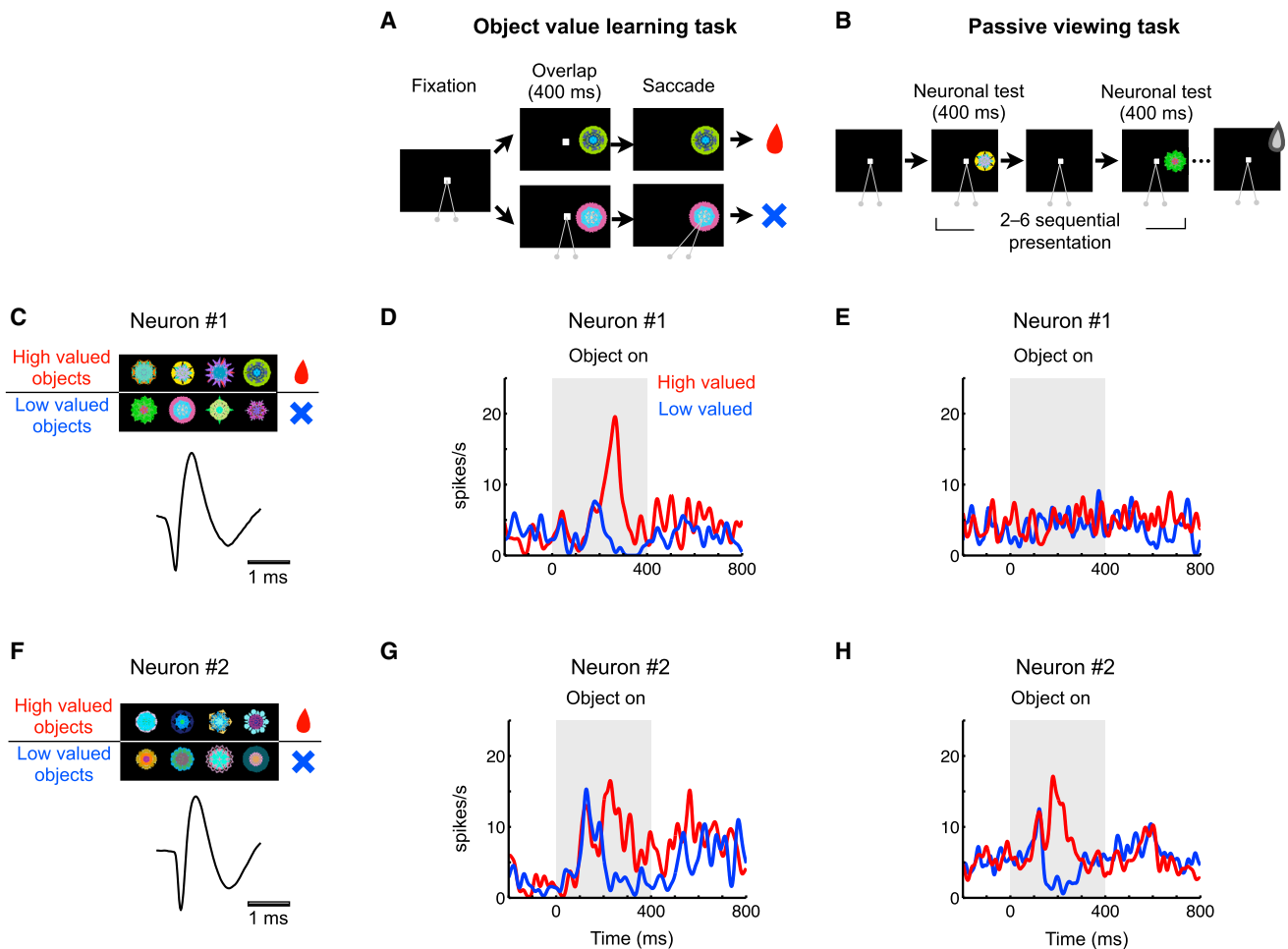


Figure 2. Neuronal Coding of Object Values during Learning and Post-Learning

Responses of two presumed DA neurons in SNc are shown during learning (object-value learning task) and post-learning (passive viewing procedure). (A) Object-value learning task (see Figure 1C).

(B) Passive viewing task. The learned objects were presented sequentially in the neuron's preferred location, while the monkey was fixating at the center. A reward was delivered non-contingently with the presented objects.

(C–E) Responses of neuron #1 (spike shape shown in C, bottom) to eight objects (shown in C, top) during the first object learning task (D), followed by the passive viewing task (E). Average activity (shown by spike density functions [SDFs]) is aligned at the onset of object presentation.

(F–H) Responses of neuron #2 in the same format.

See also Figure S2.

In order to examine the learning/memory process of these neurons, we repeated the object-value learning and passive viewing task across daily sessions. Update-type neurons continued to be non-responsive in the passive viewing task even after extensive long-term learning (greater than four daily sessions) (Figure 3E, top). In contrast, sustain-type neurons continued to be responsive in the passive viewing task (Figures 3C and 3E, bottom), and their responses were enhanced after repeated learning (Figure 3F), together with the development of the gaze bias during free viewing (Figure 1F). Their value discrimination remained robust many days after the last learning (Figure 3G, >4 days). The retention of the object-value response was affected by the amount of learning: no decrease after >4 days learning (Figure 3G, solid magenta lines); some

decrease after 1 day learning (Figure 3G, hatched magenta lines). Importantly, during the retention period, the monkeys viewed the learned objects many times without contingent reward outcomes (i.e., free viewing or passive viewing), yet sustain-type neurons showed no significant decrease in the object-value response (Figures S2E–S2G). These results suggest that sustain-type neurons contribute to the acquisition and retention of habitual visual-oculomotor behavior.

Update- and sustain-type neurons also had different sensitivities to reward itself. In the first trial of the first learning procedure when the reward outcome was unpredictable, update-type neurons were excited more strongly to reward than to no reward (Figures 4A, top, and S2B), whereas sustain-type neurons showed variable responses and overall no discrimination

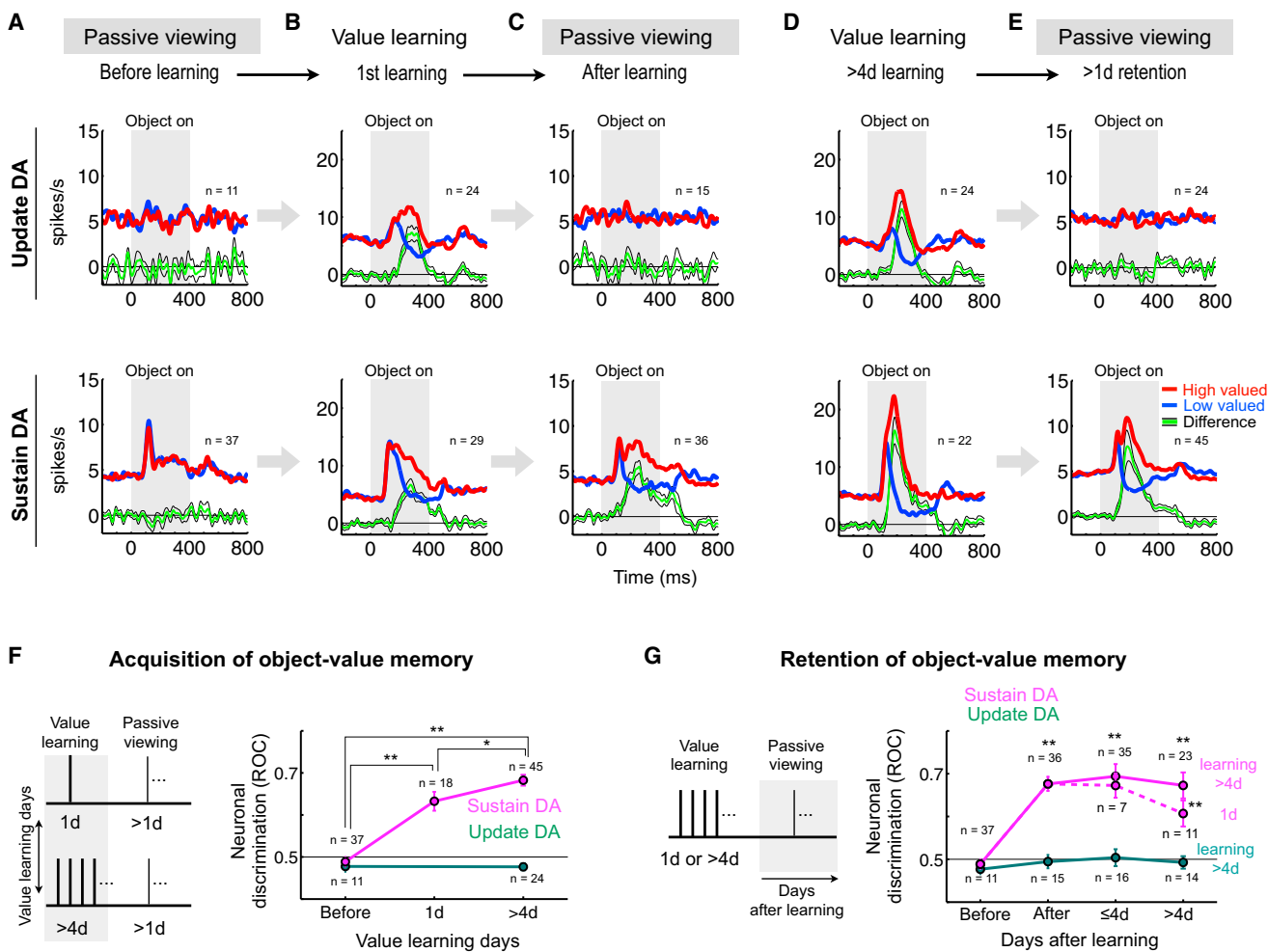


Figure 3. Distinct Patterns of Object Value Responses in Two Types of Presumed DA Neurons

(A–E) Average activity (shown by SDFs) of update-type DA neurons (top) and sustain-type DA neurons (bottom). Responses to novel objects during three steps: passive viewing (A), object value learning (B), and passive viewing (C). Responses to well learned objects (>4 days) during relearning (D) and passive viewing after >1 day retention (E). Green line indicates the difference between the high- and low-valued object responses (mean \pm SE). The number of neurons examined (n) is shown in each graph.

(F) Increase in value discrimination by repeated learning. Neuronal discrimination between high-and low-valued objects in passive viewing task (measured as ROC area, mean \pm SE) is plotted before learning (before), after 1 day learning (1d), and after more than 4 days learning (>4d). The number of neurons examined (n) is shown at each data point. *p < 0.05, **p < 0.01, ***p < 0.001 by Wilcoxon rank-sum test.

(G) Retention of value discrimination after learning. Neuronal discrimination in passive viewing task is plotted before learning (before), immediately after learning (after), 1–4 days after learning (≤ 4 d), and >4 days after learning (>4d). For sustain-type DA neurons, data are separated by the number of learning: 1 day learning (dashed line, 1d) and more than 4 days learning (solid line, >4d). The number of neurons examined (n) is shown at each data point. *p < 0.05, **p < 0.01, ***p < 0.001 by Wilcoxon rank-sum test.

See also Figures S2, S3, and S6.

(Figures 4A, bottom, and S2D). This reward response in update-type neurons disappeared in less than three trials as the reward became predictable (Figure S2B). These data suggest that update-type neurons encode RPE signals and therefore are suitable for goal-directed behavior but not for sustaining habitual behavior. In contrast, sustain-type neurons may be more suitable for habitual behavior.

These suggestions were supported by another object-value association task in which two objects reversed their values frequently (Figure S3A). Update-type neurons reversed their responses quickly and clearly following the object value reversal

(Figure S3B). In contrast, sustain-type neurons started showing value-biased responses slowly and weakly (Figure S3C). Overall, neurons showing stronger value-biased responses in the passive viewing task tended to show weaker value-biased responses in the reversal task (Figure S3F). The response to the unexpected reward outcome occurred in update-type neurons (Figure S3D), but not sustain-type neurons (Figure S3E), confirming the data in the learning procedure (Figure 4A).

Interestingly, most sustain-type neurons (29/38, 77%) responded more strongly to visual objects presented in the contralateral than ipsilateral field (p < 0.05, Wilcoxon rank-sum test)

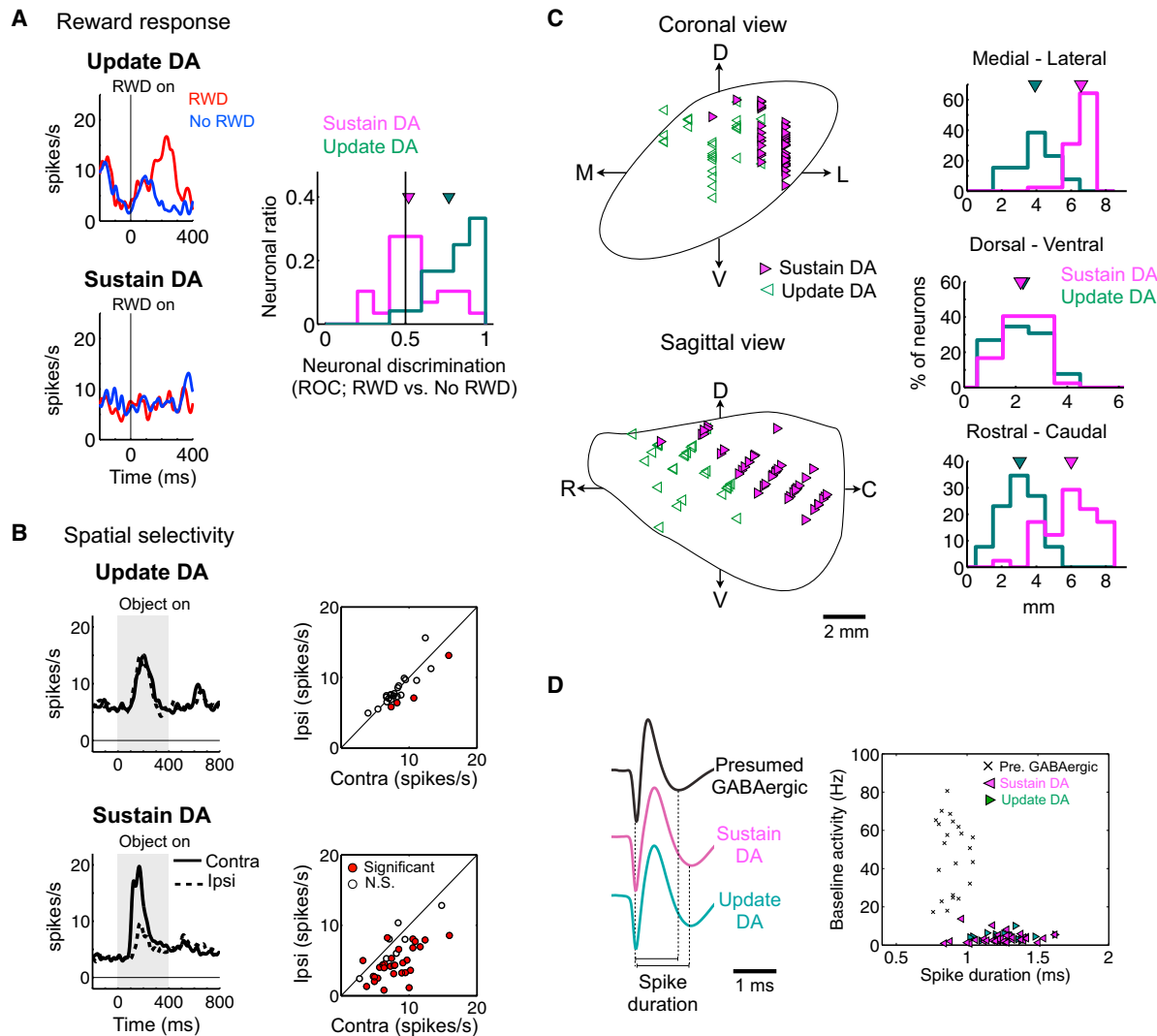


Figure 4. Differences and Similarities of Update- and Sustain-type DA Neurons

(A) Response to the unpredicted reward outcome. Data were collected only for the first trial of each object in object value learning and are shown as average SDFs (left) and individual neuronal discrimination (right) for update-type DA neurons ($n = 24$) and sustain-type DA neurons ($n = 29$). The mean neuronal discrimination (indicated by triangle, calculated as ROC area) was significantly higher than 0.5 (i.e., no discrimination) for sustain-type DA neurons (ROC = 0.78), but not for update-type DA neurons (ROC = 0.53) ($p < 0.001$, Wilcoxon rank-sum test).

(B) Spatial selectivity of visual response. This was tested for update-type DA neurons (top, $n = 24$) and sustain-type DA neurons (bottom, $n = 39$) by ipsilateral and contralateral object presentations. Data are shown by averaged SDFs (left) (dashed line: ipsilateral, solid line: contralateral). In scatterplots (right), each data point indicates the responses of each neuron to ipsilateral (ordinate) and contralateral (abscissa) objects. Red dots indicate neurons whose spatial selectivity is statistically significant (Wilcoxon rank-sum test, $p < 0.05$). NS, non-significant.

(C) Stereotaxic locations of sustain- and update-type DA neurons in SN in coronal (top left) and sagittal (down left) views. D, dorsal; V, ventral; M, medial; L, lateral; R, rostral; C, caudal. Their distributions are projected to each of 3D axes (right). Number 0 indicates the midline (medial-lateral), the dorsal end of SN (dorsal-ventral), and the rostral end of SN (rostral-caudal). Their means (triangles) were statistically different in the medial-lateral and rostral-caudal dimensions ($p < 0.001$ by Wilcoxon rank-sum test). The coordinates 0, 0, 0 (abscissa) are rostral, medial, and dorsal edges of SN.

(D) Electrophysiological properties. Sustain- and update-type DA neurons had similar spike shapes, which are different from non-DA (presumed GABAergic) neurons (left). Relationship between spike duration and baseline firing rate for sustain- and update-type DA neurons and non-DA neurons (right).

See also Figures S2, S3, and S4.

(Figures 4B, bottom, and S3C), unlike update-type neurons (Figures 4B, top, and S3B). Neurons showing stronger value-biased responses in the passive viewing task tended to show stronger spatial selectivity (Figure S3G). The scattered data in Figures S3F and S3G may suggest that presumed DA neurons can be

divided into update- and sustain-type neurons along a gradient in multiple features, rather than as two distinct groups of neurons.

We also found that the locations of update- and sustain-type neurons were largely separate: the update-type neurons more

Table 1. Electrophysiological Properties for Sustain-type DA, Update-type DA, and Presumed GABAergic Neurons

	Sustain DA (mean ± SD)	Update DA (mean ± SD)	Presumed GABAergic (mean ± SD)
Spike duration (ms)	1.3 ± 0.2	1.3 ± 0.2	0.9 ± 0.1
Baseline firing rate (spikes/s)	4.7 ± 2.9	5.0 ± 2.3	53.7 ± 19.7

rostral and medial part of SNC (rmSNC); sustain-type neurons more caudal and lateral part (clSNC) (Figure 4C). Overall, the response in the passive viewing task was stronger in the caudal and lateral parts (Figure S4A). The same tendencies were present for the spatial selectivity (Figure S4B). In contrast, the reversal response was stronger in the rostral and medial parts (Figure S4C).

Despite all of the differences described above, the update- and sustain-type neurons showed similar electrophysiological properties (Figure 4D; Table 1). Compared with presumed GABAergic neurons in SNr, both update- and sustain-type neurons had longer spike durations and lower baseline activity. These features are similar to those used previously to characterize DA neurons in the monkey SNC (Schultz, 1986), suggesting that both update- and sustain-type neurons were dopaminergic.

Update-type neurons apparently correspond to the RPE-sensitive DA neurons that have been investigated repeatedly in various animal species including humans (Cohen et al., 2012; D'Ardenne et al., 2008; Schultz, 1998). In contrast, sustain-type neurons are a novel finding, and their functions are unknown so far. In pursuing this question, we hypothesized that the value signal encoded by sustain-type neurons is sent to CDt, because we previously showed that CDt receive inputs from DA neurons in the caudal-dorsal-lateral part of SNC (cdlSNC) (Kim et al., 2014), the distribution similar to that of sustain-type neurons (Figure 4C).

Sustain-type DA Neurons Connecting with Caudate Tail

To test this hypothesis further, we examined whether the sustain-type neurons were activated antidromically by the electrical stimulation of CDt (Figures 5). We placed the stimulating electrode accurately in CDt by recording single neuronal activity with the electrode (Figure 5A). Among 31 SNC neurons tested, seven neurons were activated antidromically (hereafter called Anti(+) neurons). One example is shown in Figure 5B. The CDt stimulation evoked spikes at a fixed latency (6.9 ms) (Figure 5B, top). The antidromic nature was confirmed by a collision test: when the stimulation was followed by a spontaneous spike by <7.9 ms, the stimulation no longer evoked a spike (Figure 5B, bottom). Among the seven Anti(+) neurons, the antidromic response appeared sometimes as a partial initial segment (IS) spike in four neurons (Figures S5A–S5D), a feature common among DA neurons (Grace and Bunney, 1983).

We then examined the responses of six out of the seven Anti(+) neurons using our object-value procedures (Figures 1 and S5E–S5G). These Anti(+) neurons shared the same features common to the sustain-type neurons: (1) Anti(+) neurons showed strong value-differential responses in the passive viewing task (average activity in Figure 5C; individual activity in Figures S4A and S5F);

(2) Anti(+) neurons showed only weak value-differential responses in the reversal task (Figure S4C); (3) Anti(+) neurons were insensitive to the reward outcome (Figure S5G); (4) Anti(+) neurons responded more strongly to contralateral objects (Figure S4B); and (5) Anti(+) neurons were located within a cluster of sustain-type neurons (Figures 6F and S4). These results suggest that the sustained value signal is sent from SNC to CDt.

We also found that CDt stimulation induced orthodromic effects (Figures 5D–5F). Among 15 sustain-type neurons examined, ten neurons showed a phasic increase in activity (Figures 5D and 5F). Their locations are shown in Figure S4. The latency of the excitatory response as a population was 7 ms. In contrast, none of the update-type neurons examined ($n = 6$) showed an orthodromic response (Figures 5E and 5F). These data raise the possibility that sustain-type SNC neurons not only send signals to CDt but also receive signals from CDt, possibly through SNr (Figure 5A; see Discussion).

Given their projections to CDt, the Anti(+) neurons were likely to be dopaminergic. To test this hypothesis, we anatomically reconstructed dopaminergic neurons in SNC that projected to CDt. We injected cholera toxin B subunit (CTB, retrograde tracer) into CDt and immunohistochemically processed SNC-containing sections to detect both CTB and tyrosine hydroxylase (TH, DA neuronal marker) (Figures 6B–6D). Before this process, we marked the recording site of one Anti(+) neuron by passing a small DC current through the recording electrode. The marking lesion was found in the caudal-lateral part of SNC (clSNC) (Figures 6A and 6C). It was surrounded by many TH-positive cells (green cell somas in Figure 6D), some of which were also CTB-positive and therefore projected to CDt (orange cell somas in Figure 6D). These CTB-positive cells were clustered in clSNC and most of them (98.5%, 338/343) were TH-positive (Figures 6E and S6A), confirming our previous study (Kim et al., 2014). Importantly, the recording sites of sustain-type neurons (Figure 6F) were included in the clSNC region where DA neurons projected specifically to CDt (Figure 6E). These results suggest that sustain-type neurons are dopaminergic and project to CDt.

DISCUSSION

Anatomical and Functional Segregation of DA Effects

Our experiments showed that two types of DA neurons encoded reward values of visual objects in different manners (i.e., updating and sustaining), although they might represent two extremes of a functional gradient. Update-type DA neurons were sensitive to unpredicted changes in the values of incoming reward (i.e., RPE) and their predictors (i.e., fractal objects). These are typical features that characterize DA neurons (Schultz, 1998) and are suitable for goal-directed behavior that is modified flexibly by changes in reward outcomes (Balleine and Dickinson, 1998). In contrast, sustain-type DA neurons constitute a different group of DA neurons. After long-term learning, they became insensitive to changes in expected reward: they continued to respond to previously reward-associated visual objects even when the reward outcome was no longer expected. Their responses showed no significant decrease even when non-contingent outcomes were repeated many times across many days (Figures S2E–S2G). These extinction-resistant neuronal responses are

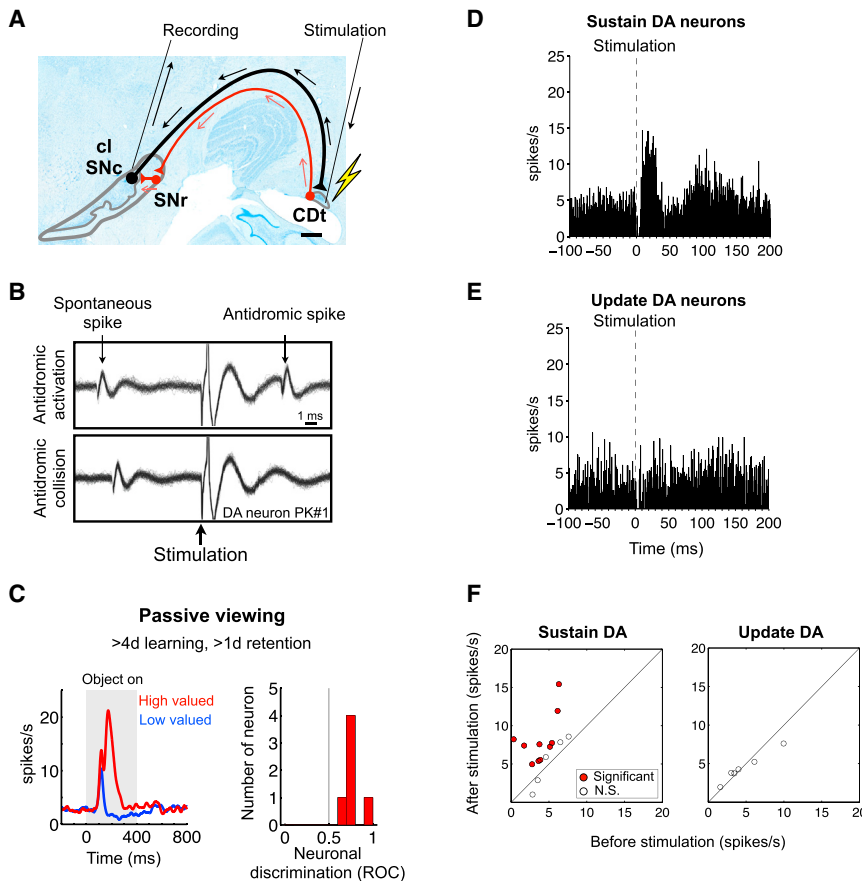


Figure 5. Efferent and Afferent Connections of Sustain-type DA Neurons

(A) Scheme showing electrical stimulation in caudate tail (CDt) and neuronal recording in caudal-lateral SNc (clSNC). SNr, substantia nigra pars reticulata. Coronal view. Scale bar, 1 mm. (B) An SNc neuron activated by electrical stimulation in CDt with a fixed latency (6.9 ms) (PK#1, Figure S5E). This activation was eliminated when CDt stimulation occurred <7.9 ms after a spontaneous spike (bottom), confirming its antidiromic nature (collision test).

(C) Value discrimination of antidiromically activated (Anti(+)) neurons ($n = 6$) in passive viewing task (>4 days learning and >1 day retention), shown as average SDFs (left) and ROC distribution (right).

(D and E) Orthodromic responses of sustain-type DA neurons (D), but not update-type DA neurons (E), by CDt stimulation. Average activity is shown by peristimulus time histogram [PSTH] is aligned on CDt stimulation (dotted line). The lack of activity just after the stimulation was caused by stimulus artifact.

(F) Responses of individual DA neurons to CDt stimulation shown by a scatterplot. Each data point indicates each neuron's activity 10–40 ms after (ordinate) and 0–80 ms before (abscissa) CDt stimulation. Red dots indicate neurons whose response is statistically significant (t test, $p < 0.05$). NS, non-significant.

See also Figures S4, S5, and S6.

compatible with habits that remain functional even after reward outcomes are eliminated (Balleine and Dickinson, 1998; Graybiel, 2008), although “devaluation” has not been applied.

The two types of DA neurons would influence behavior by their projections to separate regions of the striatum. Update-type neurons were localized in the rostral-medial part of SNc (rmSNc) where many DA neurons project to CDh (Kim et al., 2014). Indeed, depending on the expected reward outcome, neurons in CDh change their activity flexibly (i.e., mostly higher when reward is expected) similarly to update-type DA neurons (Figures S3B and S3F), and monkeys change their behavior flexibly (e.g., quicker saccades when reward is expected) (Hikosaka et al., 1989a; Kim and Hikosaka, 2013).

A different scenario applies to the other type of DA neurons: sustain-type DA neurons. Sustain-type DA neurons were localized in the caudal-lateral part of SNc (clSNC) where many DA neurons project to CDt (Kim et al., 2014). Notably, all neurons in clSNC projecting to CDt (indicated by antidiromic activation) showed sustained object-value responses. This sustained DA signal seems to control the activity of CDt neurons: most CDt neurons continued to show value-differential visual responses stably even with no contingent reward outcomes (Kim and Hikosaka, 2013; Yamamoto et al., 2013). In short, habitual object-value signals are encoded by the sustainDA-CDt circuit, but not the updateDA-CDh circuit (Figures S6C and S6D).

In fact, these two circuits seem to control gaze-oriented behavior (saccade) in distinctly different manners. The flexible saccade bias (i.e., caused by expected reward) is reduced by the inactivation of CDh, but not CDt; in contrast, the stable saccade bias (i.e., caused by previous reward associations) is reduced by the inactivation of CDt, but not CDh (Kim and Hikosaka, 2013). This distinct value-signal processing is supported by mostly separate downstream circuits (Figure S6E): CDh outputs through the rostral-ventral-medial part of SNr (rvmSNr) and CDt outputs through the caudal-dorsal-lateral part of SNr (cdlSNr), both of which converge to the superior colliculus (SC) (Yasuda and Hikosaka, 2015; Yasuda et al., 2012).

To summarize, short-term and long-term memories of object values are processed separately by the two basal ganglia circuits (Figure S6E). Relying on short-term memories, the updateDA-CDh circuit contributes to voluntary, goal-directed saccades. Relying on long-term memories, the sustainDA-CDt circuit contributes to automatic, habitual saccades.

Sustain-type DA Neurons for Habitual Visual-Oculomotor Behavior

A remarkable feature of sustain-type DA neurons is that, once they have acquired memories of object values, they rarely unlearn the object values (Figures 3G and S2E–S2G). The resistance to extinction apparently allowed them to accumulate value

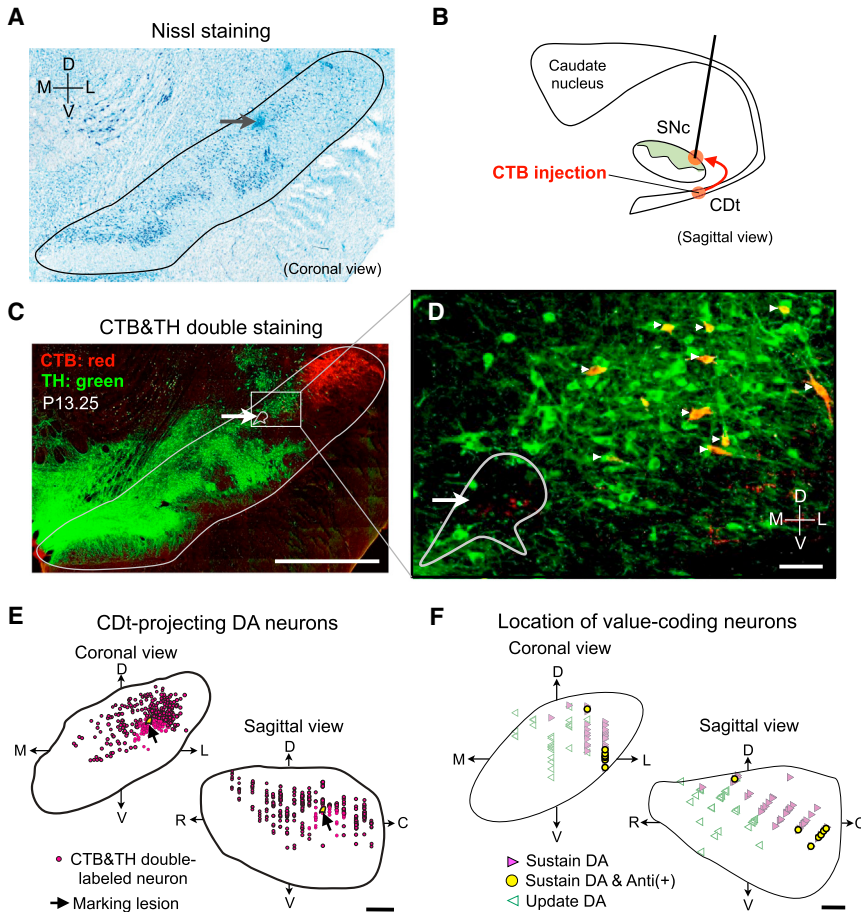


Figure 6. Colocalization of Sustain-type DA Neurons and CDt-Projecting DA Neurons

(A) Location of an Anti(+) neuron (PK#3), indicated by a marking lesion (black arrow) in a Nissl-stained coronal section. Black line indicates the border of SN.

(B) Combination of antidromic and retrograde tracer experiments in monkey PK. A retrograde tracer, cholera toxin subunit B (CTB), was injected in CDt.

(C) An adjacent section (50 μm from the section in (A) showing sensitivity to TH (green) and CTB (red) and the location of the marking lesion (white arrow). A red plexus in the dorsolateral SNr indicates the anterogradely labeled axon terminals of CDt neurons. Scale bar, 2 mm.

(D) Enlarged view of the area around the marking lesion. Among many TH-positive DA neurons (green) are TH and CTB double-labeled neurons (yellow or orange color, indicated by white arrowheads). Scale bar, 100 μm.

(E) Stereotaxic locations of CDt-projecting neurons (retrogradely CTB-labeled). Note that 98.5% of them were TH-positive. The locations of neurons are projected to the coronal and sagittal perspectives of SN based on MRI. Scale bar, 1 mm.

(F) Recording sites of sustain-type and update-type SNC neurons in stereotaxic coordinates. Anti(+) neurons among the sustain-type are indicated by yellow dots. The locations of sustain-type neurons were included in cSNC where DA neurons projected to CDt (E). The locations of neurons are projected to the coronal and sagittal perspectives of SN based on histological sections. Scale bar, 1 mm.

See also Figure S6.

memories as the monkey experienced more objects. The cumulative value memories of sustain-type DA neurons seem translated into the extremely high capacity of visual object memories in their target neurons in CDt and cdlSNr (Hikosaka et al., 2013; Yamamoto et al., 2013; Yasuda et al., 2012). This was clearly shown for cdlSNr neurons that discriminate >300 visual objects by their stable values and retain the value memories for >100 days (Yasuda et al., 2012).

How can sustain-type DA neurons process object values consistently regardless of the immediate reward outcomes? To address this question, we will discuss their detailed properties. First, sustain-type DA neurons showed little response to water reward itself even when the reward was unpredicted (Figures 4A and S2D). Instead, they responded to visual objects even when they were novel (Figure 3A) and then became consistently sensitive to the values of visual objects. These results suggest that sustain-type DA neurons rely on another mechanism that can identify the valuable object based on its association with reward outcomes; in fact, this is what update-type DA neurons would do. This might be accomplished by the connection of update-type DA neurons to SC (Figure S6E) that projects back to the DA neurons via excitatory connections (Comoli et al., 2003). Specifically, update-type DA neurons would guide SC neurons to signal attention/gaze based on recent reward experi-

ences (Ikeda and Hikosaka, 2003, 2007), and this signal may be sent to sustain-type DA neurons. Consistent with this hypothesis, sustain-type DA neurons responded to visual objects more strongly when they appeared on the contralateral side (Figure 4B), similarly to SC visual neurons (Goldberg and Wurtz, 1972). According to this scenario, sustain-type DA neurons appear to rely on conditioned reinforcement (Taylor and Robbins, 1986), not reward itself, as the source of object values.

Second, the extinction-resistant memories for habitual visual-oculomotor behavior might be facilitated by a loop-circuit mechanism. Electrical stimulation of CDt induced orthodromic excitations in many of the sustain-type DA neurons (Figures 5D and 5F), in addition to occasional antidromic activations (Figures 5A–5C). Notably, cdlSNr neurons are inhibited by CDt stimulation through the direct GABAergic connection (Yasuda and Hikosaka, 2015). SNr neurons are known to have GABAergic axon collaterals that synapse on adjacent DA neurons (Deniau et al., 1982; Tepper et al., 1995). Therefore, the CDt-induced excitation of sustain-type DA neurons may be caused by a disinhibition mediated by cdlSNr neurons. In fact, sustain-type DA neurons were located very close to cdlSNr neurons that encode stable value memories (Kim et al., 2014; Yasuda et al., 2012). The presumed loop circuit (CDt-cdlSNr-sustainDA-CDt in Figure S6E) would act as a positive loop, since the DA effect on direct pathway neurons in the

striatum is mediated through D1 receptors (Gerfen, 1992) and is thought to be facilitatory (Surmeier et al., 2007; West and Grace, 2002). This mechanism might underlie the long-term memories for habitual visual oculomotor behavior.

Implications of Sustain-type DA Neurons in Unconscious Memories

CDt has long been implicated in unconscious memories of visual objects. This “visual habit” concept was initiated by studies on macaque monkeys using a concurrent discrimination task (Fernandez-Ruiz et al., 2001) and was confirmed by human studies: people with extensive lesions in the medial temporal lobe including hippocampus may lose conscious memories (i.e., amnesia), but can learn to choose high-valued objects, even though they cannot recognize the objects (Bayley et al., 2005). Our data suggest that CDt-projecting DA neurons contribute to the unconscious visual memories and automatic gaze orienting. In fact, people with Parkinson’s disease (PD) showed no learning in the concurrent discrimination task unless conscious memories are deployed (Moody et al., 2010).

Implications of Sustain-type DA Neurons in Basal Ganglia Dysfunctions

Our study provides new perspectives in basal ganglia dysfunctions. In Parkinson’s disease, DA cell loss tends to occur in the lateral part of SNC (Goto et al., 1989) where sustain-type neurons dominate. As predicted from our data, people with Parkinson’s disease often have difficulties in performing daily routines automatically (Kim and Hikosaka, 2015; Redgrave et al., 2010). This may be caused partly by the dysfunction of the CDt-cdISNr-SC circuit. In contrast, people with drug abuse are persistently and often unconsciously attracted by visual cues associated with addictive drugs (Goldstein et al., 2009). This might be caused by malfunctioning of sustain-type DA neurons in SNC targeting the CDt-cdISNr-SC circuit.

Heterogeneity of DA Neurons

Recent studies suggest that DA neurons are heterogeneous in terms of their functions (Brischoux et al., 2009; Lerner et al., 2015; Matsumoto and Hikosaka, 2009). Our experiments support this idea. In macaque monkeys, another kind of heterogeneity was reported from our lab (Matsumoto and Hikosaka, 2009). In response to visual cues that predicted an aversive stimulus, DA neurons in the ventromedial SNC were inhibited (value-coding), whereas DA neurons in the dorsolateral SNC were excited (salience-coding). Their locations roughly match the locations of update-type and sustain-type neurons, respectively. However, it is still unknown how individual DA neurons are involved in these two kinds of functional categories. This remains a crucial question to integratively understand the functions of DA neurons.

EXPERIMENTAL PROCEDURES

General Procedures

Two adult male rhesus monkeys (*Macaca mulatta*), PK (8 kg) for neuronal recording and histology and DW (11 kg) for neuronal recording, were used for the experiments. All animal care and experimental procedures were approved by the National Eye Institute Animal Care and Use Committee and complied with the Public Health Service Policy on the humane care and use

of laboratory animals. We implanted a plastic head holder and two plastic recording chambers to the skull under general anesthesia and sterile surgical conditions. One chamber aiming at CDt was tilted laterally by 25°, and another chamber aiming at SNC was tilted posteriorly by 40°. Two search coils were surgically implanted under the conjunctiva of the eyes to record eye movements. After the monkeys fully recovered from surgery, we started training them with object value learning and passive viewing task.

Single Unit Recording

While the monkey was performing a task, activity of single neurons in SNC and CDt was recorded using conventional methods. The recording sites were determined with 1 mm spacing grid system, with the aid of MR images (4.7 T, Bruker) obtained along the direction of the chamber. Single-unit recording was performed using glass-coated electrode (Alpha-Omega). The electrode was inserted into the brain through a stainless-steel guide tube and advanced by an oil-driven micromanipulator (MO-97A, Narishige). The electric signal from the electrode was amplified with a band-pass filter (0.2–10 kHz; BAK). Neuronal spikes were isolated online using a custom voltage-time window discrimination software (MEX, Laboratory of Sensorimotor Research, National Eye Institute-National Institutes of Health [LSR/NEI/NIH]) and their timings were detected at 1 kHz. The waveforms of individual spikes were collected at 50 kHz.

Identification of Dopamine Neurons by Electrophysiological Properties

Presumed dopamine (DA) neurons were identified by their tonic baseline activity around five spikes per second and broad spike potential. To characterize the electrophysiological properties of recorded neurons, we used two parameters: (1) baseline firing rate, and (2) spike waveform. Baseline firing rate is the mean firing rate during 1 s before the onset of the fixation dot in passive viewing task. To quantify spike waveform, we measured the spike duration that was defined as the time between the first and second negative peaks.

Behavioral Procedure

Behavioral procedure was controlled by QNX-based real-time experimentation data acquisition system (REX, LSR/NEI/NIH). The monkey sat in a primate chair, facing a frontoparallel screen in a sound-attenuated and electrically shielded room. Visual stimuli generated by an active matrix liquid crystal display projector (PJ550, ViewSonic) were rear projected on the screen. We created the visual stimuli using fractal geometry (Yamamoto et al., 2012). Their sizes were ~8° × 8°.

The behavioral procedure consisted of two phases: learning (object-value learning task) and testing (passive viewing task for neuronal testing, free viewing procedure for behavioral testing). Importantly, the learning was guided by reward (i.e., water), but the testing was done with no reward outcome. Details are explained below.

Object-Value Learning Task

In this task, monkeys viewed visual objects repeatedly in association with consistent reward outcomes and thus learned their stable values (Figure 1C) (Yamamoto et al., 2013). In each session of this and the following tasks, a set of eight computer-generated fractals was used as visual objects. While the monkey was fixating on a central white dot, one of the objects was presented at a neurons’ preferred position (ipsilateral or contralateral position, 15° from center). The center fixation spot turned off 400 ms later, and the monkey was required to make a saccade to the object. Half of the objects were always associated with a liquid reward (high-valued objects), whereas the other half were associated with no reward (low-valued objects). A tone was presented with either outcome. One training session consisted of 112 trials (14 trials for each object). Each set was learned in one learning session in 1 day. The same sets of objects were repeatedly learned with the same object-value associations across days, while new sets of fractals were introduced for learning across days. At the time of the neuronal recording and behavioral experiments started, there were many objects (40–440 for monkey PK, 608–840 for monkey DW) whose levels of learning varied (from 0 day to 1,053 days), which allowed us to examine how neuronal and behavioral responses changed during long-term learning. When this learning task was used while a presumed DA neuron was being recorded, the fractal was mostly presented at a contralateral

position (15° from center), because these neurons often showed contralateral spatial selectivity (Figure 4B).

Passive Viewing Task

This task was used to examine how a presumed DA neuron responded to the value-learned objects, but now without any contingent reward outcome (Figure 2B) (Kim and Hikosaka, 2013; Yamamoto et al., 2013; Yasuda et al., 2012). While the monkey was fixating on a central white dot, some of the fractals ($n = 2–6$) were chosen pseudorandomly and presented sequentially at a contralateral position (15° from center, presentation time: 400 ms, inter-object interval: 500–700 ms). Reward was delivered 300 ms after the last object was presented. The reward was thus not contingently associated with any object. Each object was presented at least six times in one session. The value-coding activity of DA neurons was tested before learning, immediately after first learning, and after long-term learning (more than four daily learning sessions) with a sufficient retention period (>1 day after the last learning session). For each neuron, we used multiple sets of well-learned objects (two to four sets, or 16–32 objects) to test its stable value-coding during retention.

Reversal Task

To examine value-updating activity, we used a task in which the object-value contingency was reversed in every block of 20–35 trials (Kim and Hikosaka 2013; Yamamoto et al., 2013; Yasuda et al., 2012). The procedure in each trial was the same as the object-value learning task (above). Unlike the object-value learning task, the same two fractal objects (two and three pairs for monkey PK and DW) were used as the saccade target. In each trial, one of them was presented at a right or left position pseudorandomly (15° from center). In a block of 20–35 trials, one of the objects was associated with a reward and the other with no reward. In the next block, the object-reward contingency was reversed. At least four blocks were included in one experiment.

Free Viewing Procedure

This task was used to examine how the monkey responded to the value-learned objects, but without any reward outcome (Kim and Hikosaka, 2013; Yamamoto et al., 2013; Yasuda et al., 2012). After the monkey fixated on a central white dot for 300 ms, four objects were chosen pseudorandomly and presented simultaneously in four symmetric positions (15° from center) (Figure 1E). The monkey was free to look at them for 2 s without any reward outcome. After a blank period (500 ms), another four objects were presented. On half of the trials, a white dot was presented at one of eight positions. If the monkey made a saccade to it, a liquid reward was delivered. Each object was presented at least 16 times in one session.

Neuronal Spatial Preference

To test the spatial preference of presumed DA neurons, we presented fractal objects in either left or right position (15° from center) in a saccade task. The task was similar to object value learning task, but only two familiar fractals were used while the object-value association was reversed after each block of 20–35 trials.

Identifying the CDt-Projecting Neurons by Antidromic Activation

To test if a presumed DA neuron projected to CDt, we inserted two electrodes in CDt and SNC through the lateral and posterior chambers, respectively (Figure 5A). First, to determine the stimulation site, we lowered the CDt electrode until we found neurons that had typical electrophysiological properties of striatal output neurons (Figure S6B) (Hikosaka et al., 1989b). If we found that the neurons responded to fractal objects with stable value-coding (Kim and Hikosaka, 2013; Yamamoto et al., 2013), we fixed the position of the electrode for stimulation. We then lowered another electrode to SNC while stimulating CDt, until we found spikes that were evoked with a fixed latency. The antidromic nature of the spikes was confirmed by a collision test. A biphasic pulse with cathodal and anodal components was used for the stimulation. The currents for cathodal pulse ranged from 100 μ A to 1,000 μ A (anodal pulse lower). The biphasic negative-positive pulse was delivered with 0.4 ms per phase duration. The CDt stimulation site measured from the anterior commissure was at 8.5 mm posterior for monkey PK and 13 mm posterior for monkey DW.

Testing the Influence of CDt on SNC Neurons by Orthodromic Activation

We noticed that CDt stimulation induced changes in activity in some of the presumed DA neurons, but with no fixed latencies. The data were collected as the orthodromic effects on the SNC neurons (Figures 5D–5F).

Data Analysis

To assess the neuronal discrimination, we first measured the magnitude of the neuron's response to each fractal object and reward outcome by counting the numbers of spikes within a test window in individual trials. The test window was set to 0–400 ms after the onset of the object and after the onset of the reward outcome in both object value learning and passive viewing tasks. The neuronal discrimination was defined as the area under the receiver operating characteristic (ROC) based on the response magnitudes of the neurons to high-valued objects versus low-valued objects, reward versus no reward, or before reward versus after reward. The statistical significance of the neuronal discrimination and its changes was tested using Wilcoxon rank-sum test. To assess the behavioral discrimination, we used several measures. For object value learning task, we computed the target acquisition time that was measured as the time after the fixation dot disappeared until the gaze reached the object. For free viewing procedure, we measured saccade-choice rate and gazing duration rate. The saccade-choice rate was defined as follows: $(nSACh - nSACl)/(nSACh + nSACl)$ where $nSACh$ and $nSACl$ are the numbers of saccades toward high-valued and low-valued objects, respectively. The gazing duration rate was defined as follows: $(tGAZh - tGAZl)/(tGAZh + tGAZl)$ where $tGAZh$ and $tGAZl$ are the durations of gaze on high-valued and low-valued objects, respectively.

Anatomical Procedures

Electric marking lesion, retrograde tracer injection, histology, and immunohistochemistry are described in the Supplemental Experimental Procedures.

SUPPLEMENTAL INFORMATION

Supplemental Information includes Supplemental Experimental Procedures and six figures and can be found with this article online at <http://dx.doi.org/10.1016/j.cell.2015.10.063>.

AUTHOR CONTRIBUTIONS

A.G. and O.H. did pilot experiments. H.F.K. and O.H. designed the main part of the experiments. H.F.K. collected and analyzed data. H.F.K., O.H., and A.G. wrote the paper.

ACKNOWLEDGMENTS

We thank M. Yasuda for discussions and D. Parker, I. Bunea, M.K. Smith, G.Tansey, A.M. Nichols, T.W. Ruffner, J.W. McClurkin, and A.V. Hays for technical assistance. This research was supported by the Intramural Research Program at the National Institutes of Health, National Eye Institute.

Received: June 3, 2015

Revised: August 28, 2015

Accepted: October 23, 2015

Published: November 19, 2015

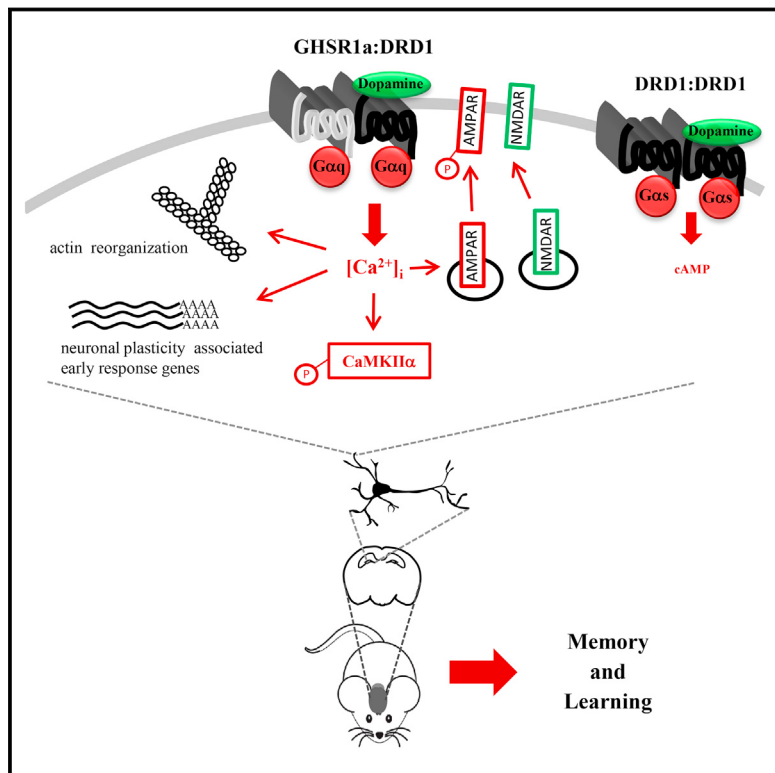
REFERENCES

- Balleine, B.W., and Dickinson, A. (1998). Goal-directed instrumental action: contingency and incentive learning and their cortical substrates. *Neuropharmacology* 37, 407–419.
- Balleine, B.W., and O'Doherty, J.P. (2010). Human and rodent homologies in action control: corticostriatal determinants of goal-directed and habitual action. *Neuropsychopharmacology* 35, 48–69.
- Bayley, P.J., Frascino, J.C., and Squire, L.R. (2005). Robust habit learning in the absence of awareness and independent of the medial temporal lobe. *Nature* 436, 550–553.

- Brischoux, F., Chakraborty, S., Brierley, D.I., and Ungless, M.A. (2009). Phasic excitation of dopamine neurons in ventral VTA by noxious stimuli. *Proc. Natl. Acad. Sci. USA* 106, 4894–4899.
- Cohen, J.Y., Haesler, S., Vong, L., Lowell, B.B., and Uchida, N. (2012). Neuron-type-specific signals for reward and punishment in the ventral tegmental area. *Nature* 482, 85–88.
- Comoli, E., Coizet, V., Boyes, J., Bolam, J.P., Canteras, N.S., Quirk, R.H., Overton, P.G., and Redgrave, P. (2003). A direct projection from superior colliculus to substantia nigra for detecting salient visual events. *Nat. Neurosci.* 6, 974–980.
- D'Ardenne, K., McClure, S.M., Nystrom, L.E., and Cohen, J.D. (2008). BOLD responses reflecting dopaminergic signals in the human ventral tegmental area. *Science* 319, 1264–1267.
- Deniau, J.M., Kitai, S.T., Donoghue, J.P., and Grofova, I. (1982). Neuronal interactions in the substantia nigra pars reticulata through axon collaterals of the projection neurons. An electrophysiological and morphological study. *Exp. Brain Res.* 47, 105–113.
- Fernandez-Ruiz, J., Wang, J., Aigner, T.G., and Mishkin, M. (2001). Visual habit formation in monkeys with neurotoxic lesions of the ventrocaudal neostriatum. *Proc. Natl. Acad. Sci. USA* 98, 4196–4201.
- Gerfen, C.R. (1992). The neostriatal mosaic: multiple levels of compartmental organization. *Trends Neurosci.* 15, 133–139.
- Goldberg, M.E., and Wurtz, R.H. (1972). Activity of superior colliculus in behaving monkey. I. Visual receptive fields of single neurons. *J. Neurophysiol.* 35, 542–559.
- Goldstein, R.Z., Craig, A.D.B., Bechara, A., Garavan, H., Childress, A.R., Paulus, M.P., and Volkow, N.D. (2009). The neurocircuitry of impaired insight in drug addiction. *Trends Cogn. Sci.* 13, 372–380.
- Goto, S., Hirano, A., and Matsumoto, S. (1989). Subdivisional involvement of nigrostriatal loop in idiopathic Parkinson's disease and striatonigral degeneration. *Ann. Neurol.* 26, 766–770.
- Grace, A.A., and Bunney, B.S. (1983). Intracellular and extracellular electrophysiology of nigral dopaminergic neurons—1. Identification and characterization. *Neuroscience* 10, 301–315.
- Graybiel, A.M. (2008). Habits, rituals, and the evaluative brain. *Annu. Rev. Neurosci.* 31, 359–387.
- Hikosaka, O., Sakamoto, M., and Usui, S. (1989a). Functional properties of monkey caudate neurons. III. Activities related to expectation of target and reward. *J. Neurophysiol.* 61, 814–832.
- Hikosaka, O., Sakamoto, M., and Usui, S. (1989b). Functional properties of monkey caudate neurons. I. Activities related to saccadic eye movements. *J. Neurophysiol.* 61, 780–798.
- Hikosaka, O., Nakahara, H., Rand, M.K., Sakai, K., Lu, X., Nakamura, K., Miyachi, S., and Doya, K. (1999). Parallel neural networks for learning sequential procedures. *Trends Neurosci.* 22, 464–471.
- Hikosaka, O., Yamamoto, S., Yasuda, M., and Kim, H.F. (2013). Why skill matters. *Trends Cogn. Sci.* 17, 434–441.
- Ikeda, T., and Hikosaka, O. (2003). Reward-dependent gain and bias of visual responses in primate superior colliculus. *Neuron* 39, 693–700.
- Ikeda, T., and Hikosaka, O. (2007). Positive and negative modulation of motor response in primate superior colliculus by reward expectation. *J. Neurophysiol.* 98, 3163–3170.
- Kim, H.F., and Hikosaka, O. (2013). Distinct basal ganglia circuits controlling behaviors guided by flexible and stable values. *Neuron* 79, 1001–1010.
- Kim, H.F., and Hikosaka, O. (2015). Parallel basal ganglia circuits for voluntary and automatic behaviour to reach rewards. *Brain* 138, 1776–1800.
- Kim, H.F., Ghazizadeh, A., and Hikosaka, O. (2014). Separate groups of dopamine neurons innervate caudate head and tail encoding flexible and stable value memories. *Front. Neuroanat.* 8, 120.
- Lehéricy, S., Benali, H., Van de Moortele, P.F., Pélégriini-Issac, M., Waechter, T., Ugurbil, K., and Doyon, J. (2005). Distinct basal ganglia territories are engaged in early and advanced motor sequence learning. *Proc. Natl. Acad. Sci. USA* 102, 12566–12571.
- Lerner, T.N., Shilyansky, C., Davidson, T.J., Evans, K.E., Beier, K.T., Zalcousky, K.A., Crow, A.K., Malenka, R.C., Luo, L., Tomer, R., and Deisseroth, K. (2015). Intact-brain analyses reveal distinct information carried by SNC dopamine subcircuits. *Cell* 162, 635–647.
- Matsumoto, M., and Hikosaka, O. (2009). Two types of dopamine neuron distinctly convey positive and negative motivational signals. *Nature* 459, 837–841.
- Moody, T.D., Chang, G.Y., Vanek, Z.F., and Knowlton, B.J. (2010). Concurrent discrimination learning in Parkinson's disease. *Behav. Neurosci.* 124, 1–8.
- Redgrave, P., Rodriguez, M., Smith, Y., Rodriguez-Oroz, M.C., Lehericy, S., Bergman, H., Agid, Y., DeLong, M.R., and Obeso, J.A. (2010). Goal-directed and habitual control in the basal ganglia: implications for Parkinson's disease. *Nat. Rev. Neurosci.* 11, 760–772.
- Richfield, E.K., Young, A.B., and Penney, J.B. (1987). Comparative distribution of dopamine D-1 and D-2 receptors in the basal ganglia of turtles, pigeons, rats, cats, and monkeys. *J. Comp. Neurol.* 262, 446–463.
- Schultz, W. (1986). Responses of midbrain dopamine neurons to behavioral trigger stimuli in the monkey. *J. Neurophysiol.* 56, 1439–1461.
- Schultz, W. (1998). Predictive reward signal of dopamine neurons. *J. Neurophysiol.* 80, 1–27.
- Schultz, W., Dayan, P., and Montague, P.R. (1997). A neural substrate of prediction and reward. *Science* 275, 1593–1599.
- Seger, C.A., and Spiering, B.J. (2011). A critical review of habit learning and the Basal Ganglia. *Front. Syst. Neurosci.* 5, 66.
- Surmeier, D.J., Ding, J., Day, M., Wang, Z., and Shen, W. (2007). D1 and D2 dopamine-receptor modulation of striatal glutamatergic signaling in striatal medium spiny neurons. *Trends Neurosci.* 30, 228–235.
- Sutton, R.S. (1988). Learning to predict by the methods of temporal differences. *Mach. Learn.* 3, 9–44.
- Taylor, J.R., and Robbins, T.W. (1986). 6-Hydroxydopamine lesions of the nucleus accumbens, but not of the caudate nucleus, attenuate enhanced responding with reward-related stimuli produced by intra-accumbens d-amphetamine. *Psychopharmacology (Berl.)* 90, 390–397.
- Tepper, J.M., Martin, L.P., and Anderson, D.R. (1995). GABA_A receptor-mediated inhibition of rat substantia nigra dopaminergic neurons by pars reticulata projection neurons. *J. Neurosci.* 15, 3092–3103.
- Tobler, P.N., Fiorillo, C.D., and Schultz, W. (2005). Adaptive coding of reward value by dopamine neurons. *Science* 307, 1642–1645.
- West, A.R., and Grace, A.A. (2002). Opposite influences of endogenous dopamine D1 and D2 receptor activation on activity states and electrophysiological properties of striatal neurons: studies combining *in vivo* intracellular recordings and reverse microdialysis. *J. Neurosci.* 22, 294–304.
- Yamamoto, S., Monosov, I.E., Yasuda, M., and Hikosaka, O. (2012). What and where information in the caudate tail guides saccades to visual objects. *J. Neurosci.* 32, 11005–11016.
- Yamamoto, S., Kim, H.F., and Hikosaka, O. (2013). Reward value-contingent changes of visual responses in the primate caudate tail associated with a visuomotor skill. *J. Neurosci.* 33, 11227–11238.
- Yasuda, M., and Hikosaka, O. (2015). Functional territories in primate substantia nigra pars reticulata separately signaling stable and flexible values. *J. Neurophysiol.* 113, 1681–1696.
- Yasuda, M., Yamamoto, S., and Hikosaka, O. (2012). Robust representation of stable object values in the oculomotor Basal Ganglia. *J. Neurosci.* 32, 16917–16932.
- Yin, H.H., and Knowlton, B.J. (2006). The role of the basal ganglia in habit formation. *Nat. Rev. Neurosci.* 7, 464–476.

Hippocampal Dopamine/DRD1 Signaling Dependent on the Ghrelin Receptor

Graphical Abstract



Authors

Andras Kern, Maria Mavrikaki,
Celine Ullrich, Rosie Albaran-Zeckler,
Alicia Faruzzi Brantley, Roy G. Smith

Correspondence

akern@scripps.edu (A.K.),
rgsmith@scripps.edu (R.G.S.)

In Brief

GPCR heteromerization between a dopamine receptor and a ghrelin receptor (that is not liganded to ghrelin) initiates a non-canonical, cAMP-independent signaling pathway that regulates dopaminergic regulation of hippocampal memory.

Highlights

- In hippocampal neurons GHSR1a and DRD1 forms heteromers in a complex with G_{α_q}
- DRD1-induced hippocampal synaptic plasticity is dependent on GHSR1a and G_{α_q}
- DRD1 mediated learning and memory is dependent on G_{α_q} -PLC rather than G_{α_s} signaling
- DRD1-induced hippocampal memory is regulated by allosteric DRD1:GHSR1a interactions

Hippocampal Dopamine/DRD1 Signaling Dependent on the Ghrelin Receptor

Andras Kern,^{1,*} Maria Mavrikaki,^{1,3} Celine Ullrich,^{1,4} Rosie Albaran-Zeckler,¹ Alicia Faruzzi Brantley,² and Roy G. Smith^{1,*}

¹Department of Metabolism and Aging

²Department of Neuroscience and Behavioral Core

The Scripps Research Institute, Jupiter, FL 33458, USA

³Present address: Department of Psychiatry, Harvard Medical School Mailman Research Center, McLean Hospital, 02478 Belmont, MA, USA

⁴Present address: Department of Biomedicine, University of Basel, 4056 Basel, Switzerland

*Correspondence: akern@scripps.edu (A.K.), rgsmith@scripps.edu (R.G.S.)

<http://dx.doi.org/10.1016/j.cell.2015.10.062>

SUMMARY

The ghrelin receptor (GHSR1a) and dopamine receptor-1 (DRD1) are coexpressed in hippocampal neurons, yet ghrelin is undetectable in the hippocampus; therefore, we sought a function for apo-GHSR1a. Real-time single-molecule analysis on hippocampal neurons revealed dimerization between apo-GHSR1a and DRD1 that is enhanced by DRD1 agonism. In addition, proximity measurements support formation of preassembled apo-GHSR1a:DRD1:G α_q heteromeric complexes in hippocampal neurons. Activation by a DRD1 agonist produced non-canonical signal transduction via G α_q -PLC-IP₃-Ca²⁺ at the expense of canonical DRD1 G α_s cAMP signaling to result in CaMKII activation, glutamate receptor exocytosis, synaptic reorganization, and expression of early markers of hippocampal synaptic plasticity. Remarkably, this pathway is blocked by genetic or pharmacological inactivation of GHSR1a. In mice, GHSR1a inactivation inhibits DRD1-mediated hippocampal behavior and memory. Our findings identify a previously unrecognized mechanism essential for DRD1 initiation of hippocampal synaptic plasticity that is dependent on GHSR1a, and independent of cAMP signaling.

INTRODUCTION

G-protein-coupled receptors (GPCRs) belong to a large family of cell surface receptors that transduce their signal by activating a trimeric G protein complex (G $\alpha\beta\gamma$). Since GPCRs are important regulators of cell signaling, developing agonists and antagonists to target GPCRs is a major focus of drug discovery. However, traditional approaches to identify drug candidates based on specificity and functional activity in “artificial” cell-based assays has failed to accurately predict clinical outcomes. GPCRs are perceived to signal as monomers, but emerging evidence also implicates signal transduction through homomers and heteromers. Heteromers may play a crucial role in allosteric interactions that occur between protomers to alter signal transduction

and modify biological function. Therefore, knowing the physiological pathways regulated by GPCR heteromers, homomers, and monomers in target cells is clinically relevant.

Our research focuses on Class A GPCRs, and in particular the orphan growth hormone secretagogue receptor (GHSR1a) that was subsequently deorphanized by the discovery of ghrelin in stomach extracts (Howard et al., 1996; Kojima et al., 1999; Smith et al., 1997). We previously showed that GHSR1a forms heteromers with dopamine receptor-2 (DRD2) in hypothalamic neurons and that signaling through GHSR1a:DRD2 is essential for DRD2 agonist-induced suppression of food intake (Kern et al., 2012).

Paradoxically, despite expression of GHSR1a in the hippocampal structures (Guan et al., 1997), ghrelin is undetectable in the CNS, with the exception of trace amounts in the hypothalamus (Cowley et al., 2003; Furness et al., 2011; Grouselle et al., 2008; Sakata et al., 2009). Based on this observation, we set out to identify a function for apo-GHSR1a in the hippocampus. Using immunohistochemistry on brain sections of *Ghsr-IRES-tau-GFP* knock-in mice, we identified hippocampal neurons that coexpress GHSR1a and DRD1 (Jiang et al., 2006). Although DRD1 is implicated in regulating hippocampal synaptic plasticity involved in memory and learning, the mechanisms involved are incompletely understood (Hamilton et al., 2010; Rossato et al., 2009). We speculated that determining the function of apo-GHSR1a in DRD1 expressing hippocampal neurons would provide new insight into these mechanisms. Previously, studies on dopamine/DRD1 signaling in the hippocampus have focused mainly on canonical signaling, with DRD1 coupling to G α_s that enhances cyclic AMP (cAMP) accumulation and activation of protein kinase A (PKA) (Abel et al., 1997; Huang and Kandel, 1995). However, DRD1 signaling through G α_q has also been described (Jin et al., 2003; Lezcano and Bergson, 2002); nevertheless, what determines G α_q over G α_s signaling had not been elucidated.

Here, we shed light on DRD1 signaling in the hippocampus by illustrating formation of apo-GHSR1a:DRD1 heteromers that by an allosteric mechanism result in DRD1 coupling to G α_q at the expense of G α_s . Activation of apo-GHSR1a:DRD1 by a DRD1 agonist mobilizes intracellular Ca²⁺ ([Ca²⁺]_i) and initiates hippocampal synaptic plasticity, independent of cAMP signaling. An essential modulatory role for apo-GHSR1a on hippocampal DRD1 signaling would not have been recognized previously because experiments were performed in animals that express GHSR1a endogenously. By establishing that apo-GHSR1a is an essential modifier of DRD1 signaling in the hippocampus,

we resolve the conundrum of hippocampal GHSR1a expression in the absence of endogenous ghrelin, and provide a mechanism for how DRD1 activation of $G\alpha_q$ -signaling in hippocampal neurons is regulated. While it is generally agreed that memory consolidation involves DRD1-induced PKA and cAMP signaling, our results support an essential and fundamental role for $G\alpha_q$ -PLC-Ca²⁺ signal transduction in initiating this process.

RESULTS

GHSR1a:DRD1 Heteromers in Native Hippocampal Neurons

Following confirmation of the selectivity of the DRD1 antibody (Figure S1A), immunohistochemistry on *Ghsr-IRES-tauGFP* mouse brain sections revealed highest levels of GHSR1a and DRD1 coexpression in the Cornu Ammonis region III of hippocampus (CA3) and dentate gyrus (DG) of the hippocampal structures (Figure 1A). Hypothalamic regions also stained for GHSR1a, but lacked detectable DRD1 staining (Figure 1A).

To test for formation of GHSR1a:DRD1 heteromers in hippocampal neurons, we employed confocal fluorescence resonance energy transfer (FRET) microscopy on hippocampal brain slices. Biotin-ghrelin labeled with FITC-avidin (green) was used to detect GHSR1a, and a fluorescently labeled DRD1 antagonist (red-SKF83566) was used for DRD1. We validated the utility of fluorescently labeled ligands for FRET and binding specificity of each fluorophore (Figures S1B–S1D). FRET confocal microscopy and image analysis showed GHSR1a and DRD1 in close proximity (6.8 ± 0.1 nm) with a FRET efficiency of 0.51 ± 0.02 , consistent with formation of GHSR1a:DRD1 heteromers (Figure 1B). Parallel incubations using hippocampal slices from *Ghsr*–/– mice illustrated red-SKF83566 labeling of DRD1 receptors without green fluorescence labeling (Figure 1B).

GPCRs are recruited and dynamically assembled on the cell membrane (Kasai and Kusumi, 2014). To monitor real-time dynamics of DRD1 and GHSR1a interactions in primary hippocampal neuronal cultures, we performed two-color single-molecule analyses using total-internal reflection fluorescence microscopy (TIRF-M). Qdot565-avidin-labeled biotinylated-ghrelin was used to detect GHSR1a, and Qdot655-labeled DRD1 monoclonal antibody for DRD1. GHSR1a and DRD1 exhibited mobility and co-localization in the membrane (Figure S1C). Analysis of the individual trajectories of GHSR1a and DRD1 molecules illustrated significantly slower diffusion within the complex, rather than outside the complex (Figures 1C and 1D). Treatment with a DRD1-specific agonist (SKF81297) increased co-localization compared to vehicle treatment ($312\% \pm 31.2\%$ versus $100\% \pm 9\%$, $p < 0.001$; Figure 1E) and augmented the number of co-localization events ($163.8\% \pm 17.1\%$ versus $100\% \pm 8.5\%$, $p < 0.01$; Figure 1E). By measuring diffusion of the individual GHSR1a molecules, we showed that SKF81297 significantly increased the confinement of GHSR1a in a complex with DRD1, as indicated by a reduction in the steady state of the mean square displacement (MSD) curve ($p < 0.001$; Figure 1F). The diffusion coefficient of mobile receptors was higher before SKF81297 treatment (0.033 ± 0.009), than after treatment (0.0072 ± 0.002 ; $p < 0.01$; Figure 1F); hence, single-molecule analysis revealed

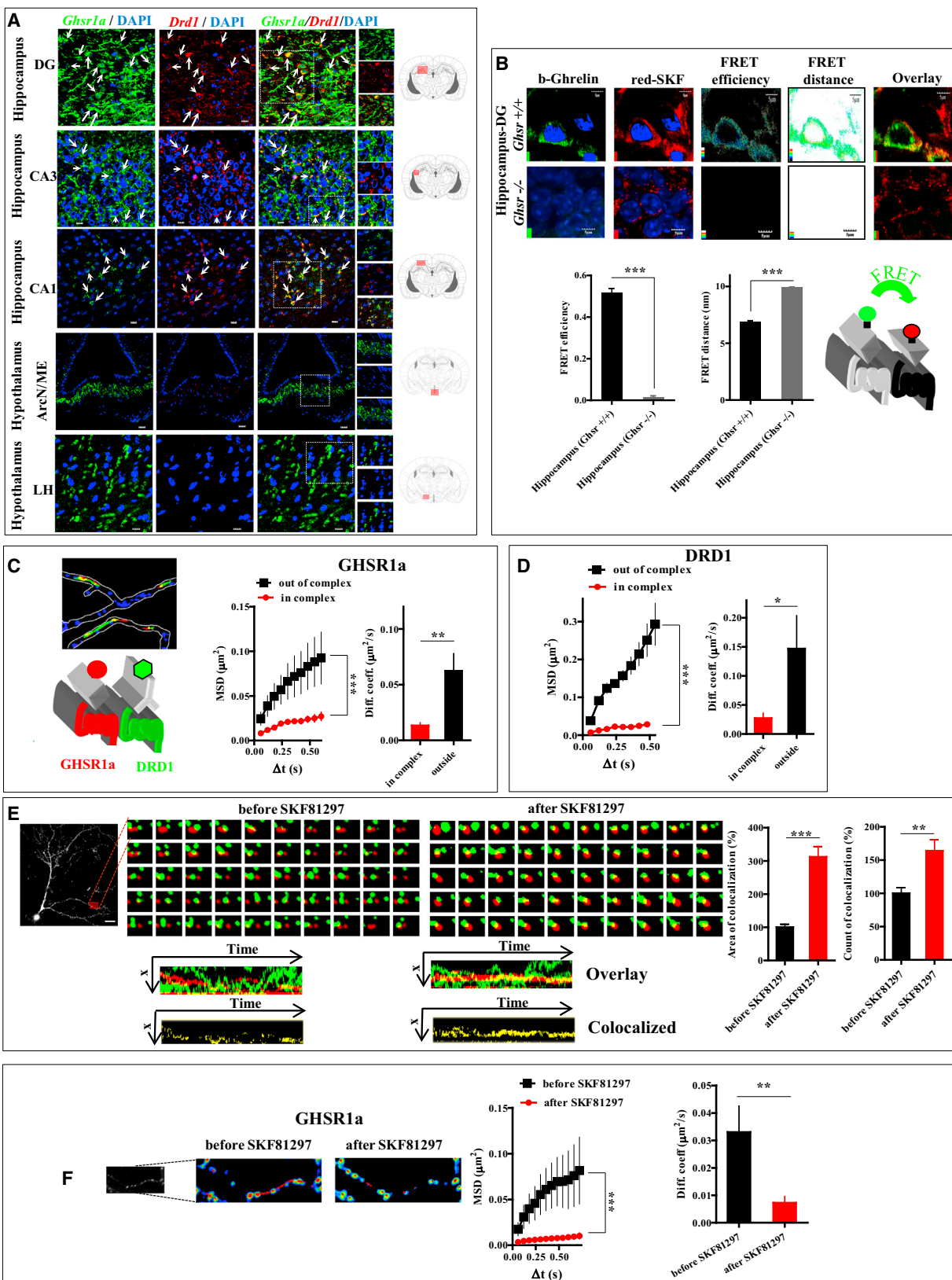
that a DRD1 agonist enhances formation of GHSR1a:DRD1 heteromeric complexes on mouse hippocampal neurons.

DRD1 Agonist Activation of GHSR1a:DRD1 Induces Ca²⁺ Transients via $G\alpha_q$ at the Expense of $G\alpha_s$ Coupling in Hippocampal Neurons

Having demonstrated close proximity and dynamic interactions of GHSR1a and DRD1 in hippocampal neurons, we asked whether these interactions modified canonical DRD1 signal transduction. To test for mobilization of [Ca²⁺]_i, we transduced primary cultures of mouse hippocampal pyramidal neurons with lentivirus expressing the genetically encoded Ca²⁺ sensor GCaMP3. Treatment with SKF81297 dose-dependently induced rapid Ca²⁺ transients ($EC_{50} = 50.37 \pm 0.12$ nM; Figure 2A). Post-treatment with ghrelin induced Ca²⁺ transient in the same neurons that responded to SKF81297 (Figure 2A), which confirmed coexpression of GHSR1a and DRD1. To test for GHSR1a dependence, we compared the effects of SKF81297 in organotypic hippocampal slices from *Ghsr*+/+ and *Ghsr*–/– mice expressing GCaMP3. Ca²⁺ transients were induced by SKF81297 in slices from *Ghsr*+/+ mice, but not in slices from *Ghsr*–/– mice; thus, Ca²⁺ mobilization is dependent on interactions between DRD1 and GHSR1a (Figure 2B, $p < 0.001$). A characteristic property of GPCR heteromers is the ability of an antagonist of one protomer to modify signaling of its protomer partner (Smith and Milligan, 2010). Pretreating organotypic hippocampal slices from *Ghsr*+/+ mice with the GHSR1a neutral antagonist JMV2959 blocked SKF81297-induced Ca²⁺ mobilization ($p < 0.05$; Figure 2C), which is consistent with modification of allosteric interactions between GHSR1a and DRD1 in the GHSR1a:DRD1 heteromeric complex.

We next asked whether SKF81297-induced [Ca²⁺]_i mobilization was mediated by DRD1:G α_q coupling through a preassembled GHSR1a:DRD1:G α_q complex. G α_q and DRD1 showed punctate co-localization in neuritic processes, indicating formation of signalosomes (Figure 2D). FRET confocal microscopy showed G α_q and DRD1 in close proximity (5.45 ± 0.2 nm; FRET efficiency, 0.416 ± 0.06 ; Figure 2D), consistent with GHSR1a:DRD1:G α_q preassembly in hippocampal neurons. In contrast to DRD1:G α_q , the FRET distance (9.98 ± 0.035 nm) and FRET efficiency (0.005 ± 0.02 ; Figure 2D) measured for DRD2 and G α_q in hippocampal neurons is inconsistent with their close proximity.

In the striatum, DRD2 and DRD1 are reported to form heteromers that couple to G α_q ; concomitant agonist activation of DRD2 and DRD1 mobilized Ca²⁺, which was blocked by a DRD2 antagonist (Hasbi et al., 2009). While proximity measurements did not support DRD2:G α_q interactions in hippocampal neurons (Figure 2D), the possibility remained that DRD1 agonist-induced [Ca²⁺]_i mobilization was explained by DRD1 coupling to G α_q in a DRD2:DRD1 complex rather than GHSR1a:DRD1. To address this possibility, we measured [Ca²⁺]_i release after treatment with pharmacologic agents: DRD1 agonist, SKF81297; DRD2 agonist, quinpirole; DRD2 antagonist, raclopride. Quinpirole neither mobilized, nor enhanced, SKF81297-induced [Ca²⁺]_i mobilization (Figure 2E), and raclopride did not attenuate SKF81297-induced Ca²⁺ release (Figure 2F); thus, signaling through a DRD2:DRD1:G α_q complex does not explain



(legend on next page)

SKF81297-induced Ca^{2+} release in hippocampal neurons. In addition, SKF81297 did not mobilize Ca^{2+} in hypothalamic neurons or in striatal neurons (Figure 2G). Further supporting hippocampal specificity, confocal FRET microscopy showed no evidence of GHSR1a:DRD1 heteromers in hypothalamic or striatal neurons (Figure 2H).

To test whether SKF81297 activation of $[\text{Ca}^{2+}]_i$ release through GHSR1a:DRD1 was mediated by Phospholipase C (PLC), we monitored, in real-time, the localization of phosphatidylinositol 4,5-bisphosphate (PIP₂). Primary hippocampal neurons from *Ghsr*^{+/+} and *Ghsr*^{-/-} mice were transduced with lentivirus encoding the PIP₂ biosensor, GFP-PH (Stauffer et al., 1998). In the basal state, GFP-PH was confined to the plasma membrane, indicating that the GHSR1a:DRD1 complex was not constitutively active. Treatment with SKF81297 rapidly induced cytoplasmic accumulation of GFP-PH in the soma and in neuritic processes of hippocampal neurons from *Ghsr*^{+/+}, but not in neurons from *Ghsr*^{-/-} mice (Figure 3A); thus, translocation of PIP₂ is dependent on GHSR1a. Pretreatment of hippocampal neurons with the PLC inhibitor U73122 inhibited DRD1 agonist-induced Ca^{2+} mobilization, further supporting dependence on PLC ($p < 0.001$; Figure 3B). To determine whether $\text{G}\alpha_q$ coupling and PLC activation occurred at the expense of canonical DRD1 $\text{G}\alpha_s$ coupling, membranes isolated from the hippocampus of *Ghsr*^{+/+} and *Ghsr*^{-/-} mice were treated with SKF81297 or vehicle, and cAMP production measured. Hippocampal membranes from *Ghsr*^{+/+} mice produced markedly less cAMP in response to SKF81297 compared to those from *Ghsr*^{-/-} mice (Figure 3C). Therefore, the presence of GHSR1a on the membranes reduces DRD1 coupling to $\text{G}\alpha_s$ in favor of $\text{G}\alpha_q$, suggesting an equilibrium between GHSR1a:DRD1 and DRD1:DRD1 on the hippocampal neuron to allow signaling through $\text{G}\alpha_q$ and $\text{G}\alpha_s$, respectively.

DRD1 Agonist-Induced $[\text{Ca}^{2+}]_i$ Mobilization Correlates with GHSR1a:DRD1 Heteromer Formation

To further characterize interactions between apo-GHSR1a and DRD1, and to determine whether GHSR1a heteromerization and dopamine activation of non-canonical DRD1 signaling is conserved across species, we expressed human GHSR1a and DRD1 in the human embryonic kidney (HEK293) cell line. We monitored heteromerization by time-resolved (Tr)-FRET using GHSR1a and DRD1 with a SNAP- or CLIP- tagged N terminus, using methods described previously (Kern et al., 2012). Tr-FRET

receptor titration assays and competition assays supported the formation of GHSR1a and DRD1 homomers and heteromers on the plasma membrane (Figures S2A and S2B). As additional proof of heteromer formation, bioluminescence resonance energy transfer (BRET) saturation, type-2 BRET, and microscopic BRET assays were conducted. The results ruled out random stochastic interactions between apo-GHSR1a and DRD1 and confirmed formation of GHSR1a:DRD1 heteromers (Figures S2C–S2E).

We employed HEK293-AEQ cells that stably express the bioluminescence Ca^{2+} sensor aequorin to monitor $[\text{Ca}^{2+}]_i$ mobilization. Dopamine and SKF81297 dose-dependently induced Ca^{2+} mobilization with dependence on apo-GHSR1a, which was blocked by the DRD1 antagonist, SCH23390, but not by the DRD2 antagonist, raclopride (Figures S3A–S3C). In control experiments, Ca^{2+} release was not detected when GHSR1a or DRD1 were coexpressed with other $\text{G}\alpha_s$ - or $\text{G}\alpha_q$ -coupled GPCRs (Figure S3D), which was consistent with their failure to form heteromers (Figure S2B). Collectively, these results show that dopamine-induced $[\text{Ca}^{2+}]_i$ mobilization correlates with GHSR1a:DRD1 heteromer formation rather than cross-talk between $\text{G}\alpha_q$ and $\text{G}\alpha_s$ signaling. To quantify the correlation between GHSR1a:DRD1 formation and $[\text{Ca}^{2+}]_i$ release, we constructed GHSR1a fusion proteins containing inducible homodimerization domains at the C terminus (GHSR1a-Hom). The cross linking agent, B/B, dose-dependently reduced dopamine-induced $[\text{Ca}^{2+}]_i$ mobilization by 40%–50% in HEK293-AEQ cells expressing GHSR1a-Hom + DRD1 compared to cells expressing GHSR1a + DRD1 (Figures 4A and 4B). B/B itself did not attenuate Ca^{2+} release or cell surface expression of either GHSR1a-Hom or DRD1 (Figures 4C and Figures S3E–S3G). TIRF-M analyses showed B/B treatment enhanced GHSR1a-Hom homodimerization by ~50%, thereby reducing the concentration of GHSR1a-Hom monomers available for forming heteromers (Figure S3H). The resulting reduction in the concentration of GHSR1a-Hom:DRD1 heteromers correlated with dopamine-induced $[\text{Ca}^{2+}]_i$ mobilization (Figure 4B).

Additional experiments tested whether dopamine-induced Ca^{2+} release involved cross-talk between $\text{G}\alpha_s$ and $\text{G}\alpha_q$ within the heteromeric complex or involved GHSR1a constitutive activity. We found that dopamine-induced $[\text{Ca}^{2+}]_i$ mobilization by GHSR1a:DRD1 was not dependent on signaling through $\text{G}\alpha_s$, AC-PKA, $\text{G}\alpha_{i/o}$ -G $\beta\gamma$, or PKC (Figures S4A–S4E). Coexpressing DRD1 with GHSR1a mutants lacking constitutive activity

Figure 1. Co-expression of GHSR1a and DRD1 in Mouse Hippocampal Neurons and Heteromer Formation Measured by FRET Confocal Microscopy and TIRF-M

(A) Brain sections from *Ghsr*-IRES-tauGFP mice stained for DRD1 (red) and GHSR1a (green). White arrows indicate individual neurons co-expressing GHSR1a and DRD1 (ArcN/ME, arcuate nucleus and median eminence; LH, lateral hypothalamus). Coexpression of GHSR1a and DRD1: 46%, DG; 17%, CA3; 10%, CA1 regions. Scale bar, 10 μm .

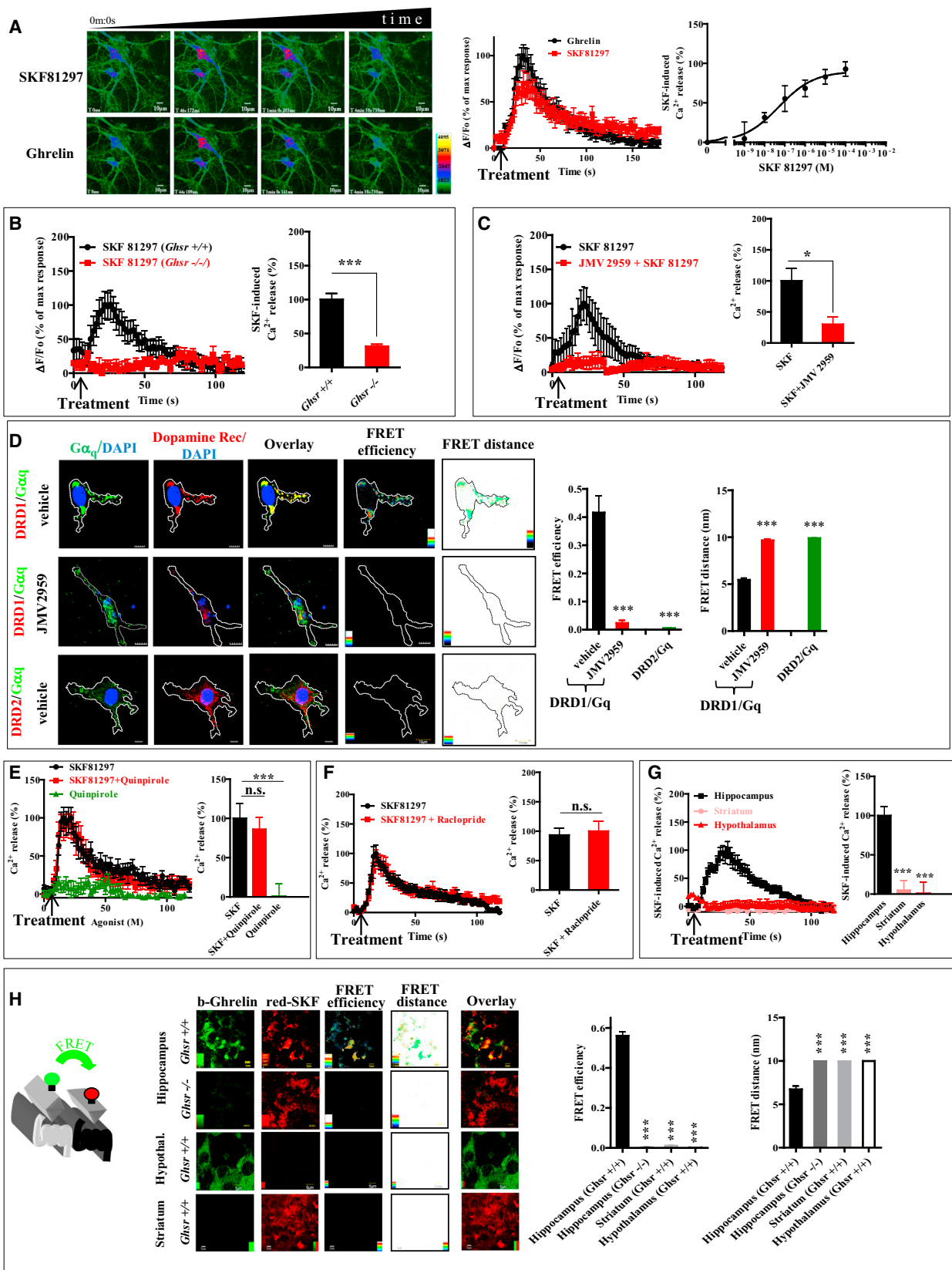
(B) Confocal microscopic FRET analysis of GHSR1a:DRD1 heteromers in DG, Scale bar, 5 μm .

(C and D) Quantification of trajectories of GHSR1a and DRD1 in neuron processes: GHSR1a (red), DRD1 (green), overlapping (yellow). MSD versus time, and diffusion coefficients of GHSR1a trajectories in and outside a complex with DRD1(C; $n_{\text{trajectories}} = 236$), and DRD1 trajectories in and outside a complex with GHSR1a (D; $n_{\text{trajectories}} = 111$).

(E) Two-color single-molecule TIRF-M images of interactions of GHSR1a with DRD1 in dendritic processes of hippocampal neurons before and after SKF81297 (1 μM) treatment: GHSR1a (red), DRD1 (green). Kymographs images of co-localization (yellow); quantitative analysis of the interactions measured by area of co-localization and counts of co-localization.

(F) Individual GHSR1a trajectories by TIRF-M before and after SKF81297 treatment: MSD versus time, diffusion coefficients.

Data represent the mean \pm SEM of at least three experiments (* $p < 0.05$ versus control; ** $p < 0.01$ versus control; *** $p < 0.001$ versus control).



(legend on next page)

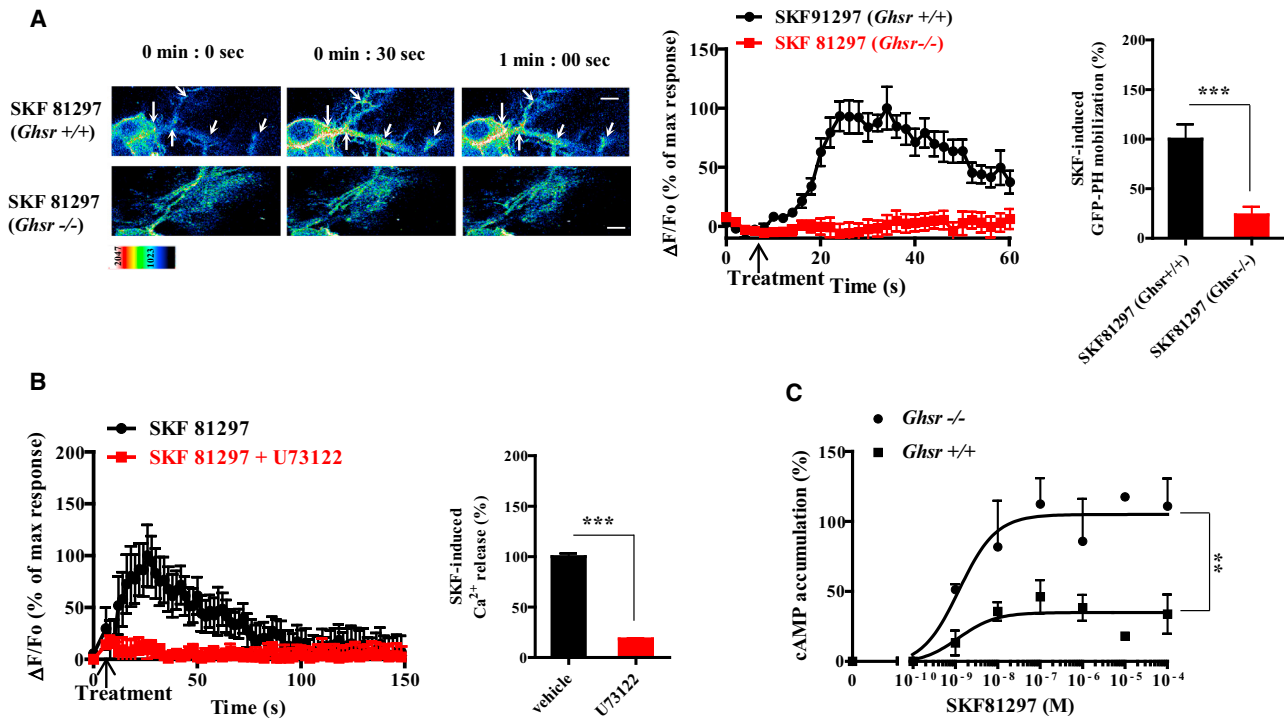


Figure 3. In Hippocampal Neurons, GHSR1a Modifies DRD1 Canonical Signaling to Induce $[Ca^{2+}]_i$ Release via $G\alpha_q$ at the Expense of $G\alpha_s$ Coupling

(A) SKF81297 (10 μ M) induces translocation of the PLC sensor (GFP-PH) to cytoplasm in neurons of *Ghsr* $^{+/+}$ mice (upper row), but not neurons of *Ghsr* $^{-/-}$ mice (lower row); Scale bar, 5 μ m.

(B) PLC inhibitor (U73122, 10 μ M) blocks SKF81297 (10 μ M)-induced $[Ca^{2+}]_i$ release in hippocampal neurons.

(C) Dose-dependent effects of SKF81297 treatment on cAMP accumulation is lower in hippocampal membranes from *Ghsr* $^{+/+}$ (■) than in membranes from *Ghsr* $^{-/-}$ (●) mice.

Data represent the mean \pm SEM of at least three independent experiments (** $p < 0.01$ versus control; *** $p < 0.001$ versus control).

(F279L and A204E) resulted in dopamine-induced Ca^{2+} release (Figure S4F); hence, non-canonical DRD1 signaling is independent of GHSR1a constitutive activity. The observed 30%–40% reduction in the Ca^{2+} response is likely explained by the lower affinity of the mutants for forming heteromers with DRD1 (Figure S4G).

To test for formation of an apo-GHSR1a:DRD1: $G\alpha_q$ complex in HEK293 cells, we combined bimolecular fluorescence complementation (BiFC) and BRET analysis (Galés et al., 2006). Co-expression of split YFP-tagged GHSR1a and DRD1 (GHSR1a-YFP-C and DRD1-YFP-N) produced YFP fluores-

cence localized on the plasma membrane, confirming formation of GHSR1a:DRD1 heteromers (Figure S5A). Expression of $G\alpha_q$ -Rluc8 with the split YFP-tagged GHSR1a and DRD1 produced a robust BRET signal, consistent with $G\alpha_q$ in a preassembled complex with GHSR1a:DRD1, which was not observed in control experiments ($G\alpha_q$ -Rluc coexpressed with DRD1-YFP-N + DRD1-YFP-C or empty vector) (Figure S5A). Agonist treatment markedly reduced the BRET signal associated with the GHSR1a-YFP-C:DRD1-YFP-N: $G\alpha_q$ -Rluc8 complex, illustrating agonist-induced dissociation of $G\alpha_q$ (Figure S5A). To assess direct coupling to the $G\alpha_q\beta\gamma$ trimer, $G\alpha_q$ -Rluc8 and split

Figure 2. In Hippocampal Neurons, DRD1 Agonist-Induced $[Ca^{2+}]_i$ Mobilization Is Dependent on GHSR1a, but Not on DRD2

(A) SKF81297 (10 μ M, upper row) produced a transient Ca^{2+} response in hippocampal neurons; after removing SKF81297 the same cells responded to ghrelin (100 nM, lower row). SKF81297 induced dose-dependent $[Ca^{2+}]_i$ release (right). Scale bar, 10 μ m.

(B) SKF81297-induced $[Ca^{2+}]_i$ mobilization in hippocampal organotypic slices from *Ghsr* $^{+/+}$ and *Ghsr* $^{-/-}$ mice (left).

(C) JMV2959 (10 μ M) inhibits SKF81297 (10 μ M) induced $[Ca^{2+}]_i$ mobilization in hippocampal organotypic slices.

(D) Hippocampal neurons treated with vehicle (upper) or JMV2959 (middle); $G\alpha_q$ (green) and DRD1 (red) images analyzed by FRET microscopy. Lower row: DRD2 (red), $G\alpha_q$ (green); quantitative analysis of FRET efficiency and FRET distance (right). Scale bar, 10 μ m.

(E and F) $[Ca^{2+}]_i$ mobilization in hippocampal organotypic slices in the presence of SKF81297 (10 μ M), SKF81297 (10 μ M) + Quinpirole (10 μ M), and Quinpirole (10 μ M) (E); or SKF81297 (10 μ M) and SKF81297 (10 μ M) + Raclopride (10 μ M) (F).

(G) SKF81297-induced (10 μ M) $[Ca^{2+}]_i$ mobilization in neurons from hippocampus, hypothalamus, and striatum (left).

(H) FRET confocal microscopy images on organotypic brain slices from hippocampus, hypothalamus, and striatum of *Ghsr* $^{+/+}$ mice; slices from *Ghsr* $^{-/-}$ as control. GHSR1a (green), DRD1 (red); Scale bar, 5 μ m.

Data represent the mean \pm SEM of at least three independent experiments in duplicate (* $p < 0.05$ versus control; *** $p < 0.001$ versus control).

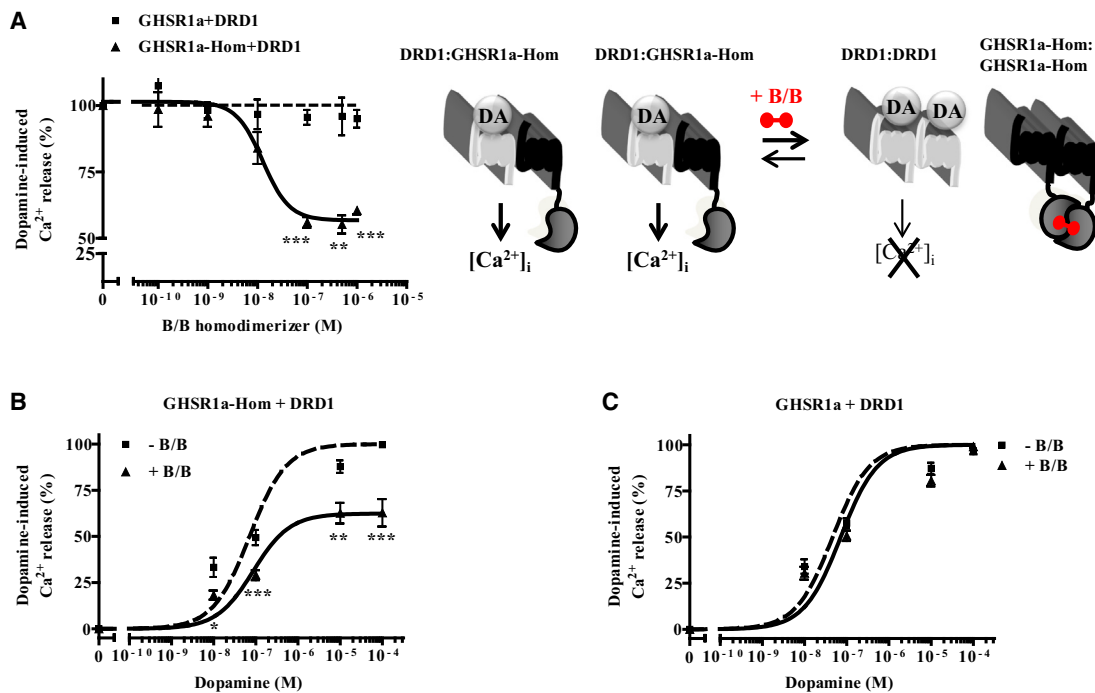


Figure 4. Dopamine-Induced $[Ca^{2+}]_i$ Mobilization Correlates with Formation of GHSR1a:DRD1 Heteromers

(A) Dopamine-induced $[Ca^{2+}]_i$ mobilization measured in HEK-AEQ cells expressing DRD1 with either GHSR1a (■) or GHSR1a-Hom (▲) preincubated with increasing concentrations of homodimerization inducer (B/B).

(B and C) Dose-dependent dopamine-induced $[Ca^{2+}]_i$ release in the absence or presence of B/B in cells coexpressing GHSR1a-Hom and DRD1 (B) or in cells coexpressing GHSR1a and DRD1 (C).

Data represent the mean \pm SEM of at least three independent experiments (*p < 0.05 versus control; **p < 0.01 versus control; ***p < 0.001 versus control).

Venus-G β_1 and -G γ_2 proteins were coexpressed with GHSR1a and DRD1 (Figure S5B). The BRET signal was attenuated by SKF81297 treatment ($p < 0.001$; Figure S5B, middle panel), consistent with DRD1 pre-coupling to G α_q and agonist-induced dissociation of the heterotrimeric G protein complex. Pretreatment with JMV2959 dose-dependently inhibited the SKF81297-induced decrease in BRET ($IC_{50} = 477 \pm 45$ nM; Figure S5B, right panel); hence, GHSR1a is intimately involved in DRD1:G α_q coupling. Dopamine-induced cAMP accumulation was reduced when DRD1 was expressed with GHSR1a, indicating GHSR1a promotes DRD1 coupling to G α_q at the expense of G α_s coupling (Figure S5C).

To determine whether GHSR1a antagonists inhibit dopamine-induced Ca $^{2+}$ mobilization by interfering with allosteric interactions between GHSR1a and DRD1, three structurally distinct GHSR1a neutral antagonists (JMV2959, JMV3002, and BIM-28163) equipotent in inhibiting ghrelin activation of GHSR1a were tested (Figure S5D). The antagonists had no effect on DRD1-induced cAMP accumulation (Figure S5E). JMV2959 was a full antagonist of dopamine-induced $[Ca^{2+}]_i$ release, while JMV3002 and BIM were partial antagonists (Figure S5F). BRET titration employing Nluc-GHSR1a and SNAP-DRD1 in the presence or absence of each GHSR1a antagonist was performed. JMV2959 did not affect the BRET $_{50}$, but significantly changed the BRET $_{max}$ (BRET $_{max}$ control, 0.0038 ± 0.0008 , and BRET $_{max}$ JMV2959, 0.0017 ± 0.0005 ; $p < 0.05$; Figure S5G), indicating JMV2959 modifies

allosteric interactions between GHSR1a and DRD1 (Hamdan et al., 2006). Furthermore, in agreement with their inhibitory effects on dopamine-induced $[Ca^{2+}]_i$ mobilization (Figure S5F), JMV3002 and BIM-28163 were less active than JMV2959 in the BRET assay (Figure S5H). These results support an allosteric mechanism for GHSR1a dependent non-canonical DRD1 signaling.

Although the collective data supported formation of a preassembled apo-GHSR1a:DRD1:G α_q complex, and indicated dopamine-induced $[Ca^{2+}]_i$ release is mediated via DRD1:G α_q , an alternative explanation is that dopamine binding to DRD1 modifies the conformation of DRD1 that in turn allosterically induces apo-GHSR1a:G α_q coupling. To test this possibility we generated a GHSR1a mutant where residues in the third intracellular loop necessary for G α_q coupling were inactivated by alanine substitution. A(237-244)-GHSR1a did not couple to G α_q and was refractory to activation by ghrelin, and ELISA assays confirmed expression on the cell surface (Figures S6A–S6D); Tr-FRET assays illustrated heteromer formation with DRD1 (Figures S6E and S6F). Despite the inability of A(237-244)-GHSR1a to couple to G α_q , dopamine treatment of A(237-244)-GHSR1a:DRD1 heteromers dose-dependently induced Ca $^{2+}$ transients, confirming direct coupling of DRD1 to G α_q . However, the amplitude of the Ca $^{2+}$ response was ~50% that of WT-GHSR1a:DRD1 (Figure S6G), suggesting that signaling via WT-GHSR1a:DRD1 heteromers is mediated by a combination of DRD1:G α_q and apo-GHSR1a:G α_q coupling (Figure S6H).

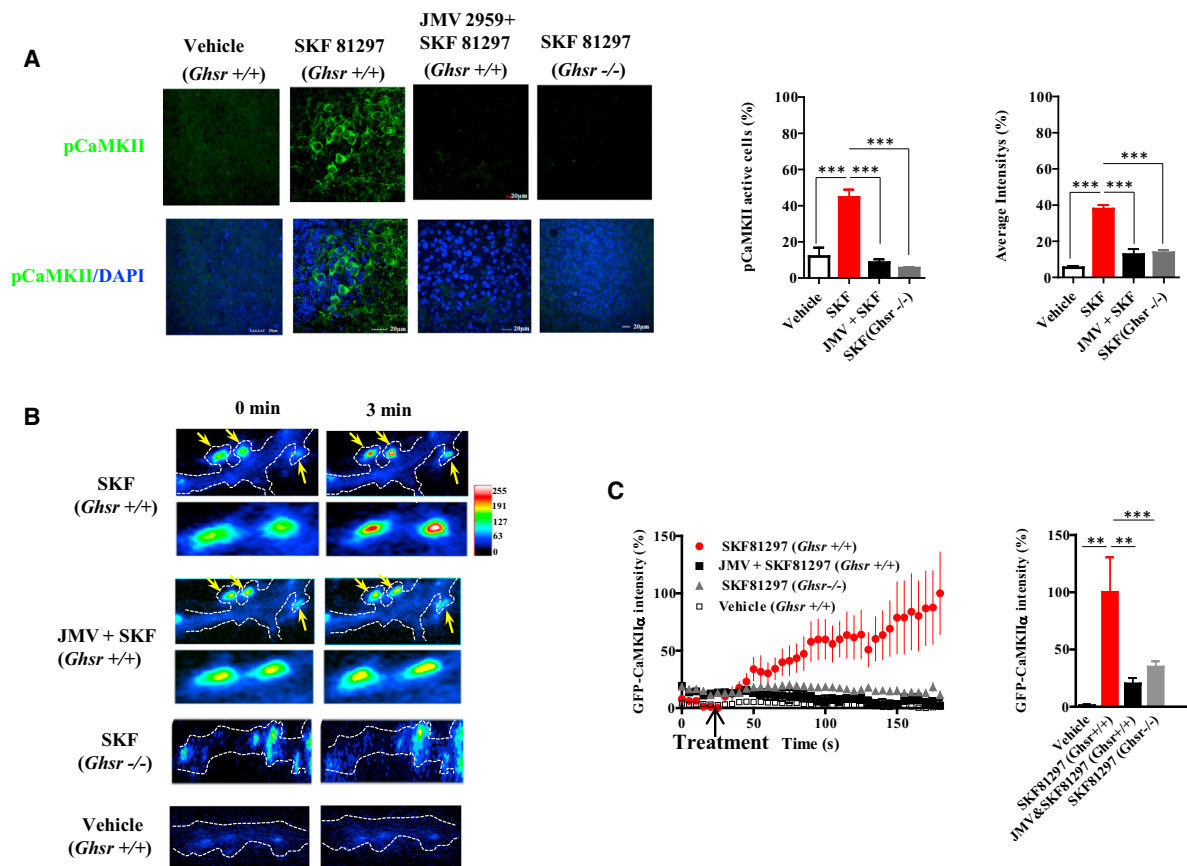


Figure 5. DRD1 Agonist-Induced CaMKII Activation in Hippocampal Neurons Is Dependent upon GHSR1a:DRD1 Interactions

(A) Hippocampal slices from *Ghsr* +/+ and *Ghsr* -/- mice treated with SKF81297 (10 μ M) \pm JMV2959 illustrating phosphorylation of CaMKII (left) and quantitative analysis (right panels).

(B and C) Representative TIRF-M images (B) and time lapse plot (C; left graph) with quantitative analysis (C; right graph) from neurons of *Ghsr* +/+ or *Ghsr* -/- mice expressing GFP-CaMKII α following treatment with SKF81297 \pm JMV2959.

Data represent the mean \pm SEM of at least three independent experiments: **p < 0.01 versus control; ***p < 0.001 versus control.

DRD1 Agonist-Induced Activation of Synaptic Plasticity Markers in Hippocampal Neurons Is Dependent on apo-GHSR1a

Phosphorylation of CaMKII is involved in activation of synaptic plasticity and is regulated by Ca^{2+} ; therefore, we asked if apo-GHSR1a was essential for DRD1 agonist activation of CaMKII. When we treated organotypic hippocampal slices from *Ghsr* +/+ mice with SKF81297, the number of pCaMKII-positive neurons was markedly enhanced ($44.56\% \pm 4.3\%$ versus vehicle $11.94\% \pm 4.9\%$, p < 0.001; Figure 5A), as was the intensity of staining ($37.8\% \pm 2.2\%$ versus vehicle $5.4\% \pm 1\%$, p < 0.001; Figure 5A). Pretreatment with JMV2959 inhibited the effect of SKF81297. Also, hippocampal slices from *Ghsr* -/- mice were refractory to SKF81297-induced CaMKII phosphorylation (Figure 5A), further illustrating dependence on GHSR1a. Synaptic activity results in pCaMKII translocation from the dendritic cytoplasm to the synapse. Time-lapse imaging of hippocampal neurons from *Ghsr* +/+ mice expressing GFP-CaMKII α cDNA showed that SKF81297-induced accumulation of GFP-CaMKII at synapses (Figure 5B); this phenomenon was markedly attenuated in hippocampal neurons from *Ghsr* -/- mice ($100\% \pm$

30.5% versus $34.78\% \pm 4.8\%$, p < 0.01; Figure 5C). Pretreating *Ghsr* +/+ neurons with JMV2959 inhibited SKF81297-induced CaMKII translocation ($20\% \pm 4.9\%$, p < 0.01; Figure 5C). Hence, DRD1 agonist-mediated CaMKII activation and translocation is dependent on GHSR1a. Synaptic localization of translocated GFP-CaMKII α was confirmed using the post-synaptic marker PSD95-DsRed (Figure S7A).

Synaptic plasticity and hippocampal memory formation are regulated by glutamate receptors. Phosphorylation of the GluR1 subunit of AMPAR at Ser831 by CaMKII is critical for AMPAR function and trafficking (Barria et al., 1997). SKF81297 increased Ser831 phosphorylation in organotypic hippocampal slices from *Ghsr* +/+ mice that was inhibited by pretreatment with either the CaMKII inhibitor (KN93), or JMV2959 (p < 0.001; Figure 6A). In *Ghsr* -/- hippocampal slices, SKF81297 activation of AMPAR was markedly lower, illustrating dependence on GHSR1a (p < 0.001; Figure 6A). To determine whether exocytosis of glutamate receptors in hippocampal neurons was dependent on GHSR1a:DRD1 signaling, we employed pHluorin-tagged NR1 and GluR1 subunits (SEP-NR1 and SEP-GluR1). When hippocampal neurons from *Ghsr* +/+ expressing SEP-NR1 or

SEP-GluR1 were treated with SKF81297, significant increases in fluorescence intensity were observed, indicating exocytosis of glutamate receptors at synapses (Figures 6B and 6C); similarly treated neurons from *Ghsr*^{-/-} mice were unresponsive. Pretreatment of *Ghsr*^{+/+} mouse neurons with JMV2959 inhibited SKF81297-induced exocytosis of NR1 and GluR1 ($p < 0.001$; Figures 6B and 6C), confirming that DRD1 agonist-induced exocytosis of glutamate receptors is dependent on interactions between GHSR1a and DRD1. Lifeact was used to measure actin accumulation (Riedl et al., 2008): SKF81297 treatment enhanced actin accumulation in hippocampal neurons, which was significantly reduced by JMV2959 pretreatment, indicating that SKF81297-mediated synaptic reorganization is dependent on GHSR1a ($p < 0.001$; Figure 6D).

If DRD1 agonist activation of neuronal plasticity in hippocampal neurons is dependent on GHSR1a, transcription of genes involved in initiation of neuronal plasticity should also be dependent on GHSR1a. Neuronal activity frequently correlates with signaling pathways that induce phosphorylation of ribosomal protein S6. We applied ribosome capture to enrich for mRNAs expressed in response to SKF81297 activation of hippocampal neurons and to enhance the dynamic range of enrichment employed pS6-244 selective immunoprecipitation (Knight et al., 2012). SKF81297 markedly increased pS6-244 immunofluorescent cells in hippocampal slices from *Ghsr*^{+/+} mice relative to vehicle treatment ($52.43\% \pm 7\%$ versus, $8.84\% \pm 1.18\%$ $p < 0.001$; Figures 6E and 6F); fluorescence intensity was also enhanced ($100\% \pm 6.85\%$ versus $9.57\% \pm 1\%$, $p < 0.001$, Figures 6E and 6G). JMV2959 pretreatment markedly lowered SKF81297-induced S6-244 phosphorylation in *Ghsr*^{+/+} slices; slices from *Ghsr*^{-/-} mice were refractory to SKF81297 treatment ($p < 0.001$; Figures 6E–6G). Treatment with 2-aminoethoxydiphenyl borate (2-APB) inhibited SKF81297-induced S6-244 phosphorylation (Figure S7B), indicating activation is dependent on release of $[Ca^{2+}]_i$. Analysis of mRNA eluted from immunoprecipitated pS6-244-positive ribosomes from SKF81297-treated *Ghsr*^{+/+} hippocampal slices showed enriched expression of genes associated with initiation of synaptic plasticity: Nr4a1, Nr4a2, Nr4a3, Ntrk2, Arc, and Zif268 (Figure 6H). Pretreatment with JMV2959 inhibited SKF81297-induced expression of these genes (Figure 6H). In addition, enhanced expression of these genes was not observed when slices from *Ghsr*^{-/-} mice were treated with SKF81297 (Figure 6H). These data illustrate that DRD1-induced initiation of hippocampal synaptic plasticity is GHSR1a-dependent and further support an important functional role for apo-GHSR1a:DRD1 heteromers.

Dependence on Hippocampal GHSR1a for DRD1 Regulated Behaviors

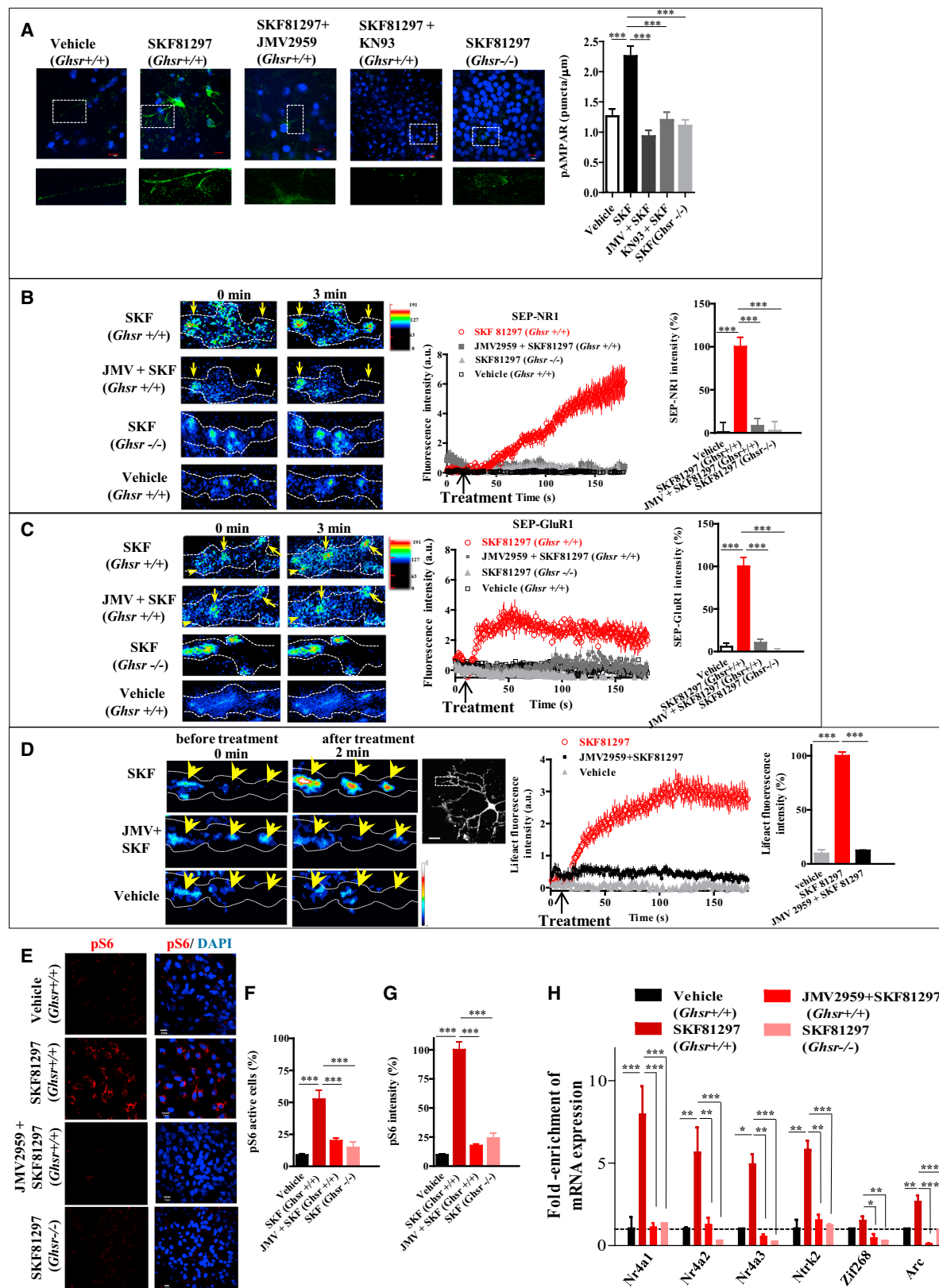
We next examined the biological relevance of apo-GHSR1a-dependent DRD1 signaling in the hippocampus by measuring DRD1 agonist-induced behavioral responses when GHSR1a was either genetically or pharmacologically inactivated. Pre-pulse inhibition (PPI) is a measure of sensorimotor gating that determines how well an animal can integrate and inhibit sensory information (Mansbach et al., 1988). Although the nucleus accumbens was once viewed as the primary structure involved in dopamine-induced interference with PPI, subsequent studies

with DRD1 selective agonists and antagonists applied systemically or directly to the hippocampus showed that disruption of PPI involved DRD1 agonist action on the dorsal hippocampus (Ellenbroek et al., 2002). Given these findings, we tested whether DRD1-induced interference with PPI was dependent upon GHSR1a by comparing PPI in DRD1agonist-treated *Ghsr*^{+/+} and *Ghsr*^{-/-} mice. In the absence of the DRD1 agonist, both genotypes produced identical PPI responses (Figure 7A). When mice were injected with the DRD1 agonist, PPI was disrupted in *Ghsr*^{+/+} mice, but not in *Ghsr*^{-/-} mice (Figure 7A); therefore, DRD1-induced interference with PPI is dependent upon GHSR1a.

Coexpression of GHSR1a and DRD1 is most abundant in the DG of the hippocampal structures and neuronal activity that influences synaptic potentiation and memory is propagated through the DG. Our ex vivo experiments showed that DRD1 agonist induced biochemical changes associated with initiation of hippocampal synaptic plasticity are blocked by JMV2959. Therefore, we selected behavioral tests of memory associated with activation of synaptic plasticity that is enhanced by hippocampal DRD1 agonism and asked if enhanced performance was inhibited by JMV2959.

DRD1 signaling in the DG is implicated in contextual fear conditioning (CFC) (Sariñana et al., 2014), and agonist activation of DRD1 in the dorsal hippocampus results in consolidation of CFC extinction (Fiorenza et al., 2012). Therefore, we asked whether DRD1-mediated extinction of CFC was dependent on GHSR1a. Mice were trained in the CFC apparatus and then placed in their home cage. The mice were returned to the apparatus 24 hr later and Extinction-1 phase (20 min) was measured (Figure 7B). The freezing response of the mice declined as a function of time (compare 0–3 min with 17–20 min, Figure 7B). Immediately after Extinction-1, mice received intra-DG infusions of vehicle, SKF81297, SKF81297 + JMV2959, or JMV2959 alone (Figure S7C). Twenty-four hours later Extinction-2 was performed. Mice treated with SKF81297 exhibited a significant decrease in freezing behavior compared to the vehicle-treated group, consistent with DRD1 agonist-induced consolidation of extinction memory (Figure 7B). In mice coadministered JMV2959 and SKF81297, the freezing response was equal to that in vehicle-treated controls; hence, JMV2959 inhibits SKF81297-induced consolidation of extinction (Figure 7B), illustrating dependence on allosteric interactions between GHSR1a and DRD1.

To determine if allosteric interactions between GHSR1a and DRD1 in the DG are important for DRD1-mediated enhancement of working memory, we utilized the T-maze alternation test (Deacon and Rawlins, 2006). Alternation is viewed as an excellent test for determining hippocampal function in mice and for mice is a more robust test than the Morris water maze (Deacon and Rawlins, 2006). Mice were trained to learn a food pellet is placed in alternate arms of the T-maze. Training is considered complete when the mice make the correct choice 75% of the time (Figure 7C). On the test day, mice received intra-DG infusion of vehicle, SKF81297, SKF81297 + JMV2959, or JMV2959 alone. The mice were retested without delay and then after a 90 s delay. In contrast to vehicle infusion, mice infused with SKF81297 continued to make 75% correct choices following the 90 s delay,



(legend on next page)

consistent with enhanced working memory ($p < 0.05$; **Figure 7C**). Coadministration of JMV2959 with SKF81297 blocked the beneficial effect of SKF81297 on working memory ($p < 0.05$; **Figure 7C**). Infusion of JMV2959 alone had no effect on immediate performance, but performance was impaired following a 90 s delay and inferior to that of vehicle infused mice (**Figure 7C**), indicating that JMV2959 inhibited endogenous dopamine/DRD1 signaling. These results provide additional evidence for the biological significance of allosteric interactions between GHSR1a and DRD1 in the DG.

DISCUSSION

Our objective was to determine the functional role of the ghrelin receptor (GHSR1a) in the hippocampus where endogenous ghrelin is undetectable ([Banks et al., 2002](#); [Furness et al., 2011](#); [Grouselle et al., 2008](#); [Sakata et al., 2009](#)). The absence of endogenous ghrelin in the mouse brain is supported by pharmacokinetic studies following i.v. administration of mouse ^{131}I -ghrelin ([Banks et al., 2002](#)). When administered systemically to mice, ghrelin binding in the CNS is confined to hypothalamic neurons ([Schaeffer et al., 2013](#)); c-Fos is activated in the arcuate nucleus, paraventricular nucleus (PVN), and lateral hypothalamus (LH) ([Pirnik et al., 2011](#)). Infusing ghrelin directly into the LH releases orexin, and orexin acts on ventral tegmental area (VTA) neurons causing dopamine release ([Cone et al., 2014](#)). Dopaminergic neurons in the VTA innervate the hippocampus, implicating a VTA-hippocampal loop that regulates hippocampal plasticity ([Gasbarri et al., 1994](#); [Lisman and Grace, 2005](#); [Swanson, 1982](#)). These data argue that the effects of pharmacological doses of ghrelin on the hippocampus that have been proposed to be a direct effect on synaptic plasticity are instead indirect and mediated by dopamine. Physiologically, the absence of endogenous ghrelin in the hippocampus allows apo-GHSR1a to modify dopamine signaling locally through apo-GHSR1a:DRD1 heteromer formation, which initiates synaptic plasticity through DRD1 coupling to $\text{G}\alpha_q$.

Intriguingly, dynamic studies in hippocampal neurons show DRD1 agonism enhances interactions between DRD1 and GHSR1a. DRD1 agonism also regulates the dynamics of DRD1 and N-methyl-D-aspartate (NMDA) receptor interactions in synapses ([Ladepeche et al., 2013](#)). Studies in WT rodents that express GHSR1a endogenously demonstrated that DRD1 regu-

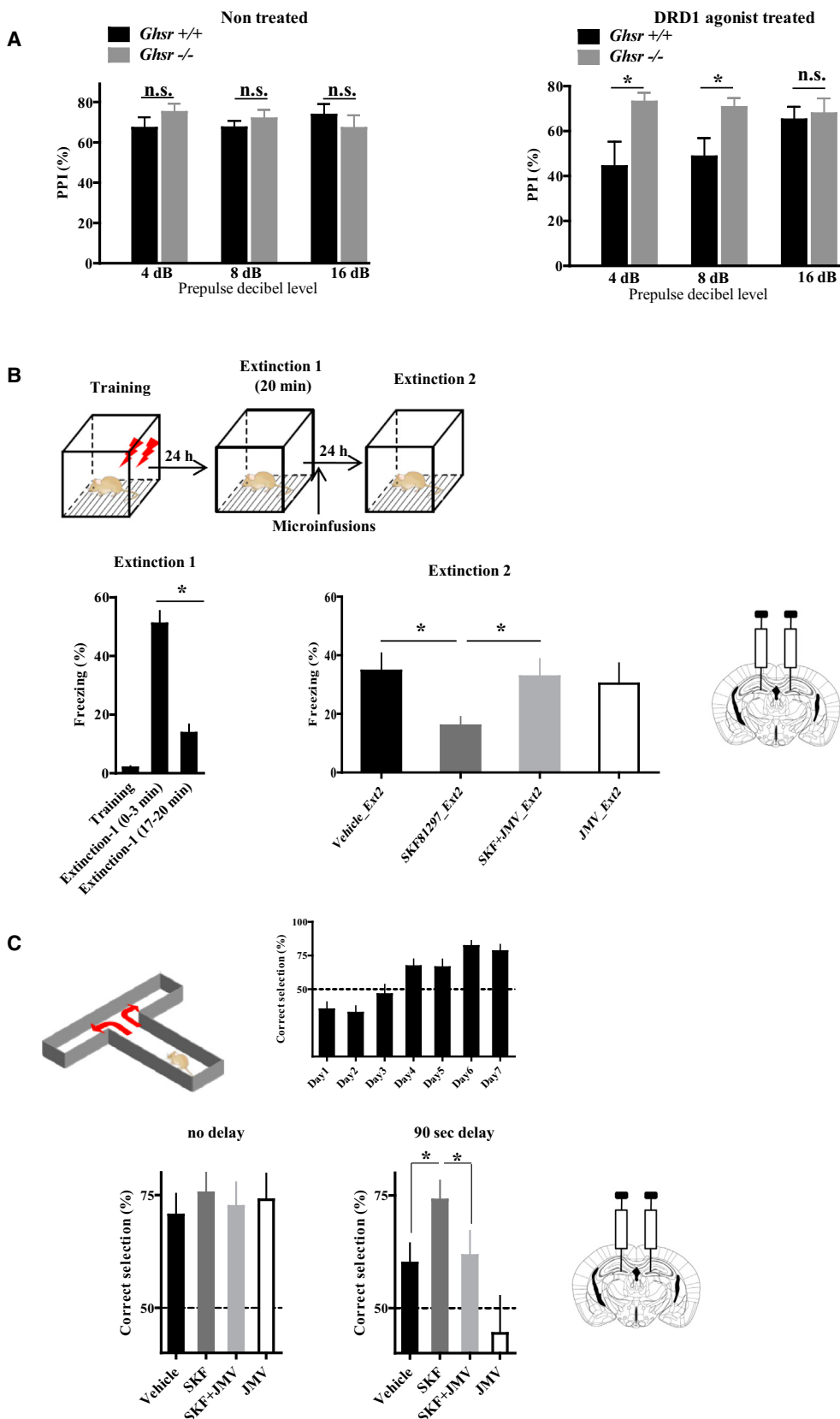
lates synaptic plasticity and long-term potentiation (LTP) by enhancing NMDA responses. DRD1 and NMDA receptor (NMDAR) interact through intracellular signaling involving heteromerization ([Cepeda and Levine, 2006](#)). DRD1 agonism enhances NMDA responses in the hippocampus, cortex, and striatum through signaling cascades involving release of $[\text{Ca}^{2+}]_i$ and activation of CaMKII, PKC, and PKA ([Cepeda and Levine, 2006](#)). Our results support this mechanism and further suggest dopamine activation of GHSR1a:DRD1 as an initiation step for enhancing NMDA currents. Indeed, dependence on GHSR1a for DRD1-induced exocytosis of NR1 supports GHSR1a:DRD1 heteromers as enhancers of the NMDA response. In hippocampal neurons, dissociation of DRD1:NR1 complexes upon DRD1 activation facilitates CaMKII activity ([Nai et al., 2010](#)), which is consistent with the idea that dissociation of the DRD1:NR1 heteromer could shift stoichiometry toward an increase in GHSR1a:DRD1 heteromers, and as a consequence increase dopamine activation of CaMKII as observed here. Clearly, additional studies are needed to elucidate the role of GHSR1a:DRD1 in DRD1 regulation of NMDA signaling and relationships to DRD1:NR1 complex formation.

Elucidating the mechanism of signaling through GHSR1a:DRD1 hippocampal neurons revealed preassembly of an apo-GHSR1a:DRD1: $\text{G}\alpha_q$ macro-complex. Proximity measurements and biochemical studies implicate a mechanism where dopamine-induced $[\text{Ca}^{2+}]_i$ mobilization is mediated by direct coupling of DRD1 to $\text{G}\alpha_q$. DRD1: $\text{G}\alpha_q$ coupling was confirmed by substituting WT-GHSR1a for a GHSR1a mutant where sites for $\text{G}\alpha_q$ coupling were inactivated and showing that dopamine activation of the mutant-GHSR1a:DRD1 heteromer mobilized $[\text{Ca}^{2+}]_i$. Nevertheless, compared to WT-GHSR1a:DRD1 the magnitude of dopamine-induced Ca^{2+} release was reduced by $\sim 50\%$, suggesting that with WT-GHSR1a:DRD1, both DRD1: $\text{G}\alpha_q$ and apo-GHSR1a: $\text{G}\alpha_q$ coupling was involved. What is the stoichiometry? In lipid nanodiscs, apo-GHSR1a homomers assemble asymmetrically with only one protomer actively coupling to $\text{G}\alpha_q$, while the other protomer is inactive, and in the case of an apo-GHSR1a heteromer, apo-GHSR1a is not actively coupled to $\text{G}\alpha_q$ ([Mary et al., 2013](#)). Based on these findings, we speculate that dopamine-induced $[\text{Ca}^{2+}]_i$ release is mediated through an asymmetric heterotetramer ($\text{G}\alpha_q$:GHSR1a:DRD1:GHSR1a:DRD1: $\text{G}\alpha_q$) where asymmetry allows just one GHSR1a and one DRD1 molecule to actively couple to $\text{G}\alpha_q$. $\text{G}\alpha_q$ coupling and signaling through PLC is fundamentally important for DRD1 agonist activation of

Figure 6. DRD1 Activation of Neuronal Plasticity Markers in Hippocampal Neurons Is Dependent on GHSR1a:DRD1 Interactions

- (A) Phosphorylation of AMPAR (p831-GluR1) in organotypic hippocampal slices from *Ghsr*^{+/+} mice treated with vehicle, SKF81297 (10 μM), JMV2959 (10 μM) + SKF81297 (10 μM), and CaMKII inhibitor (KN93) + SKF81297 (10 μM); control, slices from *Ghsr*^{-/-} mice treated with SKF81297 (10 μM) (left); and quantitative analyses (right). Scale bar, 10 μm .
- (B and C) SKF81297-induced exocytosis of NR1 or GluR1 detected by TIRF-M. Hippocampal neurons from *Ghsr*^{+/+} and *Ghsr*^{-/-} mice expressing SEP-NR1 (B) or SEP-GluR1 (C) treated with SKF81297 (10 μM) and \pm JMV2959 (10 μM); representative images before and after treatment (left); time lapse plot and quantitative analysis (right).
- (D) Representative images of hippocampal neuronal processes expressing mCherry-Lifeact, following treatment with SKF81297 (10 μM) \pm JMV2959 (10 μM) (left); time lapse plot (middle) and quantitative analysis (right); scale bar, 20 μm .
- (E) Activation of hippocampal neurons in organotypic slices measured by pS6 immunofluorescence (red); nuclei (blue); scale bar, 10 μm .
- (F and G) Quantitative analysis according to number of pS6-positive cells (F) or to pS6 immunofluorescence intensity (G).
- (H) Gene expression of early markers associated with initiation of neuronal plasticity in hippocampal organotypic slices treated with vehicle or SKF81297 (10 μM) \pm JMV2959 (10 μM).

Data represent the mean \pm SEM of at least three independent experiments (* $p < 0.05$ versus control; ** $p < 0.01$ versus control; *** $p < 0.001$ versus control).



(legend on next page)

Ca^{2+} transients and induction of hippocampal synaptic plasticity. When GHSR1a is inactivated, DRD1 couples to $\text{G}\alpha_s$ and DRD1 agonism augments cAMP accumulation, but synaptic plasticity is not initiated. We conclude that $\text{G}\alpha_q$ coupling via GHSR1a:DRD1 is essential for initiating synaptic plasticity and priming hippocampal neurons for subsequent events involving cAMP signaling and protein synthesis-dependent long-term memory formation (Abel et al., 1997). Do $\text{G}\alpha_q$ and $\text{G}\alpha_s$ sequentially and/or synergistically regulate downstream pathways that lead to memory formation? By dissociating DRD1-induced $\text{G}\alpha_q$ -PLC from $\text{G}\alpha_s$ -PKA signaling, we provide a strategy for dissecting these mechanisms.

Since GHSR1a:DRD1 heteromers are abundantly expressed in the DG, the gateway for regulating hippocampal function, we asked whether dependence on GHSR1a for activating hippocampal synaptic plasticity ex vivo translates to performance in vivo. In the DG, contextual memory is dependent on DRD1 (Sariñana et al., 2014). We showed that direct infusion of a DRD1 agonist into the DG of WT mice augments extinction of CFC, and extinction was blocked by co-infusion of the GHSR1a antagonist JMV2959. Similarly, DRD1 agonist infusion into the DG improved working memory that was also blocked by JMV2959 coinfusion. The results of these behavioral tests show that DRD1 agonist-induced behaviors are dependent on interactions between DRD1 and GHSR1a in the DG, confirming the biological relevance of conclusions derived from ex vivo experiments in hippocampal neurons.

In the dorsal hippocampus, DRD1 plays a role in integrating and filtering sensory information (Ellenbroek et al., 2002). Impairments in this process have been linked to neuropsychiatric disorders, which can be assessed in rodents and humans by measuring PPI of the acoustic startle response. Peripheral administration of a DRD1 agonist to WT mice caused disruption of PPI, but *Ghsr*-null mice were resistant. Hence, by selectively blocking dopamine signaling in GHSR1a:DRD1 expressing neurons, GHSR1a antagonists may have utility in treating psychoses, such as schizophrenia. As a further illustration of dependence on GHSR1a for sensorimotor gating, a recent report showed that disruption of PPI in rats by the noncompetitive inhibitor of the NMDA receptor phencyclidine was blocked by JMV2959 (Engel et al., 2015).

In conclusion, we show apo-GHSR1a is fundamentally important for dopamine/DRD1-induced initiation of hippocampal synaptic plasticity and formation of hippocampal memory. All previously reported studies that elucidated mechanisms of dopamine regulation of hippocampal function were conducted in rodents expressing GHSR1a endogenously; therefore, the critical role of apo-GHSR1a would have been overlooked. The results we describe—combined with conclusions from our previous work showing a functional role for apo-

GHSR1a:DRD2 heteromers in native hypothalamic neurons (Kern et al., 2012)—illustrate a previously unrecognized, but critical role for apo-GHSR1a as a modulator of dopamine signaling. Of significance toward CNS drug discovery, the GHSR1a antagonists tested allosterically inhibit dopamine-induced Ca^{2+} mobilization through apo-GHSR1a:DRD1. Based on this mechanism, different structural classes of GHSR1a antagonists have the potential to enhance, rather than inhibit, dopamine signaling. This concept has profound therapeutic implications because it allows selective pharmacological fine-tuning of dopamine signaling in subsets of neurons that express GHSR1a:DRD2 or GHSR1a:DRD1, without affecting neurons expressing DRD2 or DRD1 alone. Broader application of this concept involves identifying neutral molecules that target the unique structural interface formed by GPCR protomers in a GPCR heteromeric complex. Finally, our results reinforce the importance of knowing the GPCR composition of the clinically important native target cell when developing pharmacologic agents, because the presence or absence of a potential GPCR protomer partner markedly affects biological responses. Indeed, antagonists, agonists, and biased agonists for GPCRs have the potential to modify signal transduction, depending on whether signaling proceeds via GPCR monomers, homomers, or heteromers.

EXPERIMENTAL PROCEDURES

Hippocampal Primary Cell Isolation and Organotypic Brain Slice Preparation

Primary cells were isolated from hippocampi of P1–P3 mice. Organotypic brain slices (300 μm) were prepared from hippocampi of post-natal day 5–7 mice and cultured on membrane inserts (see *Supplemental Experimental Procedures* for more details).

Intracellular Ca^{2+} Mobilization, Inducible Homomerization, and cAMP Accumulation

In hippocampal primary cells and organotypic brain slices, Ca^{2+} was detected using GCaMP3. For the inducible homomerization assay, Ca^{2+} was detected in HEK-AEQ cells (Kern et al., 2012) in the absence or presence of homodimerizer (B/B; Clontech). cAMP production in hippocampal brain membranes was measured with LANCE Ultra cAMP assay (Perkin Elmer) (see *Supplemental Experimental Procedures* for more details).

Microscopic TIRF Measurements

TIRF imaging was performed using Olympus Fluoview 1000 equipped with commercially available objective-based TIRF (Olympus); see *Supplemental Experimental Procedures* for more details.

Microscopic FRET Analysis of Hippocampal Neurons and Brain Slices

$\text{G}\alpha_q$ proximity and GHSR1a:DRD1 heteromers in brain slices were detected by FRET microscopy using Olympus Fluoview 1000 (see *Supplemental Experimental Procedures* for more details).

Figure 7. DRD1-Agonist Specific Behaviors Dependent on GHSR1a:DRD1 Interactions

- (A) *Ghsr* +/+ and *Ghsr* –/– mice exhibit a normal PPI response in absence of DRD1 agonist (left). DRD1 agonist treatment interferes with PPI in *Ghsr* +/+ mice, but *Ghsr* –/– mice are resistant (right) ($n = 8$ –12 animals per group).
 - (B) Bilateral infusion of SKF81297 (SKF) into the DG induces extinction of CFC that is blocked by coinfusion of JMV2959 (JMV) (7–10 animals per group).
 - (C) Alternating T-maze test of working memory. Bilateral infusion of SKF81297 (SKF) into the DG enhances of working memory that is blocked by coinfusion of JMV2959 (JMV) (9–10 animals/group).
- Data represent the mean \pm SEM (* $p < 0.05$ versus control).

Immunofluorescence Microscopy of Mouse Brain Sections and Organotypic Brain Slices

GHSR1a and DRD1 immunofluorescence was performed on brain sections from adult male *Ghsr-IRES-tauGFP* mice as described previously (Kern et al., 2012) with modifications.

After treatments, organotypic brain slices were processed for immunofluorescence staining. See more details in *Supplemental Experimental Procedures*.

Ribosome Immunoprecipitation, Purification of mRNA, and qPCR

Ribosomal pS6 immunoprecipitation, mRNA purification, and qRT-PCR was performed on hippocampal organotypic slices as previously described (Knight et al., 2012) (see *Supplemental Experimental Procedures* for more details).

Behavioral Tests

PPI was performed as described previously (Geyer and Dulawa, 2003), CFC was performed as described (Fiorenza et al., 2012), and the delayed alternation T-maze task was performed as described (Deacon and Rawlins, 2006); all the above tests were performed with modifications (see *Supplemental Experimental Procedures* for more details).

Data Analysis

Values are given as means \pm SEM and obtained from the number of separate experiments indicated. Comparisons between the different groups were made using Student's t test or one-way ANOVA test. Data were analyzed using GraphPad Instat software, and a difference of $p < 0.05$ was considered significant.

SUPPLEMENTAL INFORMATION

Supplemental Information includes Supplemental Experimental Procedures and seven figures and can be found with this article online at <http://dx.doi.org/10.1016/j.cell.2015.10.062>.

AUTHOR CONTRIBUTIONS

A.K. and R.G.S. conceived and designed the study. A.K. performed most of the experiments and data analysis. M.M. contributed to design and performance of mice cannulation and the CFC behavioral experiment. C.U. contributed to organotypic brain slice preparation. R.A.-Z. and A.F.B. designed, performed, and analyzed the PPI behavioral experiment. A.K. and R.G.S. wrote the manuscript with input from all authors.

ACKNOWLEDGMENTS

The authors thank Bryan Wharram and Dr. Sukhvir Mahal (TSRI) for assistance in managing the mouse colonies, and Dr. Cristina Grande (TSRI) for help with intracranial drug delivery. We thank Æterna Zentaris, Inc. (Germany) for providing JMV2959; IPSEN (Milford, MA, USA) for BIM-28163; and Dr. Jeffry M. Friedman (Rockefeller University, NY) for 3P peptide used in pS6 experiments. We thank Dr. Courtney Miller and Dr. Sukhvir Mahal (TSRI) for helpful comments on the manuscript. This work was supported by NIH grant R01AG019230 to R.G.S.

Received: March 31, 2015

Revised: September 17, 2015

Accepted: October 26, 2015

Published: November 19, 2015

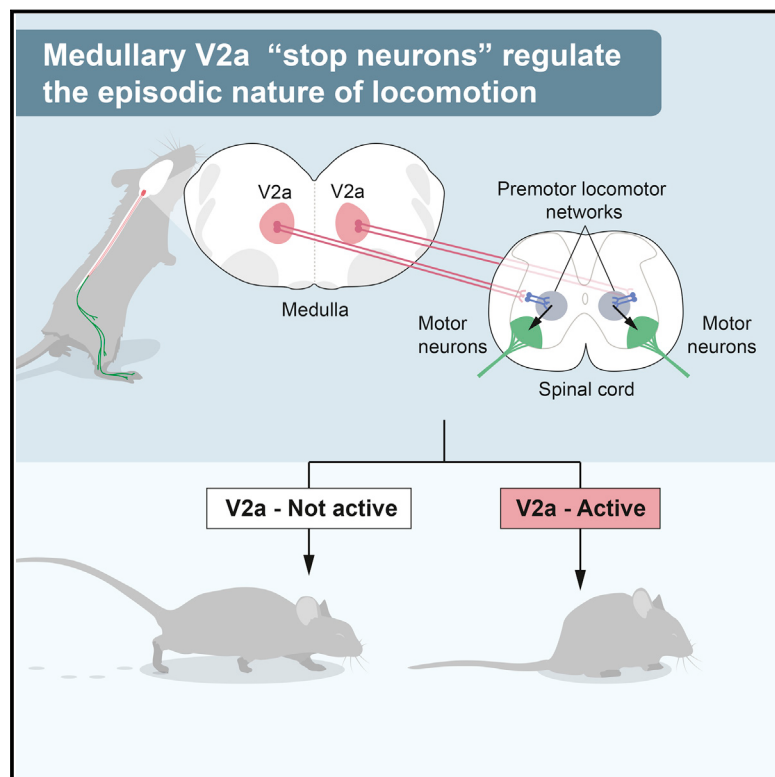
REFERENCES

- Abel, T., Nguyen, P.V., Barad, M., Deuel, T.A., Kandel, E.R., and Bourchou-ladze, R. (1997). Genetic demonstration of a role for PKA in the late phase of LTP and in hippocampus-based long-term memory. *Cell* 88, 615–626.
- Banks, W.A., Tschöp, M., Robinson, S.M., and Heiman, M.L. (2002). Extent and direction of ghrelin transport across the blood-brain barrier is determined by its unique primary structure. *J. Pharmacol. Exp. Ther.* 302, 822–827.
- Barria, A., Muller, D., Derkach, V., Griffith, L.C., and Soderling, T.R. (1997). Regulatory phosphorylation of AMPA-type glutamate receptors by CaM-KII during long-term potentiation. *Science* 276, 2042–2045.
- Cepeda, C., and Levine, M.S. (2006). Where do you think you are going? The NMDA-D1 receptor trap. *Sci. STKE* 2006, pe20.
- Cone, J.J., McCutcheon, J.E., and Roitman, M.F. (2014). Ghrelin acts as an interface between physiological state and phasic dopamine signaling. *J. Neurosci.* 34, 4905–4913.
- Cowley, M.A., Smith, R.G., Diano, S., Tschöp, M., Pronchuk, N., Grove, K.L., Strasburger, C.J., Bidlingmaier, M., Esterman, M., Heiman, M.L., et al. (2003). The distribution and mechanism of action of ghrelin in the CNS demonstrates a novel hypothalamic circuit regulating energy homeostasis. *Neuron* 37, 649–661.
- Deacon, R.M., and Rawlins, J.N. (2006). T-maze alternation in the rodent. *Nat. Protoc.* 1, 7–12.
- Ellenbroek, B.A., Lubbers, L.J., and Cools, A.R. (2002). The role of hippocampal dopamine receptors in prepulse inhibition. *Eur. J. Neurosci.* 15, 1237–1243.
- Engel, J.A., Jerlhag, E., Svensson, L., Smith, R.G., and Egecioglu, E. (2015). Blockade of growth hormone secretagogue receptor 1A signaling by JMV 2959 attenuates the NMDAR antagonist, phencyclidine-induced impairments in prepulse inhibition. *Psychopharmacology (Berl.)* 232, 4285–4292.
- Fiorenza, N.G., Rosa, J., Izquierdo, I., and Myskiw, J.C. (2012). Modulation of the extinction of two different fear-motivated tasks in three distinct brain areas. *Behav. Brain Res.* 232, 210–216.
- Furness, J.B., Hunne, B., Matsuda, N., Yin, L., Russo, D., Kato, I., Fujimiya, M., Patterson, M., McLeod, J., Andrews, Z.B., and Bron, R. (2011). Investigation of the presence of ghrelin in the central nervous system of the rat and mouse. *Neuroscience* 193, 1–9.
- Galés, C., Van Durm, J.J., Schaak, S., Pontier, S., Percherancier, Y., Audet, M., Paris, H., and Bouvier, M. (2006). Probing the activation-promoted structural rearrangements in preassembled receptor-G protein complexes. *Nat. Struct. Mol. Biol.* 13, 778–786.
- Gasbarri, A., Verney, C., Innocenzi, R., Campana, E., and Pacitti, C. (1994). Mesolimbic dopaminergic neurons innervating the hippocampal formation in the rat: a combined retrograde tracing and immunohistochemical study. *Brain Res.* 668, 71–79.
- Geyer, M.A., and Dulawa, S.C. (2003). Assessment of murine startle reactivity, prepulse inhibition, and habituation. *Curr. Protoc. Neurosci. Chapter 8*, 17.
- Grouselle, D., Chaillou, E., Caraty, A., Bluet-Pajot, M.T., Zizzari, P., Tillet, Y., and Epelbaum, J. (2008). Pulsatile cerebrospinal fluid and plasma ghrelin in relation to growth hormone secretion and food intake in the sheep. *J. Neuroendocrinol.* 20, 1138–1146.
- Guan, X.M., Yu, H., Palyha, O.C., McKee, K.K., Feighner, S.D., Sirinathsinghji, D.J., Smith, R.G., Van der Ploeg, L.H., and Howard, A.D. (1997). Distribution of mRNA encoding the growth hormone secretagogue receptor in brain and peripheral tissues. *Brain Res. Mol. Brain Res.* 48, 23–29.
- Hamdan, F.F., Percherancier, Y., Breton, B., and Bouvier, M. (2006). Monitoring protein-protein interactions in living cells by bioluminescence resonance energy transfer (BRET). *Curr. Protoc. Neurosci. Chapter 5*, 23.
- Hamilton, T.J., Wheatley, B.M., Sinclair, D.B., Bachmann, M., Larkum, M.E., and Colmers, W.F. (2010). Dopamine modulates synaptic plasticity in dendrites of rat and human dentate granule cells. *Proc. Natl. Acad. Sci. USA* 107, 18185–18190.
- Hasbi, A., Fan, T., Alijaniaran, M., Nguyen, T., Perreault, M.L., O'Dowd, B.F., and George, S.R. (2009). Calcium signaling cascade links dopamine D1-D2 receptor heteromer to striatal BDNF production and neuronal growth. *Proc. Natl. Acad. Sci. USA* 106, 21377–21382.
- Howard, A.D., Feighner, S.D., Cully, D.F., Arena, J.P., Liberator, P.A., Rosenblum, C.I., Hamelin, M., Hreniuk, D.L., Palyha, O.C., Anderson, J., et al. (1996). A receptor in pituitary and hypothalamus that functions in growth hormone release. *Science* 273, 974–977.

- Huang, Y.Y., and Kandel, E.R. (1995). D1/D5 receptor agonists induce a protein synthesis-dependent late potentiation in the CA1 region of the hippocampus. *Proc. Natl. Acad. Sci. USA* 92, 2446–2450.
- Jiang, H., Betancourt, L., and Smith, R.G. (2006). Ghrelin amplifies dopamine signaling by cross talk involving formation of growth hormone secretagogue receptor/dopamine receptor subtype 1 heterodimers. *Mol. Endocrinol.* 20, 1772–1785.
- Jin, L.Q., Goswami, S., Cai, G., Zhen, X., and Friedman, E. (2003). SKF83959 selectively regulates phosphatidylinositol-linked D1 dopamine receptors in rat brain. *J. Neurochem.* 85, 378–386.
- Kasai, R.S., and Kusumi, A. (2014). Single-molecule imaging revealed dynamic GPCR dimerization. *Curr. Opin. Cell Biol.* 27, 78–86.
- Kern, A., Albarran-Zeckler, R., Walsh, H.E., and Smith, R.G. (2012). Apo-ghrelin receptor forms heteromers with DRD2 in hypothalamic neurons and is essential for anorexigenic effects of DRD2 agonism. *Neuron* 73, 317–332.
- Knight, Z.A., Tan, K., Birsoy, K., Schmidt, S., Garrison, J.L., Wysocki, R.W., Emiliano, A., Ekstrand, M.I., and Friedman, J.M. (2012). Molecular profiling of activated neurons by phosphorylated ribosome capture. *Cell* 151, 1126–1137.
- Kojima, M., Hosoda, H., Date, Y., Nakazato, M., Matsuo, H., and Kangawa, K. (1999). Ghrelin is a growth-hormone-releasing acylated peptide from stomach. *Nature* 402, 656–660.
- Ladepeche, L., Dupuis, J.P., Bouchet, D., Doudnikoff, E., Yang, L., Campagne, Y., Bézard, E., Hosy, E., and Groc, L. (2013). Single-molecule imaging of the functional crosstalk between surface NMDA and dopamine D1 receptors. *Proc. Natl. Acad. Sci. USA* 110, 18005–18010.
- Lezcano, N., and Bergson, C. (2002). D1/D5 dopamine receptors stimulate intracellular calcium release in primary cultures of neocortical and hippocampal neurons. *J. Neurophysiol.* 87, 2167–2175.
- Lisman, J.E., and Grace, A.A. (2005). The hippocampal-VTA loop: controlling the entry of information into long-term memory. *Neuron* 46, 703–713.
- Mansbach, R.S., Geyer, M.A., and Braff, D.L. (1988). Dopaminergic stimulation disrupts sensorimotor gating in the rat. *Psychopharmacology (Berl.)* 94, 507–514.
- Mary, S., Fehrentz, J.A., Damian, M., Gaibelet, G., Orcel, H., Verdié, P., Mouillac, B., Martinez, J., Marie, J., and Banères, J.L. (2013). Heterodimerization with its splice variant blocks the ghrelin receptor 1a in a non-signaling conformation: a study with a purified heterodimer assembled into lipid discs. *J. Biol. Chem.* 288, 24656–24665.
- Nai, Q., Li, S., Wang, S.H., Liu, J., Lee, F.J., Frankland, P.W., and Liu, F. (2010). Uncoupling the D1-N-methyl-D-aspartate (NMDA) receptor complex promotes NMDA-dependent long-term potentiation and working memory. *Biol. Psychiatry* 67, 246–254.
- Pirnik, Z., Bundziková, J., Holubová, M., Pýchová, M., Fehrentz, J.A., Martinez, J., Zelezná, B., Maletinská, L., and Kiss, A. (2011). Ghrelin agonists impact on Fos protein expression in brain areas related to food intake regulation in male C57BL/6 mice. *Neurochem. Int.* 59, 889–895.
- Riedl, J., Crevenna, A.H., Kessenbrock, K., Yu, J.H., Neukirchen, D., Bista, M., Bradke, F., Jenne, D., Holak, T.A., Werb, Z., et al. (2008). Lifeact: a versatile marker to visualize F-actin. *Nat. Methods* 5, 605–607.
- Rossato, J.I., Bevilaqua, L.R., Izquierdo, I., Medina, J.H., and Cammarota, M. (2009). Dopamine controls persistence of long-term memory storage. *Science* 325, 1017–1020.
- Sakata, I., Nakano, Y., Osborne-Lawrence, S., Rovinsky, S.A., Lee, C.E., Perello, M., Anderson, J.G., Coppari, R., Xiao, G., Lowell, B.B., et al. (2009). Characterization of a novel ghrelin cell reporter mouse. *Regul. Pept.* 155, 91–98.
- Sariñana, J., Kitamura, T., Künzler, P., Sultzman, L., and Tonegawa, S. (2014). Differential roles of the dopamine 1-class receptors, D1R and D5R, in hippocampal dependent memory. *Proc. Natl. Acad. Sci. USA* 111, 8245–8250.
- Schaeffer, M., Langlet, F., Lafont, C., Molino, F., Hodson, D.J., Roux, T., Lamarche, L., Verdié, P., Bourrier, E., Dehouck, B., et al. (2013). Rapid sensing of circulating ghrelin by hypothalamic appetite-modifying neurons. *Proc. Natl. Acad. Sci. USA* 110, 1512–1517.
- Smith, N.J., and Milligan, G. (2010). Allostery at G protein-coupled receptor homo- and heteromers: uncharted pharmacological landscapes. *Pharmacol. Rev.* 62, 701–725.
- Smith, R.G., Van der Ploeg, L.H., Howard, A.D., Feighner, S.D., Cheng, K., Hickey, G.J., Wyvratt, M.J., Jr., Fisher, M.H., Nargund, R.P., and Patchett, A.A. (1997). Peptidomimetic regulation of growth hormone secretion. *Endocr. Rev.* 18, 621–645.
- Stauffer, T.P., Ahn, S., and Meyer, T. (1998). Receptor-induced transient reduction in plasma membrane PtdIns(4,5)P₂ concentration monitored in living cells. *Curr. Biol.* 8, 343–346.
- Swanson, L.W. (1982). The projections of the ventral tegmental area and adjacent regions: a combined fluorescent retrograde tracer and immunofluorescence study in the rat. *Brain Res. Bull.* 9, 321–353.

Descending Command Neurons in the Brainstem that Halt Locomotion

Graphical Abstract



Authors

Julien Bouvier, Vittorio Caggiano,
Roberto Leiras, ..., Kira Balueva,
Andrea Fuchs, Ole Kiehn

Correspondence

julien.bouvier@inaf.cnrs-gif.fr (J.B.),
ole.kiehn@ki.se (O.K.)

In Brief

The ability to stop locomotion is regulated by genetically- and spatially-confined excitatory neurons in the brainstem that project to the spinal cord where they depress locomotor rhythm generation.

Highlights

- Mouse V2a brainstem neurons are excitatory and project to the ventral spinal cord
- Optogenetic activation of V2a neurons of the rostral medulla halts locomotion
- These “V2a stop neurons” act by depressing locomotor rhythm generation
- V2a stop neurons are needed for episodic locomotion

Descending Command Neurons in the Brainstem that Halt Locomotion

Julien Bouvier,^{1,2,4,*} Vittorio Caggiano,^{1,4} Roberto Leiras,¹ Vanessa Caldeira,¹ Carmelo Bellardita,¹ Kira Balueva,³ Andrea Fuchs,¹ and Ole Kiehn^{1,*}

¹Mammalian Locomotor Laboratory, Department of Neuroscience, Karolinska Institutet, 17177 Stockholm, Sweden

²Paris-Saclay Institute of Neuroscience, UMR 9197 - CNRS and Université-Paris 11, 91190 Gif-sur-Yvette, France

³Institute of Physiology, Christian Albrechts University of Kiel, 24098 Kiel, Germany

⁴Co-first author

*Correspondence: julien.bouvier@inaf.cnrs-gif.fr (J.B.), ole.kiehn@ki.se (O.K.)

<http://dx.doi.org/10.1016/j.cell.2015.10.074>

SUMMARY

The episodic nature of locomotion is thought to be controlled by descending inputs from the brainstem. Most studies have largely attributed this control to initiating excitatory signals, but little is known about putative commands that may specifically determine locomotor offset. To link identifiable brainstem populations to a potential locomotor stop signal, we used developmental genetics and considered a discrete neuronal population in the reticular formation: the V2a neurons. We find that those neurons constitute a major excitatory pathway to locomotor areas of the ventral spinal cord. Selective activation of V2a neurons of the rostral medulla stops ongoing locomotor activity, owing to an inhibition of premotor locomotor networks in the spinal cord. Moreover, inactivation of such neurons decreases spontaneous stopping in vivo. Therefore, the V2a “stop neurons” represent a glutamatergic descending pathway that favors immobility and may thus help control the episodic nature of locomotion.

INTRODUCTION

Locomotion is one of many motor acts that the brain controls. It is a rhythmic and episodic behavior that is initiated and stopped according to behavioral needs. The timing and sequence of muscle contractions underlying locomotion originate from neuronal networks in the spinal cord called central pattern generators (CPGs; Goulding, 2009; Grillner and Jessell, 2009; Kiehn, 2006). The command for locomotion is integrated in supraspinal centers, which convey the initiating signal to the spinal cord through excitatory reticulospinal neurons of the lower brainstem (Dubuc et al., 2008; Grillner and Georgopoulos, 1996; Jordan et al., 2008; Roberts et al., 2008; Ryczko and Dubuc, 2013). Activity in these neurons is thought to provide the direct activation signal for locomotor CPG networks in all vertebrates. In addition, neural activity related to locomotion is observed in groups of reticulospinal neurons (Deliagina et al., 2000; Drew et al., 1986), suggesting that a sustained descending activity may determine

the duration of the locomotor episode. Yet, other studies have indicated that such initiating and maintenance signals may be complemented by a dedicated stop command to allow for a precisely timed locomotor arrest according to behavioral needs. In the *Xenopus* tadpole, head contact with obstacles activates GABAergic descending pathways that immediately terminate swimming (Perrins et al., 2002). Likewise, in the cat, electrical stimulation of the rostral medullary and caudal pontine reticular formations leads to a general motor inhibition (Mori, 1987; Takakusaki et al., 2003).

Excitatory and inhibitory brainstem descending neurons are largely intermingled in the reticular formation (Esposito et al., 2014; Holstege, 1991), which have made it difficult to ascribe locomotor initiating or terminating signals to defined cell populations with standard electrophysiological methods. More recently, developmental genetics has allowed manipulating discrete groups of reticular neurons in mice and addressing their function in motor control (Bouvier et al., 2010; Esposito et al., 2014). In zebrafish caudal-most brainstem V2a neurons, excitatory neurons defined by the expression of the transcription factor Chx10, have been shown to project to the spinal cord and to participate in the initiation and maintenance of locomotion (Kimura et al., 2013). In mouse, V2a neurons are found in the spinal cord, where they play distinct roles in controlling locomotion (Al-Mosawie et al., 2007; Crone et al., 2008; Crone et al., 2009; Dougherty and Kiehn, 2010; Kiehn, 2011; Lundfald et al., 2007; Zhong et al., 2010), and in the brainstem, where they send descending axons to the spinal cord (Bretzner and Brownstone, 2013; Cepeda-Nieto et al., 2005). In mice, locomotor episodes are associated with the expression of c-fos—a biochemical correlate of increased firing—in brainstem V2a neurons (Bretzner and Brownstone, 2013), but no direct link between their activation and locomotor initiation, maintenance, or termination has thus far been described. Here, we functionally evaluate this question *in vitro* and *in vivo* and identify a restricted contingent of V2a neurons of the rostral medulla/caudal pons that, upon activation, mediates an immediate arrest of ongoing locomotor activity. V2a “stop neurons” gain their effect via excitatory descending projections to the lumbar ventral spinal cord that may in turn provide an indirect inhibition of the spinal premotor locomotor networks. Our findings thus identify an excitatory functional pathway that favors immobility and thus helps control the episodic nature of locomotion.

RESULTS

V2a Brainstem Neurons Project to the Lumbar Spinal Cord and Are Excitatory

Brainstem V2a neurons were shown to project to the cervical spinal cord (Bretzner and Brownstone, 2013). We thus addressed the possibility that their projections reach the lumbar spinal cord, which contains the networks controlling hindlimb locomotion (Kiehn, 2006). V2a neurons were made permanently detectable by crossing a *Chx10::Cre* mouse line (Azim et al., 2014), which selectively drives Cre recombinase in Chx10⁺ neurons (Figure S1), with conditional eYFP or Tdtomato lines (hereafter called *Chx10-reporter* mice). Bilateral injections of the retrograde marker Cholera Toxin B (CTB) were targeted to the second lumbar (L2) spinal segment (Figure 1A). CTB⁺/Chx10-reporter labeled neurons were detected throughout the medulla and caudal pons and accounted for roughly half of ventrally located, retrogradely labeled neurons. In particular, we considered the fraction of reticulospinal neurons that are V2a at four representative levels (Figures 1B–1E): the caudal pons (caudal pontine reticular nucleus, PnC: 48% ± 4%; n = 4 animals), the rostral and caudal portion of the gigantocellularis nucleus (rGi: 44% ± 4% and cGi: 64% ± 2% respectively), and the reticular formation of the caudal medulla (hereafter referred to as the magnocellular contingent, Mc: 60% ± 5%).

In agreement with previous reports (Al-Mosawie et al., 2007; Bretzner and Brownstone, 2013; Lundfalld et al., 2007), we found that almost all V2a neurons express the mRNA for the vesicular glutamate transporter type 2 (Vglut2) regardless of their rostro-caudal or medio-lateral positioning (> 95%, n = 3, Figure 1F) and are thus exclusively excitatory. Additionally, in spite of the medial extension of Chx10-reporter labeling seen in the rostral medulla, we never observed co-expression with serotonergic neurons (Tryptophane Hydroxylase [TPH] positive, 0/584 cells, n = 4 animals, Figure 1G). We next evaluated the possibility for co-expression of inhibitory neurotransmitters within V2a neurons. Overall, and regardless of their medial or lateral localization, V2a neurons rarely co-expressed GlyT2 (PnC: 5/164 cells, 3%; rGi: 8/258, 3%; cGi: 3/242, 1%; Mc: 2/232, < 1%, n = 2 animals; Figure S2A and S2B) or GAD67 (PnC: 3/347 cells, < 1%; rGi: 2/547, < 1%; cGi: 4/433, < 1%; Mc: 6/406, 1.5%, n = 3 animals; Figures S2C and S2D). Altogether, these data indicate that most if not all V2a brainstem neurons bear a unique glutamatergic phenotype.

Optogenetic Activation of V2a Brainstem Neurons Stops Locomotor-like Activity In Vitro

To address the functional role of V2a neurons in locomotor initiation or termination, we recorded locomotor-like activities by electrophysiologically monitoring flexor-related L2 and extensor related L5 ventral roots in *in vitro* brainstem-spinal cord preparations of newborn mice (Figure 2). Selective activation of V2a neurons was achieved by expressing the light-activated Channelrhodopsin (ChR2) in Chx10⁺ cells (*Chx10::Cre; R26ChR2-YFP* mice, Hägglund et al., 2013; Figures 2 and S1). To optimally expose reticulospinal neurons to incident light and favor their depolarization, the brainstem was opened along the transverse plane—leading to an “open-book” preparation (Figures 2A and

2B)—and stimulated broadly. Under such conditions, continuous light-activation of brainstem V2a neurons did not induce any detectable changes in ventral root activity when preparations were superfused with normal Ringer solutions (naive preparation; Figure 2B; n > 10).

To test for the possibility that the role of descending V2a neurons may be revealed during ongoing locomotor-like activity, we bath-applied the minimal concentrations of neuroactive substances N-methyl-D-aspartate (NMDA) (5–7 µM) and serotonin (5-HT) (8–10 µM) sufficient to induce slow and intermediate frequency, locomotor-like activity (up to 0.45 Hz; Talpalar et al., 2013; Talpalar and Kiehn, 2010). In those conditions, light-activation of the brainstem V2a neurons induced an immediate stopping of ongoing activity (in 8/9 preparations; Figure 2C). Upon light offset, the activity immediately resumed and the first three to five cycles exhibited a rebound of activity. Similar rebound excitation has been seen after the termination of a hyperpolarization driven by current injection or optogenetic inhibition of spinal interneurons (Dougherty and Kiehn, 2010; Dougherty et al., 2013; Wilson et al., 2005; Zhong et al., 2010), suggesting that spinal locomotor neurons may have undergone synaptic inhibition during light exposure.

We questioned whether the arrest of locomotor-like activity is mediated by the recruitment of an inhibitory descending pathway in the brainstem (Holstege, 1991) or is integrated in the lumbar spinal cord. For this, the perfusion was separated between the brainstem and the spinal cord at the lower thoracic level (T8–T12) using a split-bath. This allowed blocking glutamatergic transmission selectively in the brainstem with 4 mM of kynurenic acid (KYN), known to completely block NMDA and AMPA/Kainate receptors at this concentration (Hägglund et al., 2010; Figure 2D). In those conditions, brainstem light exposure still induced an arrest of locomotor-like activity followed by a rebound of activity (Figures 2D and 2E). This observation indicates that the descending signal is directly conveyed by descending excitatory V2a brainstem neurons acting through an inhibitory network located in the lower-thoracic or lumbar segments. Both flexor- (L2, n = 8) or extensor- (L5) dominated ventral roots (n = 5, Figure 2D) were similarly abolished. Finally, light-activation of brainstem V2a neurons was efficient in suppressing neuronally evoked locomotor-like activities (n = 4; Figures 2F and 2G). These findings suggest that a population of brainstem V2a neurons provides a direct signal to the spinal locomotor networks to arrest ongoing locomotor-like activity. We will refer to those cells as “V2a stop neurons.”

V2a Stop Neurons Act at the Rhythm Generating Layer of the Locomotor CPG

Depression of ongoing locomotor-like activity by V2a stop neurons could be mediated by tonic inhibition of the motor neurons or by an action at the premotor neuron levels, including the rhythm and patterning layers.

To differentiate these possibilities, we first probed the V2a effect on lumbar motor neurons by whole-cell recordings *in vitro* (Figures 3A–3D). In the absence of locomotor activity, most motor neurons (10/16, five preparations) responded to light

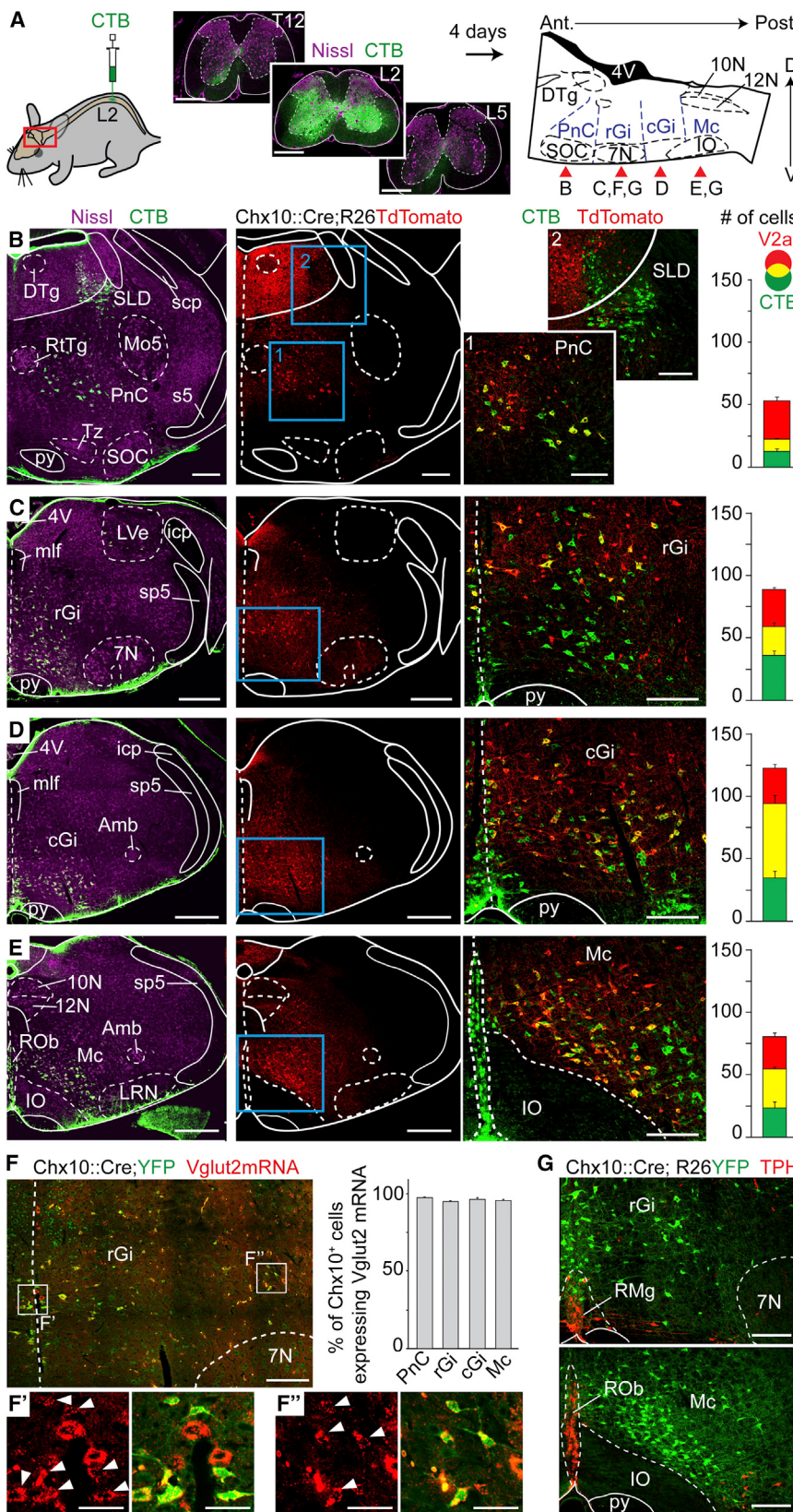


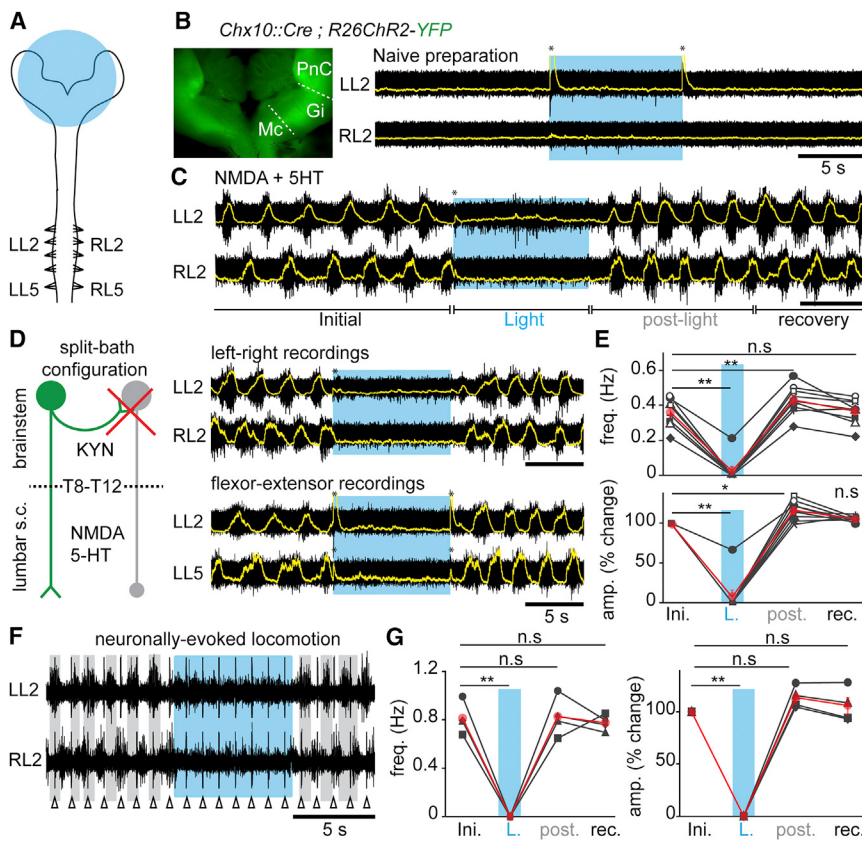
Figure 1. V2a Brainstem Neurons Project to the Lumbar Spinal Cord and Are Excitatory

(A) Bilateral injections of the retrograde marker CTB at the 2nd lumbar segment of the spinal cord (left). To the right is a sagittal schematic of the brainstem indicating the approximate rostro-caudal levels shown in the specified panels (red arrows) where CTB-labeled neurons are detected. (B–E) Transverse hemi-sections at the levels indicated in (A) stained for CTB, Nissl, and V2a neurons (Tdtomato). Right-most pictures are magnifications of the blue boxed area; V2a reticulospinal neurons appear yellow. Bar-graphs show the average number of CTB, V2a, and double-labeled neurons per hemisection ($n = 4$ animals). Error bars are SEM.

(F) Transverse hemi-section in the rGi indicating Vglut2⁺ glutamatergic (red) V2a neurons (YFP). Bar-graphs show the average percentage of Vglut2⁺;V2a neurons ($n = 3$ animals). Insets in F' and F'' are magnified views of Vglut2 expression alone (left) and merged with YFP (right) of medially-(F') and laterally positioned (F'') V2a neurons. White arrowheads indicate co-expression. Error bars are SEM.

(G) Transverse hemi-sections stained for TPH and V2a neurons (YFP). Note the absence of co-expression ($n = 4$ animals).

Scale bars (in μm): (A): 500, low magnifications in (B)–(E): 500; magnified views in (B)–(G): 200; F' and F'': 50. Abbreviations used in all figures: 10N: dorsal motor nucleus of vagus; 12N: hypoglossal nucleus; 4V: 4th ventricle; 7N: facial nucleus; Amb: ambiguus nucleus; Gi: gigantocellular reticular nucleus alpha part; icp: inferior cerebellar peduncle; IO: Inferior olive; DTg: laterodorsal tegmental nucleus; LRN: lateral reticular nucleus; LVE: lateral vestibular nucleus; Mc: magnocellular reticular nucleus; mlf: medial longitudinal fasciculus; Mo5: motor trigeminal nucleus; PnC: caudal pontine reticular nucleus; py: pyramidal tract; ROb: raphe obscurus nucleus; RMg: raphe magnus nucleus; RTg: reticulotegmental nucleus of the pons; s5: sensory root of the trigeminal nerve; SLD: Sublaterodorsal tegmentum; SOC: Superior olivary complex; sp5: spinal trigeminal tract; Tz: nucleus of the trapezoid body. See also Figure S2.



(G) Average per animal (black, $n = 4$) and grand-average among animals (red) of the instantaneous frequency and of the percent change in amplitude of descending fiber evoked locomotor bursts.

In all panels: n.s. indicates non-significant, * indicates $p < 0.05$ and ** indicates $p < 0.01$ (paired t test); Error bars in (E) and (G) are SEM.

activations by an increase in the frequency of both inhibitory and excitatory post-synaptic events (Figure S3B). The remaining cells showed increase in only excitatory events (2/16) or no changes (4/16; Figure S3A). For responsive cells, the latency from light onset to the first detectable postsynaptic excitatory and inhibitory event was on average 70 ± 4 ms and 60 ± 9 ms, respectively. Thus, in the absence of locomotor-like activity, V2a neurons may mediate a mixture of excitation and inhibition onto motor neurons. The excitatory nature of brainstem V2a neurons implies that the inhibitory connections to motor neurons are polysynaptic, while the excitatory actions may include both poly- and mono-synaptic connections (Esposito et al., 2014).

We next looked for signs of tonic inhibition of motor neurons in response to V2a activation during locomotor-like activity. When cells were held at intermediate potentials (-40 to -55 mV), most showed rhythmic oscillations of their membrane potential leading to rhythmic spiking. In response to light, motor neurons showed either a complete arrest ($n = 4$) or a significant reduction ($n = 6$) in their spiking frequency (Figures 3B and 3C), independently of the type of synaptic inputs observed before the induction of locomotor-like activity (Figure S3A and S3B). This effect was systematically associated with the disappearance of rhythmic membrane oscillations, in contrast to what is observed

following the direct hyperpolarization of the cell using current injection, where subthreshold rhythmicity remains (Figure 3B). When cells were recorded in voltage-clamp, light-activation induced a loss of the rhythmic barrages of inhibitory and/or excitatory postsynaptic currents that are normally associated with ongoing locomotor activity (Figure 3D). Together these observations suggest that the arrest of locomotor-like activity does not owe to strong direct inhibition of motor neurons, but that V2a stop neurons may depress premotor circuits.

We thus aimed at discriminating between an effect on the rhythm and/or pattern generating circuitries (Kiehn, 2006; McLean and Dougherty, 2015). Should the effect be primarily on rhythm generation, V2a-driven locomotor arrest is expected to be able to affect the frequency rather than the pattern; i.e., left-right and flexor-extensor coordination. We therefore created conditions where standardized V2a activations did not completely arrest ongoing locomotor-like activity by selectively challenging the spinal cord compartment to higher concentrations of locomotor drugs (NMDA > 8 μ M, 5-HT: 9–12 μ M). Excitatory synaptic transmission was simultaneously blocked in the brainstem using a split-bath. As reported previously, higher drug concentrations led to higher frequencies of locomotor-like activities (> 0.45 Hz; Talspalar and Kiehn, 2010). In such conditions, upon

Figure 2. V2a Brainstem Neurons Stop Slow-Frequency Locomotor-like Activity In Vitro

(A) Schematic experimental design for electrophysiological recordings in brainstem-spinal cord preparations from postnatal animals (0–4 days). The area of light stimulation is shown in blue.

(B) Inset: ChR2-YFP expression in the "open-book" brainstem preparation. Raw (black) and integrated signals (superimposed in yellow) of L2 ventral roots in normal Ringer solution. Light-activation of brainstem V2a neurons (blue epoch) does not change baseline activity. The transient voltage deflections at light onset and offset (asterisks) are light-mediated artifacts.

(C) Similar recordings during locomotor-like activity induced with 5–7 μ M NMDA and 8 μ M 5-HT. Light-activation of brainstem V2a neurons stops ongoing locomotor-like activity.

(D) Left: the possible recruitment by V2a neurons (green) of other inhibitory descending neurons (gray) was blocked by applying KYN onto the brainstem in a split-bath configuration. Right: recordings of the flexor-dominated roots bilaterally (L2, top) and of flexor and extensor (L5)-dominated roots on the same side (bottom).

(E) Average per animal (black, $n = 9$) and grand average among animals (red) of the instantaneous frequency and of the percent change in amplitude of drug-evoked locomotor bursts before (Initial: ini.), during light (L), for 5 cycles following light offset (post), and for the following 20 s (recovery: rec). Statistical significance: ** $p < 0.01$, n.s. indicates non-significant.

(F) Recordings of L2 roots bilaterally in the split-bath configuration during electrical stimulation (1Hz, Δ) at the first cervical segment. Vertical lines are stimulus artifacts.

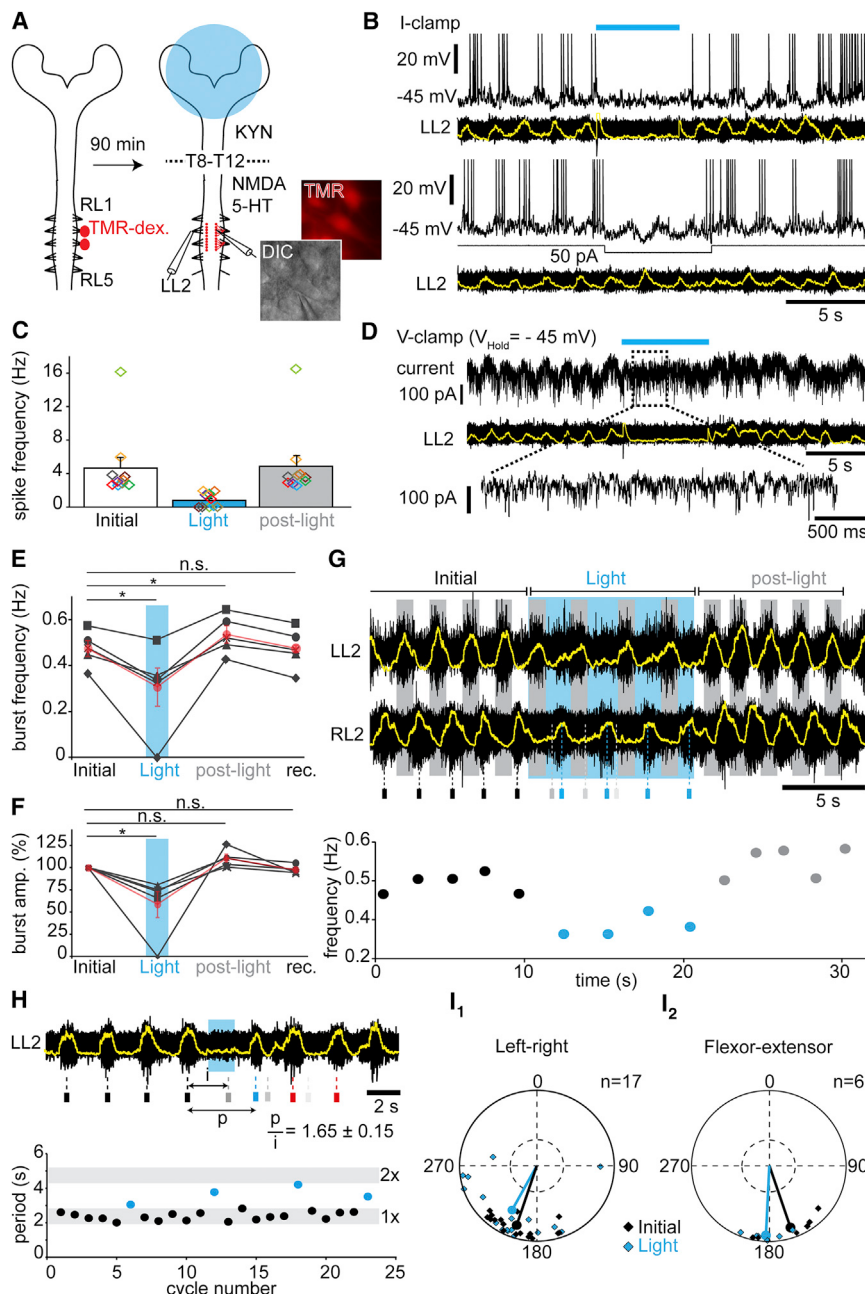


Figure 3. Light-Activation of Brainstem V2a Neurons Depresses Rhythm-Generating Levels of the Locomotor CPG

(A) Experimental design for labeling and whole-cell recording of lumbar motor neurons. TMR-dex: Tetramethyl-Rhodamine Dextran.

(B) L2 motor neuron in current-clamp during drug-evoked locomotor-like activity. V2a neurons' activation (blue bar) arrests both spiking and underlying membrane oscillations (top), while direct hyperpolarization of the same cell with current injection (bottom) preserves subthreshold oscillations.

(C) Average per cell (colored rectangles, $n = 10$) and grand-average among cells (bar-graphs) of the instantaneous spiking frequencies of lumbar motor neurons before (initial), during (Light) and after (post-light) light-activation.

(D) Same cell as in (B) recorded in voltage-clamp. Light-activation induces a loss of rhythmic currents.

(E-F) Average per animal ($n = 5$) and grand-average among animals (red) of the instantaneous frequency (E) and of the percent changes in amplitude (F) of L2 locomotor bursts on preparations facing high NMDA concentrations ($> 8 \mu M$). * indicates $p < 0.05$ (paired t test).

(G) Typical L2 ventral root recording during high-frequency locomotor-like activity (~0.5 Hz). Small rectangles below indicate the time of peak of the control RL2 bursts (black), and their forecasted (gray) and actual occurrences (blue) during light activation of brainstem V2a neurons, showing a non-graded slowing of the rhythm. Below is plotted the corresponding instantaneous frequency of RL2 bursts.

(H) L2 ventral root recording during drug-evoked locomotor-like activity. The expected burst is silenced (gray bar below) and the rhythm reset by short light-pulse, as seen by the perturbed period (p) not falling in the range of twice the initial period (I). The graph below illustrates initial (black) and perturbed periods (blue) for four consecutive trials. (I) Circular plot showing the left-right (I_1) or flexor-extensor (I_2) phase-relationships for individual trials and for the mean preferred phase among all trials before (Initial, black) and during (Light, blue) light-activation. Phase values falling in the bottom-half of the outer circles indicate alternation. There is no significant difference between control and light conditions (Watson-William's test $p > 0.05$). See also Figure S3 and S4.

Error bars in (C), (E), and (F) are SEM.

light-activation of V2a neurons, most (4/5) preparations did not show a complete arrest but a significant reduction in frequency ($76\% \pm 5\%$ of initial values) and amplitude ($74\% \pm 3\%$) of locomotor activities (Figures 3E–3G). Therefore, those conditions of high spinal excitability, by presumably preventing a complete locomotor arrest from finite light power, reveal that V2a stop neurons can modulate the frequency and amplitude of locomotor bursts. Importantly, the perturbed frequency was not an integer of the frequency prior to the light exposure (Figure 3G) and thus did not owe to skipped bursts. Moreover, shorter (1–2 s) pulses of light given at the expected occurrence of a locomotor burst caused phase-

resetting of locomotor rhythm (Figure 3H). Additionally, neither left-right nor flexor-extensor coordination, the typical manifestations of pattern formation, were significantly modified by light-activation of brainstem V2a neurons (Figure 3I). Finally, mirroring those findings, opto-inhibition of V2a brainstem neurons during drug-evoked locomotor-like activity positively modulates burst frequency and amplitude (Figure S4).

Altogether, the possibility for bidirectional modulation of locomotor frequency with preserved left-right and flexor-extensor coordination indicates that V2a stop neurons act primarily on premotor circuits involved in rhythm generation.

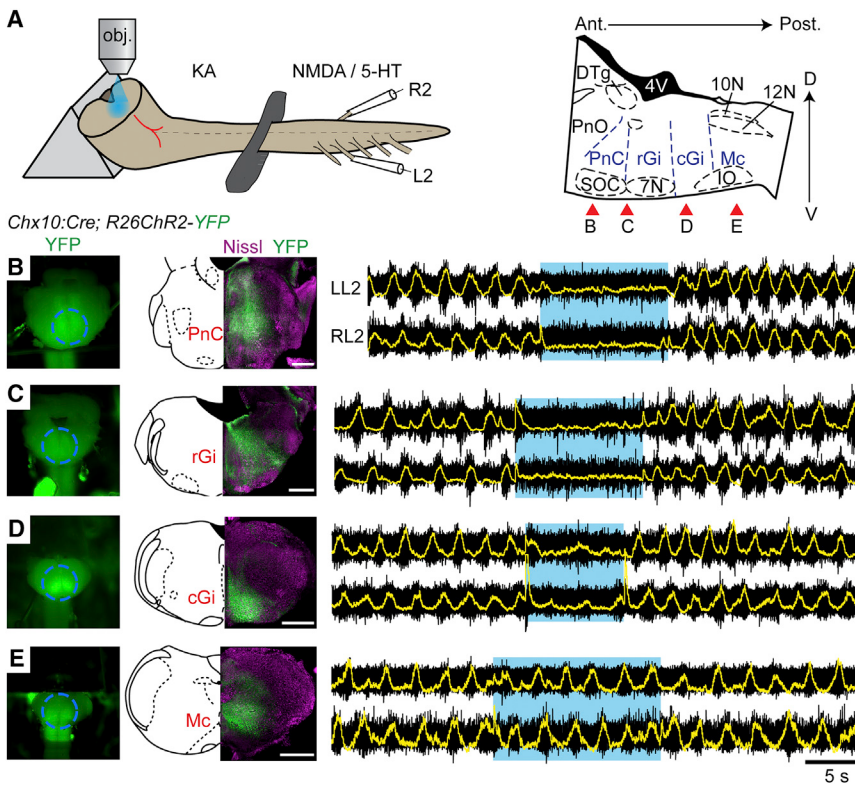


Figure 4. V2a Stop Neurons Reside in the Rostral Gigantocellularis and Caudal Pontine Reticular Nuclei

(A) Experimental set-up. The brainstem is sectioned transversally to expose a given transverse plane to the light. Red arrows on the right indicate approximate levels of the sections performed in (B)–(E).

(B–E) Simultaneous electrophysiological recordings of L2 roots on either side after a section exposing the PnC (B) and of the same preparation after having removed the PnC (C), and the rGi (D) or cGi (E). The ability of light stimulation to stop ongoing locomotion is lost when only the caudal-most medullary formation remains. The transient voltage deflections visible on the integrated traces at light onset and offset are light-mediated artifacts.

Scale bar, 500 μm

V2a Stop Neurons Reside in the Rostral Medulla and Caudal Pons

To regionally define the implicated V2a population, we sectioned the brainstem transversally at different antero-posterior levels and targeted photo-illuminations to the exposed plane (Figure 4). We performed four successive cuts on the same preparation, from the rostral to the caudal medulla. When the brainstem was sliced near the ponto-medullary junction to expose the PnC (Figure 4B), light activation of descending V2a neurons induced a complete arrest of ongoing locomotor-like activity, similar to that reported in the “open-book” preparations ($n = 3$). A similar effect was observed when the rostral (Figure 4C; $n = 2$) or caudal Gi (Figure 4D; $n = 2$) was left intact and exposed to the light, although a few low amplitude bursts occasionally occurred in the latter conditions. In contrast, after removal of the intermediate medulla, thus exposing the caudal-most descending V2a neurons (Mc), light exposure was unable to detectably modify the frequency or amplitude of ongoing locomotor-like activity (Figure 4E; $n = 3$). Light activation at any of those segmental levels in the absence of locomotor drugs was unable to elicit locomotor-like or bursting activities in the lumbar ventral roots (data not shown). Those experiments reveal that the stop command may preferentially reside in the rostral Gi and PnC, or alternatively, that a critical number of cells is required for its functional manifestation.

Activation of Brainstem V2a Neurons Halts Locomotion In Vivo

The isolated *in vitro* preparation from transgenic lines precluded investigations of V2a activations during spontaneous quadrupedal locomotion and a refined anatomical characterization of implicated cells.

To address these issues, we aimed for activation of V2a stop neurons locally, in freely-moving animals. We injected a Cre-dependent AAV-DIO-ChR2-mCherry virus bilaterally in the rGi of *Cbx10::Cre* animals (Figure S5) and implanted an optical fiber at the midline to allow for bilateral illumination of transfected cells (Figure 5A). In two animals, we collected acute brainstem slices, performed whole-cell recordings of transfected cells, and verified their functional activation under synaptic isolation (Figure 5B). Three to four weeks following viral transfection, locomotion was tested when animals were moving in a linear corridor (Bellardita and Kiehn, 2015; Talarpar et al., 2013). In this assay, light-activation of transfected V2a neurons in rGi stopped ongoing locomotion ($n = 7$; Figures 5C–5F; Movie S1). The complete locomotor arrest was on average seen 140 ms from light onset, a period allowing the ongoing step to be completed; i.e., for the dragging feet of the forelimbs and hindlimbs to be placed aligned with the leading feet. Animals thus reach a canonical stopping position with the four feet on the ground (Figure 5C). This was seen independently of the initial locomotor speed and persisted throughout the 400 ms windows of illumination (Figure 5D). Kinematic analysis of the hindlimb joints during locomotion and the stop revealed that the two conditions represent significantly different motor outputs (Figures 5E–5G): the foot was placed in front of the hip during arrest (mean angles in degrees before versus during light stimulation [all comparisons tested with U test for circular data]: 12.5° versus -26.6°, $p < 0.05$), the knee angle was more extended during arrest than locomotion (75.6° versus 101.4°, $p < 0.05$), and the feet were flat during arrest unlike during locomotion (foot: 63° versus 16.8°, $p < 0.05$).

Optical stimulation with yellow light—out of the range for activating ChR2—in the same animal or with blue light in Cre-negative animals did not produce locomotor arrest. Finally in two animals, we targeted V2a neurons of the caudal medulla (Mc).

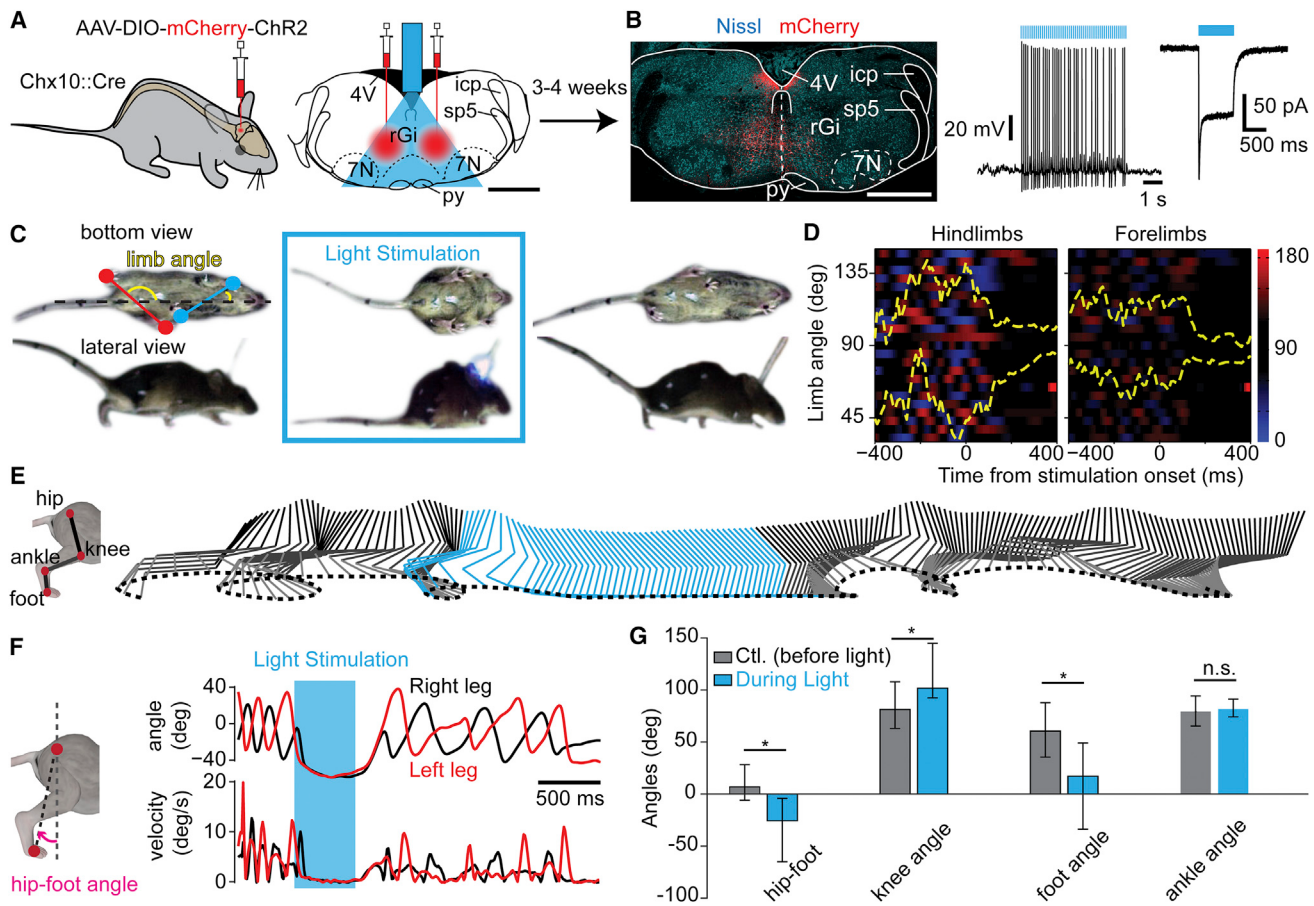


Figure 5. Optogenetic Activation of Brainstem V2a Neurons Halts Locomotion in Freely-Moving Mice

(A) Scaled reconstruction of the implantation and illumination range following the bilateral viral injection in the rGi.

(B) Transverse section showing mCherry expression (red) at the injection site. To the right is a mCherry⁺ neuron recorded in a transverse slice under synaptic isolation.

(C) Detoured snapshots of a freely-moving Chx10::Cre mouse 4 weeks post-injection before (left), during (center), and after (right) light-stimulation using pulsed blue light. The limb angle is defined as the angle between a line joining the two hindpaws (red) or forepaws (blue), with respect to the midline of the animal.

(D) Color plot of hindlimbs' and forelimbs' angles 400 ms before and after light onset. The y axis represents 23 trials from seven animals. A gradient of color to red indicates positive angle (left limb behind the right limb), to blue indicates the reverse (right limb behind left limb), and black indicates perpendicular limbs to the body axis. In yellow are shown the 25 and 75 percentile of the distribution of the angle oscillations over time. Independently of the speed before stimulation, light activation of transfected V2a neurons stopped ongoing locomotion and animals remained in a stereotypical position with the limb perpendicular to the body axis (90°).

(E) Kinematic representation of the relative movements of the hip, knee, ankle, and foot of one animal before (gray) and during (blue) light activation. Movements stopped in response to light and resumed upon light offset.

(F) Evolution of the hip-foot angle (pink) as a function of time (top) and corresponding relative velocities (bottom). Light-activation led to a configuration where the foot was kept ahead of the hip.

(G) Average ($n = 7$ mice) of the hip-foot, knee, foot, and ankle angles 400 ms before (gray) and during (blue, from 100 ms to 500 ms after light onset) light-activation of V2a neurons. Asterisks indicate significant different values ($p < 0.05$, U test for circular data).

Error bars are 25–75 percentiles. Scale bar, 1 mm (A, B). See also Figure S5.

There, light-activation did not lead to locomotor arrest. Therefore, specific activation of rGi V2a neurons *in vivo* halts quadrupedal locomotion and leads to a characteristic stopping position.

Brainstem V2a Stop Neurons Constrain the Episodic Expression of the Locomotor Behavior

To test whether brainstem V2a stop neurons are involved in the episodic manifestation of the exploratory locomotor behavior, we aimed for selectively blocking their synaptic output using

tetanus toxin light-chain (TeLC), which prevents pre-synaptic vesicle fusion at the membrane (Schiavo et al., 1992). We used a Cre-dependent TeLC-coding virus that efficiently blocks action potential-evoked synaptic transmission (AAV-FLEX-eYFP-TeLC; Murray et al., 2011), similarly to what is seen in TeLC transgenic animals (Zhang et al., 2014). Three to fourteen days after TeLC or saline (control group) injections in the rGi (Figure 6A), animals' behavior was monitored continuously for 25 min in an open-field setting. All TeLC-treated animals

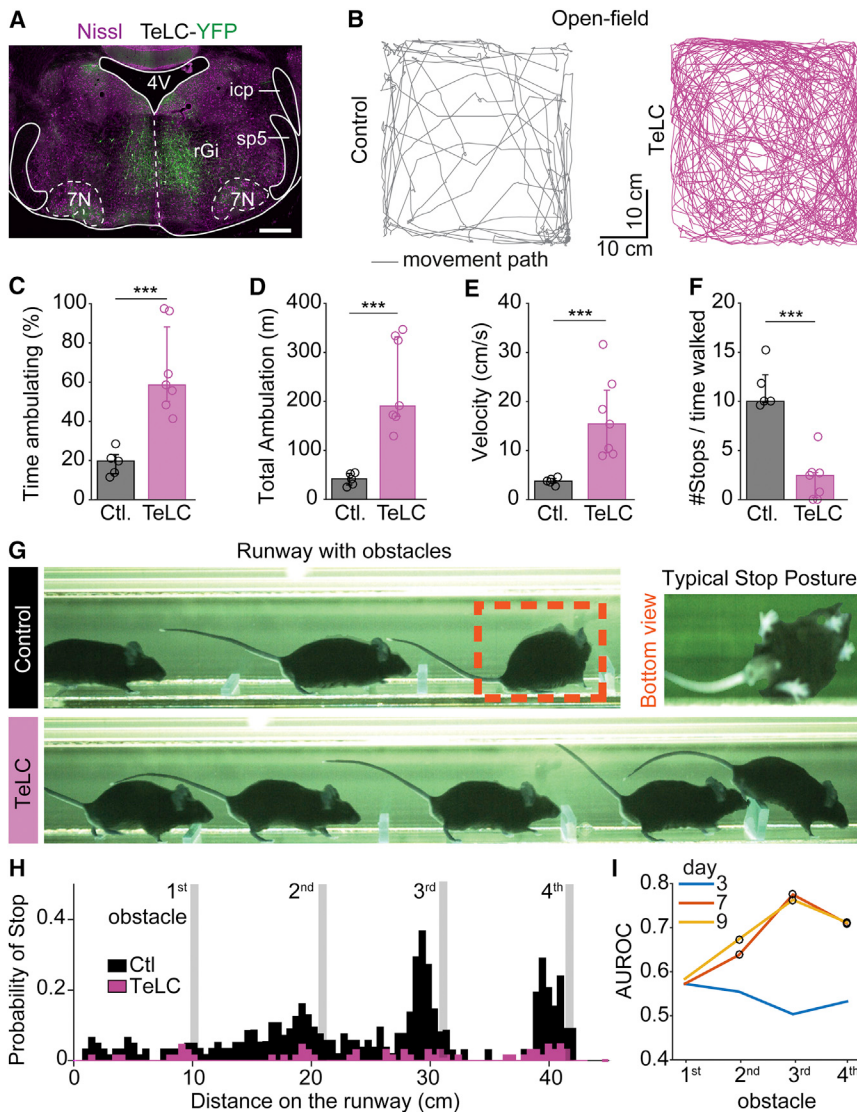


Figure 6. Blocking Synaptic Output from V2a Stop Neurons Increases Mobility

(A) Transverse brainstem section showing the expression of an AAV1/2-FLEX-TeLC-eYFP-WPRE virus following injection in the rGi bilaterally in a *Chx10::Cre* animal.

(B) Traces of movements for 10 min in an open field test 7 days after the injection of saline (control, left) or the TeLC virus (right).

(C) Averages from individual animals (open circles) and grand-average among all individuals (bar-graphs) of the percent time spent ambulating for controls (gray, n = 5) and TeLC-treated (pink, n = 8) subjects. Error bars are 25–75 percentiles. In all panels *** indicates p < 0.005 (U test).

(D–F) Similar quantifications for (D) the total distance achieved while ambulating, (E) the average velocity of ambulation, and (F) the relative number of stops to the time spent ambulating.

(G) Snapshots of a *Chx10::Cre* mouse 9 days post-injection of saline (control, top) or TeLC virus (bottom) in the rGi. The control animal shown spontaneously halts before the 3rd obstacle and adopts a stereotypical stopping position, while the TeLC-treated animal does not stop at any obstacle (see also Movie S3).

(H) Summary of the probability of stop for saline- (n = 6, black) or TeLC-injected (n = 8, pink) mice, after 9 days. Controls stopped with higher probability on the 3rd and 4th obstacles (p < 0.05, Kruskal-Wallis, Bonferroni correction for multiple comparisons) than TeLC-treated animals.

(I) Direct comparison of the probability of stop before each obstacle between controls and TeLC mice. AUROC index gauges the difference between conditions where 0.5 indicates no difference while values toward zero or one indicate that the probability curves are different. Circles indicate significant differences (p < 0.05). See also Figure S6.

(n = 8) showed a remarkable increase of overall mobility compared to controls (n = 5; Figure 6B; Movie S2). This bias toward locomotion was manifested by a significant increase in the relative time the animals spent moving (Figure 6C), indicative of a perturbed ability to reach and maintain immobility. Consequently, treated animals traveled for longer distances during the recording sessions (Figure 6D) with a higher average locomotor speed (Figure 6E). The number of stops to the time spent moving in TeLC-treated animals decreased to almost one-fourth of controls (Figure 6F). These effects were also seen in individual animals and developed over time (Figure S6A). Importantly, locomotor kinematic analysis showed that the impaired ability to stop was not due to changes in the overall locomotor capability (Figure S6B).

In sum, those observations suggest that V2a stop neurons may be normally mobilized during exploratory behavior to favor and maintain locomotor arrest and thus regulate the episodic nature of locomotion.

To further characterize the impaired ability for stopping in TeLC-treated animals and relate it to a natural behavior, we developed an assay that reveals natural and predictable stop events in wild-type mice and scored the deficiencies upon TeLC treatment. For this, four obstacles of increasing heights were spaced at regular intervals in a linear corridor. Control animals (n = 6) typically ran over the first obstacle but showed increased stopping probability as they progressed to the following higher obstacles, and most did not overcome the last obstacle (Figures 6G and 6H; Movie S3). The spontaneous locomotor arrest was typically associated with a limb configuration reminiscent of the one evoked by the optogenetic stimulation of V2a stop neurons; i.e., the foot placed in front of the hip, and hindlimbs and forelimbs perpendicular to the body axis (Figure 6G). TeLC-treated animals (n = 8) performed similarly as controls when tested 3 days post-injection but subsequently showed increased inability to stop (Figures 6I and S6C). After 9 days, TeLC-treated animals did no longer stop before the obstacles (Figures 6G–6I, Movie S3). Therefore,

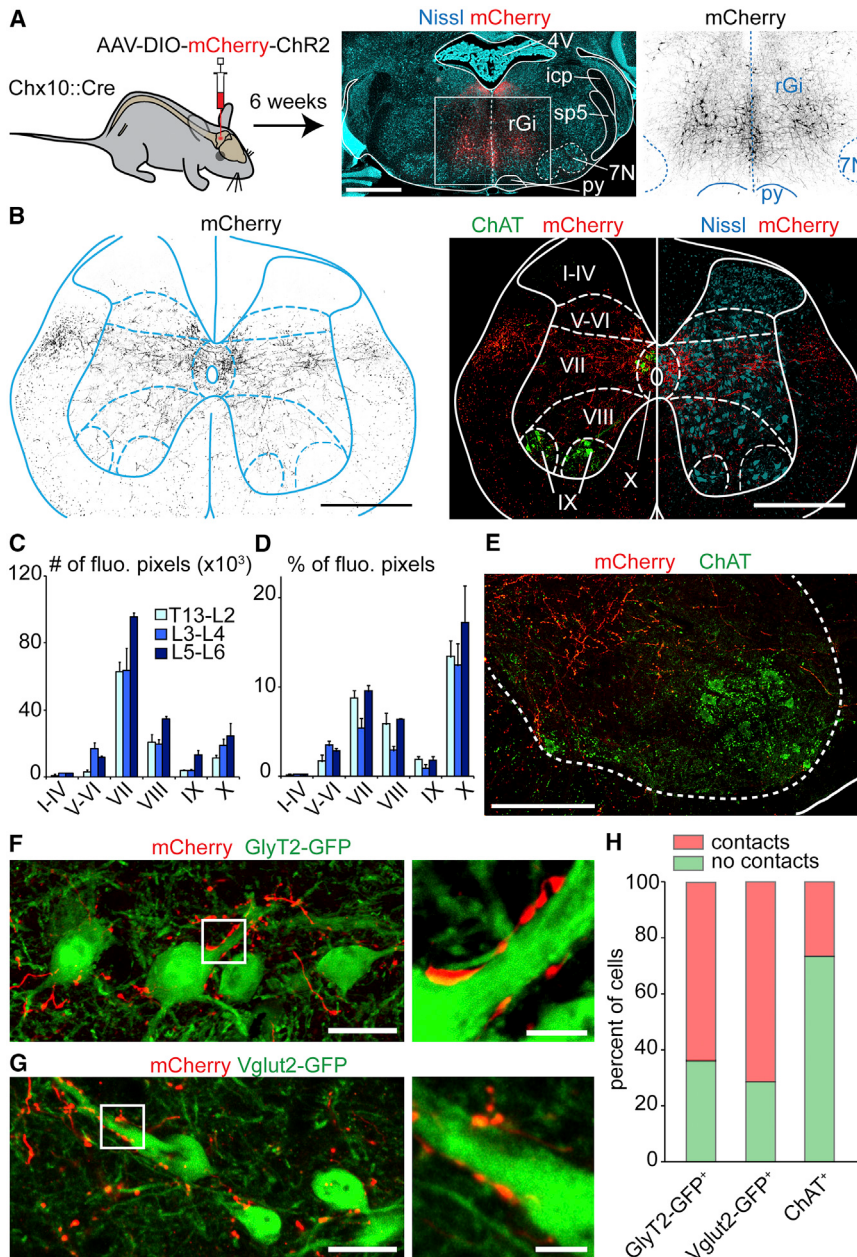


Figure 7. V2a Stop Neurons Terminate Predominantly in Lamina VII of the Lumbar Spinal Cord

(A) Bilateral injections of a Cre-dependent AAV-hChR2-mCherry-virus (middle: red; right: black) in the rGi of *Chx10::Cre* animals.

(B) Transverse L2 spinal cord section of the same animal showing transfected V2a processes (black on the left, red on the right). Rexed's laminae are delineated using ChAT and Nissl staining.

(C-D) Quantification in one animal of the number (C) or the percent (D) of fluorescent pixels in each lamina at the upper (T13-L1-L2), intermediate (L3-L4), and caudal (L5-L6) lumbar levels.

(E) Magnified view of the descending V2a innervation (red) in the vicinity of ChAT⁺ motor neurons (green).

(F, G) Similar anterograde labelings on a *Chx10::Cre; GlyT2-GFP* (E) or *Chx10::Cre; Vglut2-GFP* animal (F) showing putative V2a contacts (red) onto glycinergic and glutamatergic neurons, respectively.

(H) Percent of glycinergic (232 cells), glutamatergic (105 cells), and motor neurons somatas (124 cells) exhibiting no (green) or more than one (red) putative V2a contact.

Scale bars (in μm): (A) 1000, (B) 500, (E): 200, (F, G): 25, insets in (F, G): 5; Error bars in (C) and (D) are SEM; See also Figure S7.

blocking synaptic output from V2a neurons dramatically compromised animals' ability to naturally arrest their locomotion.

Brainstem V2a Stop Neurons Terminate in the CPG Area and Contact Inhibitory and Excitatory Neurons in the Spinal Cord

Those experiments suggest that V2a stop neurons in the rGi halt ongoing locomotion and may gain their effect by inhibiting rhythm generating circuits in the spinal cord. To start addressing this issue, we performed anterograde labeling of V2a stop neurons (bilateral injections of AAV-DIO-ChR2-mCherry in the rGi) and followed their axonal termination in the lumbar spinal cord (Figures 7 and S7). We found extensive mCherry⁺ fiber

tracts in the lateral and ventral funiculi (Figures 7B and S7B). Lamina VII—where locomotor related neurons have been described (Goulding, 2009; Grillner and Jessell, 2009; Kiehn, 2006; McLean and Dougherty, 2015)—was the most abundantly and densely innervated, followed by laminae VIII and X (Figures 7C and 7D). Innervation was more moderate in lamina IX containing motor neurons and virtually absent from dorsal laminae (I–VI). A comparable innervation pattern was detected at upper (T13-L1-L2), intermediate (L3-L4) and caudal (L5-L6) lumbar segments. We next tested whether V2a descending connectivity shows preferential innervation to excitatory versus

inhibitory neurons in ventral (VII to X) laminae. We detected a similar fraction of inhibitory glycinergic (GlyT2-GFP; Figure 7F) and excitatory (Vglut2-GFP; Figure 7G) neurons receiving one or more putative somatic synaptic contacts (Figure 7H). In contrast, most motor neurons showed no putative somatic contacts. Thus, V2a stop neurons may act onto spinal inhibitory circuits both directly and indirectly via excitatory relays.

DISCUSSION

Methodological Considerations

The function of brainstem V2a neurons in locomotor arrest is clearest when analyzed on locomotor-like activity in vitro, and

we provide numerous evidences for a functionally analog effect *in vivo*. Activities recorded in the *in vitro* rodent preparations at early postnatal stages and their perturbations following experimental interferences were previously shown to reliably forecast the consequences on limbed locomotion at later developmental stages (Andersson et al., 2012; Bellardita and Kiehn, 2015; Crone et al., 2008; Crone et al., 2009; Kullander et al., 2003; Talarpa et al., 2013; Zhang et al., 2014). Here, we extend this reasoning to long-range, descending projections. A potential limit may have resided in the unequal maturity of descending systems in the newborn animal. Nevertheless, the consistency of our *in vitro* and *in vivo* observations suggests that V2a descending projections, similar to the caudal glutamatergic (Hägglund et al., 2010) and serotonergic ones (Liu and Jordan, 2005), are functionally established and incorporated in the locomotor network at birth.

A concern that may be raised with optogenetic activation is that over-activation may cause a depolarizing block of the targeted neurons. The consequences of light-activation of ChR2-expressing V2a neurons could therefore be due to a suspension rather than a gain of their functional output. Importantly, all our experiments employed an approach with minimal light intensity, below which no response could be observed. Second, we never observed an initial excitatory signature followed by decreased activity. Third, when the same neuronal population was made to express the inhibitory opsin NpHR, light-exposure produced an acceleration of locomotor-like activity, a finding making it unlikely that the locomotor cessation observed in the ChR2 experiments is due to impaired firing of those neurons. Finally, stopping-deficiencies were seen with non-optogenetic silencing of V2a neurons (TeLC-mediated). Those observations are indicative that our strategy allows for a valid manipulation of V2a neuronal activity.

V2a Stop Neurons Constitute an Excitatory Pathway Optimally Tuned for Locomotor Arrest

The most significant finding reported here is that activation of V2a neurons of the rostral medulla/caudal pons stops ongoing locomotor activity. In accordance with previous reports (Bretzner and Brownstone, 2013; Kimura et al., 2013), we found V2a neurons to be exclusively glutamatergic. They thus represent a unique contingent that diverges from other excitatory descending systems, thought to favor excitability (Dubuc et al., 2008; Hägglund et al., 2010; Perreault and Glover, 2013; Sivertsen et al., 2014). Importantly, our split-bath experiments *in vitro* indicate that the V2a descending command is integrated in the spinal cord. The dispensable nature of inhibitory reticulospinal neurons for locomotor arrest stands as a major finding considering the abundance of the latter (Esposito et al., 2014; Holstege, 1991). A significant example is that of muscular atonia seen during REM sleep, driven by inhibitory reticulospinal neurons, themselves activated by the glutamatergic sublaterodorsal tegmental nucleus in the pons (SLD; Lu et al., 2006; Luppi et al., 2011). Although the SLD also sends direct excitatory projections to the spinal cord (Vetrivelan et al., 2009), we found it to be non-V2a (Figure 1B). Together with the absence of evident muscular atonia *in vivo*, which is due to complete loss of muscle tone (Cagiano et al., 2014; Luppi et al., 2011), those observations exclude

a prominent contribution of sleep-related descending pathways in our study. However, we cannot exclude that inhibitory reticulospinal neurons, should they be recruited by V2a stop neurons in the intact animal, may have a subsidiary role in driving locomotor arrest. Finally, our *in vivo* kinematic analysis suggests that the V2a-driven locomotor arrest differs from the defensive freezing behavior, which retains immobilization through pronounced co-contraction of muscles (Brandão et al., 2008; Yilmaz and Meister, 2013).

Our findings share similarities with works in cats (Takakusaki et al., 2003) where electrical stimulations in the dorsal tegmental field (pons) or lateral Gi evoked locomotor arrest associated with severe decrease in muscle tone due to inhibition of motor neurons. However, the low specificity of the electrical stimulation and the lack of transmitter characterization prevent a clear estimate of the putative overlap. Nevertheless, the functional analogy may point to a phylogenetic-determined system ensuring all forms of locomotion be controlled by a versatile command system with a built-in circuitry dedicated to constrain its termination, and thus its obligatory episodic nature.

Brainstem V2a Stop Neurons Arrest Locomotor Rhythm Generation

We provide strong evidence that the V2a-mediated locomotor arrest is due to a direct depression of premotor circuits, including in particular those governing rhythm generation. First, although activation of V2a brainstem neurons has both excitatory and inhibitory effects on motor neurons in the absence of locomotion, there is no sign of strong tonic inhibition during the locomotor arrest. Second, ongoing locomotor frequency can be modulated without changing left-right or flexor-extensor coordination when increased spinal excitability prevents a complete stop. This is reminiscent to what we reported recently upon selective silencing of candidate rhythm-generating neurons in the isolated spinal cord (Dougherty et al., 2013). The effect on amplitude modulation may be secondary to the effect on rhythm generation and/or imply additional effects on downstream interneurons. Moreover, a selective inhibition of pattern-generating layers has been associated with a quantal slowing of the motor bursts (Feldman and Kam, 2014) and non-resetting deletions (McCrea and Rybak, 2008), two signatures opposite from our findings. Thus, those observations are in line with a primary impact on rhythm generating layers within the locomotor network (Kiehn, 2006; McLean and Dougherty, 2015). This may allow to selectively arrest the behavior while preserving muscle tone.

The most obvious mechanisms imply the recruitment of spinal inhibitory neurons either directly, or indirectly via local excitatory neurons. Although our study did not examine specifically those targets, the dense innervation found in intermediate and ventral laminae is not overlapping with the location of Ia neurons (Hultborn et al., 1976) or Renshaw cells (Alvarez and Fyffe, 2007), making these populations less likely candidates for the inhibition. Lumbar commissural neurons have been shown to receive excitatory inputs from the brainstem (Szokol et al., 2011), but the preserved left-right coordination upon light-stimulation also suggests that these are not main actors in our study. Finally, the manifestation of the locomotor arrest *in vivo* on both fore- and hindlimbs suggests that V2a stop neurons

innervate both cervical and lumbar segments, as shown with anterograde labeling of transmitter unspecified Gi neurons (Liang et al., 2015).

Previous studies in zebrafish have shown that caudal-most brainstem excitatory V2a neurons initiate and maintain swimming activity (Kimura et al., 2013). In agreement with Bretzner and Brownstone (2013), we were unable to observe any locomotor promoting effects from stimulating the caudal-most brainstem V2a neurons in vitro. However, stimulating broadly all excitatory neurons of the caudal brainstem does initiate episodes of locomotor-like activity (Hägglund et al., 2010). Therefore, brainstem neurons providing a locomotor-initiating signal may be non-V2a in mice, and/or the abundance of V2a stop neurons and fibers may hinder selective manipulation of the putative locomotor-initiating ones. Further investigations using genetic manipulations of projection specific cell types will undoubtedly help tackle this ambiguity.

Behavioral Activation of V2a Stop Neurons

Interestingly, a unique firing pattern that correlates with the offset of swimming has been identified in lamprey reticulospinal neurons (Juvin and Dubuc, 2009). A similar functional signature has not yet been reported in mice. Further recordings taking advantage of the molecular signature described here will rapidly help address this question. Nevertheless, the deficiency in stopping we described upon V2a silencing indicates that those cells may be spontaneously mobilized during exploratory locomotor behavior to arrest it when needed. This descending stop signal may act in parallel to those initiating and controlling the speed of ongoing locomotion. When an active stop is needed the V2a neurons may be brought into action to arrest locomotion while maintaining an optimized posture to avoid collapse.

EXPERIMENTAL PROCEDURES

Mice Lines

All experiments were approved by the local ethical committee. The following transgenic lines were used: *Chx10::Cre* (kindly provided by S. Crone, K. Sharma, L. Zagoraiou, and T.M. Jessell, see Azim et al., (2014), GlyT2-GFP (Zeilhofer et al., 2005), GAD67-GFP (Tamamaki et al., 2003), Rosa26^{FloxedSTOP-YFP} or Rosa26^{FloxedSTOP-Tdtomato}, Rosa26-CAG-LSL-eNpHR3.0-EYFP-WPRE, and Rosa26-CAG-LSL-ChR2-EYFP-WPRE (all from the Jackson Laboratories).

Retrograde Labeling and Neurotransmitter Phenotyping

Chx10::Cre mice were crossed with a conditional reporter line (Rosa26^{FloxedYFP} or Rosa26^{FloxedTdtomato}) and occasionally with a GlyT2-GFP or GAD67-GFP line. CTB was injected bilaterally in the L2 spinal segment on 1–2 month old animals. Additional information on the injection procedure, in situ hybridization, immunohistochemistry, and anatomical quantifications are found in the Supplemental Experimental Procedures.

In Vitro Recording of Locomotor-Like Activity and Optogenetics

Pups (0–4 days) were anaesthetized with isoflurane, decerebrated above the ponto-medullary junction (thus preserving the PnC), and the spinal cord and brainstem were isolated in Ringer solution and transferred to a recording chamber. Locomotor-like activity was recorded with suction electrodes attached to the L2 and/or the L5 lumbar roots as previously reported. NMDA and 5-HT were bath-applied to induce locomotor-like activity. Neuro-nally evoked locomotor-like activity was elicited by electrical stimulation of the midline in upper cervical segments (Dougherty et al., 2013; Talpalar

and Kiehn, 2010). Light from a 100 W Hg lamp was filtered by 450–490 nm or 536–556 nm band-pass filters for ChR2 and eNpHR, respectively, and directed onto the preparation via a 5× objective. Details, including motor neuron recordings, are found in the Supplemental Experimental Procedures.

In Vivo Optogenetic and Genetic Silencing Experiments

Viral Injections and Ferrule Implantation

Chx10::Cre animals aged 1–2 months were used, and 600 nl of an AAVDj-EF1a-DIO-hChR2-p2A-mCheery-WPRE or 300 to 700 nl of an AAV1/2-FLEX-TeLC-eYFP-WPRE virus (Murray et al., 2011) were injected in the rGi bilaterally (~6.0 from Bregma, Lat: 0.5, D/V: −4.0). In the same surgery, an optical fiber (200 μm core, 0.22 NA, Thorlabs) held in a 1.25 mm ferrule was implanted medially (depth ~3.5 mm).

Optogenetic Stimulation

Light from a 473 nm laser (Optoduet, Ikecool Corporation) was delivered in trains of pulses (Master 8, AMPI) of 10–20 ms pulse duration, 20–40 Hz frequencies, and train durations of 0.5–1 s. The intensity of the laser was set prior to the experiment at the lowest intensity sufficient to stop locomotion (typically 5–30 mW).

Behavioral Tests

For acute optogenetic activations, mice were running spontaneously in a linear corridor (MotoRater, TSE Systems), and the locomotor behavior was recorded as described in Bellardita and Kiehn, (2015). For chronic silencing tests in the open field, mice were placed in a square Plexiglas box (45 × 45 cm); the first 30 min were considered for acclimatization and the next 25 min for the analysis. In a series of silencing experiments, we utilized the linear corridor supplemented with four obstacles of increasing height. Videos were analyzed using scripts written in Matlab (Mathworks) and R (www.r-project.org/). Details are found in the Supplemental Experimental Procedures.

SUPPLEMENTAL INFORMATION

Supplemental Information includes Supplemental Experimental Procedures, seven figures, and three movies and can be found with this article online at <http://dx.doi.org/10.1016/j.cell.2015.10.074>.

AUTHOR CONTRIBUTIONS

J.B. and O.K. conceived the in vitro study. O.K. and V. Caggiano conceived the in vivo study with contributions from R.L. and J.B. J.B. performed anatomical investigations, viral tracings, in vitro recordings, and analyzed data. V. Caggiano and R.L. performed in vivo experiments and analyzed data. C.B. contributed to spinal injections and to locomotor gait analysis. V. Caldeira carried out fluorescent in situ hybridizations. A.F. performed whole-cell recordings of transfected neurons. K.B. produced the TeLC-coding virus. J.B. and O.K. wrote the paper with contributions of all authors. O.K. supervised all aspects of the work and provided the funding of the work.

ACKNOWLEDGMENTS

We thank K. Sharma (University of Chicago), S. Crone (Cincinnati Children's), L. Zagoraiou, (Academy of Athens), and T.M. Jessell (Columbia University) for the *Chx10::cre* mouse. This work was supported by the Torsten and Ragnar Söderberg's Foundation (O.K.), Swedish Research Council (O.K.), European Research Council (O.K.), NIH R01 NS090919 (O.K.), and Hjärnfonden (O.K.). J.B. was an EMBO fellow. We thank A.C. Westerdahl and P. Löw for extensive genotyping and N. Sleiers for animal breeding in Kiehn lab. We also like to thank R. Diaz Heijtz (Karolinska) for advice on the open field test. We declare no conflict of interest regarding this work. The AAV-DIO-hChR2-mCherry virus was a kind gift from K. Deisseroth (Stanford).

Received: May 22, 2015

Revised: September 21, 2015

Accepted: October 28, 2015

Published: November 19, 2015

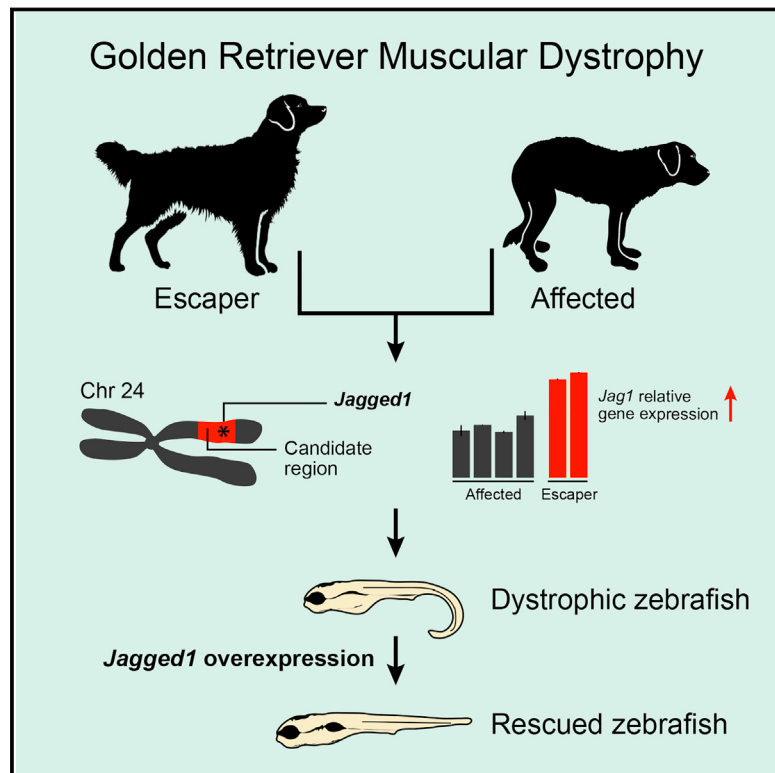
REFERENCES

- Al-Mosawie, A., Wilson, J.M., and Brownstone, R.M. (2007). Heterogeneity of V2-derived interneurons in the adult mouse spinal cord. *Eur. J. Neurosci.* 26, 3003–3015.
- Alvarez, F.J., and Fyffe, R.E. (2007). The continuing case for the Renshaw cell. *J. Physiol.* 584, 31–45.
- Andersson, L.S., Larhammar, M., Memic, F., Wootz, H., Schwochow, D., Rubin, C.J., Patra, K., Arnason, T., Wellbring, L., Hjälm, G., et al. (2012). Mutations in DMRT3 affect locomotion in horses and spinal circuit function in mice. *Nature* 488, 642–646.
- Azim, E., Jiang, J., Alstermark, B., and Jessell, T.M. (2014). Skilled reaching relies on a V2a propriospinal internal copy circuit. *Nature* 508, 357–363.
- Bellardita, C., and Kiehn, O. (2015). Phenotypic characterization of speed-associated gait changes in mice reveals modular organization of locomotor networks. *Curr. Biol.* 25, 1426–1436.
- Bouvier, J., Thoby-Brisson, M., Renier, N., Dubreuil, V., Ericson, J., Champagnat, J., Pierani, A., Chédotal, A., and Fortin, G. (2010). Hindbrain interneurons and axon guidance signaling critical for breathing. *Nat. Neurosci.* 13, 1066–1074.
- Brandão, M.L., Zanoveli, J.M., Ruiz-Martinez, R.C., Oliveira, L.C., and Landeira-Fernandez, J. (2008). Different patterns of freezing behavior organized in the periaqueductal gray of rats: association with different types of anxiety. *Behav. Brain Res.* 188, 1–13.
- Bretzner, F., and Brownstone, R.M. (2013). Lhx3-Chx10 reticulospinal neurons in locomotor circuits. *J. Neurosci.* 33, 14681–14692.
- Caggiano, V., Sur, M., and Bizzi, E. (2014). Rostro-caudal inhibition of hindlimb movements in the spinal cord of mice. *PLoS ONE* 9, e100865.
- Cepeda-Nieto, A.C., Pfaff, S.L., and Varela-Echavarria, A. (2005). Homeodomain transcription factors in the development of subsets of hindbrain reticulospinal neurons. *Mol. Cell. Neurosci.* 28, 30–41.
- Crone, S.A., Quinlan, K.A., Zagoraiau, L., Droho, S., Restrepo, C.E., Lundfeld, L., Endo, T., Setlak, J., Jessell, T.M., Kiehn, O., and Sharma, K. (2008). Genetic ablation of V2a ipsilateral interneurons disrupts left-right locomotor coordination in mammalian spinal cord. *Neuron* 60, 70–83.
- Crone, S.A., Zhong, G., Harris-Warrick, R., and Sharma, K. (2009). In mice lacking V2a interneurons, gait depends on speed of locomotion. *J. Neurosci.* 29, 7098–7109.
- Deliagina, T.G., Zelenin, P.V., Fagerstedt, P., Grillner, S., and Orlovsky, G.N. (2000). Activity of reticulospinal neurons during locomotion in the freely behaving lamprey. *J. Neurophysiol.* 83, 853–863.
- Dougherty, K.J., and Kiehn, O. (2010). Firing and cellular properties of V2a interneurons in the rodent spinal cord. *J. Neurosci.* 30, 24–37.
- Dougherty, K.J., Zagoraiau, L., Satoh, D., Rozani, I., Doobar, S., Arber, S., Jessell, T.M., and Kiehn, O. (2013). Locomotor rhythm generation linked to the output of spinal shox2 excitatory interneurons. *Neuron* 80, 920–933.
- Drew, T., Dubuc, R., and Rossignol, S. (1986). Discharge patterns of reticulospinal and other reticular neurons in chronic, unrestrained cats walking on a treadmill. *J. Neurophysiol.* 55, 375–401.
- Dubuc, R., Brocard, F., Antri, M., Fénelon, K., Gariépy, J.F., Smetana, R., Ménard, A., Le Ray, D., Viana Di Prisco, G., Pearlstein, E., et al. (2008). Initiation of locomotion in lampreys. *Brain Res. Brain Res. Rev.* 57, 172–182.
- Esposito, M.S., Capelli, P., and Arber, S. (2014). Brainstem nucleus MdV mediates skilled forelimb motor tasks. *Nature* 508, 351–356.
- Feldman, J.L., and Kam, K. (2014). Facing the challenge of mammalian neural microcircuits: Taking a few breaths may help. *J. Physiol.*
- Goulding, M. (2009). Circuits controlling vertebrate locomotion: moving in a new direction. *Nat. Rev. Neurosci.* 10, 507–518.
- Grillner, S., and Georgopoulos, A.P. (1996). Neural control. *Curr. Opin. Neurobiol.* 6, 741–743.
- Grillner, S., and Jessell, T.M. (2009). Measured motion: searching for simplicity in spinal locomotor networks. *Curr. Opin. Neurobiol.* 19, 572–586.
- Hägglund, M., Borgius, L., Dougherty, K.J., and Kiehn, O. (2010). Activation of groups of excitatory neurons in the mammalian spinal cord or hindbrain evokes locomotion. *Nat. Neurosci.* 13, 246–252.
- Hägglund, M., Dougherty, K.J., Borgius, L., Itohara, S., Iwasato, T., and Kiehn, O. (2013). Optogenetic dissection reveals multiple rhythrogenic modules underlying locomotion. *Proc. Natl. Acad. Sci. USA* 110, 11589–11594.
- Holstege, J.C. (1991). Ultrastructural evidence for GABAergic brain stem projections to spinal motoneurons in the rat. *J. Neurosci.* 11, 159–167.
- Hultborn, H., Illert, M., and Santini, M. (1976). Convergence on interneurons mediating the reciprocal Ia inhibition of motoneurons. I. Disynaptic Ia inhibition of Ia inhibitory interneurons. *Acta Physiol. Scand.* 96, 193–201.
- Jordan, L.M., Liu, J., Hedlund, P.B., Akay, T., and Pearson, K.G. (2008). Descending command systems for the initiation of locomotion in mammals. *Brain Res. Brain Res. Rev.* 57, 183–191.
- Juvín, L., and Dubuc, R. (2009). Patterns of activity of reticulospinal neurons during locomotion in lampreys. *Soc. Neurosci. Abstr.*
- Kiehn, O. (2006). Locomotor circuits in the mammalian spinal cord. *Annu. Rev. Neurosci.* 29, 279–306.
- Kiehn, O. (2011). Development and functional organization of spinal locomotor circuits. *Curr. Opin. Neurobiol.* 21, 100–109.
- Kimura, Y., Satou, C., Fujioka, S., Shoji, W., Umeda, K., Ishizuka, T., Yawo, H., and Higashijima, S. (2013). Hindbrain V2a neurons in the excitation of spinal locomotor circuits during zebrafish swimming. *Curr. Biol.* 23, 843–849.
- Kullander, K., Butt, S.J., Lebret, J.M., Lundfeld, L., Restrepo, C.E., Rydström, A., Klein, R., and Kiehn, O. (2003). Role of EphA4 and EphrinB3 in local neuronal circuits that control walking. *Science* 299, 1889–1892.
- Liang, H., Watson, C., and Paxinos, G. (2015). Terminations of reticulospinal fibers originating from the gigantocellular reticular formation in the mouse spinal cord. *Brain Struct. Funct.* Published online on January 30, 2015. <http://dx.doi.org/10.1007/s00429-015-0993-z>.
- Liu, J., and Jordan, L.M. (2005). Stimulation of the parapyramidal region of the neonatal rat brain stem produces locomotor-like activity involving spinal 5-HT and 5-HT2A receptors. *J. Neurophysiol.* 94, 1392–1404.
- Lu, J., Sherman, D., Devor, M., and Saper, C.B. (2006). A putative flip-flop switch for control of REM sleep. *Nature* 441, 589–594.
- Lundfeld, L., Restrepo, C.E., Butt, S.J., Peng, C.Y., Droho, S., Endo, T., Zeilhofer, H.U., Sharma, K., and Kiehn, O. (2007). Phenotype of V2-derived interneurons and their relationship to the axon guidance molecule EphA4 in the developing mouse spinal cord. *Eur. J. Neurosci.* 26, 2989–3002.
- Luppi, P.H., Clément, O., Sapin, E., Gervasoni, D., Peyron, C., Léger, L., Salvert, D., and Fort, P. (2011). The neuronal network responsible for paradoxical sleep and its dysfunctions causing narcolepsy and rapid eye movement (REM) behavior disorder. *Sleep Med. Rev.* 15, 153–163.
- McCrea, D.A., and Rybak, I.A. (2008). Organization of mammalian locomotor rhythm and pattern generation. *Brain Res. Brain Res. Rev.* 57, 134–146.
- McLean, D.L., and Dougherty, K.J. (2015). Peeling back the layers of locomotor control in the spinal cord. *Curr. Opin. Neurobiol.* 33, 63–70.
- Mori, S. (1987). Integration of posture and locomotion in acute decerebrate cats and in awake, freely moving cats. *Prog. Neurobiol.* 28, 161–195.
- Murray, A.J., Sauer, J.F., Riedel, G., McClure, C., Ansel, L., Cheyne, L., Bartos, M., Wisden, W., and Wulff, P. (2011). Parvalbumin-positive CA1 interneurons are required for spatial working but not for reference memory. *Nat. Neurosci.* 14, 297–299.
- Perreault, M.C., and Glover, J.C. (2013). Glutamatergic reticulospinal neurons in the mouse: developmental origins, axon projections, and functional connectivity. *Ann. N Y Acad. Sci.* 1279, 80–89.
- Perrins, R., Walford, A., and Roberts, A. (2002). Sensory activation and role of inhibitory reticulospinal neurons that stop swimming in hatchling frog tadpoles. *J. Neurosci.* 22, 4229–4240.
- Roberts, A., Li, W.C., Soffe, S.R., and Wolf, E. (2008). Origin of excitatory drive to a spinal locomotor network. *Brain Res. Brain Res. Rev.* 57, 22–28.

- Ryczko, D., and Dubuc, R. (2013). The multifunctional mesencephalic locomotor region. *Curr. Pharm. Des.* 19, 4448–4470.
- Schiavo, G., Benfenati, F., Poulain, B., Rossetto, O., Polverino de Laureto, P., DasGupta, B.R., and Montecucco, C. (1992). Tetanus and botulinum-B neurotoxins block neurotransmitter release by proteolytic cleavage of synaptobrevin. *Nature* 359, 832–835.
- Sivertsen, M.S., Glover, J.C., and Perreault, M.C. (2014). Organization of pontine reticulospinal inputs to motoneurons controlling axial and limb muscles in the neonatal mouse. *J. Neurophysiol.* 112, 1628–1643.
- Szokol, K., Glover, J.C., and Perreault, M.C. (2011). Organization of functional synaptic connections between medullary reticulospinal neurons and lumbar descending commissural interneurons in the neonatal mouse. *J. Neurosci.* 31, 4731–4742.
- Takakusaki, K., Kohyama, J., and Matsuyama, K. (2003). Medullary reticulospinal tract mediating a generalized motor inhibition in cats: III. Functional organization of spinal interneurons in the lower lumbar segments. *Neuroscience* 121, 731–746.
- Talpalar, A.E., and Kiehn, O. (2010). Glutamatergic mechanisms for speed control and network operation in the rodent locomotor CpG. *Front. Neural Circuits* 4, 4.
- Talpalar, A.E., Bouvier, J., Borgius, L., Fortin, G., Pierani, A., and Kiehn, O. (2013). Dual-mode operation of neuronal networks involved in left-right alternation. *Nature* 500, 85–88.
- Tamamaki, N., Yanagawa, Y., Tomioka, R., Miyazaki, J., Obata, K., and Kaneko, T. (2003). Green fluorescent protein expression and colocalization with calretinin, parvalbumin, and somatostatin in the GAD67-GFP knock-in mouse. *J. Comp. Neurol.* 467, 60–79.
- Vetrivelan, R., Fuller, P.M., Tong, Q., and Lu, J. (2009). Medullary circuitry regulating rapid eye movement sleep and motor atonia. *J. Neurosci.* 29, 9361–9369.
- Wilson, J.M., Hartley, R., Maxwell, D.J., Todd, A.J., Lieberam, I., Kaltschmidt, J.A., Yoshida, Y., Jessell, T.M., and Brownstone, R.M. (2005). Conditional rhythmicity of ventral spinal interneurons defined by expression of the Hb9 homeodomain protein. *J. Neurosci.* 25, 5710–5719.
- Yilmaz, M., and Meister, M. (2013). Rapid innate defensive responses of mice to looming visual stimuli. *Curr. Biol.* 23, 2011–2015.
- Zeilhofer, H.U., Studler, B., Arabadzisz, D., Schweizer, C., Ahmadi, S., Layh, B., Bösl, M.R., and Fritschy, J.M. (2005). Glycinergic neurons expressing enhanced green fluorescent protein in bacterial artificial chromosome transgenic mice. *J. Comp. Neurol.* 482, 123–141.
- Zhang, J., Lanuza, G.M., Britz, O., Wang, Z., Siembab, V.C., Zhang, Y., Velasquez, T., Alvarez, F.J., Frank, E., and Goulding, M. (2014). V1 and v2b interneurons secure the alternating flexor-extensor motor activity mice require for limbed locomotion. *Neuron* 82, 138–150.
- Zhong, G., Droho, S., Crone, S.A., Dietz, S., Kwan, A.C., Webb, W.W., Sharma, K., and Harris-Warrick, R.M. (2010). Electrophysiological characterization of V2a interneurons and their locomotor-related activity in the neonatal mouse spinal cord. *J. Neurosci.* 30, 170–182.

Jagged 1 Rescues the Duchenne Muscular Dystrophy Phenotype

Graphical Abstract



Highlights

- Escaper GRMD dogs show that a normal lifespan is possible without muscle dystrophin
- *Jagged1*, a Notch ligand, is upregulated in mildly affected dystrophin deficient dogs
- *Jagged1* overexpression can rescue the phenotype of dystrophin deficient zebrafish

Authors

Natassia M. Vieira, Ingegerd Elvers,
Matthew S. Alexander, ...,
Kerstin Lindblad-Toh, Louis M. Kunkel,
Mayana Zatz

Correspondence

kunkel@enders.tch.harvard.edu (L.M.K.),
mayazatz@usp.br (M.Z.)

In Brief

The study of two exceptional dogs that escaped from the severe phenotype associated with dystrophin deficiency unveils a genetic modifier that allows functional muscle and normal lifespan despite the complete absence of dystrophin.

Accession Numbers

GSE69040

Jagged 1 Rescues the Duchenne Muscular Dystrophy Phenotype

Natassia M. Vieira,^{1,2,3} Ingegerd Elvers,^{4,5} Matthew S. Alexander,^{1,2,6} Yuri B. Moreira,⁷ Alal Eran,² Juliana P. Gomes,³ Jamie L. Marshall,^{1,2} Elinor K. Karlsson,^{4,10} Sergio Verjovski-Almeida,^{7,8} Kerstin Lindblad-Toh,^{4,5,11} Louis M. Kunkel,^{1,2,9,11,*} and Mayana Zatz^{3,11,*}

¹The Division of Genetics and Genomics, Boston Children's Hospital, Boston, MA 02115, USA

²Department of Pediatrics and Genetics, Harvard Medical School, Boston, MA 02115, USA

³Human Genome and Stem Cell Center, Biosciences Institute, University of São Paulo, São Paulo 05508-090, Brazil

⁴Broad Institute of Harvard and Massachusetts Institute of Technology, Cambridge, MA 02142, USA

⁵Science for Life Laboratory, Department of Medical Biochemistry and Microbiology, Uppsala University, Box 597, 751 24, Uppsala, Sweden

⁶The Stem Cell Program at Boston Children's Hospital, Boston, MA 02115, USA

⁷Departamento de Bioquímica, Instituto de Química, Universidade de São Paulo, São Paulo, Brazil, 05508-000

⁸Instituto Butantan, São Paulo 05508-050, Brazil

⁹The Manton Center for Orphan Disease Research at Boston Children's Hospital, Boston, MA 02115, USA

¹⁰Program in Bioinformatics and Integrative Biology, University of Massachusetts Medical School, Worcester, MA 01605, USA

¹¹Co-senior author

*Correspondence: kunkel@enders.tch.harvard.edu (L.M.K.), mayazatz@usp.br (M.Z.)

<http://dx.doi.org/10.1016/j.cell.2015.10.049>

SUMMARY

Duchenne muscular dystrophy (DMD), caused by mutations at the *dystrophin* gene, is the most common form of muscular dystrophy. There is no cure for DMD and current therapeutic approaches to restore dystrophin expression are only partially effective. The absence of dystrophin in muscle results in dysregulation of signaling pathways, which could be targets for disease therapy and drug discovery. Previously, we identified two exceptional Golden Retriever muscular dystrophy (GRMD) dogs that are mildly affected, have functional muscle, and normal lifespan despite the complete absence of dystrophin. Now, our data on linkage, whole-genome sequencing, and transcriptome analyses of these dogs compared to severely affected GRMD and control animals reveals that increased expression of *Jagged1* gene, a known regulator of the Notch signaling pathway, is a hallmark of the mild phenotype. Functional analyses demonstrate that *Jagged1* overexpression ameliorates the dystrophic phenotype, suggesting that *Jagged1* may represent a target for DMD therapy in a dystrophin-independent manner.

INTRODUCTION

Duchenne muscular dystrophy (DMD) is an X-linked disorder caused by mutations in *dystrophin* (Hoffman et al., 1987), which affects 1 in 3,500 to 5,000 boys (Axelsson et al., 2013; Mendell et al., 2012). Deficiency of muscle dystrophin causes progressive myofiber degeneration and muscle wasting (Hoffman

et al., 1987). The first symptoms are usually evident at 3–5 years of age, with loss of ambulation between 9 and 12 years. Death occurs in the second or third decade due to respiratory or cardiac failure. While there are several treatments under development or currently in use—particularly corticotherapy, which aims to ameliorate symptoms and slow down the disease progression—there is still no cure for DMD (Bushby et al., 2010; Guiraud et al., 2015). Allelic to DMD, Becker muscular dystrophy (BMD) is caused by mutations that do not affect the reading frame of the *dystrophin* transcript; the result is a semi-functional, truncated dystrophin protein (Koenig et al., 1989). DMD muscle shows a complete absence of dystrophin, whereas in the BMD muscle there is a variable amount of partially functional dystrophin (Monaco et al., 1988). Differently from DMD, where most boys carrying null mutations show a severe phenotype, BMD patients show a variable clinical course. Genotype/phenotype correlation studies suggest that the severity of the phenotype is dependent on the amount of muscle dystrophin or the site of the mutation/deletion in the *dystrophin* gene (Koenig et al., 1989; Passos-Bueno et al., 1994; Vainzof et al., 1990).

DMD therapeutic approaches currently under development aim to rescue *dystrophin* expression in the muscle (Fairclough et al., 2013). Pre-clinical and clinical studies include exon-skipping (Goemans et al., 2011; Mendell et al., 2013; van Deutekom et al., 2007), AAV-delivery of μ -dystrophin (Mendell et al., 2010), and nonsense suppression to induce “readthrough” of nonsense mutations (Kayali et al., 2012). While AAV-delivery led to μ -dystrophin expression in skeletal muscle, T cell immunity against dystrophin epitopes was reported (Mendell et al., 2010). Also, the success of the dystrophin-based therapies relies on the quality of the recipient muscle. This requires the development of dystrophin-independent therapies to improve the muscle condition targeting the altered signaling pathways.

To explore the efficiency of the different therapeutic approaches for DMD, there is a need for animal models that mimic the human condition. However, animal models of dystrophin-deficiency

show differences in skeletal muscle pathology in response to dystrophin-deficiency (Bassett and Currie, 2004; Chapman et al., 1989; Im et al., 1996; Kornegay et al., 1988; Zucconi et al., 2010). The dystrophin-deficient fish model *sapje* shows some phenotypic variability, but nearly all fish die during the first weeks of life and all show abnormal muscle structure as measured by birefringence under polarized light (Bassett and Currie, 2004). The *mdx* mouse is the most widely used animal model for DMD, even though its mild phenotype does not mimic severe human DMD symptoms (Bulfield et al., 1984). The most similar to the human condition is the golden retriever muscular dystrophy (GRMD) dog (Bassett et al., 2003; Cooper et al., 1988; Kornegay et al., 1988; Sicinski et al., 1989). These animals carry a point mutation on a splicing site that causes the skipping of exon 7 and a premature stop codon, resulting in the absence of dystrophin. GRMD dogs and DMD patients share many similarities in disease pathogenesis, including early progressive muscle degeneration and atrophy, fibrosis, contractures, and grossly elevated serum creatine kinase (CK) levels (Kornegay et al., 1988; Sharp et al., 1992). Early death may occur within the first weeks of life but usually occurs around 1–2 years of age as a result of respiratory failure or cardiomyopathy. The great majority of GRMD dogs do not survive beyond age two. In the Brazilian GRMD colony at Biosciences Institute at the University of São Paulo, we have described two exceptional dogs presenting a very mild phenotype clearly distinguishable from other affected dogs despite the absence of muscle dystrophin. Histopathological and immunohistochemistry analysis of their muscle showed typical features of a dystrophic process with variability in fiber size, splitting, degeneration, and infiltrating connective tissue (Zucconi et al., 2010).

These two exceptional, related GRMD dogs (here called “escapers”) remained fully ambulatory with normal lifespans, a phenotype never reported before for GRMD. They fall outside the known GRMD phenotypic range of variability, differing significantly from typically affected dogs despite their dystrophic muscle, absence of muscle dystrophin, elevated serum CK levels, and lack of evidence of utrophin upregulation (Zatz et al., 2015; Zucconi et al., 2010). Most importantly, these GRMD dogs show that it is possible to have a functional muscle in a mid-size dystrophin-deficient animal.

In this study, we set out to answer the following question: how do these escaper dogs have a fully functional muscle without dystrophin? Skeletal muscle of DMD patients undergoes waves or cycles of degeneration followed by regeneration. Muscle repair is a regulated process that comprises different cell types and signaling molecules, but additional factors and genetic modifiers involved in DMD pathogenesis remain poorly understood, representing new potential therapeutic targets. Genetic modifiers have been reported in DMD patients with a slower progression, but none were associated with a nearly normal phenotype (Flanigan et al., 2013). Here, through three independent approaches, we identified a modifier gene, *Jagged1*, which can modulate the GRMD phenotype. Using a mixed model association and linkage analysis, we identified a chromosomal region associated with the escaper phenotype. One gene within this region showed altered expression when comparing muscle tissue of escaper and affected dogs. By whole-genome sequencing, we found a variant present only in escaper GRMD dogs that

creates a novel myogenin binding site in the *Jagged1* promoter. Overexpression of *jagged1* in dystrophin deficient zebrafish rescues the dystrophic phenotype in this zebrafish model. This suggests that *Jagged1*, when increased in expression in muscle, can rescue dystrophin-deficient phenotypes in two different animal models, pointing to a new potential therapeutic target.

RESULTS

Escaper GRMD Dogs Share a Common Haplotype Different from Affected

To understand the genetic basis behind the escaper phenotype in GRMD dogs, we performed a genome-wide mapping analysis comparing two related escaper GRMD dogs—the only two GRMD escapers reported to date—to 31 severely affected GRMD dogs from the same breeding population. All GRMD dogs were confirmed to carry the originally described point mutation (a change from adenine to guanine transition) in the intron 6 of the *dystrophin* gene. This mutation ablates a splicing site and exon 7 is skipped from the mature mRNA. The absence of exon 7 causes a premature stop codon at exon 8 (Cooper et al., 1988; Sharp et al., 1992). Based on survival age and functional capacity, they were classified as escaper or affected (binary). All the dogs showing the standard range of phenotypic variability seen in GRMD dogs were classified as affected in this study. Our aim was to identify a single gene responsible for the milder phenotype seen in the two escaper dogs. We performed a two-step mapping analysis. First, we carried out an association study, utilizing the power of the many severely affected dogs expected to lack the modifier locus. This was followed by segregation analysis, taking advantage of the fact that the two escapers came from a well-defined pedigree in which a transmission-based test could be used. All dogs were genotyped using the Illumina CanineHD 170K SNP array. We tested for association genome wide using the mixed model approach implemented in EMMA (Kang et al., 2010) to correct for population structure (Figure 1A) and identified strongly associated SNPs ($p < 1 \times 10^{-5}$) on chromosomes 24, 33, and 37 (Figure 1B). We then measured identity by descent (IBD) across the genome between the two escapers using Beagle (Browning and Browning, 2007). Only the associated SNPs on chromosome 24 also overlapped a segment of IBD in the two escapers, consistent with a single origin of the causative mutation (Figure 1B). The 27 Mb segment showing both IBD and association with the escaper phenotype (CanFam2, cfa24:3,073,196-30,066,497) contains approximately 350 protein-coding genes. Linkage analysis using Merlin (Abecasis et al., 2002) strongly confirmed this region, with a maximal parametric LOD score of 3.31 (dominant inheritance model with complete penetrance, Figure S1). No other genomic regions showed any signs of linkage (Figure S2). Thus, convergent IBD, association, and linkage analyses all pointed to the same 27 Mb region on chromosome 24 (Figure 1C).

Muscle Gene Expression Profile of Escaper and Affected GRMD Dogs

We then performed a genome-wide analysis for genes differentially expressed in muscle between the escapers and affected dogs. Using Agilent mRNA SurePrint Canine arrays,

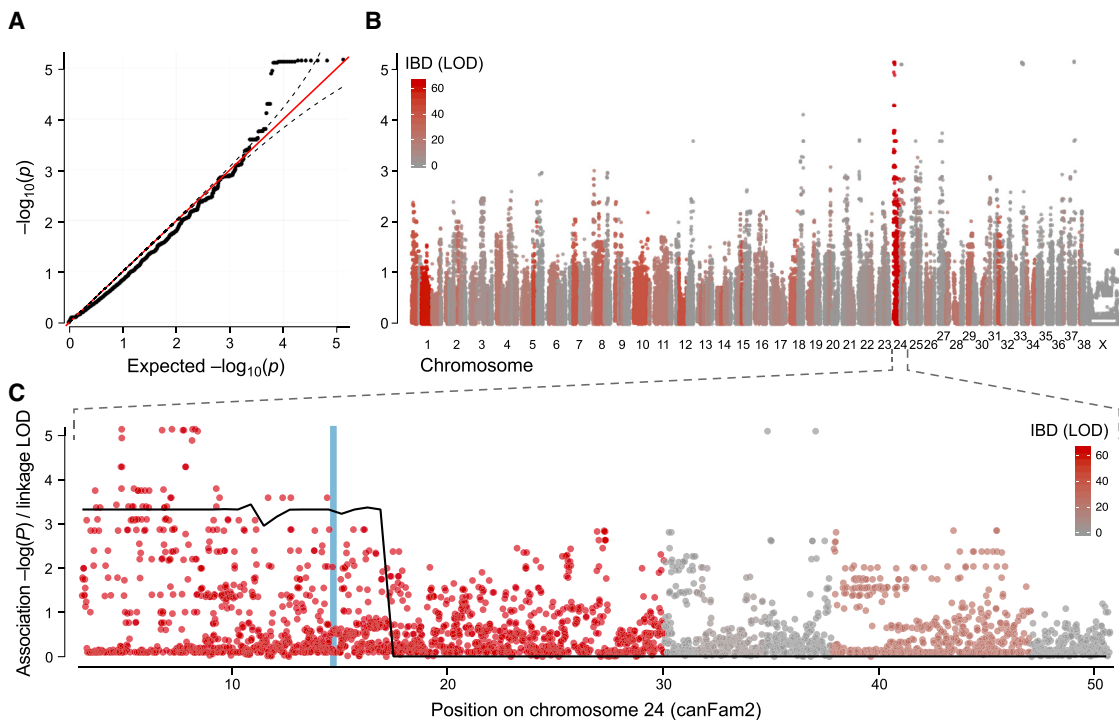


Figure 1. Combining Association, Linkage, and Identity-By-Descent Analysis Identifies a 30 Mb Candidate Region on Chromosome 24

(A) A QQ plot of 129,908 SNPs tested for association identified 27 SNPs outside the 95% confidence intervals (dashed lines) and minimal stratification relative to the expected distribution (red line), suggesting the mixed model approach corrected for close relatedness among the 2 escapers and 31 severely affected GRMD dogs. (B) Only the association on chromosome 24 also falls in a region where the two escapers (sire and offspring) share a long haplotype likely to be identical-by-descent (IBD, red). Other peaks on chromosomes 24, 33, and 37 show no evidence of IBD (gray) and are most likely false positives due to the small sample size. (C) The mapped region extends 27 Mb from the start of chromosome 24. Linkage analysis with Merlin (solid black line) detected a significant linkage peak (dominant parametric LOD > 3) overlapping the IBD and association peak that includes the putative driver gene *Jagged1* (blue line) identified through gene expression profiling. See also Figures S1 and S2.

we compared muscle gene expression of the two escapers, four affected, and four wild-type dogs at two years of age. We found very similar muscle gene expression patterns in the two escaper GRMD dogs, which were more similar to muscle from wild-type dogs than from the affected dogs. In total, 114 genes were found to be differentially expressed between escapers and affected GRMD dogs, as shown by unsupervised hierarchical clustering of all ten samples (Figure 2A). Of these, 65 genes were also differentially expressed between escapers and wild-type dogs (Table S1), implicating them in a possible compensatory mechanism active in only the escaper dogs. Only one of these 65 genes, *Jagged1*, is located under the association peak on chromosome 24. *Jagged1* mRNA levels were two times higher in the escapers when compared to both wild-type and severely affected dogs (Figure 2B). Further protein level analysis confirmed the mRNA findings (Figure 2C).

Whole-Genome Sequence of Escaper Dogs

To identify potentially causative variants behind the differential gene expression pattern observed in the escaper dogs, we performed whole-genome sequencing on three dogs (the two escapers and one severely affected related dog). We hypothesized that the compensatory variation would be novel, as the escaper phenotype had not previously been seen in GRMD

dogs worldwide. We looked for variants located under the association peak on chromosome 24 and focused on the *Jagged1* locus (including 3 KB upstream and downstream of the gene) in search for a variant present only in the escapers and not in the affected GRMD dogs. A total of ~1,300 variants were detected within the escaper-associated region on chromosome 24. All variants were lifted over to the human genome, and those present in muscle enhancer regions near the promoters of the two isoforms of *Jagged1* expressed in skeletal muscle (Figure 3A) (Hoepfner et al., 2014) were further analyzed. Since the escaper variant was hypothesized to be novel, all variants detected in previous extensive canine sequencing efforts (Axelsson et al., 2013) were excluded. After this filtering, only a single point variant was found to follow the escaper haplotype: a heterozygote G>T change in the promoter region of *Jagged1* (cfa24:11655709, Figure 3A). Sanger sequencing of the *Jagged1* candidate escaper variant was performed in the escaper extended pedigree, including the first escaper (M1M4), his offspring, and a sibling's offspring (M1M5) (Figure S3). We also sequenced key breeders of the kennel and found that the variant is specific to the escapers' pedigree and was introduced in a single outcross (B1F3 mate). All affected dogs lacked the *Jagged1* variant, while both escapers were heterozygous. Thus, the novel *Jagged1* mutation segregates with the escaper phenotype in this family. Four additional individuals

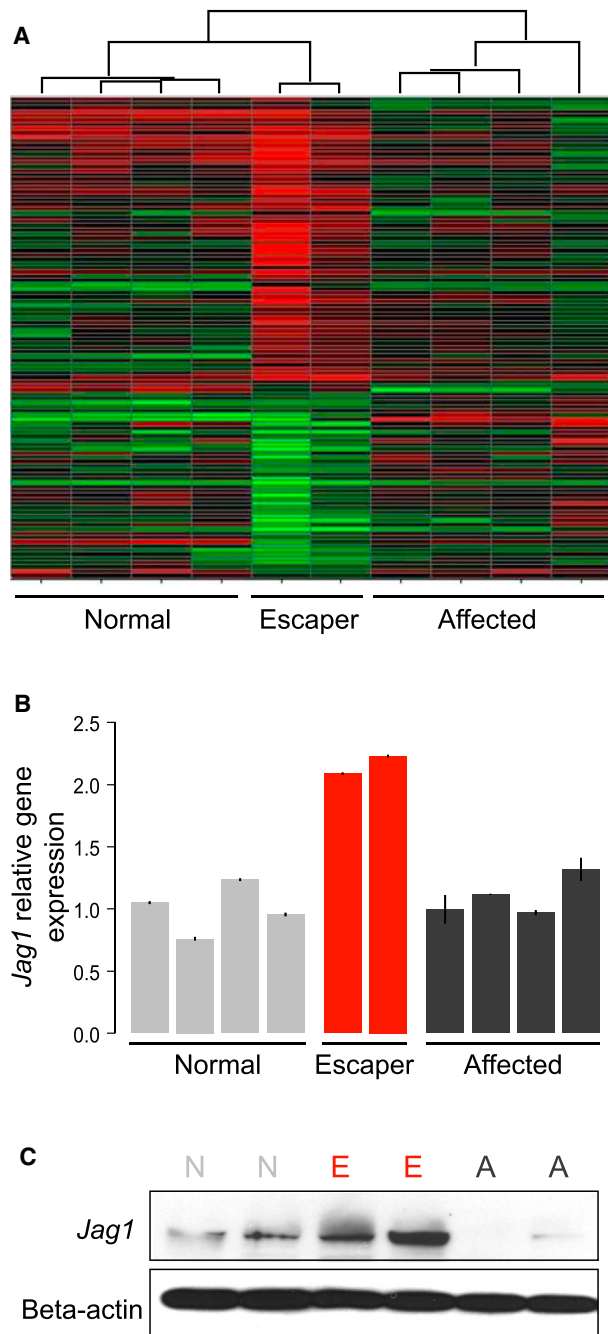


Figure 2. Altered Jagged1 Expression in Escaper GRMD Dogs

(A) mRNA microarray comparing muscle gene expression of escaper GRMD dogs with related severely affected and WT dogs.

(B) mRNA expression of escaper dogs confirming the expression array findings. Relative *Jagged1* gene expression in muscle samples of escaper GRMD dogs as compared to related severely affected and WT dogs; bars indicate SD from the mean.

(C) *Jagged1* protein levels in the muscle of escaper GRMD dogs (E) as compared to severely affected (A) and WT dog muscle (N); Beta-actin is the loading control. See also Table S1.

carried the candidate variant: three were stillborn puppies and the fourth was a GRMD puppy that died at 6 months of age from an accidental ingestion of a foreign object. This puppy (K2M11) was fully ambulatory with a similar phenotype to the two escaper dogs, but he was classified as affected in the mapping analysis since we cannot predict his adult phenotype with confidence.

Functional Analysis of Jagged1 Variant

To understand the effects of the escaper variant, we performed different functional analyses. This candidate variant was found to be conserved across 29 eutherian mammals, suggesting a regulatory potential for this region (Figures 3A and 3B). Transcription factor binding site analysis, using TRAP (Manke et al., 2010) and TRANSFAC (Matys et al., 2006), revealed that this G>T change creates a novel myogenin binding site (Figure 3C) with a high information content for the mutant allele (T) in the myogenin consensus binding motif (Figure 3D). Myogenin is a muscle-specific transcription factor involved in muscle differentiation and repair (Wright et al., 1989). To determine whether the variant affects DNA binding by myogenin, we carried out electrophoretic mobility shift assays (EMSA) using muscle cell nuclear extracts and biotin-labeled oligonucleotide probes containing either the wild-type (WT) or escaper (E) genotype. The oligonucleotide probe containing the escaper T allele robustly bound the myogenin protein, whereas an oligonucleotide probe containing the WT G allele did not bind at all (Figure 3E). A competition assay showed that an unlabeled escaper probe efficiently competed with the binding of the labeled escaper probe. In contrast, the unlabeled WT probe had no effect on the binding activity of the labeled escaper probe, indicating a specific interaction between the escaper allele and myogenin (Figure 3E). To evaluate whether the novel myogenin binding site found in the escaper dogs was driving the increased expression of *Jagged1*, we performed a luciferase reporter assay using *Jagged1* upstream promoter sequences containing either the WT sequence or the escaper variant fused to a luciferase reporter. Luciferase vectors containing either WT or escaper sequence were transfected into muscle cells (myoblasts) and human embryonic kidney cells (HEK293T) along with constructs that overexpress either myogenin or another E-box myogenic factor (MyoD) as control. On HEK293K cells, overexpression of myogenin was able to activate the expression of the escaper *Jagged1* reporter 3-fold, but showed no activation of the WT reporter (Figure 3F). As predicted, the overexpression of MyoD did not activate either the WT or escaper *Jagged1* luciferase reporter (Figure 3F). Similarly, myoblasts (that endogenously express myogenin) transfected with the escaper vector showed a similar luciferase activation that was three times higher than the WT vector, notwithstanding the presence of overexpression vectors (Figure 3F). These results demonstrate that the creation of the novel myogenin binding site in the escaper *Jagged1* promoter is essential for driving the increase of *Jagged1* expression in the escaper dog skeletal muscles.

In Vivo Overexpression of Jagged1 Rescues *sapje* Muscle Phenotype

To evaluate if the overexpression of *Jagged1* can ameliorate the dystrophic muscle phenotype in other species, we used the severely affected dystrophic *sapje* zebrafish DMD model.

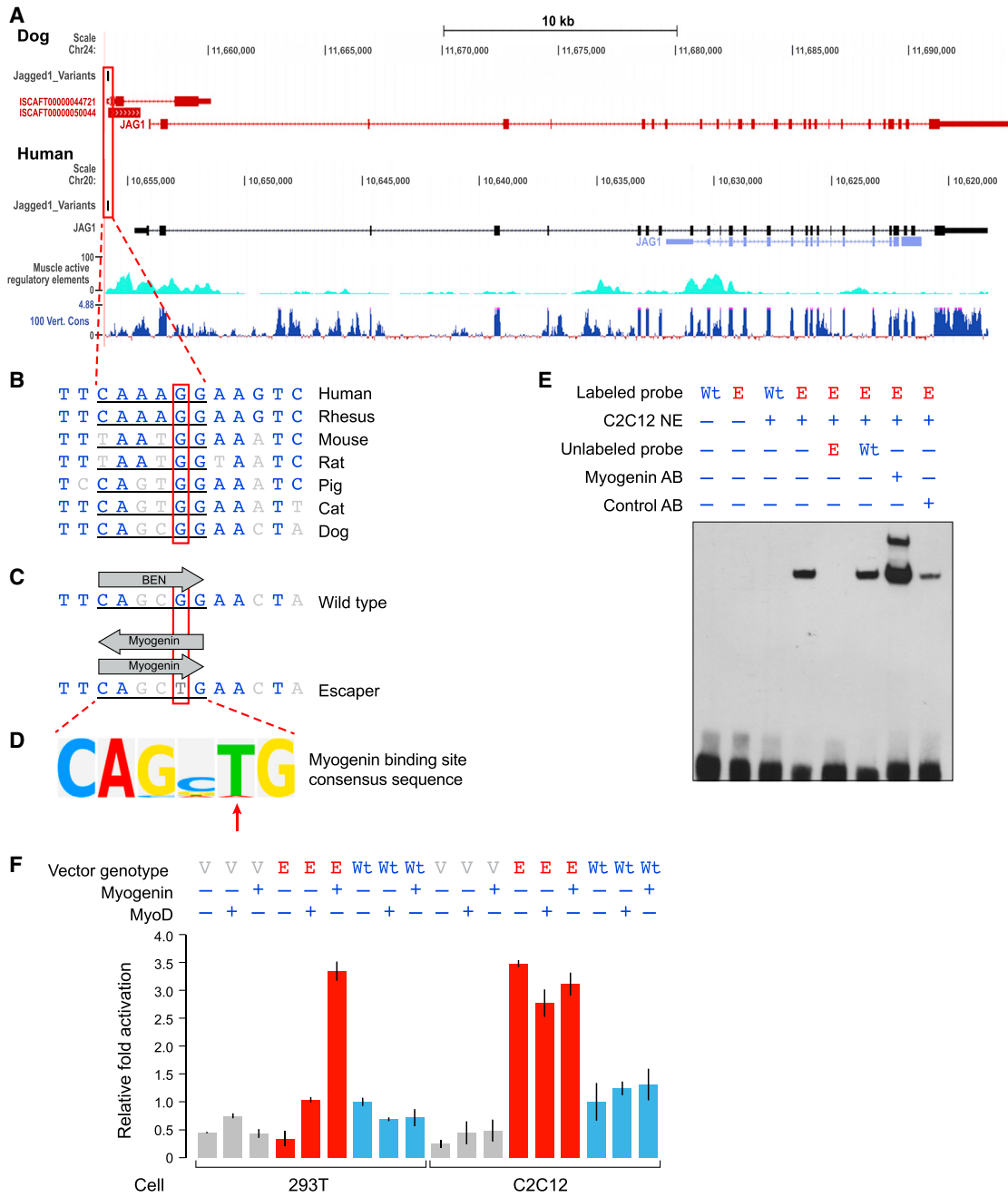


Figure 3. Variant Located in the *Jagged1* Promoter of Escaper GRMD Dogs

- (A) Dog and Human *Jagged1* locus. Box: variant at dog chr24:11,644,709.
- (B) Conservation of the variant position.
- (C) Predicted transcription factor binding site at the region with the base pair change.
- (D) Consensus sequence of myogenin binding site, demonstrating the high information content of the T allele.
- (E) Electromobility shift assay (EMSA) showing myogenin binding to mutated probe (E) and not to the WT probe.
- (F) Luciferase reporter assay showing activity of WT and E genotype vectors in both muscle cells (C2C12) and embryonic kidney cells (293T) with *Myogenin* or *MyoD* overexpression, as compared to empty vectors controls (V). Error bars indicate SEM ($n = 3$ replicates). See also Figure S3.

Muscle phenotype was assayed using birefringence, where fish are placed under a polarized light and dystrophin-negative fish show a decrease in the amount of light, indicative of muscle

tearing or muscle fiber disorganization. In four separate experiments, we injected approximately 200 fertilized one-cell stage eggs from *sapje* heterozygous fish matings with mRNA of either

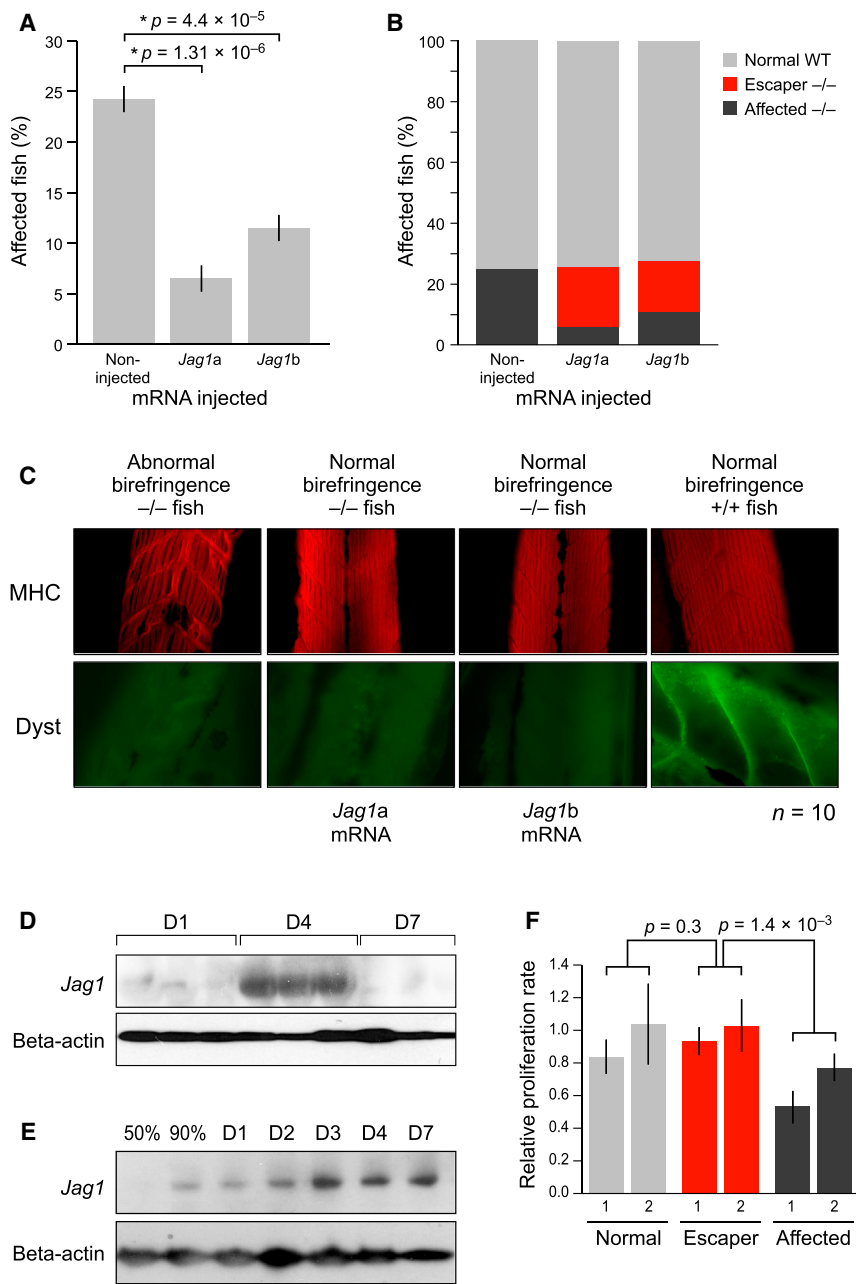


Figure 4. Functional Analysis of *jagged1* Expression

- (A) Percent affected *sapje* fish as determined by birefringence assay at 4 dpf. Note fewer affected fish in the *jagged1* injected *sapje* cohort. Four separate injection experiments were performed.
- (B) Genotype of *sapje* injected fish with *jagged1a* and *jagged1b* as compared to non-injected *sapje* fish. In red are dystrophin-null fish with a WT phenotype, recovered by *jagged1* overexpression.
- (C) Immunofluorescence of *jagged1a* and *jagged1b* overexpression in the *sapje* fish. WT, phenotypically affected homozygous fish for the dystrophin mutation and *jagged1a* and *jagged1b* injected with normal birefringence (recovered) were stained for myosin heavy chain (MCH) and dystrophin antibodies. Note the organization of the muscle fibers in the recovered fish muscle comparable to the WT fish ($n = 10$) even without dystrophin. Photographs were taken at 20x magnification.
- (D) *Jagged1* protein levels in the muscle of cardiotoxin injured mice one, four, and seven days after injury.
- (E) *Jagged1* protein levels in muscle cells during *in vitro* muscle differentiation.
- (F) Muscle cell proliferation rate, as measured by MTT, of two WT, two escaper, and two affected GRMD dogs. Error bars indicate SEM ($n = 2$, three replicates).

from the muscle lethality phenotype (Figure 4B). These results indicate that increasing *jagged1* expression rescues most dystrophin-null fish from developing the abnormalities typically seen in dystrophin-null muscle. To further evaluate the *jagged1a* and *jagged1b* overexpression *sapje* fish, we performed immunostaining on individual fish bodies using a myosin heavy chain (MHC) antibody to evaluate muscle structure. In WT fish, MHC was clearly expressed and showed that muscle fibers were normal. Interestingly, MHC staining of *jagged1* mRNA-injected dystrophin-null rescued fish showed normal myofiber structure similar to that of WT fish, whereas affected, non-injected

one of the zebrafish *jagged1* genetic copies of the mammalian *Jagged1* gene: *jagged1a* or *jagged1b*. In all experiments, an average of 24% of the non-injected *sapje* fish exhibited a typical affected dystrophic, patchy birefringence phenotype. This proportion is within the 21%–27% expected range of affected fish of a heterozygous *sapje* mating. In contrast, fish injected with either *jagged1a* or *jagged1b* showed a significantly lower percentage of fish with poor birefringence ($p = 1.31 \times 10^{-6}$ for *jagged1a*, $p = 4.4 \times 10^{-5}$ for *jagged1b*, Figure 4A). Genotypic analysis revealed that about 75% of dystrophin-null fish injected with *jagged1a* and 60% of those injected with *jagged1b* had normal birefringence, which demonstrated a common rescue

dystrophin-null fish demonstrated clear muscle abnormalities (Figure 4C).

Jagged1 Expression during Muscle Regeneration and Cell Proliferation in Mice and Dogs

When examining the effect of *Jagged1* on muscle regeneration in normal mice, we found that *Jagged1* expression is upregulated at day 4 after cardiotoxin-induced injury in mouse tibialis anterior muscle (Figure 4D). We also determined that *Jagged1* is elevated during myoblast muscle differentiation *in vitro* (Figure 4E). To examine whether muscle cells from escaper dogs proliferate faster than cells from severely affected dogs, we performed a

proliferation assay using myogenic cells from biopsies of age-matched dogs. Escaper dogs' muscle showed typical dystrophic features (Zucconi et al., 2010) as evidenced by cycles of degeneration and regeneration, which is not seen in normal muscle. Because of these cycles and consistent activation, myogenic cells from affected GRMD dogs are expected to divide less frequently. We show that muscle cells from escaper dogs divide significantly faster than those from affected dogs (Figure 4F). These results are consistent with previous findings that show that overexpression of the Notch intracellular domain (NICD) expands the proliferative capacity of activated muscle satellite cells in vitro and in vivo (Wen et al., 2012).

DISCUSSION

Animal models for DMD are important tools for developing new therapeutic approaches. Among the different animal models for muscular dystrophy, the GRMD dog is the closest to the human condition. Both GRMD dogs and DMD patients have a severe phenotype as well as many phenotypic and biochemical similarities, including early progressive muscle degeneration and atrophy, fibrosis, contractures, and elevated serum creatine kinase levels. We identified two dogs that escaped from the typical severe phenotype associated with dystrophin deficiency. Using a combined approach of mapping and identity by descent, we identified a candidate region of association with the escaper phenotype. Only one gene within this region showed altered expression in escaper and affected dogs: *Jagged1*. We found a candidate variant at an upstream, conserved position creating a new muscle-specific transcription factor binding site that drives *Jagged1* overexpression. *Jagged1* is also in the region associated to the mild phenotype observed in a muscular dystrophy mouse model on the MRL (Murphy Roths Large) "superhealing" background. These mice show enhanced muscle regeneration and reduced dystrophic pathology. This healing phenotype was mapped to a region containing 49 genes that includes the *Jagged1* locus (Heydemann et al., 2012).

The role of *Jagged1* in skeletal muscle development and disease has yet to be fully elucidated. *Jagged1* is a Notch ligand (Lindsell et al., 1995). The Notch signaling pathway represents a central regulator of gene expression and is critical for cellular proliferation, differentiation, and apoptotic signaling during all stages of embryonic muscle development. The Notch pathway also plays an important role in muscle regeneration (Conboy and Rando, 2002; Wen et al., 2012), and overexpression of Notch has been shown to improve muscle regeneration in aged mice (Conboy et al., 2003). Moreover, Notch signaling has been shown to be dysregulated in muscle satellite cells and dystrophin-deficient muscles from *mdx* mice (Jiang et al., 2014). Additionally, there is an even more pronounced dysregulation of Notch signaling in the muscle satellite cell in the severe *mdx/utrn* double knockout mice (dKO) that have early lethality at two to four months due to a breakdown of the diaphragm muscles (Church et al., 2014; Mu et al., 2015). Here, we observed greater proliferative capacity of the escaper dogs' myoblasts, suggesting that *Jagged1* overexpression might be involved in muscle cell proliferation and repair. These results are consistent with

previous findings, which demonstrate that *Jagged1* overexpression stimulates cell proliferation, suggesting that *Jagged1*-based therapy might be able to induce regeneration in a tissue-specific manner (Collesi et al., 2008). Our data show that *Jagged1* expression is upregulated at day 4 after cardiotoxin-induced injury in mouse, a time point when myoblasts proliferate and fuse to promote muscle regeneration (Couteaux et al., 1988). Furthermore, *Jagged1*/Notch signaling has been shown to promote the expansion and differentiation capacity of bone marrow-derived stromal/stem cells (BMSCs) to promote skeletal regeneration (Dong et al., 2014). In endothelial cells, genetic *Jagged-1* overexpression resulted in endothelial branching of vasculature processes; while conversely, *Jagged-1* endothelial deletion blocked angiogenic growth in *Jagged-1* eKO mice (Pedorosa et al., 2015). Indeed, *Jagged-1* overexpression leads to the activation of vasculature progenitor cells from quiescence, in a manner similar to that of muscle satellite cell activation (Ottone et al., 2014). Thus, it is likely that the endogenous overexpression of *Jagged-1* that occurs in the muscles of the escaper dogs is driving myogenic cell proliferation and potential muscle growth that occurs in mesodermal lineages. A proof-of-principle experiment in which the Notch downstream transcription factor Rbp-Jk was deleted in muscle satellite cells demonstrated that inhibition of Notch activation was detrimental to both muscle growth and muscle satellite cell expansion (Bjornson et al., 2012). All these findings suggest that *Jagged1* is likely to be a mediator of the regenerative process that is disrupted in dystrophin-deficient muscles and has potential as a novel therapy target to mitigate DMD pathological progression.

Although the great majority of DMD patients show a severe course, exceptional cases of dystrophin-deficient patients with a milder phenotype have been identified. We have previously reported two patients carrying null mutations, with no skeletal muscle dystrophin present via immunofluorescent staining or western blot analysis, and a milder course including the maintenance of ambulation well into their second decade of life (Zatz et al., 2014). More recently, a dystrophin-negative patient who remained ambulant until age 30 was also reported (Castro-Gago, 2015). Several other genetic modifiers are known to affect the severity of the clinical symptoms of Duchenne muscular dystrophy (*LTBP4*, *SPP1*, *TGFB2*). However, none of these genetic variants have been shown to fully restore or delay substantially the symptoms of dystrophin-deficiency in DMD boys (Bello et al., 2012; Flanigan et al., 2013; Pegoraro et al., 2011; Piva et al., 2012). Furthermore, it would be of great interest to examine the genomes of DMD boys with varying clinical symptoms and determine if variants in *Jagged1* or other Notch signaling factors exist and are causative for any variation of the dystrophic disease progression. The Notch signaling pathway, specifically *Jagged1* overexpression, represents a novel therapeutic entry point for the treatment of DMD. Full restoration of Notch signaling must be achieved in the muscle satellite cell if one expects to correct the dysregulated Notch-dependent signaling that is affected in dystrophin-deficiency (Church et al., 2014). Direct injection of exogenous, soluble Jagged-1 ligand is not a viable therapeutic option, as external Jagged1 weakens Notch signaling even more than dystrophin-deficiency (Xiao et al., 2013). Thus, one might envision finding a small molecule or

transcription factor that could increase expression of *Jagged1* in all of the skeletal muscles of DMD patient.

There is currently no cure for DMD, and existing therapies aiming to rescue *dystrophin* expression are only partially effective. Here, we show that the overexpression of *Jagged1* is likely to modulate the dystrophic phenotype in dystrophin-deficient GRMD dogs. We also show that overexpression of *jagged1* rescues the dystrophic phenotype in a severe DMD model: the *sapje* zebrafish. Our study highlights the possibilities of across-species analysis to identify and validate disease-modifying genes and associated pathways. These results suggest that *Jagged1* may be a new target for DMD therapeutic efforts in a dystrophin-independent manner, which will complement existing approaches. In addition, further investigation on the gene target *Jagged1* will contribute to a better understanding of the disease pathogenesis and molecular physiology.

EXPERIMENTAL PROCEDURES

GRMD dogs were classified for this study in two groups based on full ambulatory capacity and survival age. The escapers group included the GRMD dogs that were fully ambulatory (can walk and run) at 9 years old. One escaper dog (M1M4) died at 11 years old from a cardiac arrest (Zatz et al., 2015) and the second one (H3M10) is now 9.5 years old and shows full ambulation. The affected group included the GRMD dogs that died before 5 years old with ambulatory difficulties, respiratory failure, and cardiopathy; this group includes stillbirths, neonatal death, and one dog that was full ambulatory when he died by ingesting a foreign object at 6-months-old (K2M11); all were confirmed to carry the GRMD mutation. DNA from GRMD dogs with and without the escaper phenotype was genotyped using the Illumina canine 170,000 SNP array and was compared using association, linkage, and IBD mapping. The threshold for genome-wide significance for each association analysis was defined based on the 95% confidence intervals (CIs) calculated from the beta distribution of observed p values, as previously described (Wellcome Trust Case Control, 2007). The likelihood of the two escapers being identity by descent (IBD) at each SNP was estimated based on haplotype frequencies in the full pedigree using Beagle 4 (release v4.r1274) with default parameter settings (Browning and Browning, 2007). Linkage analysis was performed using MERLIN (Abecasis et al., 2002) 1.1.2 to first remove inconsistent genotypes and then calculate LOD scores (logarithm of the odds ratios) using a dominant parametric model with complete penetrance. Expression analysis from the same dogs was performed using two-color microarray-based gene expression analysis. Genes differentially expressed between WT, escaper, and affected animals were identified with the significance analysis of microarray (SAM) statistical approach. False discovery rate (FDR) was 5%. Whole-genome sequencing was performed to 30x depth of three dogs (two escapers and one affected dog). Samples were sequenced on an Illumina HiSeq 2000, and sequencing reads were aligned to the CanFam 3.1 reference sequence using BWA. Following GATK base quality score recalibration, indel realignment, and duplicate removal, SNP and INDEL discovery was performed. To assess myogenin binding to candidate mutation, EMSA was performed using biotin labeled or unlabeled competitors probes and the LightShift Chemiluminescent EMSA kit (Thermo Scientific) following manufacturer's instructions. Luciferase reporter assay was performed cloning WT and GRMD dog *Jagged1* promoter region containing the G>T change into the pIRE2-2a-hrGFP expression plasmid (Stratagene). HEK293T or C2C12 cells were transfected with affected or escaper 3'UTR *jagged1*-luc reporter constructs, Myogenin or MyoD overexpression plasmid, and renilla as internal control. Cells were lysed and assayed with luciferase substrate using the Dual Reporter Assay (Promega). Luciferase measurements were normalized to the renilla luciferase control on each well. Zebrafish were used for *jagged1* overexpression assay, where fertilized one-cell stage eggs from a *sapje* heterozygous fish mating were injected with mRNA from either one of the zebrafish *jagged1* gene copies: *jagged1a* or *jagged1b*. Zebrafish injected with either mRNA or non-injected

controls were assessed for phenotypic changes at 4 days post-fertilization (4dpf). Methods for cell growth assay and cardiotoxin injury are described in *Supplemental Experimental Procedures*.

Supplemental Experimental Procedures are available as supplemental materials.

ACCESSION NUMBERS

The accession number for the gene expression data reported in this paper is GEO: GSE69040.

SUPPLEMENTAL INFORMATION

Supplemental Information includes Supplemental Experimental Procedures, three figures, and one table and can be found with this article online at <http://dx.doi.org/10.1016/j.cell.2015.10.049>.

AUTHOR CONTRIBUTIONS

N.M.V., I.E., M.S.A., Y.B.M., S.V.-A., L.M.K., K.L.T., and M.Z. designed the study. N.M.V., Y.B.M., M.S.A., and J.L.M. performed experiments. N.M.V., I.E., Y.B.M., E.K.K., A.E., and K.L.T. performed data analysis and interpretation. N.M.V., I.E., K.L.T., L.M.K., and M.Z. wrote the paper with input from the other authors.

ACKNOWLEDGMENTS

Funding for this work was generously provided by the Duchenne Foundation (M.Z.), FAPESP-CEPID under award number 2013/08028-1 (M.Z., N.M.V.), CNPq under award number 705019/2009 (M.Z.), INCT under award number 2008/578997 (M.Z.), AACD (M.Z.), FID under award number 000663/2014 (M.Z.) the Bernard F. and Alva B. Gimbel Foundation (L.M.K.). Research reported in this publication was supported by the National Institute of Arthritis and Musculoskeletal and Skin Diseases of the NIH under award number R01AR064300 (to L.M.K.). Additional funding for this project came from the, Swedish Research Council (I.E.) and ERC (K.L.-T.). N.M.V. is supported by a Muscular Dystrophy Association (MDA) Development Grant MDA352465. M.S.A. is supported by a Muscular Dystrophy Association (MDA) Development Grant MDA255059. Some of the sequencing was performed in the Molecular Genetics Core laboratory of the Boston Children's Hospital Intellectual and Developmental Disabilities Research Center (IDDRC) supported by NIH grant (5P30 -HD18655-34). We would like to thank Munira Guilhon, Jessica Alfoldi, Peter Serafini, Marcos Valadares, Eder Zucconi, Mariane Secco, Emanuela Gussoni, Fedik Rahimov, José Visintin, and Jeremy Johnson for support and helpful suggestions, and Leslie Gaffney for help with figures. We thank the Broad Institute Genomics Platform for sequencing, and Chris Lawrence and Jason Best, who managed the fish facility at Boston Children's Hospital. We are extremely grateful for the extraordinary care and dedication of the veterinarians Vivian Landini, Thais Andrade, and Erica Cangussu from the Institute of Biosciences GRMD dogs kennel at the University of São Paulo. L.M.K. has research funding from Pfizer to develop small molecules which would increase *Jagged1* expression in mice.

Received: August 11, 2015

Revised: September 28, 2015

Accepted: October 19, 2015

Published: November 12, 2015

REFERENCES

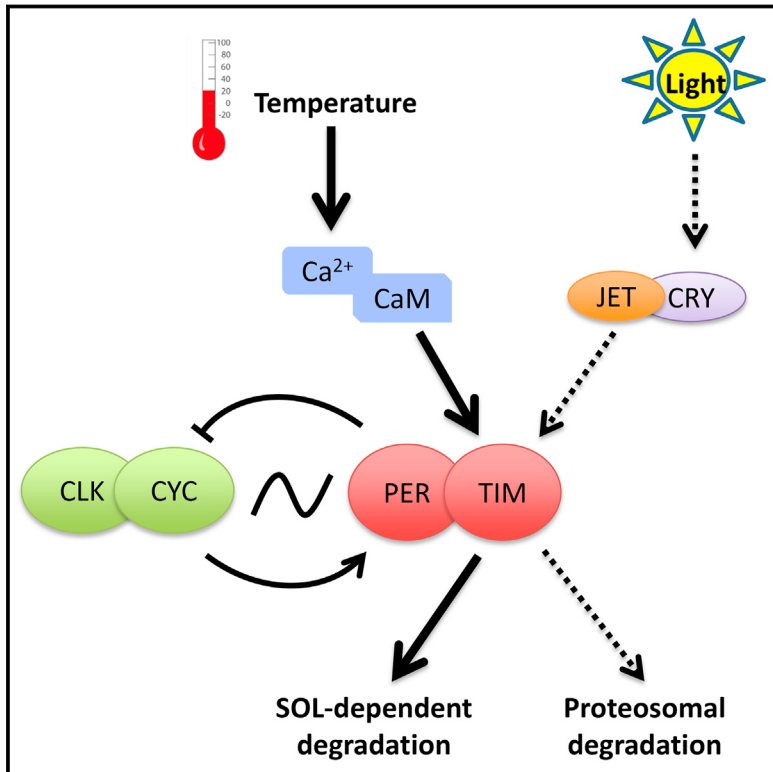
- Abecasis, G.R., Cherny, S.S., Cookson, W.O., and Cardon, L.R. (2002). Merlin-rapid analysis of dense genetic maps using sparse gene flow trees. *Nat. Genet.* 30, 97–101.
- Axelsson, E., Ratnakumar, A., Arendt, M.L., Maqbool, K., Webster, M.T., Perssoni, M., Liberg, O., Arnemo, J.M., Hedhammar, A., and Lindblad-Toh, K.

- (2013). The genomic signature of dog domestication reveals adaptation to a starch-rich diet. *Nature* 495, 360–364.
- Bassett, D., and Currie, P.D. (2004). Identification of a zebrafish model of muscular dystrophy. *Clin. Exp. Pharmacol. Physiol.* 31, 537–540.
- Bassett, D.I., Bryson-Richardson, R.J., Daggett, D.F., Gautier, P., Keenan, D.G., and Currie, P.D. (2003). Dystrophin is required for the formation of stable muscle attachments in the zebrafish embryo. *Development* 130, 5851–5860.
- Bello, L., Piva, L., Barp, A., Taglia, A., Picillo, E., Vasco, G., Pane, M., Previtali, S.C., Torrente, Y., Gazzero, E., et al. (2012). Importance of SPP1 genotype as a covariate in clinical trials in Duchenne muscular dystrophy. *Neurology* 79, 159–162.
- Bjornson, C.R., Cheung, T.H., Liu, L., Tripathi, P.V., Steeper, K.M., and Rando, T.A. (2012). Notch signaling is necessary to maintain quiescence in adult muscle stem cells. *Stem Cells* 30, 232–242.
- Browning, S.R., and Browning, B.L. (2007). Rapid and accurate haplotype phasing and missing-data inference for whole-genome association studies by use of localized haplotype clustering. *Am. J. Hum. Genet.* 81, 1084–1097.
- Bulfield, G., Siller, W.G., Wight, P.A., and Moore, K.J. (1984). X chromosome-linked muscular dystrophy (*mdx*) in the mouse. *Proc. Natl. Acad. Sci. USA* 81, 1189–1192.
- Bushby, K., Finkel, R., Birnkrant, D.J., Case, L.E., Clemens, P.R., Cripe, L., Kaul, A., Kinnett, K., McDonald, C., Pandya, S., et al.; DMD Care Considerations Working Group (2010). Diagnosis and management of Duchenne muscular dystrophy, part 2: implementation of multidisciplinary care. *Lancet Neurol.* 9, 177–189.
- Castro-Gago, M. (2015). Milder course in Duchenne patients with nonsense mutations and no muscle dystrophin. *Neuromuscul. Disord.* 25, 443.
- Chapman, V.M., Miller, D.R., Armstrong, D., and Caskey, C.T. (1989). Recovery of induced mutations for X chromosome-linked muscular dystrophy in mice. *Proc. Natl. Acad. Sci. USA* 86, 1292–1296.
- Church, J.E., Trieu, J., Chee, A., Naim, T., Gehrig, S.M., Lamon, S., Angelini, C., Russell, A.P., and Lynch, G.S. (2014). Alterations in Notch signalling in skeletal muscles from *mdx* and *dko* dystrophic mice and patients with Duchenne muscular dystrophy. *Exp. Physiol.* 99, 675–687.
- Collesi, C., Zentilin, L., Sinagra, G., and Giacca, M. (2008). Notch1 signaling stimulates proliferation of immature cardiomyocytes. *J. Cell Biol.* 183, 117–128.
- Conboy, I.M., and Rando, T.A. (2002). The regulation of Notch signaling controls satellite cell activation and cell fate determination in postnatal myogenesis. *Dev. Cell* 3, 397–409.
- Conboy, I.M., Conboy, M.J., Smythe, G.M., and Rando, T.A. (2003). Notch-mediated restoration of regenerative potential to aged muscle. *Science* 302, 1575–1577.
- Cooper, B.J., Winand, N.J., Stedman, H., Valentine, B.A., Hoffman, E.P., Kunkel, L.M., Scott, M.O., Fischbeck, K.H., Kornegay, J.N., Avery, R.J., et al. (1988). The homologue of the Duchenne locus is defective in X-linked muscular dystrophy of dogs. *Nature* 334, 154–156.
- Couteaux, R., Mira, J.C., and d'Albis, A. (1988). Regeneration of muscles after cardiotoxin injury. I. Cytological aspects. *Biol. Cell* 62, 171–182.
- Dong, Y., Long, T., Wang, C., Mirando, A.J., Chen, J., O'Keefe, R.J., and Hilton, M.J. (2014). NOTCH-Mediated Maintenance and Expansion of Human Bone Marrow Stromal/Stem Cells: A Technology Designed for Orthopedic Regenerative Medicine. *Stem Cells Transl. Med.* 3, 1456–1466.
- Fairclough, R.J., Wood, M.J., and Davies, K.E. (2013). Therapy for Duchenne muscular dystrophy: renewed optimism from genetic approaches. *Nat. Rev. Genet.* 14, 373–378.
- Flanigan, K.M., Ceco, E., Lamar, K.M., Kaminoh, Y., Dunn, D.M., Mendell, J.R., King, W.M., Pestronk, A., Florence, J.M., Mathews, K.D., et al.; United Dystrophinopathy Project (2013). LTBP4 genotype predicts age of ambulatory loss in Duchenne muscular dystrophy. *Ann. Neurol.* 73, 481–488.
- Goemans, N.M., Tulinius, M., van den Akker, J.T., Burm, B.E., Ekhart, P.F., Heuvelmans, N., Holling, T., Janson, A.A., Platenburg, G.J., Sipkens, J.A., et al. (2011). Systemic administration of PRO051 in Duchenne's muscular dystrophy. *N. Engl. J. Med.* 364, 1513–1522.
- Guiraud, S., Aartsma-Rus, A., Vieira, N.M., Davies, K.E., van Ommeren, G.J., and Kunkel, L.M. (2015). The Pathogenesis and Therapy of Muscular Dystrophies. *Annu. Rev. Genomics Hum. Genet.* 16, 281–308.
- Heydemann, A., Swaggart, K.A., Kim, G.H., Holley-Cuthrell, J., Hadhazy, M., and McNally, E.M. (2012). The superhealing MRL background improves muscular dystrophy. *Skelet. Muscle* 2, 26.
- Hoepfner, M.P., Lundquist, A., Pirun, M., Meadows, J.R., Zamani, N., Johnson, J., Sundström, G., Cook, A., FitzGerald, M.G., Swofford, R., et al. (2014). An improved canine genome and a comprehensive catalogue of coding genes and non-coding transcripts. *PLoS ONE* 9, e91172.
- Hoffman, E.P., Brown, R.H., Jr., and Kunkel, L.M. (1987). Dystrophin: the protein product of the Duchenne muscular dystrophy locus. *Cell* 51, 919–928.
- Im, W.B., Phelps, S.F., Copen, E.H., Adams, E.G., Slightom, J.L., and Chamberlain, J.S. (1996). Differential expression of dystrophin isoforms in strains of *mdx* mice with different mutations. *Hum. Mol. Genet.* 5, 1149–1153.
- Jiang, C., Wen, Y., Kuroda, K., Hannon, K., Rudnicki, M.A., and Kuang, S. (2014). Notch signaling deficiency underlies age-dependent depletion of satellite cells in muscular dystrophy. *Dis. Model. Mech.* 7, 997–1004.
- Kang, H.M., Sul, J.H., Service, S.K., Zaitlen, N.A., Kong, S.Y., Freimer, N.B., Sabatti, C., and Eskin, E. (2010). Variance component model to account for sample structure in genome-wide association studies. *Nat. Genet.* 42, 348–354.
- Kayali, R., Ku, J.M., Khitrov, G., Jung, M.E., Prikhodko, O., and Bertoni, C. (2012). Read-through compound 13 restores dystrophin expression and improves muscle function in the *mdx* mouse model for Duchenne muscular dystrophy. *Hum. Mol. Genet.* 21, 4007–4020.
- Koenig, M., Beggs, A.H., Moyer, M., Scherpf, S., Heindrich, K., Bettecken, T., Meng, G., Müller, C.R., Lindlöf, M., Kaariainen, H., et al. (1989). The molecular basis for Duchenne versus Becker muscular dystrophy: correlation of severity with type of deletion. *Am. J. Hum. Genet.* 45, 498–506.
- Kornegay, J.N., Tuler, S.M., Miller, D.M., and Levesque, D.C. (1988). Muscular dystrophy in a litter of golden retriever dogs. *Muscle Nerve* 11, 1056–1064.
- Lindsell, C.E., Shawber, C.J., Boulter, J., and Weinmaster, G. (1995). Jagged: a mammalian ligand that activates Notch1. *Cell* 80, 909–917.
- Manke, T., Heinig, M., and Vingron, M. (2010). Quantifying the effect of sequence variation on regulatory interactions. *Hum. Mutat.* 31, 477–483.
- Matys, V., Kel-Margoulis, O.V., Fricke, E., Liebich, I., Land, S., Barre-Dirrie, A., Reuter, I., Chekmenev, D., Krull, M., Hornischer, K., et al. (2006). TRANSFAC and its module TRANSCompel: transcriptional gene regulation in eukaryotes. *Nucleic Acids Res.* 34, D108–D110.
- Mendell, J.R., Campbell, K., Rodino-Klapac, L., Sahenk, Z., Shilling, C., Lewis, S., Bowles, D., Gray, S., Li, C., Galloway, G., et al. (2010). Dystrophin immunity in Duchenne's muscular dystrophy. *N. Engl. J. Med.* 363, 1429–1437.
- Mendell, J.R., Shilling, C., Leslie, N.D., Flanigan, K.M., al-Dahhak, R., Gastier-Foster, J., Kneile, K., Dunn, D.M., Duval, B., Aoyagi, A., et al. (2012). Evidence-based path to newborn screening for Duchenne muscular dystrophy. *Ann. Neurol.* 71, 304–313.
- Mendell, J.R., Rodino-Klapac, L.R., Sahenk, Z., Roush, K., Bird, L., Lowes, L.P., Alfano, L., Gomez, A.M., Lewis, S., Kota, J., et al.; Eteplirsen Study Group (2013). Eteplirsen for the treatment of Duchenne muscular dystrophy. *Ann. Neurol.* 74, 637–647.
- Monaco, A.P., Bertelson, C.J., Liechti-Gallati, S., Moser, H., and Kunkel, L.M. (1988). An explanation for the phenotypic differences between patients bearing partial deletions of the DMD locus. *Genomics* 2, 90–95.
- Mu, X., Tang, Y., Lu, A., Takayama, K., Usas, A., Wang, B., Weiss, K., and Huard, J. (2015). The role of Notch signaling in muscle progenitor cell depletion and the rapid onset of histopathology in muscular dystrophy. *Hum. Mol. Genet.* 24, 2923–2937.
- Ottone, C., Krusche, B., Whitby, A., Clements, M., Quadrato, G., Pitulescu, M.E., Adams, R.H., and Parrinello, S. (2014). Direct cell-cell contact with the vascular niche maintains quiescent neural stem cells. *Nat. Cell Biol.* 16, 1045–1056.

- Passos-Bueno, M.R., Vainzof, M., Marie, S.K., and Zatz, M. (1994). Half the dystrophin gene is apparently enough for a mild clinical course: confirmation of its potential use for gene therapy. *Hum. Mol. Genet.* 3, 919–922.
- Pedrosa, A.R., Trindade, A., Fernandes, A.C., Carvalho, C., Gigante, J., Tavares, A.T., Diéguez-Hurtado, R., Yagita, H., Adams, R.H., and Duarte, A. (2015). Endothelial Jagged1 antagonizes Dll4 regulation of endothelial branching and promotes vascular maturation downstream of Dll4/Notch1. *Arterioscler. Thromb. Vasc. Biol.* 35, 1134–1146.
- Pegoraro, E., Hoffman, E.P., Piva, L., Gavassini, B.F., Cagnin, S., Ermani, M., Bello, L., Soraru, G., Pacchioni, B., Bonifati, M.D., et al.; Cooperative International Neuromuscular Research Group (2011). SPP1 genotype is a determinant of disease severity in Duchenne muscular dystrophy. *Neurology* 76, 219–226.
- Piva, L., Gavassini, B.F., Bello, L., Fanin, M., Soraru, G., Barp, A., Ermani, M., Angelini, C., Hoffman, E.P., and Pegoraro, E. (2012). TGFBR2 but not SPP1 genotype modulates osteopontin expression in Duchenne muscular dystrophy muscle. *J. Pathol.* 228, 251–259.
- Sharp, N.J., Kornegay, J.N., Van Camp, S.D., Herbstreith, M.H., Secore, S.L., Kettle, S., Hung, W.Y., Constantinou, C.D., Dykstra, M.J., Roses, A.D., et al. (1992). An error in dystrophin mRNA processing in golden retriever muscular dystrophy, an animal homologue of Duchenne muscular dystrophy. *Genomics* 13, 115–121.
- Sicinski, P., Geng, Y., Ryder-Cook, A.S., Barnard, E.A., Darlison, M.G., and Barnard, P.J. (1989). The molecular basis of muscular dystrophy in the mdx mouse: a point mutation. *Science* 244, 1578–1580.
- Vainzof, M., Pavanello, R.C., Pavanello Filho, I., Passos-Bueno, M.R., Rapaport, D., Hsi, C.T., and Zatz, M. (1990). Dystrophin immunostaining in muscles from patients with different types of muscular dystrophy: a Brazilian study. *J. Neurol. Sci.* 98, 221–233.
- van Deutekom, J.C., Janson, A.A., Ginjaar, I.B., Frankhuizen, W.S., Aartsma-Rus, A., Bremmer-Bout, M., den Dunnen, J.T., Koop, K., van der Kooi, A.J., Goemans, N.M., et al. (2007). Local dystrophin restoration with antisense oligonucleotide PRO051. *N. Engl. J. Med.* 357, 2677–2686.
- Wellcome Trust Case Control, C.; Wellcome Trust Case Control Consortium (2007). Genome-wide association study of 14,000 cases of seven common diseases and 3,000 shared controls. *Nature* 447, 661–678.
- Wen, Y., Bi, P., Liu, W., Asakura, A., Keller, C., and Kuang, S. (2012). Constitutive Notch activation upregulates Pax7 and promotes the self-renewal of skeletal muscle satellite cells. *Mol. Cell. Biol.* 32, 2300–2311.
- Wright, W.E., Sassoon, D.A., and Lin, V.K. (1989). Myogenin, a factor regulating myogenesis, has a domain homologous to MyoD. *Cell* 56, 607–617.
- Xiao, Y., Gong, D., and Wang, W. (2013). Soluble JAGGED1 inhibits pulmonary hypertension by attenuating notch signaling. *Arterioscler. Thromb. Vasc. Biol.* 33, 2733–2739.
- Zatz, M., Pavanello, R.C., Lazar, M., Yamamoto, G.L., Lourenço, N.C., Cerqueira, A., Nogueira, L., and Vainzof, M. (2014). Milder course in Duchenne patients with nonsense mutations and no muscle dystrophin. *Neuromuscul. Disord.* 24, 986–989.
- Zatz, M., Vieira, N.M., Zucconi, E., Pelatti, M., Gomes, J., Vainzof, M., Martins-Bach, A.B., Garcia Otaduy, M.C., Bento dos Santos, G., Amaro, E., Jr., et al. (2015). A normal life without muscle dystrophin. *Neuromuscul. Disord.* 25, 371–374.
- Zucconi, E., Valadares, M.C., Vieira, N.M., Bueno, C.R., Jr., Secco, M., Jazedje, T., da Silva, H.C., Vainzof, M., and Zatz, M. (2010). Ringo: discordance between the molecular and clinical manifestation in a golden retriever muscular dystrophy dog. *Neuromuscul. Disord.* 20, 64–70.

Calcium and SOL Protease Mediate Temperature Resetting of Circadian Clocks

Graphical Abstract



Authors

Ozgur Tataroglu, Xiaohu Zhao,
Ania Busza, Jinli Ling, John S. O'Neill,
Patrick Emery

Correspondence

patrick.emery@umassmed.edu

In Brief

Temperature phase shifts the *Drosophila* circadian clock through the regulated degradation of the pacemaker protein TIMELESS.

Highlights

- Calcium and the protease SOL trigger TIM degradation in response to thermal input
- Thermal TIM degradation resets the *Drosophila* circadian pacemaker
- TIM integrates light and temperature input
- In mammals, the SOL homolog also impacts circadian thermal responses

Calcium and SOL Protease Mediate Temperature Resetting of Circadian Clocks

Ozgur Tataroglu,¹ Xiaohu Zhao,¹ Ania Busza,¹ Jinli Ling,¹ John S. O'Neill,² and Patrick Emery^{1,*}

¹Department of Neurobiology, University of Massachusetts Medical School, Worcester, MA 01605, USA

²MRC Laboratory of Molecular Biology, Cambridge CB2 0QH, UK

*Correspondence: patrick.emery@umassmed.edu

<http://dx.doi.org/10.1016/j.cell.2015.10.031>

SUMMARY

Circadian clocks integrate light and temperature input to remain synchronized with the day/night cycle. Although light input to the clock is well studied, the molecular mechanisms by which circadian clocks respond to temperature remain poorly understood. We found that temperature phase shifts *Drosophila* circadian clocks through degradation of the pacemaker protein TIM. This degradation is mechanistically distinct from photic CRY-dependent TIM degradation. Thermal TIM degradation is triggered by cytosolic calcium increase and CALMODULIN binding to TIM and is mediated by the atypical calpain protease SOL. This thermal input pathway and CRY-dependent light input thus converge on TIM, providing a molecular mechanism for the integration of circadian light and temperature inputs. Mammals use body temperature cycles to keep peripheral clocks synchronized with their brain pacemaker. Interestingly, downregulating the mammalian SOL homolog SOLH blocks thermal mPER2 degradation and phase shifts. Thus, we propose that circadian thermosensation in insects and mammals share common principles.

INTRODUCTION

Circadian rhythms result from endogenous biological clocks found in most organisms, which enable them to adapt to and predict daily changes in their environment to increase their fitness. They drive a wide range of behaviors and physiological functions. Consequently, perturbation of clock function is associated with various ailments in mice and humans (Davidson et al., 2006; Knutsson, 2003; Reddy and O'Neill, 2010). A fundamental property of circadian clocks is their ability to respond to environmental inputs and thereby remain correctly synchronized with the day/night cycle. Light and temperature are critical inputs to circadian clocks, acting synergistically in natural settings. As such, reception and integration of these environmental signals is essential for optimizing daily behavior and physiology.

Biological clocks are universally observed to be temperature compensated, presumably since a circadian rhythm strongly affected by ambient temperature would confer little adaptive advantage. Critically however, the phase of circadian clocks shifts in response to an applied daily temperature cycle (Bruce, 1960; Bruce and Pittendrigh, 1956; Pittendrigh, 1954), but in contrast to light, the molecular mechanisms underlying temperature input to the clock are poorly understood.

Circadian timekeeping occurs cell autonomously, with a molecular mechanism that is highly conserved from *Drosophila* to humans (Weaver and Emery, 2013). The fly clock consists of a transcriptional feedback loop, whereby the transcription factors CLOCK (CLK) and CYCLE (CYC) form a heterodimer and drive rhythmic expression of target genes, such as *period* (*per*) and *timeless* (*tim*), which encode a heterodimeric repressor of CLK/CYC activity. Throughout the day, PER and TIM abundance and activity are tightly regulated by various transcriptional, post-transcriptional, and post-translational mechanisms (Zhang and Emery, 2012). This results in rhythmic repression of CLK/CYC activity, which ultimately determines circadian period.

In addition to its role in rhythm generation, TIM has an essential role in the circadian light input pathway. Light induces a conformational change in the photoreceptor CRYPTOCHROME (CRY), which enables it to bind to JETLAG (JET) and TIM and thus to trigger TIM's proteasomal degradation (Busza et al., 2004; Koh et al., 2006; Ozturk et al., 2011; Peschel et al., 2009). PER degradation occurs as a consequence, ultimately resetting the molecular pacemaker, because PER abundance is supported by TIM (Ko et al., 2002; Price et al., 1995). Therefore, photic TIM degradation results in a delay or advance in the phase of the circadian clock, depending on the timing of the light signal.

In *Drosophila*, NOCTE functions in peripheral thermo- and mechano-sensors (the chordotonal organs) to synchronize brain circadian rhythms with temperature cycles (Sehadova et al., 2009). In addition, cationic TRANSIENT RECEPTOR POTENTIAL A1 (TRPA1) and PYREXIA (PYX) channels participate in temperature entrainment of circadian behavior (Lee and Montell, 2013; Wolfgang et al., 2013). How these molecules communicate with brain circadian pacemakers, however, is completely unknown. Body clocks found in most fly tissues are autonomously sensitive to temperature (Glaser and Stanewsky, 2005), but again the mechanism of peripheral clock temperature sensing remains essentially unexplained. Very high temperature pulses (37°C) were found to affect PER and TIM levels and to shift circadian

behavior in a CRY-dependent manner (Kaushik et al., 2007; Siodorek et al., 1998). However, CRY is not required for responses to temperature ranges usually experienced by fruit flies in the wild (Busza et al., 2007; Stanewsky et al., 1998) and even appears to inhibit thermal entrainment (Gentile et al., 2013).

The mammalian clockwork shares a similar logic and many molecular components with *Drosophila*. Mammalian CRY proteins (mCRY1/2) no longer function as photoreceptors but have instead replaced TIM as partners with mammalian PER proteins (mPER1/2). Thus, mPER1/2 interact with mCRY1/2 as key repressors of the CLK/BMAL1 transactivator (homologs of *Drosophila* CLK/CYC) (Griffin et al., 1999; Kume et al., 1999), with mPERs being the rate-limiting factors driving interactions between CLK/BMAL1 and CRY1/2 (Chen et al., 2009). Outside the retina, the molecular clockwork in mammalian cells is not directly photosensitive. Rather, ambient lighting information is conveyed via the retinohypothalamic tract to be integrated within the brain's master pacemaker, the suprachiasmatic nuclei (SCN) (Weaver and Emery, 2013). SCN timing cues are then communicated with peripheral cells and tissues through a diversity of endocrine and other signaling mechanisms, including circadian body temperature rhythms. These body temperature rhythms are sufficient to entrain and synchronize mammalian cells and tissues in vivo and ex vivo (Brown et al., 2002; Buhr et al., 2010). The heat-induced transcription factor HSF1 plays an important role in temperature entrainment, although it does not appear to be essential (Buhr et al., 2010; Saini et al., 2012), nor is the mechanism whereby HSF1 resets the mammalian circadian clock clear at present.

In summary, previous studies in *Drosophila* and mammals provide intriguing clues to how temperature information is relayed to the clock but do not yet explain its molecular effects on the circadian pacemaker. TRPA1 and PYX are cationic channels, HSF1 is a transcription factor and nocte is a protein of unknown function not conserved in mammals. Therefore, the connection between these proposed pathways is uncertain. These studies also suggest that various mechanisms might be employed for temperature input and entrainment of circadian clocks. Therefore, we decided to elucidate the temperature input mechanism using a bottom-up strategy, hypothesizing that all environmental cues must ultimately converge on the core molecular circadian pacemaker and affect its critical components. Here, we provide strong evidence that in *Drosophila*, a calcium (Ca^{2+})-dependent mechanism triggers TIM degradation by the protease Small Optic Lobe (SOL) in response to temperature input, and that a similar mechanism mediates thermal response in mammals.

RESULTS

Temperature Increase Induces Specific Degradation of TIM

To begin to understand how temperature cycles could affect the *Drosophila* circadian pacemaker, we expressed the critical pacemaker proteins PER and TIM in *Drosophila* S2 cells. An ecologically relevant temperature shift (TS) from 20°C to 30°C degraded TIM in S2 cells (Figure 1A), but not PER (data not shown). The proteasomal inhibitor MG-132, which blocks light-induced TIM degradation (Koh et al., 2006), failed to protect TIM against thermal degradation (Figure 1A). Moreover, it was

not necessary to co-transfect CRY or JET to observe thermal TIM degradation, while photic degradation requires these proteins (Koh et al., 2006). We confirmed this result in vivo with *Drosophila* head extracts and observed a similar specific degradation of TIM after 4 hr TS, while PER was not affected (Figures 1B and S1A).

To measure TIM degradation in real time, we fused TIM and PER with LUCIFERASE (TIM-LUC, PER-LUC) and expressed these proteins in S2 cells. Similar to the results described above, a 20°C to 30°C TS induced rapid TIM degradation, while PER was not affected (Figure 1C). We then created flies expressing TIM-LUC under the *tim* promoter (*ptim*). The TIM-LUC fusion protein was functional in vivo since it rescued normal rhythmicity to *tim⁰* flies with a period of 24.04 ± 0.37 hr in constant darkness (DD). The rescued flies also entrained normally to light/dark (LD) cycles (Figure S1B). We were able to quantitatively measure in whole flies TIM-LUC degradation induced by TS from 20°C to 30°C when TIM level is at its highest (Zeitgeber Time 18, ZT18) (Figure 1D). Similar results were observed with TS from 16°C to 25°C (Figure S1C). In both experiments, PER levels, monitored with the BG-LUC transgene (Stanewsky et al., 1997), did not respond acutely to TS (Figures 1D and S1C). Interestingly, TIM was not degraded when the temperature was lowered from 30°C to 20°C (Figure S1D). These results fit with the observation that TIM levels decrease during the warm phase of a temperature cycle, even in the absence of rhythmic *tim* transcription (Goda et al., 2014).

We tested whether the 4-hr temperature increase that specifically degrades TIM in vivo could also shift the circadian clock in flies. We found that a 4- or 6-hr temperature pulse (TP) from 20°C to 30°C at ZT18 advanced the phase of the clock as measured with TIM-LUC or BG-LUC (Figures 1E and 1F) or locomotor behavior (Figures 1G and S1E). Locomotor behavior is representative of the brain clocks, while luciferase recordings represent primarily peripheral clocks. We observed that a TP longer than 4 hr did not significantly increase the magnitude of phase advances (Figure 1F), which was approximately 3.4 hr in the periphery (Luciferase) and 2.0 hr in the brain (locomotor behavior; data not shown). Pulses shorter than 3 hr failed to advance locomotor behavior rhythms (data not shown). We did not see a significant difference between two wild-type fly strains (*y w* and *w¹¹¹⁸*) carrying two different alleles of *tim* (*s-tim* and *ls-tim*), which have different sensitivity to light (Sandrelli et al., 2007). We also observed similar phase shifts with *tim⁰;ptim-TIM-LUC* flies (Figure 1G).

Thermal TIM Degradation Is Dependent on Intracellular Ca^{2+}

We hypothesized that Ca^{2+} could mediate thermal TIM degradation and phase shifts for two reasons. First, brain pacemaker neurons receive thermal inputs through cationic channels (TRPA1, PYX) (Lee and Montell, 2013; Wolfgang et al., 2013). Second, TIM carries predicted Calmodulin binding sites (see below). Thus, we tested whether a TP from 20°C to 30°C at ZT18 can elicit an intracellular Ca^{2+} increase in circadian tissues. We quantitatively measured intracellular Ca^{2+} levels in isolated fly heads from flies expressing GFP-AEQUORIN under the control of the circadian *tim-GAL4* driver. GFP-AEQUORIN is a well-established in vivo reporter of Ca^{2+} levels (Baubet et al., 2000).

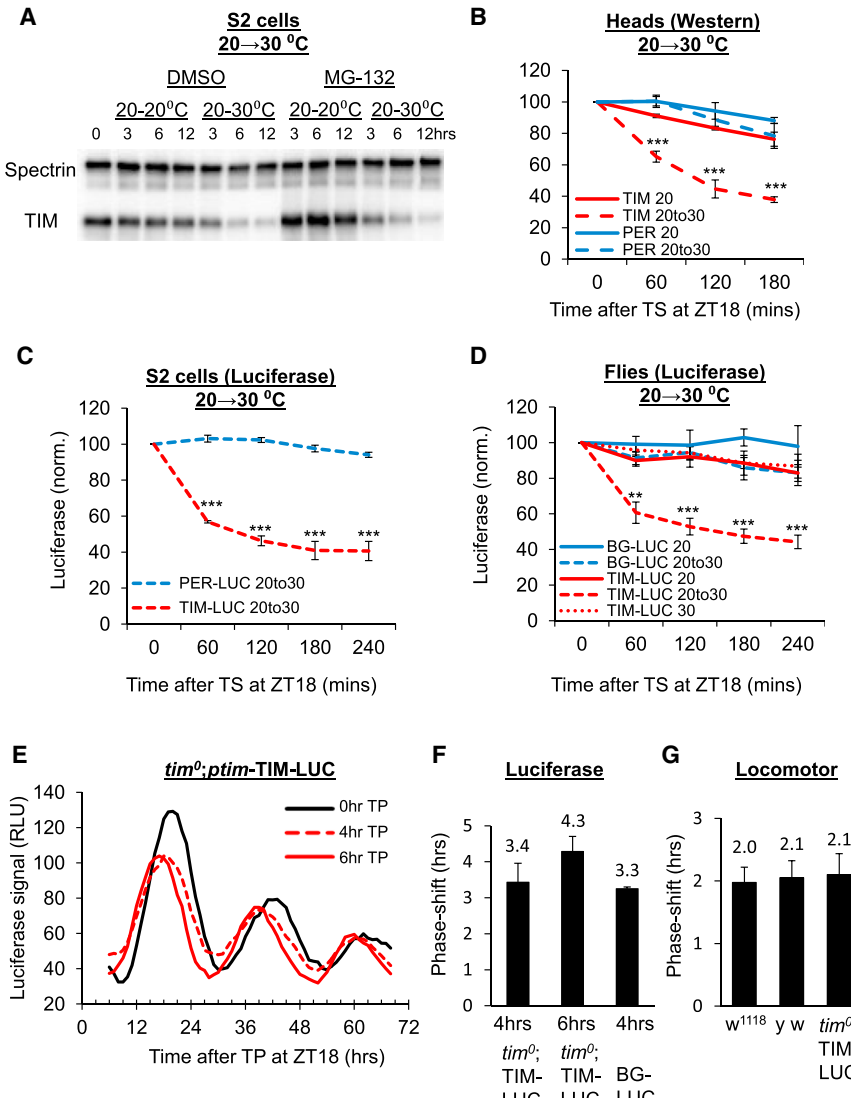


Figure 1. A Temperature Increase Degrades TIM and Resets the *Drosophila* Circadian Clock

(A) A 20°C to 30°C temperature shift (TS) degrades TIM in *Drosophila* S2 cell culture. Western blots (WB) show TIM degradation even in the presence of MG-132. Spectrin is the loading control.

(B) Quantification of WB from fly head extracts shows similar TIM (red), but not PER (blue), degradation induced by TS.

(C and D) TS-induced TIM (red), but not PER (blue), degradation is reproduced using luciferase fusion proteins in S2 cells (C) and in whole flies (D). BG-LUC is an *in vivo* PER-luciferase fusion protein (Stanewsky et al., 1997).

(E) Representative long-term luciferase recordings from TIM-LUC flies show that a 4-hr temperature pulse (TP) from 20°C to 30°C shifts the circadian clock in flies. Traces show a 6-hr moving average of TIM-LUC rhythms in flies.

(F and G) Quantification of phase advances induced by a 4-hr TP at ZT18 in peripheral (TIM-LUC) (F) and brain (locomotor behavior) clocks (G). Error bars represent SEM for (B)–(D) or SD for (F) and (G). p < 0.01 or p < 0.001 from at least five independent experiments (n ≥ 6 each) is indicated with *** or ****, respectively.

See also Figure S1.

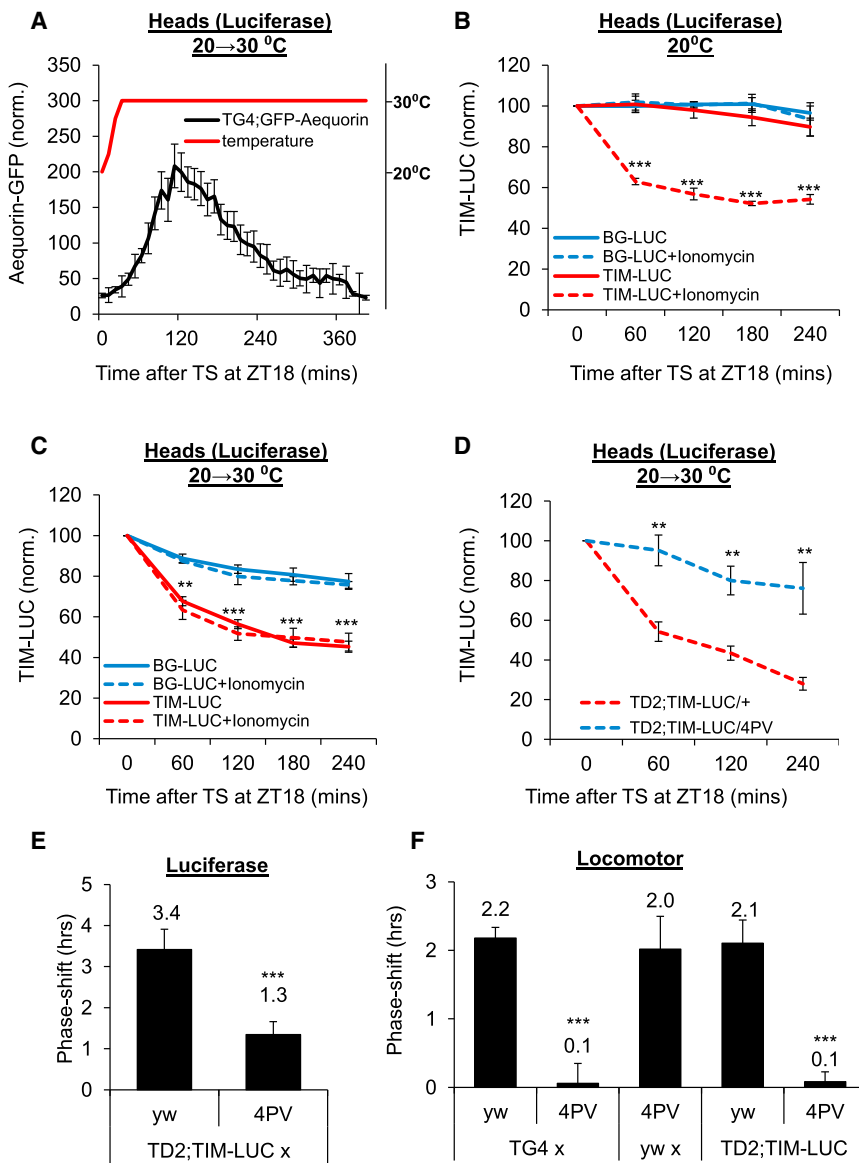
We found that temperature increases intracellular Ca²⁺ levels with a slow kinetics that peaks after ca. 2 hr (Figure 2A). To mimic the effects of TP on Ca²⁺ levels, we pharmacologically increased intracellular Ca²⁺ in fly heads using the bacterial ionophore ionomycin (Figure 2B). Its application at 20°C resulted in acute TIM degradation with a kinetic similar to TP-induced TIM degradation. In contrast, ionomycin had no effect on PER levels (Figure 2B). We also found that TP had no additive effect on ionomycin-induced TIM degradation, suggesting that Ca²⁺ is in the circadian thermal pathway (Figure 2C).

We then buffered intracellular Ca²⁺ levels *in vivo* using PARVALBUMIN (PV), an albumin-like protein that binds Ca²⁺ through multiple EF-hand motifs. PV overexpression was previously used in flies to show that intracellular Ca²⁺ affects circadian rhythmicity in DD, but not light entrainment (Harris et al., 2007). Expressing four copies of a PV-encoding transgene with *tim-gal4* strongly compromised thermal TIM degradation (Figure 2D). Furthermore, PV flies showed reduced phase advances

that Ca²⁺ plays an important role in *Drosophila* circadian thermal responses. The slow kinetics of Ca²⁺ increase likely explain the need for a prolonged temperature pulse to elicit phase shifts. TRPA1 conducts Ca²⁺ and has been implicated in temperature entrainment of circadian behavior (Lee and Montell, 2013). However, TIM degradation was not affected in *trpa1*¹ mutant flies (Figure S2G), indicating that another Ca²⁺ conductance is implicated.

Calmodulin Binding Is Required for Thermal TIM Degradation

Calcium signaling can work through several effectors, such as Calmodulin (CaM). Upon binding Ca²⁺, CaM changes conformation and binds to target proteins (Chin and Means, 2000). We predicted six putative CaM binding sites on TIM (Figure 3A). We therefore assessed whether CaM could be involved in the effects of temperature on the circadian clock. Downregulating CaM *in vivo*—using a previously validated double-stranded RNA (dsRNA) (Melom and Littleton, 2013) or another non-overlapping



dsRNA-blocked thermal phase advances both in the periphery (Figures 3B and S3A) and brain (Figures 3C and S3B). Thermal TIM degradation was also significantly reduced in CaM RNAi flies (Figure 3D).

To test whether the predicted CaM binding sites are indeed critical for thermal TIM degradation, we performed an N- and C-terminal deletion analysis in S2 cells using TIM-LUC. The results showed a progressive thermal stabilization of TIM as more putative CaM binding sites were deleted (Figure 3E). We also performed site-directed mutagenesis on these sites and found that significant reduction of thermal degradation required mutations of at least five sites (Figure 3F; data not shown). Because mutagenizing the most N-terminal CaM binding site also affected photic TIM degradation in S2 cells (data not shown), we used a mutant TIM-LUC protein for in vivo experiments.

Figure 2. Thermal TIM Degradation Is Dependent on Cytosolic Ca^{2+}

(A) A 20°C to 30°C temperature shift (TS) increases intracellular Ca^{2+} in fly head circadian tissues as measured by luminescence from GFP-Aequorin ($n = 72$). (B) An ionomycin-induced intracellular Ca^{2+} increase triggers TIM-LUC (red), but not PER (blue), degradation in isolated heads in culture at 20°C. (C) Simultaneous application of TS and ionomycin has no additive effect on TIM degradation. (D–F) Buffering intracellular Ca^{2+} in vivo with PV (blue) reduces thermal TIM degradation (D), thermal phase shifts in the periphery (E) and in the brain (F). Both *tim-Gal4* (TG4) and *tim-GAL4* combined with *UAS-dcr2* (TD2) were used to express PV (see the *Supplemental Experimental Procedures*). Error bars represent SEM for (A)–(D) or SD for (E) and (F). $p < 0.01$ or $p < 0.001$ from at least four independent experiments ($n \geq 6$ each) is indicated with “**” or “***,” respectively. See also Figure S2.

Although TIM-LUC 5C could not sustain rhythms in *tim⁰* flies (data not shown), it was rhythmically expressed and did not interfere with LD or DD behavior when expressed in wild-type flies (Figures S3C and S3D). Similar to the results in S2 cells, TIM-LUC 5C was protected from thermal degradation in vivo (Figure 3G), but was degraded normally by light (Figure S2E). Furthermore, TIM-LUC 5C acted as dominant negative for thermal responses and blocked molecular (Figures 3H and S3D) and behavioral phase advances (Figures 3I and S3E). The dominant-negative effect was not caused by abnormally high TIM levels, as TIM-LUC 5C was expressed at levels similar to wild-type TIM-LUC (Figure S3F). In support of these results, we also found that CaM could bind to TIM-LUC (but not to LUC alone)

in a Ca^{2+} -dependent manner in vitro and that this binding was lost with the TIM-LUC 5C mutant (Figure S3G). Similar to PV, TIM-LUC 5C or CaM RNAi did not have an effect on temperature compensation (Figure S2F).

TIM Is Degraded by the Calpain SOL in Response to Temperature

Since thermal TIM degradation is not dependent on the proteasome (Figure 1A), we turned our attention to calpains, which are Ca^{2+} -responsive proteases (Zhao et al., 2012). In *Drosophila*, there are four calpains: Calpain A, B, and C and small optic lobes (SOL) (Friedrich et al., 2004). Using RNAi in S2 cells, we found that thermal TIM degradation was reduced with SOL dsRNAs, while dsRNAs against other calpains had no effect (Figure 4A). Moreover, TP-induced phase shifts in peripheral circadian tissues were significantly reduced when SOL was downregulated

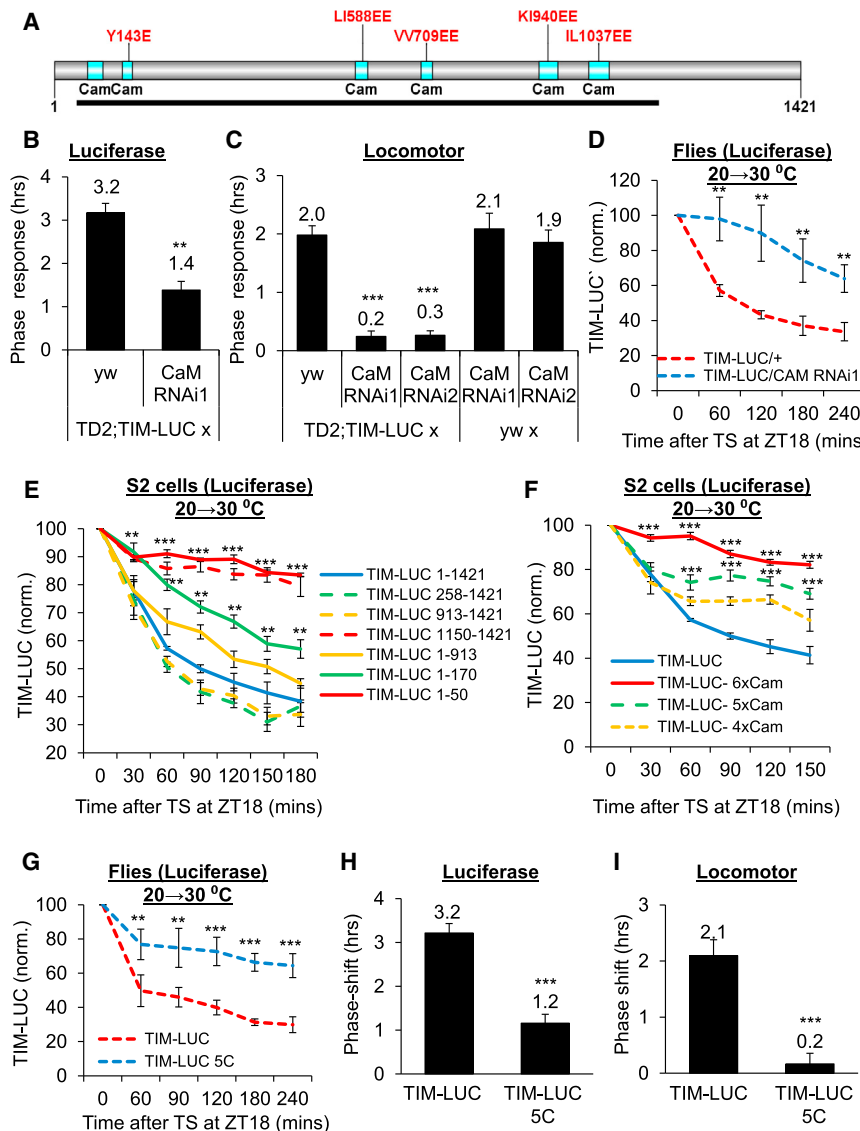


Figure 3. The Effects of Temperature on TIM Stability and the Circadian Clock Are Mediated by CaM

(A) TIM harbors six putative CaM binding sites (blue) that are distributed among amino acids 64–1057 (black bar). Mutations to abolish CaM binding are indicated (red).

(B and C) In vivo CaM downregulation using two non-overlapping RNAi blocks thermal phase advances in the periphery (B) and brain (C).

(D) CaM RNAi (blue) causes reduced TIM degradation in response to TS.

(E) N- and C-terminal deletion of TIM results in progressive thermal stabilization in *Drosophila* S2 cells.

(F) Mutations of at least five CaM binding sites on TIM (TIM-LUC 5C) are required to reduce strongly TS-induced TIM degradation in S2 cells, due to redundancy.

(G) A TIM-LUC 5C mutant, which lacks the five C-terminal CaM-binding sites, also shows diminished thermal degradation in vivo.

(H and I) TIM-LUC 5C acts as a dominant negative and blocks thermal phase advances in the peripheral (H) and brain clocks (I). Error bars represent SD for (B), (C), (H), and (I) or SEM for (D)–(G). $p < 0.01$ or $p < 0.001$ from at least five independent experiments ($n \geq 6$ each) is indicated with “***” or “****,” respectively. Significance for less stable mutants is not shown to keep the figures clear.

See also Figure S3.

Phase Delays and Temperature Entrainment Are Also Mediated by SOL-Dependent TIM Degradation

Drosophila circadian behavior can respond to 2°C temperature cycles (Wheeler et al., 1993). Thus, we tested whether such small changes in temperature could induce TIM degradation. We found that a 25°C to 27°C TP caused rapid TIM degradation just as well as a 10°C TP, in both the advance and delay zones (Busza et al., 2007). These responses were reduced in CaM RNAi, SOL RNAi, and TIM-LUC 5C flies (Figures S5A and S5B). Next, we tested the effects of TIM-LUC 5C and SOL RNAi on entrainment to thermal cycles (TC). We subjected flies to a LD cycle at 25°C and then applied an 8-hr shifted 25°C/27°C TC for 7 days in constant darkness (DD), followed by constant 25°C in DD. Release into constant conditions is critical to determine whether the circadian pacemaker underlying rhythmic behavior was indeed entrained to the shifted TC. Strikingly, both TIM-LUC 5C and SOL RNAi flies showed significantly reduced entrainment to TC in both advance and delay directions (Figure 5).

SOLH Promotes mPER2 Degradation and Thermal Phase Shifts in Mammals

Temperature is also an important timing cue for peripheral clocks in mammals. We tested whether the temperature input

using two non-overlapping dsRNA, while RNAi against calpains A, B, or C had no effect (Figures 4B and S4A). In addition, SOL downregulation by RNAi or using a deficiency caused a strong reduction in TP-induced behavioral phase advances (Figures 4C and S4B). Consistently, we also found that thermal TIM degradation was reduced in vivo (Figure 4D). In contrast, SOL overexpression in clock cells increased the amplitude of the phase shifts (Figure 4C). We confirmed SOL knockdown and overexpression using RT-PCR (Figure S4C). It is interesting to note that thermal phase shifts are very sensitive to SOL, since a 50% reduction in SOL is sufficient to strongly attenuate them. SOL is thus rate limiting. Photic TIM degradation and temperature compensation were not affected by SOL RNAi (Figures S2E and S2F). Since blocking either SOL or CaM activity caused severe disruption of thermal TIM degradation, we concluded that these proteins function in the same pathway, rather than in independent pathways converging on TIM.

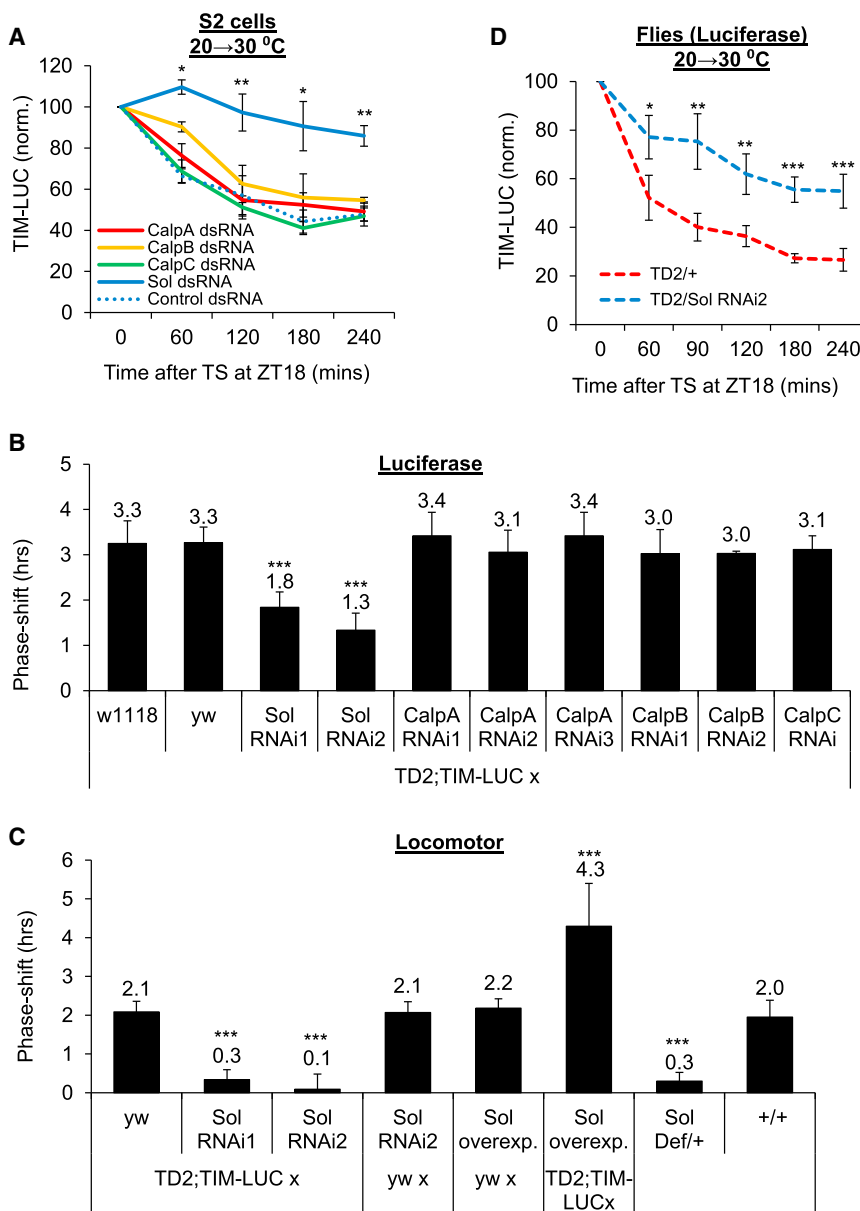


Figure 4. Thermal TIM Degradation and Phase Advances Are Mediated by SOL

(A) Downregulation of *Drosophila* SOL, but not calpain A, B, or C, impairs TIM degradation in S2 cells. (B and C) Two non-overlapping SOL RNAis block thermal phase advances in the periphery (B) and brain (C), while RNAi against the other calpains has no effect. SOL overexpression increases, and deficiency blocks phase shifts in the brain. (D) SOL RNAi reduces TS-induced TIM degradation in whole flies in vivo. Error bars represent SEM for (A) and SD for (B) and (C). $p < 0.05$, $p < 0.01$, or $p < 0.001$ from at least five independent experiments ($n \geq 6$ each) is indicated with “*,” “**,” or “***,” respectively.

See also Figure S4.

RNAs (shRNAs) directed against *Solh* using lentivirus. By RT-PCR, we determined that two of the four shRNAs we tested efficiently downregulated *Solh* (Figure S6B). These two shRNAs do not overlap. We found a striking correlation between *Solh* downregulation efficacy and disruption of thermal phase shifts (Figures 6B, S6B, and S6C). We also found that thermal mPER2 degradation was disrupted by *Solh* RNAi compared to eGFP RNAi control (Figure 6C). Interestingly, ionomycin induced mPER2 degradation in a dose-dependent manner in lung fibroblasts (Figures 6D and S6D). This degradation occurs both at CT8 and CT12 (Figure 6E), but results in a phase delay only at CT12 (Figures 6F, 6G, and S6E). Ionomycin-induced mPER2 degradation was also observed in liver cells. As with *Drosophila* TIM degradation, ionomycin and temperature shift had no additive effect on mPER2 degradation, indicating that Ca^{2+} is also in the mammalian circadian thermal input pathway. Moreover, *Solh* RNAi reduced ionomycin-induced mPER2 degradation (Figure 6H). We therefore

propose that as in flies, a sustained temperature increase triggers an increase in Ca^{2+} signaling to activate the atypical calpain SOLH, resetting the mammalian circadian pacemaker in a phase-specific manner.

Next, we asked whether the sole mammalian SOL homolog (SOLH) (Kamei et al., 1998, 2000) is involved in thermal mPER2 degradation and phase shifts of the mammalian clock. We generated immortalized liver cells expressing short hairpin

propose that as in flies, a sustained temperature increase triggers an increase in Ca^{2+} signaling to activate the atypical calpain SOLH, resetting the mammalian circadian pacemaker in a phase-specific manner.

DISCUSSION

Our results reveal a specific molecular pathway that allows circadian pacemakers to respond to temperature and thus to remain properly synchronized with their environment. In *Drosophila*, a temperature increase results in a delayed, yet sustained, increase in cytosolic Ca^{2+} , which triggers the CaM-mediated degradation of TIM by the atypical protease SOL. In mammals, our results indicate that SOLH also plays an important role in

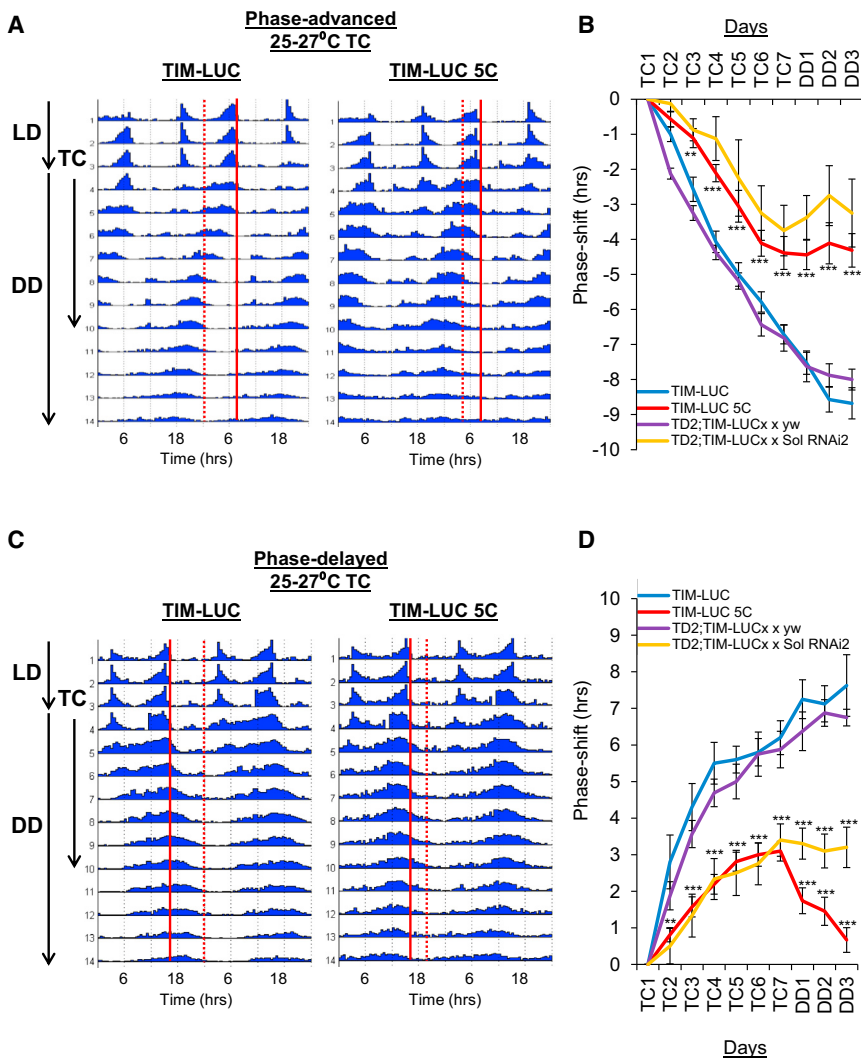


Figure 5. CaM Binding Mutations and SOL RNAi Impair Thermal Entrainment

(A) Representative actograms of flies entrained to a 12/12-hr LD cycle for 4 days at 25°C, then to an 8-hr advanced temperature cycle (TC) of 25°C/27°C for 7 days in DD, and finally released to constant 25°C in DD. Red bars indicate the circadian phase before (solid) and after TC (dashed).

(B) Quantification of circadian phases from at least five independent advanced TC experiments ($n \geq 8$ each) is shown.

(C and D) Similar experiments using an 8-hr delayed TC and their quantification from at least five independent experiments ($n \geq 8$ each) are shown. Error bars represent SEM for (B) and (D). $p < 0.01$ or $p < 0.001$ is indicated with “**” or “***,” respectively. See also Figure S5.

are targeted by SOL/SOLH; nor do we suggest that SOL/SOLH is the sole mechanism whereby Ca^{2+} affects the clock, since Ca^{2+} and other second messengers clearly engage multiple mechanisms to effect phase resetting at different times during the circadian cycle, e.g., through functional $\text{Ca}^{2+}/\text{cAMP}$ response elements in the *period1* and 2 promoters (Balsalobre et al., 2000; O’Neill et al., 2008).

Rather, our investigation focuses on a simple post-translational mechanism for the integration of multiple environmental inputs into the cellular clockwork. Indeed, light, through CRY photoreception, and temperature, through Ca^{2+} , both converge on TIM to entrain the molecular clock in flies. This explains how light and temperature cooperate to entrain molecular and behavioral circadian rhythms (Boothroyd

circadian thermal responses, triggering mPER2 degradation. Although we have not yet determined the role of mammalian CaMs in circadian thermal entrainment, we have strong evidence that Ca^{2+} is also implicated. Indeed, we show that Ca^{2+} phase shifts the mammalian clock in a time-dependent manner and triggers SOLH-mediated mPER2 degradation. Moreover, Ca^{2+} and temperature effects on mPER2 degradation are not additive, indicating that Ca^{2+} is likely to be the second messenger responsible for communicating physiological temperature increases to the molecular clockwork. mPER1 responded to temperature shifts as well. Consistent with this, mammalian PER1 and PER2 contain a highly conserved CaM recognition motif.

The SOL/SOLH thermal input pathway is thus likely to be preserved in flies and mammals, although its final target is different. It is worth noting, however, that both TIM and mPER2 levels are critical in determining circadian phase, and both are also light input targets, albeit through different mechanisms (Naidoo et al., 1999; Shearman et al., 1997; Suri et al., 1998; Yang et al., 1998). It should also be noted that we do not exclude the possibility that additional elements of the circadian pacemaker

et al., 2007; Yoshii et al., 2009). In natural environments, both inputs are noisy and their integration enables a more accurate estimation of external time, rather than by relying upon either input separately. Indeed, in the wild, temperature plays a particularly important role in entraining and modulating circadian behavior (Menegazzi et al., 2012; Vanin et al., 2012). For circadian behavior, neural networks probably also play a role in input integration. Indeed, several studies indicate that light and temperature can be preferentially detected by specific groups of circadian neurons, which would then communicate with the ventral lateral neurons, the master pacemaker neurons in *Drosophila* (Busza et al., 2007; Lamba et al., 2014; Picot et al., 2009; Shang et al., 2008; Tang et al., 2010; Yoshii et al., 2010).

Previous studies have identified three candidate sensory mechanisms for circadian temperature detection in *Drosophila*. Interestingly, two of them (TRPA1, PYX) are Ca^{2+} channels, although probably only TRPA1 is expressed in specific circadian neurons (Lee and Montell, 2013; Wolfgang et al., 2013). Thus, TRPA1 is a plausible candidate for synchronizing the molecular clock of these neurons through the SOL pathway. PYX is

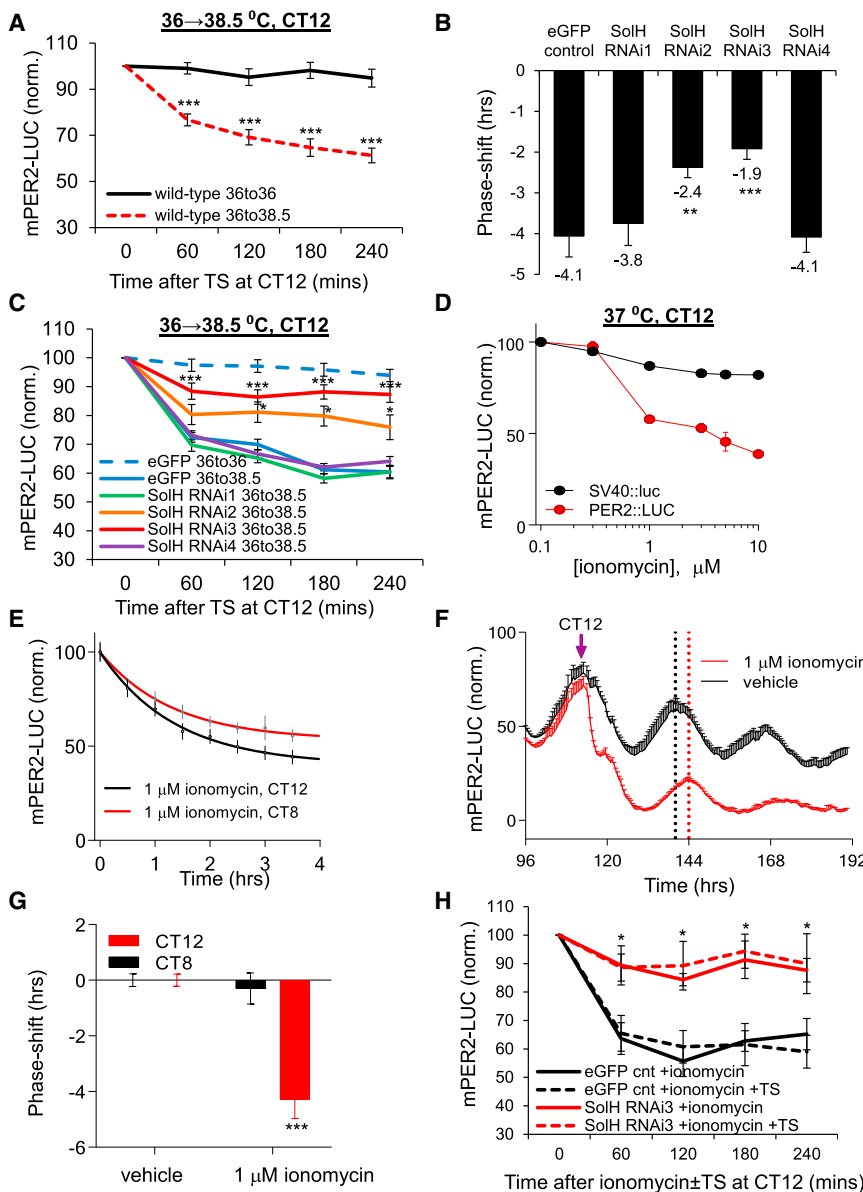


Figure 6. Temperature Shifts the Mammalian Clock through SOLH-Mediated Degradation of mPER2

(A) A 4-hr temperature shift triggers mPER2 degradation at CT12 (defined by peak PER2::LUC bioluminescence) in mammalian immortalized liver cells.

(B and C) SOLH downregulation using shRNA reduces thermal phase shifts (B) and mPER2 degradation in immortalized liver cells at CT12 (C). (D) Intracellular Ca^{2+} induced by ionomycin degrades mPER2 in a dose-dependent manner at CT12 in lung fibroblasts.

(E–G) Ionomycin results in mPER2 degradation both at CT8 and CT12 (E), and phase delays molecular rhythms at CT12 in lung cells (F and G).

(H) Ionomycin-induced mPER2 degradation in liver cells is SOLH dependent and not additive with TP, suggesting that Ca^{2+} and temperature are on the same pathway. Error bars represent SD for (B) and SEM for others. $p < 0.05$, $p < 0.01$, or $p < 0.001$ from at least three independent experiments ($n \geq 6$ each) is indicated with *, **, or ***, respectively.

See also Figure S6.

and for entrainment to light inputs (Guo et al., 2014; Lamba et al., 2014; Shang et al., 2008; Tang et al., 2010; Yao and Shafer, 2014), might also rely on Ca^{2+} -mediated TIM degradation.

This said, our results show that SOL functions cell autonomously, since we observe TIM degradation in *Drosophila* cell cultures. In flies, we observe that both peripheral and brain clocks are entrained to temperature cycles by this mechanism. Accordingly, peripheral clocks have previously been shown to entrain autonomously to temperature cycles (Glaser and Stanewsky, 2005). Surprisingly, however, Sehadova et al. (2009) proposed that brain circadian clocks are not directly sensitive to thermal cycles, but are dependent on the chordotonal organs and NOCTE. However, in our hands, at least the Dorsal Neurons—which include neurons specifically sensitive to temperature (Busza et al., 2007; Picot et al., 2009; Yoshii et al., 2010)—can synchronize to temperature cycles in cultured dissected brains (Figures S5C–S5F), disconnected from chordotonal organs and thus from NOCTE input. Sehadova et al. (2009) used constant light conditions, while all our experiments are done under constant darkness. Constant light strongly reduces the amplitude of circadian rhythms and might thus sensitize brain circadian clocks to non-autonomous NOCTE input. Based on all our results, we propose that even in the brain, temperature entrainment can function cell autonomously. TRPA1 expression in a subset of clock neurons (Lee and Montell, 2013) fits with this notion. However, TRPA1 is not the conductance that triggers TIM degradation in most circadian tissues, since TIM

apparently not expressed in the brain (Sun et al., 2009) and would thus have to rely on neural circuitry. This is also the case for the third circadian thermal sensory candidate, which is dependent on the expression of NOCTE in chordotonal organs (Sehadova et al., 2009). However, since neural communication relies heavily on Ca^{2+} as a second messenger, SOL-dependent TIM degradation might also be crucial for those non-autonomous thermal inputs. Actually, Ca^{2+} -dependent TIM degradation could be necessary for other sensory inputs to reach the circadian pacemaker neurons, such as visual (Helfrich-Förster et al., 2001), mechanical (Simoni et al., 2014), and olfactory cues (Levine et al., 2002). We note that in larvae, visual inputs trigger TIM degradation in a CRY-independent manner (Mazzoni et al., 2005). In addition, communication between circadian neurons, critical for maintaining properly synchronized circadian rhythms

tonal organs and NOCTE. However, in our hands, at least the Dorsal Neurons—which include neurons specifically sensitive to temperature (Busza et al., 2007; Picot et al., 2009; Yoshii et al., 2010)—can synchronize to temperature cycles in cultured dissected brains (Figures S5C–S5F), disconnected from chordotonal organs and thus from NOCTE input. Sehadova et al. (2009) used constant light conditions, while all our experiments are done under constant darkness. Constant light strongly reduces the amplitude of circadian rhythms and might thus sensitize brain circadian clocks to non-autonomous NOCTE input. Based on all our results, we propose that even in the brain, temperature entrainment can function cell autonomously. TRPA1 expression in a subset of clock neurons (Lee and Montell, 2013) fits with this notion. However, TRPA1 is not the conductance that triggers TIM degradation in most circadian tissues, since TIM

degradation is not affected in whole-head protein extracts. Thus, as for light (Helfrich-Förster et al., 2001), a combination of cell-autonomous and non-autonomous mechanisms might be involved in thermal behavior entrainment. Indeed, none of our manipulations completely eliminate thermal entrainment, although it should also be noted that our genetic manipulations are unlikely to have completely blocked the thermal TIM degradation pathway (RNAi and dominant-negative mutants were used).

That Ca^{2+} plays such an important role in thermal entrainment in both mammals and flies is intriguing. Indeed, intracellular Ca^{2+} has other important circadian functions. In organotypic mouse SCN, cytosolic Ca^{2+} levels oscillate and the appropriate manipulation of intracellular Ca^{2+} is sufficient to determine the phase, period, and amplitude of circadian gene expression (Brancaccio et al., 2013). Similarly in plants, flies, and non-excitable mammalian cells, Ca^{2+} signaling is intimately intertwined with molecular timekeeping (Harris singh et al., 2007; Noguchi et al., 2012; Xu et al., 2007). Ca^{2+} signaling in SCN neurons is also important for light input from retinal ganglionic cells (Ding et al., 1998). Are these functions for Ca^{2+} separate, or are they interconnected? We have identified the SOL pathway as a cellular mechanism that responds to a gradual Ca^{2+} increase over the course of hours and thereby elicits a specific phase-dependent resetting of the cellular clockwork through clock protein degradation. Therefore, prolonged exposure to temperature is needed to get a response to this input, and this fits perfectly with the slow pace of behavior synchronization to temperature cycles (Busza et al., 2007; Currie et al., 2009). This slow kinetics probably separates the thermal function of Ca^{2+} from at least some of its other circadian functions, such as those involving fast neural communication. SOLH might, on the other hand, turn out to contribute to the effect of Ca^{2+} oscillations in the SCN or on circadian period, since they have a much longer time frame.

In mammals, HSF1 has been implicated in circadian thermal responses, where it clearly contributes to, but is not essential for, entrainment to applied thermal cycles (Buhr et al., 2010; Saini et al., 2012). Intriguingly, HSF1 is regulated by Ca^{2+} (Buhr et al., 2010; Ding et al., 1996). Since neither HSF1 knockout nor down-regulation of SOLH completely blocks thermal responses, these proteins could be on two parallel branches of a complex Ca^{2+} -activated circadian thermal pathway. Alternative models are possible, such as a regulatory role for HSF1 upon SOLH-mediated mPER2 degradation. We also note that a CLK mutant protein that cannot be phosphorylated partially disrupts thermal entrainment of *Drosophila* circadian behavior (Lee et al., 2014). Conceivably, CLK phosphorylation could affect TIM's sensitivity to SOL in clock neurons since CLK and TIM physically interact.

In summary, our results point to a striking conservation of entrainment pathways in animals that tune the cellular clock to thermal cycles. In addition, our work uncovers how the atypical calpain SOL/SOLH, which lacks EF domains for Ca^{2+} binding found in most calpains, can be activated physiologically. Moreover, we identify a specific biological function for this poorly studied protease. It will be interesting to determine whether Ca^{2+} and SOL/SOLH play additional roles in other thermal responses.

In developed nations, ~15% of the work force engage in shift work and as a consequence suffer from a significantly increased

risk of chronic diseases, such as type 2 diabetes and many cancers. Preventive strategies that directly target the transcriptional clockwork would be highly likely to result in adverse off-target effects. In contrast, as an endogenous means of circadian entrainment to systemic cues, SOLH could have clear potential as a target for pharmacological resetting of the body clock, thereby alleviating the deleterious acute and long-term effects of jetlag and shift work.

EXPERIMENTAL PROCEDURES

For detailed protocols, see the [Supplemental Experimental Procedures](#).

Temperature Pulses

2- to 7-day-old male flies were entrained to 12/12-hr LD cycles for 3 days at constant temperature. Flies were then moved to a pre-warmed dark incubator for 4 hr for the temperature pulse experiments at ZT18 and then moved back to the original incubator. Control flies were handled similarly but were returned to the original incubator. Locomotor activity or luciferase rhythms were then monitored for several days in constant conditions as indicated. Luciferase data were normalized to *tim(enh-mut)-LUC* controls (Allada et al., 2003). A *pactin-LUC* plasmid was used as control for S2R+ cells for normalization.

Data analysis was done in Excel (Microsoft) using raw data for short-term experiments (<4 hr) and by fitting a 6-hr moving average for long-term experiments (>7 days) for added reliability. Circadian phase was calculated using at least three troughs of the locomotor activity or luminescence rhythm from pulsed and non-pulsed samples, because we found troughs to be the most reliable phase marker. Flies that did not show overt rhythmicity or did not survive until the end of the experiment were excluded from the analysis.

In Vivo Ca^{2+} Recording with GFP-Aequorin

Isolated heads from TG4:Aequorin-GFP flies were cultured in Shields and Sang M3 insect medium (Sigma; + 10% fetal bovine serum+ penicillin-streptomycin+ insulin-transferrin-selenium) in the presence of native coelenterazine (Gold-biotech) substrate (1 mM final) for 4 hr and then moved from 20°C to a pre-warmed 30°C incubator and continuously monitored for luciferase activity. Four independent experiments were performed. Most heads (74.2%) responded to the temperature shift (Figure 2A). Heads that did not show a significant response within 2.5 hr of the temperature shift were excluded from the analysis.

Culture and Manipulation of Mammalian Cells

Animal work was licensed under the UK Animals (Scientific Procedures) Act of 1986 with local ethical approval or approved by the Institutional Animal Care and Use Committee of UMass Medical School. Immortalized fibroblasts homozygous for PER2::LUC (Yoo et al., 2004) were cultured, and luminescence was recorded as described previously (O'Neill and Hastings, 2008). Data were detrended to remove baseline changes and then fit with a damped sine wave in order to determine circadian period, amplitude, and phase. Statistical analyses were performed using Graphpad Prism. In order to be able to interpret our observations with respect to the accepted timetable of molecular events established in organotypic mouse SCN (Brancaccio et al., 2013), we arbitrarily defined CT12 as the peak of PER2:LUC bioluminescence under constant conditions.

Liver cells were extracted from PER2:LUC mice and immortalized. Solh knockdown viruses (or control viruses) were added to the liver cells followed by selection with 2 mg/ml puromycin for 1 week. Bioluminescence assays were performed with cells seeded into 96-well plates, sealed with PCR film, and entrained to 36°C/38.5°C thermal cycles for 2 days in puromycin-containing complete Williams' E medium with luciferin (400 μM).

SUPPLEMENTAL INFORMATION

Supplemental Information includes Supplemental Experimental Procedures and six figures and can be found with this article online at <http://dx.doi.org/10.1016/j.cell.2015.10.031>.

AUTHOR CONTRIBUTIONS

O.T. and P.E. designed the project. X.Z. generated the liver cell lines expressing *Solh* shRNAs. A.B. conducted the initial S2 cell experiments on thermal TIM degradation. J.L. performed experiments on cultured brains. J.S.O. designed and performed the lung fibroblast experiments. All other experiments were performed by O.T., O.T., J.S.O., and P.E. wrote the manuscript.

ACKNOWLEDGMENTS

We specially thank D. Weaver for discussions and help with mammalian experiments and antibodies and R. Stanewsky for sharing unpublished results. We thank D. Wentworth, D. Szydlik, and C. Yuan for technical assistance, Y. Zhang and S. Antolin for discussions, M. Nitabach for PV and GFP-Aequorin flies, M. Rosbash for LUC control flies, A. Seghal for anti-TIM antibody, R. Stanewsky for anti-PER antibody and BG-LUC flies, the Bloomington and VDRC *Drosophila* stock centers for fly stocks, and the UMass Medical School shRNA core for viruses expressing *Solh* shRNAs. This work was supported by NIH grants (GM079182 and GM066777) (to P.E.). J.S.O. is supported by the Medical Research Council (MC_UP_12014) and the Wellcome Trust (093734/Z/10/Z).

Received: April 10, 2015

Revised: July 24, 2015

Accepted: September 30, 2015

Published: November 19, 2015

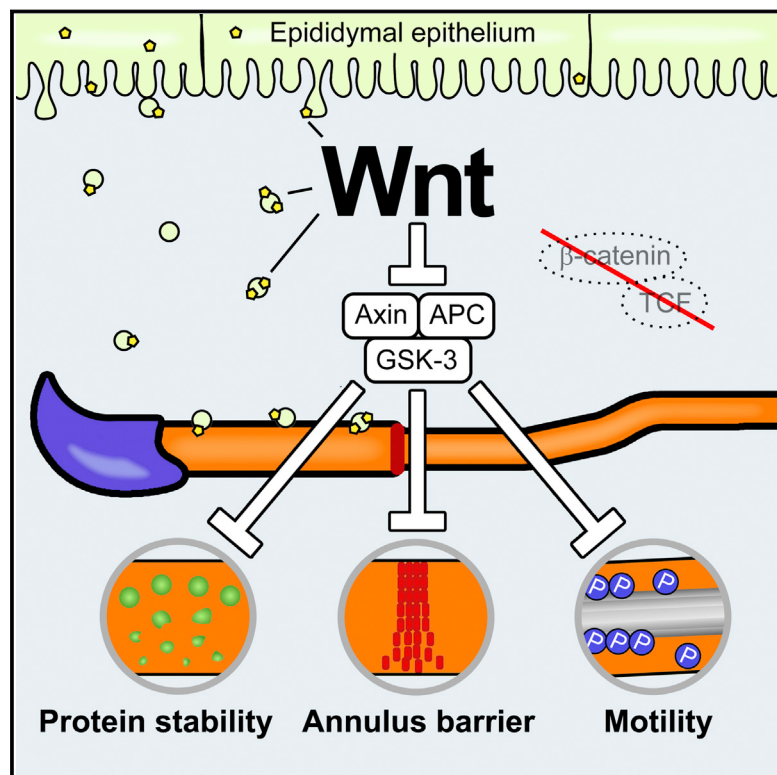
REFERENCES

- Allada, R., Kadener, S., Nandakumar, N., and Rosbash, M. (2003). A recessive mutant of *Drosophila Clock* reveals a role in circadian rhythm amplitude. *EMBO J.* 22, 3367–3375.
- Balsalobre, A., Marcacci, L., and Schibler, U. (2000). Multiple signaling pathways elicit circadian gene expression in cultured Rat-1 fibroblasts. *Curr. Biol.* 10, 1291–1294.
- Baubet, V., Le Mouellic, H., Campbell, A.K., Lucas-Meunier, E., Fossier, P., and Brûlé, P. (2000). Chimeric green fluorescent protein-aequorin as bioluminescent Ca²⁺ reporters at the single-cell level. *Proc. Natl. Acad. Sci. USA* 97, 7260–7265.
- Boothroyd, C.E., Wijnen, H., Naef, F., Saez, L., and Young, M.W. (2007). Integration of light and temperature in the regulation of circadian gene expression in *Drosophila*. *PLoS Genet.* 3, e54.
- Brancaccio, M., Maywood, E.S., Chesham, J.E., Loudon, A.S., and Hastings, M.H. (2013). A Gq-Ca²⁺ axis controls circuit-level encoding of circadian time in the suprachiasmatic nucleus. *Neuron* 78, 714–728.
- Brown, S.A., Zumbrunn, G., Fleury-Olela, F., Preitner, N., and Schibler, U. (2002). Rhythms of mammalian body temperature can sustain peripheral circadian clocks. *Curr. Biol.* 12, 1574–1583.
- Bruce, V.G. (1960). Environmental entrainment of circadian rhythms. *Cold Spring Harb. Symp. Quant. Biol.* 25, 29–48.
- Bruce, V.G., and Pittendrigh, C.S. (1956). Temperature independence in a unicellular “clock”. *Proc. Natl. Acad. Sci. USA* 42, 676–682.
- Buhr, E.D., Yoo, S.H., and Takahashi, J.S. (2010). Temperature as a universal resetting cue for mammalian circadian oscillators. *Science* 330, 379–385.
- Busza, A., Emery-Le, M., Rosbash, M., and Emery, P. (2004). Roles of the two *Drosophila* CRYPTOCHROME structural domains in circadian photoreception. *Science* 304, 1503–1506.
- Busza, A., Murad, A., and Emery, P. (2007). Interactions between circadian neurons control temperature synchronization of *Drosophila* behavior. *J. Neurosci.* 27, 10722–10733.
- Chen, R., Schirmer, A., Lee, Y., Lee, H., Kumar, V., Yoo, S.H., Takahashi, J.S., and Lee, C. (2009). Rhythmic PER abundance defines a critical nodal point for negative feedback within the circadian clock mechanism. *Mol. Cell* 36, 417–430.
- Chin, D., and Means, A.R. (2000). Calmodulin: a prototypical calcium sensor. *Trends Cell Biol.* 10, 322–328.
- Currie, J., Goda, T., and Wijnen, H. (2009). Selective entrainment of the *Drosophila* circadian clock to daily gradients in environmental temperature. *BMC Biol.* 7, 49.
- Davidson, A.J., Sellix, M.T., Daniel, J., Yamazaki, S., Menaker, M., and Block, G.D. (2006). Chronic jet-lag increases mortality in aged mice. *Curr. Biol.* 16, R914–R916.
- Ding, X.Z., Smallridge, R.C., Galloway, R.J., and Kiang, J.G. (1996). Increases in HSF1 translocation and synthesis in human epidermoid A-431 cells: role of protein kinase C and [Ca²⁺]_i. *J. Investig. Med.* 44, 144–153.
- Ding, J.M., Buchanan, G.F., Tischkau, S.A., Chen, D., Kuriashkina, L., Faiman, L.E., Alster, J.M., McPherson, P.S., Campbell, K.P., and Gillette, M.U. (1998). A neuronal ryanodine receptor mediates light-induced phase delays of the circadian clock. *Nature* 394, 381–384.
- Friedrich, P., Tompa, P., and Farkas, A. (2004). The calpain-system of *Drosophila melanogaster*: coming of age. *BioEssays* 26, 1088–1096.
- Gentile, C., Sehadova, H., Simoni, A., Chen, C., and Stanewsky, R. (2013). Cryptochrome antagonizes synchronization of *Drosophila*'s circadian clock to temperature cycles. *Curr. Biol.* 23, 185–195.
- Glaser, F.T., and Stanewsky, R. (2005). Temperature synchronization of the *Drosophila* circadian clock. *Curr. Biol.* 15, 1352–1363.
- Goda, T., Sharp, B., and Wijnen, H. (2014). Temperature-dependent resetting of the molecular circadian oscillator in *Drosophila*. *Proc. Biol. Sci.* 281, pii: 20141714.
- Griffin, E.A.J., Jr., Staknis, D., and Weitz, C.J. (1999). Light-independent role of CRY1 and CRY2 in the mammalian circadian clock. *Science* 286, 768–771.
- Guo, F., Cerullo, I., Chen, X., and Rosbash, M. (2014). PDF neuron firing phase-shifts key circadian activity neurons in *Drosophila*. *eLife* 3. <http://dx.doi.org/10.7554/eLife.02780>.
- Harris, M.C., Wu, Y., Lnenicka, G.A., and Nitabach, M.N. (2007). Intracellular Ca²⁺ regulates free-running circadian clock oscillation in vivo. *J. Neurosci.* 27, 12489–12499.
- Helfrich-Förster, C., Winter, C., Hofbauer, A., Hall, J.C., and Stanewsky, R. (2001). The circadian clock of fruit flies is blind after elimination of all known photoreceptors. *Neuron* 30, 249–261.
- Kamei, M., Webb, G.C., Young, I.G., and Campbell, H.D. (1998). SOLH, a human homologue of the *Drosophila melanogaster* small optic lobes gene is a member of the calpain and zinc-finger gene families and maps to human chromosome 16p13.3 near CATM (cataract with microphthalmia). *Genomics* 51, 197–206.
- Kamei, M., Webb, G.C., Heydon, K., Hendry, I.A., Young, I.G., and Campbell, H.D. (2000). Solh, the mouse homologue of the *Drosophila melanogaster* small optic lobes gene: organization, chromosomal mapping, and localization of gene product to the olfactory bulb. *Genomics* 64, 82–89.
- Kaushik, R., Nawathean, P., Busza, A., Murad, A., Emery, P., and Rosbash, M. (2007). PER-TIM interactions with the photoreceptor cryptochrome mediate circadian temperature responses in *Drosophila*. *PLoS Biol.* 5, e146.
- Knutsson, A. (2003). Health disorders of shift workers. *Occup. Med. (Lond.)* 53, 103–108.
- Ko, H.W., Jiang, J., and Edery, I. (2002). Role for Slimb in the degradation of *Drosophila* Period protein phosphorylated by Doubletime. *Nature* 420, 673–678.
- Koh, K., Zheng, X., and Sehgal, A. (2006). JETLAG resets the *Drosophila* circadian clock by promoting light-induced degradation of TIMELESS. *Science* 312, 1809–1812.
- Kume, K., Zylka, M.J., Sriram, S., Shearman, L.P., Weaver, D.R., Jin, X., Maywood, E.S., Hastings, M.H., and Reppert, S.M. (1999). mCRY1 and mCRY2 are essential components of the negative limb of the circadian clock feedback loop. *Cell* 98, 193–205.
- Lamba, P., Bilodeau-Wentworth, D., Emery, P., and Zhang, Y. (2014). Morning and evening oscillators cooperate to reset circadian behavior in response to light input. *Cell Rep.* 7, 601–608.

- Lee, Y., and Montell, C. (2013). Drosophila TRPA1 functions in temperature control of circadian rhythm in pacemaker neurons. *J. Neurosci.* 33, 6716–6725.
- Lee, E., Jeong, E.H., Jeong, H.J., Yildirim, E., Vanselow, J.T., Ng, F., Liu, Y., Mahesh, G., Kramer, A., Hardin, P.E., et al. (2014). Phosphorylation of a central clock transcription factor is required for thermal but not photic entrainment. *PLoS Genet.* 10, e1004545.
- Levine, J.D., Funes, P., Dowse, H.B., and Hall, J.C. (2002). Resetting the circadian clock by social experience in *Drosophila melanogaster*. *Science* 298, 2010–2012.
- Mazzoni, E.O., Desplan, C., and Blau, J. (2005). Circadian pacemaker neurons transmit and modulate visual information to control a rapid behavioral response. *Neuron* 45, 293–300.
- Melom, J.E., and Littleton, J.T. (2013). Mutation of a NCKX eliminates glial microdomain calcium oscillations and enhances seizure susceptibility. *J. Neurosci.* 33, 1169–1178.
- Menegazzi, P., Yoshii, T., and Helfrich-Förster, C. (2012). Laboratory versus nature: the two sides of the *Drosophila* circadian clock. *J. Biol. Rhythms* 27, 433–442.
- Naidoo, N., Song, W., Hunter-Ensor, M., and Sehgal, A. (1999). A role for the proteasome in the light response of the timeless clock protein. *Science* 285, 1737–1741.
- Noguchi, T., Wang, C.W., Pan, H., and Welsh, D.K. (2012). Fibroblast circadian rhythms of PER2 expression depend on membrane potential and intracellular calcium. *Chronobiol. Int.* 29, 653–664.
- O'Neill, J.S., and Hastings, M.H. (2008). Increased coherence of circadian rhythms in mature fibroblast cultures. *J. Biol. Rhythms* 23, 483–488.
- O'Neill, J.S., Maywood, E.S., Chesham, J.E., Takahashi, J.S., and Hastings, M.H. (2008). cAMP-dependent signaling as a core component of the mammalian circadian pacemaker. *Science* 320, 949–953.
- Ozturk, N., Selby, C.P., Annayev, Y., Zhong, D., and Sancar, A. (2011). Reaction mechanism of *Drosophila* cryptochrome. *Proc. Natl. Acad. Sci. USA* 108, 516–521.
- Peschel, N., Chen, K.F., Szabo, G., and Stanewsky, R. (2009). Light-dependent interactions between the *Drosophila* circadian clock factors cryptochrome, jetlag, and timeless. *Curr. Biol.* 19, 241–247.
- Picot, M., Klarsfeld, A., Chélot, E., Malpel, S., and Rouyer, F. (2009). A role for blind DN2 clock neurons in temperature entrainment of the *Drosophila* larval brain. *J. Neurosci.* 29, 8312–8320.
- Pittendrigh, C.S. (1954). On temperature independence in the clock-system controlling emergence time in *Drosophila*. *Proc. Natl. Acad. Sci. USA* 40, 1018–1029.
- Price, J.L., Dembinska, M.E., Young, M.W., and Rosbash, M. (1995). Suppression of PERIOD protein abundance and circadian cycling by the *Drosophila* clock mutation timeless. *EMBO J.* 14, 4044–4049.
- Reddy, A.B., and O'Neill, J.S. (2010). Healthy clocks, healthy body, healthy mind. *Trends Cell Biol.* 20, 36–44.
- Saini, C., Morf, J., Stratmann, M., Gos, P., and Schibler, U. (2012). Simulated body temperature rhythms reveal the phase-shifting behavior and plasticity of mammalian circadian oscillators. *Genes Dev.* 26, 567–580.
- Sandrelli, F., Tauber, E., Pegoraro, M., Mazzotta, G., Cisotto, P., Landskron, J., Stanewsky, R., Piccin, A., Rosato, E., Zordan, M., et al. (2007). A molecular basis for natural selection at the timeless locus in *Drosophila melanogaster*. *Science* 316, 1898–1900.
- Sehdeva, H., Glaser, F.T., Gentile, C., Simoni, A., Giesecke, A., Albert, J.T., and Stanewsky, R. (2009). Temperature entrainment of *Drosophila*'s circadian clock involves the gene nocte and signaling from peripheral sensory tissues to the brain. *Neuron* 64, 251–266.
- Shang, Y., Griffith, L.C., and Rosbash, M. (2008). Light-arousal and circadian photoreception circuits intersect at the large PDF cells of the *Drosophila* brain. *Proc. Natl. Acad. Sci. USA* 105, 19587–19594.
- Shearman, L.P., Zylka, M.J., Weaver, D.R., Kolakowski, L.F.J., Jr., and Reppert, S.M. (1997). Two period homologs: circadian expression and photic regulation in the suprachiasmatic nuclei. *Neuron* 19, 1261–1269.
- Sidote, D., Majercak, J., Parikh, V., and Edery, I. (1998). Differential effects of light and heat on the *Drosophila* circadian clock proteins PER and TIM. *Mol. Cell. Biol.* 18, 2004–2013.
- Simoni, A., Wolfgang, W., Topping, M.P., Kavlie, R.G., Stanewsky, R., and Albert, J.T. (2014). A mechanosensory pathway to the *Drosophila* circadian clock. *Science* 343, 525–528.
- Stanewsky, R., Jamison, C.F., Plautz, J.D., Kay, S.A., and Hall, J.C. (1997). Multiple circadian-regulated elements contribute to cycling period gene expression in *Drosophila*. *EMBO J.* 16, 5006–5018.
- Stanewsky, R., Kaneko, M., Emery, P., Beretta, B., Wager-Smith, K., Kay, S.A., Rosbash, M., and Hall, J.C. (1998). The cryb mutation identifies cryptochrome as a circadian photoreceptor in *Drosophila*. *Cell* 95, 681–692.
- Sun, Y., Liu, L., Ben-Shahar, Y., Jacobs, J.S., Eberl, D.F., and Welsh, M.J. (2009). TRPA channels distinguish gravity sensing from hearing in Johnston's organ. *Proc. Natl. Acad. Sci. USA* 106, 13606–13611.
- Suri, V., Qian, Z., Hall, J.C., and Rosbash, M. (1998). Evidence that the TIM light response is relevant to light-induced phase shifts in *Drosophila melanogaster*. *Neuron* 21, 225–234.
- Tang, C.H., Hinteregger, E., Shang, Y., and Rosbash, M. (2010). Light-mediated TIM degradation within *Drosophila* pacemaker neurons (s-LNvs) is neither necessary nor sufficient for delay zone phase shifts. *Neuron* 66, 378–385.
- Vanin, S., Bhutani, S., Montelli, S., Menegazzi, P., Green, E.W., Pegoraro, M., Sandrelli, F., Costa, R., and Kyriacou, C.P. (2012). Unexpected features of *Drosophila* circadian behavioural rhythms under natural conditions. *Nature* 484, 371–375.
- Weaver, D.R., and Emery, P. (2013). Circadian timekeeping. In *Fundamental Neuroscience*, L.R. Squire, ed. (Elsevier), pp. 819–846.
- Wheeler, D.A., Hamblen-Coyle, M.J., Dushay, M.S., and Hall, J.C. (1993). Behavior in light-dark cycles of *Drosophila* mutants that are arrhythmic, blind, or both. *J. Biol. Rhythms* 8, 67–94.
- Wolfgang, W., Simoni, A., Gentile, C., and Stanewsky, R. (2013). The Pyrexia transient receptor potential channel mediates circadian clock synchronization to low temperature cycles in *Drosophila melanogaster*. *Proc. Biol. Sci.* 280, 20130959.
- Xu, X., Hotta, C.T., Dodd, A.N., Love, J., Sharrock, R., Lee, Y.W., Xie, Q., Johnson, C.H., and Webb, A.A. (2007). Distinct light and clock modulation of cytosolic free Ca²⁺ oscillations and rhythmic CHLOROPHYLL A/B BINDING PROTEIN2 promoter activity in *Arabidopsis*. *Plant Cell* 19, 3474–3490.
- Yang, Z., Emerson, M., Su, H.S., and Sehgal, A. (1998). Response of the timeless protein to light correlates with behavioral entrainment and suggests a nonvisual pathway for circadian photoreception. *Neuron* 21, 215–223.
- Yao, Z., and Shafer, O.T. (2014). The *Drosophila* circadian clock is a variably coupled network of multiple peptidergic units. *Science* 343, 1516–1520.
- Yoo, S.H., Yamazaki, S., Lowrey, P.L., Shimomura, K., Ko, C.H., Buhr, E.D., Siepka, S.M., Hong, H.K., Oh, W.J., Yoo, O.J., et al. (2004). PERIOD2: LUCIFERASE real-time reporting of circadian dynamics reveals persistent circadian oscillations in mouse peripheral tissues. *Proc. Natl. Acad. Sci. USA* 101, 5339–5346.
- Yoshii, T., Vanin, S., Costa, R., and Helfrich-Förster, C. (2009). Synergic entrainment of *Drosophila*'s circadian clock by light and temperature. *J. Biol. Rhythms* 24, 452–464.
- Yoshii, T., Hermann, C., and Helfrich-Förster, C. (2010). Cryptochrome-positive and -negative clock neurons in *Drosophila* entrain differentially to light and temperature. *J. Biol. Rhythms* 25, 387–398.
- Zhang, Y., and Emery, P. (2012). Molecular and neural control of insects circadian rhythms. In *Insect Molecular Biology and Biochemistry*, L.I. Gilbert, ed. (Academic Press), pp. 513–551.
- Zhao, S., Liang, Z., Demko, V., Wilson, R., Johansen, W., Olsen, O.A., and Shalchian-Tabrizi, K. (2012). Massive expansion of the calpain gene family in unicellular eukaryotes. *BMC Evol. Biol.* 12, 193.

Post-transcriptional Wnt Signaling Governs Epididymal Sperm Maturation

Graphical Abstract



Authors

Stefan Koch, Sergio P. Acebron, Jessica Herbst, Gencay Hatiboglu, Christof Niehrs

Correspondence

niehrs@dkfz-heidelberg.de

In Brief

Although the impact of canonical Wnt signaling is predominantly thought to necessitate β-catenin-dependent transcription, a multifaceted set of Wnt functions in sperm development is implemented post-transcriptionally through mechanisms that maybe relevant to other tissues as well.

Highlights

- Mammalian spermatozoa are Wnt-responsive cells
- Wnt signaling controls sperm maturation independent of β-catenin
- Wnt ligands promote sperm proteome stability (Wnt/STOP) and sperm motility
- GSK3 is a septin 4 kinase that inhibits septin clustering

Post-transcriptional Wnt Signaling Governs Epididymal Sperm Maturation

Stefan Koch,^{1,4} Sergio P. Acebron,^{1,4} Jessica Herbst,¹ Gencay Hatiboglu,² and Christof Niehrs^{1,3,*}

¹Division of Molecular Embryology, DKFZ-ZMBH Alliance, 69120 Heidelberg, Germany

²Department of Urology, University of Heidelberg, 69120 Heidelberg, Germany

³Institute of Molecular Biology (IMB), 55128 Mainz, Germany

⁴Co-first author

*Correspondence: niehrs@dkfz-heidelberg.de

<http://dx.doi.org/10.1016/j.cell.2015.10.029>

SUMMARY

The canonical Wnt signaling pathway is of paramount importance in development and disease. An emergent question is whether the upstream cascade of the canonical Wnt pathway has physiologically relevant roles beyond β -catenin-mediated transcription, which is difficult to study due to the pervasive role of this protein. Here, we show that transcriptionally silent spermatozoa respond to Wnt signals released from the epididymis and that mice mutant for the Wnt regulator Cyclin Y-like 1 are male sterile due to immotile and malformed spermatozoa. Post-transcriptional Wnt signaling impacts spermatozoa through GSK3 by (1) reducing global protein polyubiquitination to maintain protein homeostasis; (2) inhibiting septin 4 phosphorylation to establish a membrane diffusion barrier in the sperm tail; and (3) inhibiting protein phosphatase 1 to initiate sperm motility. The results indicate that Wnt signaling orchestrates a rich post-transcriptional sperm maturation program and invite revisiting transcription-independent Wnt signaling in somatic cells as well.

INTRODUCTION

Canonical Wnt signaling is an evolutionarily conserved pathway, which plays a key role in numerous processes of development and disease (Anastas and Moon, 2013; Clevers and Nusse, 2012; Holland et al., 2013). At the heart of canonical Wnt signaling is the transcriptional regulator β -catenin, which in unstimulated cells is phosphorylated by glycogen synthase kinase 3 (GSK3) and then polyubiquitinated and thereby targeted for proteasomal degradation. Binding of Wnt proteins to the Frizzled (Fz) receptors and their low-density lipoprotein receptor related protein (LRP) 5 and 6 co-receptors triggers GSK3 inhibition to stabilize β -catenin, which enter the nucleus and regulate downstream target genes (Kikuchi et al., 2011; MacDonald et al., 2009).

The canonical Wnt signaling cascade is well characterized, and it is widely assumed that this pathway acts primarily through transcriptional response of β -catenin-dependent target genes.

However, we have previously shown that Wnt signaling peaks in the G₂/M phase of the cell cycle in a variety of cells (Davidson et al., 2009). It appeared paradoxical that Wnt signaling should peak in G₂/M, when the hallmark of the pathway is transcriptional regulation, which in mitosis comes to a standstill. Importantly, De Robertis and colleagues showed that Wnt signaling stabilizes many other cellular proteins in addition to β -catenin (Taelman et al., 2010). Building on this discovery, we introduced Wnt-dependent stabilization of proteins (Wnt/STOP), which is independent of β -catenin, and peaks during mitosis to slow down protein degradation as cells prepare to divide (Acebron et al., 2014). This post-transcriptional branch of canonical Wnt signaling is required for proper chromosome segregation, endolysosomal biogenesis, as well as for cell growth and cell-cycle progression (Acebron et al., 2014; Huang et al., 2015; Ploper et al., 2015; Stolz et al., 2015). Wnt stabilizes proteins by inhibiting GSK3, a kinase, which creates phospho-degrons to target proteins for proteasomal degradation. GSK3 inhibition by Wnt signaling peaks in mitosis because the Wnt coreceptor LRP6 is activated by cyclin Y (Ccny) and its target kinase CDK14 (cyclin-dependent kinase 14) in a cell-cycle-dependent manner (Acebron et al., 2014; Davidson et al., 2009). In addition to Wnt/STOP, other post-transcriptional signals have been shown to branch off downstream of GSK3. For instance, Wnt-induced GSK3 regulation activates mTOR to increase protein translation and cell growth (Inoki et al., 2006) and modulates the activity of microtubule-associated proteins during axon growth (Salinas, 2007).

A main caveat of this post-transcriptional Wnt signaling model is the lack of genetic proof. This is because *in vivo* it is challenging to study Wnt responses under conditions where β -catenin transcriptional effects can be ruled out, e.g., in β -catenin mutant background, since such cells are often heavily perturbed due to the pervasive role of β -catenin in transcription and cell adhesion (Valenta et al., 2011). Given the paramount importance of Wnt signaling, it is essential to clarify whether the upstream cascade of the canonical pathway can act independent of β -catenin transcriptional response by obtaining genetic proof *in vivo*, which is the subject of this study.

One class of cells where confounding transcription-dependent effects of Wnt signaling can be ruled out is spermatozoa. These cells are akin to mitotic cells; i.e., they are arrested in a cell-cycle phase where the chromosomes are condensed and transcription has come to a halt (Braun, 1998). Coincidentally, mitosis is also

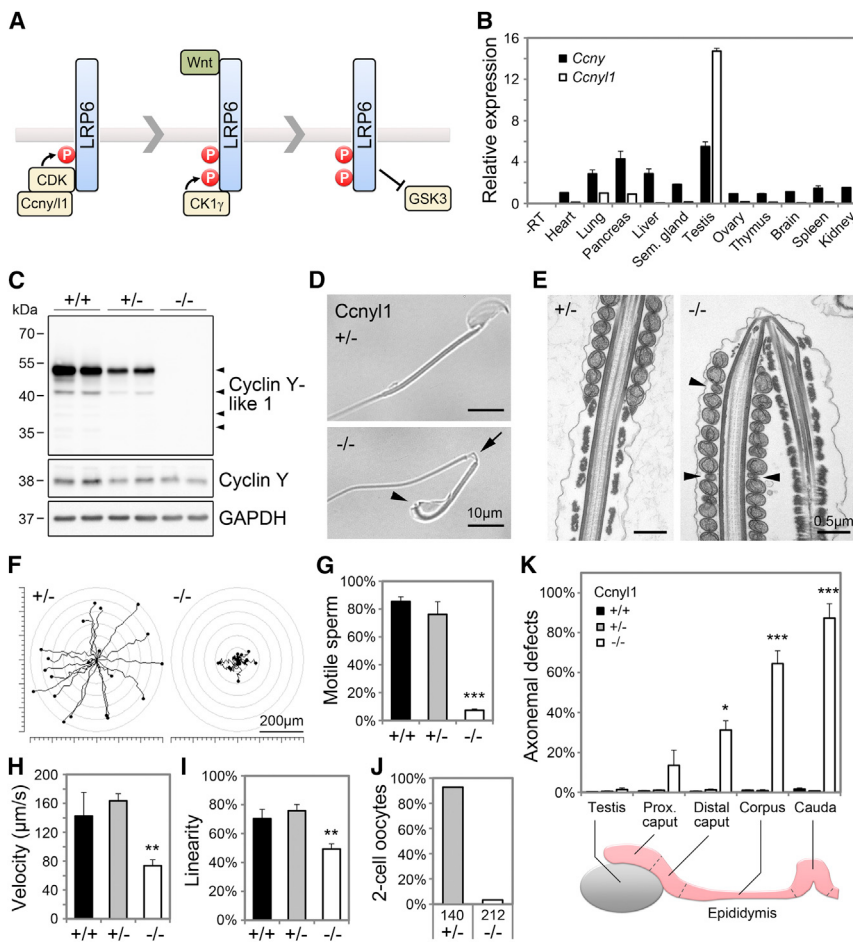


Figure 1. *Ccnyl1* Mutant Mice Show Sperm Maturation Defects

(A) Illustration of Cyclin Y-like 1-dependent LRP6 priming, required for Wnt-induced receptor activation.

(B) qPCR of cyclin Y (*Ccny*) and cyclin Y-like 1 (*Ccnyl1*) in wild-type mouse tissues, normalized to *HPRT*.

(C) Immunoblot of *Ccnyl1* in testis lysates of 2 *Ccnyl1* mutant mice each.

(D) Bright field microscopy highlighting axonemal defects at the annulus (arrow) and connecting piece (arrowhead) of *Ccnyl1* -/- cauda sperm.

(E) Electron micrographs of the annulus region showing axonemal bending and heteromorphic mitochondria (arrowheads) in *Ccnyl1* -/- sperm.

(F) Representative track plots of cauda sperm from *Ccnyl1* +/- and *Ccnyl1* -/- mice. The graphs show 20 sperm each tracked for 2 s.

(G) Quantification of total motile cauda sperm. $n \geq 3$ mice per genotype.

(H and I) Computer-assisted sperm motility analysis showing that the (H) curvilinear velocity and (I) linearity of the remaining motile cauda sperm were significantly decreased in *Ccnyl1* -/- mice.

(J) Quantification of B6/F1 oocytes in 2-cell stage after IVF with *Ccnyl1* mutant cauda sperm. Sperm were pooled from two mice per genotype. The total number of oocytes is indicated below.

(K) Quantification of sperm axonemal defects in different parts of the reproductive tract. *Ccnyl1* -/- sperm exhibit progressive structural defects during epididymal transit. $n = 3$ mice per genotype. See also Figure S1.

the cell-cycle phase where responsiveness to Wnt signaling is expected to peak (Davidson et al., 2009; Hadjihannas et al., 2012; Olmeda et al., 2003). Importantly, germ-cell-specific deletion of β -catenin has no effect on male fertility, with spermatocyte differentiation and sperm maturation proceeding normally (Rivas et al., 2014).

Despite their compacted structure, spermatozoa are not signaling inert. During a week-long maturation process mammalian spermatozoa respond to maturation signals as they transit the epididymis, a coiled tubule connected to the testis. Epididymal maturation of spermatozoa involves changes in protein composition and subcellular localization, necessary for motility and fertilization (Sipilä et al., 2009; Turner, 2008; Yeung and Cooper, 2002). Maturation is thus induced by factors secreted from the epididymis while spermatozoa are transcriptionally silent. The identity of the epididymal maturation factors has remained unresolved. Here, we show that spermatozoa respond to Wnt signals released from the epididymis. The Wnt regulator Cyclin Y-like 1 (*Ccnyl1*) is highly expressed in germ cells, and *Ccnyl1* -/- mice are male sterile due to immotile and malformed spermatozoa. Wnt signaling impacts spermatozoa through GSK3 by (1) reducing global protein poly-ubiquitination to maintain protein homeostasis; (2) inhibiting septin 4 phosphorylation to establish a membrane diffusion

barrier in the sperm tail; (3) and inhibiting protein phosphatase 1 to initiate sperm motility. The results indicate that Wnt signaling orchestrates a post-transcriptional sperm maturation program.

RESULTS

Ccnyl1 Mutant Mice Show Sperm Maturation Defects

To investigate post-transcriptional Wnt signaling in mammalian physiology, we generated mice deficient for cyclin Y-like 1 (*Ccnyl1*) (Figure 1A). In contrast to its ubiquitously expressed homolog *Ccny*, *Ccnyl1* RNA and protein are largely restricted to germ cells in the testis (Figures 1B, 1C, S1A, and S1B). As is the case for *Ccny* (Acebron et al., 2014; Davidson et al., 2009), *Ccnyl1* protein also localizes to the plasma membrane in mammalian cell lines, where it associates with LRP6 and collaborates with *Ccny* in promoting Wnt signaling (Figures S1C–S1E; see also Davidson et al., 2009). *Ccnyl1* -/- mice appeared normal, but male *Ccnyl1* -/- mice were sterile due to severe sperm structural and motility defects. Sperm tails displayed hairpin bending at the annulus (Figure 1D) and in electron microscopy presented axonemal breakage at the junction between midpiece and principal piece (Figure 1E). Additionally, *Ccnyl1* -/- sperm exhibited heteromorphic mitochondria and a partial denudation of the distal midpiece

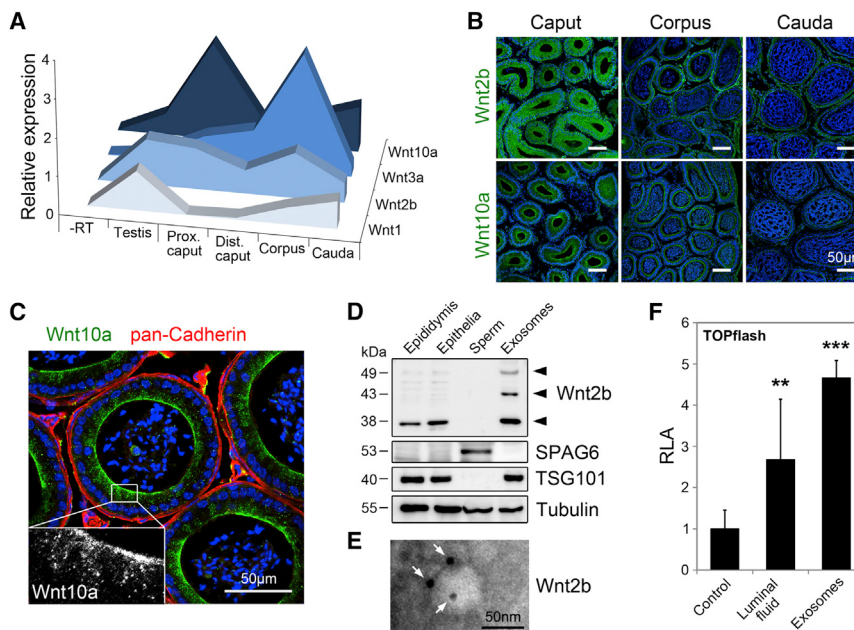


(Figure 1E). Moreover, *Ccny1*^{-/-} sperm showed a severe motility defect, with less than 10% of mutant sperm exhibiting progressive motility, while sperm movement was unaffected in heterozygous mice (Figures 1F and 1G). Residual motile mutant spermatozoa had reduced curvilinear velocity and linearity (Figures 1H and 1I). Consequently, *Ccny1*^{-/-} sperm had a greatly reduced capacity to fertilize wild-type oocytes in vitro (Figure 1J). Thus, loss of *Ccny1* results in a complex sperm structure and motility phenotype, ultimately causing male infertility (see also Zi et al., 2015).

Dysfunctional spermatozoa can arise from defects in spermatogenesis and spermiogenesis in the testis, or aberrant sperm maturation during epididymal transit. Analysis of sperm from different regions of the male reproductive tract revealed that the hairpin phenotype appeared gradually (Figure 1K), suggesting a defect in sperm maturation. In agreement with this interpretation, total caudal sperm count, meiotic cell divisions, and germ cell differentiation in the testis were unaffected in *Ccny1*^{-/-} mice (Figures S1F–S1H). Moreover, testicular *Ccny1*^{-/-} sperm were indistinguishable from controls and exhibited no axonemal damage (Figure S1I). Similarly, the epididymides of *Ccny1*^{-/-} mice showed no structural abnormalities, and the distribution of major epididymal cell populations was unchanged compared to controls (Figures S1J and S1K). This indicates that the cellular malformations result from a sperm-intrinsic defect manifesting during epididymal transit.

Exosomal Wnt Signaling in the Epididymis

Consistent with a role for Wnt signaling in epididymal sperm maturation, qPCR showed expression of multiple Wnt ligands in the epididymis, including the canonical Wnt ligands *Wnt1*,

Figure 2. Exosomal Wnt Signaling in the Epididymis

(A) Real-time RT-PCR identified site-specific expression of indicated Wnt ligands in different parts of the male reproductive tract. The graph depicts the mean expression levels of six wild-type mice.

(B) Immunostaining of wild-type mouse epididymides showing a proximal-to-distal gradient of Wnt2b and Wnt10a protein.

(C) Immunolocalization of Wnt10a in caput epididymal sections of wild-type mice showing vesicle-like punctae that accumulate at the apical plasma membrane. The tubule margin is indicated by pan-Cadherin staining.

(D) Immunoblot of Wnt2b in exosome-enriched epididymal vesicle fractions of wild-type mice. Note the molecular weight shift of Wnt2b, characteristic for mature Wnt ligands.

(E) Immunogold labeling of Wnt2b in epididymal exosomes of wild-type mice. Arrows highlight the Wnt2b staining.

(F) Epididymal luminal fluid and exosomes were used for TOPflash reporter assays in HEK293T cells. Tissue from eight to ten wild-type mice was pooled for each experiment. The graph is representative of two experiments and shows relative luciferase activity (RLA) \pm SD.

See also Figure S2.

Wnt2b, *Wnt3a*, and *Wnt10a* (Figure 2A) (Wang et al., 2013). Interestingly, these Wnts displayed compartmentalized expression patterns within the epididymis, and immunostaining of Wnt2b and Wnt10a in particular showed a proximal-to-distal protein gradient (Figures 2B and S2A). Active Wnt signaling in the proximal epididymis was confirmed by examining *BAT-gal* reporter mice, which express nuclear β -galactosidase under the control of β -catenin/TCF (Marett et al., 2003) (Figure S2B). Reporter activity in these mice correlated with Wnt protein expression; i.e., it was high in the caput epididymis where peak Wnt2b and Wnt10a protein levels were seen but virtually absent in the cauda (Figures S2C and S2D). Interestingly, Wnt10a accumulated in vesicle-like punctae at the apical plasma membrane of epididymal principal cells (Figure 2C). This pattern is characteristic for vesicles released as epididymal exosomes, which are essential for sperm maturation (Sullivan et al., 2007). Since Wnt ligands can be transported on epithelial exosomes to facilitate long-range Wnt signaling (Gross et al., 2012; Luga et al., 2012), we asked whether epididymal exosomes can activate Wnt signaling. We therefore isolated extracellular vesicles from epididymal luminal fluid (Figures 2D and 2E). This exosome-enriched fraction harbored mature Wnt2b, which in immunoelectron microscopy localized to vesicles (Figures 2E and 2F). Importantly, this vesicle fraction robustly induced Wnt signaling in vitro (Figure 2F). In *Ccny1*^{-/-} mice, epididymal Wnt activity was unaffected, and there was no difference in Wnt signaling in testis and epididymis (Figures S2E and S2F). We conclude that (1) the epididymis expresses multiple Wnt genes, (2) Wnt signaling decreases from caput to cauda, and (3) the epididymis releases active Wnt ligands on exosomes into the epithelial lumen.

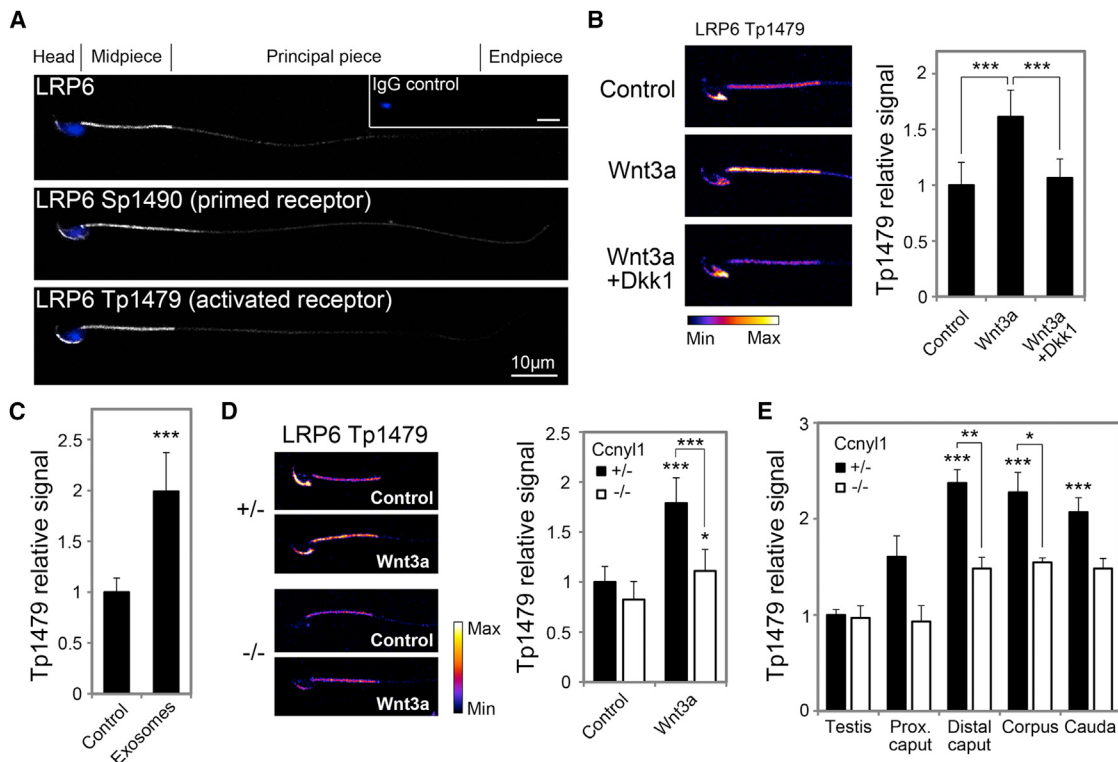


Figure 3. Mammalian Spermatozoa Are Wnt-Responsive Cells

(A) Immunostaining of LRP6 with the indicated antibodies in wild-type mouse cauda sperm showed localization along the tail, which was largely restricted to the midpiece, with sporadic staining in the acrosomal cap.

(B) Immunostaining of wild-type cauda sperm treated with Wnt3a CM for 1 hr showed increased LRP6 Tp1479 staining in the midpiece, which was blocked by co-administration of recombinant Dkk1. Exemplary heatmaps are shown on the left. The average signal intensity along the midpiece was measured and normalized to control treated sperm. n = 6 mice.

(C) Relative Tp1479 staining intensity in sperm treated with epididymal exosomes for 1 hr was increased compared to controls. n = 3 wild-type mice.

(D) Ccnyl1^{-/-} sperm showed both lower basal LRP6 activity and reduced Wnt responsiveness. Heatmaps are shown on the left. n = 5 mice per genotype.

(E) Endogenous LRP6 activity monitored by Tp1479 staining in sperm isolated from indicated parts of the reproductive tract, normalized to total LRP6. Ccnyl1^{-/-} mice exhibited reduced Tp1479 signal in all areas of the epididymis compared to controls. n = 5 mice per genotype.

See also Figure S3.

Mammalian Spermatozoa Are Wnt-Responsive Cells

Is it possible then that Wnt ligands signal to transcriptionally silent sperm? Active Wnt signaling can be monitored with LRP6 antibodies specific for the CK1 γ phosphorylation site Tp1479 ("active LRP6") (Davidson et al., 2005), adjacent to the cyclin Y/CDK14 priming phosphorylation site Sp1490 ("primed LRP6") (Figure 1A). Both primed and active LRP6 proteins were detectable in mouse and bull spermatozoa, where they primarily localized to the midpiece, with additional staining in the head (Figures 3A and S3A). LRP6 activation was induced by exogenous Wnt3a treatment and was blocked by addition of the Wnt antagonist Dkk1 (Figures 3B and S3B). Additionally, epididymal exosomes activated LRP6 ex vivo (Figure 3C). Endogenous LRP6 phosphorylation was highest in sperm collected from the distal caput epididymis of wild-type mice (Figure S3C), consistent with peak Wnt signaling activity in this region, and decayed rapidly after removal of sperm from the epididymis (Figure S3D). Importantly, Ccnyl1^{-/-} sperm had a blunted response to stimulation with exogenous Wnt3a, and they exhibited reduced LRP6 activation in all parts of the epidid-

ymis (Figures 3D and 3E). Taken together, the data (1) identify mammalian spermatozoa as Wnt-responsive cells and (2) suggest that deficiency in Ccnyl1-dependent Wnt signal transduction leads to malformed spermatozoa during their epididymal transit.

Ccnyl1 Mutant Spermatozoa Show Reduced Wnt/STOP Signaling

Since the results suggested that Wnts act as sperm maturation factors in the epididymis, we tested the involvement of Wnt/STOP signaling (Acebron et al., 2014). In this signaling mode, Ccnyl-dependent Wnt signaling protects part of the proteome from GSK3-dependent ubiquitination and proteasomal degradation, independent of β -catenin (Figure 4A). Consistent with this model, Ccnyl1^{-/-} cauda sperm showed globally increased K48-linked protein ubiquitination (Figure 4B). In immunofluorescence analysis, bulk ubiquitinated proteins co-localized with proteasomes (20S subunit α 5) in the sperm tail, in particular, in the distal midpiece of Ccnyl1^{-/-} cells (Figure 4C). Moreover, protein levels of several Wnt/GSK3 targets, including

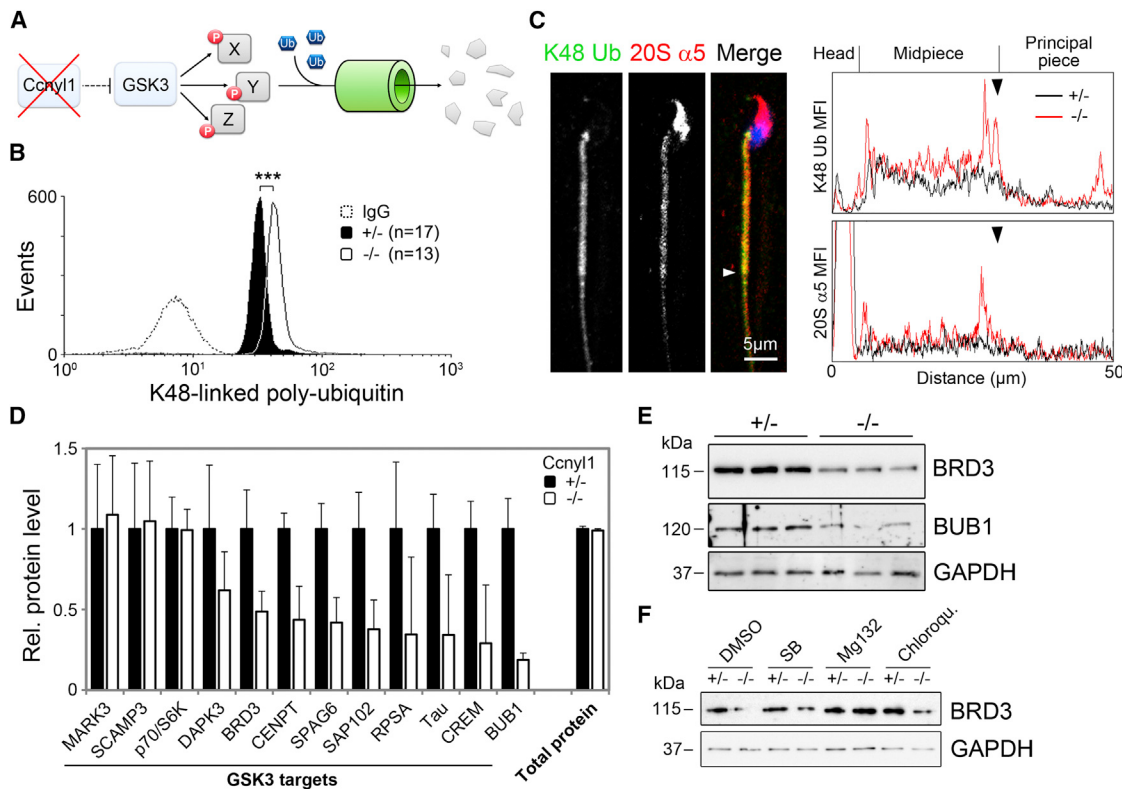


Figure 4. *Ccny1*^{-/-} Spermatozoa Show Reduced Wnt/STOP Signaling

(A) Schematic depiction of GSK3-dependent destabilization of target proteins by phosphorylation, which leads to protein ubiquitination and proteasomal degradation.

(B) Fluorescence-activated cell sorting (FACS) profile of K48-linked poly-ubiquitin in cauda sperm of *Ccny1* mutant mice.

(C) Co-immunolocalization of K48-linked poly-ubiquitin and 20S proteasomal subunit α 5 in *Ccny1*^{-/-} cauda sperm showed overlapping staining in the distal midpiece. Representative profile plots of the mean fluorescence intensity (MFI) are shown on the right. Arrowheads indicate the position of the annulus.

(D) The protein level of GSK3 targets in cauda sperm samples were determined by immunoblot and normalized to GAPDH. Total protein levels were measured by bicinchoninic acid assay. n = 3–6 mice per genotype.

(E) Exemplary immunoblot of GSK3 target proteins BRD3 and BUB1 in sperm lysates of three *Ccny1* mutant mice each.

(F) BRD3 levels in *Ccny1* mutant cauda sperm after treatment with GSK3 inhibitor SB-216763 (20 μ M), proteasomal inhibitor Mg132 (10 μ M), or lysosomal inhibitor chloroquine (16 μ M) for 6 hr at 37°C. Sperm were pooled from four mice per genotype.

See also Figure S4.

Bromodomain-containing protein (BRD) 3 and serine/threonine protein kinase BUB1 (Acebron et al., 2014; Taelman et al., 2010; Xu et al., 2009), were markedly decreased in *Ccny1*^{-/-} sperm, whereas other specific proteins and bulk protein were unaffected (Figures 4D and 4E).

Importantly, treatment of sperm with inhibitors against GSK3, proteasome, or to a lesser extent lysosome increased BRD3 levels in *Ccny1*^{-/-} cells (Figure 4F), suggesting that the sperm proteome is subject to GSK3-dependent degradation. We conclude that *Ccny1*^{-/-} spermatozoa show aberrant GSK3/ubiquitination-dependent protein degradation. It has been proposed that sperm GSK3 activity is regulated by inhibitory serine phosphorylation (Somanath et al., 2004). However, in *Ccny1*^{-/-} sperm, which exhibit enhanced GSK3 activity, GSK3 serine phosphorylation was unchanged in caput epididymal sperm, and even increased in caudal sperm (Figure S4), indicating that PKB/GSK3-dependent derepression of GSK3 does not account for increased GSK3 activity in *Ccny1*^{-/-} mice.

Post-transcriptional Wnt Signaling Regulates Sperm Diffusion Barrier Function via Septin 4

Considering the large number of potential GSK3 target proteins that may be misregulated in *Ccny1*^{-/-} sperm, their complex mutant phenotype may result from loss-of-function of multiple proteins. Yet, we sought to identify key regulators of sperm maturation that are controlled by GSK3. An intriguing candidate GSK3 target is septin 4, knockout mice of which share many features of *Ccny1* mutants, including male sterility, sperm tail hairpin bending, and dysmorphic mitochondria (Kissel et al., 2005; Matsuda et al., 2005). Septin 4 is a filament-forming GTPase, which during sperm maturation is required for the formation of a membrane diffusion barrier at the annulus, a cortical ring separating the midpiece and principal piece of the sperm tail (Figure 5A). Sequence inspection of septin 4 revealed three putative GSK3 phosphorylation sites in its N-terminal proline-rich domain (S68, S100, and S107), of which the latter two are highly conserved in vertebrates (Figure 5B). Of note, these sites are also

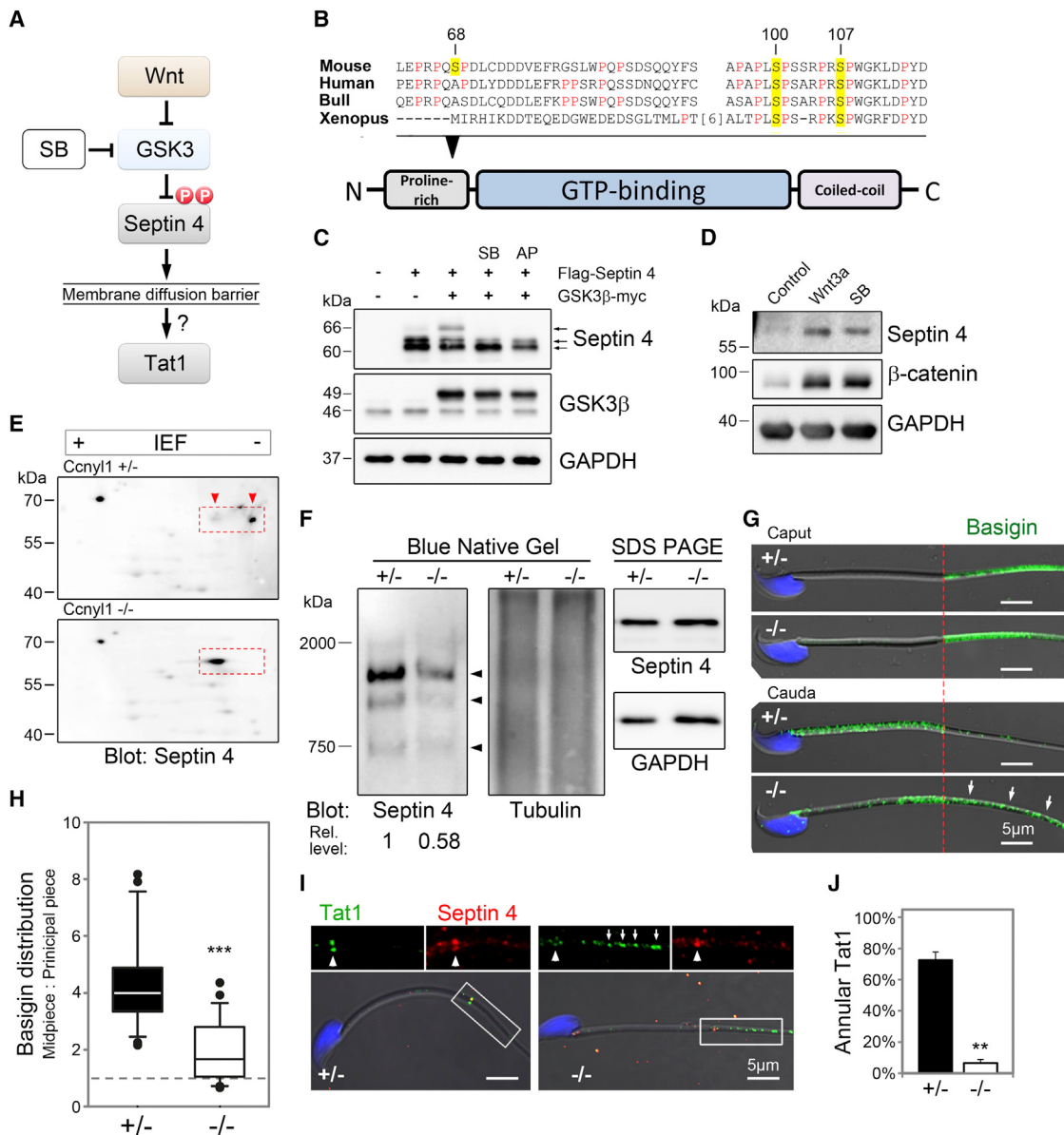


Figure 5. Wnt Signaling Regulates Sperm Diffusion Barrier Function via Septin 4

(A) Schematic presentation of the investigated signaling module.

(B) Partial sequence alignment of septin 4. Multiple putative phosphorylation sites (yellow) were identified in the N-terminal proline-rich domain. Proline residues are highlighted in red. Numbers indicate amino acid positions in the mouse protein.

(C) Immunoblot of mouse Flag-septin 4 co-expressed with GSK3 β -myc in HEK293T cells with or without GSK3 inhibitor (SB) or alkaline phosphatase treatment (AP). GSK3 induced increased septin 4 phosphorylation. Arrows indicate major septin 4 species.

(D) Mouse spermatocyte-derived GC-2spd cells were treated with Wnt3a CM or SB for 72 hr. Both treatments increased endogenous septin 4 protein levels.

(E) Cauda sperm were analyzed by 2D gel electrophoresis. Arrowheads highlight a mobility shift of septin 4 in Ccnyl1 $^{-/-}$ sperm.

(F) Protein extracts from cauda sperm were analyzed by blue native gel electrophoresis, which showed a loss of high-molecular-weight septin 4 complexes in Ccnyl1 $^{-/-}$ cells (arrowheads). Membranes were reprobed for α -tubulin. An aliquot of each sample was subjected to reducing SDS electrophoresis to confirm equal loading. Data in (E) and (F) are representative of three independent experiments with samples pooled from three to five mice per genotype.

(G) Representative staining of basigin showing loss of diffusion barrier integrity specifically in cauda epididymis sperm of Ccnyl1 $^{-/-}$ mice. The position of the annulus is indicated by the red line. Arrows highlight aberrant localization of basigin in the principal piece.

(H) Quantification of basigin distribution in Ccnyl1 mutant cauda sperm. n = 3 mice per genotype.

(I) Co-localization of Tat1 and septin 4 in the sperm tail. Boxed areas are magnified above. Arrowheads indicate the position of the annulus. Arrows highlight mislocalized Tat1 in Ccnyl1 $^{-/-}$ sperm.

(J) Quantification of Tat1 annular localization in Ccnyl1 mutant cauda sperm. n = 3 mice per genotype.

See also Figure S5.

found in the pro-apoptotic septin 4 splice variant ARTS, which in sperm is implicated in protein degradation (Kissel et al., 2005). Co-expression of septin 4 with GSK3 β in HEK293T cells induced a phosphorylation super-shift that was blocked by GSK3 inhibition (Figure 5C). Mutation of individual or all putative phosphorylation sites identified S100 as the major GSK3 target residue, while S107 most likely acts as a priming site that can also be phosphorylated by other kinases (Sitz et al., 2008) (Figure S5A). Septin 4 physically associated with endogenous GSK3 (Figure S5B); however, this interaction was inhibited when either one or all of the putative phosphorylation sites were replaced with alanine. In addition, in HeLa cells expression of GSK3 β reduced septin 4 levels by protein destabilization, which was partially rescued by mutation of S100 and S107 (Figures S5C–S5F). Moreover, in mouse spermatocyte-derived GC-2spd cells, Wnt3a treatment or pharmacological GSK3 inhibition increased endogenous septin 4 levels (Figure 5D).

In sperm, Wnt signaling alters the polymerization properties of septin 4, rather than promoting its stabilization. In *Ccny1* $^{−/−}$ sperm, septin 4 levels were unchanged, but 2D gel electrophoresis showed a shift of septin 4 toward the positive pole, consistent with increased GSK3-dependent phosphorylation (Figure 5E). Moreover, septin 4 isolated from mutant sperm failed to form high-molecular-weight complexes, as revealed by blue native gel electrophoresis (Figure 5F). Septins form a membrane diffusion barrier at the annulus, and this barrier function restricts the localization of proteins, including basigin (Kwitny et al., 2010). In caput sperm, basigin is confined to the principal piece and undergoes relocation to the midpiece during sperm epididymal transit (Figure 5G). In *Sept4* $^{−/−}$ sperm basigin localizes over the whole tail length (Kwitny et al., 2010). *Ccny1* $^{−/−}$ sperm exhibited normal basigin localization in caput sperm but lost midpiece restriction during epididymal transit toward the cauda (Figures 5G and 5H), in line with an epididymal maturation defect. Moreover, the testis anion transporter 1 (Tat1/Slc26a8), which normally localizes to the sperm annulus and is essential for sperm terminal differentiation (Touré et al., 2007), was dispersed along the tail in the majority of *Ccny1* $^{−/−}$ sperm (Figures 5I and 5J).

It was suggested that during epididymal transit spermatozoa receive an unknown signal that triggers a post-translational modification of, e.g., septins, which opens a one-way gate to regulate protein diffusion in the sperm tail (Kwitny et al., 2010). Our results support this idea, whereby epididymal Wnt signaling inhibits GSK3, a septin 4 kinase, which negatively regulates the barrier function of septin filaments.

Wnt Signaling Unlocks Sperm Motility through GSK3

Although the morphological changes of *Ccny1* $^{−/−}$ sperm are consistent with septin 4 malfunction, this may not satisfactorily explain the reduced motility of overtly normal sperm (Figure 1H). It is known that the potential for motility already exists in immature sperm, and that serine/threonine protein phosphatase 1 (PP1) holds motility in check before epididymal passage (Vijayaraghavan et al., 1996). PP1 is a ubiquitous enzyme that dephosphorylates a wide range of protein substrates, and that is kept in an active state by GSK3-dependent phosphorylation of its inhibitory subunit PPP1R2 (Cohen, 1989; Vijayaraghavan et al.,

1996). Together with our findings, this suggests a simple mechanism for inducing sperm motility during epididymal transit: Caput Wnt signals inhibit GSK3 and thereby inactivate PP1, thus removing the roadblock to sperm motility (Figure 6A). To test this model, we first confirmed phosphorylation of PPP1R2 T72 by GSK3, using two GSK3 inhibitors in HeLa cells (Figure S6A). PPP1R2 Tp72 was greatly increased in mitotic compared to non-mitotic HeLa cells and was reduced by Wnt3a treatment (Figures 6B and S6B). PPP1R2 phosphorylation was also greatly increased in *Ccny1* $^{−/−}$ sperm (Figure 6C), and this should lead to higher PP1 activity and hence reduced protein phosphorylation. Indeed, total phospho-serine in the tail of *Ccny1* $^{−/−}$ sperm was markedly reduced (Figure 6D). The phospho-serine differences, as well as changes in protein ubiquitination (Figure 4B), were only apparent in epididymal spermatozoa, but not in sperm progenitor cells or somatic cells in testis and epididymis, and they were not caused by differential gene expression (Figures S6C–S6F). Moreover, GSK3 inhibition was sufficient to increase pan-serine phosphorylation in caput sperm of *Ccny1* $^{−/−}$ mice (Figure S6G). Consistent with these findings, Wnt3a stimulation or pharmacological GSK3 inhibition both increased the velocity of submotile spermatozoa isolated from the distal caput epididymis of wild-type mice (Figure 6E). Likewise, in *Ccny1* heterozygous mice, Wnt3a, the GSK3 inhibitor BIO, and phosphatase inhibitor okadaic acid significantly increased the velocity of caput sperm to approximately the same extent (Figure 6F). In contrast, *Ccny1* $^{−/−}$ sperm completely failed to respond to Wnt3a. However, inhibition of either GSK3 or phosphatase, which act downstream of *Ccny1* in the Wnt-PP1 cascade, partially rescued their motility.

Since motility defects are a major cause of male infertility, we also analyzed human sperm. We confirmed that (phospho)-LRP6 localizes to the midpiece of human testicular spermatozoa (Figure 6G). We then treated two independent disaggregated testicular biopsies with Wnt3a, or okadaic acid as a positive control. Wnt treatment increased the number of sperm with notable flagellar beating in both samples approximately twofold (Figure 6H). Low Wnt signaling in sperm could potentially be a cause for male infertility, and analysis of a published data set (Platts et al., 2007) showed that sperm from men with teratozoospermia, i.e., structural defects of the sperm, show remarkably reduced *Ccny1* RNA levels (Figure S6H).

Sperm Maturation Involves Epididymal Wnt Signaling and the Axin/APC Complex

We confirmed the requirement for epididymal Wnt signaling in sperm maturation by transgenic overexpression of the Wnt antagonist Dkk1 in the proximal epididymis. Mice harboring the proximal epididymis-specific *Lcn5-CreERT2* (Xie et al., 2013) were crossed with *Rosa26-Dkk1* mice, containing a floxed transcriptional stop signal (Wu et al., 2008). Tamoxifen injection in *Lcn5-CreERT2/Rosa26-Dkk1* mice induced moderate *Dkk1* expression in the caput epididymis (Figures S7A and S7B). *Dkk1* induction partially phenocopied the sperm phenotype of *Ccny1* $^{−/−}$ mice, including reduced LRP6 activation, increased PPP1R2 Tp72 levels, and decreased pan-serine phosphorylation (Figures 7A–7E). Importantly, sperm motility was significantly decreased following tamoxifen

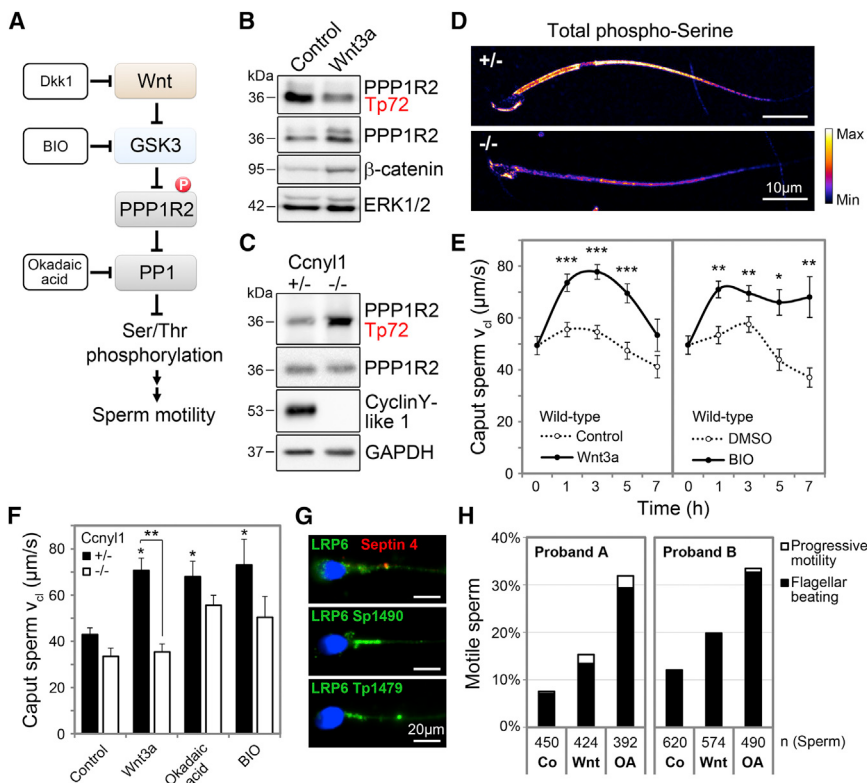


Figure 6. Wnt Signaling Unlocks Sperm Motility via GSK3

(A) Schematic representation of the investigated signaling module, and its inhibitors.

(B) Immunoblot of PPP1R2 phosphorylation in G₂/M-synchronized HeLa cells. Wnt3a reduced PPP1R2 inhibition.

(C) Representative immunoblot of PPP1R2 Tp72 in Ccny1^{-/-} mutant cauda sperm lysates pooled from three mice per genotype.

(D) Heatmap of serine phosphorylation in cauda sperm. Staining in the tail was decreased in Ccny1^{-/-} cells.

(E) Wild-type sperm isolated from the distal caput epididymis were incubated with Wnt3a-conditioned media or 1 μM BIO, and curvilinear velocity was measured at the indicated times. n = 5 mice.

(F) Caput sperm were incubated with Wnt3a CM,

okadaic acid, or BIO, and the velocity of motile

sperm was measured after 3 hr. Ccny1^{-/-} cells did not respond to Wnt3a but showed increased motility following phosphatase and GSK3 inhibition.

(G) LRP6 staining in human testicular sperm.

Primed and active receptor localized to the mid-

piece, as in mouse and bull sperm. The annulus is

indicated in the top panel by septin 4 staining.

(H) Quantification of sperm motility in testicular

biopsies of two volunteers. Wnt treatment

increased the number of motile sperm in both

cases. OA, Okadaic acid.

See also Figure S6.

injection in *Lcn5-CreERT2/Rosa26-Dkk1* mice, but not in control animals (Figures 7F and S7C). These results corroborate that Wnt signals trigger the cascade that inhibits PP1 and activates motility as immature sperm pass through the epididymis.

To further corroborate the cell-autonomous Wnt signaling defect, we assessed the involvement of the GSK3/Axin/APC destruction complex in sperm maturation and Wnt/STOP. The tankyrase inhibitor XAV-939, which stabilizes Axin and thereby inhibits Wnt signaling (Huang et al., 2009), increased GSK3-dependent PPP1R2 phosphorylation in wild-type sperm (Figure 7G), decreased pan-serine phosphorylation in the sperm tail (Figure 7H), and blocked the Wnt-induced increase in caput sperm motility (Figure 7I). Moreover, XAV treatment increased overall protein ubiquitination in sperm, consistent with reduced Wnt/STOP (Figure S7D). Conversely, APC loss of function, which upregulates Wnt signaling, reduced PPP1R2 phosphorylation in MDA-MB-231 cells in vitro (Figure 7J). In addition, total serine phosphorylation and sperm motility were increased in APC^{min} sperm (Figures 7K and 7L), as was the stability of Wnt/STOP targets BRD3 and CREM (Figure S7E). Collectively, these observations outline a critical role for the GSK3/Axin/APC complex in sperm maturation and Wnt/STOP.

DISCUSSION

Wnts Act as an Epididymal Sperm Maturation Signal

The role of the epididymis in sperm maturation is well established, but the secreted signals inducing the maturation

process are poorly understood. The first main conclusion of this study therefore is the discovery of Wnts as an epididymal sperm maturation signal. Our results support the following model: Wnt ligands produced by epithelial cells in the proximal epididymis are released into the lumen on signaling-competent exosomes, where they signal to transitioning spermatozoa. Epididymal Wnt ligands activate LRP6, which is phospho-primed via Ccny1. Wnt signaling inhibits GSK3, to promote sperm maturation through at least three distinct mechanisms: (1) inhibiting protein poly-ubiquitination to maintain protein homeostasis (Wnt/STOP signaling); (2) promoting septin 4 polymerization, thereby maintaining the annular protein diffusion barrier; and (3) inhibiting PP1 to unlock sperm motility. In Ccny1^{-/-} mutants, GSK3 fails to be inhibited, leading to sperm structural and motility defects and infertility.

The results indicate that Wnt signaling is particularly important in the caput epididymis, since LRP6 phosphorylation peaked in caput spermatozoa, and Wnt inhibition in the caput was sufficient to block sperm maturation. Moreover, Wnt reporter activity was most prominent in caput epididymis, which expresses high levels of β-catenin (Wang et al., 2013). Wnt ligands with high expression in the caput epididymis include *Wnt10a*, *Wnt2b*, and *Wnt1*, but *Wnt10a* and *Wnt2b* mutants apparently do not display male fertility deficits (Tsukiyama and Yamaguchi, 2012; Yang et al., 2015), while *Wnt1*-null mutants die perinatally (McMahon and Bradley, 1990). Multiple Wnts may

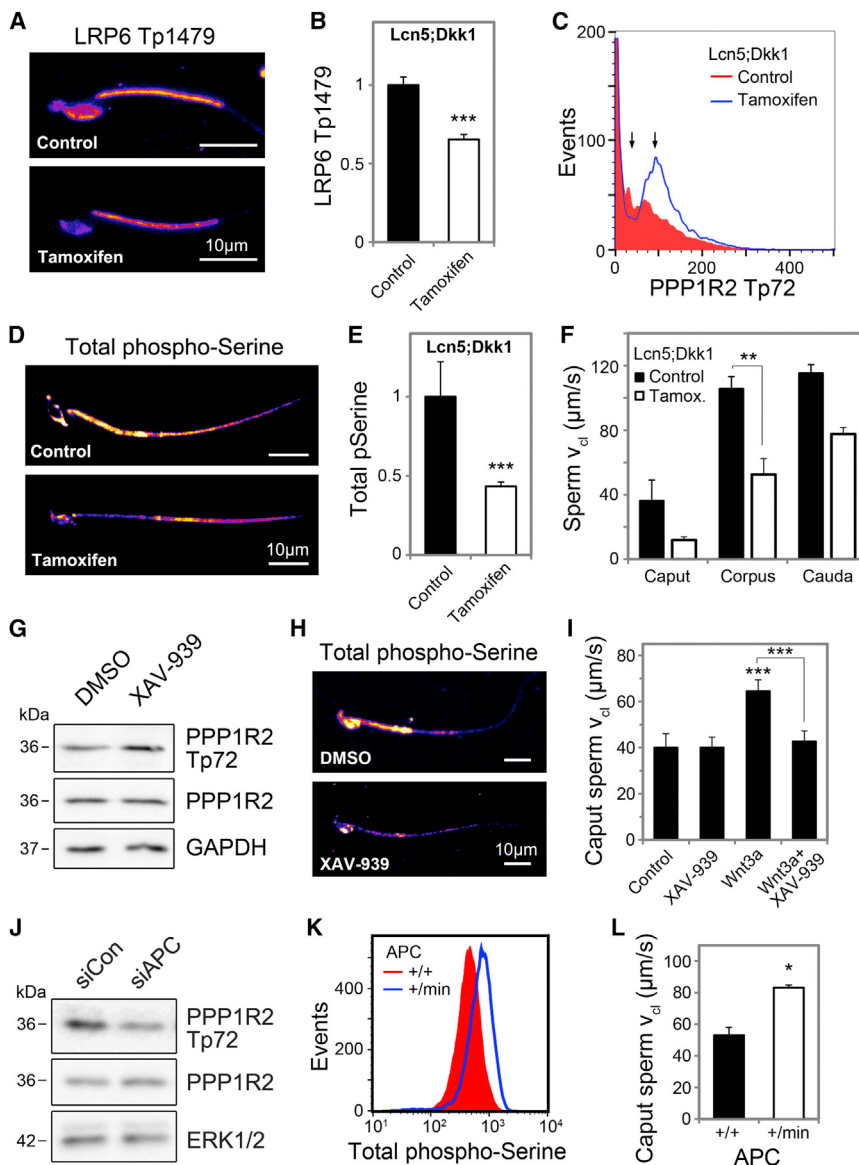


Figure 7. Sperm Maturation Involves Epididymal Wnt Signaling and the Axin/APC Complex

(A) Heatmaps and (B) quantification of LRP6 Tp1479 staining in *Lcn5-CreERT2/Rosa26-Dkk1* (*Lcn5;Dkk1*) cauda sperm following *Dkk1* induction. n = 3 mice per group.

(C) Flow cytometric analysis of PPP1R2 phosphorylation in *Lcn5;Dkk1* cauda sperm. Samples were pooled from three mice per group.

(D and E) Heatmaps (D) and quantification (E) of total serine phosphorylation in *Lcn5;Dkk1* sperm. n = 3 mice per group.

(F) Sperm motility analysis of *Lcn5;Dkk1* mice. Motility was markedly decreased in all regions of the epididymis after *Dkk1* induction. n = 3 mice per group.

(G) Immunoblot of PPP1R2 phosphorylation in wild-type sperm treated with 5 μM tankyrase inhibitor XAV-939 for 1 hr.

(H) Heatmaps of total serine phosphorylation in wild-type sperm treated with XAV-939 for 1 hr. Samples in (G) and (H) were pooled from eight mice.

(I) Sperm motility analysis after treatment with Wnt3a-conditioned medium and XAV-939 for 1 hr. n = 4 wild-type mice.

(J) Immunoblot of PPP1R2 phosphorylation following APC depletion in MDA-MB-231 cells for 24 hr.

(K) FACS profile of total serine phosphorylation in APC^{min} cauda sperm. Samples were pooled from three mice per group.

(L) Motility analysis of APC^{min} sperm. n = 3 mice per group.

See also Figure S7.

therefore function redundantly and co-operatively in sperm maturation.

Previous studies with various Wnt pathway mutants have implicated Wnt signaling in adult testicular spermatogenesis, including germ cell apoptosis, differentiation, and proliferation (Boyer et al., 2012; Das et al., 2013; Li et al., 2005), but not in epididymal sperm maturation. The severe spermatogenic defects in previous genetic mouse models likely masked later defects in sperm maturation. Importantly, however, β-catenin is dispensable for all steps of spermatocyte development and sperm maturation (Rivas et al., 2014), consistent with our model of Wnts as post-transcriptional maturation signal. Interestingly, mutants of *Cdk16*, one of the five *Ccny*-dependent CDKs (CDK14 to 18), show sperm maturation deficits similar to *Ccny1* mice, and the two proteins can interact in vivo (Mikolcevic et al., 2012; Zi et al., 2015), suggesting that a *Ccny1/CDK16* complex mediates Wnt signaling during

sperm maturation. *Cdk16* mutants additionally display terminal spermatogenesis defects, and this somewhat severer phenotype compared to *Ccny1*^{-/-} sperm is probably due to partial redundancy of *Ccny1* with *Ccny*.

We note finally that the involvement of a druggable signaling pathway in sperm maturation may provide new opportunities for male infertility and contraception.

Post-transcriptional Wnt Signaling through a Canonical Upstream Cascade

It is commonly thought that the Wnt-Fzd-LRP-GSK3 signaling module acts predominantly by regulating β-catenin and its target genes. Various arguments have been raised against canonical Wnt signaling regulating proteins other than β-catenin (reviewed in, e.g., Metcalfe and Bienz, 2011; Wu and Pan, 2010). The main controversy is whether Wnt signaling regulates phosphorylation of kinase substrates beyond β-catenin and whether this is physiologically relevant. Studying this question genetically *in vivo* is challenging due to the pervasive role of Wnt signaling in transcriptional regulation. Here, we establish sperm maturation as the first genetic model to study Wnt signaling by the upstream

canonical pathway, where confounding transcriptional effects can be ruled out. Hence, the second main conclusion of this study is that post-testicular sperm are Wnt responsive, i.e., that Wnt signaling acts in transcriptionally silent sperm cells. Our data support the concept that the upstream canonical Wnt pathway can elicit a rich post-transcriptional response (Acebron et al., 2014; Kim et al., 2009; Taelman et al., 2010; Vinyoles et al., 2014).

We identified a number of Wnt/STOP target proteins in sperm and showed that stabilization of proteins is but one of the post-transcriptional functions of the Wnts that govern sperm maturation. Another role of Wnt signaling is to regulate protein function of septin 4 and the activity state of PP1 via PPP1R2. Septins are GTPases involved in cytokinesis, and hence our results suggest septin 4 to be a target of post-transcriptional Wnt signaling also in mitosis in somatic cells. In addition, the septin 4 variant ARTS is known to regulate critical homeostatic functions such as stem cell apoptosis and calcium signaling (Fuchs et al., 2013; Sharma et al., 2013) and may similarly be under Wnt control in somatic cells. PP1 regulates the β -catenin degradation complex (Kim et al., 2013; Luo et al., 2007), and hence in somatic cells Wnt signaling may inhibit PP1 possibly in a negative feedback loop.

Wnt signaling is thought to target a sub-pool of GSK3 in complex with the scaffold protein Axin, and only this pool of GSK3 β participates in Wnt signaling and is insulated from other inhibitory signals, such as HGF and insulin (reviewed in Wu and Pan, 2010). GSK3 substrates other than β -catenin also require Axin for Wnt regulation (Acebron et al., 2014; Huang et al., 2015; Inoki et al., 2006; Kim et al., 2009, 2015; Stolz et al., 2015; Taelman et al., 2010; Vinyoles et al., 2014). This indicates that Axin mediates Wnt pathway insulation also in post-transcriptional Wnt signaling. Limiting amounts of Axin may achieve this by undergoing phosphorylation-dephosphorylation cycles, proposed to stabilize β -catenin (and presumably other GSK3 targets as well) across broad component stoichiometries (Kim et al., 2013). In agreement with this model, we found that both Axin and APC are involved in the regulation of sperm maturation and Wnt/STOP, which corroborates that the destruction complex is involved in regulation of proteins other than β -catenin.

In conclusion, we show that Wnt signaling elicits an unexpectedly rich response in transcriptionally silent spermatozoa. In light of this important lesson from germ cells, it appears fruitful to revisit also in somatic cells the degree to which Wnt signaling exerts its effects post-transcriptionally, notably during mitosis. There is evidence that Wnt pathway components upstream of mutated β -catenin or APC are also relevant in tumorigenesis (e.g., SFZD1 and DKK1; Vincan and Barker, 2008), and hence targeting of post-transcriptional Wnt signaling may offer new pharmaceutical avenues.

EXPERIMENTAL PROCEDURES

Mice

Sperm from mice carrying a flanked by loxP (floxed) allele of cyclin Y-like 1 (*Ccnyl1*^{tm1a(EUCOMM)Wtsi}/*H*) was obtained from the European Mouse Mutant Archive (EMMA) and used for in vitro fertilization of wild-type C57BL/6N oocytes. Heterozygous *Ccnyl1*-flox mice were bred with transgenic animals expressing Cre recombinase under the control of CMV promoter to achieve organism-wide gene knockout. β -catenin/TCF reporter mice (BAT-gal; Maretto

et al., 2003) in a C57BL/6J genetic background were purchased from The Jackson Laboratory and bred with *Ccnyl1*-null mice. Mice with or without reporter element showed identical sperm phenotypes and were used interchangeably in most experiments. *Lcn5-CreERT2* mice were generated as reported (Xie et al., 2013). *APC*^{min} and R26-Dkk1 mice harboring full-length mouse Dkk1 with a floxed transcriptional stop signal have been described (Moser et al., 1990; Wu et al., 2008). Wild-type (C57BL/6N) mice were obtained from Charles River Laboratories. All mouse experiments were approved by the State review board of Baden-Württemberg (protocol no. G159/13 to S.K. and C.N.) and performed according to federal and institutional guidelines.

Human Samples

Acquisition of human testicular biopsies was approved by the institutional review board at the University of Heidelberg Medical Center (protocol no. S-267/2014 to G.H.). Samples were obtained from volunteers undergoing scheduled surgery for testicular sperm extraction (TESE), following written, informed consent.

Data Analysis

Data were analyzed with an unpaired Student's t test in Excel 2007 (Microsoft) or Holm-Sidak post hoc test following one-way analysis of variance (ANOVA) in SigmaPlot 12 (Systat Software), assuming normal distribution. Data in Figure S6H were from data set GEO: GSE6969 (Platts et al., 2007) and analyzed by Mann-Whitney rank-sum test in SigmaPlot. Data are displayed as arithmetic mean \pm SEM, unless indicated otherwise. Statistically significant results in all figures are indicated as * $p < 0.05$; ** $p < 0.01$; and *** $p < 0.001$.

SUPPLEMENTAL INFORMATION

Supplemental Information includes Supplemental Experimental Procedures and seven figures and can be found with this article online at <http://dx.doi.org/10.1016/j.cell.2015.10.029>.

AUTHOR CONTRIBUTIONS

S.K. and S.P.A. conceived, performed, and analyzed experiments. J.H. supervised animal husbandry and assisted with experiments. G.H. procured human samples. C.N. supervised all aspects of the project. S.K. and C.N. wrote the manuscript with input from all authors.

ACKNOWLEDGMENTS

Expert technical support by the DKFZ core facilities for flow cytometry, transgenics, light microscopy, electron microscopy, and the central animal laboratory is gratefully acknowledged. We thank X. Huang and Y. Zhang for *Lcn5-CreERT2* mice, D. Baumann for *Cela2a;Kras* mice, N. Soshnikova for *APC*^{min} mice, and W. Becker and L. Leyns for reagents. This work was supported by the Deutsche Forschungsgemeinschaft (DFG), SFB 873.

Received: April 10, 2015

Revised: September 3, 2015

Accepted: September 23, 2015

Published: November 19, 2015

REFERENCES

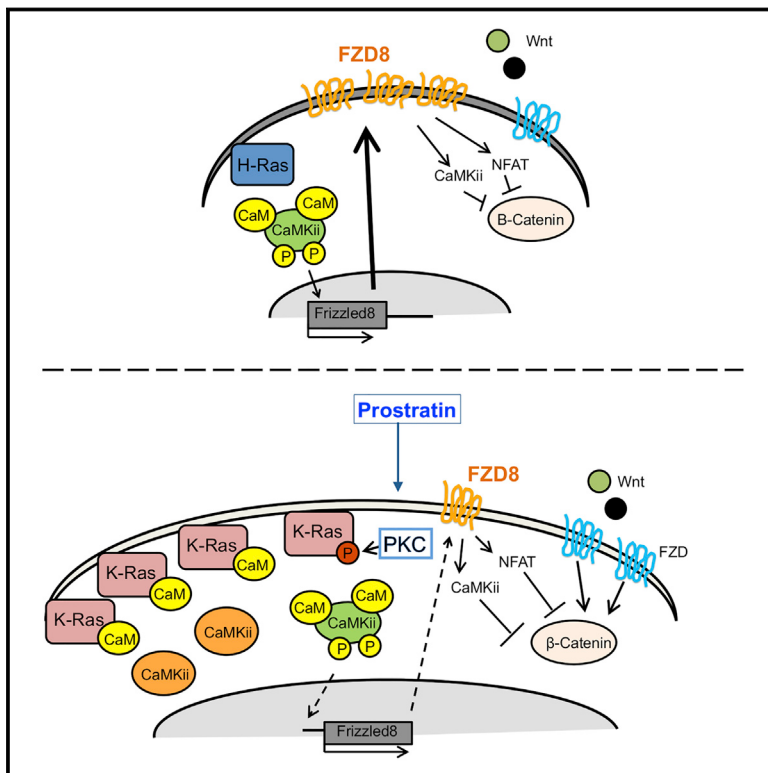
- Acebron, S.P., Karaulanov, E., Berger, B.S., Huang, Y.L., and Niehrs, C. (2014). Mitotic wnt signaling promotes protein stabilization and regulates cell size. *Mol. Cell* 54, 663–674.
- Anastas, J.N., and Moon, R.T. (2013). WNT signalling pathways as therapeutic targets in cancer. *Nat. Rev. Cancer* 13, 11–26.
- Boyer, A., Yeh, J.R., Zhang, X., Paquet, M., Gaudin, A., Nagano, M.C., and Boerboom, D. (2012). CTNNB1 signaling in sertoli cells downregulates spermatogonial stem cell activity via WNT4. *PLoS ONE* 7, e29764.
- Braun, R.E. (1998). Post-transcriptional control of gene expression during spermatogenesis. *Semin. Cell Dev. Biol.* 9, 483–489.

- Clevers, H., and Nusse, R. (2012). Wnt/β-catenin signaling and disease. *Cell* 149, 1192–1205.
- Cohen, P. (1989). The structure and regulation of protein phosphatases. *Annu. Rev. Biochem.* 58, 453–508.
- Das, D.S., Wadhwa, N., Kunj, N., Sarda, K., Pradhan, B.S., and Majumdar, S.S. (2013). Dickkopf homolog 3 (DKK3) plays a crucial role upstream of WNT/β-CATENIN signaling for Sertoli cell mediated regulation of spermatogenesis. *PLoS ONE* 8, e63603.
- Davidson, G., Wu, W., Shen, J., Bilic, J., Fenger, U., Stannek, P., Glinka, A., and Niehrs, C. (2005). Casein kinase 1 gamma couples Wnt receptor activation to cytoplasmic signal transduction. *Nature* 438, 867–872.
- Davidson, G., Shen, J., Huang, Y.L., Su, Y., Karaulanov, E., Bartscherer, K., Hassler, C., Stannek, P., Boutros, M., and Niehrs, C. (2009). Cell cycle control of wnt receptor activation. *Dev. Cell* 17, 788–799.
- Fuchs, Y., Brown, S., Gorenc, T., Rodriguez, J., Fuchs, E., and Steller, H. (2013). Sept4/ARTS regulates stem cell apoptosis and skin regeneration. *Science* 341, 286–289.
- Gross, J.C., Chaudhary, V., Bartscherer, K., and Boutros, M. (2012). Active Wnt proteins are secreted on exosomes. *Nat. Cell Biol.* 14, 1036–1045.
- Hadjhannas, M.V., Bernkopf, D.B., Brückner, M., and Behrens, J. (2012). Cell cycle control of Wnt/β-catenin signalling by conductin/axin2 through CDC20. *EMBO Rep.* 13, 347–354.
- Holland, J.D., Klaus, A., Garratt, A.N., and Birchmeier, W. (2013). Wnt signaling in stem and cancer stem cells. *Curr. Opin. Cell Biol.* 25, 254–264.
- Huang, S.M., Mishina, Y.M., Liu, S., Cheung, A., Stegmeier, F., Michaud, G.A., Charlat, O., Wiellette, E., Zhang, Y., Wiessner, S., et al. (2009). Tankyrase inhibition stabilizes axin and antagonizes Wnt signalling. *Nature* 461, 614–620.
- Huang, Y.L., Anvarian, Z., Döderlein, G., Acebron, S.P., and Niehrs, C. (2015). Maternal Wnt/STOP signaling promotes cell division during early Xenopus embryogenesis. *Proc. Natl. Acad. Sci. USA* 112, 5732–5737.
- Inoki, K., Ouyang, H., Zhu, T., Lindvall, C., Wang, Y., Zhang, X., Yang, Q., Bennett, C., Harada, Y., Stankunas, K., et al. (2006). TSC2 integrates Wnt and energy signals via a coordinated phosphorylation by AMPK and GSK3 to regulate cell growth. *Cell* 126, 955–968.
- Kikuchi, A., Yamamoto, H., Sato, A., and Matsumoto, S. (2011). New insights into the mechanism of Wnt signaling pathway activation. *Int. Rev. Cell Mol. Biol.* 291, 21–71.
- Kim, N.G., Xu, C., and Gumbiner, B.M. (2009). Identification of targets of the Wnt pathway destruction complex in addition to beta-catenin. *Proc. Natl. Acad. Sci. USA* 106, 5165–5170.
- Kim, S.E., Huang, H., Zhao, M., Zhang, X., Zhang, A., Semonov, M.V., MacDonald, B.T., Zhang, X., Garcia Abreu, J., Peng, L., and He, X. (2013). Wnt stabilization of β-catenin reveals principles for morphogen receptor-scaffold assemblies. *Science* 340, 867–870.
- Kim, H., Vick, P., Hedtke, J., Ploper, D., and De Robertis, E.M. (2015). Wnt Signaling Translocates Lys48-Linked Polyubiquitinated Proteins to the Lysosomal Pathway. *Cell Rep.* 11, 1151–1159.
- Kissel, H., Georgescu, M.M., Larisch, S., Manova, K., Hunnicutt, G.R., and Steller, H. (2005). The Sept4 septon locus is required for sperm terminal differentiation in mice. *Dev. Cell* 8, 353–364.
- Kwitny, S., Klaus, A.V., and Hunnicutt, G.R. (2010). The annulus of the mouse sperm tail is required to establish a membrane diffusion barrier that is engaged during the late steps of spermiogenesis. *Biol. Reprod.* 82, 669–678.
- Li, Q., Ishikawa, T.O., Miyoshi, H., Oshima, M., and Taketo, M.M. (2005). A targeted mutation of Nkd1 impairs mouse spermatogenesis. *J. Biol. Chem.* 280, 2831–2839.
- Luga, V., Zhang, L., Viloria-Petit, A.M., Ogunjimi, A.A., Inanlou, M.R., Chiu, E., Buchanan, M., Hosein, A.N., Basik, M., and Wrana, J.L. (2012). Exosomes mediate stromal mobilization of autocrine Wnt-PCP signaling in breast cancer cell migration. *Cell* 151, 1542–1556.
- Luo, W., Peterson, A., Garcia, B.A., Coombs, G., Kofahl, B., Heinrich, R., Shabanowitz, J., Hunt, D.F., Yost, H.J., and Virshup, D.M. (2007). Protein phosphatase 1 regulates assembly and function of the beta-catenin degradation complex. *EMBO J.* 26, 1511–1521.
- MacDonald, B.T., Tamai, K., and He, X. (2009). Wnt/beta-catenin signaling: components, mechanisms, and diseases. *Dev. Cell* 17, 9–26.
- Maretto, S., Cordenonsi, M., Dupont, S., Braghetta, P., Broccoli, V., Hassan, A.B., Volpin, D., Bressan, G.M., and Piccolo, S. (2003). Mapping Wnt/beta-catenin signaling during mouse development and in colorectal tumors. *Proc. Natl. Acad. Sci. USA* 100, 3299–3304.
- Matsuda, T., Ihara, M., Inoguchi, H., Kwon, I.K., Takamizawa, K., and Kidoaki, S. (2005). Mechano-active scaffold design of small-diameter artificial graft made of electrospun segmented polyurethane fabrics. *J. Biomed. Mater. Res. A* 73, 125–131.
- McMahon, A.P., and Bradley, A. (1990). The Wnt-1 (int-1) proto-oncogene is required for development of a large region of the mouse brain. *Cell* 62, 1073–1085.
- Metcalfe, C., and Bienz, M. (2011). Inhibition of GSK3 by Wnt signalling—two contrasting models. *J. Cell Sci.* 124, 3537–3544.
- Mikolcevic, P., Sigl, R., Rauch, V., Hess, M.W., Pfaller, K., Barisic, M., Pelli-niemi, L.J., Boesl, M., and Geley, S. (2012). Cyclin-dependent kinase 16/PCTAIRE kinase 1 is activated by cyclin Y and is essential for spermatogenesis. *Mol. Cell. Biol.* 32, 868–879.
- Moser, A.R., Pitot, H.C., and Dove, W.F. (1990). A dominant mutation that predisposes to multiple intestinal neoplasia in the mouse. *Science* 247, 322–324.
- Olmeda, D., Castel, S., Vilaró, S., and Cano, A. (2003). Beta-catenin regulation during the cell cycle: implications in G2/M and apoptosis. *Mol. Biol. Cell* 14, 2844–2860.
- Platts, A.E., Dix, D.J., Chemes, H.E., Thompson, K.E., Goodrich, R., Rockett, J.C., Rawe, V.Y., Quintana, S., Diamond, M.P., Strader, L.F., and Krawetz, S.A. (2007). Success and failure in human spermatogenesis as revealed by teratozoospermic RNAs. *Hum. Mol. Genet.* 16, 763–773.
- Ploper, D., Taelman, V.F., Robert, L., Perez, B.S., Titz, B., Chen, H.W., Graeber, T.G., von Euw, E., Ribas, A., and De Robertis, E.M. (2015). MITF drives endolysosomal biogenesis and potentiates Wnt signaling in melanoma cells. *Proc. Natl. Acad. Sci. USA* 112, E420–E429.
- Rivas, B., Huang, Z., and Agoulnik, A.I. (2014). Normal fertility in male mice with deletion of β-catenin gene in germ cells. *Genesis* 52, 328–332.
- Salinas, P.C. (2007). Modulation of the microtubule cytoskeleton: a role for a divergent canonical Wnt pathway. *Trends Cell Biol.* 17, 333–342.
- Sharma, S., Quintana, A., Findlay, G.M., Mettlen, M., Baust, B., Jain, M., Nilsson, R., Rao, A., and Hogan, P.G. (2013). An siRNA screen for NFAT activation identifies septins as coordinators of store-operated Ca²⁺ entry. *Nature* 499, 238–242.
- Sipilä, P., Jalkanen, J., Huhtaniemi, I.T., and Poutanen, M. (2009). Novel epididymal proteins as targets for the development of post-testicular male contraception. *Reproduction* 137, 379–389.
- Sitz, J.H., Baumgärtel, K., Hämmeler, B., Papadopoulos, C., Hekerman, P., Tejedor, F.J., Becker, W., and Lutz, B. (2008). The Down syndrome candidate dual-specificity tyrosine phosphorylation-regulated kinase 1A phosphorylates the neurodegeneration-related septon 4. *Neuroscience* 157, 596–605.
- Somanath, P.R., Jack, S.L., and Vijayaraghavan, S. (2004). Changes in sperm glycogen synthase kinase-3 serine phosphorylation and activity accompany motility initiation and stimulation. *J. Androl.* 25, 605–617.
- Stolz, A., Neufeld, K., Erych, N., and Bastians, H. (2015). Wnt-mediated protein stabilization ensures proper mitotic microtubule assembly and chromosome segregation. *EMBO Rep.* 16, 490–499.
- Sullivan, R., Frenette, G., and Girouard, J. (2007). Epididymosomes are involved in the acquisition of new sperm proteins during epididymal transit. *Asian J. Androl.* 9, 483–491.
- Taelman, V.F., Dobrowolski, R., Plouhinec, J.L., Fuentealba, L.C., Vorwald, P.P., Gumper, I., Sabatini, D.D., and De Robertis, E.M. (2010). Wnt signaling requires sequestration of glycogen synthase kinase 3 inside multivesicular endosomes. *Cell* 143, 1136–1148.

- Touré, A., Lhuillier, P., Gossen, J.A., Kuil, C.W., Lhôte, D., Jégou, B., Escalier, D., and Gacon, G. (2007). The testis anion transporter 1 (*Slc26a8*) is required for sperm terminal differentiation and male fertility in the mouse. *Hum. Mol. Genet.* 16, 1783–1793.
- Tsukiyama, T., and Yamaguchi, T.P. (2012). Mice lacking Wnt2b are viable and display a postnatal olfactory bulb phenotype. *Neurosci. Lett.* 512, 48–52.
- Turner, T.T. (2008). De Graaf's thread: the human epididymis. *J. Androl.* 29, 237–250.
- Valenta, T., Gay, M., Steiner, S., Draganova, K., Zemke, M., Hoffmans, R., Cincelli, P., Aguet, M., Sommer, L., and Basler, K. (2011). Probing transcription-specific outputs of β -catenin in vivo. *Genes Dev.* 25, 2631–2643.
- Vijayaraghavan, S., Stephens, D.T., Trautman, K., Smith, G.D., Khatra, B., da Cruz e Silva, E.F., and Greengard, P. (1996). Sperm motility development in the epididymis is associated with decreased glycogen synthase kinase-3 and protein phosphatase 1 activity. *Biol. Reprod.* 54, 709–718.
- Vincan, E., and Barker, N. (2008). The upstream components of the Wnt signalling pathway in the dynamic EMT and MET associated with colorectal cancer progression. *Clin. Exp. Metastasis* 25, 657–663.
- Vinyoles, M., Del Valle-Pérez, B., Curto, J., Viñas-Castells, R., Alba-Castellón, L., García de Herreros, A., and Duñach, M. (2014). Multivesicular GSK3 sequestration upon Wnt signaling is controlled by p120-catenin/cadherin interaction with LRP5/6. *Mol. Cell* 53, 444–457.
- Wang, K., Li, N., Yeung, C.H., Li, J.Y., Wang, H.Y., and Cooper, T.G. (2013). Oncogenic Wnt/ β -catenin signalling pathways in the cancer-resistant epididymis have implications for cancer research. *Mol. Hum. Reprod.* 19, 57–71.
- Wu, D., and Pan, W. (2010). GSK3: a multifaceted kinase in Wnt signaling. *Trends Biochem. Sci.* 35, 161–168.
- Wu, X., Tu, X., Joeng, K.S., Hilton, M.J., Williams, D.A., and Long, F. (2008). Rac1 activation controls nuclear localization of beta-catenin during canonical Wnt signaling. *Cell* 133, 340–353.
- Xie, S., Xu, J., Ma, W., Liu, Q., Han, J., Yao, G., Huang, X., and Zhang, Y. (2013). Lcn5 promoter directs the region-specific expression of cre recombinase in caput epididymidis of transgenic mice. *Biol. Reprod.* 88, 71.
- Xu, C., Kim, N.G., and Gumbiner, B.M. (2009). Regulation of protein stability by GSK3 mediated phosphorylation. *Cell Cycle* 8, 4032–4039.
- Yang, J., Wang, S.K., Choi, M., Reid, B.M., Hu, Y., Lee, Y.L., Herzog, C.R., Kim-Berman, H., Lee, M., Benke, P.J., et al. (2015). Taurodontism, variations in tooth number, and misshapened crowns in Wnt10a null mice and human kindreds. *Mol. Genet. Genomic Med.* 3, 40–58.
- Yeung, C.-H., and Cooper, T. (2002). Acquisition and development of sperm motility upon maturation in the epididymis. In *The Epididymis: From Molecules to Clinical Practice*, B. Robaire and B. Hinton, eds. (Springer), pp. 417–434.
- Zi, Z., Zhang, Z., Li, Q., An, W., Zeng, L., Gao, D., Yang, Y., Zhu, X., Zeng, R., Shum, W.W., et al. (2015). CCNYL1, but not CCNY, cooperates with CDK16 to regulate spermatogenesis in mouse. *PLoS Genet.* 11, e1005485.

K-Ras Promotes Tumorigenicity through Suppression of Non-canonical Wnt Signaling

Graphical Abstract



Authors

Man-Tzu Wang, Matthew Holderfield, Jacqueline Galeas, Reyno Delrosario, Minh D. To, Allan Balmain, Frank McCormick

Correspondence

mccormic@cc.ucsf.edu

In Brief

The interaction between K-Ras and calmodulin (CaM) modulates tumor formation through inhibition of CaM kinase activity and suppression of Fzd8-mediated Wnt/Ca²⁺ signaling. This interaction does not occur with H-Ras or N-Ras, and disruption of the K-Ras-CaM interaction by the orally active natural product prostratin represses tumor growth.

Highlights

- Oncogenic K-Ras and H-Ras differ in tumor initiation via non-canonical Wnt signaling
- Suppression of Fzd8-mediated Wnt/Ca²⁺ signaling is essential to K-Ras malignancy
- K-Ras-CaM interaction modulates the Wnt/Ca²⁺ signaling pathway
- Prostratin compromises the K-Ras-CaM interaction and so prevents tumorigenicity

K-Ras Promotes Tumorigenicity through Suppression of Non-canonical Wnt Signaling

Man-Tzu Wang,¹ Matthew Holderfield,¹ Jacqueline Galeas,¹ Reyno Delrosario,¹ Minh D. To,¹ Allan Balmain,¹ and Frank McCormick^{1,*}

¹Helen Diller Family Comprehensive Cancer Center, University of California, San Francisco, 1450 3rd Street, San Francisco, CA 94158, USA

*Correspondence: mccormic@cc.ucsf.edu

<http://dx.doi.org/10.1016/j.cell.2015.10.041>

SUMMARY

K-Ras and H-Ras share identical effectors and have similar properties; however, the high degree of tumor-type specificity associated with K-Ras and H-Ras mutations suggests that they have unique roles in oncogenesis. Here, we report that oncogenic K-Ras, but not H-Ras, suppresses non-canonical Wnt/Ca²⁺ signaling, an effect that contributes strongly to its tumorigenic properties. K-Ras does this by binding to calmodulin and so reducing CaMKII activity and expression of Fzd8. Restoring Fzd8 in K-Ras mutant pancreatic cells suppresses malignancy, whereas depletion of Fzd8 in H-Ras^{V12}-transformed cells enhances their tumor initiating capacity. Interrupting K-Ras-calmodulin binding using genetic means or by treatment with an orally active protein kinase C (PKC)-activator, prostratin, represses tumorigenesis in K-Ras mutant pancreatic cancer cells. These findings provide an alternative way to selectively target this “undruggable” protein.

INTRODUCTION

H-Ras, N-Ras, and K-Ras genes are frequently mutated in human tumors and affect a multitude of cellular processes. They share a high degree of sequence homology as well as identical regulators and effectors. However, they may also have unique roles in physiological and pathological processes. K-Ras mutations occur at high frequency in pancreatic and colorectal cancers and in lung adenocarcinomas, while N-Ras and H-Ras mutations are far less common (Prior et al., 2012). Furthermore, K-Ras deficiency results in embryonic lethality, whereas N- and H-Ras knockout mice develop normally (Johnson et al., 1997; Koera et al., 1997; Malumbres and Barbacid, 2003). In a model of tumor initiation and differentiation, K-Ras, but not H-Ras or N-Ras, initiated tumors through a mechanism involving stem cell expansion (Quinlan et al., 2008). H-Ras can replace K-Ras when expressed from the endogenous K-Ras locus, suggesting that the genetic locus is more important than the isoform of Ras that is expressed (To et al., 2008). However, tumors driven by K-Ras are more metastatic than those driven by H-Ras (Wong et al., 2013). Together, these data suggest a potentially unique role for K-Ras in tumor biology. Here, we report that oncogenic

K-Ras uniquely elicits a tumorigenic phenotype through down-regulation of non-canonical Wnt/Ca²⁺ signaling. Binding of calmodulin (CaM) to K-Ras, but not to H-Ras or N-Ras, appears to be responsible for this major difference. These data provide an alternative avenue to inhibit this “undruggable” protein. Indeed, treatment of mice with prostratin, a natural product that promotes dissociation of K-Ras from CaM, suppressed tumorigenesis in pancreas cancer models and papillomas driven specifically by oncogenic K-Ras.

RESULTS

K-Ras^{V12} and H-Ras^{V12} Differ in Tumor Initiation Despite Comparable Canonical MAPK and Akt Signaling

To identify distinct properties of H-Ras and K-Ras, we expressed oncogenic H-Ras and K-Ras(4B) in NIH/3T3 cells and looked for phenotypic differences. However, H-Ras^{V12}- and K-Ras^{V12}-transformed cells had almost identical phenotypes: similar morphologies, comparable levels of GTP-loaded Ras (Figure 1A), similar levels of Erk (Figures 1B and S1A), and similar Akt activity (Figures 1B and S1B).

Next, we examined their ability to self-renew at the single-cell level, using a sphere-forming assay (Fang et al., 2005; Fujii et al., 2009; Gou et al., 2007; Ponti et al., 2005; Singh et al., 2003). With limited numbers of seeded cells, K-Ras^{V12}-transformed NIH/3T3 cells showed significantly increased sphere-forming efficiency compared with H-Ras^{V12} (Figure 1C). Re-plating revealed that spheres from K-Ras^{V12}-transformed cells were viable and able to re-initiate exponentially growing cells in 2D culture, whereas H-Ras^{V12}-transformed cells were not (Figure S1C).

We next evaluated their tumorigenic potential, using limited and serial transplantation (Clarke et al., 2006). When 1,000 cells were engrafted subcutaneously, H-Ras^{V12} and K-Ras^{V12} tumors arose at similar rates. However, when the number was reduced to 100, K-Ras^{V12}-transformed cells displayed enhanced tumor initiating rates compared to H-Ras^{V12} cells (Figure 1D, left). We then re-transplanted cells from primary tumors into a second cohort of mice. Upon injection of 500 K-Ras^{V12} cells, all ten injections gave rise to tumors. In contrast, only two out of ten injections of H-Ras^{V12} cells initiated tumors (Figure 1D, right).

To examine whether K-Ras and H-Ras play distinct roles in inducing tumorigenicity in human cancers, we first examined their roles in BxPC3 cells, a pancreatic cancer-cell line expressing wild-type H-Ras and K-Ras. Knock down of K-Ras, but not H-Ras, significantly reduced sphere-forming efficiency in response to EGF and reduced the size of initiated spheres

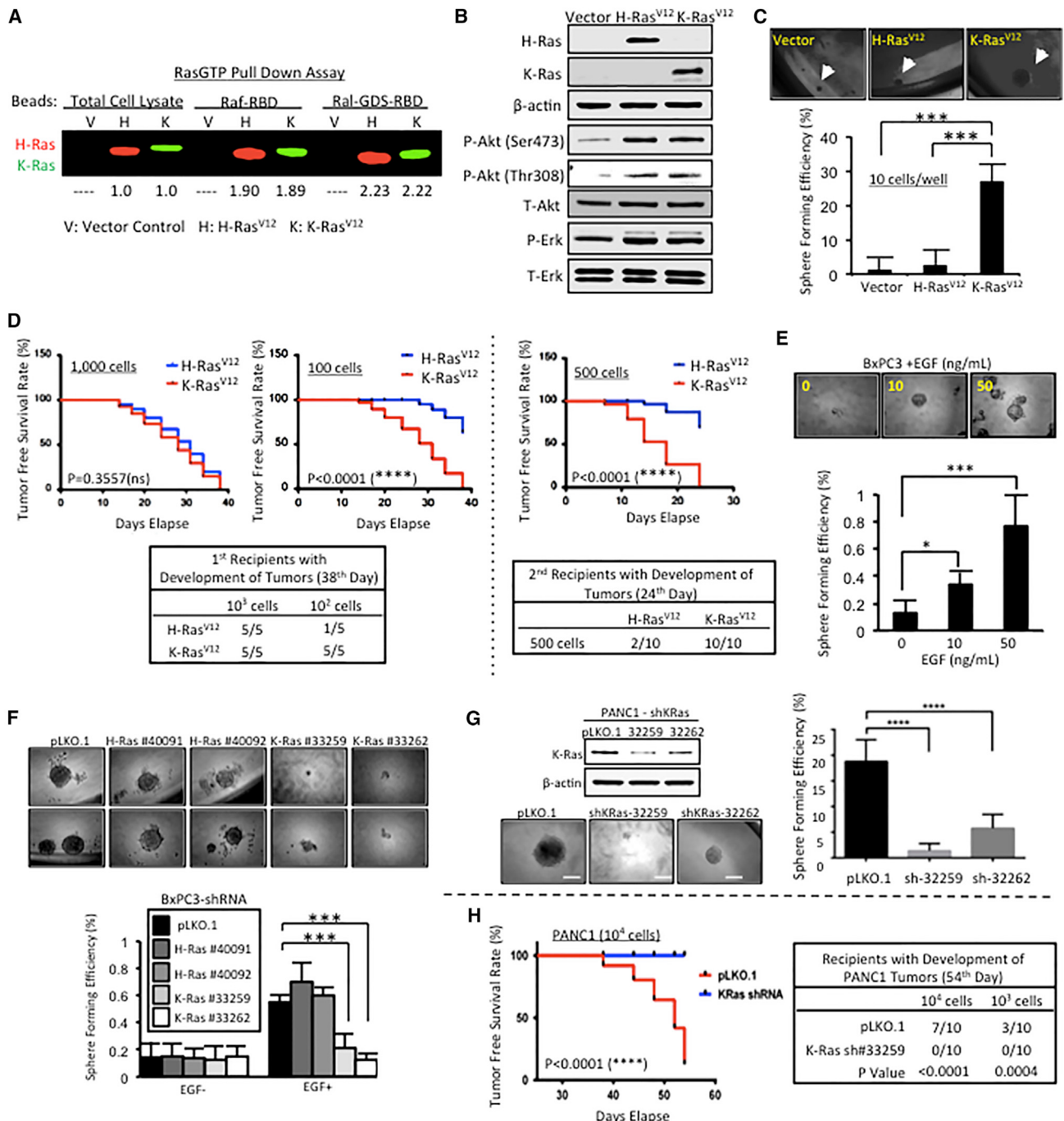


Figure 1. K-Ras^{V12} and H-Ras^{V12} Have Differential Tumor-Initiating Properties, Despite Comparable Canonical Signaling Outputs

- (A) Comparable levels of total Ras proteins and GTP-bound Ras as measured by Raf-RBD or Raf-GDS-RBD pull-down assays.
- (B) Comparable levels of phosphorylated Erk and Akt in cells transformed by H-Ras^{V12} or K-Ras^{V12}.
- (C) K-Ras^{V12}-transformed NIH/3T3 cells presented increased sphere formation. Top: morphology of spheres formed. Bottom: sphere formation efficiency ($n = 6$).
- (D) The tumor initiating abilities of H-Ras^{V12}-transformed and K-Ras^{V12}-transformed NIH/3T3 cells when the number of injected cells was 1,000 (top left) or 100 (top right). K-Ras^{V12}-transformed cells presented increased tumor initiating capacity, in comparison with H-Ras^{V12}-transformed cells, when the number of cells injected became limited (bottom table). Right: cells derived from K-Ras^{V12} driven tumors had enhanced tumor recapitulating ability than H-Ras^{V12}.
- (E) Promotion of BxPC3 sphere formation by EGF. Top: morphology of spheres formed. Bottom: sphere formation efficiency as calculated by the number of spheres normalized by the number of cells seeded ($n = 6$).
- (F) Knockdown of K-Ras, but not H-Ras, attenuated EGF stimulation of BxPC3 sphere-forming efficiency ($n = 6$).

(legend continued on next page)

(Figures 1E, 1F, and S1D–S1F). We next determined whether oncogenic K-Ras is required for the maintenance of “stemness” in human pancreatic tumor cells PANC2.13 and PANC1, both of which express oncogenic K-Ras. Upon knock down of K-Ras, both cell lines showed a differentiated morphology, reduced expression of CD44 and CD24 (Figures S1G–S1I), and reduced ability to form spheres with re-plating potential (Figures 1G and S1J). PANC1 is K-Ras-independent in 2D culture (Scholl et al., 2009; Singh et al., 2009; Wei et al., 2012). However, using a limited number of transplanted cells, K-Ras knockdown significantly reduced their rate of tumor initiation (Figure 1H), suggesting that oncogenic K-Ras mediates tumorigenicity through a function, distinct from its role in maintaining viability in 2D.

K-Ras Suppresses Frizzled 8 and CaMKii Activity

We next investigated the mechanisms through which K-Ras promotes tumorigenicity and stem-ness more efficiently than H-Ras, despite comparable levels of canonical Ras signaling. We used PCR arrays to profile stem cell-related gene expression mediated by K-Ras or H-Ras (Figure 2A; Tables S1 and S2). Three stem cell-related genes were expressed with a >4-fold change between H-Ras^{V12}- and K-Ras^{V12}-transformed NIH/3T3 cells (Figure 2B; Table S2): *Bmpr1b* was upregulated in K-Ras^{V12}-transformed cells, whereas *Gli2* and *Frizzled 8* (*Fzd8*) were downregulated. We did not pursue *bmpr1b* due to its low expression, or *Gli2*, because it plays different roles in mouse and human cells (Sasaki et al., 1999).

Frizzled proteins are G protein-coupled receptors involved in Wnt signaling. *Fzd1*, *Fzd4*, and *Fzd10* activate the canonical Wnt/β-catenin pathway, whereas, *Fzd8* is a major mediator of non-canonical Wnt/Ca²⁺ signaling in stem cells (Sugimura et al., 2012). The non-canonical Wnt/Ca²⁺ pathway involves activation of CaMKii and the transcription factor NF-AT and inhibition of β-catenin/TCF signaling (Saneyoshi et al., 2002; Semenov et al., 2007; Sugimura and Li, 2010). Figure 2C confirms that *Fzd8* was downregulated in K-Ras^{V12}-transformed cells compared with H-Ras^{V12}-transformed cells and vector controls. K-Ras^{V12}-transformed cells also had reduced levels of activated CaMKii, as indicated by phosphorylation at Threonine-286 (Figure 2C). Activation and nuclear translocation of NF-AT was reduced in NIH/3T3-K-Ras^{V12} cells (Figure 2C). The phosphorylated form of β-catenin was also reduced in these cells (Figure 2C).

The non-canonical Wnt/Ca²⁺pathway and CaMKii suppress canonical Wnt signaling by blocking β-catenin/TCF4 interaction (Semenov et al., 2007; Sugimura and Li, 2010). In K-Ras^{V12}-transformed cells, where CaMKii was barely phosphorylated, the β-catenin/TCF4 interaction was significantly increased compared with H-Ras^{V12}-transformed cells, in which CaMKii activity was elevated (Figure 2D). Furthermore, reduced activation of CaMKii and NF-AT in NIH/3T3-K-Ras^{V12} cells led to increased nuclear localization of β-catenin, whereas in vector controls and NIH/

3T3-H-Ras^{V12} cells, in which CaMKii and NF-AT were highly activated, nuclear β-catenin was barely detectable (Figure 2C). TOP-Flash assay confirmed that the transcriptional activity of β-catenin was greatly elevated in NIH/3T3-K-Ras^{V12} cells (Figure 2E). Consequentially, the mRNA expressions of β-catenin-target genes, *c-Myc* and *TCF1*, were upregulated in K-Ras^{V12}-transformed cell in comparison with control or H-Ras^{V12}-transformed cells (Figure S2A).

Next, we asked whether non-canonical Wnt/Ca²⁺ signaling differs in tumors driven by H-Ras or K-Ras in vivo. We compared tumors from wild-type mice with tumors from a genetically engineered mouse model devoid of endogenous H-Ras, but expressing wild-type *H-Ras* from the endogenous *K-Ras* locus. *K-Ras* or *H-Ras* mutations were then induced by topical treatment with 7,12-dimethylbenz[a]anthracene/12-O-tetradecanoylphorbol-13-acetate (DMBA/TPA). This model allows comparison of K-Ras and H-Ras oncogenes under control of the same endogenous regulatory elements in the same cellular background (Potenza et al., 2005; To et al., 2008). Figure 2G shows that mutant *H-Ras* driven skin tumors had elevated level of *Fzd8* protein and increased levels of phosphorylated-CaMKii compared to skin tumors with *K-Ras* mutations. This shows that this unique K-Ras-mediated signaling cannot be recapitulated by H-Ras even when it is knocked in at the *K-Ras* locus.

Canonical and non-canonical Wnt signaling pathways are both regulated by binding of WNT ligands to frizzled receptors. WNT3a preferentially activates Wnt/β-catenin signaling, whereas WNT5a activates non-canonical Wnt signaling (Weekes and Winn, 2011). To assess whether different WNT ligands are involved in modulating the distinct Wnt/Ca²⁺ signaling activities of oncogenic H-Ras and K-Ras, we evaluated the expression levels and functions of WNT-5a and WNT-3a in Ras^{V12}-transformed NIH/3T3 cells. As shown in the Figure S2B, oncogenic Ras^{V12}-transformed cells expressed more WNT-3a and WNT-5a protein than control cells, but there was no difference in expression levels between H-Ras^{V12} and K-Ras^{V12}. Furthermore, addition of WNT ligands did not alter CaMKii activity, β-catenin/TCF/LEF transcriptional activity, or sphere-forming efficiency in H-Ras^{V12} or K- Ras^{V12}-transformed cells (Figures S2C–S2E). The divergence between H-Ras and K-Ras in non-canonical Wnt/Ca²⁺ signaling is therefore not dependent upon the presence of WNT ligands.

We next determined the effect of K-Ras on non-canonical Wnt/Ca²⁺ signaling in human cancer-derived cell lines. In PANC2.13 cells, K-Ras knockdown increased *Fzd8* expression, increased phosphorylation of CaMKii (Figure 2H), and reduced β-catenin activity (Figure 2I). We therefore conclude that oncogenic K-Ras, but not H-Ras, represses *Fzd8* expression and CaMKii activity, a major effector of the Wnt/Ca²⁺ pathway, in both mouse fibroblasts, mouse tumors, and in human cancer cells.

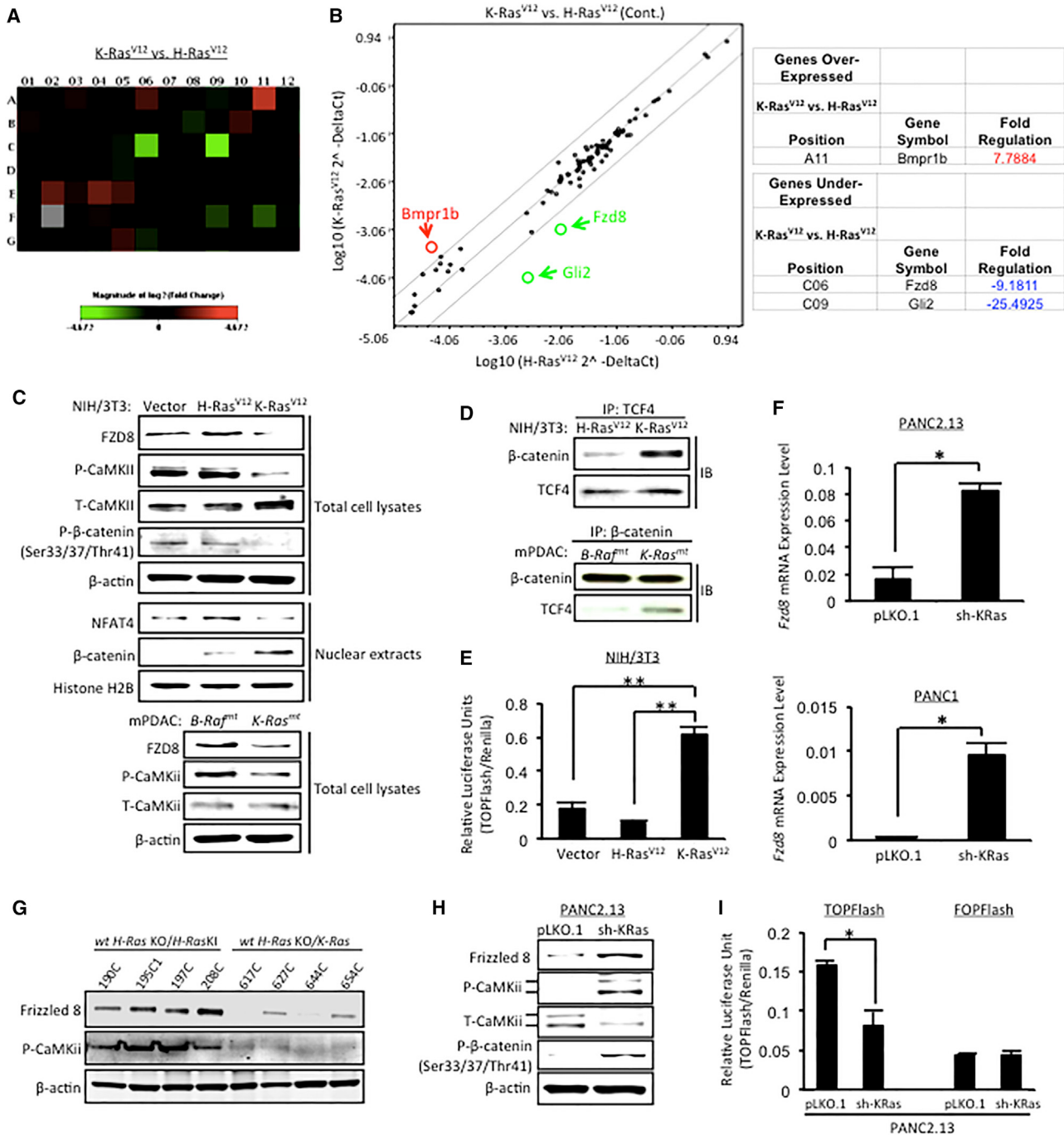
Canonical Wnt/β-catenin signaling is modulated by the non-canonical Wnt/Ca²⁺ pathway in K-Ras^{V12}-transformed cells

(G) Knockdown of mutant K-Ras repressed PANC1 sphere formation efficiency. Top left: western blot confirmed the knockdown efficiency. Bottom left and right: PANC1 with K-Ras shRNA expression formed spheres in smaller sizes and numbers when compared to vector control (n = 6).

(H) Knockdown of mutant K-Ras reduced PANC1 tumor-initiating capacity. Left: tumor free survival curve. Right: tumor formation frequency.

NS, no significance. *p < 0.05; **p < 0.001; ***p < 0.0001.

See also Figure S1.

**Figure 2. K-Ras, but Not H-Ras, Suppresses Fzd8**

- (A) Heat map of stem cell factors differentially expressed in H-Ras^{V12} and K-Ras^{V12}-transformed NIH/3T3 cells as evaluated by qPCRarray ($n = 3$).
- (B) Scatter plot (left) and identification of *Bmpr1b*, *Fzd8*, and *Gli2* as genes differentially expressed in H-Ras^{V12} and K-Ras^{V12}-transformed NIH/3T3 cells.
- (C) Reduced *Fzd8* expression and Wnt/Ca²⁺ signaling in K-Ras-transformed NIH/3T3 cells when compared with the vector control or H-Ras^{V12}-transformed cells (Top eight panels) and in mouse PDAC cells with oncogenic K-Ras mutation when compared with those with mutant Raf (Bottom four panels).
- (D) Increased TCF4 and β-catenin complexes in K-Ras^{V12}-transformed NIH/3T3 cells (Top panel) and in mouse PDAC cells with K-Ras mutations (Bottom panel) when compared to those with H-Ras^{V12} or B-Raf, respectively.
- (E) Increased TCF/β-catenin activities in K-Ras^{V12}-transformed NIH/3T3 cells as compared to the vector control or H-Ras^{V12}-transformed cells ($n = 4$).
- (F) Knockdown of K-Ras led to increased *Fzd8* expression at mRNA level in PANC2.13 and PANC1 cells ($n = 3$).
- (G) Reduction in the levels of *Fzd8* expression and CaMKII phosphorylation in skin tumors harboring WT H-Ras KO with mutations in either Kras or HrasKI alleles.

(legend continued on next page)

and in pancreatic cancer cells containing oncogenic K-Ras (above). This suggests that activation of canonical Wnt/β-catenin may be responsible for stem-like properties induced by K-Ras. However, in colorectal cancers, the canonical Wnt/β-catenin signaling pathway is strongly activated through inactivation of the APC gene or mutation of β-catenin potentially rendering K-Ras irrelevant with regard to stem-ness in these cells. Knock down of K-Ras promoted expression of Fzd8 and the activation of NF-AT and CaMKii in multiple colon cancer cell lines regardless of the status of wild-type or mutant APC (Figure S3A). As expected from our model, knock down of K-Ras significantly repressed β-catenin/TCF/LEF transcriptional activity in SW480 (mutant APC), which express wild-type β-catenin, yet not in either HCT15 (mutant APC) or HCT116 (wild-type APC) that have a gain-of-function mutation in β-catenin (Figure S3B). However, although repression of K-Ras expression by short hairpin RNA (shRNA) did not alter β-catenin/TCF/LEF transcriptional activity, or even the proliferation rates, in HCT15 and HCT116 cells, it still inhibited their sphere formation ability in 3D culture (Figures S3C and S3D). Therefore, K-Ras-mediated stem-ness is independent from canonical Wnt/β-catenin/TCF/LEF transcriptional activity. To confirm this, we treated NIH/3T3 cells transformed by H-Ras^{V12} or K-Ras^{V12} with the tankyrase inhibitors JW55 and JW67 and with cardionogen1. JW55 and JW67 function as potent inhibitors of canonical Wnt/β-catenin signaling pathway by degrading β-catenin, and cardionogen1 inhibits the β-catenin/TCF/LEF transcriptional activity. Tankyrase inhibitors repressed β-catenin/TCF/LEF transcriptional activity in Ras^{V12}-transformed cells (Figure S3E), but this did not affect their growth in 3D culture and formation of spheres (Figure S3F). These suggest that β-catenin/TCF/LEF transcriptional activity is affected by non-canonical Wnt/Ca²⁺ signaling activity, but K-Ras driven stem-ness is independent from the canonical Wnt/β-catenin signaling pathway and β-catenin/TCF/LEF activation.

Inhibition of CaMKii Enhances Sphere Formation by H-Ras^{V12} Cells

To determine whether suppression of CaMKii observed in K-Ras-transformed cells is responsible for the acquisition of stem-ness properties, we treated NIH/3T3-H-Ras^{V12} with KN-93, a selective CaMKii inhibitor (Figure 3A). Inhibition of CaMKii reduced Fzd8 expression (Figure 3B) and increased β-catenin transcriptional activity, confirming the inhibitory effects of Wnt/Ca²⁺/CaMKii signaling on the canonical Wnt pathway (Figure 3C). Moreover, KN-93 treatment enhanced the sphere-forming efficiency and the size of spheroid colonies in NIH/3T3-H-Ras^{V12} cells (Figure 3D). Downregulation of CaMKii activity is therefore essential for induction of malignant features observed in K-Ras-transformed cells.

Knockdown of Fzd8 Induces Tumorigenicity in H-Ras^{V12} Cells

To further determine the role of Fzd8 in Wnt/Ca²⁺ signaling, we knocked Fzd8 down in NIH/3T3-H-Ras^{V12} cells (Figures 3A and

3E). We observed reduced phospho-CaMKii level and enhanced β-catenin activity (Figures 3E and 3F). Formation of spheres with re-plating ability was also enhanced upon Fzd8 knockdown (Figure 3G). Importantly, mice injected subcutaneously with 50 NIH/3T3-H-Ras^{V12} cells showed significantly reduced tumor-free survival following shRNA suppression of Fzd8 (Figure 3H). Thus, suppression of Fzd8 expression pheno-copies the effects of oncogenic K-Ras in these stem-ness assays.

Roles of Fzd8 in K-Ras-Driven Malignancy

Next, we tested whether downregulation of Fzd8 is required for NIH/3T3-K-Ras^{V12} cells to promote tumor formation. Restoration of Fzd8 expression in NIH/3T3-K-Ras^{V12} cells enhanced levels of phosphorylated CaMKii (Figure 4A) and reduced β-catenin/TCF/LEF activity (Figure 4B). Furthermore, restoration of Fzd8 significantly reduced sphere formation in NIH/3T3-K-Ras^{V12} cells (Figure 4C). Fzd8 overexpression also abolished tumor formation in nude mice (Figure 4D). Interestingly, exogenously added WNT3a or WNT5a ligand did not affect the increased phospho-CaMKii and inhibited β-catenin activity caused by the overexpression of Fzd8 in NIH 3T3-K-Ras^{V12} cells (Figures S4A and S4B). These suggest that the altered Wnt/Ca²⁺ signaling pathway and β-catenin activity resulting of Fzd8 overexpression cannot be rescued by canonical or non-canonical Wnt pathway ligands.

When Fzd8 was overexpressed in PANC2.13 cells, we observed an increase in phospho-CaMKii level, with a concurrent reduction in the expression of CD44 and CD24 (Figure S4C). When compared with control cells, Fzd8-overexpressing PANC2.13 cells displayed significant downregulation of multiple β-catenin targeted genes, including CCND-1, LEF1, and c-Myc (Herbst et al., 2014), consistent with repressed β-catenin transcriptional activity (Figure S4D). Overexpression of Fzd8 in PANC1 cells, resulted in elevated NF-AT transcriptional activity, decreased activity of β-catenin, and reduced expression of CD44 and CD24 (Figures 4E and S4E). Overexpression of Fzd8 in these pancreatic cancer lines induced differentiation-like morphological changes, phenocopying those observed upon K-Ras knockdown (Figure S4F). Furthermore, nude mice with subcutaneous xeno-transplants of Fzd8-overexpressing PANC1 had increased tumor-free survival rates (Figure 4F). Thus, restoration of Fzd8 expression, which enhances Wnt/Ca²⁺ signaling and suppresses canonical Wnt signaling, reduces tumor formation by K-Ras^{V12}-transformed cells or pancreatic tumor cells possessing oncogenic K-Ras.

Human Fzd8 is normally expressed in brain, heart, kidney, and muscle, as well as in the pancreas (Saitoh et al., 2001). Immunohistochemistry of four human pancreatic tissue arrays revealed that while Fzd8 expression was abundant in normal pancreatic acini, islet, and ductal cells, its expression was frequently lost in malignant pancreatic adenocarcinomas (Figures 4G and S4G). Tissue array T143, B1, B2, B5, and B6 revealed no reduction in Fzd8 expression in islet cell tumors, which are mostly

(H) Knockdown of K-Ras increased Fzd8 protein level, non-canonical Wnt signaling (p-CaMKii), and increased phosphorylation of β-catenin.

(I) Knockdown of K-Ras in PANC2.13 cells reduced canonical Wnt signaling as revealed by TOPFlash assay (n = 4).

*p < 0.05; **p < 0.01.

See also Figures S2 and S3 and Tables S1 and S2.

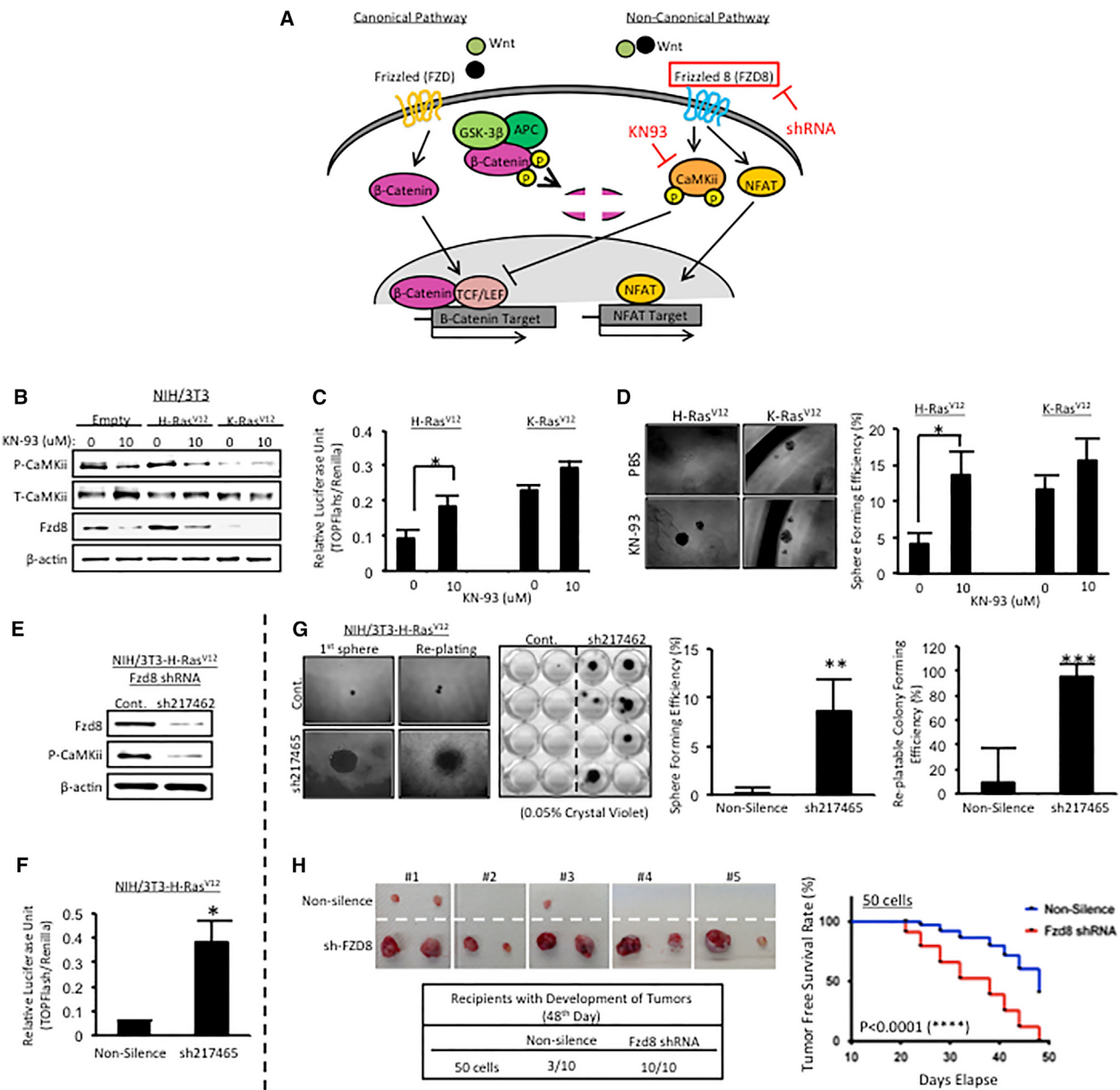


Figure 3. Fzd8-Mediated Non-canonical Wnt/Ca²⁺ Signaling Suppresses the Tumor-Promoting Properties of H-Ras^{V12}-Transformed NIH/3T3 Cells

(A) Schematic illustration of Fzd8 in non-canonical Wnt/Ca²⁺ signaling pathway and its crosstalk with canonical Wnt signaling. Small molecule, KN-93, and shRNA against Fzd8 were used to block CaMKII activity and Fzd8 expression for following experiments.

(B) Inhibition of CaMKII by KN-93 reduced phosphorylation of CaMKII and reduced the expression of Fzd8.

(C) KN-93 treatment stimulated β-catenin transcriptional activities in H-Ras^{V12}-transformed NIH/3T3 cells ($n = 4$).

(D) Inhibition of CaMKII by KN-93 enhanced sphere formation in H-Ras^{V12}-transformed NIH/3T3 cells, but not in K-Ras^{V12}-transformed NIH/3T3 cells ($n = 6$).

(E and F) Knockdown of Fzd8 in H-Ras^{V12}-transformed NIH/3T3 cells. Reduced phospho-CaMKII levels (D) and stimulated β-catenin transcriptional activities ($n = 4$) (E).

(G) Knockdown of Fzd8 in H-Ras^{V12}-transformed NIH/3T3 cells promoted sphere formation and re-plate efficiency ($n = 6$).

(H) Knockdown of Fzd8 in H-Ras^{V12}-transformed NIH/3T3 cells enhanced their tumor initiating abilities.

*p < 0.05; **p < 0.01; ***p < 0.001.

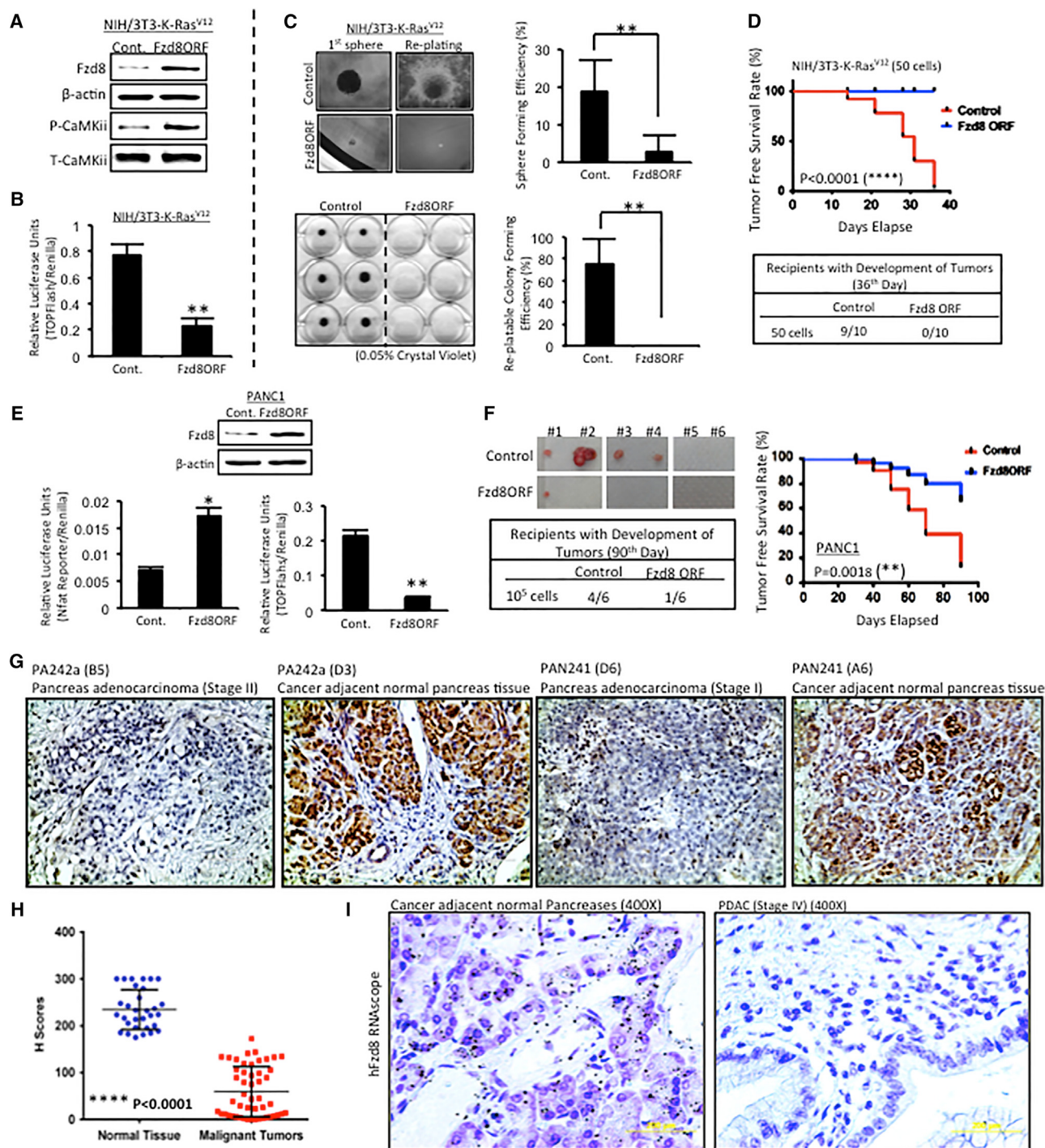


Figure 4. Downregulation of Fzd8 Is Required for K-Ras to Enhance Tumor Initiation

(A and B) Restoration of Fzd8 expression in K-Ras^{V12}-transformed NIH/3T3 cells enhanced Wnt/Ca²⁺ signaling (A) and reduced β-catenin transcriptional activities (B) (n = 4).

(C) Restoration of Fzd8 in K-Ras^{V12}-transformed NIH/3T3 cells reduced sphere formation and re-plating efficiency (n = 6).

(D) Restoration of Fzd8 reduced tumor initiation capacity of K-Ras^{V12}-transformed NIH/3T3 cells.

(E) Fzd8 restoration in PANC1 cells enhanced Wnt/Ca²⁺ signaling as revealed by NF-AT transcriptional activities (n = 4) and reduced β-catenin activities (n = 4).

(F) Fzd8 restoration reduced the tumor initiating ability of PANC1 cells.

(G) Downregulation of Fzd8 in human pancreatic tumor tissues: micrographs of tissue sections immunostained for Fzd8 in human pancreatic cancer adjacent normal tissue and adenocarcinomas (magnification = 200×).

(legend continued on next page)

benign and in which K-Ras is rarely mutated (Figure S4G). In addition, Fzd8 expression was strongly repressed in stage I pancreatic adenocarcinomas (Figure 4G), in which oncogenic activation of K-Ras has most likely already occurred. H-scoring further provided semiquantitative analysis indicating Fzd8 was significantly repressed in human malignant pancreatic specimens when compared with normal pancreases including cancer-adjacent normal tissues (Figure 4H; Data S1).

To further confirm the expression of Fzd8 in human pancreas tissues, we used an *in situ* hybridization method, RNAscope (Wang et al., 2012). As shown in Figure 4I, normal pancreases and cancer-adjacent normal tissues hybridized with the probes specifically for human Fzd8, whereas malignant pancreatic tissue showed no detectable Fzd8 expression. Moreover, Oncomine software (Life Technologies), showed that Fzd8 was significantly downregulated in human pancreatic ductal adenocarcinomas and multiple types of human cancer (Figure S4H). Taken together, we conclude that expression of Fzd8 is repressed in multiple cancers and suggest it may have a role as a tumor suppressor.

Wnt/Ca²⁺ Signaling Is Modulated by K-Ras-Calmodulin Interaction

Calmodulin (CaM) binds preferentially to GTP-bound K-Ras4B, but not to H-Ras, N-Ras, or K-Ras4A (Klee and Vanaman, 1982; Schulman, 1993; Villalonga et al., 2001) (Figure 5A). This specific interaction between CaM and K-Ras can change its subcellular localization and thus reduce the pool of CaM available to activate CaMKii and its subsequent non-canonical Wnt/Ca²⁺ signaling. The hypervariable region of K-Ras4B is essential for CaM binding, and phosphorylation of Ser181 of K-Ras4B abolishes this interaction (Lopez-Alcalá et al., 2008; Villalonga et al., 2001). We generated retroviruses encoding either a mutant (S181D) that mimics phosphorylation or mutant (S181A) form of K-Ras^{V12} that cannot undergo phosphorylation and introduced these mutants into NIH/3T3 cells (Figure S5A). K-Ras^{V12}-S181D did not co-immunoprecipitate with CaM, whereas wild-type and the S181A mutant maintained interaction with CaM under identical conditions (Figure 5B). K-Ras^{V12}-S181D-expressing cells showed increased levels of phospho-CaMKii and marked increase in Fzd8 promoter activity, as well as increased expression of Fzd8, in comparison with K-Ras^{V12}- or K-Ras^{V12}-S181A-transformed cells (Figures 5C–5E). Even though they exhibited comparable levels of K-Ras protein expression and phospho-Erk, K-Ras^{V12}-S181D-infected NIH/3T3 cells showed elevated levels of active CaMKii when compared with K-Ras^{V12}- or K-Ras^{V12}-S181A-transformed cells (Figure 5E). K-Ras^{V12}-S181D-expressing cells further showed increased transcriptional activity of NF-AT, another major down-stream mediator of Wnt/Ca²⁺ signaling pathway, and repression of β-catenin transcriptional activity (Figure 5F). These data show that K-Ras regulates Fzd8-mediated non-canonical Wnt/Ca²⁺

signaling and sequential canonical Wnt/β-catenin signaling by specific interaction with CaM. In contrast, oncogenic H-Ras-transformed tumor cells contain sufficient free CaM to activate CaMKii. N-Ras, like H-Ras, is unable to bind to CaM (Figure S5C). As a result, cells transformed by N-Ras resemble those transformed by H-Ras, including the phosphorylation of CaMKii, elevated expression of Fzd8, and decreased β-catenin/TCF/LEF transcriptional activity (Figures S5D–S5F).

Taken together, these data suggest that the differential interactions between CaM and Ras proteins are the key components that distinguish down-stream CaMKii activity and Fzd8 expression and that disrupting the interaction between K-Ras and CaM by stimulating phosphorylation of S181 is an attractive approach to suppress oncogenic K-Ras-driven malignancy.

Phosphorylation of K-Ras by Treatment with Prostratin Compromises Its Binding to CaM and Suppresses Tumorigenicity

Protein kinase C (PKC) regulates K-Ras by phosphorylation of S181 (Bivona et al., 2006). While typical phorbol esters, such as PMA, activate PKC and promote tumor formation, an atypical PKC activator, prostratin (12-deoxyphorbol-13-acetate), is not a tumor promoter (Szallasi et al., 1993; Zayed et al., 1984). Here, we determined whether this non-tumor promoting PKC activator could be used as an anti-cancer agent to reduce K-Ras-mediated malignancy (Figure 5G).

Prostratin activates PKC in a dose-dependent manner (Figure S6A) and abolishes the interaction between K-Ras and CaM in Ras^{V12}-transformed cells and human pancreatic cancer cell lines (Figure 5H) and increased levels of phospho-CaMKii (Figures 5H and 5I). Prostratin also increased expression of Fzd8 and reduced expression of the β-catenin targeted gene, LEF1 (Figure S6B). Of note, prostratin did not alter the activity of CaMKii in cells transformed by H-Ras^{V12} or K-Ras^{V12}-S181D (Figure 5I). Moreover, K-Ras^{V12}, but not H-Ras^{V12} or K-Ras^{V12}-S181D-transformed NIH/3T3 cells, were sensitive to prostratin and showed dramatically reduced cell viability (Figure 5J). These in vitro responses led us to ask whether prostratin could be used to treat K-Ras-driven malignancies. Indeed, prostratin administered either orally or intra-peritoneally strongly suppressed tumorigenicity of K-Ras^{V12}-transformed cells with no evidence of systemic toxicity (Figure S6C). A single, small subcutaneous tumor derived from K-Ras^{V12}-NIH/3T3 cells in the presence of prostratin showed greatly increased phospho-CaMKii compared with vehicle control (Figure S6D).

Prostratin Suppresses Tumor Initiation and Growth of Human Pancreatic Cancers

In response to prostratin, human pancreatic cancer cells showed morphological changes, phenocopying those observed with knock down of K-Ras or overexpression of Fzd8 (Figure S7A, left panel). Moreover, treatment of prostratin significantly reduced

(H) H-scores of Fzd8 immunoreactivities in pancreatic tissue arrays including normal and malignant tissues.

(I) RNAscope *in situ* hybridization probed for human Fzd8 in cancer adjacent pancreatic normal tissue and pancreatic adenocarcinoma.

*p < 0.05; **p < 0.01.

See also Figure S4.

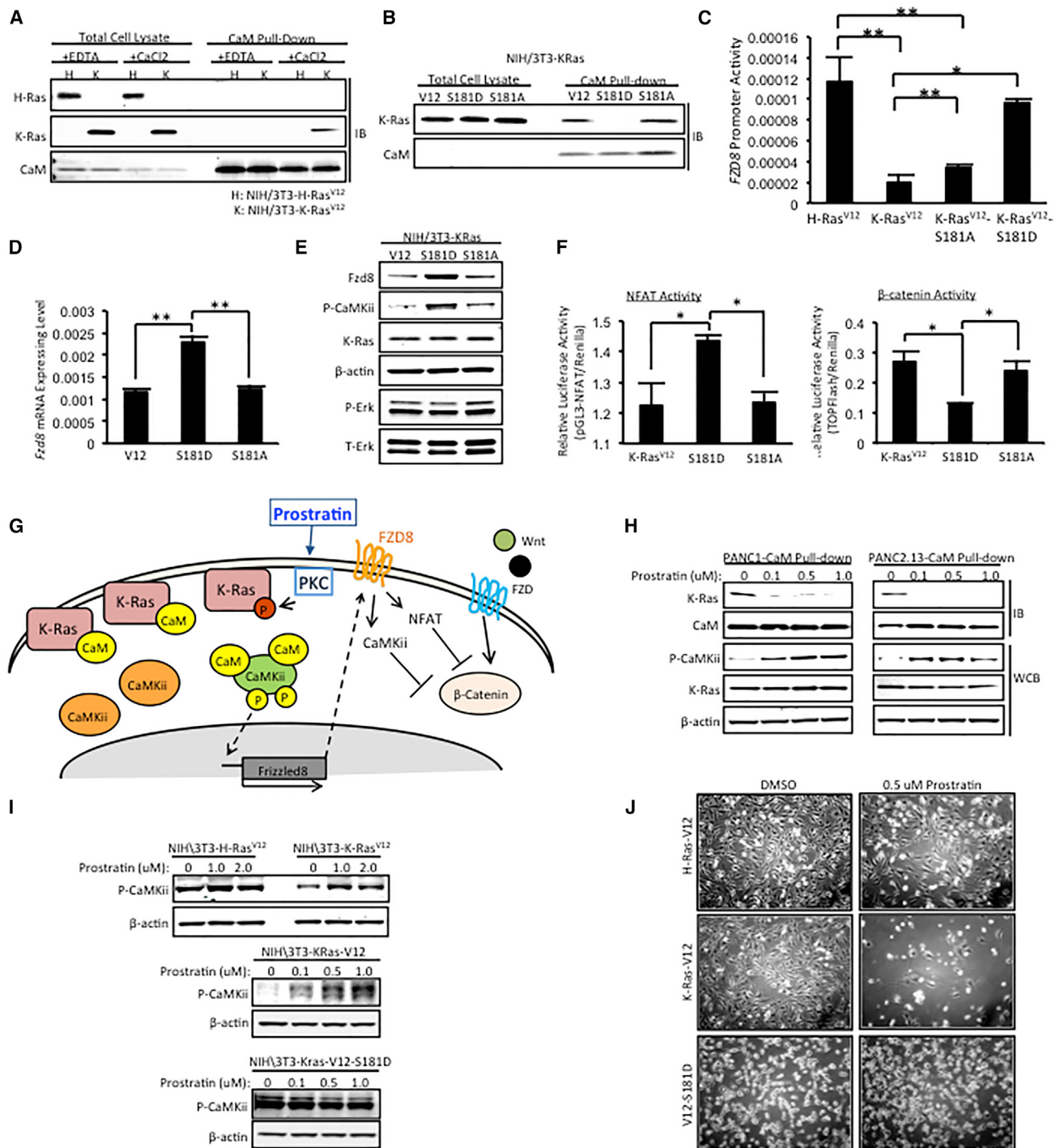


Figure 5. CaM-KRas Interaction Is Essential for Suppression of CaMKii Activity and Fzd8 Expression in K-Ras^{V12}-Transformed NIH/3T3 Cells

- (A) CaM interaction with K-Ras^{V12}, but not with H-Ras^{V12}, as revealed by CaM pull-down assay in the presence of EDTA or Ca²⁺.
- (B) Loss of interaction between CaM with K-Ras^{V12}-S181D mutant when compared with K-Ras^{V12} or K-Ras^{V12}-S181A mutant.
- (C) K-Ras^{V12}-S181D mutant presented reduced capability to suppress Fzd8 promoter activities when compared with K-Ras^{V12} or K-Ras^{V12}-S181A mutant (n = 4).
- (D) Increased Fzd8 expressions in NIH/3T3-K-Ras^{V12}-S181D cells when compared with K-Ras^{V12} or K-Ras^{V12}-S181A group at RNA level (n = 3).
- (E) K-Ras^{V12}-S181D-expressing NIH/3T3 cells showed increased levels of Fzd8 expression and phospho-CaMKii when compared with NIH/3T3-K-Ras^{V12} or NIH/3T3-K-Ras^{V12}-S181A cells. There was no significant difference in the levels of K-Ras protein and phospho-Erk among three cell lines.
- (F) NIH/3T3-K-Ras^{V12}-S181D cells presented significantly increased NF-AT transcriptional activity (left) and reduced Wnt/β-catenin activity (right) when compared with K-Ras^{V12} or K-Ras^{V12}-S181A group (n = 4).

(legend continued on next page)

both cell viability and proliferation rates of these cells (Figure S7A, right panel).

To test the effects of prostratin on K-Ras-driven human pancreatic cancers *in vivo*, we first asked whether prostratin can prevent pancreatic tumor formation in a xenograft model. As Figure 6A shows, prostratin significantly reduced the frequency of tumor formation at subcutaneous sites. Moreover, the average size of established tumors was much smaller than tumors in the control group (Figure 6B). Pancreatic tumor cells were labeled with luciferase for detecting tumor formation more accurately. Bioluminescence imaging (BLI) confirmed that treatment with prostratin profoundly suppressed tumor initiation and tumor size (Figure 6C). In addition, xenografted pancreatic tumors treated with prostratin showed reduced tumor growth rates during therapy, as well as reduced expression of Ki67 (Figure 6D).

We next evaluated the effects of prostratin in orthotopic models of human pancreatic cancer cells with mutant *K-Ras*. PKC activity assays revealed that the oral route was preferable for delivering prostratin efficiently into the pancreas relative to the intraperitoneal route (Figure S6E). Immuno-compromised NOD-SCID mice receiving daily oral treatment of prostratin had lower tumor burden in the orthotopic sites compared to control mice. BLI analysis revealed that prostratin reduced the sizes of orthotopic tumors (Figures 6E and S7B). Moreover, prostratin reduced metastasis to the peritoneum in orthotopic pancreatic cancer models (Figures 6E and S7C). As shown in Figures 6F and S7B, H&E staining revealed that most of prostratin-treated mice did not show formation of primary tumors in the pancreas, whereas mice in the control group had obvious orthotopic tumors and normal pancreatic tissue was barely detectable. In addition, orthotopic tumors in the prostratin-treated group expressed much lower Ki67 (Figures 6G and S7B). Our data suggest that prostratin significantly reduces tumor initiation frequency of human pancreatic cancers in xenograft models.

Next, we tested the anti-tumor effects of prostratin on established human pancreatic xenograft tumors, subcutaneously or orthotopically transplanted into immune-compromised mice. Daily oral prostratin treatment started around 10–14 days post-injection, depending on the cell lines and models (Figure 7A). Prostratin showed anti-tumor activity on human pancreatic subcutaneous tumors, defined by reduced growth rate when compared to vehicle-treated tumors (Figure 7A). Additionally, prostratin-treated subcutaneous tumors showed enhanced expression of cleaved caspase 3 (Figure S7D), suggesting it exerts cytotoxic effects on established tumors.

Cell-free DNA (cfDNA) in the bloodstream shows a nearly perfect correlation with primary tumor size following effective

therapy or tumor recurrence (Anker et al., 1999; Sozzi et al., 2003). Therefore, the quantification of cfDNA can be a useful tool for monitoring certain cancers, including pancreatic malignancies (Sikora et al., 2015). Here, we used Taqman probes specifically detecting human cfDNA in mice in which human pancreatic cancer cells had been orthotopically implanted (Cheng et al., 2009) (Figure 7B). The level of human cfDNA increased more than six times above baseline on day 14 post-tumor implantation. The concentration of human-specific cfDNA decreased in prostratin-treated animals over time, whereas it showed positive dynamic changes in controls (Figure 7B). These data demonstrate that prostratin significantly represses the burden of human pancreatic cancers in orthotopic xenograft models.

Taken together, our data suggest that prostratin, an activator of atypical PKCs, can efficiently reduce the interaction of K-Ras and CaM, rewire Wnt/Ca²⁺ signaling, and suppress malignancy mediated by oncogenic K-Ras in pancreatic cancers.

Prostratin Specifically Represses K-Ras^{G12V}-Induced Papilloma

While the xenografts described above demonstrate the potential of human tumor cells to respond to prostratin *in vivo*, the effects of the tumor microenvironment and immune system are not recapitulated in these models. Therefore, we examined the effects of prostratin in a genetically engineered mouse model (GEMM). We used a papilloma model driven by oncogenic H-Ras or K-Ras under the control of a skin stem cell promoter, Lrig1 (Figure 7C) (Jackson et al., 2001; Jaks et al., 2010; Page et al., 2013; Powell et al., 2012; Tuveson et al., 2004). In this GEMM, tamoxifen-inducible Cre recombinase initiates the expression of oncogenic H-Ras or K-Ras, inducing papillomas during wound-healing (Figure 7C).

Starting from day 5 post-tamoxifen induction and 2 days before wounding, daily oral prostratin treatment was administered to Lrig1-Cre/ER/LSL/K-Ras^{G12D} and Lrig1-Cre/ER/LSL/H-Ras^{G12V} mice (Figure 7C). Six of six Lrig1-Cre/ER/LSL-K-Ras^{G12D} mice receiving placebo treatment had detectable papillomas within 7 days post-wounding; however, only two of six Lrig1-Cre/ER/LSL/K-Ras^{G12D} mice treated with prostratin showed papilloma formation, at a delayed point in time (between 14 and 26 days post-wounding) (Figure 7D, bottom panel). In addition, prostratin significantly reduced the invasive signatures and the growth rate of K-Ras^{G12D}-induced papillomas (Figures 7E and S7E). Lrig1-Cre/ER/LSL/H-Ras^{G12V} mice showed no significant difference in tumor initiation rates and tumor sizes between control (7/9) and prostratin-treated group (8/9) (Figures 7D, S7F, and S7G). In conclusion, prostratin significantly

(G) Schematic illustration of CaM-K-Ras interaction in K-Ras-mediated repression of Fzd8 expression and Fzd8-promoted stem-ness. Prostratin is proposed to interfere the interaction through phosphorylation of K-Ras by the activation of PKC.

(H) CaM interaction with K-Ras^{V12} was suppressed by the treatments of prostratin, as revealed by CaM pull-down assay. WCB, whole cell lysate; IB, immunoblotting.

(I) Elevated activation of CaMKII by prostratin treatments in NIH/3T3 cells transformed by K-Ras^{V12}, not K-Ras^{V12}-S181A mutant or H-Ras^{V12}.

(J) Cell morphologies of NIH/3T3 cells transformed by K-Ras^{V12}, K-Ras^{V12}-S181A mutant, and H-Ras^{V12} in the response to prostratin treatments. DMSO was used as the vehicle control.

*p < 0.05; **p < 0.01.

See also Figures S5 and S6.

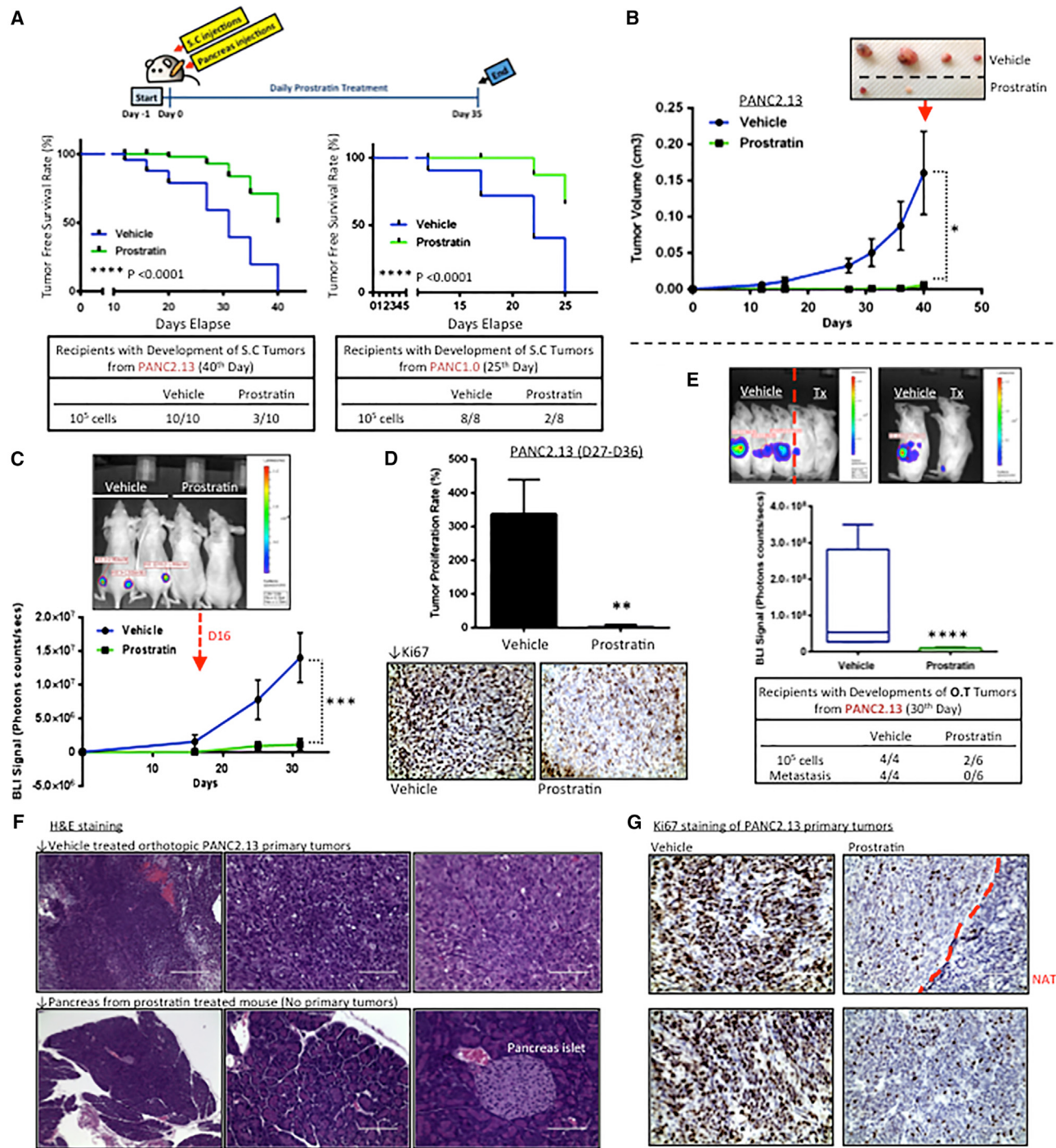


Figure 6. Prostratin Prevented Tumor Initiation of Human Pancreatic Cancers with Mutant K-Ras

(A) Tumor initiation rates of subcutaneously injected PANC1 and PANC2.13 in the response to either vehicle or prostratin treatments. Top panel: schematic illustration of experimental design. Oral prostratin administration was given 1 day before tumor implantation. Nude mice were used for subcutaneous injections, and SCID mice were used for orthotopic implantation.

(B) Tumor growth curve of the subcutaneous tumors derived from PANC2.13 in the response to drug treatments (n = 10).

(C) Bioluminescence imaging (BLI) signaling changes of the subcutaneous tumors derived from PANC2.13 in the response to drug treatments (n = 10).

(D) Tumor proliferation rate and Ki67 staining of the subcutaneous tumors derived from PANC2.13 in the response to drug treatments. Tumor proliferation rate (D27-D36) = (size of tumor on D36 – size of tumor on D27)/size of tumor on D36 × 100.

(E) Tumor initiation rate and bioluminescence imaging (BLI) signaling activity of the orthotopic tumors derived from PANC2.13 in the response to drug treatments.

(legend continued on next page)

reduced the formation of papillomas driven by K-Ras^{G12D}, whereas it showed no effect on H-Ras^{G12V}-induced tumors.

All the described experiments in xenograft and GEMM models are approved by UCSF IACUC (protocol number: AN092211-03D).

DISCUSSION

Historically, the high degree of sequence homology, coupled with similar ability of mutant *H-Ras*, *N-Ras*, and *K-Ras* oncogenes to transform cells in culture and to activate common cellular signaling pathways, supported the idea that these three *Ras* gene products are functionally redundant (Bos, 1989; Castellano and Santos, 2011; Chesa et al., 1987; Furth et al., 1987; Leon et al., 1987). Here, we report that *H-Ras* and *K-Ras* actually differ in their abilities to induce tumor initiation and that this is directly related to the ability of K-Ras to suppress the Fzd8-mediated non-canonical Wnt/Ca²⁺ signaling pathway. One consequence of suppressing this pathway is the induction of canonical Wnt signaling. However, our data, and those of others, suggest that this induction is not sufficient to promote malignancy, at least in pancreatic tissue.

To be noted, two key down-stream effectors of non-canonical Wnt/Ca²⁺ signaling, NF-AT and CaMKII, are involved in the regulation of expression of multiple genes (Krebs, 1998; Rao et al., 1997). For example, NF-AT is a transcription factor and has been predicted to directly bind to the promoter regions of multiple genes that are associated with tumorigenesis, such as *TNF* and *MMP9*. The functions of NF-AT on down-stream genes and their potential crosstalk with K-Ras need to be investigated further.

CaMKII is regulated by binding to CaM (Bachs et al., 1994; Klee and Vanaman, 1982; Stewart et al., 1982). Interestingly, CaM also binds to K-Ras4B, but not to N-Ras, H-Ras, or K-Ras4A (Villalonga et al., 2001). Furthermore, the binding of K-Ras to CaM is attenuated by phosphorylation of Ser181 by PKC. The K-Ras^{V12} S181D variant lost the ability to suppress CaMKII activity and Fzd8 expression, suggesting that the interaction between K-Ras and CaM, which is GTP-dependent, is an important pathway for K-Ras to inhibit Fzd8-mediated non-canonical Wnt/Ca²⁺ signaling. Therefore, blocking this specific interaction between K-Ras and CaM may provide a novel approach to target K-Ras selectively.

Here, we report that activation of PKC by prostratin leads to the dissociation of K-Ras and CaM, activation of non-canonical Wnt/Ca²⁺ signaling, and suppression of K-Ras-mediated malignancy. Our finding leads to an open question: while the activation of PKC isozymes by phorbol esters has long been considered to promote tumorigenesis, what drives the difference between PKC activation by prostratin and other typical activators, such as PMA?

PKC has been implicated in tumorigenesis for over 30 years (Castagna et al., 1982). PKC is a family of related isoforms, cate-

gorized as conventional (α , βI , βII , and γ), novel (δ , ϵ , η , and θ), and atypical (ζ , λ/ι) (Basu and Pal, 2010), which exhibit overlapping as well as opposing functions (Steinberg, 2008). For example, PKC δ is believed to function as a tumor suppressor since downregulation rather than activation of PKC δ has been associated with tumor promotion (Lu et al., 1997). Surprisingly, the majority of cancer-associated mutations in PKC subgroups are loss-of-function (Antal et al., 2015), and several mutations are dominant negative, that suppress global PKC signaling (Antal et al., 2015). This establishes a hypothesis: PKC isozymes generally function as tumor suppressors and, therefore, anti-cancer therapies should focus on restoring, not inhibiting PKC activity. This suggestion had also been made by Bivona et al. (2006) based on their observations that PKC-mediated phosphorylation of K-Ras at Serine-181 affects K-Ras activity.

Interestingly, PMA and prostratin have been shown to differ substantially in their biological activities (activation versus sub-cellular translocation) on PKC α and PKC δ (Márquez et al., 2008), potentially explaining their distinct properties on tumor promotion. Moreover, although K-Ras is known to be phosphorylated by PKC, the specific functions of different PKC isozymes on the phosphorylation of S181 within the polybasic region of K-Ras remain to be defined. Further investigation of the specific PKC isoforms required for K-Ras phosphorylation and regulation by prostratin will be needed to clarify these unanswered questions and to develop more potent inhibitors for blocking K-Ras-CaM interactions.

In summary, K-Ras suppresses Wnt/Ca²⁺ signaling pathway by direct binding with CaM, leading to the reduced CaMKII activity and downregulating Fzd8 expression. Downregulation of Fzd8 expression by K-Ras leads to a sustained suppression of Wnt/Ca²⁺ signaling, which causes increased tumorigenicity. The isoform-specific activity of K-Ras, described here, can be exploited to block K-Ras oncogenic activity without affecting other Ras isoforms.

EXPERIMENTAL PROCEDURES

Cell Lines

NIH/3T3, BxPC3, PANC1, PANC2.13, SW480, LS180, HCT15, and HCT116 cells were from ATCC. Mouse pancreatic adenocarcinoma cells were from Dr. Collisson (University of California, San Francisco). Mouse cell lines were grown in DMEM with 10% FBS (or calf serum [CS] for NIH/3T3 cells) at 37°C, 5% CO₂. Human colon cancer cell lines were cultured in RPMI-1640 medium with 10% FBS. Human pancreatic cancer cell lines were maintained in RPMI-1640 medium supplemented with 15% FBS and human recombinant insulin (GIBCO 12585-014).

Animal Studies

All experiments were approved by the University of California, San Francisco (UCSF) Institutional Animal Care and Use Committee (IACUC). Ras^{V12}-transformed NIH/3T3 cells were subcutaneously injected in female nude mice (Nu/Nu) at 50, 100, or 1,000 cells per flank. Palpable tumors were measured twice a week. Mice were divided into five/group. Pancreatic adenocarcinoma cells-derived *Kras*^{LSL-G12D} mice were provided by Dr. Collisson and genotyped

(F) H&E staining of normal mouse pancreases and orthotopic tumors derived from PANC2.13.

(G) Ki67 staining of orthotopic tumors derived from PANC2.13 in the response to drug treatments.

*p < 0.05; **p < 0.01; ***p < 0.001. Data are means \pm SEM for (B) and (C).

See also Figure S6.

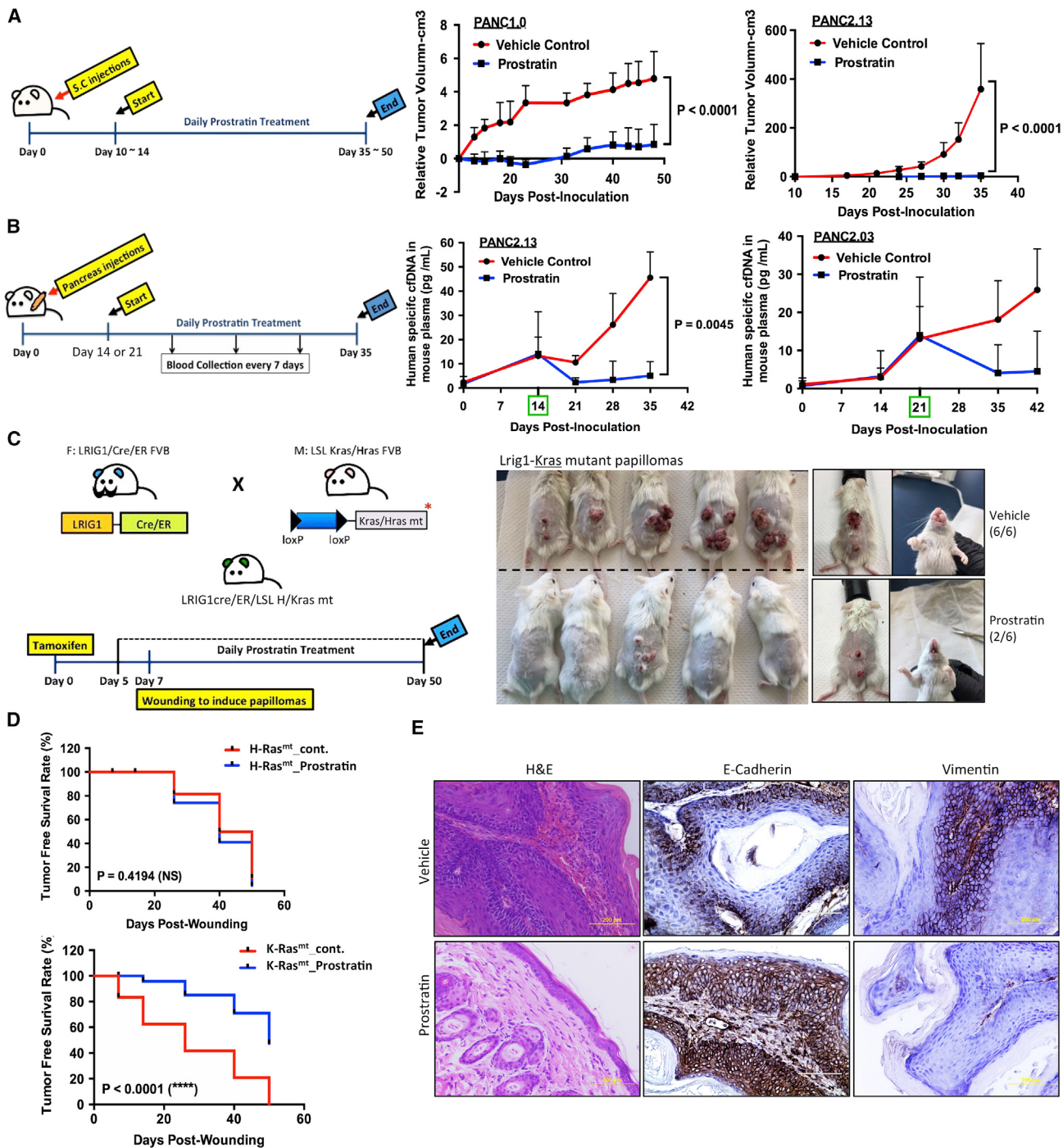


Figure 7. Prostratin Represses In Vivo Malignancy Driven by Oncogenic K-Ras

- (A) Prostratin showed anti-tumor effects on established subcutaneous tumors derived from 0.5×10^6 cells of PANC1 or PANC2.13 ($n = 7$; data are means \pm SEM).
- (B) Prostratin suppressed orthotopic tumor burdens measured by cfDNA values ($n = 5$ for PANC2.13 group; $n = 6$ for PANC2.03 group).
- (C) Prostratin reduced the incidence of papilloma formations in LRIG1cre/ER/LSL-Ras^{mutant} GEMM. Left: schematic illustration of the generation of papilloma in LRIG1cre/ER/LSL-Ras^{mutant} mice. Right: the pictures of mice carrying K-Ras^{G12D}-induced papillomas with vehicle or prostratin treatment.
- (D) Prostratin affected papilloma initiation differently in LRIG1cre/ER/LSL-H- and K-Ras^{mutant} mice.
- (E) H&E staining and IHC stained for E-cadherin and vimentin in K-Ras^{G12D}-induced papillomas with vehicle (top) or prostratin treatment (bottom).

See also Figure S7.

as described (Collisson et al., 2011; Dankort et al., 2007; Hingorani et al., 2003). One hundred cells were orthotopically implanted in 6- to 8-week-old FVB/n mice in 20 μ l 50% Matrigel using a 28.5-gauge needle. Mice were monitored for 1 month and were euthanized when distressed.

Skin tumors were induced by the two-stage chemical carcinogenesis protocol using DMBA and TPA (Balmain and Pragnell, 1983). Histologically confirmed skin carcinomas were processed for molecular analyses by conventional methods. Mutations in Kras and HrasK1 alleles were identified by direct sequencing (Karnoub and Weinberg, 2008; To et al., 2008).

Prostratin for animal treatment was from Santa Cruz Biotechnology (sc-203422A). It was administrated daily into either NOD-SCID mice or athymic NUDE mice by oral gavage at 1 mg/kg or intraperitoneal injection at 0.5 mg/kg. Ten percent DMSO, 10% cremophor, and 80% saline solutions were used as the solvent and vehicle control. The toxic effects of prostratin were evaluated by monitoring body weight for at least 30 days.

Lrig1Cre/ER/LSL Hras^{G12V} and *Lrig1Cre/ER/ LSL-Kras^{G12D}* mice have been backcrossed into the FVB/N background over multiple generations. Cre recombinase was activated in both groups of mice. A single dose of 4-OH-tamoxifen was topically applied at 8 weeks of age and on day 7. Thereafter, papilloma development was induced by wounding the back of the mice.

DNA Extraction from Mouse Plasma Samples

All blood samples were collected in K₂EDTA containing tubes (BD Microtainer; 365974) and centrifuged at 1,500 \times g for 10 min. The supernatants were collected from the top of the plasma to eliminate cell contamination. Plasma was stored at -80°C. cfDNA was extracted from 100 μ l of plasma using NucleoSpin Plasma XS kit (Macherey-Nagel; 740900). Quantification of human cfDNA in mouse plasma is described in the Supplemental Experimental Procedures.

SUPPLEMENTAL INFORMATION

Supplemental Information includes Supplemental Experimental Procedures, seven figures, two tables, and one data file and can be found with this article online at <http://dx.doi.org/10.1016/j.cell.2015.10.041>.

AUTHOR CONTRIBUTIONS

M.-T.W. performed most of the experiments. M.H. generated the K-Ras^{V12}-S181D and -S181A mutant constructs. M.D.T., R.D., and A.B. generated the chemically induced skin tumors from the *H-Ras* knockin mice and also provided tumor-bearing *Lrig1-Cre/ER-K-RasLSLG12D* and *Lrig1-H-RasLSLG12V* mice. J.G. provided technical assistance. M.-T.W. and F.M. conceived the project, designed experiments, interpreted results, and wrote the manuscript.

ACKNOWLEDGMENTS

Parts of this work were supported by grants from Daiichi Sankyo, Tokyo and the Lustgarten Foundation. We acknowledge Drs. Yu-Jen Lu and Chen-Yen Yang for helping with parts of the animal experiments, including oral gavage treatment and blood collection. We thank Dr. Bob Coffey for providing *Lrig1* mice and Drs. Kevin Haigis and Tyler Jacks for the *HrasLSLG12V* mice. F.M. and M.-T.W. are the co-founders of K-Gen, Limited.

Received: August 12, 2015

Revised: October 1, 2015

Accepted: October 13, 2015

Published: November 19, 2015

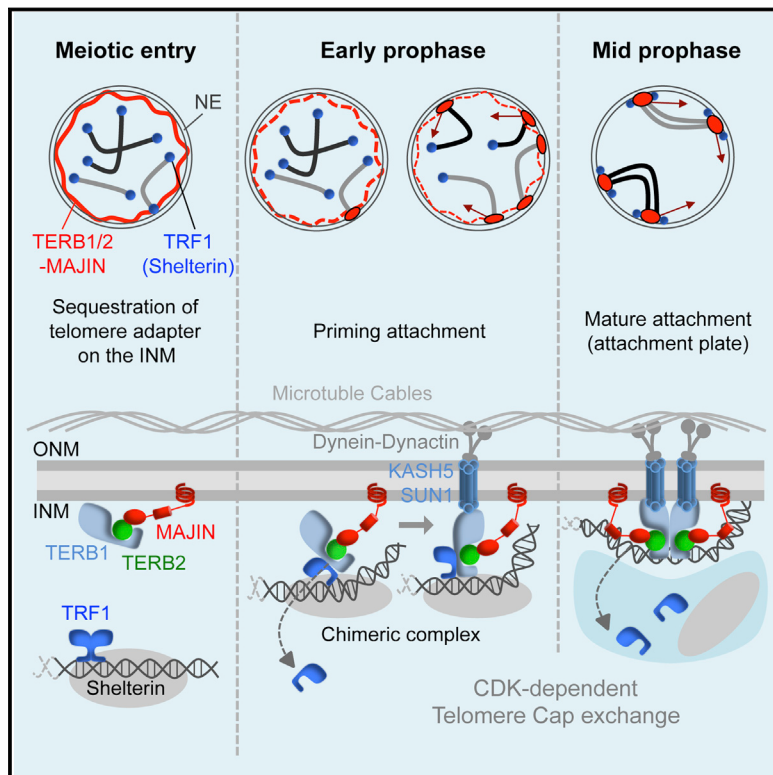
REFERENCES

- Anker, P., Mulcahy, H., Chen, X.Q., and Stroun, M. (1999). Detection of circulating tumour DNA in the blood (plasma/serum) of cancer patients. *Cancer Metastasis Rev.* 18, 65–73.
- Antal, C.E., Hudson, A.M., Kang, E., Zanca, C., Wirth, C., Stephenson, N.L., Trotter, E.W., Gallegos, L.L., Miller, C.J., Furnari, F.B., et al. (2015). Cancer-associated protein kinase C mutations reveal kinase's role as tumor suppressor. *Cell* 160, 489–502.
- Bachs, O., Agell, N., and Carafoli, E. (1994). Calmodulin and calmodulin-binding proteins in the nucleus. *Cell Calcium* 16, 289–296.
- Balmain, A., and Pragnell, I.B. (1983). Mouse skin carcinomas induced in vivo by chemical carcinogens have a transforming Harvey-ras oncogene. *Nature* 303, 72–74.
- Basu, A., and Pal, D. (2010). Two faces of protein kinase C δ : the contrasting roles of PKC δ in cell survival and cell death. *ScientificWorldJournal* 10, 2272–2284.
- Bivona, T.G., Quatela, S.E., Bodenmann, B.O., Ahearn, I.M., Soskis, M.J., Mor, A., Miura, J., Wiener, H.H., Wright, L., Saba, S.G., et al. (2006). PKC regulates a farnesyl-electrostatic switch on K-Ras that promotes its association with Bcl-XL on mitochondria and induces apoptosis. *Mol. Cell* 21, 481–493.
- Bos, J.L. (1989). ras oncogenes in human cancer: a review. *Cancer Res.* 49, 4682–4689.
- Castagna, M., Takai, Y., Kaibuchi, K., Sano, K., Kikkawa, U., and Nishizuka, Y. (1982). Direct activation of calcium-activated, phospholipid-dependent protein kinase by tumor-promoting phorbol esters. *J. Biol. Chem.* 257, 7847–7851.
- Castellano, E., and Santos, E. (2011). Functional specificity of ras isoforms: so similar but so different. *Genes Cancer* 2, 216–231.
- Cheng, C., Omura-Minamisawa, M., Kang, Y., Hara, T., Koike, I., and Inoue, T. (2009). Quantification of circulating cell-free DNA in the plasma of cancer patients during radiation therapy. *Cancer Sci.* 100, 303–309.
- Chesa, P.G., Rettig, W.J., Melamed, M.R., Old, L.J., and Niman, H.L. (1987). Expression of p21ras in normal and malignant human tissues: lack of association with proliferation and malignancy. *Proc. Natl. Acad. Sci. USA* 84, 3234–3238.
- Clarke, M.F., Dick, J.E., Dirks, P.B., Eaves, C.J., Jamieson, C.H., Jones, D.L., Visvader, J., Weissman, I.L., and Wahl, G.M. (2006). Cancer stem cells—perspectives on current status and future directions: AACR Workshop on cancer stem cells. *Cancer Res.* 66, 9339–9344.
- Collisson, E.A., Sadanandam, A., Olson, P., Gibb, W.J., Truitt, M., Gu, S., Cooc, J., Weinkle, J., Kim, G.E., Jakkula, L., et al. (2011). Subtypes of pancreatic ductal adenocarcinoma and their differing responses to therapy. *Nat. Med.* 17, 500–503.
- Dankort, D., Filenova, E., Collado, M., Serrano, M., Jones, K., and McMahon, M. (2007). A new mouse model to explore the initiation, progression, and therapy of BRAFV600E-induced lung tumors. *Genes Dev.* 21, 379–384.
- Fang, D., Nguyen, T.K., Leishear, K., Finko, R., Kulp, A.N., Hotz, S., Van Belle, P.A., Xu, X., Elder, D.E., and Herlyn, M. (2005). A tumorigenic subpopulation with stem cell properties in melanomas. *Cancer Res.* 65, 9328–9337.
- Fujii, H., Honoki, K., Tsujiuchi, T., Kido, A., Yoshitani, K., and Takakura, Y. (2009). Sphere-forming stem-like cell populations with drug resistance in human sarcoma cell lines. *Int. J. Oncol.* 34, 1381–1386.
- Furth, M.E., Aldrich, T.H., and Cordon-Cardo, C. (1987). Expression of ras proto-oncogene proteins in normal human tissues. *Oncogene* 1, 47–58.
- Gou, S., Liu, T., Wang, C., Yin, T., Li, K., Yang, M., and Zhou, J. (2007). Establishment of clonal colony-forming assay for propagation of pancreatic cancer cells with stem cell properties. *Pancreas* 34, 429–435.
- Herbst, A., Jurinovic, V., Krebs, S., Thieme, S.E., Blum, H., Göke, B., and Kolligs, F.T. (2014). Comprehensive analysis of β -catenin target genes in colorectal carcinoma cell lines with deregulated Wnt/ β -catenin signaling. *BMC Genomics* 15, 74.
- Hingorani, S.R., Petricoin, E.F., Maitra, A., Rajapakse, V., King, C., Jacobetz, M.A., Ross, S., Conrads, T.P., Veenstra, T.D., Hitt, B.A., et al. (2003). Preinvasive and invasive ductal pancreatic cancer and its early detection in the mouse. *Cancer Cell* 4, 437–450.
- Jackson, E.L., Willis, N., Mercer, K., Bronson, R.T., Crowley, D., Montoya, R., Jacks, T., and Tuveson, D.A. (2001). Analysis of lung tumor initiation and progression using conditional expression of oncogenic K-ras. *Genes Dev.* 15, 3243–3248.

- Jaks, V., Kasper, M., and Toftgård, R. (2010). The hair follicle-a stem cell zoo. *Exp. Cell Res.* 316, 1422–1428.
- Johnson, L., Greenbaum, D., Cichowski, K., Mercer, K., Murphy, E., Schmitt, E., Bronson, R.T., Umanoff, H., Edelmann, W., Kucherlapati, R., and Jacks, T. (1997). K-ras is an essential gene in the mouse with partial functional overlap with N-ras. *Genes Dev.* 11, 2468–2481.
- Karnoub, A.E., and Weinberg, R.A. (2008). Ras oncogenes: split personalities. *Nat. Rev. Mol. Cell Biol.* 9, 517–531.
- Klee, C.B., and Vanaman, T.C. (1982). Calmodulin. *Adv. Protein Chem.* 35, 213–321.
- Koera, K., Nakamura, K., Nakao, K., Miyoshi, J., Toyoshima, K., Hatta, T., Otani, H., Aliba, A., and Katsuki, M. (1997). K-ras is essential for the development of the mouse embryo. *Oncogene* 15, 1151–1159.
- Krebs, J. (1998). Calmodulin-dependent protein kinase IV: regulation of function and expression. *Biochim. Biophys. Acta* 1448, 183–189.
- Leon, J., Guerrero, I., and Pellicer, A. (1987). Differential expression of the ras gene family in mice. *Mol. Cell. Biol.* 7, 1535–1540.
- Lopez-Alcalá, C., Alvarez-Moya, B., Villalonga, P., Calvo, M., Bachs, O., and Agell, N. (2008). Identification of essential interacting elements in K-Ras/calmodulin binding and its role in K-Ras localization. *J. Biol. Chem.* 283, 10621–10631.
- Lu, Z., Hornia, A., Jiang, Y.W., Zang, Q., Ohno, S., and Foster, D.A. (1997). Tumor promotion by depleting cells of protein kinase C delta. *Mol. Cell. Biol.* 17, 3418–3428.
- Malumbres, M., and Barbacid, M. (2003). RAS oncogenes: the first 30 years. *Nat. Rev. Cancer* 3, 459–465.
- Márquez, N., Calzado, M.A., Sánchez-Duffhues, G., Pérez, M., Minassi, A., Pagani, A., Appendino, G., Diaz, L., Muñoz-Fernández, M.A., and Muñoz, E. (2008). Differential effects of phorbol-13-monoesters on human immunodeficiency virus reactivation. *Biochem. Pharmacol.* 75, 1370–1380.
- Page, M.E., Lombard, P., Ng, F., Göttgens, B., and Jensen, K.B. (2013). The epidermis comprises autonomous compartments maintained by distinct stem cell populations. *Cell Stem Cell* 13, 471–482.
- Ponti, D., Costa, A., Zaffaroni, N., Pratesi, G., Petrangolini, G., Coradini, D., Pilotti, S., Pierotti, M.A., and Daidone, M.G. (2005). Isolation and in vitro propagation of tumorigenic breast cancer cells with stem/progenitor cell properties. *Cancer Res.* 65, 5506–5511.
- Potenza, N., Vecchione, C., Notte, A., De Rienzo, A., Rosica, A., Bauer, L., Affuso, A., De Felice, M., Russo, T., Poulet, R., et al. (2005). Replacement of K-Ras with H-Ras supports normal embryonic development despite inducing cardiovascular pathology in adult mice. *EMBO Rep.* 6, 432–437.
- Powell, A.E., Wang, Y., Li, Y., Poulin, E.J., Means, A.L., Washington, M.K., Higginbotham, J.N., Juchheim, A., Prasad, N., Levy, S.E., et al. (2012). The pan-ErbB negative regulator Lrig1 is an intestinal stem cell marker that functions as a tumor suppressor. *Cell* 149, 146–158.
- Prior, I.A., Lewis, P.D., and Mattos, C. (2012). A comprehensive survey of Ras mutations in cancer. *Cancer Res.* 72, 2457–2467.
- Quinlan, M.P., Quatela, S.E., Philips, M.R., and Settleman, J. (2008). Activated Kras, but not Hras or Nras, may initiate tumors of endodermal origin via stem cell expansion. *Mol. Cell. Biol.* 28, 2659–2674.
- Rao, A., Luo, C., and Hogan, P.G. (1997). Transcription factors of the NFAT family: regulation and function. *Annu. Rev. Immunol.* 15, 707–747.
- Saitoh, T., Hirai, M., and Katoh, M. (2001). Molecular cloning and characterization of human Frizzled-8 gene on chromosome 10p11.2. *Int. J. Oncol.* 18, 991–996.
- Saneyoshi, T., Kume, S., Amasaki, Y., and Mikoshiba, K. (2002). The Wnt/calcium pathway activates NF-AT and promotes ventral cell fate in Xenopus embryos. *Nature* 417, 295–299.
- Sasaki, H., Nishizaki, Y., Hui, C., Nakafuku, M., and Kondoh, H. (1999). Regulation of Gli2 and Gli3 activities by an amino-terminal repression domain: implication of Gli2 and Gli3 as primary mediators of Shh signaling. *Development* 126, 3915–3924.
- Scholl, C., Fröhling, S., Dunn, I.F., Schinzel, A.C., Barbie, D.A., Kim, S.Y., Silver, S.J., Tamayo, P., Wadlow, R.C., Ramaswamy, S., et al. (2009). Synthetic lethal interaction between oncogenic KRAS dependency and STK33 suppression in human cancer cells. *Cell* 137, 821–834.
- Schulman, H. (1993). The multifunctional Ca²⁺/calmodulin-dependent protein kinases. *Curr. Opin. Cell Biol.* 5, 247–253.
- Semenov, M.V., Habas, R., Macdonald, B.T., and He, X. (2007). SnapShot: Noncanonical Wnt Signaling Pathways. *Cell* 131, 1378.
- Sikora, K., Bedin, C., Vicentini, C., Malpeli, G., D'Angelo, E., Sperandio, N., Lawlor, R.T., Bassi, C., Tortora, G., Nitti, D., et al. (2015). Evaluation of cell-free DNA as a biomarker for pancreatic malignancies. *Int. J. Biol. Markers* 30, e136–e141.
- Singh, S.K., Clarke, I.D., Terasaki, M., Bonn, V.E., Hawkins, C., Squire, J., and Dirks, P.B. (2003). Identification of a cancer stem cell in human brain tumors. *Cancer Res.* 63, 5821–5828.
- Singh, A., Greninger, P., Rhodes, D., Koopman, L., Violette, S., Bardeesy, N., and Settleman, J. (2009). A gene expression signature associated with "K-Ras addiction" reveals regulators of EMT and tumor cell survival. *Cancer Cell* 15, 489–500.
- Sozzi, G., Conte, D., Leon, M., Ciricione, R., Roz, L., Ratcliffe, C., Roz, E., Cirenei, N., Bellomi, M., Pelosi, G., et al. (2003). Quantification of free circulating DNA as a diagnostic marker in lung cancer. *J. Clin. Oncol.* 21, 3902–3908.
- Steinberg, S.F. (2008). Structural basis of protein kinase C isoform function. *Physiol. Rev.* 88, 1341–1378.
- Stewart, A.A., Ingebritsen, T.S., Manalan, A., Klee, C.B., and Cohen, P. (1982). Discovery of a Ca²⁺- and calmodulin-dependent protein phosphatase: probable identity with calcineurin (CaM-BP80). *FEBS Lett.* 137, 80–84.
- Sugimura, R., and Li, L. (2010). Noncanonical Wnt signaling in vertebrate development, stem cells, and diseases. *Birth Defects Res. C Embryo Today* 90, 243–256.
- Sugimura, R., He, X.C., Venkatraman, A., Arai, F., Box, A., Semerad, C., Haug, J.S., Peng, L., Zhong, X.B., Suda, T., and Li, L. (2012). Noncanonical Wnt signaling maintains hematopoietic stem cells in the niche. *Cell* 150, 351–365.
- Szallasi, Z., Krsmanovic, L., and Blumberg, P.M. (1993). Nonpromoting 12-deoxyphorbol 13-esters inhibit phorbol 12-myristate 13-acetate induced tumor promotion in CD-1 mouse skin. *Cancer Res.* 53, 2507–2512.
- To, M.D., Wong, C.E., Karnezis, A.N., Del Rosario, R., Di Lauro, R., and Balmain, A. (2008). Kras regulatory elements and exon 4A determine mutation specificity in lung cancer. *Nat. Genet.* 40, 1240–1244.
- Tuveson, D.A., Shaw, A.T., Willis, N.A., Silver, D.P., Jackson, E.L., Chang, S., Mercer, K.L., Grochow, R., Hock, H., Crowley, D., et al. (2004). Endogenous oncogenic K-ras(G12D) stimulates proliferation and widespread neoplastic and developmental defects. *Cancer Cell* 5, 375–387.
- Villalonga, P., López-Alcalá, C., Bosch, M., Chiloeches, A., Rocamora, N., Gil, J., Marais, R., Marshall, C.J., Bachs, O., and Agell, N. (2001). Calmodulin binds to K-Ras, but not to H- or N-Ras, and modulates its downstream signaling. *Mol. Cell. Biol.* 21, 7345–7354.
- Wang, F., Flanagan, J., Su, N., Wang, L.C., Bui, S., Nielson, A., Wu, X., Vo, H.T., Ma, X.J., and Luo, Y. (2012). RNAscope: a novel in situ RNA analysis platform for formalin-fixed, paraffin-embedded tissues. *J. Mol. Diagn.* 14, 22–29.
- Weekes, C.D., and Winn, R.A. (2011). The many faces of wnt and pancreatic ductal adenocarcinoma oncogenesis. *Cancers (Basel)* 3, 3676–3686.
- Wei, F., Liu, Y., Bellail, A.C., Olson, J.J., Sun, S.Y., Lu, G., Ding, L., Yuan, C., Wang, G., and Hao, C. (2012). K-Ras mutation-mediated IGF-1-induced feedback ERK activation contributes to the rapalog resistance in pancreatic ductal adenocarcinomas. *Cancer Lett.* 322, 58–69.
- Wong, C.E., Yu, J.S., Quigley, D.A., To, M.D., Jen, K.Y., Huang, P.Y., Del Rosario, R., and Balmain, A. (2013). Inflammation and Hras signaling control epithelial-mesenchymal transition during skin tumor progression. *Genes Dev.* 27, 670–682.
- Zayed, S., Sorg, B., and Hecker, E. (1984). Structure activity relations of polyfunctional diterpenes of the tigliane type. VI. Irritant and tumor promoting activities of semisynthetic mono and diesters of 12-deoxyphorbol. *Planta Med.* 50, 65–69.

MAJIN Links Telomeric DNA to the Nuclear Membrane by Exchanging Telomere Cap

Graphical Abstract



Authors

Hiroki Shibuya, Abrahan Hernández-Hernández, Akihiro Morimoto, Lumi Negishi, Christer Höög, Yoshinori Watanabe

Correspondence

ywatanab@iam.u-tokyo.ac.jp

In Brief

During meiosis, telomeres experience a cap exchange process in which a protein complex localized at the inner nuclear membrane replaces the protective cap of chromosomes to ensure telomere tethering for correct chromosome recombination.

Highlights

- Identification of the meiotic telomere complex, TERB1/2-MAJIN, in mouse germ cells
- TERB1/2-MAJIN ensures telomere-inner nuclear membrane attachment during meiosis
- Telomere cap exchange releases shelterin from the telomeric DNA

MAJIN Links Telomeric DNA to the Nuclear Membrane by Exchanging Telomere Cap

Hiroki Shibuya,¹ Abraham Hernández-Hernández,² Akihiro Morimoto,¹ Lumi Negishi,³ Christer Höög,² and Yoshinori Watanabe^{1,*}

¹Laboratory of Chromosome Dynamics, Institute of Molecular and Cellular Biosciences, University of Tokyo, 1-1-1 Yayoi, Tokyo 113-0032, Japan

²Department of Cell and Molecular Biology, Karolinska Institute, Stockholm 171 77, Sweden

³Laboratory of Protein Expression and Production, Center for Structural Biology of Challenging Proteins, Institute of Molecular and Cellular Biosciences, University of Tokyo, 1-1-1 Yayoi, Tokyo 113-0032, Japan

*Correspondence: ywatanab@iam.u-tokyo.ac.jp

<http://dx.doi.org/10.1016/j.cell.2015.10.030>

SUMMARY

In meiosis, telomeres attach to the inner nuclear membrane (INM) and drive the chromosome movement required for homolog pairing and recombination. Here, we address the question of how telomeres are structurally adapted for the meiotic task. We identify a multi-subunit meiotic telomere-complex, TERB1/2-MAJIN, which takes over telomeric DNA from the shelterin complex in mouse germ cells. TERB1/2-MAJIN initially assembles on the INM sequestered by its putative transmembrane subunit MAJIN. In early meiosis, telomere attachment is achieved by the formation of a chimeric complex of TERB1/2-MAJIN and shelterin. The chimeric complex matures during prophase into DNA-bound TERB1/2-MAJIN by releasing shelterin, forming a direct link between telomeric DNA and the INM. These hierarchical processes, termed "telomere cap exchange," are regulated by CDK-dependent phosphorylation and the DNA-binding activity of MAJIN. Further, we uncover a positive feedback between telomere attachment and chromosome movement, revealing a comprehensive regulatory network underlying meiosis-specific telomere function in mammals.

INTRODUCTION

The ends of eukaryotic chromosomes, telomeres, are composed of a tandem array of short repeat DNA, (TTAGGG)_n, in vertebrates, which is bound by an evolutionary conserved DNA-binding protein complex named shelterin. The primary function of shelterin is to protect telomeres from the aberrant activation of the DNA damage response. Without the protective function of shelterin, chromosome-ends are degraded, leading to checkpoint activation, irreversible growth arrest, and ultimately, apoptosis. Therefore, the binding of shelterin to telomeric DNA is a universal process in eukaryotic cells, the so-called protective cap of chromosomes (Palm and de Lange, 2008).

Meiosis is a specialized cell division for gametogenesis in which haploid cells are produced through two successive rounds of cell divisions following a single round of DNA replication. Errors in meiosis are a leading cause of human disease, such as congenital birth defects and miscarriages (Hassold and Hunt, 2001). During meiotic prophase I, cells establish associations between homologous chromosomes (homologs) to exchange their genetic codes and, more crucially, to correctly divide the homologs in the following cell division steps. To this end, chromosomes are tethered to the inner nuclear membrane (INM) through telomeres (or, as an exception, pairing centers in nematodes) and move along the INM throughout prophase I. At the INM, telomeres associate with the transmembrane linker of nucleoskeleton and cytoskeleton (LINC)-complex, which is composed of SUN-KASH domain proteins. The SUN domain protein interacts with telomeres at the INM, whereas the KASH domain protein interacts with cytoplasmic motors at the outer nuclear membrane (ONM). This transmembrane-linkage transduces cytoskeletal forces to telomeres and drives chromosome movements (Hiraoka and Dernburg, 2009; Link et al., 2015; Starr and Fridolfsson, 2010). The chromosome movement not only gathers the correct homologs together, but also resolves unwanted entanglements between non-homologs, ensuring the correct homolog pairing and recombination (Koszul and Kleckner, 2009; Storazzi et al., 2010).

While telomeres build the chromosome movement apparatus during meiotic prophase I (Shibuya and Watanabe, 2014), the underlying molecular architecture remains largely elusive. Accumulating evidences suggest that meiotic telomeres are decorated with the shelterin complex as telomeres in somatic cells (Scherthan et al., 2000; Siderakis and Tarsounas, 2007) and the "linker" proteins, Bqt1/2 (fission yeast), Ndj1 (budding yeast), and TERB1 (mammals) connect shelterin with the LINC-complex (Chikashige et al., 2006; Chua and Roeder, 1997; Conrad et al., 1997, 2008; Scherthan et al., 2007; Shibuya et al., 2014a; Treilles-Sticken et al., 2000).

At the same time, there have been several findings suggestive of fundamental structural reformations taking place at meiotic telomeres in higher eukaryotes. Early electron microscopic (EM) observations in rodent and human spermatocytes recognized a characteristic chromosome-INM fusion structure, termed the telomere attachment plate (Alzheimer et al., 1999;

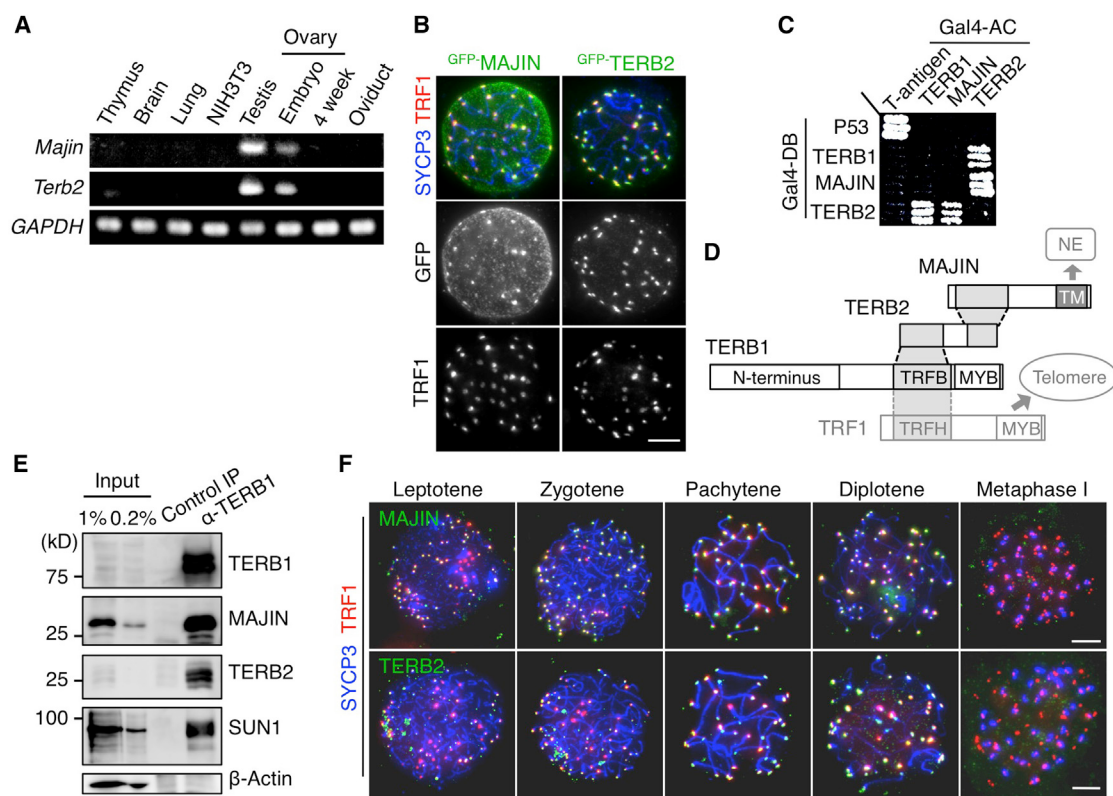


Figure 1. Identification of MAJIN and TERB2

(A) Tissue-specific expressions of *Majin* (1700123I01RIK) and *Terb2* (4933406J08RIK) mRNAs. NIH 3T3 is a mitotically rounding fibroblast cell line. *GAPDH* is a loading control.

(B) WT spermatocytes expressing ^{GFP}-MAJIN or ^{GFP}-TERB2 stained with the indicated antibodies.

(C) Yeast two-hybrid interactions between full length TERB1, MAJIN, and TERB2. The pair of p53-T serves as a positive control.

(D) Schematic of interaction domains as defined by the yeast two-hybrid assays shown in Figure S1D. TRFH, TRF-homology domain; TRFB, TRF1-binding domain; MYB, MYB-like domain; N terminus, SUN1-binding domain; TM, transmembrane domain.

(E) Immunoprecipitates from mouse testis-chromatin extracts with TERB1 antibody or control IgG, immunoblotted with the indicated antibodies. Silver-stained gel and results of mass spectrometry are shown in Figures S1A and S1B.

(F) WT spermatocytes stained with the indicated antibodies. Immunostainings of fetal oocytes are shown in Figure S1E. Scale bars, 5 μm.

See also Figure S1.

Esponda and Giménez-Martin, 1972; Holm and Rasmussen, 1977; Woollam et al., 1967). EM *in situ* hybridization assays using murine spermatocytes revealed that telomeric DNA is embedded in the attachment plate (Liebe et al., 2004), suggesting that telomeric DNA might be compacted and physically integrated into the lipid bilayer. However, the proteinaceous or membranous elements comprising the structures remain to be discovered.

In this study, we have identified meiosis-specific telomere and INM-binding proteins, telomere repeat-binding bouquet formation protein 2 (TERB2) and membrane-anchored junction protein (MAJIN), which form a complex with TERB1. TERB1/2-MAJIN establishes telomere attachment to the INM by taking over the telomeric DNA from shelterin and, concomitantly, develops the telomere attachment plate. Our results highlight elaborate molecular cross-communications between the lipid bilayer and chromatin and offer a plausible mechanism by which the transmembrane DNA binding protein dictates telomere-INM fusion.

RESULTS

Identification of MAJIN and TERB2

To identify proteins that construct the membrane-integrated telomere structures in meiosis, we analyzed TERB1 immunoprecipitates from mouse testis extracts by a mass spectrometry (Figures S1A and S1B). Among the proteins identified, we found two uncharacterized proteins, coded by 1700123I01Rik and 4933406J08Rik, which were expressed specifically in germline tissues (Figure 1A). Their GFP-fusion proteins localized to the meiotic telomeres when expressed in live-mouse testes (Figure 1B). Notably, ^{GFP}-1700123I01RIK showed additional localization on the whole nuclear envelope (Figure 1B). Both proteins are widely conserved in vertebrate species (Figure S1C). We named these proteins MAJIN (membrane-anchored junction protein, 1700123I01Rik) and TERB2 (telomere repeat-binding bouquet formation protein 2, 4933406J08Rik).

Yeast two-hybrid analyses detected interactions between MAJIN and TERB2 and also between TERB2 and TERB1

(Figures 1C and S1D, summarized in 1D). Further, immunoblotting the TERB1 immunoprecipitates indicated that TERB1 forms a complex with MAJIN and TERB2 in vivo (Figure 1E). Consistently, both endogenous MAJIN and TERB2 localize to meiotic telomeres throughout prophase I and disappear in metaphase I (Figures 1F and S1E), as does TERB1 (Shibuya et al., 2014a), leading to the conclusion that MAJIN and TERB2 are meiotic telomere-associating proteins.

MAJIN-TERB2 Is Indispensable for Meiotic Chromosome Movement

To address their functions, we raised knockout mice for *Majin* and *Terb2*, utilizing the gene-trap ES-cell lines (Figures S2A–S2C). The homozygous mice (*Majin*^{-/-} and *Terb2*^{-/-}) lacking the protein expressions displayed no overt somatic phenotype but were completely infertile and possessed degenerated germ-line tissues (Figures 2A and 2B). Histological analyses revealed the absence of post-meiotic cells in mutant gonads, suggesting that both MAJIN and TERB2 are essential for meiotic progression (Figures 2A and 2B).

Inspection of the cellular phenotypes of *Majin*^{-/-} and *Terb2*^{-/-} revealed that homologous synapsis, which is defined by the loading of the synaptonemal complex protein SYCP1 onto the lateral element (LE) of SYCP3, was severely impaired, leading to cell-cycle arrest in zygotene (partial SYCP1) stage (Figures 2C and S2E). The number of TRF1 foci remained large in mutant spermatocytes, implying that homolog pairing was largely impaired also at the telomeric regions (Figure 2D).

Since the accumulation of meiotic LINC-complex, SUN1-KASH5, to the telomere attachment site is required for meiotic chromosome movement and subsequent homolog pairing and synapsis (Ding et al., 2007; Horn et al., 2013), we suspected that this process is disturbed in the absence of MAJIN-TERB2. In fact, SUN1-KASH5 no longer accumulated at telomeres, but rather aggregated to the nuclear surface near the centrosome in mutant spermatocytes (Figures 2E and S2F). These aggregations were no longer detectable after detergent treatment, suggesting that SUN1-KASH5 loses its tight association with chromatin (Figure S2G). Time-lapse observations of live-spermatocytes revealed an almost complete cessation of rapid-chromosome movement in *Majin*^{-/-} and *Terb2*^{-/-} spermatocytes (Figure 2F) as we observed previously in *Terb1*^{-/-} and *Sun1*^{-/-} spermatocytes (Shibuya et al., 2014a). Thus, we conclude that MAJIN-TERB2 plays a crucial role in assembling SUN1-KASH5 at telomeres and, thereby, in achieving meiotic chromosome movement.

MAJIN Locally Limits TERB1/2 Assembly on the INM

Since the meiotic phenotypes of *Majin*^{-/-} and *Terb2*^{-/-} largely mimic those of *Terb1*^{-/-} (Figure 2) (Shibuya et al., 2014a), and they form a complex in vivo (Figures 1 and S1), they might function in cooperation at meiotic telomeres. To explore the relationships among TERB1, TERB2, and MAJIN, we inspected their localization hierarchy at meiotic telomeres in each mutant testis. In wild-type leptotene spermatocytes, telomeres are only partly localized at the nuclear periphery, and TERB1, TERB2, and MAJIN accumulated only to those telomeres, but not telomeres at the nuclear internal domain (Figure 3A). Strikingly, these mem-

brane-oriented assemblies were disturbed in *Majin*^{-/-}, leading to uniform distributions of TERB1 and TERB2 at telomeres, including internal ones (Figure 3A). In contrast, in *Terb1*^{-/-}, both TERB2 and MAJIN were completely absent from telomeres (from both peripheral and internal domains) (Figure 3A) and localized to the entire INM, which can be detected by a sensitive assay using GFP-fusion protein expression (Figure 3B). These results suggest that there are two distinct localization-dependent assembly mechanisms, the membrane-oriented one exerted by MAJIN and the telomere-oriented one exerted by TERB1 (Figure 3C). TERB2 shows a versatile nature, as it localized at all telomeres in *Majin*^{-/-} and on the entire INM in *Terb1*^{-/-} (Figures 3A and 3B), consistent with the fact that TERB2 interacts with both TERB1 and MAJIN (Figures 1C, 1D, and S1D).

Considering that TERB1, TERB2, and MAJIN are rarely detectable at yet-unattached telomeres in the physiological assembly process (Figure 3A; internal telomeres in wild-type leptotene spermatocytes), the membrane-oriented assembly is likely dominant, rather than the telomere-oriented one, leading to the sequestration of preassembled TERB1-TERB2-MAJIN complex on the INM (Figure 3C). Indeed, the membrane-sequestered complex became obvious when the proteins were overexpressed in wild-type spermatocytes (Figure 3D). In HeLa cells, in which the meiotic program is absent, ectopically expressed GFP or HA-MAJIN distributed on the entire INM in a manner dependent on its C terminus putative transmembrane (TM) domain (Figures S3A–S3C) and sequestered co-expressed GFP-TERB2 and TERB1^{-MYC} to the INM (Figures S3C and S3D).

TERB1/2-MAJIN Forms the Membrane-Integrated Telomere Attachment Structure

Our assays indicate that SUN1-KASH5 disappears from telomeres in all mutant spermatocytes, *Terb2*^{-/-}, *Majin*^{-/-}, and *Terb1*^{-/-} (Figures 2E and S2G) (Shibuya et al., 2014a). In contrast, the telomere localizations and membrane-oriented natures of TERB1, TERB2, and MAJIN were entirely intact in *Sun1*^{-/-} (Figures 3E and 3F), implying that TERB1/2-MAJIN assembly precedes the enrichment of SUN1-KASH5 at membrane-anchored telomeres. These results suggest the possibility that telomere attachment in *Sun1*^{-/-} might have different characteristics from those of *Terb1*^{-/-}, *Terb2*^{-/-}, and *Majin*^{-/-}. Indeed, telomere attachment defects were milder in *Sun1*^{-/-} than the other mutants, although they all arrested at the zygotene stage (Figure 3G).

To examine the telomere attachment status in these mutants, we investigated the ultrastructures of meiotic telomeres by electron microscopy (EM). The EM images of meiotic telomeres in wild-type spermatocytes show the electron-dense conical thickenings of synapsed LEs and a capping structure attached to the INM (Figures 3H and S4) (Liebe et al., 2004). These structures were completely absent, even at the ends of synapsed LEs near the INM, in *Terb1*^{-/-}, *Terb2*^{-/-}, and *Majin*^{-/-}, while preserved in *Sun1*^{-/-} spermatocytes (Figure 3H) (Link et al., 2014). Notably, in *Majin*^{-/-}, the capping structure was preserved although dissociated from the INM. In contrast, in *Terb1*^{-/-} and *Terb2*^{-/-}, the capping structure was largely disrupted, but the conical thickenings of the LEs were partly preserved, especially in *Terb2*^{-/-}, without INM attachment (Figure 3H). These various

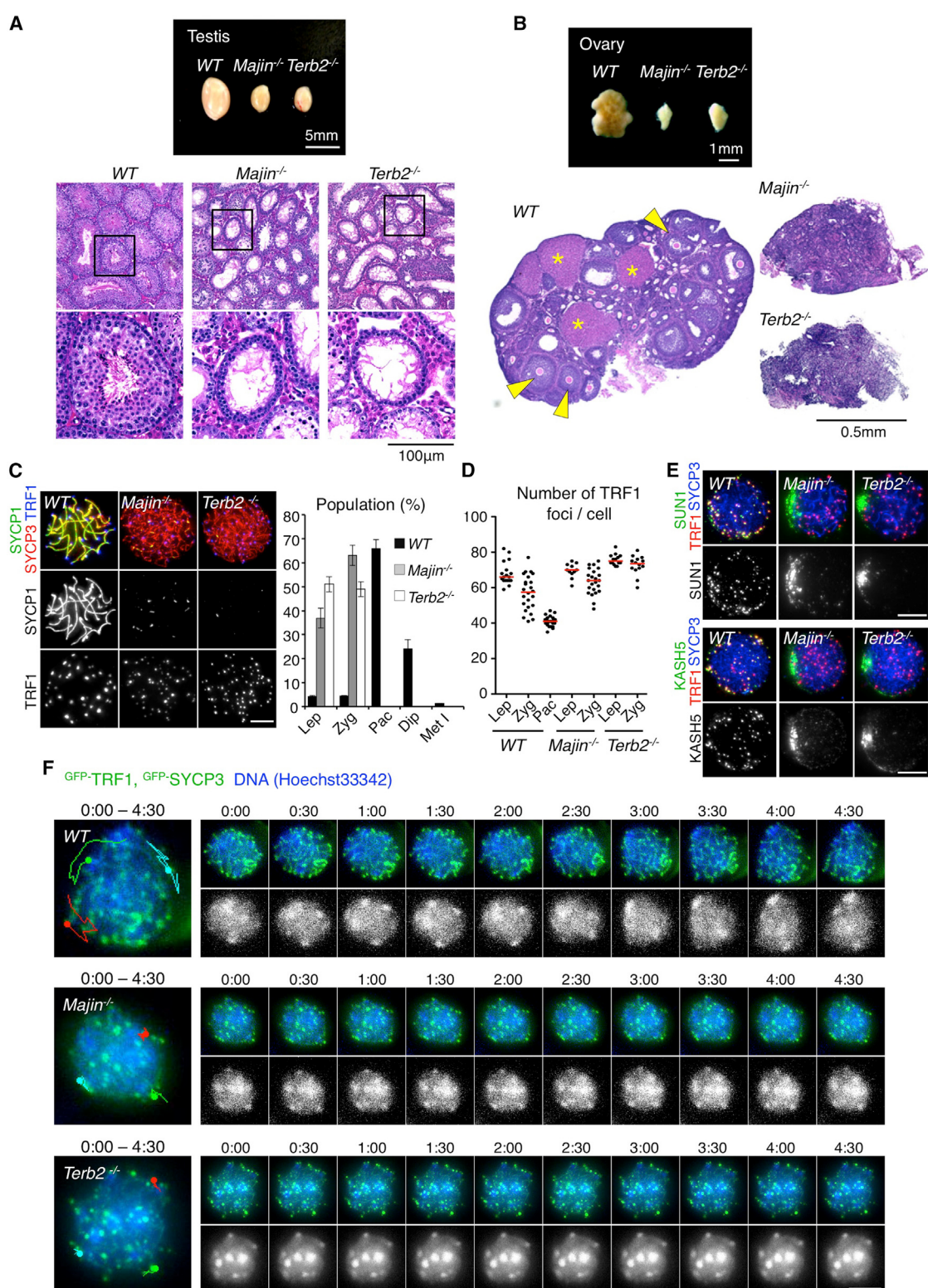


Figure 2. MAJIN-TERB2 Is Indispensable for the Meiotic Chromosome Movement

(A) Testes from 8-week-old mice of the indicated genotypes (top) and their tissue sections stained with hematoxylin and eosin (bottom). Note that post-meiotic nuclei are observed in WT seminiferous tubules but not in those of Majin^{-/-} and Terb2^{-/-}. TUNEL stainings are shown in Figure S2D.

(legend continued on next page)

structural defects may reflect the hierarchical protein assembly states at telomeres in these mutants (Figure 3C). Taken together, these results indicate that the meiotic factors TERB1/2-MAJIN play a crucial role in positioning meiotic telomeres onto the INM and in constructing the attachment plate in a manner independent of SUN1-KASH5.

TRF1 and TERB1/2-MAJIN Form a Tetrameric Complex

The foregoing results suggest that TERB1/2 is sequestered to the INM by the membrane protein MAJIN and accumulates at telomeres only when telomeres relocate to the nuclear periphery in meiotic entry (Figures 3A and 4A). Because TERB1 binds directly to the shelterin core component TRF1 (Shibuya et al., 2014a) and forms a 1:1 stoichiometric heterodimer even in the presence of accessory TERB2 binding (Figures S5A–S5D), we assumed that this molecular interaction might be a crucial step for telomere attachment to the INM. To reconstitute the telomere attachment process in vitro, we purified the ^{HIS}-TERB1^C-TERB2-MAJIN^{ΔTM} tripartite complex, mixed it with varying amounts of ^{HIS}-TRF1, and examined DNA-binding activity by electron mobility shift assay (EMSA) (Figures 4B and 4C). While the DNA-binding of ^{HIS}-TERB1^C-TERB2-MAJIN^{ΔTM} tripartite complex was weak (often forming smear bands) (Figure S5H), the addition of TRF1 enhanced DNA-binding in a dose-dependent manner by forming a tetrameric complex (Figures 4C, lanes 3–6, and S5E). The DNA-binding of the tetrameric complex is telomere-DNA-specific and depends largely on the TRF1 MYB-domain (Figures S5F and S5G). Notably, DNA binding of the TRF1 homodimer alone is not detectable with the excess amount of tripartite complex, indicating that the tetrameric complex formation occurs very efficiently. We argue that this highly efficient complex conversion from the canonical TRF1 homodimer to the chimeric complex with TERB1/2-MAJIN might be a key mechanism of telomere (TRF1) attachment to the INM.

Notably, MAJIN has a basic cluster (isoelectric points [PI] = 10) adjacent to the C terminus TM domain (Figure 4D, shown in red), a common feature of transmembrane DNA-binding proteins (Ulbert et al., 2006), and has DNA-binding activity that is not sequence-specific in vitro (Figures 4E and 4F). Mutations of the basic amino acids within the cluster (^{HIS}-MAJIN^{DBΔTM}) severely impaired the DNA-binding activity of MAJIN (Figures

4E and 4F), and this was the case also for the tripartite complex, ^{HIS}-TERB1^C-TERB2-MAJIN^{DBΔTM}, but not for the tetrameric complex containing TRF1 likely due to the predominant DNA-binding activity of TRF1 (Figures S5H and S5I). Further, ^{GFP}-MAJIN^{DB} exogenously expressed in *Majin*^{−/−} spermatocytes retained its abilities to localize on the INM and accumulated to telomeres at the INM, likely through the formation of the chimeric complex on the INM. However, ^{GFP}-MAJIN^{DB} only partially rescued the telomere attachment defects of *Majin*^{−/−} spermatocytes, while wild-type protein almost completely suppressed the defects (Figure 4G). Thus, we conclude that MAJIN has DNA-binding activity on its own that is important for the stabilization of telomere attachment on the INM.

The Telomere Cap Exchange

Zoom-in views of meiotic telomeres revealed that TERB1/2-MAJIN colocalizes with TRF1 on the INM in zygote (Figure 4A), consistent with their in vitro nature to form a stable tetrameric complex (Figure S5E). In pachytene, however, TRF1 signals are dissociated from the TERB1/2-MAJIN region and distributed in the surrounding area to form a ring-shaped structure (Figure 5A). Importantly, other shelterin components, TRF2, TIN2, ^{GFP}-RAP1, ^{GFP}-TPP1, and ^{GFP}-POT1A, also behave like TRF1 (Figure 5B). Experiments combining immunofluorescence with in situ hybridization (FISH) for telomeric DNA demonstrated that telomeric DNA signals co-localize with the TERB1/2-MAJIN complex rather than the shelterin ring structure, implying that shelterin is largely dissociated from the telomeric DNA (Figure 5C) (see Discussion). We refer to this phenomenon as the telomere cap exchange, since the majority of telomeric DNA is handed over from the canonical shelterin to the membrane-bound TERB1/2-MAJIN complex. The cap exchange is not an artifact caused by the cell-spread procedures since it was detectable even in structurally preserved nuclei (Figure S6B). Further, it is not due to differences in antibody accessibility, since the immunofluorescence signal of ^{GFP}-TRF1 detected by a GFP-antibody also showed the ring-shaped structure, while ^{GFP}-TERB1 was localized to the center of the endogenous TRF1-rings (Figures S6C and S6D). Collectively, these data demonstrate that the canonical shelterin is largely dissociated from the meiotic telomere complex after priming TERB1/2-MAJIN on the telomeric DNA.

(B) Ovaries from 8-week-old mice of the indicated genotypes (top) and their tissue sections stained with hematoxylin and eosin (bottom). Arrowheads, follicle; asterisks, corpora lutea.

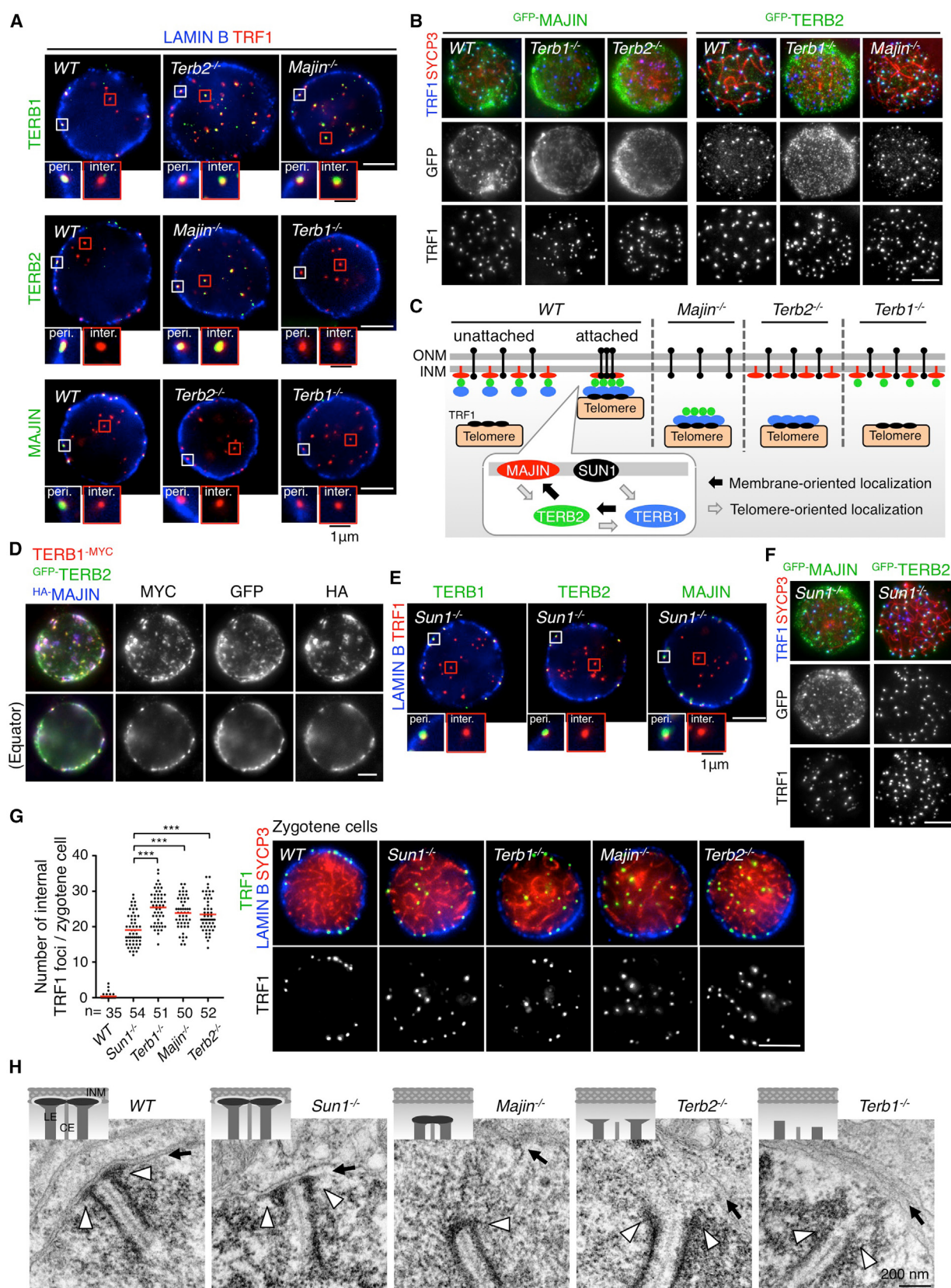
(C) Left: spermatocytes of the indicated genotypes stained with the indicated antibodies. Right: frequencies of meiotic stages in testes from 8-week-old mice of the indicated genotypes. SYCP3 positive spermatocytes (>2,400 cells for each genotype) are classified into the following substages: Lep, leptotene (no SYCP1); Zyg, zygote (partially assembled SYCP1); Pac, pachytene (fully assembled SYCP1); Dip, diplotene (disassembled SYCP1); Met I, metaphase I (no SYCP1 and SYCP3 accumulations at centromeres). Mean values of three independent experiments from three different mice are shown. Error bars, SEM (n = 3). The corresponding results of fetal oocytes are shown in Figure S2E.

(D) Quantification of TRF1 foci number with the median (n > 30 cells for each substage). Substages are defined in (C). Data are from two independent experiments from two different mice. Note that murine cells have 40 chromosomes (2n) and the number of telomeres ranges from 80 (fully unpaired) to 40 (fully paired) in WT.

(E) Zygote-spermatocytes of the indicated genotypes stained with the indicated antibodies. Immunostainings with γ -tubulin are shown in Figure S2F. Immunostainings with harsh extraction are shown in Figure S2G.

(F) Time-lapse images (30-s intervals) of live zygote-spermatocytes of the indicated genotypes, expressing ^{GFP}-TRF1 and ^{GFP}-SYCP3 (green). DNA are visualized with Hoechst33342 (blue or monotone panels). The leftmost panels are pictures at the final time points (4:30) overlaid with trajectories of three independent telomeres from times 0:00 to 4:30. More than 15 zygote-spermatocytes were observed for each mutant and all showed the same movement defects. Scale bars, 5 μ m (unless otherwise indicated).

See also Figure S2.



(legend on next page)

CDK Activity Triggers Telomere Cap Exchange

Since the expressions of M phase cyclin and cyclin-dependent kinase (CDK) rise during prophase progression (Godet et al., 2000; Wolgemuth et al., 2013), we wondered whether CDK activity might be involved in the regulation of the cap exchange. To examine this possibility, we pulse-treated wild-type spermatocytes with a CDK inhibitor, Roscovitine, and examined their telomere structures. Strikingly, the characteristic ring-shaped TRF1 signals in pachytene were totally abolished after the Roscovitine treatment; instead TRF1 appeared as a pair of punctate signals, likely corresponding to the synapsed homologous telomeres (Figures 5D and 5G). The punctate TRF1 signals that appeared after the Roscovitine treatment colocalized with MAJIN (Figure 5D), suggesting that the cap exchange is abolished after CDK inhibition.

One candidate substrate of CDK involved in the cap exchange is the threonine 647 (T647) in TERB1, an evolutionary conserved consensus site for CDK, since our previous study demonstrated that the TRF1-TERB1 interaction is reduced by the phosphomimetic mutation of T647 in TERB1 (Shibuya et al., 2014a). To examine the *in vivo* phosphorylation, we raised a phospho-specific antibody against TERB1-pT647 (pT647) (Figure 5E). Immunostaining of spermatocytes with the antibody demonstrated punctate signals at meiotic telomeres, and the signal strength increased during prophase progression (Figure 5F). We confirmed that the signals were derived from TERB1, since they were detected at membrane-anchored telomeres in wild-type but not in *Terb1*^{-/-} (Figures S6E and S6F). Accordingly, pachytene-spermatocytes treated with Roscovitine showed severely diminished pT647 signals (Figure 5G). Therefore, we conclude that TERB1-T647 is phosphorylated by CDK *in vivo*, especially in late prophase when the cap exchange is prominent. Notably, the TERB1^{T647A} mutant exhibited telomere attachment defects when expressed in *Terb1*^{-/-} spermatocytes (Figure 5H), even though the protein itself has the abilities to form a priming chimeric complex (Figure S5J) and to localize to telomeres at the INM, similar to wild-type protein (Figure 5H). Despite the defect in telomere attachment, *Terb1*^{-/-} spermatocytes expressing the TERB1^{T647A} mutant finally exhibited the cap exchange when the spermatocytes had progressed to the pachytene-like stage (Figure 5I). Thus, phosphorylation on TERB1-T647 is important for the stabilization of telomere attach-

ment but dispensable for the cap exchange. There might be other key CDK substrates that are sufficient for the cap exchange. Intriguingly, the DNA-binding defective mutant of MAJIN (MAJIN^{DB}) expressed in *Majin*^{-/-} spermatocytes showed a complete loss of the cap exchange, even in the pachytene-like stage (Figure 5J). Therefore, in addition to the activation of CDK, the direct tethering of DNA to the INM by MAJIN is necessary to achieve the cap exchange reaction (see Discussion).

Incipient Chromosome Movement Promotes the Telomere Attachment

It remains unexplained why a substantial number of telomeres are detached from the INM in *Sun1*^{-/-}, despite the fact that an intact attachment plate is formed in this mutant (Figures 3E–3H) (Ding et al., 2007; Link et al., 2014). Because chromosome movements are absent in *Sun1*^{-/-} (Shibuya et al., 2014a), we speculated that chromosome movement might influence telomere attachment. To address this issue, we utilized a testis organ-culture system (Sato et al., 2013), in which meiotic progression can be monitored for several days *in vitro*. Microtubule (MT)-dependent chromosome movements were disrupted by addition of the MT-depolymerizing drug, nocodazole, to the culture medium (Figure 6A) (Lee et al., 2015; Morimoto et al., 2012; Shibuya et al., 2014b). We cultured testes from wild-type juvenile male with EdU for 3.5 days. EdU incorporation can distinguish cells that have progressed through pre-meiotic S phase during the time in culture (Figure 6A). As a result, cells cultured in the presence of nocodazole rarely accomplished homolog synapsis, while cells cultured without nocodazole did (Figure 6B). This result is consistent with the previously established notion that the MT-dependent chromosome movement is required for homolog association during meiotic prophase I. Further, to our surprise, there were prominent telomere attachment defects in EdU-positive zygote cells cultured with nocodazole (14 ± 4.1 internal telomeres/cell), while the defects were far less pronounced in EdU-negative cells cultured with nocodazole (2 ± 4.3 internal telomeres/cell) (Figure 6C). These results suggest that MT function is needed for faithful telomere attachment to the INM during pre-meiotic S phase, when telomere relocation usually takes place (Pfeifer et al., 2001). We confirmed that the accumulations of TERB1/2-MAJIN and even SUN1 are entirely intact at peripheral telomeres in these cultured cells (Figure 6D).

Figure 3. MAJIN Locally Limits TERB1/2 Assembly at the INM

- (A) Equator images of spermatocytes of the indicated genotypes stained with the indicated antibodies. WTs are in the early leptotene stage. Mutants (*Majin*^{-/-}, *Terb2*^{-/-}, and *Terb1*^{-/-}) are in the zygote stage.
- (B) Zygote-spermatocytes of the indicated genotypes expressing ^{GFP}-MAJIN (left) and ^{GFP}-TERB2 (right) stained with the indicated antibodies.
- (C) Schematic of TERB1/2-MAJIN-SUN1 assembly under the regulations of two distinct gravities in spermatocytes of WT (unattached or attached) and the indicated mutants.
- (D) WT spermatocytes co-expressing TERB1^{-MYC}, ^{GFP}-TERB2, and ^{HA}-MAJIN stained with the indicated antibodies. Bottom, equator images.
- (E) Equator images of *Sun1*^{-/-} zygote-spermatocytes, stained with the indicated antibodies.
- (F) *Sun1*^{-/-} zygote-spermatocytes expressing ^{GFP}-MAJIN (left) and ^{GFP}-TERB2 (right) stained with the indicated antibodies.
- (G) Equator images of structurally preserved zygote-spermatocytes of the indicated genotypes stained with the indicated antibodies. Graph shows the number of internal TRF1 foci with median. Data are from three independent experiments from three different mice. ***p < 0.0001, one-way ANOVA with Bonferroni's multiple comparisons test.
- (H) Electron microscopic images of telomeres (arrowheads) and INMs (arrows) in spermatocytes of the indicated genotypes, with schematics. LE, lateral element; CE, central element; INM, inner nuclear membrane. Telomeres at the nuclear periphery (peri.) and in the internal domain (inter.) are magnified in (A) and (E). Scale bars, 5 μm (unless otherwise indicated).
- See also Figures S3 and S4.

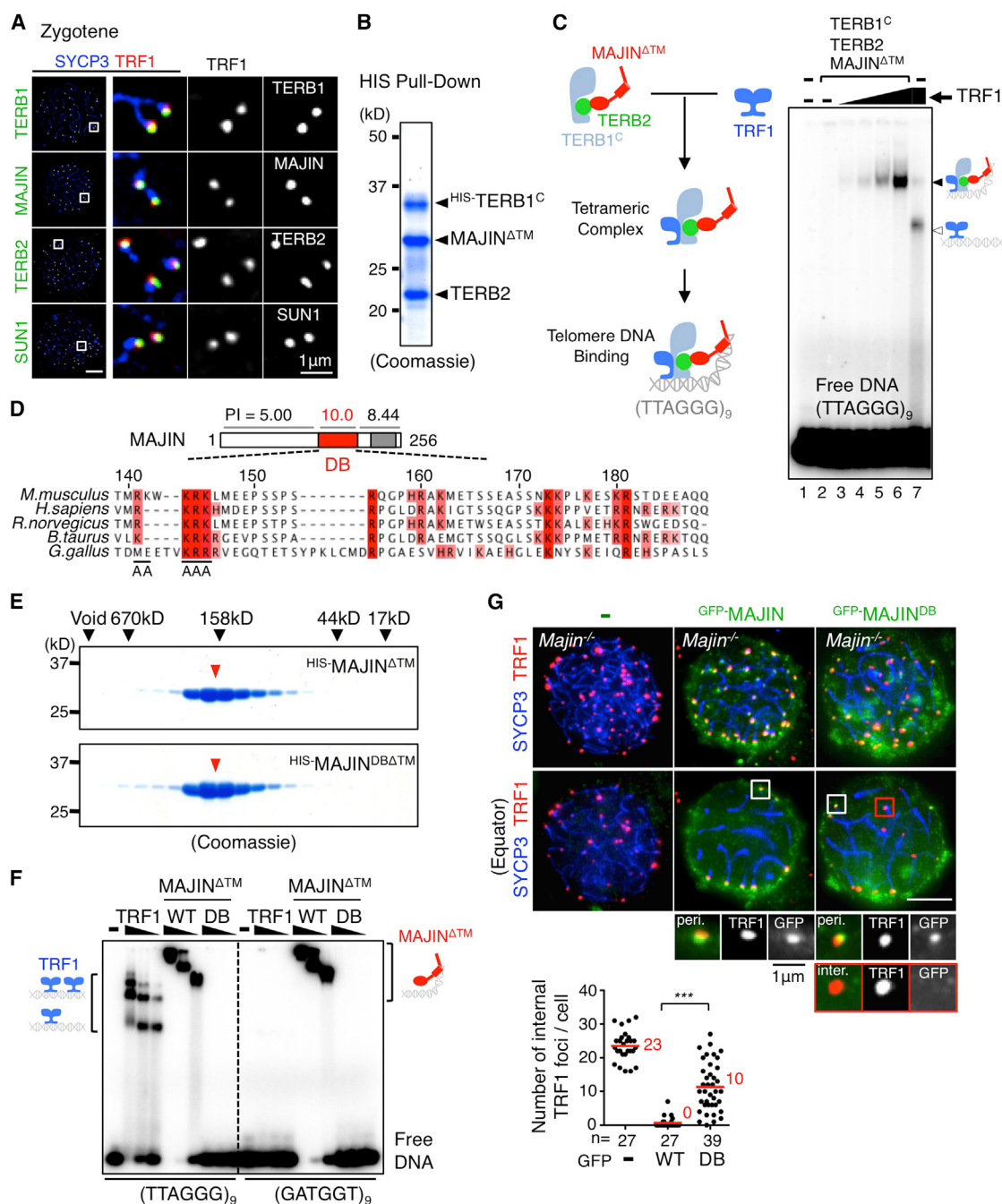


Figure 4. Meiotic Telomere-Binding Complex Forms a Chimeric Complex with TRF1 in Early Meiosis

(A) Peripheral images of WT zygote spermatocytes stained with the indicated antibodies. The pairs of juxtaposed homologous telomeres are magnified.

(B) Tripartite complex (^{HIS}-TERB1^C-TERB2-MAJIN^{ΔTM}) purified with a HIS-tag on TERB1^C from the *Escherichia coli* extract co-expressing all these subunits shown in the Coomassie-stained gel. Note that we used the truncated versions of TERB1 and MAJIN (TERB1^C lacking the N terminus SUN1-binding domain, MAJIN^{ΔTM} lacking the C terminus transmembrane domain) because these domains caused protein aggregations in vitro.

(C) EMSA assay with a concentration (17 pM) of the tripartite complex, ^{HIS}-TERB1^C-TERB2-MAJIN^{ΔTM}, premixed with increasing amounts of ^{HIS}-TRF1 (lanes 3–6, 3-fold steps up to 1.7 pM). Lane 2: 17 pM of the tripartite complex. Lane 7: 1.7 pM of ^{HIS}-TRF1. Lane 1: probe alone. White arrowhead, TRF1 homodimer; black arrowhead, the tetrameric complex (^{HIS}-TRF1-^{HIS}-TERB1^C-TERB2-MAJIN^{ΔTM}). The labeled DNA probe is a restriction fragment containing nine telomere repeats, (TTAGGG)₉. The formation of the tetrameric complex was assured by the co-expression of ^{HIS}-TERB1^C, MAJIN^{ΔTM}, TERB2, and TRF1 in *E. coli* (Figure S5E).

(D) Schematic of MAJIN divided into three domains: the N terminus domain (1–138 aa), the basic cluster (139–189 aa shown in red), and the C terminus domain (190–256 aa). The C terminus transmembrane domain is shown in gray. The isoelectric points (PI) of each domain are also shown. Amino acid sequence alignment

(legend continued on next page)

Of note, similar attachment defects are observed in *Sun1^{-/-}*, in which MT polymerization is intact but chromosome movement is impaired (Ding et al., 2007; Shibuya et al., 2014a, 2014b). Taken together, these results suggest that the MT-dependent chromosome movement promotes the initial telomere association with the nuclear periphery, probably by increasing the liquidity within the nucleus (see Discussion).

DISCUSSION

Rapid-chromosome movement along the nuclear envelope is an evolutionary conserved meiotic process essential for pairing and recombination of the homologous chromosomes. Hence, a key goal of meiosis research has been to define the regulatory mechanism that takes place at meiotic telomeres to develop the movement apparatus. In this study, we identified factors responsible for telomere attachment to the INM in mammalian meiosis and uncovered the underlying hierarchical molecular mechanisms. The key player is the membrane-associated junction protein MAJIN, named also after a Japanese word representing the “Genie in Aladdin’s Lamp.” MAJIN behaves as a membrane protein and sequesters telomere adaptors TERB1/2 to the INM. Once telomeres access the nuclear periphery during meiotic entry, MAJIN dynamically relocates to telomeres on the INM and stabilizes the attachment through a number of ingenious strategies.

A Transmembrane DNA-Binding Protein MAJIN

MAJIN stabilizes telomere attachment partly through its own DNA-binding activity, which maps adjacent to the TM-domain (Figures 4D–4F). The presence of a basic segment near the TM-domain is the common feature of the transmembrane DNA-binding proteins, although its physiological significance has been rarely addressed (most believe it to be involved in transcriptional regulation or nuclear envelope reassembly after mitosis) (Ulbert et al., 2006). Our analyses show that a mutation in the DNA-binding domain of MAJIN impairs its DNA binding activity and in vivo function in tethering telomeres to the INM. Our data suggest that the DNA-binding activity of MAJIN is relatively weak compared to that of TRF1 (~1/100 that of TRF1) and not specific for the telomere repeat sequence (Figure 4F). We, therefore, reason that the incipient telomere attachment is mediated primarily by the protein-protein interaction between TERB1 and TRF1, and the interaction of MAJIN with the telomeric DNA may develop after the priming attachment, establishing direct linkage between telomeric DNA and the lipid bilayer.

Notably, an analogous regulatory mechanism has been reported in fission yeast, in which a ubiquitous INM protein complex Bqt3/4 associates with a shelterin protein Rap1 and tethers telomeres to the nuclear periphery. This Bqt3/4-mediated telomere-INM interaction is maintained in vegetative cells and becomes a prerequisite for the recruitment of the SUN-KASH complex in meiosis (Chikashige et al., 2009). Although their overall amino acid sequences are diverged, both Bqt4 and MAJIN have a single TM-segment on their extreme C termini, which is a hallmark of tail-anchored proteins. Moreover, Bqt4 has a helix-turn-helix motif, a putative DNA-binding domain. The basic cluster in MAJIN is also predicted to compose a helix-turn-helix motif, and residues mutated in our DNA-binding defective mutant reside in the second helix, known to function in a direct DNA binding (NPS server; <https://npsa-prabi.ibcp.fr/>). Therefore, we propose that MAJIN could be an evolutionary relative of fission yeast Bqt4 and specified for meiotic telomere-INM attachment in vertebrates.

The Telomere Cap Exchange

Our analyses indicate that after the establishment of priming attachment, the cap exchange takes place depending on CDK activity, which increases gradually throughout prophase. TERB1-T647 is a substrate of CDK, the phosphorylation of which reduces the binding affinity between TERB1 and TRF1, and thus might facilitate release of TRF1 from the priming chimeric complex. However, there might be another CDK target sufficient for the cap exchange since the TERB1-T647A mutant does not prevent the cap exchange. Further, not only TRF1 but whole shelterin complex is displaced from telomeres at the time of cap exchange (Figure 5B), suggesting that there must be regulations beyond the resolution of TRF1-TERB1, such as the direct phosphorylations of TRF1 and TRF2 as observed in mitosis (Hayashi et al., 2012; McKerlie and Zhu, 2011). Crucially, the MAJIN-mediated association between DNA and the membrane is essential for triggering the cap exchange in addition to the CDK activation. Taken together, it is tenable that the electrostatic repulsion, at the hydrophobic environment very close to the lipid bilayer, may drive the shelterin away from the membrane-attached telomeres, especially when the affinity between shelterin and telomeric-DNA is diminished by CDK activity.

Because the binding of shelterin to telomeric DNA is constitutively required to prevent the DNA-damage-response at telomeres (Palm and de Lange, 2008), the cap exchange is quite a surprising phenomenon on its own. It is possible that the TERB1/2-MAJIN complex overcomes the requirement of the

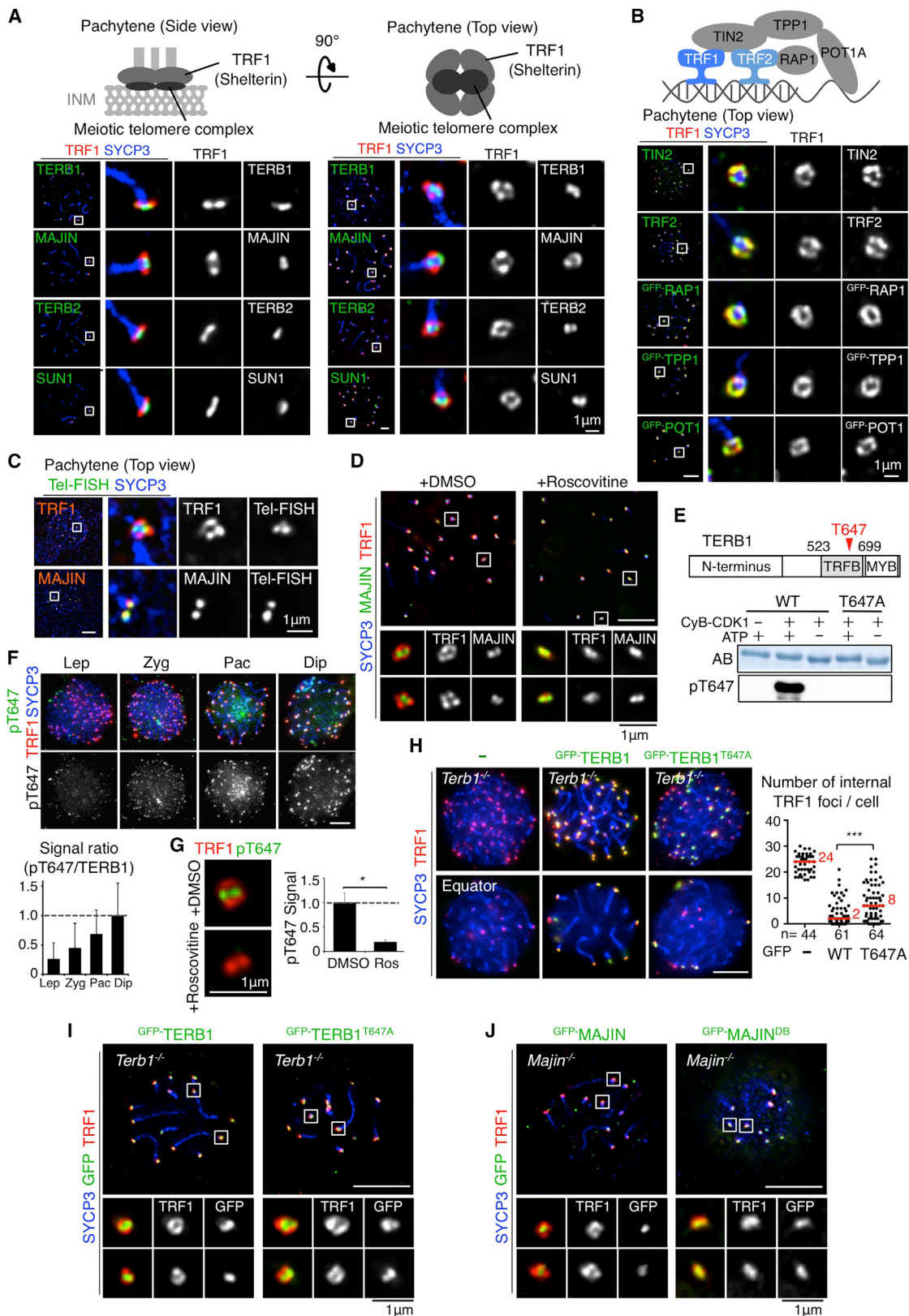
of the C terminus basic domains of MAJIN homologs (bottom). The basic amino acids are shown in red. Alanine substitutions in the basic cluster domain are underlined.

(E) Gel-filtration elution profiles of ^{HIS}-MAJIN^{ΔTM} (1–229 aa), WT (top) or the DNA-binding mutant (DB) (bottom). Note ^{HIS}-MAJIN^{ΔTM} and its DB mutant form a similar homooligomer. Red arrowheads, the peaks.

(F) EMSA assay with ^{HIS}-TRF1, ^{HIS}-MAJIN^{ΔTM} (WT), and ^{HIS}-MAJIN^{DBΔTM} (DB). The labeled DNA probes are restriction fragments containing nine of telomere repeats (TTAGGG)₉ (left 10 lanes) or scrambled repeats (GATGGT)₉ (right 10 lanes). The dilution series of ^{HIS}-TRF1 are 1/2-fold steps, 4 pM, 2 pM, and 1 pM and those of ^{HIS}-MAJIN^{ΔTM} (both WT and DB) are 400 pM, 200 pM, and 100 pM. Leftmost lanes: probe alone.

(G) *Majin^{-/-}* spermatocytes expressing ^{GFP}-MAJIN (WT), ^{GFP}-MAJIN^{DB} (DB), or control (−) stained with the indicated antibodies. Equator images are shown at the bottom. Graph shows the number of internal TRF1 foci in each cell with the median. Scale bars, 5 μm (unless otherwise indicated). Telomeres at the nuclear periphery (peri.) and in the internal domain (inter.) are magnified. ***p < 0.0001, unpaired t test.

See also Figure S5.



(legend on next page)

canonical protective function of shelterin by limiting the accessibility of damage-response proteins in the hydrophobic environment at the lipid bilayer. Notably, although shelterin is largely dissociated from the region stained by telomeric FISH after the cap exchange, it still remains at the proximal region forming a ring-shaped structure (Figure 5C). These shelterin pools after the cap exchange may be maintained in preparation for their rapid returns to the telomeric DNA after prophase I or, more actively, to act as a structural element reinforcing the telomere attachment plate. Otherwise, the shelterin ring would have distinct functions, such as the canonical repressive roles against the activation of the DNA damage response or in the development of the telomere extension machineries, which takes place during gametogenesis (Siderakis and Tarsounas, 2007; Thilagavathi et al., 2013). Future studies will address these newly arising questions.

An Attachment and Movement Are Mechanically Distinct Processes but Are Coordinated via Feedback

The SUN-KASH transmembrane complex is a conserved key regulator of the meiotic chromosome movement, a prerequisite for homolog pairing and recombination in various eukaryotic species. It is widely believed that the SUN-KASH complex mediates both the attachment and movement of meiotic telomeres (Link et al., 2015), because mutations in SUN-KASH cause significant defects in both pathways in some organisms, including budding yeast and mammals (Bupp et al., 2007; Ding et al., 2007; Horn et al., 2013; Schober et al., 2009). However, telomere

attachment to the INM might be achieved by alternative molecular mechanisms beyond the SUN-KASH complex, as proposed for the fission yeast membrane proteins Bqt3/4 and budding yeast Esc1 (Chikashige et al., 2009; Mekhail and Moazed, 2010). That is also the case in nematode meiosis, where mutations in the SUN-domain protein impair the movements of pairing centers (corresponding to telomeres), but their attachments to the INM are perfectly maintained by unknown regulatory mechanisms (Sato et al., 2009). Our present study revealed that the attachment and movement of meiotic telomeres are separately regulated by two distinct meiosis-specific transmembrane complexes, TERB1/2-MAJIN and SUN1-KASH5, in mammals.

Our analyses reveal that the suppression of incipient telomere movement by MT-depolymerization significantly reduces the efficiency of telomere attachment as seen in *Sun1^{-/-}*, while some telomeres are perfectly attached to the INM depending on TERB1/2-MAJIN. Thus, the incipient telomere attachment and movement might be initiated at telomeres that stochastically locate near the INM, possibly with the support of preceding movement of heterochromatin to the nuclear periphery (Scherthan et al., 2014). Because chromosomes are highly entangled in early prophase (Koszul and Kleckner, 2009; Storazzi et al., 2010), the incipient telomere movement might facilitate the overall chromosome motion within the nucleus, including the movements of yet-unattached chromosomes, and promote their attachments. Thus, our study reveals the coordinated feedback regulation between telomere attachment and chromosome movement (Figure 7).

Figure 5. Telomere Cap Exchange

- (A) Equator (left) or peripheral (right) images of WT pachytene-spermatocytes stained with the indicated antibodies. Top schematics show relative positions of TRF1 (shelterin) and the meiotic telomere binding complex (TERB1/2-MAJIN) at telomeres in pachytene spermatocytes. The colocalizations of TERB1, MAJIN, TERB2, and SUN1 are shown in Figure S6A.
- (B) Peripheral images of WT pachytene-spermatocytes stained for TRF1 (red), TIN2/TRF2/GFP (green), and SYCP3 (blue). The localizations of TPP1, RAP1, and POT1A were examined by expressing GFP-fusion proteins, followed by immunostainings with GFP antibody. Top schematic shows the protein composition of the shelterin complex.
- (C) Peripheral images of WT pachytene-spermatocytes stained with the indicated antibodies. Telomeric DNA are visualized by FITC-labeled FISH-probe (Tel-FISH) (green).
- (D) Peripheral images of WT pachytene-spermatocytes, treated with either CDK inhibitor (+Roscovitine) or control DMSO (+DMSO) for 2 hr, and stained with the indicated antibodies.
- (E) Schematic of the domain composition of TERB1 with the position of T647 (top). N terminus, SUN1-binding domain; TRFB, TRF1-binding domain; MYB, Myb-like domain. Western blot of recombinant ^{MBP}-TERB1-TRFB (523–699 aa), WT, or T647A mutant, immunoblotted with pT647 antibody (bottom). Prior to the western blot, the proteins were phosphorylated in vitro with (+) or without (−) recombinant cyclin B-CDK1 complex (CyB-CDK1) in the presence (+) or absence (−) of ATP. AB, Amido black staining of the membrane.
- (F) WT spermatocytes stained with the indicated antibodies. The graph shows relative signal intensities of pT647 at telomeres in comparison with TERB1. The relative intensities in each meiotic substage are normalized to that in the diplotene stage (Dip). Lep, leptotene; Zyg, zygotene; Pac, pachytene. Ten telomeres are measured in each cell (total ten cells for each substage). Error bars, SD. The signal intensities of pT647 are shown in Figure S6I. The stainings and signal intensities of TERB1 are shown in Figures S6G and S6H.
- (G) Magnified images of synapsed telomeres, at the nuclear peripheries of WT pachytene-spermatocytes, treated with either CDK inhibitor (+Roscovitine) or control DMSO (+DMSO) for 2 hr and stained with the indicated antibodies. The graph shows the relative signal intensities of pT647 in corresponding cells. Mean values of three independent experiments from three different mice, normalized to the control (DMSO), are shown. In each experiment, five telomeres are measured in each cell (total 30 cells). Error bars, SEM ($n = 3$).
- (H) *Terb1^{-/-}* spermatocytes expressing ^{GFP}-TERB1 (middle), ^{GFP}-TERB1^{T647A} (right), or control (−) (left) stained with the indicated antibodies. Equator images are shown at the bottom. The graph shows the number of internal TRF1 foci in each cell with the median indicated. Data are from two independent experiments from two different mice.
- (I) Peripheral images of *Terb1^{-/-}* spermatocytes, progressed to the pachytene-like stage following the expression of ^{GFP}-TERB1 (left) or ^{GFP}-TERB1^{T647A} (right), and stained with the indicated antibodies. Note that the cap exchange normally occurs in both situations.
- (J) Peripheral images of *Majin^{-/-}* spermatocytes progressed to the pachytene-like stage following the expression of ^{GFP}-MAJIN (left) or ^{GFP}-MAJIN^{DB} (right), and stained with the indicated antibodies. Note that the cap exchange normally occurs in cells expressing ^{GFP}-MAJIN but not ^{GFP}-MAJIN^{DB}. Scale bars, 5 μ m (unless otherwise indicated). * $p < 0.05$, ** $p < 0.0001$, unpaired t test.
- See also Figures S6 and S7.

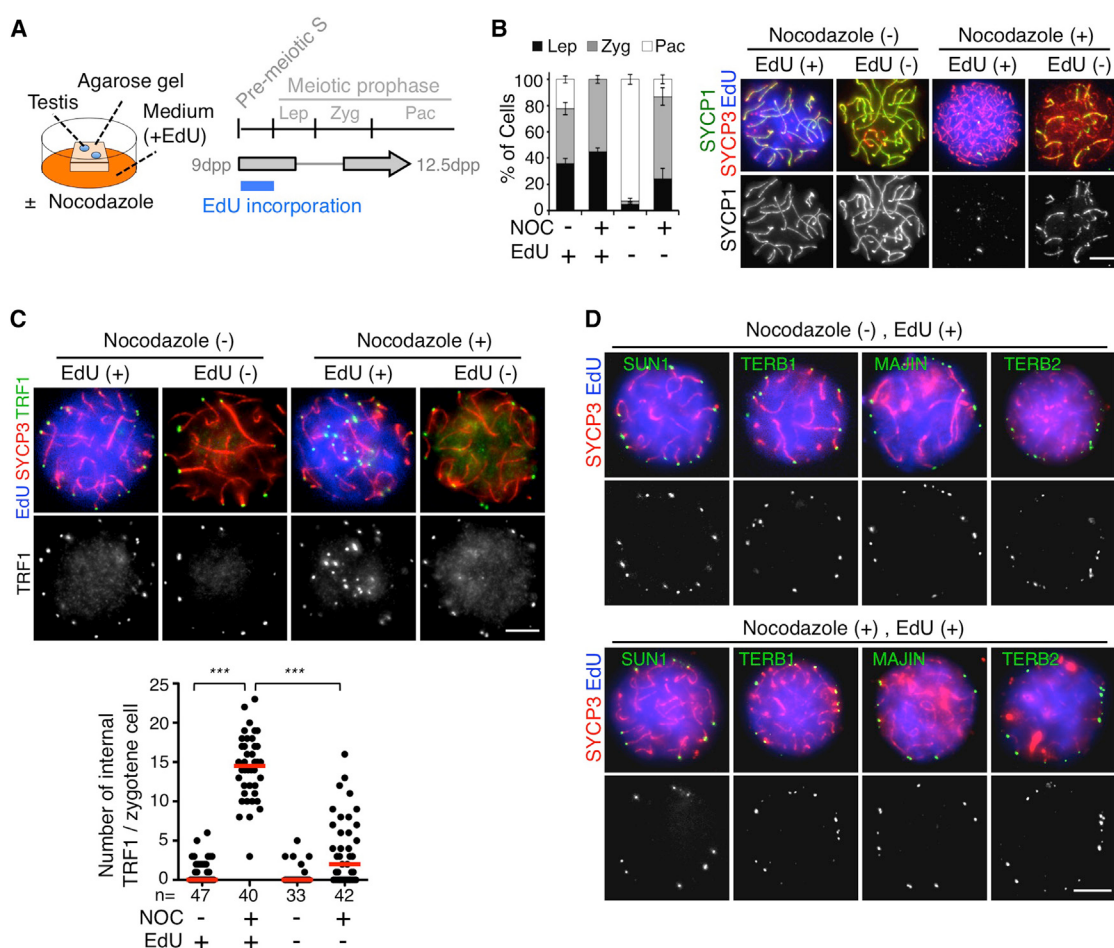


Figure 6. Incipient Telomere Movement Promotes the Telomere Attachment in Meiotic Entry

(A) Schematic of the in vitro organ culture. Testes undergoing the first wave of spermatogenesis (9 days post-partum [dpp]; the majority of spermatocytes are at pre-meiotic S to early leptotene stage) were cultured on an agarose gel half-soaked with medium containing EdU and nocodazole/DMSO. After 3.5 days in culture (12.5 dpp; the majority of spermatocytes are at pachytene stage), cells were collected from the organ, fixed, and stained.

(B) Frequencies of meiotic stages after organ culture. SYCP3-positive spermatocytes, from cultures with (+) or without (-) nocodazole are divided into two populations, EdU incorporated (+) or unincorporated (-). Substages are defined in Figure 2C. Mean frequencies of three independent cultures are shown (>200 cells for each condition). Error bars, SEM ($n = 3$). Representative cells (right), stained with the indicated antibodies and EdU.

(C) Equator images of zygotene-spermatocytes after organ culture stained with the indicated antibodies and EdU. The graph shows the number of internal TRF1 foci in zygotene-spermatocytes with the median. Zygote-spermatocytes from cultures with (+) or without (-) nocodazole, are divided into two populations, EdU incorporated (+) or unincorporated (-). Data are from three independent cultures.

(D) Equator images of zygotene-spermatocytes after organ culture stained with the indicated antibodies. *** $p < 0.0001$, unpaired t test. Scale bars, 5 μ m.

Meiosis-Specific Reformation of the INM

Our identification and characterization of the meiosis-specific nuclear membrane complex, TERB2-MAJIN, highlight the elaborate cross regulations between the meiotic nuclear envelope and telomeres. Previous studies in mice also hinted at the drastic reformations of INM proteins taking place specifically in meiosis, such as the expression of meiosis-specific short isoform of lamina protein, lamin C2 (Alzheimer et al., 1999; Jahn et al., 2010; Link et al., 2013), and the reorganization of nuclear pore complex (Scherthan et al., 2000), which may influence the telomere mobility within the INM. Further, the redistribution of SUN1 from the whole INM to the telomere attachment sites requires the meiosis-specific phospho-modifications on its N terminus domain, that are mediated possibly by CDK2 in mammals (Mar-

tinerie et al., 2014; Viera et al., 2015), as do CHK2 and PLK2 in nematode (Harper et al., 2011; Labella et al., 2011; MacQueen and Villeneuve, 2001; Penkner et al., 2009). Thus, emerging evidences indicate that there are extensive protein networks that lie underneath the INM of the nuclear envelope in meiosis. The future goals in this field will be to identify factors involved in the INM network and understand the interplay between them. Such studies will provide an important clue to solve the issues of human infertility and a wide range of diseases related to the INM dysfunction (Méjat and Misteli, 2010).

EXPERIMENTAL PROCEDURES

Detailed methods are described in the *Supplemental Experimental Procedures*.

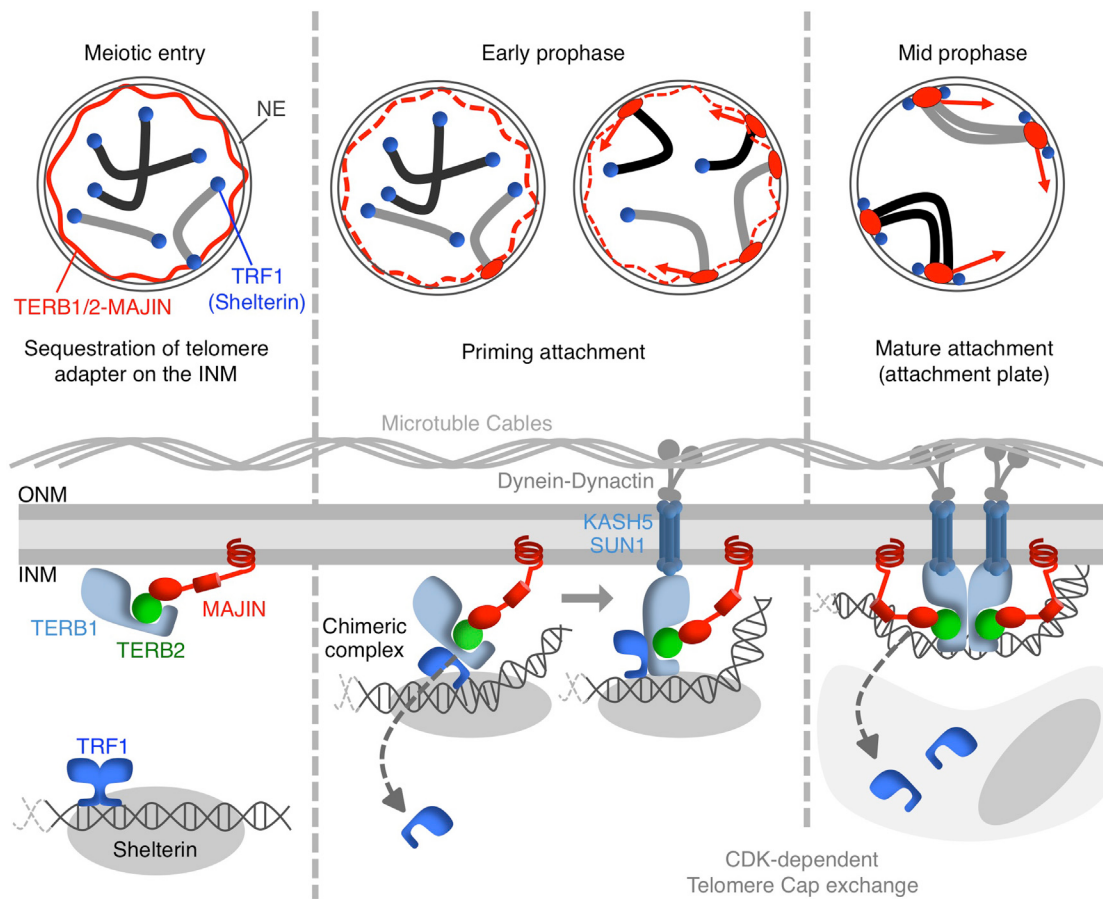


Figure 7. Schematic of Meiosis-Specific Telomere Regulations in Mammals

The meiotic telomere complex, TERB1/2-MAJIN, is sequestered to the inner nuclear membrane (INM) by the transmembrane DNA-binding protein MAJIN (meiotic entry). The priming telomere attachment is achieved via the formation of the chimeric complex, TRF1-TERB1/2-MAJIN, initially at telomeres located stochastically at the nuclear periphery. The downstream accumulation of SUN1-KASH5 to the telomere attachment site triggers the incipient chromosome movement by linking telomeres to the microtubule cables surrounding the cytoplasmic surface of the outer nuclear membrane (ONM) and its associated dynein-dynactin motors. The incipient chromosome movement further facilitates telomere attachment by producing liquidity within the nucleus (early prophase). In mid prophase, the shelterin complex, including TRF1, is removed from the membrane-anchored telomeres dependent on the CDK activity and direct DNA-membrane interaction mediated by MAJIN (telomere cap exchange).

Animal Experiments

Knockout mice for *Sun1* and *Terb1* were reported earlier (Ding et al., 2007; Shibuya et al., 2014a). All knockout mice were congenic with the C57BL/6J background. Animal experiments were approved by the Institutional Animal Care and Use Committee (approval 2711).

Electrophoretic Mobility Shift Assay and In Vitro Phosphorylation Assay

To prepare the DNA probes, EcoRI/NotI fragments containing six or nine telomere repeats (TTAGGG) or scrambled repeats (GATGGT) were radio-labeled with [α -³²P] dCTP by Klenow enzyme. Proteins were mixed with 0.5 ng of labeled probes for one reaction in binding buffer (20 mM HEPES-KOH [pH 7.9], 5% glycerol, 4% Ficoll, 0.5 μ g poly[dI-dC], 4 mM DTT, 100 mM NaCl, 1 mM MgCl₂, 0.1 mM EDTA) and electrophoresed in a 5% nondenaturing polyacrylamide gel in 0.5 \times Tris-borate-EDTA (TBE) at room temperature (RT). For in vitro phosphorylation, 1 μ l of 100 mM ATP and 1 μ l of recombinant cyclin B-CDK1 complex (NEB; P6020L) were incubated with the substrate proteins at 30°C for 1 hr.

Gel Filtration

Gel filtration was conducted on an ENrich SEC 650 column (Bio-Rad) in a buffer containing 600 mM NaCl, 0.1% NP-40, and 20 mM Tris-KCl (pH 7.5).

Fractions (500 μ l) were collected. The peaks generated by the Gel Filtration Standard (Bio-Rad; #151-1901) are marked in each figure.

Testis Organ Culture

Testis organ culture was performed based on the previous study with some modifications (Sato et al., 2013). Briefly, testes from 9 days post-partum (dpp) male mice were chopped into three to four pieces 1–3 mm in diameter with forceps and placed on the agarose gels soaked in the organ culture medium, 2 \times DMEM (Sigma). To label cells progressing to pre-meiotic S phase during organ culture, 2 μ M of EdU (Life Technologies; C10340) was supplied to the medium. To suppress microtubule-dependent chromosome movements, 5 μ M of nocodazole (or the same volume of DMSO as a control) were supplied. After 3.5 days in culture, cells were collected from the organ and subjected to the EdU labeling and immunostaining.

Immuno-FISH Assay

Immuno-FISH assay was carried out based on a previous study (Ding et al., 2007). In brief, spermatocyte spreads were treated with RNase A (100 μ g/ml) at 37°C for 30 min in 2 \times saline sodium citrate (SSC), denatured at 85°C for 10 min with fluorescein isothiocyanate (FITC)-labeled TelC (CCCTAA)₃ PNA probe (Panagene), and hybridized for 4 hr at 37°C. Preparations were washed

sequentially in 50% formamide/0.5× SSC (twice) and 1× SSC (twice) at 42°C for 5 min each time. The preparations were co-labeled with antibodies.

Statistical Analysis

Kruskal-Wallis one-way ANOVA with Bonferroni's multiple comparisons test was performed in Figure 3G and Student's t tests were performed in Figures 4G, 5G, 5H, and 6C using GraphPad Prism version 5.0d (GraphPad Software). Statistical analyses were performed for technical variability ($n = 3$ experiments) otherwise indicated.

ACCESSION NUMBERS

The accession numbers for the Murine MAJIN, human MAJIN, and Murine TERB2 reported in this paper are NCBI: LC068586, LC068587, and LC068588.

SUPPLEMENTAL INFORMATION

Supplemental Information includes Supplemental Experimental Procedures and seven figures and can be found with this article online at <http://dx.doi.org/10.1016/j.cell.2015.10.030>.

AUTHOR CONTRIBUTIONS

H.S. designed and performed most of the experiments. A.M. supported the screenings of MAJIN and TERB2. A.H. and C.H. performed the electron microscopic experiments. L.N. supported MASS spectrometry analysis. H.S., A.H., and Y.W. interpreted the data. H.S. and Y.W. wrote the paper. Y.W. supervised the project.

ACKNOWLEDGMENTS

We thank N. Takeda (University of Kumamoto) for the constructions of *Majin* and *Terb2* KO mice and T. de Lange (Rockefeller University) for anti-TIN2 antibody. We thank Y. Okada (University of Tokyo) for technical advice concerning testis organ culture. We thank H. Sasaki and Y. Tomari (University of Tokyo) for valuable discussion and advice concerning the biochemistry. We thank H. Scherthan (Ulm University), M.P. Colaiacovo (Harvard Medical School), and N. Kleckner (Harvard University) for valuable discussion. We thank all the members of our laboratory for their valuable support and discussion. This work was supported in part by a JSPS Research Fellowship (to H.S.), the Swedish Research Council and the Karolinska Institute (to A.H. and C.H.) and MEXT KAKENHI grant 25000014 (to Y.W.).

Received: August 3, 2015

Revised: September 16, 2015

Accepted: September 24, 2015

Published: November 5, 2015

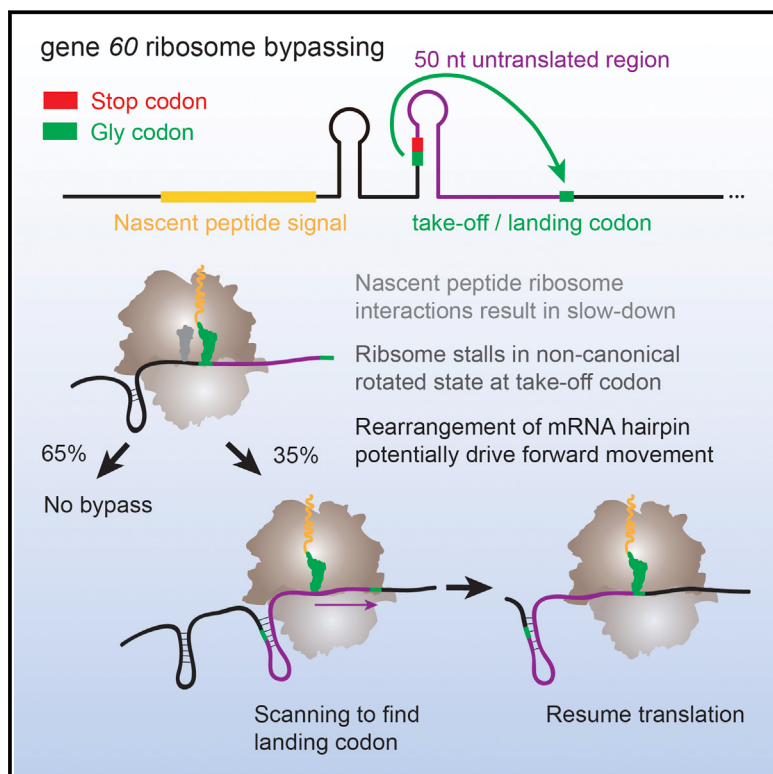
REFERENCES

- Alsheimer, M., von Glesenapp, E., Hock, R., and Benavente, R. (1999). Architecture of the nuclear periphery of rat pachytene spermatocytes: distribution of nuclear envelope proteins in relation to synaptonemal complex attachment sites. *Mol. Biol. Cell* 10, 1235–1245.
- Bianchi, A., Smith, S., Chong, L., Elias, P., and de Lange, T. (1997). TRF1 is a dimer and bends telomeric DNA. *EMBO J* 16, 1785–1794.
- Bupp, J.M., Martin, A.E., Stensrud, E.S., and Jaspersen, S.L. (2007). Telomere anchoring at the nuclear periphery requires the budding yeast Sad1-UNC-84 domain protein Mps3. *J. Cell Biol.* 179, 845–854.
- Chikashige, Y., Tsutsumi, C., Yamane, M., Okamasa, K., Haraguchi, T., and Hiraoka, Y. (2006). Meiotic proteins Bqt1 and Bqt2 tether telomeres to form the bouquet arrangement of chromosomes. *Cell* 125, 59–69.
- Chikashige, Y., Yamane, M., Okamasa, K., Tsutsumi, C., Kojidani, T., Sato, M., Haraguchi, T., and Hiraoka, Y. (2009). Membrane proteins Bqt3 and -4 anchor telomeres to the nuclear envelope to ensure chromosomal bouquet formation. *J. Cell Biol.* 187, 413–427.
- Chua, P.R., and Roeder, G.S. (1997). Tam1, a telomere-associated meiotic protein, functions in chromosome synapsis and crossover interference. *Genes Dev.* 11, 1786–1800.
- Conrad, M.N., Dominguez, A.M., and Dresser, M.E. (1997). Ndj1p, a meiotic telomere protein required for normal chromosome synapsis and segregation in yeast. *Science* 276, 1252–1255.
- Conrad, M.N., Lee, C.Y., Chao, G., Shinohara, M., Kosaka, H., Shinohara, A., Conchello, J.A., and Dresser, M.E. (2008). Rapid telomere movement in meiotic prophase is promoted by Ndj1, MPS3, and CSM4 and is modulated by recombination. *Cell* 133, 1175–1187.
- Ding, X., Xu, R., Yu, J., Xu, T., Zhuang, Y., and Han, M. (2007). SUN1 is required for telomere attachment to nuclear envelope and gametogenesis in mice. *Dev. Cell* 12, 863–872.
- Esponda, P., and Giménez-Martín, G. (1972). The attachment of the synaptonemal complex to the nuclear envelope. An ultrastructural and cytochemical analysis. *Chromosoma* 38, 405–417.
- Fairall, L., Chapman, L., Moss, H., de Lange, T., and Rhodes, D. (2001). Structure of the TRFH dimerization domain of the human telomeric proteins TRF1 and TRF2. *Mol. Cell* 8, 351–361.
- Godet, M., Thomas, A., Rudkin, B.B., and Durand, P. (2000). Developmental changes in cyclin B1 and cyclin-dependent kinase 1 (CDK1) levels in the different populations of spermatogenic cells of the post-natal rat testis. *Eur. J. Cell Biol.* 79, 816–823.
- Harper, N.C., Rillo, R., Jover-Gil, S., Assaf, Z.J., Bhalla, N., and Dernburg, A.F. (2011). Pairing centers recruit a Polo-like kinase to orchestrate meiotic chromosome dynamics in *C. elegans*. *Dev. Cell* 21, 934–947.
- Hassold, T., and Hunt, P. (2001). To err (meiotically) is human: the genesis of human aneuploidy. *Nat. Rev. Genet.* 2, 280–291.
- Hayashi, M.T., Cesare, A.J., Fitzpatrick, J.A., Lazzarini-Denchi, E., and Karl-seder, J. (2012). A telomere-dependent DNA damage checkpoint induced by prolonged mitotic arrest. *Nat. Struct. Mol. Biol.* 19, 387–394.
- Hiraoka, Y., and Dernburg, A.F. (2009). The SUN rises on meiotic chromosome dynamics. *Dev. Cell* 17, 598–605.
- Holm, P.B., and Rasmussen, S.W. (1977). Human meiosis I. The human pachytene karyotype analyzed by three dimensional reconstruction of the synaptonemal complex. *Carlsberg Res. Commun.* 42, 283–323.
- Horn, H.F., Kim, D.I., Wright, G.D., Wong, E.S., Stewart, C.L., Burke, B., and Roux, K.J. (2013). A mammalian KASH domain protein coupling meiotic chromosomes to the cytoskeleton. *J. Cell Biol.* 202, 1023–1039.
- Jahn, D., Schramm, S., Benavente, R., and Alsheimer, M. (2010). Dynamic properties of meiosis-specific lamin C2 and its impact on nuclear envelope integrity. *Nucleus* 1, 273–283.
- Koszul, R., and Kleckner, N. (2009). Dynamic chromosome movements during meiosis: a way to eliminate unwanted connections? *Trends Cell Biol.* 19, 716–724.
- Labella, S., Woglar, A., Jantsch, V., and Zetka, M. (2011). Polo kinases establish links between meiotic chromosomes and cytoskeletal forces essential for homolog pairing. *Dev. Cell* 21, 948–958.
- Lee, C.Y., Horn, H.F., Stewart, C.L., Burke, B., Bolcun-Filas, E., Schimenti, J.C., Dresser, M.E., and Pezza, R.J. (2015). Mechanism and regulation of rapid telomere prophase movements in mouse meiotic chromosomes. *Cell Rep.* 11, 551–563.
- Liebe, B., Alsheimer, M., Höög, C., Benavente, R., and Scherthan, H. (2004). Telomere attachment, meiotic chromosome condensation, pairing, and bouquet stage duration are modified in spermatocytes lacking axial elements. *Mol. Biol. Cell* 15, 827–837.
- Link, J., Jahn, D., Schmitt, J., Göb, E., Baar, J., Ortega, S., Benavente, R., and Alsheimer, M. (2013). The meiotic nuclear lamina regulates chromosome dynamics and promotes efficient homologous recombination in the mouse. *PLoS Genet.* 9, e1003261.
- Link, J., Leubner, M., Schmitt, J., Göb, E., Benavente, R., Jeang, K.T., Xu, R., and Alsheimer, M. (2014). Analysis of meiosis in SUN1 deficient mice reveals a

- distinct role of SUN2 in mammalian meiotic LINC complex formation and function. *PLoS Genet.* 10, e1004099.
- Link, J., Jahn, D., and Alsheimer, M. (2015). Structural and functional adaptations of the mammalian nuclear envelope to meet the meiotic requirements. *Nucleus* 6, 93–101.
- MacQueen, A.J., and Villeneuve, A.M. (2001). Nuclear reorganization and homologous chromosome pairing during meiotic prophase require *C. elegans* chk-2. *Genes Dev.* 15, 1674–1687.
- Martinerie, L., Manterola, M., Chung, S.S., Panigrahi, S.K., Weisbach, M., Vasileva, A., Geng, Y., Sicinski, P., and Wolgemuth, D.J. (2014). Mammalian E-type cyclins control chromosome pairing, telomere stability and CDK2 localization in male meiosis. *PLoS Genet.* 10, e1004165.
- McKerlie, M., and Zhu, X.D. (2011). Cyclin B-dependent kinase 1 regulates human TRF1 to modulate the resolution of sister telomeres. *Nat. Commun.* 2, 371.
- Méjat, A., and Misteli, T. (2010). LINC complexes in health and disease. *Nucleus* 1, 40–52.
- Mekhail, K., and Moazed, D. (2010). The nuclear envelope in genome organization, expression and stability. *Nat. Rev. Mol. Cell Biol.* 11, 317–328.
- Morimoto, A., Shibuya, H., Zhu, X., Kim, J., Ishiguro, K., Han, M., and Watanabe, Y. (2012). A conserved KASH domain protein associates with telomeres, SUN1, and dynein during mammalian meiosis. *J. Cell Biol.* 198, 165–172.
- Palm, W., and de Lange, T. (2008). How shelterin protects mammalian telomeres. *Annu. Rev. Genet.* 42, 301–334.
- Penkner, A.M., Fridkin, A., Gloggnitzer, J., Baudrimont, A., Machacek, T., Woglar, A., Csaszar, E., Pasierbek, P., Ammerer, G., Gruenbaum, Y., and Jantsch, V. (2009). Meiotic chromosome homology search involves modifications of the nuclear envelope protein Matefin/SUN-1. *Cell* 139, 920–933.
- Pfeifer, C., Thomsen, P.D., and Scherthan, H. (2001). Centromere and telomere redistribution precedes homologue pairing and terminal synapsis initiation during prophase I of cattle spermatogenesis. *Cytogenet. Cell Genet.* 93, 304–314.
- Sato, A., Isaac, B., Phillips, C.M., Rillo, R., Carlton, P.M., Wynne, D.J., Kasad, R.A., and Dernburg, A.F. (2009). Cytoskeletal forces span the nuclear envelope to coordinate meiotic chromosome pairing and synapsis. *Cell* 139, 907–919.
- Sato, T., Katagiri, K., Kubota, Y., and Ogawa, T. (2013). In vitro sperm production from mouse spermatogonial stem cell lines using an organ culture method. *Nat. Protoc.* 8, 2098–2104.
- Scherthan, H., Jerratsch, M., Li, B., Smith, S., Hultén, M., Lock, T., and de Lange, T. (2000). Mammalian meiotic telomeres: protein composition and redistribution in relation to nuclear pores. *Mol. Biol. Cell* 11, 4189–4203.
- Scherthan, H., Wang, H., Adelfalk, C., White, E.J., Cowan, C., Cande, W.Z., and Kaback, D.B. (2007). Chromosome mobility during meiotic prophase in *Saccharomyces cerevisiae*. *Proc. Natl. Acad. Sci. USA* 104, 16934–16939.
- Scherthan, H., Schöfisch, K., Dell, T., and Illner, D. (2014). Contrasting behavior of heterochromatic and euchromatic chromosome portions and pericentric genome separation in pre-bouquet spermatocytes of hybrid mice. *Chromosoma* 123, 609–624.
- Schober, H., Ferreira, H., Kalck, V., Gehlen, L.R., and Gasser, S.M. (2009). Yeast telomerase and the SUN domain protein Mps3 anchor telomeres and repress subtelomeric recombination. *Genes Dev.* 23, 928–938.
- Shibuya, H., and Watanabe, Y. (2014). The meiosis-specific modification of mammalian telomeres. *Cell Cycle* 13, 2024–2028.
- Shibuya, H., Ishiguro, K., and Watanabe, Y. (2014a). The TRF1-binding protein TERB1 promotes chromosome movement and telomere rigidity in meiosis. *Nat. Cell Biol.* 16, 145–156.
- Shibuya, H., Morimoto, A., and Watanabe, Y. (2014b). The dissection of meiotic chromosome movement in mice using an *in vivo* electroporation technique. *PLoS Genet.* 10, e1004821.
- Siderakis, M., and Tarsounas, M. (2007). Telomere regulation and function during meiosis. *Chromosome Res.* 15, 667–679.
- Starr, D.A., and Fridolfsson, H.N. (2010). Interactions between nuclei and the cytoskeleton are mediated by SUN-KASH nuclear-envelope bridges. *Annu. Rev. Cell Dev. Biol.* 26, 421–444.
- Storlazzi, A., Gargano, S., Ruprich-Robert, G., Falque, M., David, M., Kleckner, N., and Zickler, D. (2010). Recombination proteins mediate meiotic spatial chromosome organization and pairing. *Cell* 141, 94–106.
- Thilagavathi, J., Venkatesh, S., and Dada, R. (2013). Telomere length in reproduction. *Andrologia* 45, 289–304.
- Trelles-Sticken, E., Dresser, M.E., and Scherthan, H. (2000). Meiotic telomere protein Ndj1p is required for meiosis-specific telomere distribution, bouquet formation and efficient homologue pairing. *J. Cell Biol.* 151, 95–106.
- Ulbert, S., Platani, M., Boue, S., and Mattaj, I.W. (2006). Direct membrane protein-DNA interactions required early in nuclear envelope assembly. *J. Cell Biol.* 173, 469–476.
- Viera, A., Alsheimer, M., Gómez, R., Berenguer, I., Ortega, S., Symonds, C.E., Santamaría, D., Benavente, R., and Suja, J.A. (2015). CDK2 regulates nuclear envelope protein dynamics and telomere attachment in mouse meiotic prophase. *J. Cell Sci.* 128, 88–99.
- Wolgemuth, D.J., Manterola, M., and Vasileva, A. (2013). Role of cyclins in controlling progression of mammalian spermatogenesis. *Int. J. Dev. Biol.* 57, 159–168.
- Woollam, D.H., Millen, J.W., and Ford, E.H. (1967). Points of attachment of pachytene chromosomes to the nuclear membrane in mouse spermatocytes. *Nature* 213, 298–299.

Coupling of mRNA Structure Rearrangement to Ribosome Movement during Bypassing of Non-coding Regions

Graphical Abstract



Authors

Jin Chen, Arthur Coakley,
Michelle O'Connor, Alexey Petrov,
Seán E. O'Leary, John F. Atkins,
Joseph D. Puglisi

Correspondence

j.atkins@ucc.ie (J.F.A.),
puglisi@stanford.edu (J.D.P.)

In Brief

The ribosome can “hop” over a section of phage mRNA while in the midst of translating it, and single-molecule techniques indicate that these dynamics require interactions between the mRNA secondary structure, the nascent peptide, and the ribosome, which advances in a non-canonical rotated state.

Highlights

- A long, non-canonical rotated-state pause of the ribosome is a hallmark of bypassing
- Nascent peptide-ribosome interactions slow down the ribosome prior to the take-off codon
- mRNA structure rearrangements drive ribosome movement across the non-coding gap
- The ribosome scans mRNA a short distance in search of the optimal landing codon

Coupling of mRNA Structure Rearrangement to Ribosome Movement during Bypassing of Non-coding Regions

Jin Chen,^{1,2} Arthur Coakley,³ Michelle O'Connor,^{3,5} Alexey Petrov,¹ Seán E. O'Leary,¹ John F. Atkins,^{3,4,*} and Joseph D. Puglisi^{1,*}

¹Department of Structural Biology, Stanford University School of Medicine, Stanford, CA 94305-5126, USA

²Department of Applied Physics, Stanford University, Stanford, CA 94305-4090, USA

³School of Biochemistry and Cell Biology, University College Cork, Western Gateway Building, Western Road, Cork, Ireland

⁴Department of Human Genetics, University of Utah, Salt Lake City, UT 84112-5330, USA

⁵Present address: Health Information and Quality Authority, City Gate, Mahon, Cork, Ireland

*Correspondence: j.atkins@ucc.ie (J.F.A.), puglisi@stanford.edu (J.D.P.)

<http://dx.doi.org/10.1016/j.cell.2015.10.064>

SUMMARY

Nearly half of the ribosomes translating a particular bacteriophage T4 mRNA bypass a region of 50 nt, resuming translation 3' of this gap. How this large-scale, specific hop occurs and what determines whether a ribosome bypasses remain unclear. We apply single-molecule fluorescence with zero-mode waveguides to track individual *Escherichia coli* ribosomes during translation of T4's gene 60 mRNA. Ribosomes that bypass are characterized by a 10- to 20-fold longer pause in a non-canonical rotated state at the take-off codon. During the pause, mRNA secondary structure rearrangements are coupled to ribosome forward movement, facilitated by nascent peptide interactions that disengage the ribosome anticodon-codon interactions for slippage. Close to the landing site, the ribosome then scans mRNA in search of optimal base-pairing interactions. Our results provide a mechanistic and conformational framework for bypassing, highlighting a non-canonical ribosomal state to allow for mRNA structure refolding to drive large-scale ribosome movements.

INTRODUCTION

Translation normally occurs sequentially in triplets of nucleotides (codons) with strict maintenance by the ribosome of fidelity and reading frame with error rates of 10^{-3} to 10^{-4} per codon (Dunkle and Dunham, 2015; Hansen et al., 2003; Jenner et al., 2010). There are cases in which this well-established rule breaks down, where the genetic code can be recoded and altered in an mRNA-specific manner (called "programmed"). During programmed frameshifting, a portion of translating ribosomes can be stochastically diverted to a different reading frame (Chen et al., 2014b; Márquez et al., 2004; Tinoco et al., 2013). Ribosomes can even be directed to bypass, hopping over a stretch

of nucleotides to continue translating a contiguous polypeptide (Herr et al., 2000a). These events increase the richness of information encoded in DNA or RNA, where a coding sequence can specify additional protein products not predicted from the standard readout of the open reading frame, as well as adding a layer of translational control.

The best-documented case of programmed bypassing is the gene 60 mRNA of bacteriophage T4 that codes for a subunit of a viral DNA topoisomerase (Herr et al., 2000a; Huang et al., 1988; Weiss et al., 1990). During translation of the gene 60 mRNA, ribosomes translate the first 45 codons (excluding the initiator fMet tRNA, which we term codon 0) to a Gly GGA codon. Half of the translating ribosomes stop at the subsequent UAG stop codon, and the other half skips the next 50 nt and resumes translation from a downstream Gly codon (Maldonado and Herr, 1998). Instead of stopping at the stop codon, the anticodon of the peptidyl-tRNA^{Gly} (Gly-2) (Herr et al., 1999) disengages from mRNA (in a process called "take-off"), the ribosome skips over the 50-nt gap, and the peptidyl-tRNA re-pairs to mRNA downstream at a GGA codon (called the "landing site"). As a result, translation resumes at codon 46 to create a single, continuous protein product from a discontinuous open reading frame (Wills, 2010) (Figure 1A).

Biochemical, genetic, and mutational analysis relying on detection of protein products, both *in vitro* and *in vivo*, have identified the essential stimulatory elements for programmed bypassing in gene 60: (1) the tRNA^{Gly} (Gly-2) and the matching GGA take-off and landing sites bounding the non-coding gap, (2) an upstream nascent peptide sequence, (3) a stem loop consisting of the take-off codon and the adjacent UAG stop codon, and (4) a GAG Shine-Dalgarno-like sequence located 6 nt 5' to the landing site to promote precision of landing (Figure 1A). With the matched take-off/landing pairs, bypassing is the most efficient for the wild-type (WT) GGA codon; other codons are possible, but codons with G or C in the first two positions yield more efficient bypassing (Bucklin et al., 2005). With unmatched take-off/landing pairs, for example, GGA/GCA or GCA/GGA, bypassing efficiencies were greatly reduced (Weiss et al., 1990). The take-off codon is located within a potential -UUCG- hairpin stem loop in the 5' portion of the non-coding gap, which is

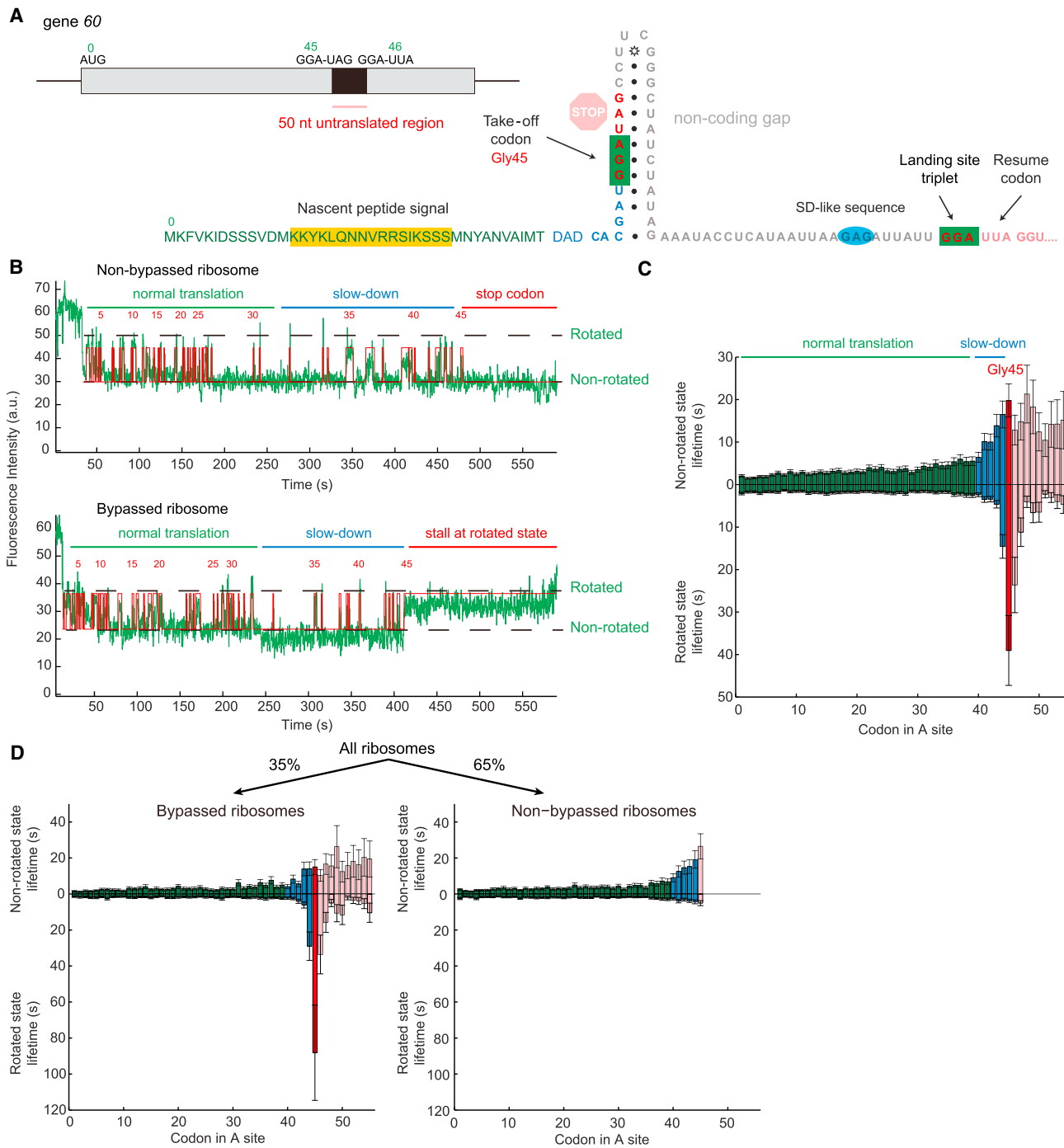


Figure 1. Dynamic Pathways of Gene 60 Bypassing

(A) The elements of the gene 60 bypass are labeled: (1) the UAG stop codon immediately 3' to the take-off GGA site at codon Gly45, (2) the tRNA^{Gly} and the matching GGA take-off and landing sites, (3) an upstream nascent peptide signal, (4) a stem loop consisting of the take-off codon, and possibly (5) a GAG Shine-Dalgarno-like sequence located 6 nt 5' to the landing site to promote precision of landing. The full sequence of the gene 60 mRNA is shown, where the first 42 codons are written as their amino acids (with Met being codon 0), and the remaining sequence is labeled with nucleotides. The coloring of the codon or nucleotide matches the coloring in (B) and (C).

(B) Representative traces of ribosomes Cy3B (green) fluorescent intensity for bypassed and non-bypassed ribosomes. For both cases, there is a phase with normal translation (labeled with a green line), a phase of slowdown (blue line), and either termination at a stop codon for non-bypassed ribosomes or entering a rotated-state pause at codon Gly45 for bypassed ribosomes. The state assignment is shown in red, with the codon counts above.

(legend continued on next page)

important for bypassing: mutations that disrupted base pairing reduced bypassing, whereas compensatory double mutations restored it. Altering the -UUCG- tetraloop sequence at the top of the stem, extending the length of the stem, or increasing loop size also reduced bypassing (Herr et al., 2000b; Weiss et al., 1990; Wills et al., 2008). In addition to the hairpin, a “nascent peptide signal,” KKYKLQNNVRRSIKSSS^{13–29}, potentially interacts with the exit tunnel of the ribosome to stimulate bypassing (Herr et al., 2004; Maldonado and Herr, 1998; Weiss et al., 1990). Lastly, there is an alternative landing site at GGG within the non-coding gap near the top of the stem loop (positions 9–11 from the take-off codon); however, the bypassing ribosome always lands at the wild-type landing codon (positions 48–50 from the take-off codon). Thus, it has been proposed that the ribosome does not scan the full non-coding gap in search of a potential landing site, but rather hops over the non-coding region (Wills et al., 2008).

How the ribosome traverses the gap remains unclear, and no definitive and testable model is proposed for the mechanism of such a large-scale movement. What stimulates the ribosome to initiate bypass, and what determines whether or not a ribosome bypasses? What are the roles of the nascent peptide and mRNA secondary structure in inducing bypass? What is the conformational state of the ribosome during bypassing? Prior investigations of frameshifting have underscored the importance of dynamics in translational recoding (Caliskan et al., 2014; Chen et al., 2014b). Here, we probe the dynamic and stochastic nature of bypassing using single-molecule fluorescence to track single translating ribosomes in real time, allowing us to define a global mechanism for bypassing.

RESULTS

Real-Time Observation of Ribosome Bypassing Dynamics

To monitor single *Escherichia coli* ribosome progression on mRNAs in real-time, we used zero-mode waveguide (ZMW) instrumentation (Chen et al., 2014a, 2014b). In this study, we followed conformational changes underlying elongation, involving rotational movements of the small (30S) ribosomal subunit with respect to the large (50S) ribosomal subunit and correlated them with binding and departure of tRNAs and elongation factors. To observe rotational movement, the 30S subunit was labeled with Cy3B on helix 44, and a non-fluorescent quencher, BHQ-2, was placed on helix 101 of the 50S subunit, allowing fluorescence resonance energy transfer (FRET) between the two dyes (Chen et al., 2012b, 2013) (Figure S1A).

During one elongation cycle, the two subunits start in a non-rotated state (characterized by high FRET, low Cy3B intensity). The EF-Tu-GTP-aa-tRNA ternary complex (TC) binds to the

vacant A site, followed by peptidyl transfer from P-site tRNA to the new A-site aa-tRNA. After peptidyl transfer, the ribosomal subunits rapidly rotate relative to each other (rotated state; lower FRET, higher Cy3B intensity). During this stage, the ribosome is “unlocked,” where the ribosome conformation and tRNA spontaneously fluctuate (Blanchard et al., 2004a; Chen et al., 2012a; Cornish et al., 2008), preparing for translocation. mRNA-tRNA interactions and ribosome-tRNA interactions are weaker at this stage (Liu et al., 2011; Valle et al., 2003). Upon translocation catalyzed by EF-G, the two subunits rotate back to their original high-FRET state and the ribosome is “relocked.” Thus, one round of high-low FRET (low-high Cy3B intensity) corresponds to a single ribosome translating one codon, allowing tracking of translation at codon resolution, and providing the timings of individual substeps at each codon (Chen et al., 2013) (Figure S1B). As opposed to previous smFRET studies with probes labeled at ribosomal proteins S6 and L9 showing spontaneous intersubunit rotations after peptidyl transfer (Cornish et al., 2008), our FRET probe positions possibly monitor a different intersubunit movement that occurs only one cycle per codon. Arrival and departure of the dye-labeled ligands, such as tRNAs, can be simultaneously observed as a sequence of fluorescent pulses (Chen et al., 2013) (Figure S1C). The correlation of single cycles of FRET to translation of a single codon has been confirmed in multiple studies (Aitken and Puglisi, 2010; Chen et al., 2012a; Marshall et al., 2008).

To follow translating ribosomes, we monitored the intersubunit conformational signal upon delivering total tRNA (tRNA_{tot}) ternary complex (aa-tRNA-EF-Tu-GTP), EF-G, and BHQ-50S to immobilized Cy3B-30S preinitiation complexes on the bottom of the ZMWs, as done previously (Johansson et al., 2014; Tsai et al., 2014). Through statistical analysis of multiple translating single ribosomes, we obtained waiting times for the non-rotated and rotated states of each codon. Continuous translation can be observed for more than 50 codons, allowing us to profile the real-time dynamics approaching, during, and after bypassing.

Dynamic Pathways of Bypassing Show a Rotated-State Pause for Bypassed Ribosomes

Translation of the first 40 codons of wild-type gene 60 mRNA proceeds normally, with expected lifetimes of the rotated (waiting for translocation) and non-rotated (waiting for peptidyl transfer) states (2–5 s at 3 μM tRNA_{tot} TC and 240 nM EF-G), demonstrating a regular elongation rate at these codons. From codons 40 to 45, i.e., before the take-off site, translation gradually slows with an increase in both rotated and non-rotated states lifetimes to roughly 15 s for each state (3- to 7-fold increase). At the bypass site at codon Gly45, an exceptionally long rotated-state pause is observed, with a 20-fold higher mean lifetime of 40 s. For a subset of ribosomes paused at codon Gly45,

(C) The mean state lifetimes. The first 39 codons, when translation occurs normally, are colored in green. Codons 40 to 44, characterized by slowdown due to nascent peptide interaction, are shown in blue. The take-off site at codon 45 is colored in red. At codon 45, there is a long rotated-state pause. Codons after bypass are shaded in pink. The number of molecules analyzed is n = 451.

(D) We can parse the subpopulation of ribosomes into bypassed and non-bypassed and separate the lifetimes shown in (C) into these two populations, giving us a bypassing efficiency of 35%. Only the bypassed ribosomes exhibit an increase in rotated state lifetime at codon Gly45. The color scheme is the same as in (C). n = 451.

See also Figures S1, S2, and S3.

translation resumes instead of stopping at the UAG stop codon after Gly45, indicating that we observe bypassing (Figures 1B, 1C, S2A, and S2B).

Translating single ribosomes cluster into three major subpopulations: (1) ribosomes that translate 45 codons and stall at the stop codon; these ribosomes do not bypass and do not exhibit the long rotated pause at Gly45, (2) ribosomes that bypass and translate at least codon 46; these ribosomes ubiquitously exhibit a long rotated state at codon 45, or (3) ribosome traces showing end of Cy3B signal during the long rotated state due to photobleaching or end of movie. Combining the second and third clusters gives a bypassing efficiency of ~35%, consistent with our *in vivo* assays (33%) and prior studies (Maldonado and Herr, 1998; Samatova et al., 2014). These results also confirm that bypassing is programmed in mRNA itself (Samatova et al., 2014); no other auxiliary factors beyond the standard factors added here are required.

Bypassing and non-bypassing ribosomes show distinct dynamics. All ribosomes exhibit the gradual increase in non-rotated state and rotated lifetimes from codons 40 to 45. This increase in lifetime upon approaching the bypass site is reminiscent of the dynamic signatures observed for nascent peptide-ribosome interactions during SecM stalling (Tsai et al., 2014). The long rotated-state pause at the bypass site (Gly45) is observed only for ribosomes that undergo bypassing and is similar to the non-canonical rotated states observed in -1 frameshifting (Chen et al., 2014b). By parsing into two distinct populations of ribosomes, we obtain a more accurate mean lifetime for the rotated-state pause (88.2 ± 26.4 s) without the convolution of non-bypassed ribosomes (Figure 1D). Resumption of normal translation post bypassing is not immediate, and the ribosome translates slowly for a few more codons before the rotated state lifetimes return to normal (mean lifetime is 5 s), while the non-rotated state lifetimes remain higher (mean lifetime is 15 s) (Figures 1B and 1C; see Figure S3).

The Role of the Nascent Peptide Signal and Its Interaction with the Ribosome Exit Tunnel: Setting the Stage for Bypassing

We hypothesized that the general slowdown in translation observed for both non-bypassed and bypassed ribosomes is due to the nascent peptide signal, KYKLQNNVRRSIKSSS^{14–29} (Weiss et al., 1990; Wills, 2010), which interacts with the ribosome exit tunnel. *In vivo*, deleting from codon 14 to codon 29 causes a 70% decrease in bypassing efficiency (Figure 2A). Mutational analysis of the nascent peptide highlighted the importance of a KKYK^{13–16} motif (Figure 2A). With our *in vitro* single-molecule system, deleting the sequence encoding KYKLQNNVRRSIKSSS^{14–29} eliminates observable bypassing and pausing: translating ribosomes no longer exhibit the increase in rotated and non-rotated state lifetimes and ribosomes now translate 29 codons to the stop codon, with only 1% of the traces showing translation beyond the UAG stop codon (Figure S4). Mutating the critical KKYK motif to AAAA resulted in a similar behavior; the increases in non-rotated and rotated states lifetimes are no longer observed (Figure 2B). Deletion of the non-coding gap, while maintaining the nascent peptide signal,

abrogates bypassing as expected, but increases in rotated and non-rotated state lifetimes approaching codon Gly45 are observed as for the wild-type sequence (Figure S4). These results indicate that the nascent peptide is responsible for the slowdown approaching the bypass site independent of the mRNA sequence and structure at the bypass site and that this slowdown is necessary for the ribosome to undergo the rotated-state pause at Gly45 for bypassing. Importantly, these interactions are different from SecM-induced stall (Figure 2C).

The Role of the mRNA Hairpin in Promoting Disengagement of Anticodon-Codon Interactions

The nascent peptide signal alone is not sufficient to promote bypass; the hairpin at the bypass site is required. Disrupting the potential base pairing in the hairpin stem abolishes the long rotated-state pause at Gly45, but we still observe the slowdown caused by the nascent peptide signal (Figure 3A). This demonstrates that the hairpin stem loop is required for the long pause in the rotated state prior to bypassing and that the action of the hairpin follows that of the nascent chain.

How the mRNA hairpin promotes such a pause is puzzling, since the –UUCG– hairpin stem loop should be fully melted by the ribosome within the mRNA channel at the take-off site, as the ribosome protects 9 nt subsequent to the P-site codon (Qu et al., 2011). We hypothesize here that the unusual stability of a UUCG tetraloop (Ennifar et al., 2000; Todd and Walter, 2013), which has a propensity to form a compact structure, may favor re-folding of the apical portions of the hairpin, providing a mechanism for the long rotated-state pause. If this hypothesis were correct, then the top portion of the hairpin would be sufficient for pausing and bypassing.

To test this hypothesis, we created two mutants, called Δ top hairpin (destabilized the three base pairs below the UUCG tetraloop) and Δ bottom hairpin (leaving the three base pairs below the tetraloop intact but disrupting seven potential base pairs in the lower part of the stem) (Figures 3B and 3C). Translation of the Δ top hairpin mutant mRNA resulted in a decrease of ribosomes that enter the rotated-state pause (12%). Translation of the Δ bottom hairpin mRNA remained similar to the wild-type sequence (36% compared to WT 35%). This highlights the importance of the UUCG tetraloop and the top portions of the hairpin in stimulating bypass, consistent with prior mutagenesis (Weiss et al., 1990; Wills et al., 2008) (~1%–30% of WT). Interestingly, destabilizing the three base pairs located 5 nt from the tetraloop did not significantly reduce bypass efficiency (~60%–90% of WT) (Weiss et al., 1990). Thus, the precise location of the UUCG tetraloop with respect to the ribosome during take-off is critical, in addition to the propensity of the tetraloop to re-fold (see the Discussion for speculations on where the hairpin refolds). It is likely that this propensity to re-fold induces a lateral tension on the mRNA-tRNA interaction, which combined with the vertical pull from the nascent peptide interaction, causes the disengagement of the anticodon-codon interaction and “slippage” uncoupling ribosomal motions from tRNA-mRNA movement, causing the ribosome to be trapped in a non-canonical rotated state, reminiscent of the uncoupled translocation in -1 frameshifting (Chen et al., 2014b).

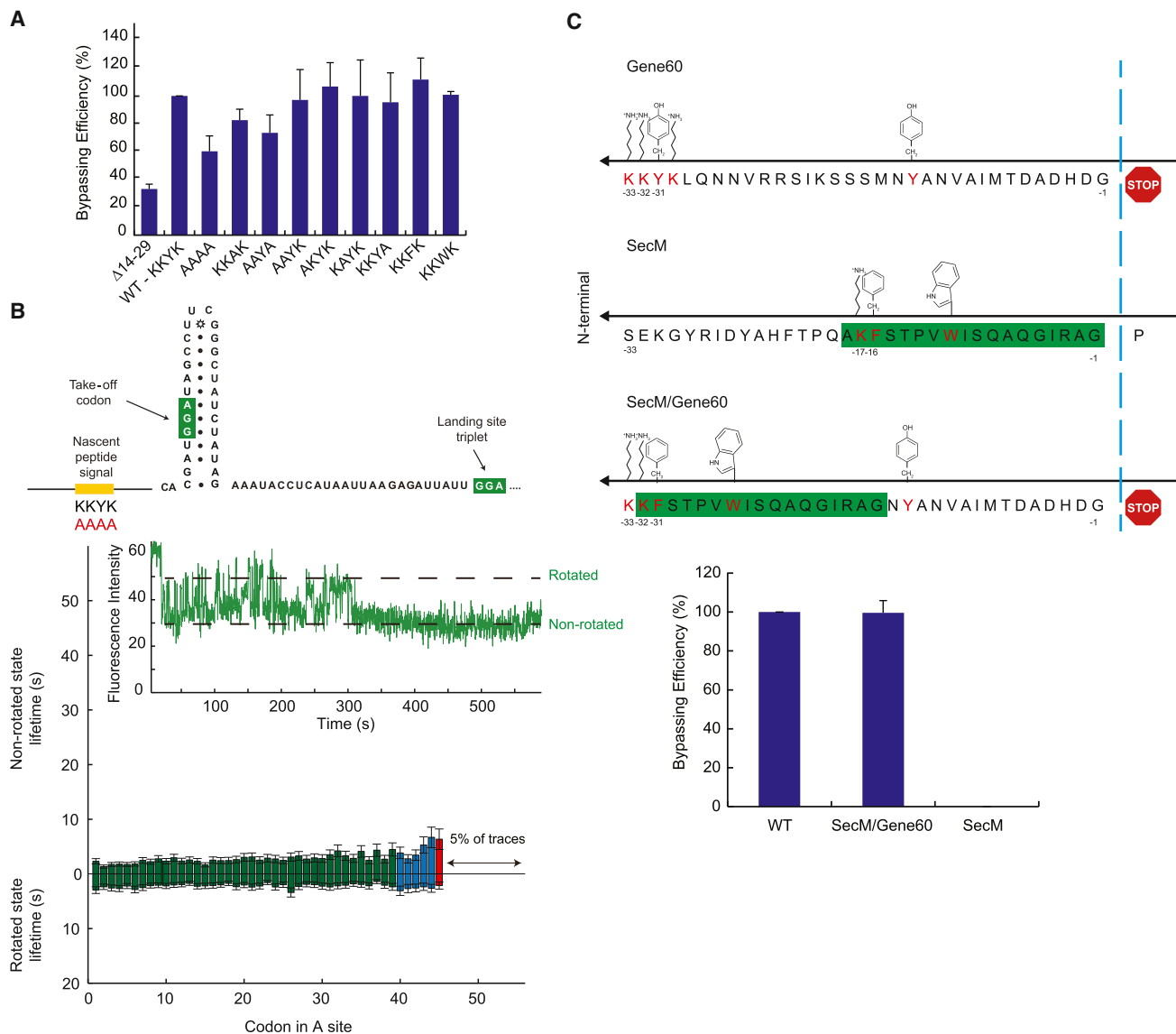


Figure 2. Mutation of the Nascent Peptide Interaction Abolishes the Slowdown

(A) In vivo analysis of bypassing with mutants of the nascent peptide. The absolute value of bypassing in these assays by WT (the second from the left) is 33%, and all other values are a percentage of it.

(B) Deleting the key interaction of the nascent peptide signal (KKYK) to AAAA did not increase non-rotated and rotated state lifetimes. Most ribosomes terminate at the stop codon after codon Gly45. An example trace is shown. The color scheme is the same as in Figure 1. n = 424.

(C) In vivo analysis of bypassing with fusions of gene 60/SecM nascent peptides. The cassette used to generate the result in the middle lane has gene 60 sequence encoding amino acids 32 to 46 in its native location 5' adjacent to the gene 60 take-off codon. The SecM nascent peptide signal encoding sequence is 5' adjacent to it. The right lane derives from a cassette with the SecM nascent peptide encoding sequence 5' adjacent to the gene 60 take-off codon. See also Figures S2 and S4.

Second Hairpin 5' to the Take-off Site Is Required for Bypassing

What provides the forward bias for the bypass? To answer this, we focused on a predicted hairpin 5' to the bypass stem loop (Figures 4 and S5) (Samatova et al., 2014; Todd and Walter, 2013). We introduced synonymous mutations that disrupt this 5' stem loop and preserve the amino acid identity and showed that the percentage of ribosomes that enter the rotated-state pause decreases to 11.8%, confirming the importance of this

stem loop. Consistently, Samatova et al. (2014) showed that the synonymous mutations that disrupt this 5' stem loop reduce bypassing efficiency in vitro (~10% of WT), while compensatory mutations partially restore bypassing. When the ribosome is positioned at the take-off Gly45 codon, the 5' stem loop is likely partially formed, except for the bottom 3–6 base pairs. The re-folding of the bottom three base pairs may provide a forward bias for the bypass movement. Alternatively, the directionality may be maintained through re-forming of the stem loop when

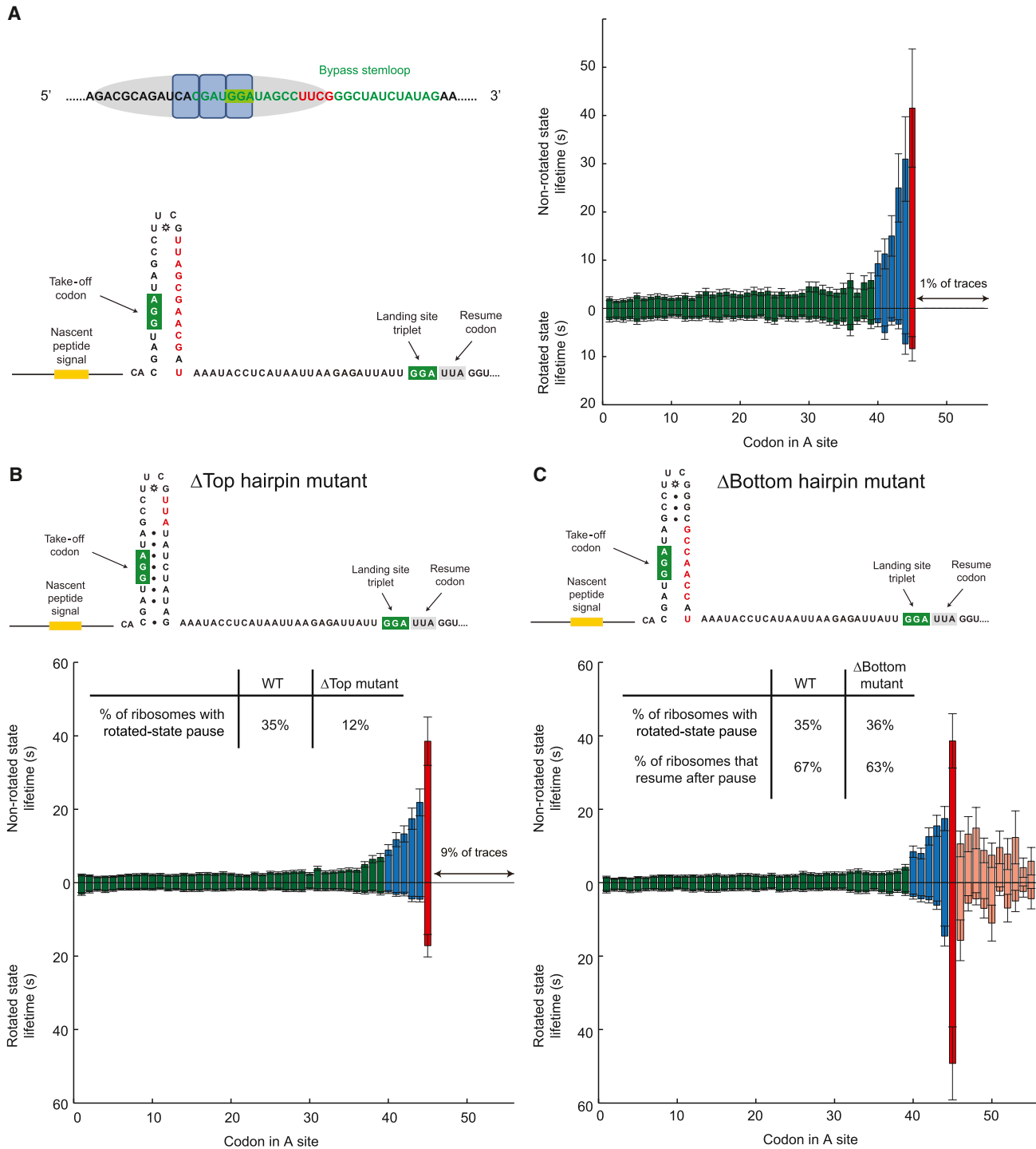


Figure 3. The –UUCG– Hairpin Stem Loop, Especially the Top Base Pairs, Is Important for the Rotated-State Pause

(A) The hairpin is shown in green, and the UUCG tetraloop is marked in red. To investigate the role of the mRNA hairpin, the base pairs were disrupted; the increase in the non-rotated state lifetime due to the nascent peptide signal is still observed, but a long rotated-state pause at Gly45, characteristic of bypassing, is no longer detected. n = 244.

(B) Mutation of 3 bp below the UUCG tetraloop decreased bypass efficiency to 12%. n = 442.

(C) Mutation of the bottom portion of the hairpin. The bypass efficiency remained the same at 36%. n = 349.

See also Figure S2.

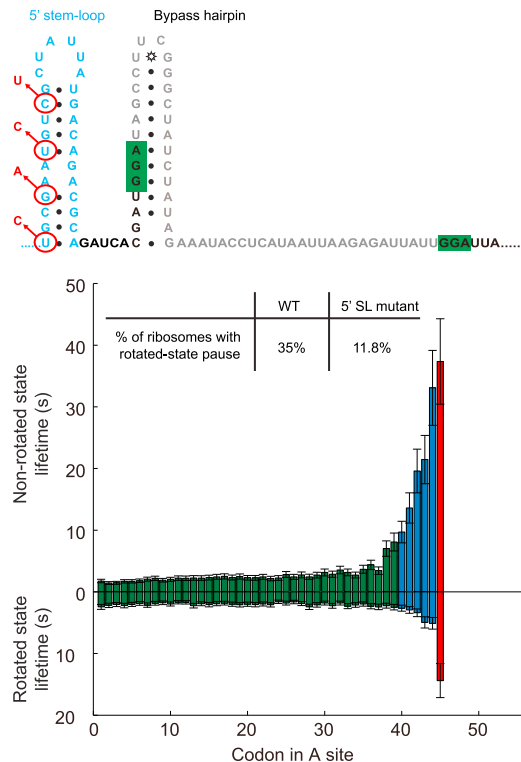


Figure 4. Effects of the 5' Stem Loop

Synonymous mutations (shown in red) of the 5' stem loop (wild-type sequence shown in blue) destabilize the secondary structure. The bypass efficiency decreased to 11.8%, with a corresponding decrease in the rotated state lifetime at codon Gly45, suggesting that the 5' stem loop is important. n = 488. See also Figures S2 and S5.

the ribosome vacates the stem loop, acting as a block for backward movement.

Take-Off and Landing Mechanisms: mRNA Refolding Causes Uncoupled Translocation

The concerted effects from the nascent peptide interaction, refolding of the 5' hairpin and the re-folding of the tetraloop, induce a long rotated-state pause characteristic of bypassing. Pausing may be caused by translocation that is uncoupled with the ribosome reverse rotation, similar to what was observed previously for -1 frameshifting in *dnaX* (Chen et al., 2014b). This leaves the ribosome in a non-canonical rotated state, resulting in the long rotated-state pause observed in frameshifting.

To test whether translocation occurs during the pause, we mutated Asp44 (the codon before Gly45) to Phe; this allows the use of Cy5-labeled tRNA^{Phe} to estimate when translocation occurs during the rotated-state pause (through the departure and disappearance of Cy5-tRNA^{Phe} with the Asp44Phe mutant) in correlation with the Cy3B ribosome conformational signal (Figure S1C). Translocation of the P-site tRNA to the E site is typically correlated with ribosome reverse rotation. Hence, the rotated state lifetime is equivalent to the time to departure of the P-site tRNA signal, and thus, ribosome reverse rotation and translocation are usually coupled. Here, we found the Cy5-tRNA^{Phe}

departs 28.1 ± 8.5 s after the rotation of the ribosome at codon Gly45, which is much shorter than the lifetime of the rotated-state pause (88.2 ± 26.4 s) (Figure 5A), indicating that translocation precedes reverse rotation and that the two are now uncoupled. Uncoupled translocation results in a ribosome in a non-canonical rotated state with a peptidyl P-site tRNA and an empty A site. During this non-canonical state, recoding events can occur when ribosome-tRNA-mRNA interactions are weaker to allow for the “take-off” to occur and peptidyl-tRNA and mRNA to dissociate.

Similarly, the timing of “landing” was probed through the Leu46Phe mutant, with the codon after the landing codon mutated to Phe. The arrival of Cy5-tRNA^{Phe} after the intersubunit rotation at Gly45 indicates successful landing of the peptidyl-tRNA to the landing Gly45 codon, with an exposed Phe codon in the A site. The arrival time of Cy5-tRNA^{Phe} in this case is 67.3 ± 13.0 s after the rotation at Gly45. These results allow us to determine the timeline of the hop (Figure 5B)—it begins during the long rotated pause and ends within it.

After translational hopping to Gly46, tRNA^{Phe} arrives at the A-site codon 46 with the ribosome in the rotated state, unlike during normal translation when tRNAs usually bind to the non-rotated state. The binding of the tRNA^{Phe} is stable, with the lifetime comparable to the remaining lifetime of the rotated-state pause. During the remainder of the pause, tRNAs re-pair with the mRNA codon and peptidyl transfer occurs, returning the ribosome to the canonical rotated state with hybrid tRNAs. EF-G can then act on the ribosome and translocate the tRNAs, allowing for normal translation to resume (see Figure S6).

To decipher the mechanism of the bypass during the long rotated-state pause, we examined the effects of simultaneous mutations to the take-off and landing codons, as well as mutations of only the landing codon to create a mismatch (Figure 5C). For unmatched take-off and landing codons, the bypassing efficiency decreases to ~5% of wild-type (Weiss et al., 1990). Upon mutation of the landing codon to a GUA (Val) to create a mismatch, 36% of the ribosomes exhibit a pause at Gly45 with the slowdown approaching Gly45 due to the nascent peptide, similar to wild-type mRNA. Thus, the behavior up to the bypass is not affected by the mutated landing codon. However, only 4% of ribosomes in the landing site mutant resume translation after the pause (within observation window) compared to 67% of for wild-type mRNA.

We determined the fate of ribosomes during the pause by examining the ending state of each ribosome at the pause. For wild-type mRNA, the vast majority of the traces (>90%) show ribosomes either resuming translation or the movie acquisition ends during the pause; for the landing site mutant, the majority of ribosomes (55%) show loss of a Cy3B signal at Gly45. This loss of signal is not due to photobleaching, since for the wild-type mRNA, under the same experimental conditions, only 5% of the traces showed a loss of Cy3B signal at Gly45. Thus, loss of a 30S-Cy3B signal is due to ribosome drop-off on the mutant mRNA, where ribosomes that initiated bypass failed to find the correct landing codon. Since these ribosomes do not stably form peptidyl-tRNA-mRNA interactions, they dissociate from mRNA (Herr et al., 2001). Accordingly, the rotated-state pause lifetime decreased from 40 s to 15 s (Figure 5C).

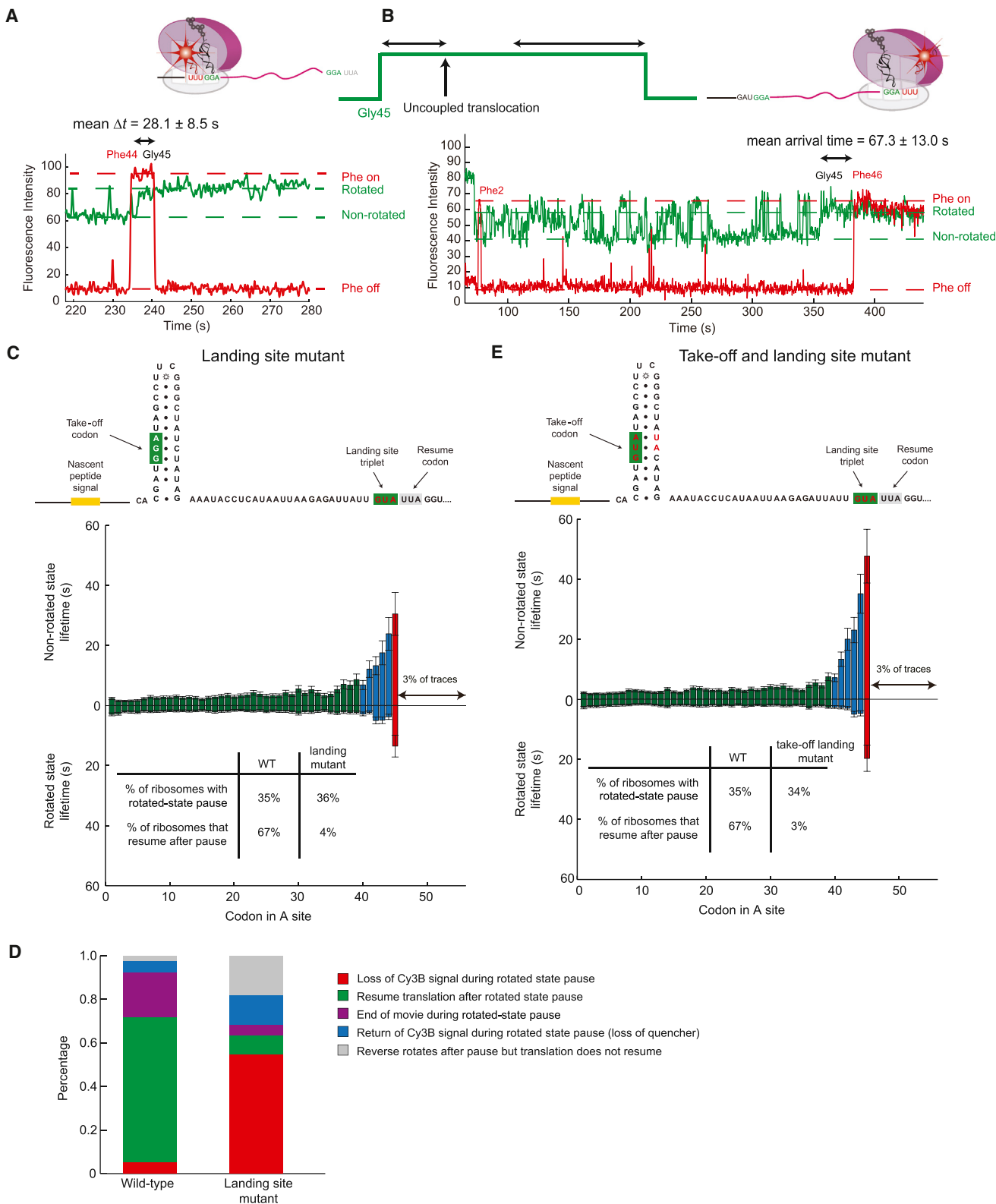


Figure 5. The Timing and Mechanism of Take-Off and Landing

(A) Using the Asp44Phe and Leu46Phe mutant mRNAs introduced in Figure S2, the timing of bypass was probed. Using the Asp45Phe mutant, we can get the timing of when the Cy5-tRNA^{Phe} (red) departs relative to the start of the rotated-state pause at Gly45. This gives an upper estimate of when translocation occurs
(legend continued on next page)

Mutation of both the landing and take-off codons from a GGA to GUA (Val) was previously shown to drop the bypass efficiency to 7% of wild-type (Bucklin et al., 2005). Similar results were observed in our experiments if both the take-off and landing codon are changed from GGA to GUA (Val) (Figure 5E). These results suggest that the identity of the take-off tRNA is not critical to start the process of bypassing; the nascent peptide and hairpins induce take-off and the rotated-state pause. The identity of the tRNA is important for successful landing; it must match the landing codon, but stable G-C-rich pairing is important for successful recognition and re-pairing of the peptidyl-tRNA and mRNA, consistent with earlier data (Bucklin et al., 2005).

Directly Monitoring the Timing of the Hop with Ribosome-mRNA FRET

To probe ribosome movement directly during bypassing, we used FRET between the ribosome and mRNA: mRNA was labeled downstream of the landing site by annealing a Cy5-labeled DNA oligonucleotide complimentary to mRNA (termed +15 Cy5-oligo, 15 nt downstream of the landing GGA codon), and 30S subunits were labeled with Cy3B on helix 33a near the beak domain, which is close to the mRNA entrance channel (Figures 6A and S1). The bypass will bring the Cy3B dye on the ribosome close to the Cy5 dye with the simultaneous appearance of FRET. Translation is followed by stable binding of Cy3.5-labeled Phe-tRNA^{Phe}. Before bypassing, we observed no FRET between translating ribosomes and downstream labels in mRNA; ribosome-mRNA FRET is thus a hallmark of attempted bypassing.

Using the Asp44Phe mutant and Leu46Phe mutant mRNAs, we can use Cy3.5-labeled tRNA^{Phe} to score for the translation of Phe44 prior to the take-off or Phe46 after successful landing. This allows us to monitor the time between uncoupled translocation (departure of Cy3.5-tRNA^{Phe} from Phe44) and bypassing (appearance of FRET), and also the time between bypassing and successful landing (arrival of Cy3.5-tRNA^{Phe} at Phe46). The hop occurs shortly after uncoupled translocation, on average after 3.4 ± 0.9 s (Figure 6B). The ribosome quickly lands near the landing Gly codon, as demonstrated by the 1–2 frame FRET transition at 100-ms frame rate. After landing, the resume codon in the A site (Leu in the wild-type and Phe in

the Leu46Phe mutant) is not immediately available for binding. Instead, Cy3.5-tRNA^{Phe} binds on average 50.5 ± 13.0 s after the hop (Figure 6C).

Does the ribosome land directly on the landing site, or does the ribosome land upstream and scan to find the optimal landing site? To distinguish between these possibilities, we note that the FRET average lifetime for the +15 Cy5-oligo is 72.3 ± 20.0 s. If we move the Cy5-oligonucleotide to 3 nt downstream of the take-off GGA codon (called +3 Cy5-oligo), such that the ribosome footprint is blocked upon landing, the FRET average lifetime decreases significantly to 10.2 ± 4.5 s (Figure 6D). Thus, even when the landing site is blocked, we still see a stable FRET signal, indicating that ribosomes land upstream and then scan before photobleaching or contact quenching the Cy5 dye. Thus, bypassing occurs in two steps: a hop in the 3' direction, followed by scanning, which is associated with finding the best stable landing site to resume translation.

DISCUSSION

By tracking single ribosomes translating in real time, we delineate here the dynamic events underlying bypassing. All determinants for bypassing are specified by the gene 60 mRNA itself. Translation of the gene 60 sequence results in a branchpoint stimulated by the nascent peptide signal and hairpin. At the take-off codon Gly45, the nascent peptide and the hairpin induce a fraction of the ribosomes (35%) to undergo a long rotated-state pause, similar to what was observed for –1 frameshifting (Chen et al., 2014b). In this state, the ribosome-tRNA-mRNA interactions are weaker, which allows for unusual and large-scale ribosome reconfiguration events to occur for bypassing. Non-bypassed ribosomes terminate at the stop codon without the pause. In this mechanism both the nascent peptide and the hairpin (especially the UUCG tetraloop with three flanking nucleotides) are critical for bypassing. A recent study by Samatova et al. (2014), as well as our findings, confirms the importance of another 5' stem loop, which provides directionality for the bypass. Here, we propose a model for bypassing that involves the sequential coupling of the re-folding of the two hairpins to ribosome movement, allowing the ribosome with weakened ribosome-tRNA-mRNA interactions induced by the nascent peptide to bypass the non-coding mRNA region.

during the pause. The mean departure time was 28.1 ± 8.5 s, which is a lot shorter than the mean lifetime of the pause (90 s), indicating that the translocation is uncoupled with reverse rotation. This gives an estimate of when the launch occurs.

(B) With the Leu46Phe mutant, A-site accessibility could be probed with Cy5-tRNA^{Phe}, giving an estimate of when landing is completed. The mean arrival time was 67.3 ± 13.0 s, which is also during the pause. Thus, bypass and landing is completed during the rotated-state pause, making the A site available for tRNA binding.

(C) The landing site was changed from GGA(Gly) to GUA(Val), and the mRNA sequence is shown. The increase in the non-rotated state lifetime due to the nascent peptide signal can be seen. The rotated-state pause at Gly45 is shorter than for wild-type. This is due to the lost Cy3B signal during the rotated-state pause, when the ribosome fails to find the correct landing codon after launching the bypass and drops off. Thus, matching take-off and landing codons are required. Consistent with this, the percentage of ribosomes undergoing the rotated-state pause at Gly45 is the same as wild-type. However, the percentage of ribosomes that resume after the pause is much lower. n = 469.

(D) The end states of the ribosome after the pause can be parsed to (1) the loss of the Cy3B signal (due to ribosome drop off or photobleaching), (2) a resume in translation after the pause, (3) the end of movie during the pause, (4) the return of the Cy3B signal (photobleaching of FRET quencher or dissociation of 50S), and (5) reverse rotates but translation does not resume.

(E) The non-rotated and rotated state lifetimes for the double mutant, where both the take-off and landing codons were changed from wild-type GGA(Gly) to GUA(Val). Behavior that is very similar to the landing site mutant can be seen. Thus, the identity of the take-off codon is not critical for initiating bypass. However, for successful landing, the identity of the tRNA is very important. n = 466.

See also Figures S2 and S6.

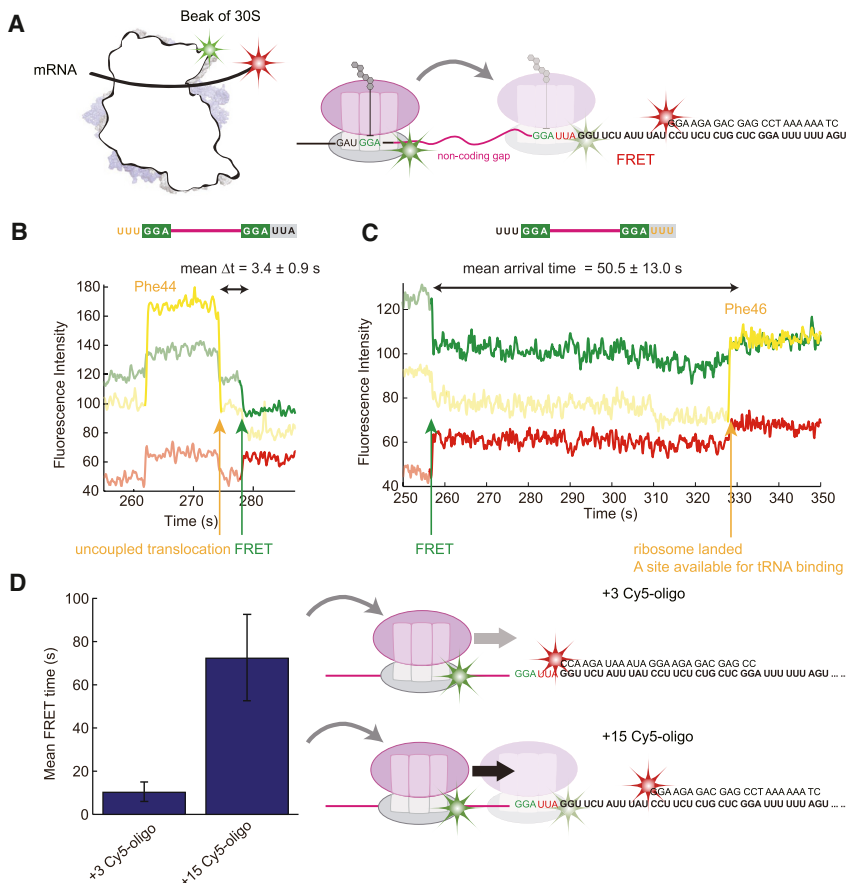


Figure 6. The Timing of Ribosomal Bypassing and Scanning Monitored by Ribosome-mRNA FRET

(A) For ribosome-mRNA FRET to monitor the hop, the 30S subunit was labeled with Cy3B on helix 33a, near the beak of 30S subunit, and mRNA is labeled with Cy5 downstream of the landing site. Landing after bypassing brings the ribosome within FRET distance to the Cy5 dye.

(B) Asp44Phe mutant mRNA allows us to use Cy3.5-labeled tRNA^{Phe} (yellow) to track when the tRNA departs at codon 44. This represents the timing of uncoupled translocation during the rotated-state pause at Gly45. The ribosome bypasses on average 3.4 ± 0.9 s after uncoupled translocation.

(C) Translation of the Leu46Phe mutant mRNA allows us to use Cy3.5-labeled tRNA^{Phe} (yellow) to track when the tRNA arrives at the A site after the bypass. This represents the timing of when successful landing occurs and the A site is available after the bypass (on average 50.5 ± 13.0 s).

(D) With the use of the +15 Cy5-oligo (15 nt downstream of the GGA landing codon, the same used for B and C), the FRET lifetime is 72.3 ± 20.0 s. By moving the Cy5-oligonucleotide to 3 nt downstream of the take-off GGA codon (called +3 Cy5-oligo), such that the ribosome footprint is blocked upon landing, the FRET average lifetime decreases significantly to 10.2 ± 4.5 s. Since there is still a stable FRET signal, the ribosome must land upstream of the oligonucleotide, then scan to find the landing site, during which time the ribosome contact quenches the Cy5 dye.

The nascent polypeptide of gene 60 causes slowdown in translation as the ribosome approaches the take-off Gly45 codon (from codons 40 to 45), which is a required prelude to bypassing. The interaction causing slowdown begins after a ribosome translates 40 codons when the key KKYK portion of the nascent peptide is ~25 amino acids from the P-site tRNA. The slowdown is defined by the increased lifetimes of both the non-rotated and rotated states, indicating increased barriers to tRNA selection/accommodation and translocation, respectively. These barriers increase progressively during translation from codon 40 to 45. At the take-off site, the KKYK portion of the nascent peptide is ~30 amino acids from the P-site tRNA (as opposed to interaction of SecM, which is 17 amino acids (Nakatogawa and Ito, 2002; Tsai et al., 2014). Thus, even though the dynamic signatures are similar to other stalling sequences, the interaction in bypassing is different from that of SecM; the SecM stalling mechanism does not promote bypassing. We recently showed that co-translational folding of a short peptide sequence upstream of the SecM sequence in the exit tunnel beyond the constriction point “pulls” on the peptide releasing the stall (Nilsson et al., 2015). Since the nascent peptide signal sequence from codons 14–29 in bypassing has been predicted to fold into a α -helical structure (Bhushan et al., 2010; Samatova et al., 2014) (see Figure S7), it may play a similar role in “pulling” on the peptidyl-tRNA to cause the disruption of anticodon-codon interactions necessary for take-off. This suggests that

for efficient bypassing, stall is insufficient; the specific interaction and force direction from the traditional SecM stall may not be conducive for bypassing (Goldman et al., 2015). The precise interactions of the nascent peptide with the tunnel will require further study using structural methods. Nonetheless, this nascent peptide interaction is a prerequisite for the ribosome pausing in the rotated state at codon Gly45.

Ribosomes at the bypass site stochastically continue translating or bypass. We propose that the -UUCG- hairpin is the origin for this branchpoint of pathways, similar to the role played by a helical stem loop for -1 frameshifting (Chen et al., 2014b). The role of the bypass hairpin, however, is puzzling, since at the take-off site, the hairpin has been melted by the ribosome. However, the stability of the UUCG tetraloop (Ennifar et al., 2000; Todd and Walter, 2013), which has a propensity to form a compact structure, may cause the apical portion of the hairpin stem loop to refold. In addition, the recent work by Samatova et al. and our work have identified a previously uncharacterized 5' stem loop that also contributes to bypassing (Samatova et al., 2014). When tRNA^{Gly} at codon 45 accommodates into the ribosome and the ribosome rotates, the A site is over codon 45, which places the ribosome such that the UUCG tetraloop is just within the 3' mRNA channel and the 5' stem loop is mostly folded except for the bottom base pairs (Figure 7). The tendency for the 5' stem loop and the UUCG tetraloop to re-fold, in addition to the “pull” on the tRNA through the cascade of nascent peptide

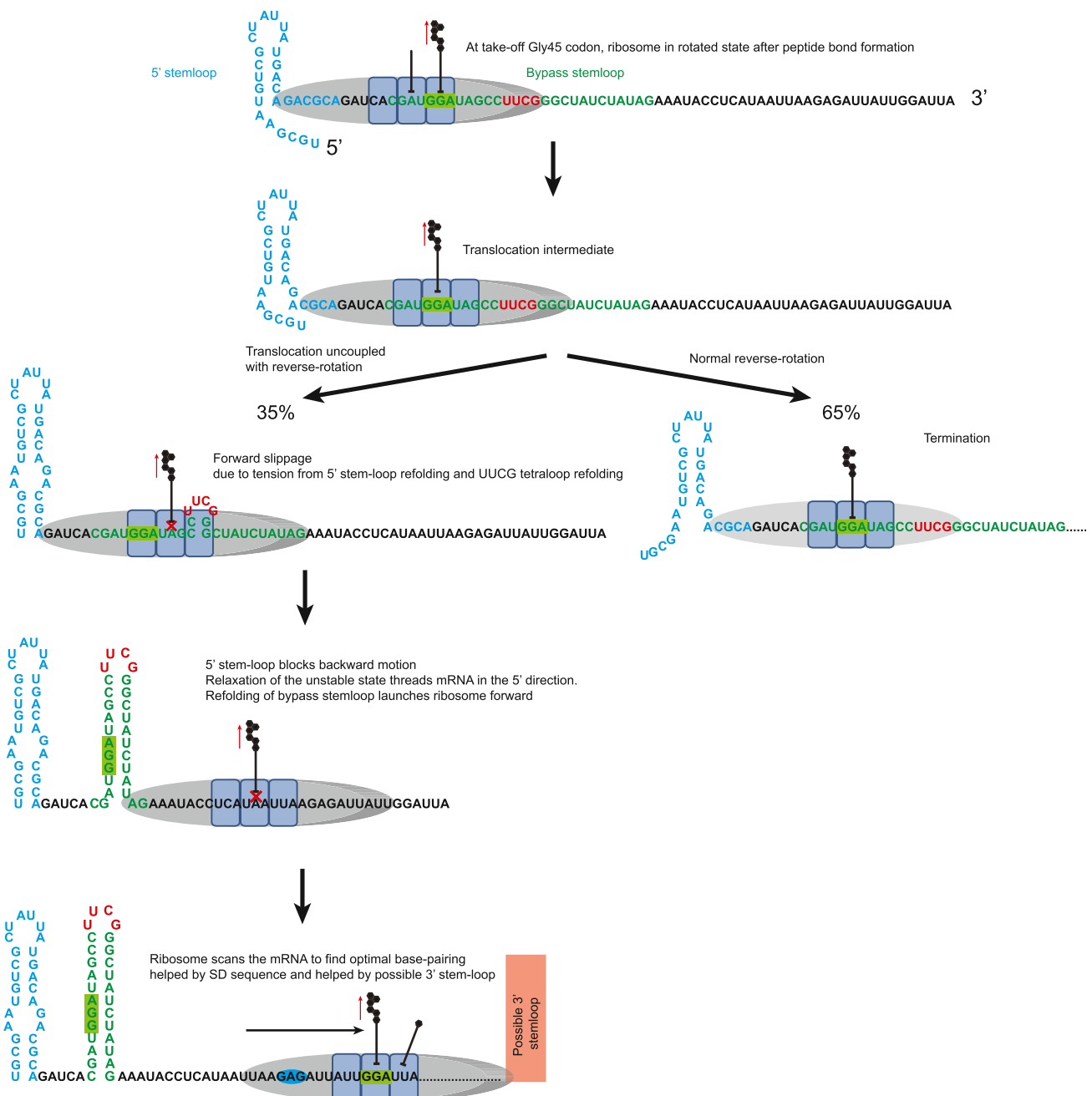


Figure 7. A Model of Translational Bypassing

At the take-off Gly45 (GGA) codon, after the arrival of tRNA^{Gly} to the A site and peptidyl transfer, the ribosome rotates. The nascent peptide signal interaction pulls on the peptidyl-tRNA, as indicated by the red arrow. The 5' stem loop is shown in blue; the bypass hairpin is shown in green; and the UUCG tetraloop is shown in red. EF-G catalyzes translocation, moving the GGA codon to the P site. Combined with the propensity of the UUCG tetraloop to re-fold, the ribosome slips forward and leads to uncoupled translocation, allowing the UUCG tetraloop and a few base pairs to re-fold within the A site and the 5' stem loop to completely refold. Since the 5' stem loop blocks backward movement, relaxation of the unstable state threads mRNA in the 5' direction. Refolding of the bypass hairpin launches the ribosome forward. The ribosome then scans mRNA to find the optimal base pairing, assisted by the GAG Shine-Dalgarno-like sequence and a possible 3' stem loop. Upon arriving at the landing site, the next tRNA accommodates into the rotated ribosome to help re-define the reading frame and translation is resumed.

See also Figure S7.

interactions, likely creates a tension in the system. Thus, the refolding of the 5' stem loop and the ribosome stochastically encountering a folded or unfolded UUCG tetraloop may cause the initial branchpoint.

EF-G catalyzed translocation occurs, and combined with the 5' stem-loop refolding, we propose that the ribosome slips forward in the 3' direction, allowing for the 5' stem loop to completely refold. This is consistent with the observation that the lower part of the secondary structure is important for bypassing (Wills et al., 2008; Samatova et al., 2014). Simultaneously, the -UUCG- tetraloop becomes positioned such that it is able to refold. In one model this is within the A site of the ribosome. The folding of a tetraloop or hairpin within the A site is not without precedent: a crystal structure of the 70S ribosome showed mRNA forming a hairpin with a 4 base pair stem and a tetraloop in the A-site, overlapping the natural codon-anticodon interaction region (Yusupova et al., 2001). Along similar lines, a previous model of bypassing suggested that the hairpin re-folds within the A site of the ribosome (Wills et al., 2008). Alternatively, mRNA may be forced a short distance in the forward direction before the tetraloop hairpin forms, perhaps even in the ribosomal E site, with formation of the stem loop it nucleates enhancing forward mRNA to position the ribosome to a more 3' position on mRNA. Here, we propose that the tetraloop hairpin forms within the A site, though only the top base pairs of the stem are formed.

We further propose that the slip caused by the refolding of the 5' stem loop and tetraloop uncouples anticodon-codon interactions and translocation from ribosome reverse-rotation. This non-canonical conformation may be hyper-rotated (Qin et al., 2014) or represent a translocation intermediate (Tourigny et al., 2013). The rotated state, with its weakened ribosome-tRNA-mRNA interactions, is key to allowing the mRNA rearrangements that promote bypassing. This ribosome state with a hairpin within the A site may be unstable, and relaxation of this unstable state threads mRNA in the 5' direction. This forward bias is due to the 5' stem loop preventing backward movement (Figure 7).

The bypass begins and ends during the long rotated-state pause, with the movement occurring in two steps. First, as soon as the tetraloop clears the ribosome on the 5' side, the high tendency for the hairpin to refold may cause mRNA to fold directionally in the 5' direction and the hairpin to fold 5' of the ribosome. This launches the ribosome forward toward the landing site. However, even with hairpin folding 5' to the ribosome, the distance threaded is not sufficient to place the ribosome over the landing codon. Thus in the second step, as we have demonstrated, the ribosome scans a short distance to find the optimal landing codon, possibly with the aid of the internal Shine-Dalgarno sequence. This is consistent with the delay between mRNA rearrangement and resumption of translation as measured here.

A combination of mRNA rearrangement-induced movement with processive scanning builds upon and reconciles inconsistencies in earlier models of bypassing (Samatova et al., 2014; Wills et al., 2008). The model proposed here, although still speculative in some aspects, explains many outstanding questions and provides a testable model for future studies. In our model,

the re-pairing of the peptidyl-tRNA to the correct position on mRNA during scanning may be stabilized by the SD-like sequence or a possible downstream 3' stem loop (Samatova et al., 2014); the SD-like sequence has a moderate effect on bypassing but may be important for the fidelity of landing site selection (Herr et al., 2004; Wills et al., 2008). All of these events happen during the rotated-state pause; the majority of the pause is the ribosome sampling and exploring the reading frame widely, with movements possibly similar to the excursions and sliding behaviors observed previously (Koutmou et al., 2015; Yan et al., 2015). In the mechanism proposed here, bypassing is not induced by A-site (UAG stop codon) starvation, explaining why the absence of RF1 did not significantly affect the bypassing efficiency (Herr et al., 2000b). Bypassing induced by A-site starvation may follow a different mechanism (Lindsley et al., 2005a; Lindsley et al., 2005b).

How does the ribosome resume translation? After successful landing and initial contact of the peptidyl-tRNA in the P site with the mRNA codon, the ribosome remains in a non-canonical rotated state with an exposed A site, similar to what was observed for frameshifting. The subsequent tRNA can bind to the ribosomal A site, which may help the ribosome re-define the correct reading frame. Peptidyl transfer in this state is slow, since the rotated ribosome may not position the A- and P-site tRNAs correctly for peptidyl transfer to occur efficiently. Subsequent to peptide bond formation, EF-G can then act on the ribosome and translocate the tRNAs, allowing for normal translation to resume. However, normal rates are not immediately resumed. The nascent peptide is major contributor to this slowdown, suggesting that it still inhibiting subsequent peptidyl transfer and slowing non-rotated state lifetimes until the key sequences leave the ribosomal exit tunnel. This is consistent with the inference from mutagenesis experiments that the nascent peptide signal also has affects at the completion stage (Herr et al., 2000b).

Our results provide a glimpse of an unexpectedly versatile translation scheme with widespread implications. Bypassing may be more widespread than previously thought, suggesting that this phenomenon is not limited to gene 60 (Lang et al., 2014; Nosek et al., 2015). Furthermore, the issue of a fidelity check may be significant for bypassing. Any mismatches upon codon-anticodon re-pairing during reading frame sampling before landing would not be susceptible to the fidelity controls governing proper mRNA decoding (Yan et al., 2015). Lastly, the mechanisms presented here may have parallel in eukaryotic scanning during initiation or other recoding events.

Here, we present a general mechanistic and conformational framework for ribosomal bypassing that may be applicable to different recoding signals. Many aspects of the framework are speculative and still require further investigation, especially the high-resolution structures of the many bypassing intermediates. Nonetheless, a long-lived, non-canonical translational state is the centerpiece of this mechanism and provides a window for reading-frame reset through mRNA structure rearrangement. This state, whose formation is driven by mRNA and nascent chain energy barriers in bypassing, may be universal for many recoding events and possibly a central feature of translational control.

EXPERIMENTAL PROCEDURES

Reagents and Buffers for Translation Experiments

Escherichia coli translation factors (IF2, EF-Tu, EF-G, and EF-Ts) and initiator fMet-tRNA for the single-molecule experiments were prepared and purified as described before (Blanchard et al., 2004b; Marshall et al., 2008). Ribosome purification, tRNA aminoacylation, preparation of biotinylated mRNA, and *in vivo* bypass assays are described in the Supplemental Experimental Procedures.

All experiments were conducted in a Tris-based polymix buffer consisting of 50 mM Tris-acetate (pH 7.5), 100 mM KCl, 5 mM ammonium acetate, 0.5 mM calcium acetate, 5 mM magnesium acetate, 0.5 mM EDTA, 5 mM putrescine-HCl, and 1 mM spermidine. All single-molecule experiments had 4 mM GTP and were performed at 20°C.

Single-Molecule Profiling Experiments

Translation experiments with ribosome Cy3B/BHQ conformational FRET were performed as described (Chen et al., 2014b). Before each experiment, 30S (helix 44 mutant) and 50S (helix 101 mutant) ribosomal subunits (at 1 μM) were mixed in a 1:1 ratio with the 3' dye-labeled oligonucleotides specific for the hairpin extensions in each subunit and incubated at 37°C for 10 min and then at 30°C for 20 min in a polymix buffer system. 30S pre-initiation complexes (PICs) were formed as described (Marshall et al., 2008) by incubating the following at 37°C for 5 min: 0.25 μM Cy3B-30S, pre-incubated with stoichiometric S1, 1 μM IF2, 1 μM fMet-tRNA^{fMet}, 1 μM mRNA, and 4 mM GTP to form 30S PICs in the polymix buffer. Before use, mRNA was heated to 90°C for 1 min and then snap cooled to 4°C for 20 min to promote mRNA folding.

Before use, we pre-incubated a SMRT Cell V3 (Pacific Biosciences), a zero-mode waveguide (ZMW) chip, with a 1 mg/ml Neutravidin solution in 50 mM Tris-acetate (pH 7.5), and 50 mM KCl at room temperature for 5 min. The cell was then washed with the Tris-based polymix buffer. After washing, 40 μl of the buffer was left in the cell to keep the cell surface wet. We then diluted the 30S PICs with polymix buffer containing 1 μM IF2 and 4 mM GTP down to 100 nM PIC concentration. A higher immobilization concentration compared to previous reports was used since not all the PICs have mRNA with biotin (Chen et al., 2014b). The diluted PICs are loaded into the SMRT cell at room temperature for 3 min to immobilize the 30S PICs into the ZMW wells. We wash away unbound material with polymix buffer containing 1 μM IF2, 4 mM GTP, 2.5 mM Trolox, and a PCA/PCD oxygen scavenging system (2.5 mM 3,4-dihydroxybenzoic acid and 250 nM protocatechuate dehydrogenase [Aitken et al., 2008]). After washing, 20 μl of the washing mix was added to the cell to keep the surface wet.

We formed ternary complexes (TCs) between total charged *E. coli* tRNAs and EF-Tu(GTP) as described (Marshall et al., 2008). Total or Δ(Phe) aminoacyl-tRNA·EF-Tu·GTP ternary complexes were pre-formed by incubating (2 min at 37°C) the aa-tRNAs with 5-fold excess of EF-Tu, GTP (1 mM), PEP (3 mM), and EF-Ts (40 μM) in polymix. The ternary complexes (3–6 μM) were added to BHQ-50S (200 nM), EF-G (240–480 nM), IF2 (1 μM), GTP (4 mM), 2.5 mM Trolox, and the oxygen-scavenging system to form a delivery mix in polymix buffer. Experiments are done at 3 μM ternary complexes and 240 nM EF-G (chosen to have well-defined, detectable FRET transition signals), unless indicated otherwise. Before an experiment, the SMRT cell is loaded into a modified PacBio RS sequencer. At the start of the elongation experiment, the instrument illuminates the SMRT cell with a green laser and then automatically delivers 20 μl of a delivery mixture onto the cell surface at t ~10 s. Experiments involving labeled tRNAs and ribosome-mRNA FRET were performed similarly. See the Supplemental Experimental Procedures.

ZMW Instrumentation and Data Analysis

All single-molecule fluorescence experiments were conducted using a modified PacBio RS sequencer that allowed the collection of single-molecule fluorescence from individual ZMW wells in four dye channels corresponding to Cy3, Cy3.5, Cy5, and Cy5.5 (Chen et al., 2014a). The RS sequencer had 532- and 632-nm excitation lasers. In all experiments, data were collected at ten frames per second (100-ms exposure time) for 10 min. The energy flux of the green laser was 0.32 μW/μm², and the red laser was at 0.14 μW/μm².

Data analysis for all experiments were conducted with MATLAB (MathWorks) scripts written in-house (see the Supplemental Experimental Procedures). All error bars are SEM.

SUPPLEMENTAL INFORMATION

Supplemental Information includes Supplemental Experimental Procedures and seven figures and can be found with this article online at <http://dx.doi.org/10.1016/j.cell.2015.10.064>.

AUTHOR CONTRIBUTIONS

J.C., J.F.A., and J.D.P. conceived of and designed the experiments. J.C. performed and analyzed the single-molecule experiments. A.C. and M.O'C performed the *in vivo* experiments. J.C. wrote the manuscript with input from all of the authors.

ACKNOWLEDGMENTS

The authors thank Gary Loughran for his support. This work was supported by U.S. NIH grants (GM51266 to J.D.P., GM099687 to J.D.P., and GM111858 to S.E.O'L.), a Stanford Interdisciplinary Graduate Fellowship (to J.C.), and Science Foundation Ireland grants (SFI grant codes 12/IP1492 and 13/1A/1853) (to J.F.A.).

Received: June 10, 2015

Revised: September 7, 2015

Accepted: October 21, 2015

Published: November 19, 2015

REFERENCES

- Aitken, C.E., and Puglisi, J.D. (2010). Following the intersubunit conformation of the ribosome during translation in real time. *Nat. Struct. Mol. Biol.* **17**, 793–800.
- Aitken, C.E., Marshall, R.A., and Puglisi, J.D. (2008). An oxygen scavenging system for improvement of dye stability in single-molecule fluorescence experiments. *Biophys. J.* **94**, 1826–1835.
- Bhushan, S., Gartmann, M., Halic, M., Armache, J.P., Jarasch, A., Mielke, T., Berninghausen, O., Wilson, D.N., and Beckmann, R. (2010). α -Helical nascent polypeptide chains visualized within distinct regions of the ribosomal exit tunnel. *Nat. Struct. Mol. Biol.* **17**, 313–317.
- Blanchard, S.C., Gonzalez, R.L., Kim, H.D., Chu, S., and Puglisi, J.D. (2004a). tRNA selection and kinetic proofreading in translation. *Nat. Struct. Mol. Biol.* **11**, 1008–1014.
- Blanchard, S.C., Kim, H.D., Gonzalez, R.L., Jr., Puglisi, J.D., and Chu, S. (2004b). tRNA dynamics on the ribosome during translation. *Proc. Natl. Acad. Sci. USA* **101**, 12893–12898.
- Bucklin, D.J., Wills, N.M., Gesteland, R.F., and Atkins, J.F. (2005). P-site pairing subtleties revealed by the effects of different tRNAs on programmed translational bypassing where anticodon re-pairing to mRNA is separated from dissociation. *J. Mol. Biol.* **345**, 39–49.
- Caliskan, N., Katunin, V.I., Belardinelli, R., Peske, F., and Rodnina, M.V. (2014). Programmed -1 frameshifting by kinetic partitioning during impeded translocation. *Cell* **157**, 1619–1631.
- Chen, J., Tsai, A., O'Leary, S.E., Petrov, A., and Puglisi, J.D. (2012a). Unraveling the dynamics of ribosome translocation. *Curr. Opin. Struct. Biol.* **22**, 804–814.
- Chen, J., Tsai, A., Petrov, A., and Puglisi, J.D. (2012b). Nonfluorescent quenchers to correlate single-molecule conformational and compositional dynamics. *J. Am. Chem. Soc.* **134**, 5734–5737.
- Chen, J., Petrov, A., Tsai, A., O'Leary, S.E., and Puglisi, J.D. (2013). Coordinated conformational and compositional dynamics drive ribosome translocation. *Nat. Struct. Mol. Biol.* **20**, 718–727.

- Chen, J., Dalal, R.V., Petrov, A.N., Tsai, A., O'Leary, S.E., Chapin, K., Cheng, J., Ewan, M., Hsiung, P.L., Lundquist, P., et al. (2014a). High-throughput platform for real-time monitoring of biological processes by multicolor single-molecule fluorescence. *Proc. Natl. Acad. Sci. USA* **111**, 664–669.
- Chen, J., Petrov, A., Johansson, M., Tsai, A., O'Leary, S.E., and Puglisi, J.D. (2014b). Dynamic pathways of -1 translational frameshifting. *Nature* **512**, 328–332.
- Cornish, P.V., Ermolenko, D.N., Noller, H.F., and Ha, T. (2008). Spontaneous intersubunit rotation in single ribosomes. *Mol. Cell* **30**, 578–588.
- Dunkle, J.A., and Dunham, C.M. (2015). Mechanisms of mRNA frame maintenance and its subversion during translation of the genetic code. *Biochimie* **114**, 90–96.
- Ennifar, E., Nikulin, A., Tishchenko, S., Serganov, A., Nevskaya, N., Garber, M., Ehresmann, B., Ehresmann, C., Nikonov, S., and Dumas, P. (2000). The crystal structure of UUCG tetraloop. *J. Mol. Biol.* **304**, 35–42.
- Goldman, D.H., Kaiser, C.M., Milin, A., Righini, M., Tinoco, I., Jr., and Bustamante, C. (2015). Ribosome. Mechanical force releases nascent chain-mediated ribosome arrest in vitro and in vivo. *Science* **348**, 457–460.
- Hansen, T.M., Baranov, P.V., Ivanov, I.P., Gesteland, R.F., and Atkins, J.F. (2003). Maintenance of the correct open reading frame by the ribosome. *EMBO Rep.* **4**, 499–504.
- Herr, A.J., Atkins, J.F., and Gesteland, R.F. (1999). Mutations which alter the elbow region of tRNA₂Gly reduce T4 gene 60 translational bypassing efficiency. *EMBO J.* **18**, 2886–2896.
- Herr, A.J., Atkins, J.F., and Gesteland, R.F. (2000a). Coupling of open reading frames by translational bypassing. *Annu. Rev. Biochem.* **69**, 343–372.
- Herr, A.J., Gesteland, R.F., and Atkins, J.F. (2000b). One protein from two open reading frames: mechanism of a 50 nt translational bypass. *EMBO J.* **19**, 2671–2680.
- Herr, A.J., Wills, N.M., Nelson, C.C., Gesteland, R.F., and Atkins, J.F. (2001). Drop-off during ribosome hopping. *J. Mol. Biol.* **311**, 445–452.
- Herr, A.J., Wills, N.M., Nelson, C.C., Gesteland, R.F., and Atkins, J.F. (2004). Factors that influence selection of coding resumption sites in translational bypassing: minimal conventional peptidyl-tRNA:mRNA pairing can suffice. *J. Biol. Chem.* **279**, 11081–11087.
- Huang, W.M., Ao, S.Z., Casjens, S., Orlandi, R., Zeikus, R., Weiss, R., Winge, D., and Fang, M. (1988). A persistent untranslated sequence within bacteriophage T4 DNA topoisomerase gene 60. *Science* **239**, 1005–1012.
- Jenner, L.B., Demeshkina, N., Yusupova, G., and Yusupov, M. (2010). Structural aspects of messenger RNA reading frame maintenance by the ribosome. *Nat. Struct. Mol. Biol.* **17**, 555–560.
- Johansson, M., Chen, J., Tsai, A., Kornberg, G., and Puglisi, J.D. (2014). Sequence-dependent elongation dynamics on macrolide-bound ribosomes. *Cell Rep.* **7**, 1534–1546.
- Koutmou, K.S., Schuller, A.P., Brunelle, J.L., Radhakrishnan, A., Djuranovic, S., and Green, R. (2015). Ribosomes slide on lysine-encoding homopolymeric A stretches. *eLife* **4**, 4.
- Lang, B.F., Jakubkova, M., Hegedusova, E., Daoud, R., Forget, L., Brejova, B., Vinar, T., Kosa, P., Fricova, D., Nebohacova, M., et al. (2014). Massive programmed translational jumping in mitochondria. *Proc. Natl. Acad. Sci. USA* **111**, 5926–5931.
- Lindsley, D., Bonhuis, P., Gallant, J., Tofoleanu, T., Elf, J., and Ehrenberg, M. (2005a). Ribosome bypassing at serine codons as a test of the model of selective transfer RNA charging. *EMBO Rep.* **6**, 147–150.
- Lindsley, D., Gallant, J., Doneanu, C., Bonhuis, P., Caldwell, S., and Fontelera, A. (2005b). Spontaneous ribosome bypassing in growing cells. *J. Mol. Biol.* **349**, 261–272.
- Liu, C.Y., Qureshi, M.T., and Lee, T.H. (2011). Interaction strengths between the ribosome and tRNA at various steps of translocation. *Biophys. J.* **100**, 2201–2208.
- Maldonado, R., and Herr, A.J. (1998). Efficiency of T4 gene 60 translational bypassing. *J. Bacteriol.* **180**, 1822–1830.
- Márquez, V., Wilson, D.N., Tate, W.P., Triana-Alonso, F., and Nierhaus, K.H. (2004). Maintaining the ribosomal reading frame: the influence of the E site during translational regulation of release factor 2. *Cell* **118**, 45–55.
- Marshall, R.A., Dorywalska, M., and Puglisi, J.D. (2008). Irreversible chemical steps control intersubunit dynamics during translation. *Proc. Natl. Acad. Sci. USA* **105**, 15364–15369.
- Nakatogawa, H., and Ito, K. (2002). The ribosomal exit tunnel functions as a discriminating gate. *Cell* **108**, 629–636.
- Nilsson, O.B., Hedman, R., Marino, J., Wickles, S., Bischoff, L., Johansson, M., Müller-Lucks, A., Trovato, F., Puglisi, J.D., O'Brien, E.P., et al. (2015). Cotranslational protein folding inside the ribosome exit tunnel. *Cell Rep.* **12**, 1533–1540.
- Nosek, J., Tomaska, L., Burger, G., and Lang, B.F. (2015). Programmed translational bypassing elements in mitochondria: structure, mobility, and evolutionary origin. *Trends Genet.* **31**, 187–194.
- Qin, P., Yu, D., Zuo, X., and Cornish, P.V. (2014). Structured mRNA induces the ribosome into a hyper-rotated state. *EMBO Rep.* **15**, 185–190.
- Qu, X., Wen, J.D., Lancaster, L., Noller, H.F., Bustamante, C., and Tinoco, I., Jr. (2011). The ribosome uses two active mechanisms to unwind messenger RNA during translation. *Nature* **475**, 118–121.
- Samatova, E., Konevega, A.L., Wills, N.M., Atkins, J.F., and Rodnina, M.V. (2014). High-efficiency translational bypassing of non-coding nucleotides specified by mRNA structure and nascent peptide. *Nat. Commun.* **5**, 4459.
- Tinoco, I., Jr., Kim, H.K., and Yan, S. (2013). Frameshifting dynamics. *Biopolymers* **99**, 1147–1166.
- Todd, G.C., and Walter, N.G. (2013). Secondary structure of bacteriophage T4 gene 60 mRNA: implications for translational bypassing. *RNA* **19**, 685–700.
- Tourigny, D.S., Fernández, I.S., Kelley, A.C., and Ramakrishnan, V. (2013). Elongation factor G bound to the ribosome in an intermediate state of translocation. *Science* **340**, 1235490.
- Tsai, A., Kornberg, G., Johansson, M., Chen, J., and Puglisi, J.D. (2014). The dynamics of SecM-induced translational stalling. *Cell Rep.* **7**, 1521–1533.
- Valle, M., Zavialov, A., Sengupta, J., Rawat, U., Ehrenberg, M., and Frank, J. (2003). Locking and unlocking of ribosomal motions. *Cell* **114**, 123–134.
- Weiss, R.B., Huang, W.M., and Dunn, D.M. (1990). A nascent peptide is required for ribosomal bypass of the coding gap in bacteriophage T4 gene 60. *Cell* **62**, 117–126.
- Wills, N.M. (2010). Translational bypassing - peptidyl-tRNA re-pairing at non-overlapping sites. In *Recoding: Expansion of Decoding Rules Enriches Gene Expression*, J.F. Atkins and R.F. Gesteland, eds. (Springer), pp. 365–381.
- Wills, N.M., O'Connor, M., Nelson, C.C., Rettberg, C.C., Huang, W.M., Gesteland, R.F., and Atkins, J.F. (2008). Translational bypassing without peptidyl-tRNA anticodon scanning of coding gap mRNA. *EMBO J.* **27**, 2533–2544.
- Yan, S., Wen, J.D., Bustamante, C., and Tinoco, I., Jr. (2015). Ribosome excursions during mRNA translocation mediate broad branching of frameshift pathways. *Cell* **160**, 870–881.
- Yusupova, G.Z., Yusupov, M.M., Cate, J.H., and Noller, H.F. (2001). The path of messenger RNA through the ribosome. *Cell* **106**, 233–241.

H3K4me3 Breadth Is Linked to Cell Identity and Transcriptional Consistency

Bérénice A. Benayoun, Elizabeth A. Pollina, Duygu Ucar, Salah Mahmoudi, Kalpana Karra, Edith D. Wong, Keerthana Devarajan, Aaron C. Daugherty, Anshul B. Kundaje, Elena Mancini, Benjamin C. Hitz, Rakhi Gupta, Thomas A. Rando, Julie C. Baker, Michael P. Snyder, J. Michael Cherry, and Anne Brunet*

*Correspondence: anne.brunet@stanford.edu

<http://dx.doi.org/10.1016/j.cell.2015.10.051>

(Cell 158, 673–688, July 31, 2014)

Our paper reported that broad H3K4me3 domains in a given cell type are associated with genes that are important for the identity/function of that cell type and that they are associated with increased transcriptional consistency, but not increased expression.

It has come to our attention that we made a programming error in the code used to generate Figure S1J. When the code is corrected, the top 5% broadest H3K4me3 domains display a statistically significant increased expression compared to the rest of the distribution (see corrected Figure S1J below). In addition, if one uses the rank-based Spearman correlation instead of the Pearson correlation we had used, H3K4me3 breadth exhibits a positive correlation with gene expression. Thus, the correct conclusion is that broad H3K4me3 domains are, on average, more expressed than non-broad H3K4me3 domains. This error does not affect our conclusions that H3K4me3 breadth is associated with cell identity and transcriptional consistency. However, we acknowledge that the increased transcriptional consistency of genes marked by broad H3K4me3 domains could be due to their increased average expression, as normalized transcriptional variability and average expression have been observed to be anti-correlated.

The corrected Figure S1J is shown below. The text changes are as follows, with additions in bold and deletions in bracketed italics:

Summary:

“Indeed, genes marked by the broadest H3K4me3 domains exhibit enhanced transcriptional consistency **and** [rather than] increased transcriptional levels.”

Page 674, second paragraph of Results:

“H3K4me3 breadth **quantiles** did not **linearly** correlate with mRNA levels (Figures 1D and 1E, **Pearson correlation**). However, **H3K4me3 breadth showed positive rank correlation with mRNA levels ($R \sim 0.19\text{--}0.31$, Spearman correlation)**. In addition, **the top 5% broadest H3K4me3 domains were more highly expressed on average compared to the rest of the distribution (Figure S1J)** [even when comparing the most extreme example to the rest of the distribution (Figure S1J)]. Thus, broad H3K4me3 domains are present in many cell types across taxa but cannot be explained as simple readouts of promoter complexity [or **high expression levels**].”

Figure 1 title:

“Breadth Is an Evolutionarily Conserved Feature [that Is Not Predictive of Expression Levels]”

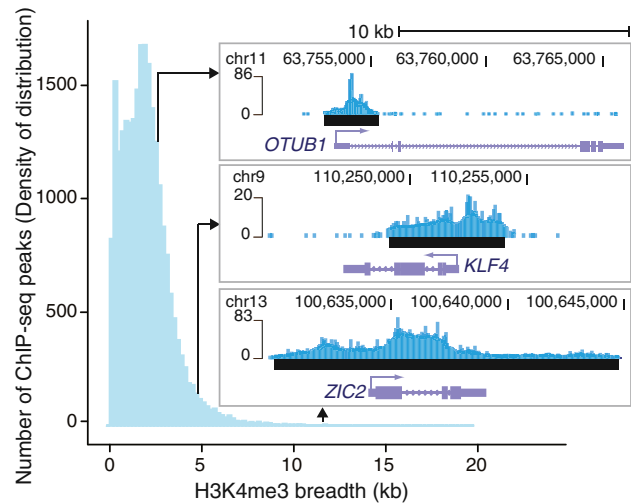
After we identified this programming error, we had the entire manuscript and lines of code independently scrutinized. This process identified the following inadvertent errors that do not affect our conclusions but that we would like to correct.

In Figures 1E and S6A, there was an incorrect attribution of datasets (C2C12 myotubes for myoblasts and H1 hESC population for single cells). The corrected Figures 1E and S6A are shown below. The conclusions are not changed.

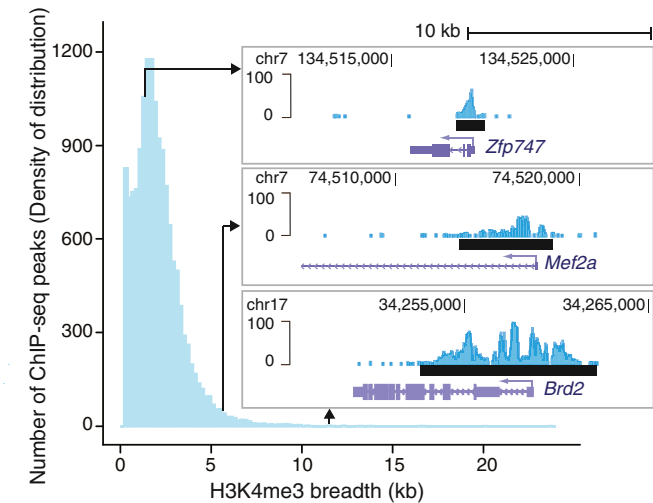
In Figures 7D, 7E, 7G, and S7L, the statistical analyses were done using two different tests (one-sided one-sample and one-sided two-sample Wilcoxon tests), but only one set of p values was reported in the original panels, and the corresponding statistical tests were not appropriately described. Results from both tests are shown in updated Figures 7D, 7E, 7G, and S7L. Upper p values (7D, 7G), black lines (7E, S7L): one-sided two-sample Wilcoxon tests for increased variability between genes with maintained versus changed H3K4me3 breadth. Lower p values (7D, 7G), gray lines (7E, S7L): one-sided one-sample Wilcoxon tests for increased variability between genes with changed H3K4me3 breadth versus the expectation of no change in variability. The overall conclusions are not changed.

We sincerely regret these errors and apologize for any inconvenience they may have caused. We would also like to thank Wei Li and Kaifu Chen from the Baylor College of Medicine for alerting us to the discrepancy between the Pearson and Spearman correlation results and for helping us to identify the error in Figure S1J.

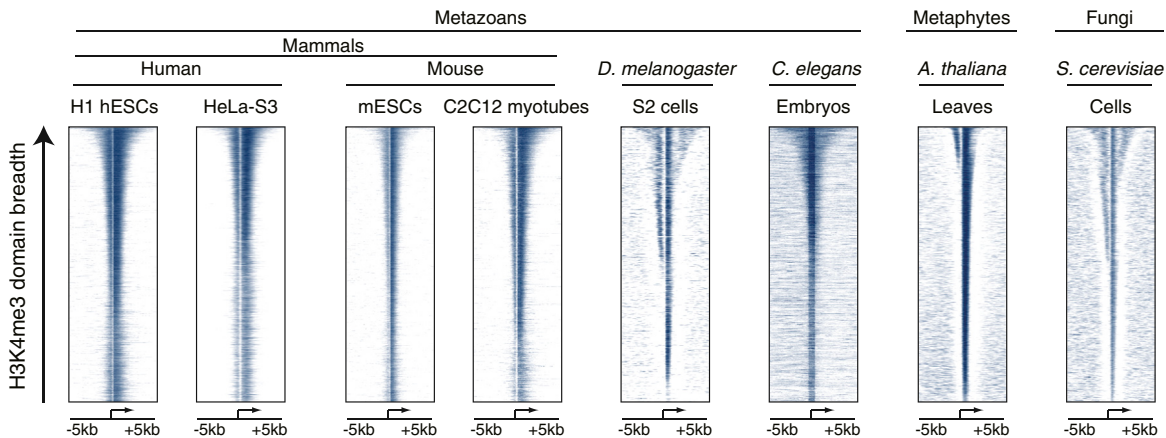
A Distribution of H3K4me3 ChIP-seq peaks in H1 hESCs



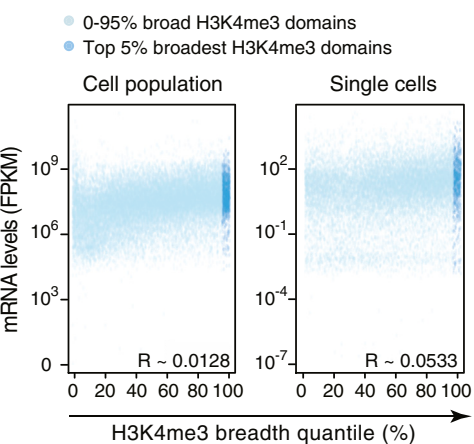
B Distribution of H3K4me3 ChIP-seq peaks in C2C12 myotubes



C H3K4me3 signal around transcription start sites



D H3K4me3 breadth and mRNA levels (H1 hESCs)



E H3K4me3 breadth and mRNA levels (C2C12 myoblasts)

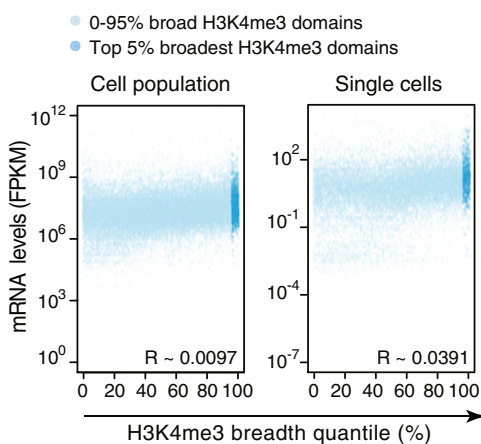


Figure 1. H3K4me3 Breadth Is an Evolutionarily Conserved Feature

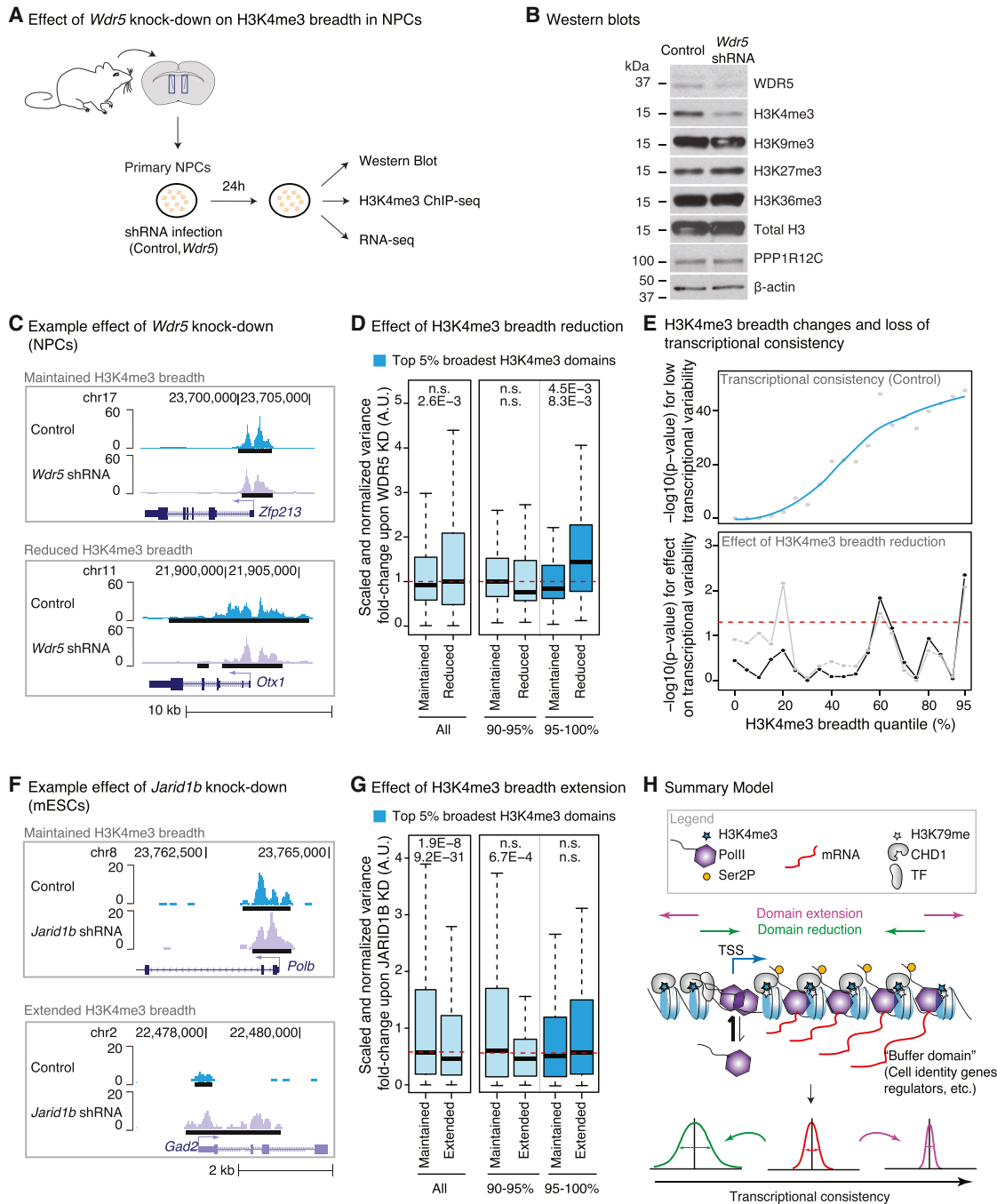


Figure 7. Experimental Perturbation of H3K4me3 Breadth Results in Changes to Transcriptional Consistency

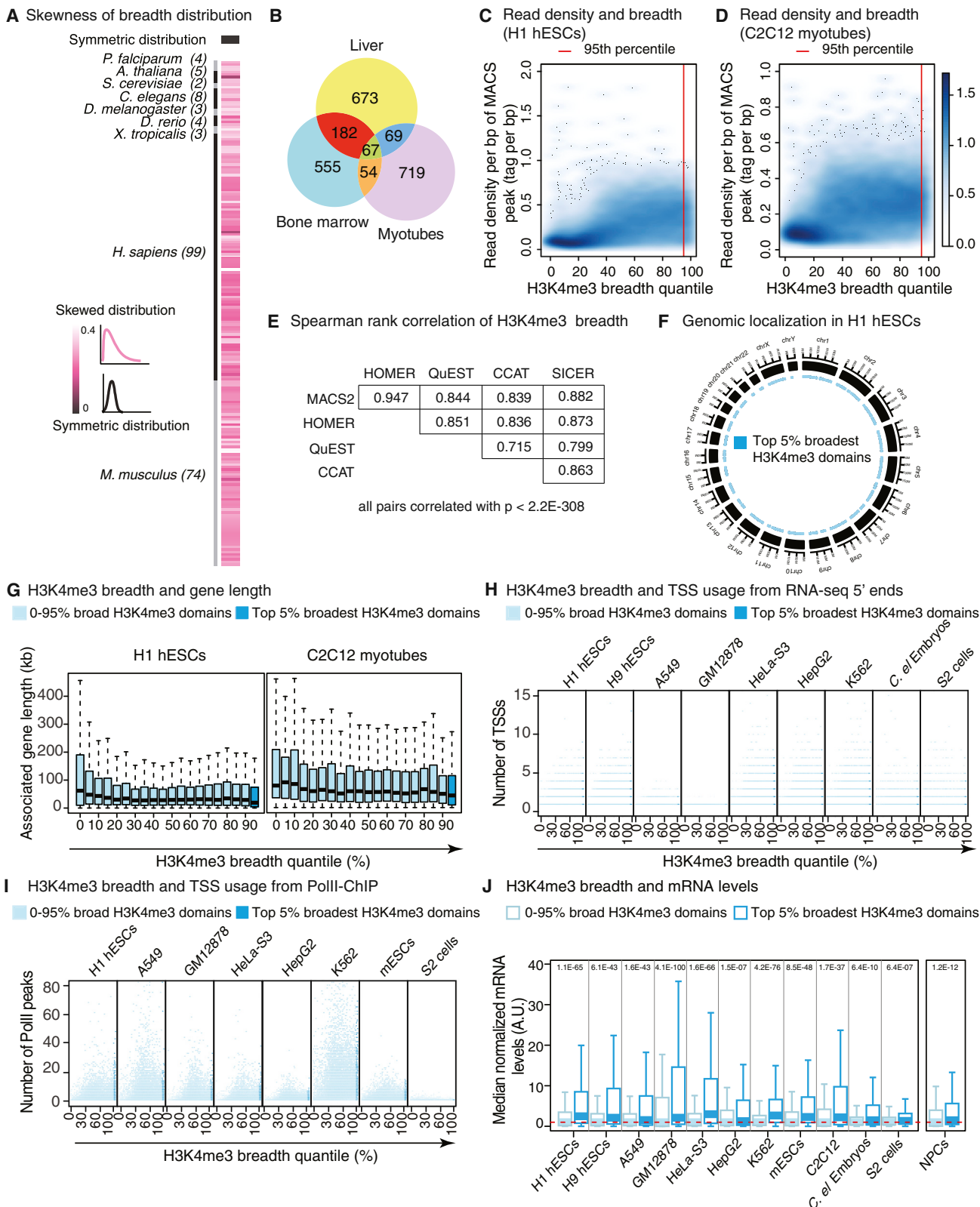


Figure S1. Broad H3K4me3 Stretches Are Present in Different Cell Types and Organisms but Are Independent of Signal Intensity, Promoter Architecture, Gene Length, and Genomic Location, Related to Figure 1

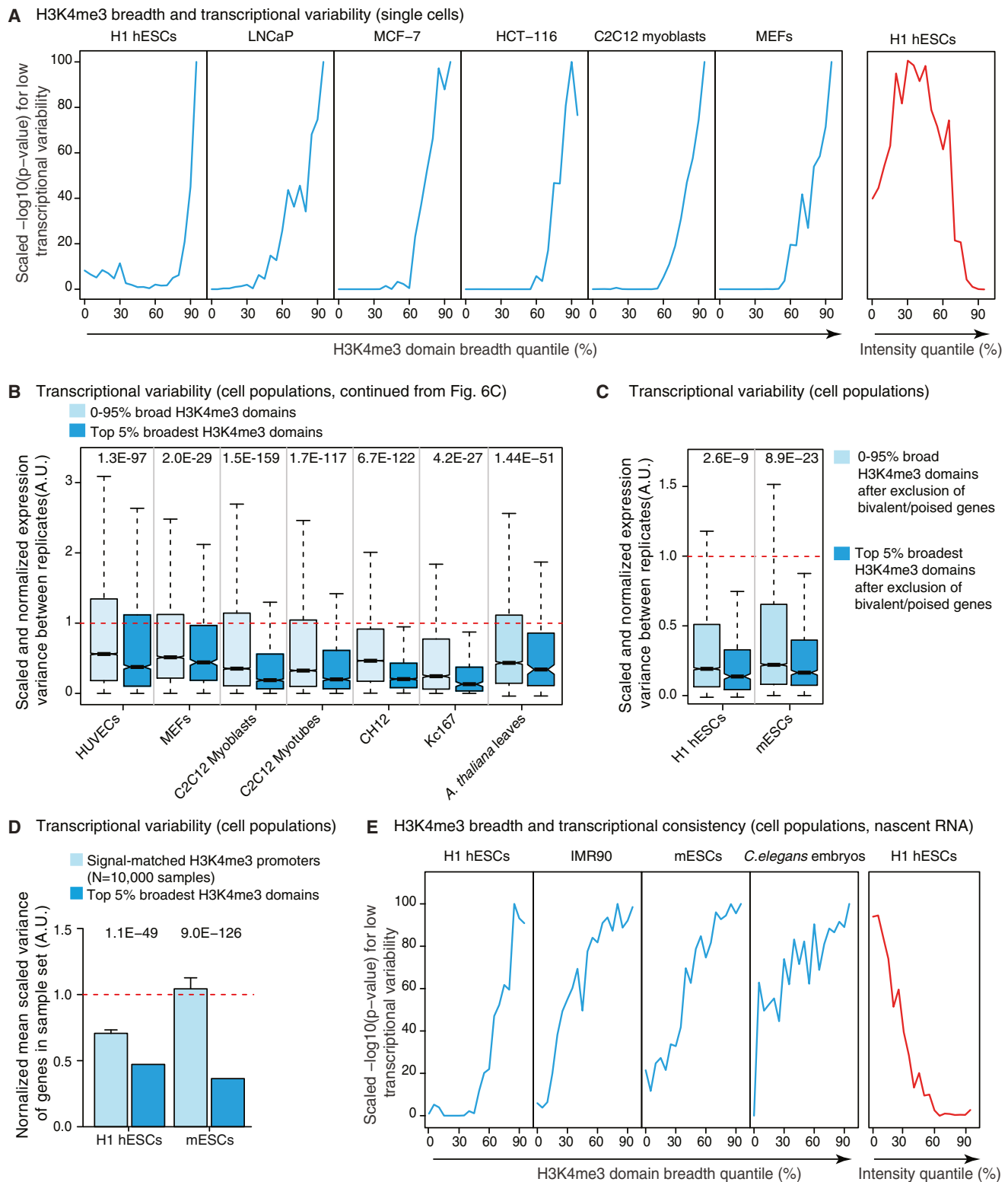


Figure S6. H3K4me3 Breadth Is Associated with Increased Transcriptional Consistency, Related to Figure 6

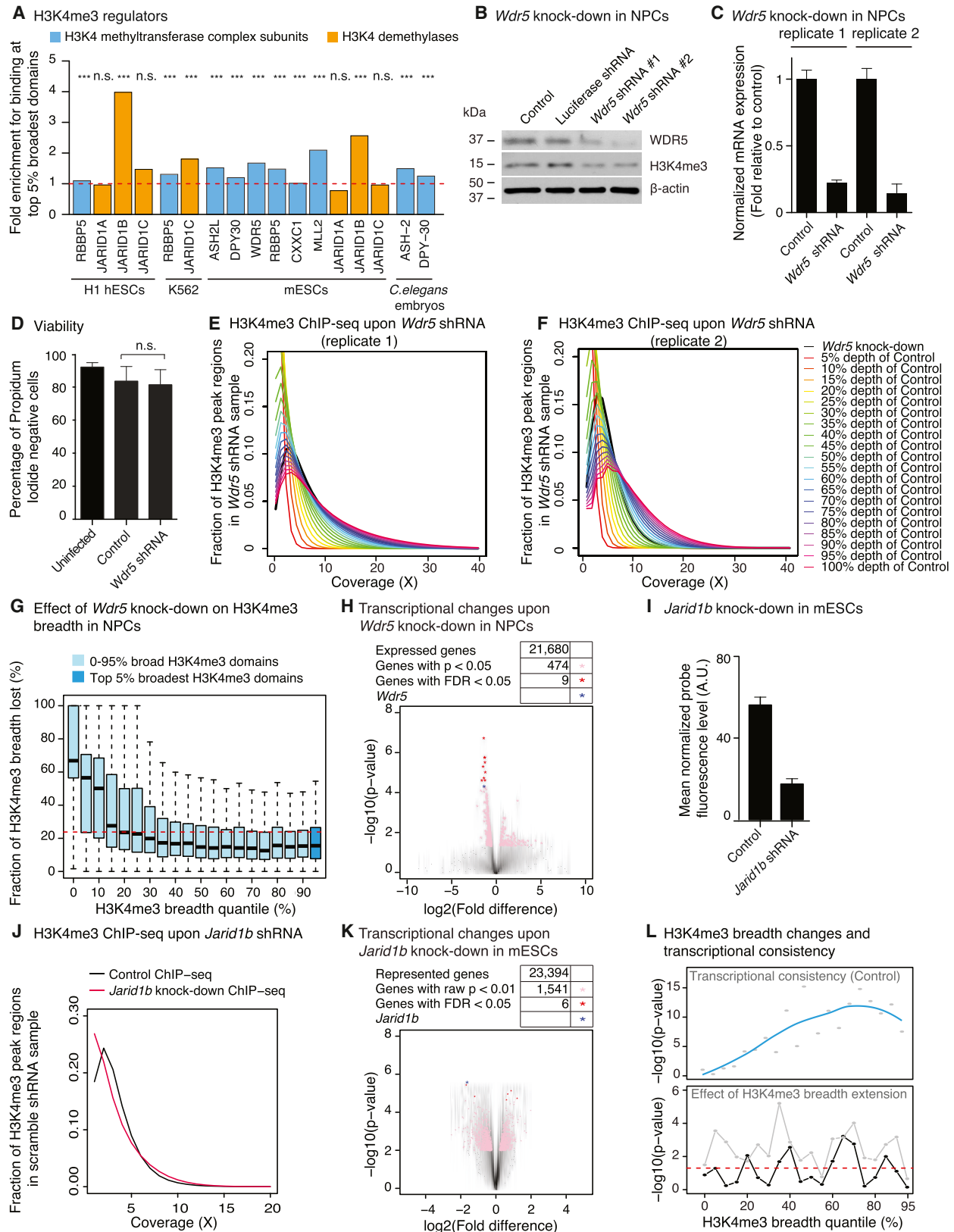
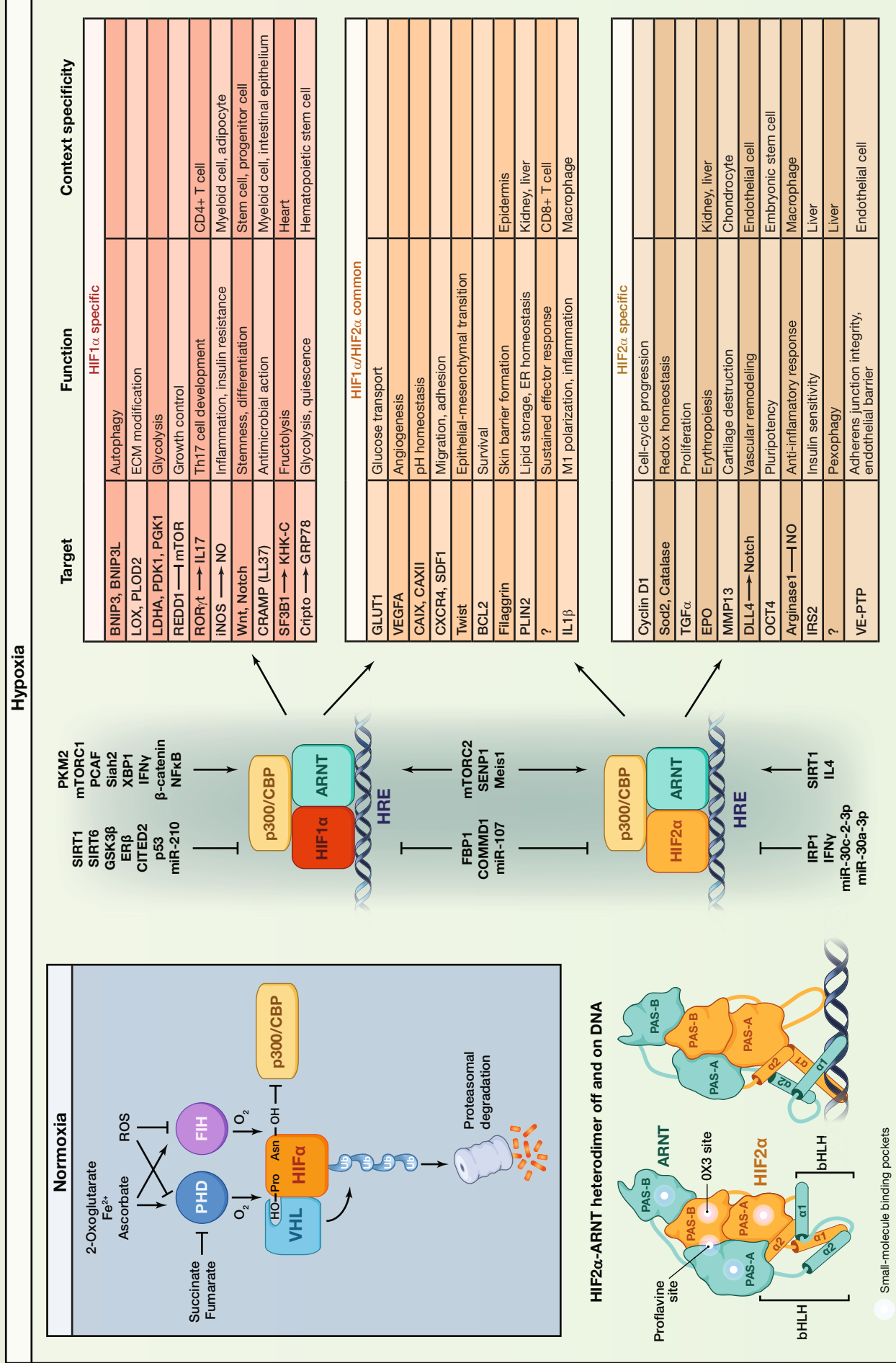


Figure S7. Effect of H3K4me3 Regulators on H3K4me3 Breadth and Transcriptional Consistency, Related to Figure 7

SnapShot: Hypoxia-Inducible Factors

Kyoung Eun Lee and M. Celeste Simon
Abramson Family Cancer Research Institute, Perelman School of Medicine at the University of Pennsylvania, Philadelphia, PA 19104, USA



SnapShot: Hypoxia-Inducible Factors

Kyoung Eun Lee and M. Celeste Simon

Abramson Family Cancer Research Institute, Perelman School of Medicine at the University of Pennsylvania,
Philadelphia, PA 19104, USA

Cell

Molecular oxygen (O_2) is a critical substrate for numerous biochemical reactions (e.g., the introduction of carbon double bonds into fatty acids), mitochondrial energy production, and the growing number of α -ketoglutarate (2-oxoglutarate)-dependent oxygenases that maintain O_2 homeostasis, promote collagen maturation, and impact the methylation status of both DNA and histones. Oxygen availability also regulates flux through important nutrient- and energy-sensing pathways, including mTOR, AMPK, and autophagy, as well as the unfolded protein response (UPR), which combats proteotoxicity. In many ways, the ongoing study of cellular, tissue, and organismal adaptations to O_2 limitation, or “hypoxia,” in physiology and disease has numerous open-ended questions: How many of the O_2/α -ketoglutarate-consuming oxygenases exhibit enzymatic activity frequently modulated by the dynamic range of O_2 concentrations typically found in healthy and/or diseased tissues? What is the scope of crosstalk between O_2 levels/metabolite pools and durable changes in the epigenome? How is O_2 sensing integrated with other environmentally regulated processes, such as circadian rhythms, neuronal activity, and zeno-biotic metabolism? How do mTORC1 or the UPR “sense” acute decreases in O_2 levels? How is the protein synthesis machinery affected by O_2 availability? What is the scope of metabolite (lactate, 2-hydroxyglutarate) influences on HIF-independent hypoxic responses (Lee et al., 2015)?

These and other fundamental questions will undoubtedly continue to fascinate researchers in the hypoxia field for years to come. Nevertheless, a number of recent papers have revealed unexpected inputs and functions for one of the best-characterized O_2 -sensing systems at this time—namely, the pVHL/PHD/HIF pathway. This pathway regulates a large transcriptome promoting hypoxic adaptations by enhancing the expression of hundreds of genes involved in metabolism, proliferation, differentiation, inflammation, angiogenesis, cell motility, and “stemness.” This SnapShot highlights several exciting new concepts, such as regulatory physical interactions between HIF1 α /HIF2 α and metabolic enzymes like PKM2 and FBP1 (Li et al., 2014; Luo et al., 2011), HIF input into T cell function (e.g., Th17 development) (Dang et al., 2011), HIF activation by commensal bacteria in GI antifungal responses (Fan et al., 2015), and hypoxic influences on adherens junction integrity. While HIF crosstalk with metabolic pathways has been appreciated for some time (glycolysis, mitochondrial O_2 consumption, glutamine metabolism, etc.) (Lee et al., 2014), new interfaces are continually being discovered, such as “pexophagy” (selective peroxisome degradation to maintain lipid homeostasis) and fructolysis, where HIF regulates ketohexokinase alternative splicing (Mirtschink et al., 2015; Walter et al., 2014).

Recent major advances based on comprehensive ChIPSeq and chromatin capture assays in multiple cell types have also contributed to our understanding of genome-wide HIF associations with DNA and target gene selectivity. In addition, new structural insights provided by Fraydoon Rastinejad and colleagues (Wu et al., 2015) also further clarify conformational changes in HIF dimers on and off DNA and contrast them with other bHLH-PAS factors, i.e., CLOCK/bMAL. This report defines binding “pockets” for previously identified small-molecule inhibitors of HIF1 α and HIF2 α at the angstrom level and raises again the possibility that HIF α s bind endogenous ligands, as ultimately revealed for the AhR bHLH-PAS family member. The notion that HIF directly and indirectly controls metabolite accumulation that could, in turn, provide allosteric regulation by post-translational modifications or covalent binding presents an exciting new line of investigation for the scientific community.

Although the pVHL/PHD/HIF axis represents the O_2 sensor studied in perhaps the greatest detail (Keith et al., 2012), much remains to be discovered. Coupled with ongoing efforts to characterize other pathways regulated by the 70+ O_2/α -ketoglutarate-consuming oxygenases, intermediate metabolism, and ion channels, the community studying the fundamental mechanisms governing adaptations to fluctuating O_2 levels during development, physiology, and disease will certainly be engaged for years to come.

ABBREVIATIONS

ARNT, aryl hydrocarbon receptor nuclear translocator; bHLH, basic helix-loop-helix; CBP, cyclic AMP response element-binding protein; FIH, factor-inhibiting hif1 α ; HIF, hypoxia-inducible factor; HRE, hypoxia response element; PAS, Per-Arnt-Sim; PHD, prolyl hydroxylase domain; Ub, ubiquitin; VHL, Von Hippel-Lindau tumor suppressor.

ACKNOWLEDGMENTS

The lower-left panel has been modified with permission from Marmorstein, R., and Simon, M.C. (2015). *Nature* 524, 298–300.

REFERENCES

- Dang, E.V., Barbi, J., Yang, H.Y., Jinnesena, D., Yu, H., Zheng, Y., Bordman, Z., Fu, J., Kim, Y., Yen, H.R., et al. (2011). *Cell* 146, 772–784.
- Fan, D., Coughlin, L.A., Neubauer, M.M., Kim, J., Kim, M.S., Zhan, X., Simms-Waldrip, T.R., Xie, Y., Hooper, L.V., and Koh, A.Y. (2015). *Nat. Med.* 21, 808–814.
- Keith, B., Johnson, R.S., and Simon, M.C. (2012). *Nat. Rev. Cancer* 12, 9–22.
- Lee, Y.S., Kim, J.W., Osborne, O., Oh, Y., Sasik, R., Schenk, S., Chen, A., Chung, H., Murphy, A., Watkins, S.M., et al. (2014). *Cell* 157, 1339–1352.
- Lee, D.C., Sohn, H.A., Park, Z.Y., Oh, S., Kang, Y.K., Lee, K.M., Kang, M., Jang, Y.J., Yang, S.J., Hong, Y.K., et al. (2015). *Cell* 161, 595–609.
- Li, B., Qiu, B., Lee, D.S., Walton, Z.E., Ochocki, J.D., Mathew, L.K., Mancuso, A., Gade, T.P., Keith, B., Nissim, I., and Simon, M.C. (2014). *Nature* 513, 251–255.
- Luo, W., Hu, H., Chang, R., Zhong, J., Knabel, M., O'Meally, R., Cole, R.N., Pandey, A., and Semenza, G.L. (2011). *Cell* 145, 732–744.
- Mirtschink, P., Krishnan, J., Grimm, F., Sarre, A., Hörl, M., Kayikci, M., Fankhauser, N., Christinat, Y., Cortijo, C., Feehan, O., et al. (2015). *Nature* 522, 444–449.
- Walter, K.M., Schönenberger, M.J., Trötzmüller, M., Horn, M., Elsässer, H.P., Moser, A.B., Lucas, M.S., Schwarz, T., Gerber, P.A., Faust, P.L., et al. (2014). *Cell Metab.* 20, 882–897.
- Wu, D., Potluri, N., Lu, J., Kim, Y., and Rastinejad, F. (2015). *Nature* 524, 303–308.